THE DEVELOPMENT AND CLINICAL APPLICATION OF INNOVATIVE OPTICAL OPHTHALMIC IMAGING TECHNIQUES

EDITED BY: Peng Xiao, Claude Boccara, Kate Grieve and Yali Jia

PUBLISHED IN: Frontiers in Medicine

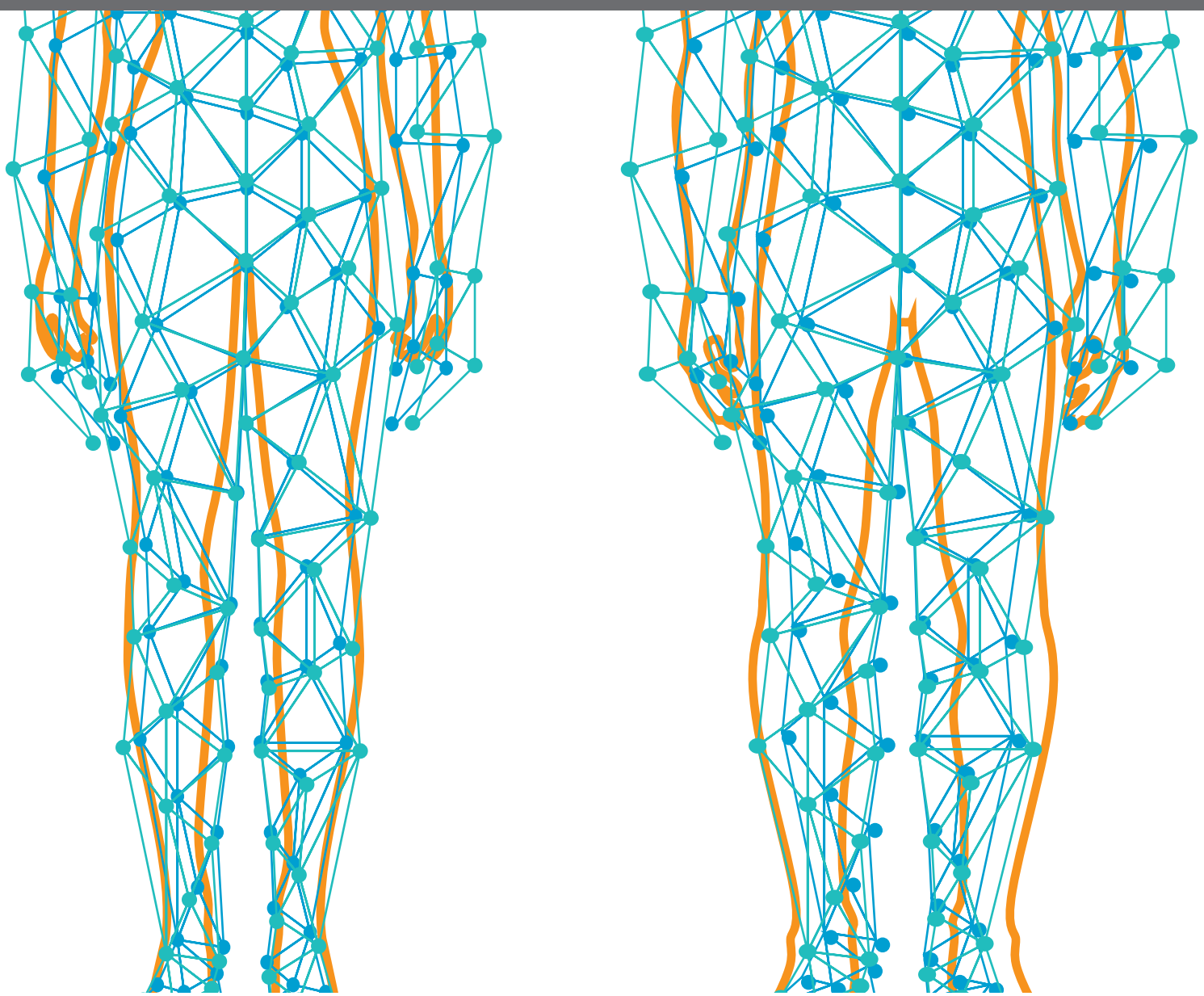

frontiers Research Topics

ISSN 1664-8714
ISBN 978-2-83250-892-3
DOI 10.3389/978-2-83250-892-3

About Frontiers

Frontiers is more than just an open-access publisher of scholarly articles: it is a pioneering approach to the world of academia, radically improving the way scholarly research is managed. The grand vision of Frontiers is a world where all people have an equal opportunity to seek, share and generate knowledge. Frontiers provides immediate and permanent online open access to all its publications, but this alone is not enough to realize our grand goals.

Frontiers Journal Series

The Frontiers Journal Series is a multi-tier and interdisciplinary set of open-access, online journals, promising a paradigm shift from the current review, selection and dissemination processes in academic publishing. All Frontiers journals are driven by researchers for researchers; therefore, they constitute a service to the scholarly community. At the same time, the Frontiers Journal Series operates on a revolutionary invention, the tiered publishing system, initially addressing specific communities of scholars, and gradually climbing up to broader public understanding, thus serving the interests of the lay society, too.

Dedication to Quality

Each Frontiers article is a landmark of the highest quality, thanks to genuinely collaborative interactions between authors and review editors, who include some of the world's best academicians. Research must be certified by peers before entering a stream of knowledge that may eventually reach the public - and shape society; therefore, Frontiers only applies the most rigorous and unbiased reviews.
Frontiers revolutionizes research publishing by freely delivering the most outstanding research, evaluated with no bias from both the academic and social point of view. By applying the most advanced information technologies, Frontiers is catapulting scholarly publishing into a new generation.

What are Frontiers Research Topics?

Frontiers Research Topics are very popular trademarks of the Frontiers Journals Series: they are collections of at least ten articles, all centered on a particular subject. With their unique mix of varied contributions from Original Research to Review Articles, Frontiers Research Topics unify the most influential researchers, the latest key findings and historical advances in a hot research area! Find out more on how to host your own Frontiers Research Topic or contribute to one as an author by contacting the Frontiers Editorial Office: frontiersin.org/about/contact

THE DEVELOPMENT AND CLINICAL APPLICATION OF INNOVATIVE OPTICAL OPHTHALMIC IMAGING TECHNIQUES

Topic Editors:
Peng Xiao, Sun Yat-sen University, China
Claude Boccara, École Supérieure de Physique et de Chimie Industrielles de la Ville de Paris, France
Kate Grieve, Institut National de la Santé et de la Recherche Médicale (INSERM), France
Yali Jia, Oregon Health and Science University, United States

Citation: Xiao, P., Boccara, C., Grieve, K., Jia, Y., eds. (2022). The Development and Clinical Application of Innovative Optical Ophthalmic Imaging Techniques. Lausanne: Frontiers Media SA. doi: 10.3389/978-2-83250-892-3

Table of Contents

frontiers | Frontiers in Medicine

TYPE Editorial
PUBLISHED 15 November 2022
DOI 10.3389/fmed.2022.1058069

OPEN ACCESS

EDITED AND REVIEWED BY
Jodhbir Mehta,
Singapore National Eye Center, Singapore

*CORRESPONDENCE
Peng Xiao
xiaopengaddis@hotmail.com

SPECIALTY SECTION
This article was submitted to Ophthalmology, a section of the journal Frontiers in Medicine

RECEIVED 30 September 2022
ACCEPTED 07 November 2022
PUBLISHED 15 November 2022

CITATION
Zhang J, Boccara C, Grieve K, Jia Y and Xiao P (2022) Editorial: The development and clinical application of innovative optical ophthalmic imaging techniques.
Front. Med. 9:1058069.
doi: 10.3389/fmed.2022.1058069

Editorial: The development and clinical application of innovative optical ophthalmic imaging techniques

Jinze Zhang[1], Claude Boccara[2], Kate Grieve[3], Yali Jia[4] and Peng Xiao[1]*

[1]State Key Laboratory of Ophthalmology, Zhongshan Ophthalmic Center, Sun Yat-sen University, Guangzhou, China, [2]Institut Langevin, ESPCI Paris, CNRS, PSL University, Paris, France, [3]Paris Eye Imaging Group, Vision Institute, Quinze Vingts National Ophthalmology Hospital, INSERM, CNRS, Paris, France, [4]Casey Eye Institute, Oregon Health and Science University, Portland, OR, United States

KEYWORDS

ophthalmic imaging, ophthalmic image analysis, artificial intelligence, optical imaging, ophthalmic optical coherence tomography (OCT) equipment

Editorial on the Research Topic
The development and clinical application of innovative optical ophthalmic imaging techniques

According to the report of the World Health Organization, ophthalmic diseases are the third major group of diseases that severely affect people's quality of life (1). As the most important sensory organization, the eye plays an irreplaceable role in obtaining external information and performing effective communication with its sophisticated optical refractive system and microvascular system. Precise structural and functional evaluation and analysis of the eye based on optical imaging modalities is important for the early and accurate diagnosis and therapeutic evaluation of ophthalmic diseases. At the same time, as the only tissue in the body where blood vessels can be directly observed *in vivo*, many systemic diseases can also be detected or diagnosed through ocular imaging. With the breakthrough of cutting-edge optical imaging and artificial intelligence technologies, high-resolution, multi-dimensional, and intelligent have become the key development trends of ophthalmic imaging methods, with their core technical features of functional imaging, multimodal information fusion, and artificial intelligence (AI) assisted analysis (2).

In fact, translational research in novel optical imaging modalities, such as optical coherence tomography (OCT) and confocal microscopy (3, 4), has greatly advanced the precise management of ocular and related diseases by facilitating ophthalmic imaging with more comprehensive physiological and pathological information due to their high-resolution or 3-dimensional (3D) imaging properties. In the meantime, new-generation optical imaging systems with specific technical features continue to emerge: non-contact full-field OCT provides cellular-resolution images of both anterior and posterior eye (5, 6); combining traditional optical imaging systems with adaptive optics (AO) enhances the resolution by removing the limits imposed by intrinsic eye aberrations (7); OCT angiography based on OCT or Doppler imaging techniques offer the possibility of assessing vascular structural network

and blood flow function (8–10); AI-assisted systems enable objective image assessment and automated disease diagnosis and large-scale screening (11, 12). Only with the development of these innovative ophthalmic imaging instruments and techniques, can we continue to advance our understanding, diagnosis, and treatment of ocular diseases.

In this Research Topic, 13 original research articles report their development or clinical verification of new ophthalmic imaging equipment or image analysis algorithms. Nine studies involved the evaluation and application of new optical ophthalmic imaging devices. Wang et al. developed and applied a visible light optical coherence tomography device to healthy eyes and determined the microvascular oxygen saturation baseline in the paracentral macular sulcus. Chen H. et al. compared the segmentation error rate of anterior chamber volume and iris volume measured automatically using anterior segment OCT in both narrow-angle and wide-angle eyes. Using fluorescence adaptive optics scanning laser ophthalmoscopy (SLO), Vienola et al. demonstrated for the first time the cellular level structural changes of the retinal pigment epithelial cell mosaic in Torpedo Maculopathy. Lu et al. evaluated the central and peripheral refraction measurement reproducibility of multispectral optometry and assessed their agreement in myopic patients with subjective refraction measurement. Chen L. et al. evaluated the performance of magnetic resonance imaging based radiomics in the differential diagnosis of orbital cavernous hemangioma and orbital nerve sheath tumor. Xin et al. found a decrease in lens thickness, outer retinal layer thickness and cone photoreceptor density in myopia subjects using swept-source OCT and AO assisted fundus photography. Fan et al. evaluated the effectiveness of a new-generation portable 3D imaging device to assess the anthropometry periocular region. Combining both SLO and OCT, Paques et al. documented the temporal changes over months of the cell-scale dynamics in lesion borders during the progression of geographic atrophy. The study by Cai et al. thoroughly characterized and quantified the human retinal axial motion using 200 kHz spectral-domain OCT (SD-OCT) with high axial resolution. Four studies proposed novel image analysis methods for ophthalmic evaluation. Xu L. et al. showed a decrease in stereopsis with magnification increase in aniseikonia using a phoropter and two 4K smartphones incorporated with contour-based and random point-based stereograms. Xu J. et al. developed a new retinal blood vessel segmentation algorithm for limited image data and gold-standard annotations based on so-called few-shot learning to assist laser surgery for central serous chorioretinopathy. To resolve the chromatic dispersion problem in OCT imaging, which was typically addressed with hardware methods, Ahmed et al. developed an numerical method with deep learning network for robust automatic dispersion compensation in OCT. Pfäffle et al. demonstrated that conducting appropriate signal post-processing in full-field swept-source OCT can provide good phase stability and spatial resolution for retinal neuronal signal processing analysis, opening up the possibility of using phase-sensitive FF-SS-OCT for functional evaluation of different retinal cell types *in vivo*.

Besides, four reviews or meta-analysis articles discuss the development and application of new ophthalmic imaging techniques. Tan et al. conducted a meta-analysis on the application of optical coherence tomography angiography in systemic hypertension. Kim et al. summarize recent advances of functional OCT for intrinsic optical signal (IOS) imaging and computational IOS processing based on OCT intensity or phase analysis. Jiang and Qi evaluated the diagnostic sensitivity and specificity of SD-OCT for polypoidal choroidal vasculopathy by conducting a meta-analysis study. Alexopoulos et al. thoroughly summarized the recent advances in various optical ophthalmic imaging techniques, discussed their potential contributions for daily clinical settings, and also evaluated the important contribution of artificial intelligence in the field of ophthalmic imaging.

In summary, this Research Topic focuses on the development of a new generation of ophthalmic optical imaging equipment and intelligent quantitative image analysis techniques; their clinical application for more accurate and effective imaging diagnosis and pathogenesis of ophthalmic related diseases; and finally provides insights into the latest translational optical ophthalmic imaging research and its applications in resolving clinical needs.

Author contributions

All authors listed have made a substantial, direct, and intellectual contribution to the work and approved it for publication.

Funding

This work is supported by the National Natural Science Foundation of China (No. 81901788), Guangdong Basic and Applied Basic Research Foundation (No. 2022A1515011486), and Guangzhou Science and Technology Program (No. 202002030412).

Acknowledgments

We appreciate all the significant works and thank the contributors to this Research Topic.

Conflict of interest

The authors declare that the research was conducted in the absence of any commercial or financial relationships that could be construed as a potential conflict of interest.

Publisher's note

References

1. World Health Organization. "*World Report on Vision*." (2019).

2. Ting DS, Pasquale LR, Peng L, Campbell JP, Lee AY, Raman R, et al. Artificial intelligence and deep learning in ophthalmology. *Br. J. Ophthalmology.* (2019) 103:167–75. doi: 10.1136/bjophthalmol-2018-313173

3. Reilly WM, Obara CJ. Advances in confocal microscopy and selected applications. *Methods Mol Biol.* (2021) 2304:1–35. doi: 10.1007/978-1-0716-1402-0_1

4. Huang D, Swanson EA, Lin CP, Schuman JS, Stinson WG, Chang W, et al. Optical coherence tomography. *Science.* (1991) 254:1178–81. doi: 10.1126/science.1957169

5. Xiao P, Mazlin V, Grieve K, Sahel J-A, Fink M, Boccara AC. In vivo high-resolution human retinal imaging with wavefront-correctionless full-field OCT. *Optica.* (2018) 5:409. doi: 10.1364/OPTICA.5.000409

6. Mazlin V, Irsch K, Paques M, Sahel J-A, Fink M, Boccara CA. Curved-field optical coherence tomography: large-field imaging of human corneal cells and nerves. *Optica.* (2020) 7:872. doi: 10.1364/OPTICA.396949

7. Jonnal RS, Kocaoglu OP, Zawadzki RJ, Liu Z, Miller DT, Werner JS. A review of adaptive optics optical coherence tomography: technical advances, scientific applications, and the future. *Investig. Ophthalmol. Vis. Sci.* (2016) 57, OCT51–68 doi: 10.1167/iovs.16-19103

8. Spaide RF, Fujimoto JG, Waheed NK, Sadda SR, Staurenghi G. Optical coherence tomography angiography. *Prog Retin Eye Res.* (2018) 64:1–55. doi: 10.1016/j.preteyeres.2017.11.003

9. Gao SS, Jia Y, Zhang M, Su JP, Liu G, Hwang TS, Bailey ST, Huang D. Optical coherence tomography angiography. *Investig. Ophthalmol. Vis. Sci.* (2016) 57, OCT27–36. doi: 10.1167/iovs.15-19043

10. Puyo L, Paques M, Fink M, Sahel JA, Atlan M. In vivo laser doppler holography of the human retina. *Biomed Opt Express.* (2018) 9:4113–29. doi: 10.1364/BOE.9.004113

11. Ting DSW, Peng L, Varadarajan AV, Keane PA, Burlina PM, Chiang MF, et al. Deep learning in ophthalmology: The technical and clinical considerations. *Prog Retin Eye Res.* (2019) 72:100759. doi: 10.1016/j.preteyeres.2019.04.003

12. Deng Y, Wang Q, Luo Z, Li S, Wang B, Zhong J, et al. Quantitative analysis of morphological and functional features in meibography for meibomian gland dysfunction: diagnosis and grading. *EClinical Med.* (2021) 40:101132. doi: 10.1016/j.eclinm.2021.101132

frontiers in Medicine

SYSTEMATIC REVIEW
published: 08 November 2021
doi: 10.3389/fmed.2021.778330

The Application of Optical Coherence Tomography Angiography in Systemic Hypertension: A Meta-Analysis

Wilson Tan[1,2†], *Xinwen Yao*[1,3,4†], *Thu-Thao Le*[5,6], *Anna C. S. Tan*[1,6], *Carol Y. Cheung*[7], *Calvin Woon Loong Chin*[5,6], *Leopold Schmetterer*[1,3,4,6,8,9,10] *and Jacqueline Chua*[1,6*]

[1] Singapore Eye Research Institute, Singapore National Eye Centre, Singapore, Singapore, [2] Yong Loo Lin School of Medicine, National University of Singapore and National University Health System, Singapore, Singapore, [3] School of Chemical and Biomedical Engineering, Nanyang Technological University, Singapore, Singapore, [4] SERI-NTU Advanced Ocular Engineering (STANCE), Singapore, Singapore, [5] National Heart Centre Singapore, National Heart Research Institute Singapore, Singapore, Singapore, [6] Ophthalmology and Visual Sciences Academic Clinical Program, Duke-National University of Singapore Medical School, Singapore, Singapore, [7] Department of Ophthalmology and Visual Sciences, The Chinese University of Hong Kong, Shatin, Hong Kong SAR, China, [8] Department of Clinical Pharmacology, Medical University of Vienna, Vienna, Austria, [9] Center for Medical Physics and Biomedical Engineering, Medical University of Vienna, Vienna, Austria, [10] Institute of Molecular and Clinical Ophthalmology, Basel, Switzerland

Objective: Multiple studies have compared various optical coherence tomography angiography (OCTA) parameters in participants with systemic hypertension vs. controls and have presented discordant findings. We conducted a meta-analysis to pool together data from different studies to generate an overall effect size and find out whether OCTA parameter(s) significantly differed in participants with systemic hypertension as compared to controls.

Methods: We conducted a literature search through a search of electronic databases to identify studies before 19 June 2021, which compared OCTA parameters in non-diabetic participants with systemic hypertension vs. controls. If the OCTA parameter had a minimum number of 3 studies that analyzed it, the mean difference between participants with systemic hypertension and controls were analyzed using a random-effects model.

Results: We identified 11 eligible studies. At the macula, 9 studies analyzed vessel density at the superficial capillary plexus (SVD), 7 analyzed vessel density at the deep capillary plexus (DVD), and 6 analyzed the area of the superficial foveal avascular zone (FAZ). Participants with systemic hypertension had significantly lower SVD (standardized mean difference [SMD], −0.50 [−0.70, −0.30], P < 0.00001, $I^2 = 63\%$), lower DVD (SMD, −0.38 [−0.64, −0.13], $P = 0.004$, $I^2 = 67\%$) and larger superficial FAZ (SMD, 0.32 [0.04, 0.61], $P = 0.020$, $I^2 = 77\%$).

Conclusion: The eyes of people with systemic hypertension have robustly lower superficial and deep vascular densities at the macula when compared to control eyes. Our results suggest that OCTA can provide information about pre-clinical microvascular changes from systemic hypertension.

Keywords: hypertension, blood pressure, optical coherence tomography angiography, OCTA, biological marker, biomarker, retina

OPEN ACCESS

Edited by:
Kate Grieve,
Institut National de la Santé et de la Recherche Médicale (INSERM), France

Reviewed by:
Irini Chatziralli,
National and Kapodistrian University of Athens, Greece
Rana Saad,
National Hospital Center of Ophthalmology Quinze-Vingts, France

***Correspondence:**
Jacqueline Chua
jacqueline.chua.y.m@seri.com.sg

*These authors have contributed equally to this work and share first authorship

Specialty section:
This article was submitted to Ophthalmology, a section of the journal Frontiers in Medicine

Received: *16 September 2021*
Accepted: *20 October 2021*
Published: *08 November 2021*

Citation:
Tan W, Yao X, Le T-T, Tan ACS, Cheung CY, Chin CWL, Schmetterer L and Chua J (2021) The Application of Optical Coherence Tomography Angiography in Systemic Hypertension: A Meta-Analysis. Front. Med. 8:778330. doi: 10.3389/fmed.2021.778330

INTRODUCTION

Systemic hypertension remains the leading contributor to the global burden of disease and global all-cause mortality, leading to 9.4 million deaths and 212 million lost healthy life years (8.5% of the global total) each year (1). In 2015, an estimated 874 million adults had a systolic blood pressure of 140 mmHg or higher globally (2). Systemic hypertension, damages the body's microvasculature, and leads to increased risk of complications known as target end-organ damage (Chua J), which include cerebrovascular accidents, cardiovascular diseases, renal failure, and retinal vascular disease.

The retina is a highly vascularized tissue which is susceptible to microvascular damage due to hypertension and retinal imaging provides a unique opportunity to non-invasively assess these pathological changes. The current systems of grading hypertensive retinopathy, the Keith-Wagner-Barker or Wong-Mitchell classification systems, are based on a clinician's subjective assessment of retinal fundus photographs (3). Signs assessed from retinal fundus photographs (e.g., arteriolar narrowing, arteriovenous nicking, hemorrhages) are limited to the visible larger arterioles and venules in the more superficial layers of the retinal circulation and earlier microvascular changes which may be subclinical biomarkers of disease may be missed (**Figure 1**).

The advent of optical coherence tomography angiography (OCTA) has provided us with depth-resolved high-resolution images of both the superficial and deep retinal vascular layer and the choroid, without the administration of intravenous dye (4). OCTA technology has the ability to non-invasively assess and quantify the vessels of all layers of the retinal vasculature and choroid (5), in both disease and healthy states (**Figure 2**). Therefore, detecting pre-clinical changes in the retinal microvascular in response to hypertension, that correlates to disease states in other microvascular systems, may provide the potential opportunity to discover novel objective biomarkers of early microvascular changes. Detecting and monitoring pre-clinical microvascular changes before irreversible end-organ damage occurs may alter practice patterns with earlier and stricter interventions to control blood pressure, with the aim of preventing life-threatening hypertensive-related complications.

Recently, multiple studies have been conducted comparing various quantitative OCTA parameters (e.g., vessel density), in patients with systemic hypertension vs. healthy controls and have presented discordant findings. For example, a 2021 study by Donati et al. (6) found no significant reduction in superficial vessel density in patients with systemic hypertension when compared to healthy controls. However, a 2020 study by Sun et al. (7) found otherwise. We hypothesize that there are quantitative OCTA parameters which significantly differ in patients with systemic hypertension when compared with healthy controls and present a meta-analysis of studies investigating measurements by OCTA in patients with systemic hypertension.

METHODS

This meta-analysis is reported in accordance with the Meta-analysis Of Observational Studies in Epidemiology (MOOSE) group guidelines (8). Minor deviations are described below.

SEARCH STRATEGY AND STUDY SELECTION

We systematically searched PubMed, Embase, The Cochrane Library, Scopus, and Web of Science, for all human studies published until 19 June 2021 in all languages. The concepts identified for this review are (1) OCTA; (2) Hypertension. The keywords searched for the concept OCTA are (1) OCTA; (2) Optical Coherence Tomography Angiography (3) OCT Angiography. The keywords searched for the concept Hypertension are (1) Hypertension; (2) cardiovascular disease; (3) CVD; (4) high blood pressure; (5) high mean arterial pressure;

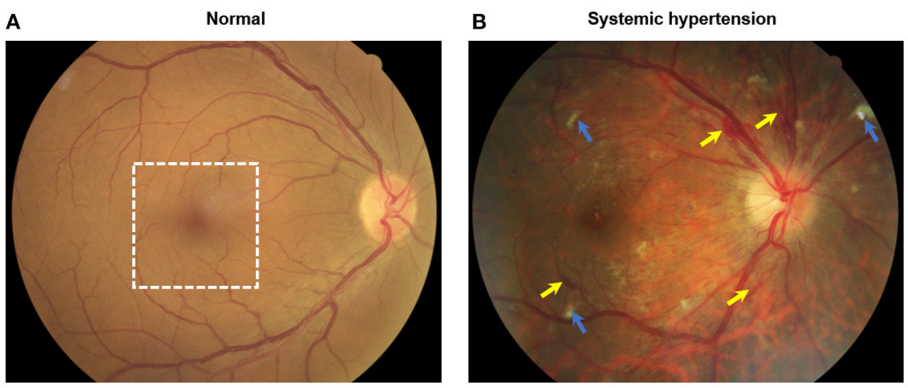

FIGURE 1 | Color fundus photographs of **(A)** an individual without systemic hypertension with normal eye and **(B)** a hypertensive person with signs of moderate hypertensive retinopathy. Notably features include flame hemorrhages (yellow arrows) and cotton wool spots (blue arrows). White dotted box indicates the optical coherence tomography angiography (OCTA, 3 × 3 mm^2) scanned region as seen in **Figure 2**.

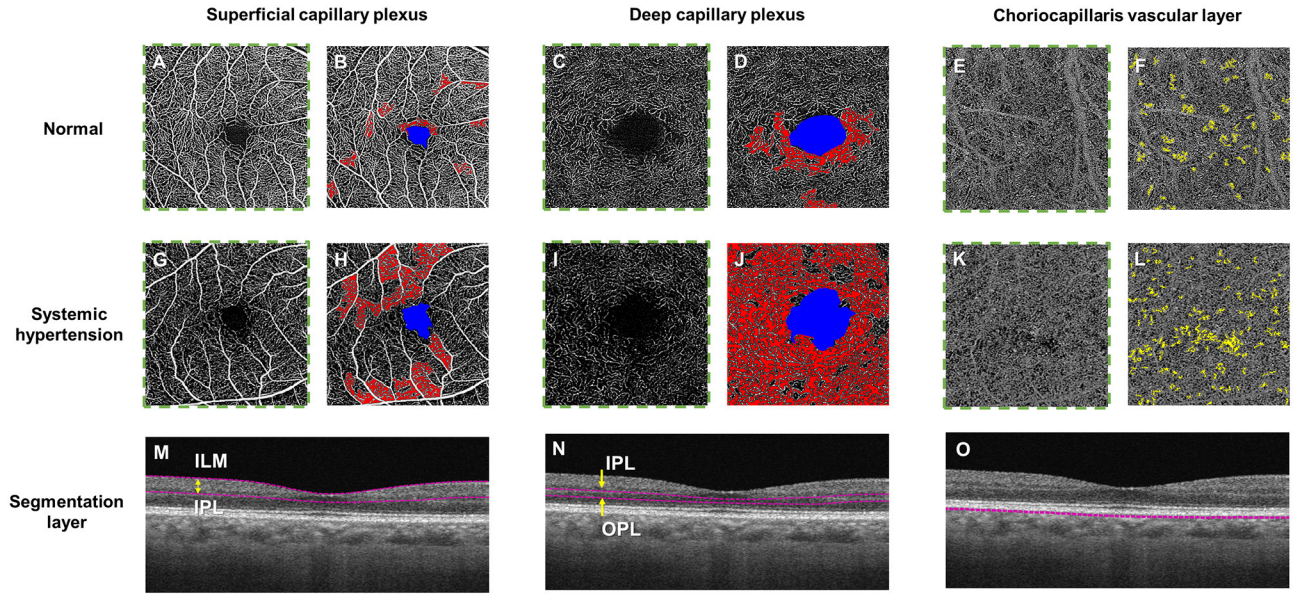

FIGURE 2 | Optical coherence tomography angiography (OCTA) and color-coded maps of a healthy control individual (Top panel; **A–F**) and a hypertensive individual with poorly controlled blood pressure (Middle panel; **G–L**) and the horizontal B-scan images of the corresponding layer (Bottom row, **M–O**). OCTA metrics, including fovea avascular zone (FAZ) area (in blue), retinal vessel density and choriocapillaris flow void deficits, can be calculated automatically. **(M)** The superficial plexus was segmented from the internal limiting membrane (ILM) to the inner plexiform layer (IPL), **(N)** the deep plexus was segmented from the IPL to the outer plexiform layer (OPL) and the choriocapillaris layer was segmented within a thin 10 μm thick slab (31–40 μm) below the retinal pigmented epithelium. The presence of larger non-perfusion area (in red) can be detected in both the superficial and deep capillary plexuses and more choriocapillaris flow voids (in yellow) in a hypertensive eye **(H, J, L)** as compared to the healthy eye **(B, D, F)**.

(6) hypertensive crisis; (7) hypertensive crises. The search results were then exported to Endnote where duplicates were excluded. The remaining studies were then screened by Title/Abstract using Rayyan (9) by two independent reviewers (W.T and J.C). Discrepancies between reviewer selections were resolved by the decision of a third independent reviewer (Y.X). Studies selected by Title/Abstract then underwent a full-text review by two independent reviewers (W.T and J.C). Discrepancies between reviewer selections were resolved by the decision of a third independent reviewer (Y.X).

INCLUSION AND EXCLUSION CRITERIA

Inclusion criteria for studies were: (1) studies with hypertensive patients and non-hypertensive controls; (2) studies which analyzed microvascular parameters using OCTA; (3) cross-sectional or longitudinal studies. We excluded the following studies: (1) reviews; (2) case reports; (3) non-human research; (4) conference presentations or summaries. The inclusion criteria for hypertensive patients were: (1) diagnosis of systemic hypertension as defined by systolic blood pressure ≥140 mmHg, and/or diastolic blood pressure ≥90 mmHg, and/or history of antihypertensive medication, and/or physician diagnosed hypertension in clinic setting. The exclusion criteria for hypertensive patients were: (1) abnormal fundus findings or ophthalmological disease except for hypertensive retinopathy; (2) age <18 years. The inclusion criteria for controls were: (1) no diagnosis of systemic hypertension and the exclusion criteria were: (1) abnormal fundus findings or ophthalmological disease; (2) age <18 years.

DATA EXTRACTION AND SYNTHESIS

Studies selected after full-text review underwent data extraction. The data extracted were: (1) title; (2) first author; (3) year of publication; (4) study design; (5) number of hypertensive eyes analyzed; (6) number of hypertensive participants; (7) number of control eyes analyzed; (8) number of control participants; (9) Mean age and sex of hypertensives and controls; (10) Major modifiable cardiovascular risk factor characteristics (10) of hypertensives and controls; (11) OCTA parameters analyzed; (12) mean values of OCTA parameters analyzed; (13) diagnostic criteria; (14) participant selection criteria; (15) method of imaging and analysis used.

One researcher (W.T) performed data extraction, while another researcher (J.C) reviewed the extracted data for possible inclusion in this meta-analysis. Discrepancies between reviewer selections were resolved by the decision of a third independent reviewer (Y.X). As some studies studied both eyes of each participant, analysis was performed at the eye level instead of at the participant level; the total number of eyes is similar to the total number of participants for all meta-analyses as outlined in the results section below. OCTA parameters used for comparison between patients with systemic hypertension and controls were

synthesized for analysis if they were reported in a minimum number of 3 papers. The mean and standard deviation of the OCTA parameters from individual studies were combined using a random effects meta-analysis, for both the hypertensive and control group. If a study had the hypertensive patients split into subgroups, the mean and standard deviation of the subgroups were combined to produce a mean and standard deviation for the hypertensive patients as a whole (https://training.cochrane.org/handbook/current/chapter-06; https://www.statstodo.com/CombineMeansSDs_Pgm.php). Similarly, if a study divided a specific OCTA parameter into subgroups, the mean and standard deviation of the subgroups was combined to produce a total mean and standard deviation for the specific OCTA parameter. The difference in mean value of the specific OCTA parameter(s) in patients with systemic hypertension vs. healthy controls was then used as the main outcome measure.

ASSESSMENT OF STUDY QUALITY

Study quality was assessed with the Newcastle-Ottawa Scale (NOS) for Quality Assessment. Since the NOS is not suitable for cross-sectional studies, adapted scales have been created (11, 12). We adapted the NOS scale for cross-sectional studies (12) for our research question. Studies were graded as unsatisfactory ($\leq$4 stars), satisfactory (5–6 stars), good (7–8 stars) and very good (9–10 stars) (12). One researcher (W.T) performed the quality assessment, while another researcher (J.C) reviewed the assessment. Discrepancies between quality assessment were resolved by the decision of a third independent reviewer (Y.X).

STATISTICAL ANALYSES

Meta-analyses of continuous outcomes was conducted with the Cochrane Collaboration's Review Manager software (RevMan 5) (Review Manager (RevMan) [Computer program]. Version 5.4) using an inverse variance with random-effects in the model. We chose random effects instead of fixed effects analysis because of the different OCTA devices used in the studies. The *z*-test was performed to assess the difference between the OCTA measures from the patient cohort and healthy controls, where a *P*-value of $<$0.05 was considered significant. Statistical heterogeneity of data synthesized was assessed by utilizing the Higgins I^2 value, ranging from 0 to 100%, that measures the degree of inconsistency across studies, and tentatively assigned as low, moderate, and high to I^2 values of 25, 50, and 75% (13).

A potentially important source of heterogeneity is the type of OCTA device used in different studies, as manufacturers' proprietary built-in software algorithms and segmentation algorithms to obtain the specific vascular plexuses vary between machines (**Supplementary Figure S1**). There was a variety of OCTA machines used in these studies, namely the AngioVue (Optovue Inc., Fremont, CA, USA), Cirrus 5000 AngioPlex (Carl Zeiss Meditec Inc., Dublin, CA., USA), and PLEX Elite 9000 (Carl Zeiss Meditec Inc., Dublin, CA., USA). Both AngioVue and Cirrus AngioPlex 5000 are spectral-domain systems, based on an 800 nm optical window, while PLEX Elite 9000 is a swept-source system that utilizes a longer wavelength (1,060 nm), allowing for better penetration and higher sensitivity at deeper layers such as choroid. In addition, different manufactures employed different techniques to identify blood vessels from the change in the OCT signals induced by the moving blood cells. Both Zeiss AngioPlex and PLEX Elite 9000 employed an optical microangiography (OMAG) algorithm, which calculates the decorrelation in the phase and intensity between repeated B-scans. On the other hand, Optovue AngioVue is based on the split spectrum amplitude decorrelation angiography (SSADA) algorithm, which uses a small sliding window to split the spectrum into small bands and calculates the decorrelation. A small discrepancy exists in layer segmentation provided by each machine as well. Specifically, the segmentation algorithm for the superficial retinal layer slab (which is bounded by the internal limiting membrane and inner plexiform layer) is the same for Zeiss AngioPlex and PLEX Elite 9000 but shifted slightly downward in Optovue by a few microns.

Heterogeneity was investigated using planned subgroup analysis on the different OCTA devices when I^2 was above 50%. We then tested for subgroup differences, considering *p*-values of 0.05 or less as significant. Following Cochrane guidelines (https://training.cochrane.org/handbook/current/chapter-10#section-10-11-4), meta-regression was not performed as there were fewer than 10 studies for each OCTA parameter that was meta-analyzed. To assess publication bias, funnel plots were used.

RESULTS

Supplementary Figure S2 summarizes the selection process for the 11 eligible studies, using the 2020 Preferred Reporting Items for Systematic Reviews and Meta-Analyses (PRISMA) flow diagram. The literature search yielded 783 studies, of which 374 were unique. Of these, 358 were removed after they were determined to not meet the inclusion/exclusion criteria after a title and abstract screen. The full-text version of the remaining 16 studies relevant to OCTA and hypertension were retrieved and assessed for eligibility. We omitted five studies due to a lack of control group (14, 15), not meeting the diagnostic criteria for systemic hypertension (16), not screening participants for concurrent ophthalmological conditions (17), and involving participants $<$18 years of age (18).

Table 1 summarizes the key characteristics of the 11 eligible studies that were included for meta-analyses. For the macula, nine studies analyzed the superficial vessel density (6, 7, 19, 20, 22, 24–27), seven analyzed the deep vessel density (6, 7, 19, 20, 22, 24, 25), five analyzed the superficial foveal avascular zone (6, 7, 19, 26, 27), two analyzed vessel density (length) (26, 27), two analyzed skeleton density (19, 22), two analyzed vessel diameter index (19, 22), and one analyzed fractal dimension (19). For the optic nerve head, five studies analyzed peripapillary vessel density (6, 20, 23–25), two analyzed inside disc perfusion density (20, 25), one analyzed vessel caliber (19), and one analyzed vessel density (length) (23). For the choriocapillaris, two studies analyzed density of flow deficits (21, 22), two analyzed size of flow deficits (21, 22), and two analyzed number of flow

TABLE 1 | Key characteristics of the 11 eligible studies.

References	Country	Study design	Number of hypertensive eyes	Number of hypertensives	Number of control eyes	Number of controls	Age and Sex (male)	Major modifiable cardiovascular risk factors	Type of hypertensive patients	Type of OCTA machine used	OCTA parameters analyzed
Xu et al. (19)	China	Cross-sectional	137	77	79	43	**Age:** hypertensives (59.2 +/– 7.6), controls (57 +/– 6.8) **Sex:** hypertensives (26), controls (15)	**Smoking:** – **BMI: – Dyslipidemia: – Diabetes: – Systolic BP: – Diastolic BP: –**	77 patients (137 eyes) with untreated hypertension	AngioVue	**Macula:** vessel density, skeleton density, foveal avascular zone, vessel diameter index, fractal dimension **Optic nerve head:** vessel caliber
Hua et al. (20)	China	Cross-sectional	73	73	40	40	**Age:** hypertensives (64.32 +/– 2.99), controls (65.65 +/– 2.89) **Sex:** hypertensives (32), controls (17)	**Smoking: – BMI: – Dyslipidemia: – Diabetes: – Systolic BP:** hypertensives (125.76 +/– 12.92), controls (119.6 +/– 8.72) **Diastolic BP:** hypertensives (80.01 +/– 7.88), controls (76.8 +/– 5.92)	**Group A:** 32 hypertensive patients (32 eyes) with intensive BP control (systolic BP < 120) **Group B:** 26 hypertensive patients (26 eyes) with standard BP control (systolic BP 120–140) **Group C:** 15 hypertensive patients (26 eyes) with poor BP control (systolic pressure >140)	AngioVue	**Macula:** vessel density **Optic nerve head:** peripapillary vessel density, inside disc perfusion density
Donati et al. (6)	Italy	Cross-sectional	60	30	30	15	**Age:** hypertensives (54.1 +/– 5.38), controls (52.18 +/– 4.73) **Sex:** hypertensives (15), controls (8)	**Smoking: – BMI: – Dyslipidemia: – Diabetes: – Systolic BP:** Hypertensives (130.83 +/– 5.91), Controls (113.2 +/– 7.41) **Diastolic BP:** hypertensives (81.64 +/– 6.09), controls (69.82 +/– 6.73)	**Group 2**: 15 patients (30 eyes) with newly diagnosed hypertension **Group 3**: 15 patients (30 eyes) with treated hypertension	AngioVue	**Macula:** vessel density, foveal avascular zone **Optic nerve head:** peripapillary vessel density

(Continued)

TABLE 1 | Continued

References	Country	Study design	Number of hypertensive eyes	Number of hypertensives	Number of control eyes	Number of controls	Age and Sex (male)	Major modifiable cardiovascular risk factors	Type of hypertensive patients	Type of OCTA machine used	OCTA parameters analyzed
Chua et al. (21)	Singapore	Cross-sectional	116	71	74	41	**Age:** hypertensives (56.75 +/– 9.09), controls (55 +/– 14) **Sex:** hypertensives (44), controls (25)	**Smoking:** hypertensives (2), controls (2) **BMI: – Dyslipidemia:** hypertensives (25), controls (11) **Diabetes: – Systolic BP:** hypertensives (129.83 +/– 12.46), controls (124 +/– 11) **Diastolic BP:** hypertensives (80.04 +/– 8.36), controls (72 +/– 8)	**Good BP control** (systolic BP < 140 and/or diastolic BP < 90): 53 hypertensive patients (87 eyes) **Poor BP control** (systolic BP > 140 and/or diastolic BP > 90): 18 hypertensive patients (29 eyes)	PLEX Elite 9000	**Choriocapillaris flow deficits (macula):** density, size, number
Terheyden et al. (22)	Germany	Cross-sectional	28	17	31	18	**Age:** hypertensives (56 +/– 19), controls (52 +/– 16) **Sex: –**	**Smoking: – Dyslipidemia: – Diabetes: – Systolic BP: – Diastolic BP: –**	17 patients (28 eyes) with hypertensive crisis (systolic BP ≥ 180 and/or diastolic BP ≥ 110)	PLEX Elite 9000	Macula: vessel density, skeleton density, vessel diameter index **Choriocapillaris flow deficits (macula):** density, size, number
Sun et al. (7)	Singapore	Cross-sectional	94	94	46	46	**Age:** Hypertensives (64.77 +/– 9.03), controls (58.3 +/– 4.62) **Sex:** hypertensives (47), controls (21)	**Smoking: – BMI: – Dyslipidemia: – Diabetes: – Systolic BP:** hypertensives (150.82 +/– 17.37), controls (123.35 +/– 11.04) **Diastolic BP:** hypertensives (78.64 +/– 8.52), controls (70.97 +/– 6.62)	94 patients (94 eyes) with systemic hypertension	AngioVue	**Macula:** vessel density, foveal avascular zone

(Continued)

TABLE 1 | Continued

References	Country	Study design	Number of hypertensive eyes	Number of hypertensives	Number of control eyes	Number of controls	Age and Sex (male)	Major modifiable cardiovascular risk factors	Type of hypertensive patients	Type of OCTA machine used	OCTA parameters analyzed
Shin et al. (23)	South Korea	Cross-sectional	78	78	90	90	**Age:** hypertensives (61.72 +/– 9.27), controls (60.1 +/– 8.9) **Sex (Male):** hypertensives (37), controls (38)	**Smoking: – BMI: Dyslipidemia: – Diabetes: – Systolic BP:** hypertensive: (118.07 +/– 8.56), controls (115.6 +/– 9.7) **Diastolic BP:** hypertensives (81.93 +/– 7.34), controls (79.8 +/– 7.6)	**Group 1**: 38 patients (38 eyes) with hypertension < 10 years **Group 2**: 40 patients (40 eyes) with hypertension ≥ 10 years	Cirrus AngioPlex 5000	**Optic nerve head:** vessel density (length), peripapillary vessel density
Peng et al. (24)	China	Cross-sectional	169	169	30	30	**Age:** hypertensives (53.54 +/– 10.85), controls (53.6 +/– 9.2) **Sex (male):** hypertensives (83), controls (15)	**Smoking:** hypertensives (16), controls (3) **BMI:** hypertensives (24.53 +/– 3.06), controls (24.1 +/– 1.9) **Dyslipidemia: – Diabetes: – Systolic BP:** hypertensives [with retinopathy (135; range 130–149), no retinopathy (136; range 127–147)], controls (117; range 110–122) **Diastolic BP:** hypertensives [with retinopathy (85; range 80–95), no retinopathy (85; range 79–93)], controls (75; range 65–81)	**Group A:** 113 patients (113 eyes) with hypertensive retinopathy **Group B:** 56 patients (56 eyes) without hypertensive retinopathy	AngioVue	**Macula:** vessel density **Optic Nerve Head:** peripapillary vessel density

(Continued)

TABLE 1 | Continued

References	Country	Study design	Number of hypertensive eyes	Number of hypertensives	Number of control eyes	Number of controls	Age and Sex (male)	Major modifiable cardiovascular risk factors	Type of hypertensive patients	Type of OCTA machine used	OCTA parameters analyzed
Hua et al. (25)	China	Cross-sectional	57	57	40	40	**Age:** Hypertensives (65.67 +/– 3.02), controls (65.65 +/– 2.89) **Sex:** Hypertensives (22), controls (17)	**Smoking: – BMI: – Dyslipidemia: – Diabetes: – Systolic BP (mmHg):** hypertensives (120.75 +/– 8.42), controls (119.6 +/– 8.72) **Diastolic BP (mmHg):** hypertensives (78.35 +/– 5.27), controls (76.80 +/– 5.92)	**Group A:** 35 patients (35 eyes) with a history of hypertension for >10 years **Group B:** 22 patients (22 eyes) with a history of hypertension for 5–10 years	AngioVue	**Macula:** vessel density **Optic nerve head:** inside disc perfusion density
Lim (27)	South Korea	Cross-sectional	84	84	117	117	**Age:** hypertensives (58.53 +/– 9.14), controls (56.4 +/– 12.68) **Sex:** hypertensives (38), controls (53)	**Smokers:** hypertensives (24), controls (19) **BMI: – Dyslipidemia: – Diabetes: – Systolic BP:** hypertensives (122.9 +/– 13.8), controls (119.2 +/– 14.4) **Diastolic BP:** hypertensives (82.9 +/– 8.7), controls (81.0 +/– 7.4)	**Group 1:** 32 patients (32 eyes) with hypertension < 5 years **Group 2:** 52 patients (52 eyes) with hypertension ≥ 5 years	Cirrus AngioPlex 5000	**Macula:** vessel density (superficial only), foveal avascular zone
Lee (26)	South Korea	Cross-sectional	85	85	100	100	**Age:** hypertensives (51.8 +/– 12.2), controls (50.4 +/– 12.6) **Sex:** hypertensives (45), controls (51)	**Smoking: – BMI: – Dyslipidemia: – Diabetes: – Systolic BP: – Diastolic BP: –**	**Group A:** 45 patients (45 eyes) with hypertension of at least 10 years **Group B:** 40 patients (40 eyes) with relieved hypertensive retinopathy (grade IV, <1 year prior)	Cirrus AngioPlex 5000	**Macula:** vessel density (superficial only), foveal avascular zone

Age is shown as mean +/– SD in years, sex is shown as number of males, smoking is shown as number of smokers, BMI is shown as mean +/– SD in kg/m2, dyslipidemia is shown as number of participants with dyslipidemia, diabetes is shown as number of participants with diabetes, systolic and diastolic BP is shown as mean +/– SD in mmHg.

deficits (21, 22). Nine studies used spectral domain OCTA (SD-OCTA) devices, while two used swept source OCTA (SS-OCTA). Regarding the OCTA models, six studies used the AngioVue (Optovue RTVue XR Avanti; Optovue Inc., Fremont, CA), three studies used the Cirrus 5000 AngioPlex (Carl Zeiss Meditec, Dublin, CA, USA), and two studies used the PLEX Elite 9000 (Carl Zeiss Meditec, Inc., Dublin, USA). All studies were cross-sectional and there were no longitudinal studies published before 19 June 2021. The populations sampled were from China (four), Italy (one), Singapore (two), Germany (one), and South Korea (three). Age of participants was recorded in all studies. Sex of participants was recorded in all studies except for one (22). As for major modifiable cardiovascular risk factors, smoking status was available for three studies (21, 24), BMI was available for one study (24), dyslipidemia status was available for one study (21), diabetic patients were not included in any studies, and mean systolic and diastolic blood pressure readings were available in all studies except for three (19, 22, 26). As for quality assessment, all studies included in our meta-analyses had either a good or very good rating; the complete assessment of study quality is shown in **Supplementary Figure S3**.

SUPERFICIAL VASCULAR DENSITY (SVD) AT MACULA

Of the 11 studies, nine published results featuring the SVD in 787 eyes of 659 patients with systemic hypertension and 513 eyes of 449 healthy controls. Reduction of the SVD of standardized mean difference [SMD], −0.50 [−0.70, −0.30], $P < 0.00001$ occurred in eyes of patients with systemic hypertension as compared with control eyes (**Figure 3**). Given the heterogeneity in the SVD analysis was considered significant ($I^2 = 63\%$ and $P = 0.005$), we then performed a subgroup analysis by OCTA devices. Our analysis did not reveal any statistically significance heterogeneity introduced by the type of OCTA machine ($I^2 = 0\%$ and $P = 0.740$).

DEEP VASCULAR DENSITY (DVD) AT MACULA

For the DVD, the meta-analysis of seven studies (**Figure 4**), totaling 618 eyes of 517 patients with systemic hypertension and 296 eyes of 232 healthy controls, revealed significantly reduced vascular density in patients with systemic hypertension when compared to controls (SMD, −0.38 [−0.64, −0.13], $P = 0.004$). The heterogeneity in the DVD analysis was considered significant ($I^2 = 67\%$ and $P = 0.006$). Subgroup analysis by OCTA machines did not show statistically significant heterogeneity ($I^2 = 0\%$ and $P = 0.670$).

FOVEAL AVASCULAR ZONE (FAZ)

For the FAZ, meta-analysis of six studies (**Figure 5**), totaling 517 eyes of 400 patients with systemic hypertension and 412 eyes of 361 healthy controls, revealed a statistically significant increase in foveal avascularity in patients with systemic hypertension when compared to controls (SMD, 0.32 [0.04, 0.61], $P = 0.030$). The heterogeneity in the FAZ analysis was considered significant ($I^2 = 77\%$ and $P < 0.001$). The test for subgroup differences revealed no statistically significant heterogeneity introduced by the type of OCTA machine used to measure the FAZ ($I^2 = 0\%$ and $P = 0.340$).

PERIPAPILLARY VASCULAR DENSITY (PVD)

For PVD, meta-analysis of five studies (**Supplementary Figure S4**), totaling 407 eyes of 377 patients with systemic hypertension and 204 eyes of 189 healthy controls, revealed no significant difference in vascular density in patients with systemic hypertension when compared to controls (SMD, −0.35 [−1.11, 0.42], $P = 0.370$).

ADDITIONAL ANALYSES

Publication biases were investigated by plotting funnel plots, which revealed a symmetrical distribution of studies about the SMD of −0.50, −0.38, and 0.33, indicating little to no publication bias nor small study bias in the analysis for SVD, DVD and FAZ area, respectively (**Supplementary Figures S5–S7**).

We also performed a sensitivity analysis by removing the 2020 study by Terheyden et al. (22) as the study involved hypertensive patients with recent history (<7 days prior) of hypertensive crisis as defined by systolic blood pressure greater or ≥180 mmHg and/or diastolic blood pressure ≥120 mmHg. Results remained similar after sensitivity analysis, where both SVD and DVD were significantly reduced in hypertensives as compared to controls (SMD, −0.52 [−0.73, −0.30], $P < 0.00001$, $I^2 = 67\%$) and SMD, −0.37 [−0.66, −0.08], $P = 0.010$, $I^2 = 72\%$; **Supplementary Figures S8, S9**), respectively.

DISCUSSION

In this meta-analysis, the data (6, 7, 19–27) shows that systemic hypertension is associated with reduction of vascular density in the superficial capillary plexus (SVD and FAZ area) and deep capillary plexus (DVD) at the macula (**Figure 2**). This outcome suggests the potential of OCTA technology to serve as tool for pre-clinical retinal microvascular changes in systemic hypertension, where changes in the small retinal vessels may potentially be imaging biomarkers to risk stratify hypertensive complications in end-organs such as the brain, heart, and kidney (28).

POTENTIAL OCTA MEASURES OF MICROCIRCULATION IN SYSTEMIC HYPERTENSION

Superficial and Deep Vascular Densities

The reduced superficial and deep vascular densities on OCTA that we observed in the hypertensive subjects could be the

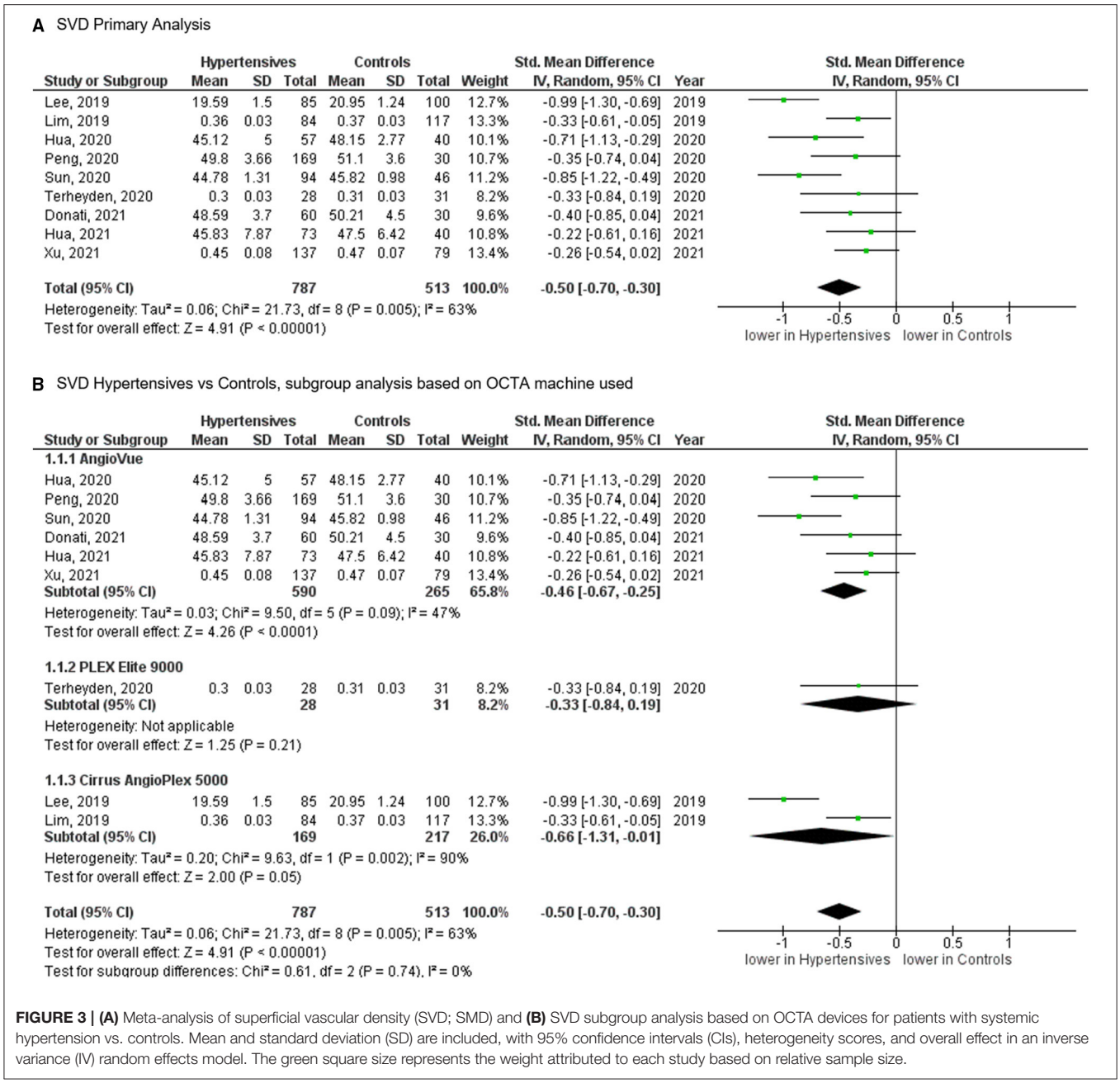

FIGURE 3 | (A) Meta-analysis of superficial vascular density (SVD; SMD) and **(B)** SVD subgroup analysis based on OCTA devices for patients with systemic hypertension vs. controls. Mean and standard deviation (SD) are included, with 95% confidence intervals (CIs), heterogeneity scores, and overall effect in an inverse variance (IV) random effects model. The green square size represents the weight attributed to each study based on relative sample size.

result of either capillary dropout (structural absence of capillaries) or functional non-perfusion. Since OCTA relies on the change between consecutive scans, it will detect flow only above a minimum threshold (29) and regions that have flow below the slowest detectable flow would therefore be visualized as non-perfusion using the OCTA imaging technique. Coupling OCTA and adaptive optics may be an exciting avenue. Adaptive optics is another novel ocular imaging approach that provides *in vivo* ultra-high-resolution imaging of retinal vessel morphology in humans (30).

FAZ Area

We observed a weak association between hypertension and FAZ area, which may be explained by the substantial heterogeneity among the studies. Investigations into potential sources revealed that the type of OCTA machine was not the source of the heterogeneity for FAZ area. Previous studies have shown that the size of the FAZ is notoriously variable among normal individuals (31). Another limitation is the difference in reporting of FAZ where traditional analyses (26, 27) (prior to 2020) splits the reporting of superficial vs. deep FAZ, whereas the newer analyses give a combined FAZ parameter. Taken together, it prevents us

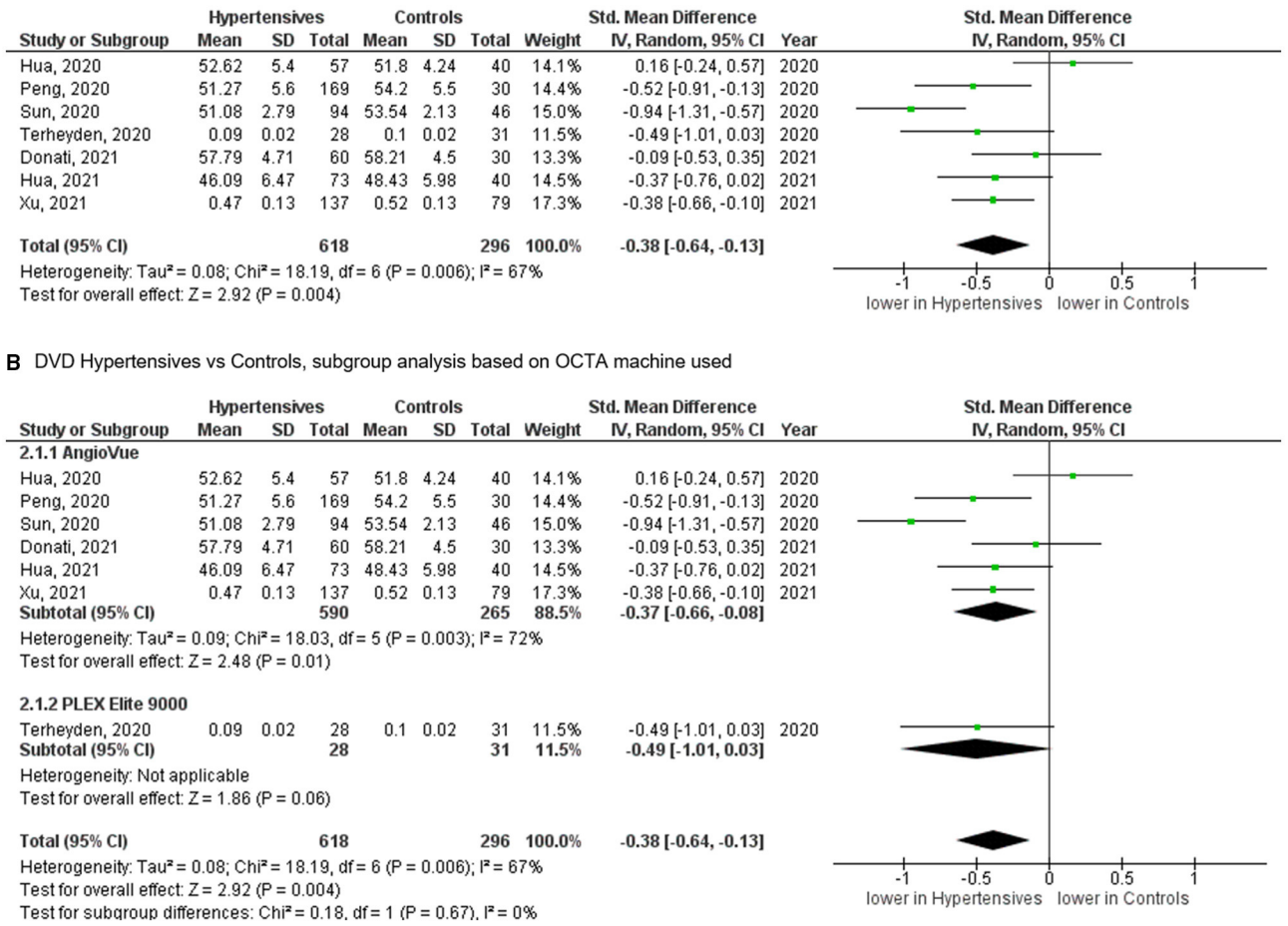

FIGURE 4 | (A) Meta-analysis of deep vascular density (DVD; SMD) and **(B)** DVD subgroup analysis based on OCTA devices for patients with systemic hypertension vs. controls. Mean and standard deviation (SD) are included, with 95% confidence intervals (CIs), heterogeneity scores, and overall effect in an inverse variance (IV) random effects model. The green square size represents the weight attributed to each study based on relative sample size.

from recommending the FAZ area as a parameter in systemic hypertension research.

Peripapillary Vascular Density

We are not able to draw a conclusion on the utility of peripapillary vascular density in differentiating systemic hypertension cases from controls. The wide degree of imprecision of this estimate may be due to the marked inter-individual variation in the blood supply of the optic nerve head, requiring a larger sample size (32).

Additional OCTA Parameters

In the present meta-analysis, only four OCTA parameters have been meta-analyzed. Other parameters identified through this systematic review may be promising but do not yet have enough data to pool together. These include fractal dimension of the retina, and capillary density inside the optic nerve head (20, 24). Of particular interest is the choroidal circulation. In a 2019 study by Lee et al. (33), choroidal blood was found to increase and be affected before retinal circulation in patients with elevated blood pressure. This may indicate that the choroidal circulation is the earliest vasculature in the eye to be affected in systemic hypertension. However, our systematic review only found two papers, 2021 study by Chua et al. (21) and 2020 study by Terheyden et al. (22), to have compared the patterns of choriocapillaris flow deficits at the macula of patients with systemic hypertension with healthy controls.

RECOMMENDATIONS FOR FUTURE STUDY DESIGNS

Ocular microvascular dysfunction can be due to eye diseases or hypertension. This explains why most studies screened in the meta-analysis excluded participants for concurrent ophthalmological conditions, except for one study (17). As we know that hypertension is a risk factor for age-related macular degeneration (34) and glaucoma (35), an unanswered question now is to determine if hypertensive capillary damage participates to the disease or if it is another

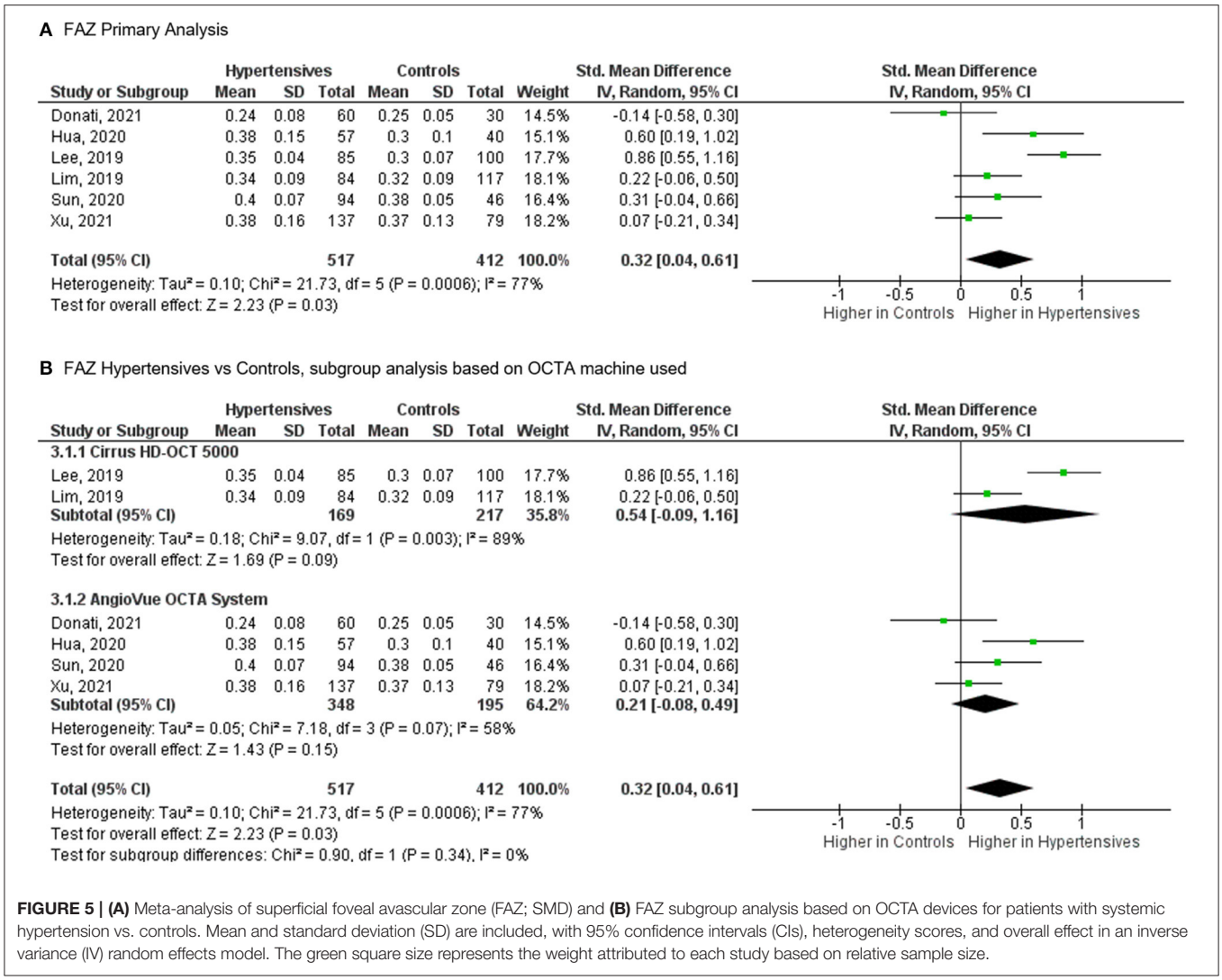

FIGURE 5 | (A) Meta-analysis of superficial foveal avascular zone (FAZ; SMD) and **(B)** FAZ subgroup analysis based on OCTA devices for patients with systemic hypertension vs. controls. Mean and standard deviation (SD) are included, with 95% confidence intervals (CIs), heterogeneity scores, and overall effect in an inverse variance (IV) random effects model. The green square size represents the weight attributed to each study based on relative sample size.

mechanism. Future studies wanting to corroborate the level of hypertensive retinopathy/choroidopathy, and the degree of retinal damage could consider including hypertensive patients in control groups.

Apart from eye diseases, three other factors can bias the relationship between hypertension and OCTA: aging, diabetes, and methods of blood pressure measurement. Aging is associated with decreased retinal tissue perfusion (36, 37). OCTA metrics, such as areas of retinal non-perfusion have been found in eyes of patients with diabetes without retinopathy (38, 39). Methods of blood pressure measurement i.e., ambulatory vs. office, can affect the accuracy of blood pressure readings (40). It will be important for future studies to consider confounders during the interpretation of results as confounding variables can distort the observed association between OCTA and hypertension.

It may also be interesting for future studies to note the presence of major modifiable cardiovascular risk factors (10) of study participants apart from hypertension, namely smoking status, body mass index, dyslipidemia, and investigate whether variations in OCTA parameters are influenced by these other factors. This may also allow future meta-analyses to perform meta-regression analyses of the effects of continuous variables such as body mass index, blood pressure, or lipid levels on retinal/choroidal vessel density.

POTENTIAL USE OF OCTA AS A QUICK AND NON-INVASIVE MEASURE OF MICROCIRCULATION

OCTA Parameters and Blood Pressure Control

Several papers have examined how the retinal microcirculation, as measured by OCTA parameters, is affected by blood pressure control. However, pooling these studies is challenging due to differences in stratification of blood pressure control. For example, the 2021 study by Hua et al. (20) attempted to classify hypertensive patients into three groups based on blood pressure control, in accordance with the Systolic Blood Pressure

Intervention Trial (SPRINT study) (41), where intensive blood pressure control was defined as systolic blood pressure <120 mmHg; standard blood pressure control was defined as systolic blood pressure 120–140 mmHg; and poor blood pressure control was defined as systolic blood pressure >140 mmHg. On the other hand, the 2021 study by Chua et al. (21) attempted to stratify patients into two groups by defining well-controlled ambulatory blood pressure defined as systolic blood pressure <140 mmHg and/or diastolic blood pressure <90 mmHg and poorly controlled blood pressure defined as systolic blood pressure ≥140 mmHg and/or diastolic blood pressure ≥90 mmHg. The extreme heterogeneity in which patients are currently being stratified in studies make it challenging for meta-analyses to be done. There is a need to harmonize these criteria for future OCTA studies.

OCTA Parameters and Class of Anti-hypertensive Treatments

It has been proposed that different classes of anti-hypertensive treatments have differing effects at the microvascular levels (42). The hypothesis is, however, largely unproven because of the lack of microvascular imaging. As such, OCTA is an attractive technique to study the effects anti-hypertensive treatments on the microvasculature. However, caution must be taken. For example, though the 2020 study by Peng et al. (24) attempted to investigate the use of anti-hypertensive treatments on OCTA parameters, it was difficult to ascertain the duration the patient was on the specific anti-hypertensive or whether he/she had been recently switched over from a different class. This may erroneously attribute a certain OCTA outcome to a specific class of anti-hypertensive drugs when in fact it was due to a previous medication that the patient was recently on. Considering this, it may be most appropriate for future studies to conduct randomized-control trials where OCTA parameters of untreated/newly diagnosed essential hypertensives starting on different hypertensive medications are measured at various time points longitudinally.

OCTA Parameters and Hypertensive End-Organ Damage

Whether the OCTA adds value to risk prediction of hypertensive end-organ damage remains to be determined. Two small studies have shown the association of retinal capillary rarefaction and impaired kidney function (estimated glomerular filtration rate levels) in hypertensive individuals (14, 43). To investigate the prognostic value of OCTA parameters for hypertensives end-organ damage, prospective longitudinal follow-up studies can be done to, for example, correlate SVD or DVD values with the incidence/risk of renal failure at 5 years. Correlation of retinal findings with other systemic measures of microvasculature in other organs will help shed further light on the significance of these retinal microvascular changes.

CONCLUSION

Our results suggest that certain OCTA parameters can provide objective information about pre-clinical microvascular changes from systemic hypertension and have the potential to act as novel biomarkers of these changes.

DATA AVAILABILITY STATEMENT

The original contributions presented in the study are included in the article/**Supplementary Material**, further inquiries can be directed to the corresponding author/s.

AUTHOR CONTRIBUTIONS

WT, XY, and JC contributed to the conception and design of the study, literature search, data extraction and synthesis, and assessment of study quality. WT performed the statistical analysis and wrote the first draft of the manuscript. XY and JC wrote sections of the manuscript. All authors contributed to manuscript revision, read, and approved the submitted version.

FUNDING

Funding received for this work from the Duke-NUS Medical School (Duke-NUS-KP(Coll)/2018/0009A), the National Medical Research Council (CG/C010A/2017; OFIRG/0048/2017; OFLCG/004c/2018; TA/MOH-000249-00/2018 and MOH-OFIRG20nov-0014), National Research Foundation Singapore (NRF2019-THE002-0006 and NRF-CRP24-2020-0001), A*STAR (A20H4b0141), the Singapore Eye Research Institute & Nanyang Technological University (SERI-NTU Advanced Ocular Engineering (STANCE) Program), and the SERI-Lee Foundation (LF1019-1) Singapore.

SUPPLEMENTARY MATERIAL

The Supplementary Material for this article can be found online at: https://www.frontiersin.org/articles/10.3389/fmed.2021.778330/full#supplementary-material

REFERENCES

1. Forouzanfar MH, Afshin A, Alexander LT, Anderson HR, Bhutta ZA, Biryukov S, et al. Global, regional, and national comparative risk assessment of 79 behavioural, environmental and occupational, and metabolic risks or clusters of risks, 1990–2015: a systematic analysis for the Global Burden of Disease Study 2015. *Lancet.* (2016) 388:1659–724. doi: 10.1016/S0140-6736(16)31679-8
2. Forouzanfar MH, Liu P, Roth GA, Ng M, Biryukov S, Marczak L, et al. Global burden of hypertension and systolic blood pressure of at least 110 to 115 mm Hg, 1990–2015. *JAMA.* (2017) 317:165. doi: 10.1001/jama.2016.19043
3. Tsukikawa M, Stacey AW. A review of hypertensive retinopathy and chorioretinopathy. *Clin Optom Vol.* (2020) 12:67–73. doi: 10.2147/OPTO.S183492
4. Chalam KV, Sambhav K. Optical coherence tomography angiography in retinal diseases. *J Ophthalmic Vis Res.* (2016) 11:84–92. doi: 10.4103/2008-322X.180709

5. Spaide RF, Klancnik JM, Cooney MJ. Retinal vascular layers imaged by fluorescein angiography and optical coherence tomography angiography. *JAMA Ophthalmol.* (2015) 133:45. doi: 10.1001/jamaophthalmol.2014.3616
6. Donati S, Maresca AM, Cattaneo J, Grossi A, Mazzola M, Caprani SM, et al. Optical coherence tomography angiography and arterial hypertension: a role in identifying subclinical microvascular damage? *Eur J Ophthalmol.* (2021) 31:158–65. doi: 10.1177/1120672119880390
7. Sun C, Ladores C, Hong J, Nguyen DQ, Chua J, Ting D, et al. Systemic hypertension associated retinal microvascular changes can be detected with optical coherence tomography angiography. *Sci Rep.* (2020) 10:9580. doi: 10.1038/s41598-020-66736-w
8. Stroup DF, Berlin JA, Morton SC, Olkin I, Williamson GD, Rennie D, et al. Meta-analysis of observational studies in epidemiology: a proposal for reporting. Meta-analysis Of Observational Studies in Epidemiology (MOOSE) group. *JAMA.* (2000) 283:2008–12. doi: 10.1001/jama.283.15.2008
9. Ouzzani M, Hammady H, Fedorowicz Z, Elmagarmid A. Rayyan—a web and mobile app for systematic reviews. *Syst Rev.* (2016) 5. doi: 10.1186/s13643-016-0384-4
10. Patel SA, Winkel M, Ali MK, Narayan KM, Mehta NK. Cardiovascular mortality associated with 5 leading risk factors: national and state preventable fractions estimated from survey data. *Ann Intern Med.* (2015) 163:245–53. doi: 10.7326/M14-1753
11. Herzog R, Álvarez-Pasquin MJ, Díaz C, Del Barrio JL, Estrada JM, Gil Á. Are healthcare workers' intentions to vaccinate related to their knowledge, beliefs and attitudes? a systematic review. *BMC Publ Health.* (2013) 13:154. doi: 10.1186/1471-2458-13-154
12. Naafs JC, Vendrig LM, Limpens J, Van Der Lee HJ, Duijnhoven RG, Marchal JP, et al. Cognitive outcome in congenital central hypothyroidism: a systematic review with meta-analysis of individual patient data. *Eur J Endocrinol.* (2020) 182:351–61. doi: 10.1530/EJE-19-0874
13. Higgins JP, Thompson SG, Deeks JJ, Altman DG. Measuring inconsistency in meta-analyses. *BMJ.* (2003) 327:557–60. doi: 10.1136/bmj.327.7414.557
14. Chua J, Chin CWL, Hong J, Chee ML, Le TT, Ting DSW, et al. Impact of hypertension on retinal capillary microvasculature using optical coherence tomographic angiography. *J Hypertens.* (2019) 37:572–80. doi: 10.1097/HJH.0000000000001916
15. Chua J, Chin CWL, Tan B, Wong SH, Devarajan K, Le TT, et al. Impact of systemic vascular risk factors on the choriocapillaris using optical coherence tomography angiography in patients with systemic hypertension. *Sci Rep.* (2019) 9:5819. doi: 10.1038/s41598-019-41917-4
16. Pascual-Prieto J, Burgos-Blasco B, Ávila Sánchez-Torija M, Fernández-Vigo JI, Arriola-Villalobos P, Barbero Pedraz MA, et al. Utility of optical coherence tomography angiography in detecting vascular retinal damage caused by arterial hypertension. *Eur J Ophthalmol.* (2020) 30:579–85. doi: 10.1177/1120672119831159
17. Liang J, Li Y, Chen L, Xia W, Wu G, Tong X, et al. Systemic microvascular rarefaction is correlated with dysfunction of late endothelial progenitor cells in mild hypertension: a substudy of EXCAVATION-CHN1. *J Transl Med.* (2019) 17:368. doi: 10.1186/s12967-019-2108-8
18. Dereli Can G, Korkmaz MF, Can ME. Subclinical retinal microvascular alterations assessed by optical coherence tomography angiography in children with systemic hypertension. *J AAPOS.* (2020) 24:147.e141–7.e146. doi: 10.1016/j.jaapos.2020.02.006
19. Xu Q, Sun H, Huang X, Qu Y. Retinal microvascular metrics in untreated essential hypertensives using optical coherence tomography angiography. *Graefe's Arch Clin Exp Ophthalmol.* (2021) 259:395–403. doi: 10.1007/s00417-020-04714-8
20. Hua D, Xu Y, Zhang X, He T, Chen C, Chen Z, et al. Retinal microvascular changes in hypertensive patients with different levels of blood pressure control and without hypertensive retinopathy. *Curr Eye Res.* (2021) 46:107–14. doi: 10.1080/02713683.2020.1775260
21. Chua J, Le TT, Tan B, Ke M, Li C, Wong DWK, et al. Choriocapillaris microvasculature dysfunction in systemic hypertension. *Sci Rep.* (2021) 11:4603. doi: 10.1038/s41598-021-84136-6
22. Terheyden JH, Wintergerst MWM, Pizarro C, Pfau M, Turski GN, Holz FG, et al. Retinal and choroidal capillary perfusion are reduced in hypertensive crisis irrespective of retinopathy. *Trans Vis Sci Technol.* (2020) 9:1–7. doi: 10.1167/tvst.9.8.42
23. Shin YI, Nam KY, Lee WH, Ryu CK, Lim HB, Jo YJ, et al. Peripapillary microvascular changes in patients with systemic hypertension: An optical coherence tomography angiography study. *Sci Rep.* (2020) 10:6541. doi: 10.1038/s41598-020-63603-6
24. Peng Q, Hu Y, Huang M, Wu Y, Zhong P, Dong X, et al. Retinal neurovascular impairment in patients with essential hypertension: an optical coherence tomography angiography study. *Invest Opthalmol Vis Sci.* (2020) 61:42. doi: 10.1167/iovs.61.8.42
25. Hua D, Xu Y, Zeng X, Yang N, Jiang M, Zhang X, et al. Use of optical coherence tomography angiography for assessment of microvascular changes in the macula and optic nerve head in hypertensive patients without hypertensive retinopathy. *Microvasc Res.* (2020) 129. doi: 10.1016/j.mvr.2019.103969
26. Lee WH, Park JH, Won Y, Lee MW, Shin YI, Jo YJ, et al. Retinal microvascular change in hypertension as measured by optical coherence tomography angiography. *Sci Rep.* (2019) 9:156. doi: 10.1038/s41598-018-36474-1
27. Lim HB, Lee MW, Park JH, Kim K, Jo YJ, Kim JY. Changes in ganglion cell-inner plexiform layer thickness and retinal microvasculature in hypertension: an optical coherence tomography angiography study. *Am J Ophthalmol.* (2019) 199:167–76.
28. Bhargava M, Cheung CY, Sabanayagam C, Huang L, Lamoureux EL, Wang JJ, et al. Prevalence and risk factors for retinopathy in persons without diabetes: the Singapore Indian Eye Study. *Acta Ophthalmol.* (2014) 92:e602–609. doi: 10.1111/aos.12446
29. De Carlo TE, Romano A, Waheed NK, Duker JS. A review of optical coherence tomography angiography (OCTA). *Int J Retina Vitreous.* (2015) 1:5. doi: 10.1186/s40942-015-0005-8
30. Bakker E, Dikland FA, Van Bakel R, Andrade De Jesus D, Sanchez Brea L, Klein S, et al. (2021). Adaptive optics ophthalmoscopy: a systematic review of vascular biomarkers. *Surv Ophthalmol*. doi: 10.1016/j.survophthal.2021.05.012
31. Chui TY, Zhong Z, Song H, Burns SA. Foveal avascular zone and its relationship to foveal pit shape. *Optom Vis Sci.* (2012) 89:602–10. doi: 10.1097/OPX.0b013e3182504227
32. Hayreh SS. Inter-individual variation in blood supply of the optic nerve head: its importance in various ischemic disorders of the optic nerve head, and glaucoma, low-tension, glaucoma, and allied, disorders. *Doc Ophthalmol.* (1985) 59:217–46. doi: 10.1007/BF00159262
33. Lee CS, Choi EY, Lee M, Kim H, Chung H. Serous retinal detachment in preeclampsia and malignant hypertension. *Eye.* (2019) 33:1707–14. doi: 10.1038/s41433-019-0461-8
34. Hyman L, Schachat AP, He Q, Leske MC. Hypertension, cardiovascular disease, and age-related macular degeneration. Age-related macular degeneration risk factors study group. *Arch Ophthalmol.* (2000) 118:351–8. doi: 10.1001/archopht.118.3.351
35. Bae HW, Lee N, Lee HS, Hong S, Seong GJ, Kim CY. Systemic hypertension as a risk factor for open-angle glaucoma: a meta-analysis of population-based studies. *PLoS ONE.* (2014) 9:e108226. doi: 10.1371/journal.pone.0108226
36. Bata AM, Fondi K, Szegedi S, Aschinger GC, Hommer A, Schmidl D, et al. Age-related decline of retinal oxygen extraction in healthy subjects. *Invest Ophthalmol Vis Sci.* (2019) 60:3162–9. doi: 10.1167/iovs.18-26234
37. Lin Y, Jiang H, Liu Y, Rosa Gameiro G, Gregori G, Dong C, et al. Age-related alterations in retinal tissue perfusion and volumetric vessel density. *Invest Opthalmol Vis Sci.* (2019) 60:685. doi: 10.1167/iovs.18-25864
38. Chua J, Sim R, Tan B, Wong D, Yao X, Liu X, et al. Optical coherence tomography angiography in diabetes and diabetic retinopathy. *J Clin Med.* (2020) 9:1723. doi: 10.3390/jcm9061723
39. Chua J, Cheung CYL, Schmetterer L, Wong TY. Hypertensive fundus, changes. In: *Retinal Vascular Disease*. Singapore: Springer (2020). p. 85–97. doi: 10.1007/978-981-15-4075-2_9
40. Roerecke M, Kaczorowski J, Myers MG. Comparing automated office blood pressure readings with other methods of blood pressure measurement for identifying patients with possible hypertension. *JAMA Intern Med.* (2019) 179:351. doi: 10.1001/jamainternmed.2018.6551

41. A randomized trial of intensive vs. standard blood-pressure control. *N Engl J Med.* (2015) 373, 2103–2116. doi: 10.1056/NEJMoa1511939
42. Levy BI, Ambrosio G, Pries AR, Struijker-Boudier, HAJ. Microcirculation in hypertension. *Circulation.* (2001) 104:735–40. doi: 10.1161/hc3101.091158
43. Frost S, Nolde JM, Chan J, Joyson A, Gregory C, Carnagarin R, et al. Retinal capillary rarefaction is associated with arterial and kidney damage in hypertension. *Sci Rep.* (2021) 11:1001. doi: 10.1038/s41598-020-79594-3
44. *StatsToDo: Combine Means and SDs Into One Group Program.* (n.d.). StatsToDo. Retrieved from: https://www.statstodo.com/CombineMeansSDs.php (accessed June 19, 2021).
45. Review Manager (Revman). (2020). [Computer Program]. Version 5.4, The Cochrane Collaboration.
46. Higgins JPT, Li T, Deeks JJ. Chapter 6: Choosing effect measures and computing estimates of effect. In: Higgins JPT, Thomas J, Chandler J, Cumpston M, Li T, Page MJ, Welch VA, editors. *Cochrane Handbook for Systematic Reviews of Interventions, 2nd Ed.* (2019). Retrieved from: https://training.cochrane.org/handbook/current/chapter-06 (accessed June 19, 2021).
47. Higgins JPT, Li T, Deeks JJ. Chapter 10: Analysing data and undertaking meta-analyses. In: Higgins JPT, Thomas J, Chandler J, Cumpston M, Li T, Page MJ, Welch VA, editors. *Cochrane Handbook for Systematic Reviews of Interventions, 2nd Ed.* (2019). Retrieved from: https://training.cochrane.org/handbook/current/chapter-10 (accessed June 19, 2021).

Conflict of Interest: The authors declare that the research was conducted in the absence of any commercial or financial relationships that could be construed as a potential conflict of interest.

Publisher's Note: All claims expressed in this article are solely those of the authors and do not necessarily represent those of their affiliated organizations, or those of the publisher, the editors and the reviewers. Any product that may be evaluated in this article, or claim that may be made by its manufacturer, is not guaranteed or endorsed by the publisher.

frontiers in Medicine

ORIGINAL RESEARCH
published: 09 December 2021
doi: 10.3389/fmed.2021.777685

Agreement and Repeatability of Central and Peripheral Refraction by One Novel Multispectral-Based Refractor

*Weicong Lu†, Rongyuan Ji†, Wenzhi Ding, Yuyin Tian, Keli Long, Zhen Guo and Lin Leng**

State Key Laboratory Cultivation Base, Shandong Provincial Key Laboratory of Ophthalmology, Eye Institute of Shandong First Medical University, Qingdao Eye Hospital of Shandong First Medical University, Qingdao, China

Purpose: To evaluate the repeatability of a multispectral-based refractor in central and peripheral refraction measurement, and to assess the agreement of such measurements with objective refraction (OR) and subjective refraction (SR) in patients with myopia.

Methods: A total of 60 subjects were recruited in this prospective research. Patients were divided into three groups according to the refractive error. Next, the central and peripheral refraction parameters were measured using multispectral refractive tomography (MRT) before and after cycloplegia. In addition, OR and SR measurements were also performed. The intraobserver repeatability was analyzed using within-subject standard deviation (Sw), test–retest repeatability (TRT), and intraclass correlation coefficient (ICC). Agreement was evaluated using Bland-Altman plot and 95% limits of agreement (LoA).

Results: The ICC value of central and peripheral refraction were all higher than 0.97 with or without cycloplegia. The peripheral refraction in the nasal, temporal, superior, and inferior quadrants was slightly worse than other parameters, with the largest error interval being 1.43 D. The 95% LoA of the central refraction and OR or SR ranged from −0.89 to 0.88 D and −1.24 to 1.16 D without cycloplegia, respectively, and from −0.80 to 0.42 D and −1.39 to −0.84 D under cycloplegia, respectively.

Conclusions: The novel multispectral refraction topography demonstrated good repeatability in central and peripheral refraction. However, the refraction in the nasal, temporal, superior, and inferior quadrants were not as good as that of central and circle peripheral refraction.

Keywords: agreement, repeatability, refraction, myopia, ophthalmology

OPEN ACCESS

Edited by:
Peng Xiao,
Sun Yat-sen University, China

Reviewed by:
FangJun Bao,
Affiliated Eye Hospital of Wenzhou Medical College, China
Jun Jiang,
Wenzhou Medical University, China

***Correspondence:**
Lin Leng
coollin.1987@163.com

†These authors have contributed equally to this work

Specialty section:
This article was submitted to Ophthalmology, a section of the journal Frontiers in Medicine

Received: *15 September 2021*
Accepted: *11 November 2021*
Published: *09 December 2021*

Citation:
Lu W, Ji R, Ding W, Tian Y, Long K, Guo Z and Leng L (2021) Agreement and Repeatability of Central and Peripheral Refraction by One Novel Multispectral-Based Refractor. Front. Med. 8:777685. doi: 10.3389/fmed.2021.777685

INTRODUCTION

In the past few decades, myopia has emerged as a worldwide public health issue due to its rapidly increasing prevalence (1). The overall prevalence of myopia is ∼40% in the United States and >80% in young adults in China (2). In developed countries, 15 to 49% of the adult population suffer from myopia (3). It is worth noting that myopia is a complex disease. Evidence suggests that genetic and

environmental factors play important roles in its occurrence and development (4). However, its pathogenesis has not yet been fully elucidated. In recent years, many clinical studies have proposed that visual signals from the peripheral retina might induce myopia (5). Moreover, studies involving animal models have demonstrated that the peripheral retina refraction status dominated refractive changes whenever conflicts occur between the fovea and the peripheral visual signals (6). Therefore, this finding calls for the measurement of both the central and relative peripheral refractive errors with the overarching goal of elucidating the mechanisms of myopic development (7). It has been reported that inhibiting the progression of myopia by reducing the hyperopic defocus of the peripheral retina following a refractive correction is an effective method (8).

A study has revealed that using an autorefractor for objective refraction during the initial process in myopia examination is a reliable method compared with the use of subjective refraction (9). WAM-5500 (Grand Seiko Co., Hiroshima, Japan), a binocular, open-field, infrared, and ref/keratometer, is generally used in the clinic to measure central and peripheral retina refractive because of its well-documented repeatability (10, 11). However, its use is associated with certain difficulties and challenges in patients wearing optic lenses, and the measurement region is limited to a few specific spots only (12). To address these limitations, multispectral refractive tomography (MRT) (version 1.0.5T05C; Thondar, Inc. China), a novel multispectral-based computing system, was designed to measure the spherical equivalent (SE) of a 53-degree fundus field of view within 2–3 s. MRT simultaneously obtains the refractive power of all retinal regions, including the central and peripheral retina, within a certain range. In MRT, there is one internal fixation point rather than having the fixation point being moved in different positions and angles. Given that MRT is a newly introduced device, its repeatability should be investigated to broaden its clinical application. This study aimed to explore the repeatability of the measurements obtained using the MRT device and assess the agreement among the refractive measurements made using MRT, Topcon KR-1 (Topcon, Tokyo, Japan), and subjective refraction.

MATERIALS AND METHODS

Patients

In this prospective study, 60 subjects who visited the Qingdao Eye Hospital of Shandong First Medical University for regular examination in August 2021 were recruited. Only the right eye of each patient was examined in this study. Patients were divided into three groups according to the SE measured by the subjective refraction (NIDEK AOS1500+SSC3): low myopia group (−3.00 D<SE≤-0.50 D), moderate myopia group (−6.00 D<SE≤-3.00 D), and high myopia group (SE≤-6.00 D) (13). The study was approved by the Ethics Committee of Qingdao Eye Hospital of Shandong First Medical University (ChiCTR2100049050) and adhered to the tenets of the Declaration of Helsinki. Signed informed consent was obtained from all patients prior to the conduct of this study.

The enrolled patients met the following inclusion criteria: age > 18 years, astigmatism diopter < 3.0 D, no history of cornea refractive surgery, no history of ocular trauma, and agreed to stop wearing contact lenses for at least 2 weeks for soft contact lenses and 4 weeks for rigid gas-permeable contact lenses before the examination.

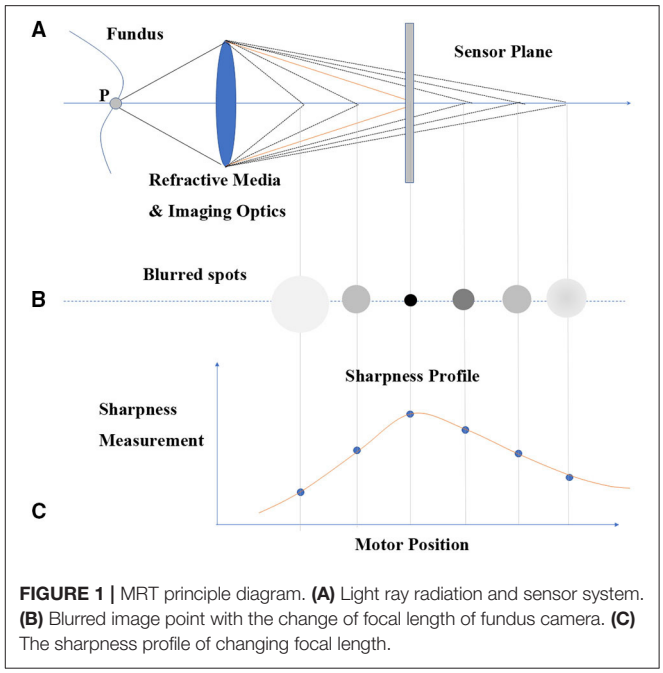

FIGURE 1 | MRT principle diagram. **(A)** Light ray radiation and sensor system. **(B)** Blurred image point with the change of focal length of fundus camera. **(C)** The sharpness profile of changing focal length.

Instrument and Methods

MRT was designed according to the simplified reduced optical model. Light rays were radiated from one ideal point (P) of fundus and were transmitted via an optical path, comprising the refractive media of human eye and imaging optics of fundus camera. Images were ultimately formed on the sensor plane (**Figure 1A**). When the focal length of the fundus camera was adjusted, the image point was accommodated accordingly into relative defocused status, shaping into a blurred spot with different sizes and gray levels (**Figure 1B**). In the fundus camera imaging process, the radiation originated from a fundus surface rather than from an ideal point. Consequently, the fundus image was blurred to different degrees in different focal lengths, which was controlled by the focus motor. A focus measure, such as the Sobel operator, was applied to measure the sharpness of each region of interest (ROI) in the fundus, representing a particular viewing angle such as the central view, nasal 10° eccentricity, and temporal 25°. As shown in **Figure 1C**, a sharpness profile of the changes in focal length was obtained for a particular viewing angle. The maximum sharpness of the sharpness profile correlated with the situation when point P was focused on the sensor plane. The motor position when the maximum sharpness was obtained in a given imaging optical system represents the specific optic setup from which the human eye refraction was calculated. A sequential calculation for all ROIs in the defined field of view generated a refraction tomography. Notably, the device can provide both central and peripheral refractive errors with different eccentricities.

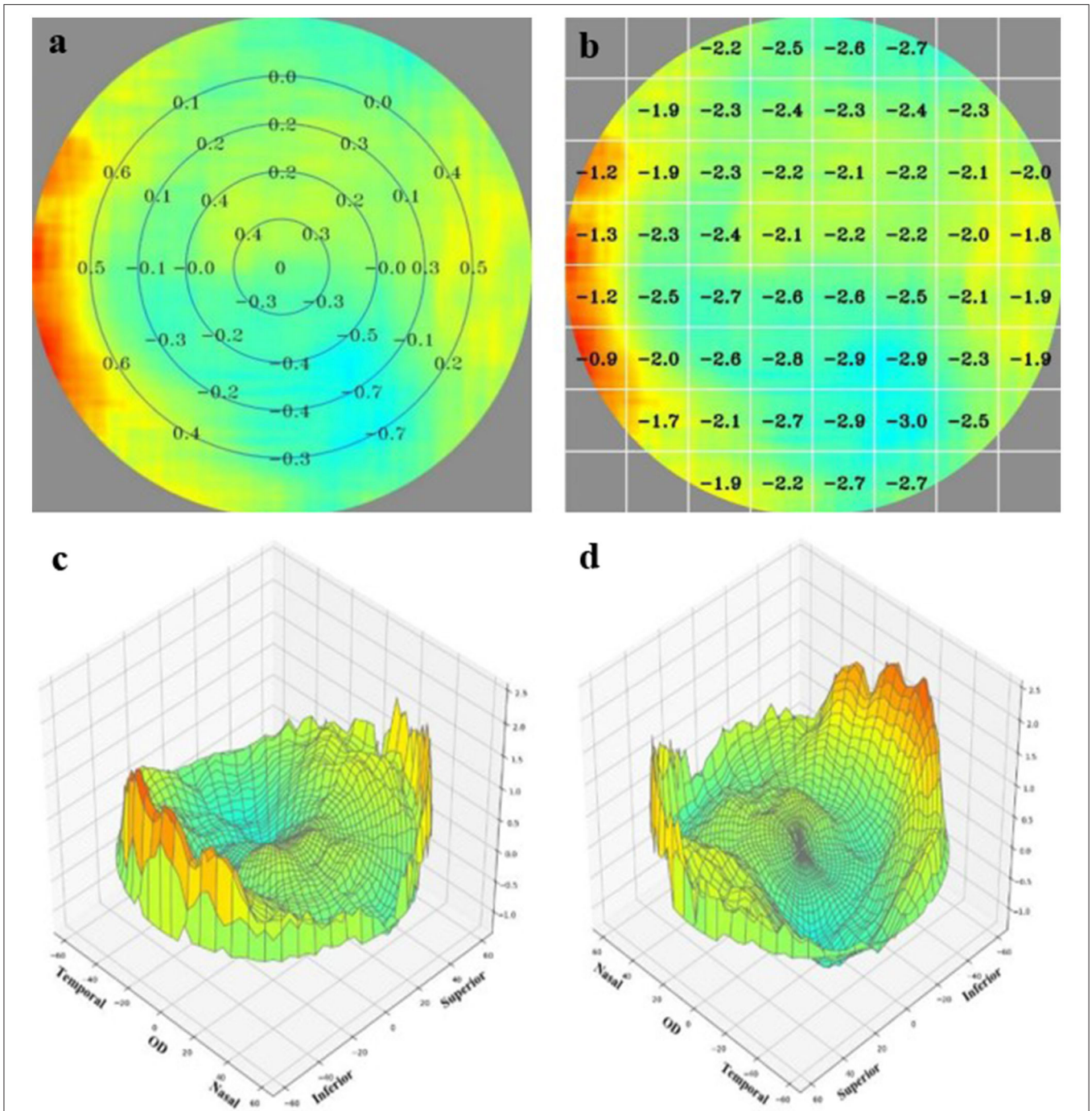

FIGURE 2 | The result provided by the MRT analysis system. **(a)** The relative peripheral refraction defocus value. **(b)** The block-refraction of absolute refraction value. **(c,d)** A direct view of the relative fraction status of the retinal by three-dimensional images viewing from superotemporal and inferonasal, respectively.

Next, image analysis was performed and an algorithm was used to decouple and generate the refractive value of each imaging data point. This approach could determine the SE of 128 × 128 points on a 53-degree field of view of the fundus, with a data point of 0.5° in between. After each data point was acquired, a set of images processed by a custom compensation software was obtained using the color-coded approach (**Figure 2**). Relative peripheral refraction defocus was the difference between the absolute refraction and the central macular refraction and was translated into color images (**Figure 2a**). Block-refraction provided an absolute refraction value using each value as mean data for each corresponding

TABLE 1 | Intraobserver repeatability outcomes of central and peripheral refraction using MRT without cycloplegia.

Parameters	Mean	SD	Sw	TRT	ICC
CRE	−5.28	1.96	0.37	1.04	0.988
TRDV	−4.53	1.89	0.36	1.02	0.987
RDV-15	−5.09	1.89	0.42	1.16	0.983
RDV-30	−4.77	1.88	0.38	1.06	0.986
RDV-45	−4.55	1.88	0.35	0.98	0.988
RDV-S	−4.80	1.88	0.51	1.43	0.974
RDV-I	−4.41	1.94	0.50	1.39	0.977
RDV-T	−4.85	2.04	0.43	1.20	0.984
RDV-N	−4.07	1.94	0.51	1.42	0.976

CRE, central refractive error; TRDV, peripheral refractive error from center to peripheral 53°of retina; RDV-15, the difference of CRE and paracentral refractive error from center to 15°of retina; RDV-30, the difference of CRE and paracentral refractive error from center to 30°of retina; RDV-45, the difference of CRE and paracentral refractive error from center to 45°of retina; RDV-S, refraction difference value-superior; RDV-I, refraction difference value-inferior; RDV-T, refraction difference value- refraction difference value-temporal; RDV-N, refraction difference value-nasal; SD, standard deviation; Sw, standard deviation; TRT, test–retest repeatability; ICC, intraclass correlation coefficient.

block (**Figure 2b**). The three-dimensional (3D) images of superotemporal and inferonasal retina provide a direct view of the relative fraction status of the retina (**Figures 2c,d**).

Prior to the experiment, the patients were subjected to routine examinations, including visual acuity examination, slit-lamp examination of the anterior segment, and fundus evaluations. The examinations were conducted between 1,000 and 1,700 h by an experienced doctor to avoid the influence of diurnal variation (14). Initially, patients were positioned on the headrest and asked to fix their attention to the internal target. Next, the patients were asked to blink twice before measurement to ensure that the tear film coating cornea surface was intact. All MRT measurements were carried out by an experienced doctor. Each patient was examined three times to evaluate the intraobserver repeatability. Objective refraction (OR) using Topcon KR-1 and subjective refraction (SR) were conducted by another doctor who was blinded to the previous examination results. Next, compound tropicamide 0.5% and phenylephrine 0.5% (SINQI Pharmaceutical Co., Ltd., Shenyang, China) was used three times, with an interval of 5 min to induce cycloplegia until the pupil diameter reached 7–8 mm to relax the accommodation. The MRT, OR, and SR examinations were repeated by the same doctor to minimize the operator-related error.

The parameters obtained using MRT for further analysis were as follows: central refractive error (CRE); total refraction difference value, which indicates the average peripheral refractive error from the center to the peripheral 53° of the retina (TRDV); refraction difference value-15 which indicates the average paracentral refractive error from the center to 15° of the retina (RDV-15); refraction difference value-30 and 45 (RDV-30, and RDV-45, respectively) which indicate the average peripheral refractive error at 30 and 45° of the posterior retina, respectively, refraction difference value-inferior (RDV-I); refraction difference value-superior (RDV-S); refraction difference value-nasal (RDV-N); and refraction difference value-temporal (RDV-T). The measurement quality was estimated by a computer to avoid the influence of iris reflection, eye blinking, and dim illumination, and only those results with a quality score of >80% were recorded for further analysis. For the SR examination, the OR was used as the baseline value instead of the MRT so as not to influence the examination being conducted.

Statistical Analysis

All statistical analyses were performed using SPSS software (version 24.0; IBM Corporation, Armonk, NY) and Medcalc software (version 24.0; IBM Corporation, Armonk, NY). All data were recorded as mean ± standard deviation (SD). Data distribution was analyzed by the Kolmogorov–Smirnov test to determine normally distributed data ($P > 0.05$). To assess the intraoperator repeatability of MRT, one-way analysis of variance (ANOVA) was used to calculate the within-subject standard deviation (Sw), the test–retest repeatability (TRT), and the intraclass correlation coefficient (ICC). The Sw is the intraoperator deviation derived from the three consecutive measurements. When the TRT is equal to 2.77 Sw represents the 95% measurement deviation interval within which the measurement error should lie. ICC is a common parameter used to evaluate repeatability and is defined as the ratio of variance between individual measurements to the sum. In clinical application, an ICC value larger than 0.9 indicates high repeatability. However, an ICC value of 0.75 is acceptable in statistical applications (15).

The mean of the three consecutive measurements was used in assessing agreement with the SR and OR. For the agreement evaluation, the MedCalc statistical software (version 18.2.1, Ostend, Belgium) was used to draw the Bland-Altman plots. The 95% limit of agreement (LoA) was drawn according to the mean difference ± 1.96 SD between two methods, and it indicates the measurement error of these methods (16).

RESULTS

Sixty patients were recruited in this study, and the average age was 27.25 ± 6.70 years (range: 18–36 years). The mean SE before and after cycloplegia was −5.28 ± 1.95 D and −4.93 ± 1.94 D for OR, respectively, and −5.32 ± 1.82 D and 5.01 ± 1.85 D for SR, respectively. The mean SE in each group with sample sizes of 19,

21, and 20 was −2.51 ± 0.82 D, −5.02 ± 0.61 D, and −7.13 ± 0.87 D, respectively.

Intraoperator Repeatability

Table 1 shows the repeatability of MRT in central and peripheral refraction measurements in patients with myopia before cycloplegia. The ICC values were all above 0.97. Similarly, the Sw and TRT results supported the good repeatability of CRE, TRDV, RDV-15, RDV-30, and RDV-45, but the RDV of different quadrants was slightly worse. The largest error interval was 1.43 D, indicating that the variation among the measurements for superior peripheral refraction could reach 1.43 D. However, the repeatability of these parameters significantly improved after cycloplegia, with all ICC values higher than 0.99. The Sw and TRT were smaller in CRE, TRDV, RDV-15, RDV-30, and RDV-45 in the cycloplegia group than in the non-cycloplegia group (**Table 2**). Notably, the RDV for the different quadrants remained the same in the cycloplegia group compared with that in the non-cycloplegia group, with the exception of RDV-I measurement, as its repeatability improved.

Furthermore, we analyzed the repeatability of different refractive errors. As shown in **Tables 3**–**5**, the CRE, TRDV, RDV-15, RDV-30, and RDV-45 all showed good repeatability, and the high myopia group without cycloplegia showed the highest degree of repeatability. Moreover, the RDV-I, RDV-S, RDV-N, and RDV-T demonstrated a lower degree of repeatability than the CRE, TRDV, RDV-15, RDV-30, and RDV-45, and patients in the low myopia group were the most easily influenced by these parameters. The ICC values for the RDV-I, RDV-S, RDV-N, and RDV-T in the low myopia group ranged from 0.83 to 0.89, and increased with the increment of myopia diopter. **Tables 6**–**8** show the results obtained after cycloplegia. Moreover, the repeatability of the measurements in the quadrants were slightly of lower degree than that of CRE, TRDV, RDV-15, RDV-30, and RDV-45. However, all ICC values were higher than 0.9, indicating that repeatability remained good for the three groups.

Agreement

Figure 3 shows the Bland-Altman plots comparing MRT and OR before cycloplegia. Results demonstrated that there was no significant difference in CRE and OR, and the 95% LoA ranged from −0.89 to 0.88 D, indicating a good agreement. However, the difference between peripheral refraction and OR is higher compared with the difference between CRE and OR. In addition, the refractive error in the peripheral retina was smaller than the OR, although the interval of 95% LoA was stable (nearly 2.5 D). Meanwhile, the RDV-I, RDV-S, RDV-N, and RDV-T values increased up to nearly 3.0 D. A similar result as regard the agreement between MRT and SR was observed (**Figure 4**). The 95% LoA of CRE and SR ranged from −1.24 to 1.14 D, and RDV-I, RDV-S, RDV-N, and RDV-T demonstrated a lower degree of agreement.

Similarly, the 95% LoA of CRE and OR ranged from −0.80 to 0.42 D after cycloplegia, suggesting that cycloplegia could enhance the agreement given that the accommodation was relaxed (**Figure 5**). Notably, the peripheral refraction was more remarkable in RDV-45. RDV-S demonstrated the largest 95% LoA, which ranged from −3.0 to 0.6 D, indicating a low degree of agreement in different quadrants. Moreover, RDV-S showed a higher degree of the agreement with the OR group than with the SR group, and it had the largest interval that ranged from −3.3 to 0.7 D (**Figure 6**).

DISCUSSION

Myopia, a multi-factor-related disease, is the most prevalent disorder worldwide (17). Previous studies have confirmed that peripheral hyperopia refractive status plays a crucial role in myopia progression, especially in patients who need spectacle correction (18). Therefore, measurement of the peripheral refractive error is an important aspect in clinical application (19). Although the measurement can be done using the WAM-5500, the intrinsic limitations of spots calculation restrict its further application (11). Such disadvantages can be overcome by MRT, a novel device that can measure the large areas of peripheral refraction. This study explored the repeatability of using MRT to measure central and peripheral refraction before and after cycloplegia in different groups. The results were also compared with the OR and SR measurements obtained under the same conditions.

The current results demonstrated that MRT could provide reproducible results for CRE, TRDV, RDV-15, RDV-30, and RDV-45 without cycloplegia, and the RDV showed a slightly lower degree of repeatability in the four different quadrants. It should be noted that MRT adopts a mechanism similar to that of autorefractors. To our best knowledge, this study was the first to evaluate the repeatability of MRT. Our findings were consistent with that of other studies that evaluated the repeatability of autorefractors in non-cycloplegia refractive error. For example, Nguyen and Berntsen (10) found that the sphere was −0.34 D, with a 95% LoA ranging from −0.37 to 0.32 D without cycloplegia. Allen et al. (20) reported that the repeatability of an autorefractor had a 95% LoA ranging from −0.45 to 0.47 D. Moreover, Elliott et al. (21) investigated the repeatability of Nikon NRK-8000, Nidek AR-1000, and SR, and they have found that the COR values for these three methods were 0.71, 0.26, and 0.61 D, respectively. The above findings are consistent with our results, confirming that MRT could demonstrate a good repeatability in central refraction measurement. In addition, the repeatability of MRT was significantly enhanced after the cycloplegia, which may be attributed to the fact that the cycloplegia could have relaxed the ciliary muscle, thereby reducing the accommodation reflex. Nguyen and Berntsen (10) found that when the pupil size was 6 mm, the repeatability of sphere diopter was ± 0.32 D. Hernandez-Moreno et al. (22) also investigated the repeatability of SE in a pediatric population, and they found that a 95% LoA ranging from −0.66 to +0.65 D with cycloplegia and from −1.38 to +1.74 D without cycloplegia. These findings suggested that the autorefractor had a low repeatability under non-cycloplegia conditions, but such a degree of repeatability is acceptable under cycloplegic conditions. Their results are consistent with our finding showing that cycloplegia could enhance the repeatability of MRT.

TABLE 2 | Intraobserver repeatability outcomes of central and peripheral refraction using MRT with cycloplegia.

Parameters	Mean	SD	Sw	TRT	ICC
CRE	−4.74	1.89	0.27	0.76	0.993
TRDV	−3.56	1.82	0.27	0.75	0.992
RDV-15	−4.32	1.90	0.33	0.92	0.990
RDV-30	−3.95	1.86	0.30	0.852	0.991
RDV-45	−3.63	1.85	0.28	0.79	0.992
RDV-S	−3.71	1.90	0.45	1.25	0.980
RDV-I	−3.49	1.90	0.37	1.03	0.987
RDV-T	−3.87	1.95	0.50	1.39	0.978
RDV-N	−3.09	1.98	0.50	1.41	0.977

CRE, central refractive error; TRDV, peripheral refractive error from center to peripheral 53°of retina; RDV-15, the difference of CRE and paracentral refractive error from center to 15°of retina; RDV-30, the difference of CRE and paracentral refractive error from center to 30°of retina; RDV-45, the difference of CRE and paracentral refractive error from center to 45°of retina; RDV-S, refraction difference value-superior; RDV-I, refraction difference value-inferior; RDV-T, refraction difference value- refraction difference value-temporal; RDV-N, refraction difference value-nasal; SD, standard deviation; Sw, standard deviation; TRT, test–retest repeatability; ICC, intraclass correlation coefficient.

TABLE 3 | Intraobserver repeatability outcomes of central and peripheral refraction using MRT without cycloplegia of low myopia group.

Parameters	Mean	SD	Sw	TRT	ICC
CRE	−2.97	0.82	0.41	1.13	0.909
TRDV	−2.45	0.84	0.38	1.07	0.917
RDV-15	−3.03	1.01	0.42	1.17	0.937
RDV-30	−2.71	0.95	0.38	1.06	0.942
RDV-45	−2.47	0.86	0.36	1.01	0.934
RDV-S	−2.75	0.84	0.52	1.44	0.833
RDV-I	−2.43	1.19	0.63	1.76	0.889
RDV-T	−2.65	0.92	0.48	1.34	0.896
RDV-N	−1.98	1.08	0.62	1.71	0.869

CRE, central refractive error; TRDV, peripheral refractive error from center to peripheral 53°of retina; RDV-15, the difference of CRE and paracentral refractive error from center to 15°of retina; RDV-30, the difference of CRE and paracentral refractive error from center to 30°of retina; RDV-45, the difference of CRE and paracentral refractive error from center to 45°of retina; RDV-S, refraction difference value-superior; RDV-I, refraction difference value-inferior; RDV-T, refraction difference value- refraction difference value-temporal; RDV-N, refraction difference value-nasal; SD, standard deviation; Sw, standard deviation; TRT, test–retest repeatability; ICC, intraclass correlation coefficient.

TABLE 4 | Intraobserver repeatability outcomes of central and peripheral refraction using MRT without cycloplegia of moderate myopia group.

Parameters	Mean	SD	Sw	TRT	ICC
CRE	−5.41	0.95	0.39	1.09	0.936
TRDV	−4.76	1.09	0.39	1.09	0.955
RDV-15	−5.31	1.05	0.50	1.39	0.912
RDV-30	−5.00	1.05	0.44	1.24	0.933
RDV-45	−4.78	1.07	0.39	1.09	0.953
RDV-S	−5.05	1.11	0.57	1.59	0.897
RDV-I	−4.56	1.23	0.46	1.27	0.949
RDV-T	−5.12	1.33	0.42	1.16	0.964
RDV-N	−4.33	1.09	0.53	1.47	0.920

CRE, central refractive error; TRDV, peripheral refractive error from center to peripheral 53°of retina; RDV-15, the difference of CRE and paracentral refractive error from center to 15°of retina; RDV-30, the difference of CRE and paracentral refractive error from center to 30°of retina; RDV-45, the difference of CRE and paracentral refractive error from center to 45°of retina; RDV-S, refraction difference value-superior; RDV-I, refraction difference value-inferior; RDV-T, refraction difference value- refraction difference value-temporal; RDV-N, refraction difference value-nasal; SD, standard deviation; Sw, standard deviation; TRT, test–retest repeatability; ICC, intraclass correlation coefficient.

TABLE 5 | Intraobserver repeatability outcomes of central and peripheral refraction using MRT without cycloplegia of high myopia group.

Parameters	Mean	SD	Sw	TRT	ICC
CRE	−7.33	0.85	0.32	0.89	0.954
TRDV	−6.39	0.81	0.35	0.98	0.931
RDV-15	−6.97	0.78	0.30	0.85	0.948
RDV-30	−6.63	0.76	0.30	0.84	0.945
RDV-45	−6.43	0.78	0.33	0.92	0.936
RDV-S	−6.60	0.92	0.46	1.29	0.902
RDV-I	−6.26	0.90	0.41	1.15	0.920
RDV-T	−6.79	0.94	0.46	1.29	0.904
RDV-N	−5.92	0.90	0.38	1.05	0.936

CRE, central refractive error; TRDV, peripheral refractive error from center to peripheral 53°of retina; RDV-15, the difference of CRE and paracentral refractive error from center to 15°of retina; RDV-30, the difference of CRE and paracentral refractive error from center to 30°of retina; RDV-45, the difference of CRE and paracentral refractive error from center to 45°of retina; RDV-S, refraction difference value-superior; RDV-I, refraction difference value-inferior; RDV-T, refraction difference value- refraction difference value-temporal; RDV-N, refraction difference value-nasal; SD, standard deviation; Sw, standard deviation; TRT, test–retest repeatability; ICC, intraclass correlation coefficient.

TABLE 6 | Intraobserver repeatability outcomes of central and peripheral refraction using MRT with cycloplegia of low myopia group.

Parameters	Mean	SD	Sw	TRT	ICC
CRE	−2.46	0.54	0.24	0.67	0.921
TRDV	−1.45	0.65	0.20	0.57	0.965
RDV-15	−2.03	0.63	0.22	0.63	0.952
RDV-30	−1.71	0.63	0.19	0.54	0.966
RDV-45	−1.44	0.65	0.21	0.60	0.962
RDV-S	−1.68	0.83	0.36	1.02	0.925
RDV-I	−1.31	0.77	0.29	0.81	0.951
RDV-T	−1.65	0.73	0.23	0.65	0.964
RDV-N	−0.92	0.97	0.35	0.97	0.952

CRE, central refractive error; TRDV, peripheral refractive error from center to peripheral 53°of retina; RDV-15, the difference of CRE and paracentral refractive error from center to 15°of retina; RDV-30, the difference of CRE and paracentral refractive error from center to 30°of retina; RDV-45, the difference of CRE and paracentral refractive error from center to 45°of retina; RDV-S, refraction difference value-superior; RDV-I, refraction difference value-inferior; RDV-T, refraction difference value- refraction difference value-temporal; RDV-N, refraction difference value-nasal; SD, standard deviation; Sw, standard deviation; TRT, test–retest repeatability; ICC, intraclass correlation coefficient.

TABLE 7 | Intraobserver repeatability outcomes of central and peripheral refraction using MRT with cycloplegia of moderate myopia group.

Parameters	Mean	SD	Sw	TRT	ICC
CRE	−4.86	0.81	0.31	0.88	0.943
TRDV	−3.74	1.00	0.28	0.78	0.972
RDV-15	−4.50	0.88	0.36	1.00	0.939
RDV-30	−4.13	0.88	0.32	0.88	0.954
RDV-45	−3.82	0.95	0.28	0.79	0.968
RDV-S	−3.83	1.31	0.54	1.51	0.934
RDV-I	−3.72	1.04	0.37	1.04	0.953
RDV-T	−4.17	1.28	0.67	1.86	0.895
RDV-N	−3.21	1.12	0.56	1.56	0.899

CRE, central refractive error; TRDV, peripheral refractive error from center to peripheral 53°of retina; RDV-15, the difference of CRE and paracentral refractive error from center to 15°of retina; RDV-30, the difference of CRE and paracentral refractive error from center to 30°of retina; RDV-45, the difference of CRE and paracentral refractive error from center to 45°of retina; RDV-S, refraction difference value-superior; RDV-I, refraction difference value-inferior; RDV-T, refraction difference value- refraction difference value-temporal; RDV-N, refraction difference value-nasal; SD, standard deviation; Sw, standard deviation; TRT, test–retest repeatability; ICC, intraclass correlation coefficient.

The peripheral refraction error determined using MRT also showed that the repeatability of the TRDV, RDV-15, RDV-30, and RDV-45 was better than that of the peripheral refractive error measured in the quadrants. RDV-S showed the lowest degree of repeatability in the non-cycloplegia group, but its repeatability was better under cycloplegic conditions. Notably,

TABLE 8 | Intraobserver repeatability outcomes of central and peripheral refraction using MRT with cycloplegia of high myopia group.

Parameters	Mean	SD	Sw	TRT	ICC
CRE	−6.77	0.86	0.25	0.71	0.968
TRDV	−5.39	0.94	0.31	0.86	0.961
RDV-15	−6.30	0.83	0.38	1.05	0.919
RDV-30	−5.88	0.85	0.37	1.03	0.926
RDV-45	−5.52	0.90	0.33	0.93	0.949
RDV-S	−5.52	1.09	0.41	1.13	0.948
RDV-I	−5.32	1.09	0.43	1.19	0.944
RDV-T	−5.66	1.10	0.47	1.32	0.933
RDV-N	−5.01	1.16	0.56	1.57	0.905

CRE, central refractive error; TRDV, peripheral refractive error from center to peripheral 53°of retina; RDV-15, the difference of CRE and paracentral refractive error from center to 15°of retina; RDV-30, the difference of CRE and paracentral refractive error from center to 30°of retina; RDV-45, the difference of CRE and paracentral refractive error from center to 45°of retina; RDV-S, refraction difference value-superior; RDV-I, refraction difference value-inferior; RDV-T, refraction difference value- refraction difference value-temporal; RDV-N, refraction difference value-nasal; SD, standard deviation; Sw, standard deviation; TRT, test–retest repeatability; ICC, intraclass correlation coefficient.

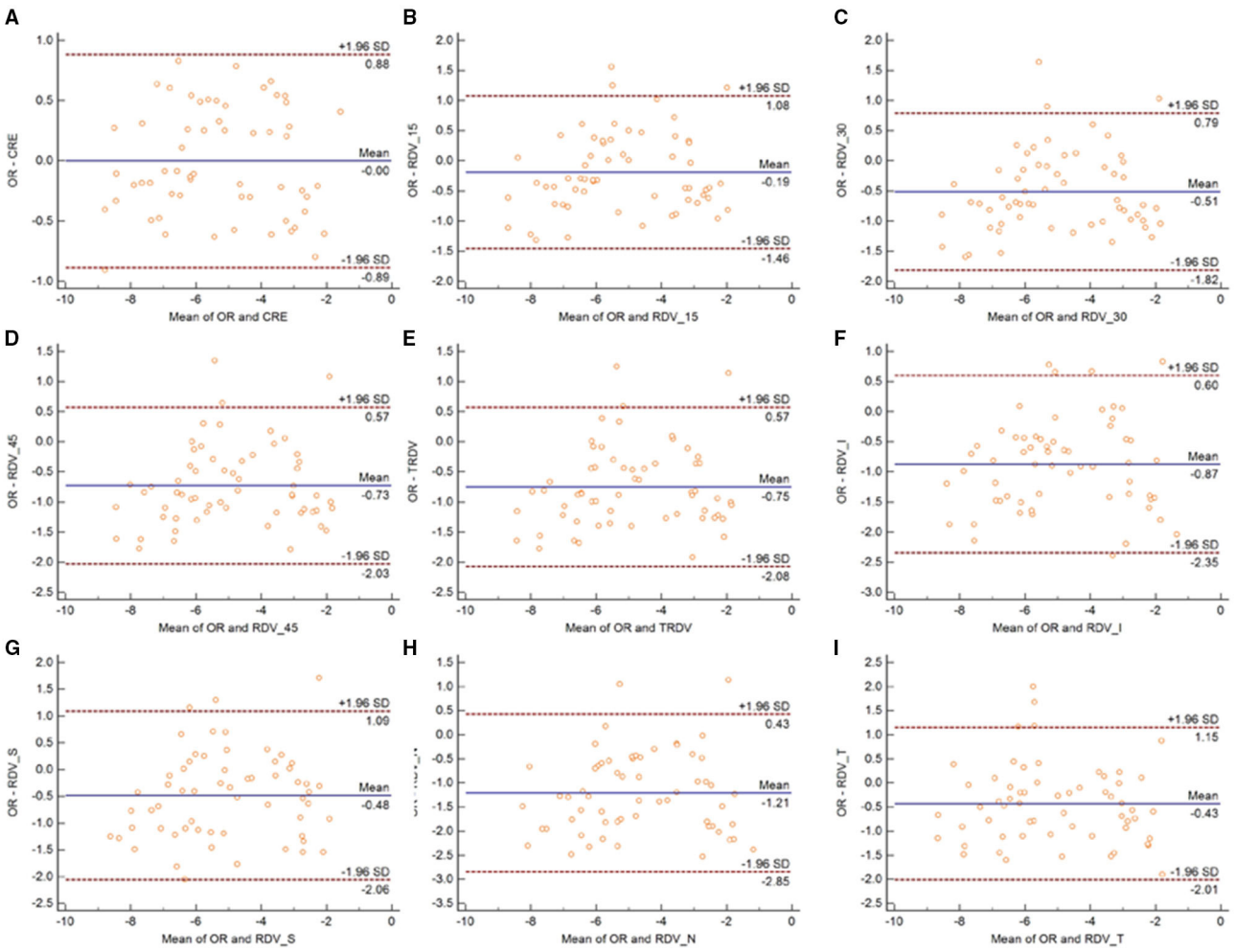

FIGURE 3 | Bland–Altman plots between SR and CRE **(A)**, RDV-15 **(B)**, RDV-30 **(C)**, RDV-45 **(D)**, TRVD **(E)**, RDV-I **(F)**, RDV-S **(G)**, RDV-N **(H)**, and RDV-T **(I)** in non-cycloplegia eyes. The solid line shows the mean difference (bias), and the upper and lower lines represent 95% limits of agreement.

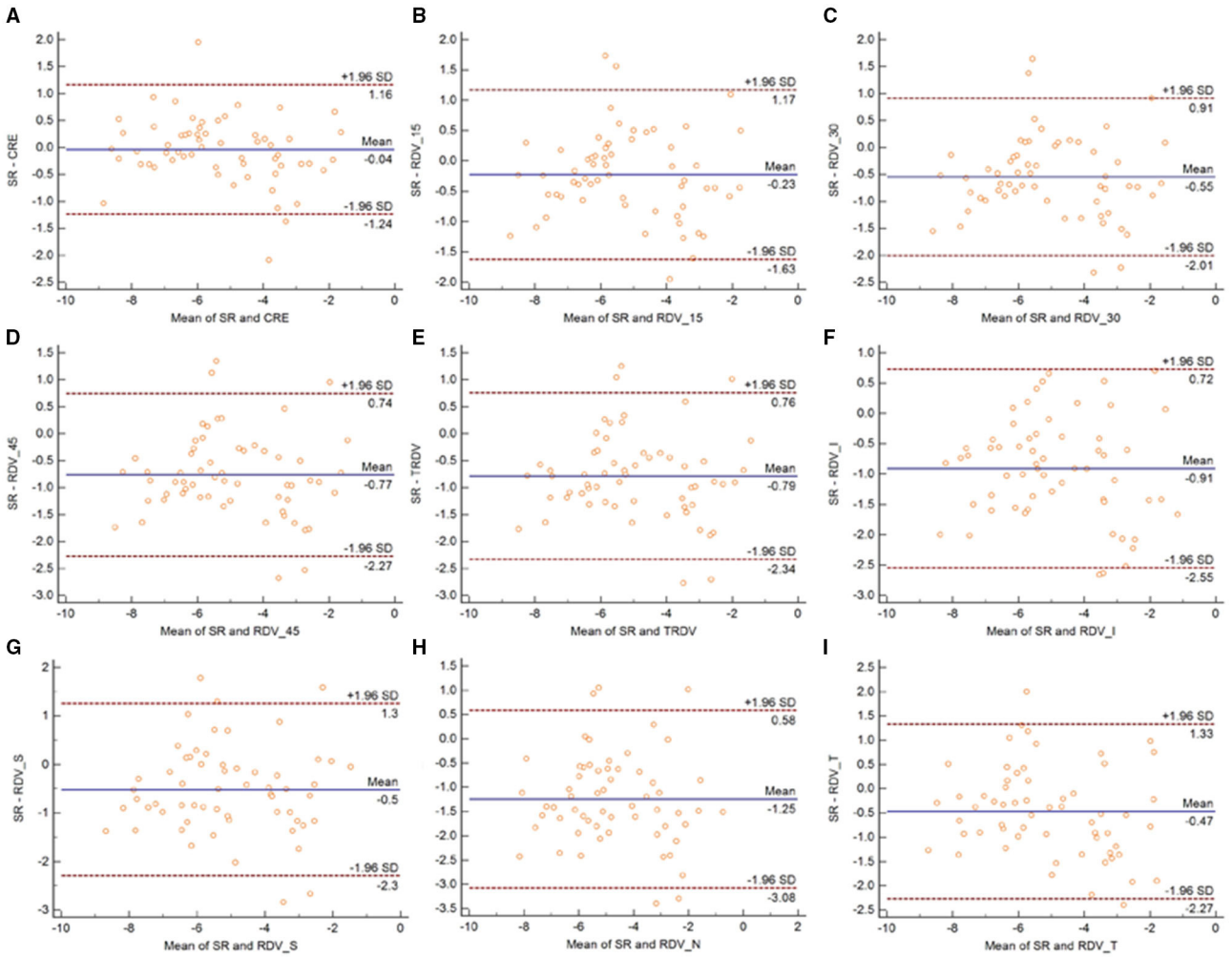

FIGURE 4 | Bland–Altman plots between OR and CRE **(A)**, RDV-15 **(B)**, RDV-30 **(C)**, RDV-45 **(D)**, TRVD I **(E)**, RDV-I **(F)**, RDV-S **(G)**, RDV-N **(H)**, and RDV-T **(I)** in non-cycloplegia eyes. The solid line shows the mean difference (bias), and the upper and lower lines represent 95% limits of agreement.

the RDV-N was the least easily influenced. We hypothesize that the upper eyelid pressure plays a role in peripheral refraction. As previously reported, eyelid pressure could induce corneal topographic changes and eyelid morphometry, so peripheral refraction would also be influenced by corneal topographic changes (23). Collectively, these results confirmed that the repeatability of MRT for the peripheral refraction measurements was associated with the measurement regions. The asphericity of the retina (especially in myopic eyes) may cause differences in the intensity of light ray distribution on the retina in different regions. This may explain the worse measurement results of the quadrants than the data of the circle. WAM-5500, frequently used in peripheral autorefraction, was selected as the reference since no research about the novel MRT has been published (11). In an investigation by Moore and Berntsen (11), the repeatability of cycloplegia autorefraction in normal eyes was ± 0.21 D, ± 0.42 D, ± 0.60 D, ± 0.73 D, ± 0.36 D, ± 0.47 D, and ± 0.88 D for central, 20°, 30°, 40° nasal, 20°, 30°, and 40°temporal, respectively, which are consistent with our results. By contrast, we found that the repeatability did not decrease as eccentricity increased. This phenomenon may be attributed to the fact that the spot measurement made by the WAM 5500, which has an open-field design, was based on the fixation point the patient stared at. When autorefractor measurements are being obtained at higher eccentricities, any changes in fixation could induce a measurement error and a lateral pupil misalignment, which also influence repeatability. Fedtke et al. (24) reported that even a 0.27 mm lateral misalignment of the pupil center would cause a 0.25 D change in peripheral defocus when measuring at 30° in the periphery of a myopic eye. Meanwhile, the MRT could calculate the entire retinal refraction in one measurement and analyze the peripheral refraction through adjustment in the focal length of the fundus camera in order to eliminate influence of misalignment of the pupil center.

This study found that the agreement of MRT with the OR or SR decreased as eccentricity increased. The majority of the

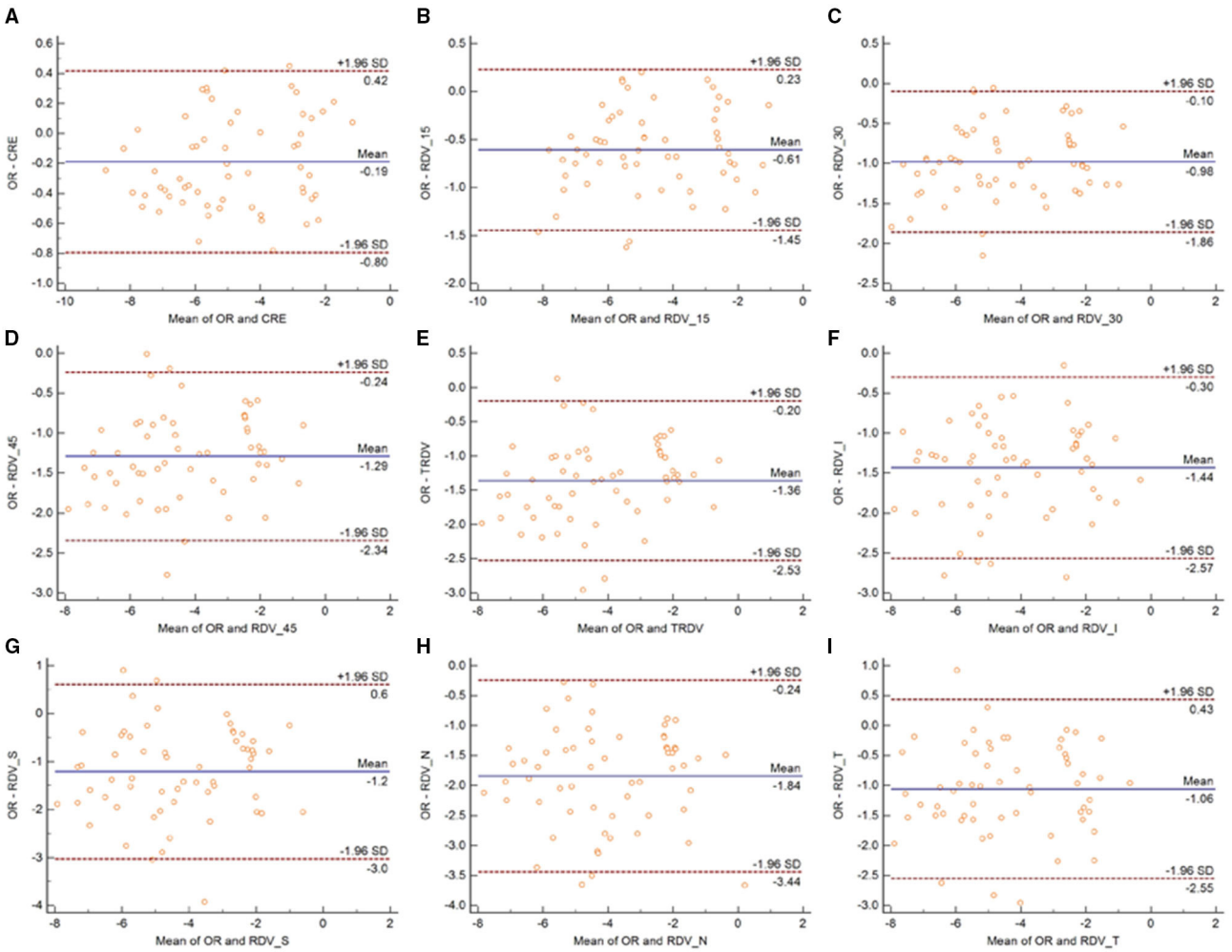

FIGURE 5 | Bland–Altman plots between SR and CRE **(A)**, RDV-15 **(B)**, RDV-30 **(C)**, RDV-45 **(D)**, TRVD **(E)**, RDV-I **(F)**, RDV-S **(G)**, RDV-N **(H)**, and RDV-T **(I)** in cycloplegia eyes. The solid line shows the mean difference (bias), and the upper and lower lines represent 95% limits of agreement.

patients had a noticeable peripheral hyperopia, consistent with previous findings (24). However, the average difference in the peripheral refractive error between MRT and OR was smaller than that between MRT and SR, and the central refractive error in OR was better than that in SR. This may be due to the fact that the SR could measure the exact macular refractive error and could consider the posterior retina as a sphere although its actual shape is ellipse. Liao et al. (25) have reported that the 95% LoA between MRT and autorefractometer ranged from −1.43 to 1.83 D. Similarly, we found that the same conclusion and the 95% interval of LoA was narrower. The MRT measurement in the peripheral retina may increase the difference compared with central retina, but it would still maintain the reliability. Carracedo et al. (26) compared two wavefront autorefractors (Eye Refract and VX110), and discovered the 95% LoA of refraction ranged from −0.99 to 0.59 D. We obtained the same conclusion: MRT is a good technique for central refractive error measurement, even under induced cycloplegia. The results showed that the cycloplegia group had significant peripheral hyperopia compared with the non-cycloplegia group, indicating that the patients could have more peripheral hyperopia status (0.5 D). This finding suggested that care should be taken during peripheral refractive measurement in patients with cycloplegia.

Although the repeatability of all patients with or without cycloplegia showed acceptable repeatability in central and peripheral refraction, we further investigated the relationship between repeatability and the degree of myopia. It was found that the repeatability in the quadrants was worse than others in all three groups, and cycloplegia could improve repeatability. We speculate that cycloplegia improved the repeatability because it enlarged the pupil by nearly 6.0 mm, which is significantly larger than the pupil under natural conditions. Therefore, peripheral measurements of a large pupil size could be easily conducted, and the lens was relaxed under cycloplegia, ensuring constant peripheral lens refraction.

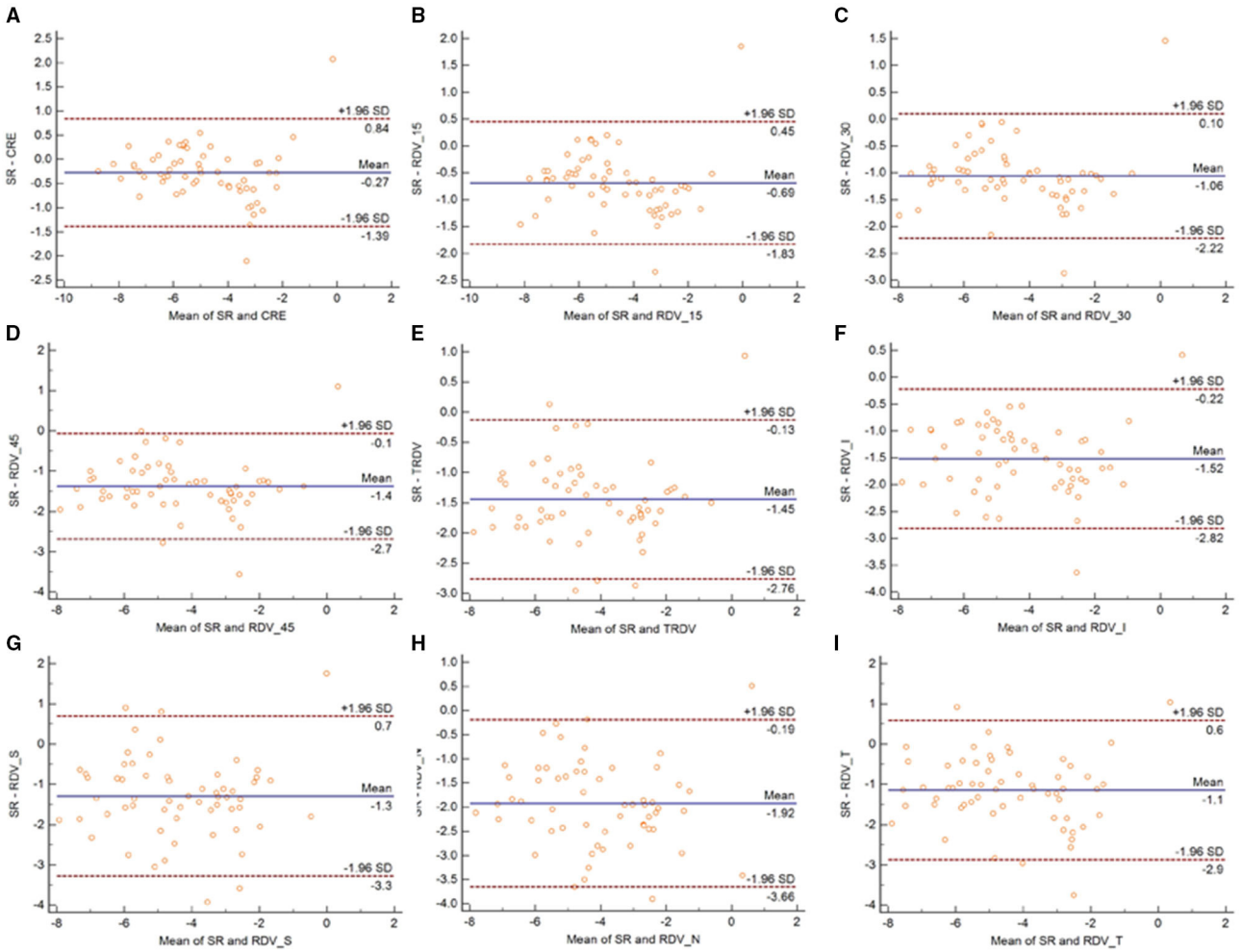

FIGURE 6 | Bland–Altman plots between OR and CRE **(A)**, RDV-15 **(B)**, RDV-30 **(C)**, RDV-45 **(D)**, TRVD **(E)**, RDV-I **(F)**, RDV-S **(G)**, RDV-N **(H)**, and RDV-T **(I)** in cycloplegia eyes. The solid line shows the mean difference (bias), and the upper and lower lines represent 95% limits of agreement.

One limitation of this study was that we only evaluated the intraoperator repeatability, whereas repeatability in different time points was not evaluated. In addition, the patients were asked to remove their glasses during measurement. However, as is well-known, peripheral hyperopia inducing myopia mostly happens in patients wearing glasses or lenses. Therefore, future studies should evaluate patients with glasses and lenses. In this study, we only assessed the repeatability of MRT without comparing it with other peripheral wavefront autorefractors. A gold standard in measuring peripheral refraction remains inexistent. Future studies should compare MRT with other devices to gain insights on the introduction of MRT in clinical applications.

CONCLUSION

The novel MRT demonstrated good repeatability in central and peripheral refraction measurements. However, the repeatability of the measurements in the nasal, temporal, superior, and inferior quadrants were not as good as that in the central and circle peripheral refractions. Furthermore, we found that cycloplegia relaxed the accommodation and thus could improve repeatability.

DATA AVAILABILITY STATEMENT

The raw data supporting the conclusions of this article will be made available by the authors, without undue reservation.

ETHICS STATEMENT

The studies involving human participants were reviewed and approved by the Ethics Committee of Qingdao Eye Hospital of Shandong First Medical University. The patients/participants provided their written informed consent to participate in this study. Written informed consent was obtained from the individual(s) for the publication of any potentially identifiable images or data included in this article.

AUTHOR CONTRIBUTIONS

All authors listed have made a substantial, direct, and intellectual contribution to the work and approved it for publication.

FUNDING

This work was supported by the Medical and Health Development Grant of Shandong Province, China (202007020431).

REFERENCES

1. Huang J, Wen D, Wang Q, McAlinden C, Flitcroft I, Chen H, et al. Efficacy comparison of 16 interventions for myopia control in children: a network meta-analysis. *Ophthalmology*. (2016) 123:697–708. doi: 10.1016/j.ophtha.2015.11.010
2. Baird PN, Saw SM, Lanca C, Guggenheim JA, Smith Iii EL, Zhou X, et al. Myopia. *Nat Rev Dis Primers*. (2020) 6:99. doi: 10.1038/s41572-020-00231-4
3. Pan CW, Ramamurthy D, Saw SM. Worldwide prevalence and risk factors for myopia. *Ophthal Physiol Opt*. (2012) 32:3–16. doi: 10.1111/j.1475-1313.2011.00884.x
4. Morgan I, Rose K. How genetic is school myopia? *Prog Retinal Eye Res*. (2005) 24:1–38. doi: 10.1016/j.preteyeres.2004.06.004
5. Smith EL, Hung LF, Huang J. Relative peripheral hyperopic defocus alters central refractive development in infant monkeys. *Vis Res*. (2009) 49:2386–92. doi: 10.1016/j.visres.2009.07.011
6. Smith EL. Prentice Award Lecture 2010: a case for peripheral optical treatment strategies for myopia. *Optom Vis Sci*. (2011) 88:1029–44. doi: 10.1097/OPX.0b013e3182279cfa
7. Leung TW, Li RW, Kee CS. Meridional anisotropy of foveal and peripheral resolution acuity in adults with emmetropia, myopia, and astigmatism. *Invest Ophthalmol Vis Sci*. (2021) 62:11. doi: 10.1167/iovs.62.10.11
8. Smith EL, Ramamirtham R, Qiao-Grider Y, Hung LF, Huang J, Kee CS, et al. Effects of foveal ablation on emmetropization and form-deprivation myopia. *Invest Ophthalmol Vis Sci*. (2007) 48:3914–22. doi: 10.1167/iovs.06-1264
9. Cleary G, Spalton DJ, Patel PM, Lin PF, Marshall J. Diagnostic accuracy and variability of autorefraction by the Tracey Visual Function Analyzer and the Shin-Nippon NVision-K 5001 in relation to subjective refraction. *Ophthal Physiol Opt*. (2009) 29:173–181. doi: 10.1111/j.1475-1313.2008.00627.x
10. Nguyen MT, Berntsen DA. Aberrometry repeatability and agreement with autorefraction. *Optom Vis Sci*. (2017) 94:886–93. doi: 10.1097/OPX.0000000000001107
11. Moore KE, Berntsen DA. Central and peripheral autorefraction repeatability in normal eyes. *Optom Vis Sci*. (2014) 91:1106–12. doi: 10.1097/OPX.0000000000000351
12. Nagra M, Akhtar A, Huntjens B, Campbell P. Open versus closed view autorefraction in young adults. *J Optom*. (2021) 14:86–91. doi: 10.1016/j.optom.2020.06.007
13. Leng L, Zhang J, Xie S, Ding W, Ji R, Tian Y, et al. Effect of sunshine duration on myopia in primary school students from Northern and Southern China. *Int J Gen Med*. (2021) 14:4913–22. doi: 10.2147/IJGM.S328281
14. Read SA, Collins MJ. Diurnal variation of corneal shape and thickness. *Optom Vis Sci*. (2009) 86:170–80. doi: 10.1097/OPX.0b013e3181981b7e
15. Muller R, Buttner P. A critical discussion of intraclass correlation coefficients. *Stat Med*. (1994) 13:2465–76. doi: 10.1002/sim.4780132310
16. Bland JM, Altman DG. Statistical methods for assessing agreement between two methods of clinical measurement. *Lancet*. (1986) 1:307–10. doi: 10.1016/S0140-6736(86)90837-8
17. Holden BA, Fricke TR, Wilson DA, Jong M, Naidoo KS, Sankaridurg P, et al. Global prevalence of myopia and high myopia and temporal trends from 2000 through 2050. *Ophthalmology*. (2016) 123:1036–42. doi: 10.1016/j.ophtha.2016.01.006
18. Bowrey HE, Zeng G, Tse DY, Leotta AJ, Wu Y, To CH, et al. The effect of spectacle lenses containing peripheral defocus on refractive error and horizontal eye shape in the guinea pig. *Invest Ophthalmol Vis Sci*. (2017) 58:2705–14. doi: 10.1167/iovs.16-20240
19. Mutti DO, Sinnott LT, Reuter KS, Walker MK, Berntsen DA, Jones-Jordan LA, et al. Peripheral refraction and eye lengths in myopic children in the Bifocal Lenses In Nearsighted Kids (BLINK) study. *Transl Vis Sci Technol*. (2019) 8:17. doi: 10.1167/tvst.8.2.17
20. Allen PM, Radhakrishnan H, O'Leary DJ. Repeatability and validity of the PowerRefractor and the Nidek AR600-A in an adult population with healthy eyes. *Optom Vis Sci*. (2003) 80:245–51. doi: 10.1097/00006324-200303000-00014
21. Elliott M, Simpson T, Richter D, Fonn D. Repeatability and accuracy of automated refraction: a comparison of the Nikon NRK-8000, the Nidek AR-1000, and subjective refraction. *Optom Vis Sci*. (1997) 74:434–8. doi: 10.1097/00006324-199706000-00028
22. Hernandez-Moreno L, Vallelado-Alvarez A, Martin R. Repeatability of ARK-30 in a pediatric population. *Indian J Ophthalmol*. (2018) 66:1262–7. doi: 10.4103/ijo.IJO_266_18
23. Shaw AJ, Collins MJ, Davis BA, Carney LG. Eyelid pressure: inferences from corneal topographic changes. *Cornea*. (2009) 28:181–8. doi: 10.1097/ICO.0b013e31818a7d61
24. Fedtke C, Ehrmann K, Ho A, Holden BA. Lateral pupil alignment tolerance in peripheral refractometry. *Optom Vis Sci*. (2011) 88:E570–9. doi: 10.1097/OPX.0b013e31821041e2
25. Liao Y, Yang Z, Li Z, Zeng R, Wang J, Zhang Y, et al. A quantitative comparison of multispectral refraction topography and autorefractometer in young adults. *Front Med*. (2021) 8:715640. doi: 10.3389/fmed.2021.715640
26. Carracedo G, Carpena-Torres C, Batres L, Serramito M, Gonzalez-Bergaz A. Comparison of two wavefront autorefractors: binocular open-field versus monocular closed-field. *J Ophthalmol*. (2020) 2020:8580471. doi: 10.1155/2020/8580471

Conflict of Interest: The authors declare that the research was conducted in the absence of any commercial or financial relationships that could be construed as a potential conflict of interest.

Publisher's Note: All claims expressed in this article are solely those of the authors and do not necessarily represent those of their affiliated organizations, or those of the publisher, the editors and the reviewers. Any product that may be evaluated in this article, or claim that may be made by its manufacturer, is not guaranteed or endorsed by the publisher.

frontiers in Medicine

ORIGINAL RESEARCH
published: 09 December 2021
doi: 10.3389/fmed.2021.769308

Multimodal Imaging of Torpedo Maculopathy With Fluorescence Adaptive Optics Imaging of Individual Retinal Pigmented Epithelial Cells

Kari V. Vienola[1], Kunal K. Dansingani[1], Andrew W. Eller[1], Joseph N. Martel[1], Valerie C. Snyder[1] and Ethan A. Rossi[1,2,3]*

[1] Department of Ophthalmology, University of Pittsburgh, Pittsburgh, PA, United States, [2] Department of Bioengineering, University of Pittsburgh Swanson School of Engineering, Pittsburgh, PA, United States, [3] McGowan Institute for Regenerative Medicine, University of Pittsburgh, Pittsburgh, PA, United States

OPEN ACCESS

Edited by:
Peng Xiao,
Sun Yat-sen University, China

Reviewed by:
Elisabetta Pilotto,
University Hospital of Padua, Italy
Xiaoyan Ding,
Sun Yat-sen University, China
John Nickerson,
Emory University, United States

***Correspondence:**
Kari V. Vienola
kvienola@ucdavis.edu

Specialty section:
This article was submitted to Ophthalmology, a section of the journal Frontiers in Medicine

Received: *01 September 2021*
Accepted: *08 November 2021*
Published: *09 December 2021*

Citation:
Vienola KV, Dansingani KK, Eller AW, Martel JN, Snyder VC and Rossi EA (2021) Multimodal Imaging of Torpedo Maculopathy With Fluorescence Adaptive Optics Imaging of Individual Retinal Pigmented Epithelial Cells. Front. Med. 8:769308. doi: 10.3389/fmed.2021.769308

Torpedo maculopathy (TM) is a rare congenital defect of the retinal pigment epithelium (RPE). The RPE is often evaluated clinically using fundus autofluorescence (AF), a technique that visualizes RPE structure at the tissue level from the intrinsic AF of RPE fluorophores. TM lesions typically emit little or no AF, but this macroscopic assessment is unable to resolve the RPE cells, leaving the organization of the RPE cell mosaic in TM unknown. We used fluorescence adaptive optics scanning laser ophthalmoscopy (AOSLO) to show here for the first time the microscopic cellular-level structural alterations to the RPE cell mosaic in TM that underlie the tissue-level changes seen in conventional clinical imaging. We evaluated two patients with TM using conventional clinical imaging techniques and adaptive optics (AO) infrared autofluorescence (IRAF) in AOSLO. Confocal AOSLO revealed relatively normal cones outside the TM lesion but altered cone appearance within it and along its margins in both patients. We quantified cone topography and RPE cell morphometry from the fovea to the margin of the lesion in case 1 and found cone density to be within the normal range across the locations imaged. However, RPE morphometric analysis revealed disrupted RPE cells outside the margin of the lesion; the mean RPE cell area was greater than two standard deviations above the normative range up to approximately 1.5 mm from the lesion margin. Similar morphometric changes were seen to individual RPE cells in case 2. Multi-modal imaging with AOSLO reveals that RPE cells are abnormal in TM well beyond the margins of the characteristic TM lesion boundary defined with conventional clinical imaging. Since the TM fovea appears to be fully formed, with normal cone packing, it is possible that the congenital RPE defect in TM occurs relatively late in retinal development. This work demonstrates how cellular level imaging of the RPE can provide new insight into RPE pathologies, particularly for rare conditions such as TM.

Keywords: torpedo maculopathy, retinal pigment epithelium, autofluorescence, adaptive optic systems, scanning laser ophthalmoscopy, fluorescence imaging

INTRODUCTION

Torpedo maculopathy (TM) is characterized by the presence of a well-circumscribed lesion of the macula featuring elements of hyperpigmentation and atrophy at the level of the retinal pigment epithelium (RPE) and named for its typical shape and orientation with respect to the fovea (1, 2). TM appears to be congenital, non-progressive, and uncommon. Prevalence has been estimated to be 2 per 100,000 (3) with fewer than 100 cases reported as of 2019 (4). Early conjectures about the most appropriate classification included a subclass of congenital nevus of the RPE, or a form of congenital hypertrophy of the RPE (5, 6), but these descriptions pre-date optical coherence tomography (OCT).

In TM, OCT sometimes reveals neurosensory retinal layers detached from the RPE, forming a cavity (7, 8). Based on this, Wong et al. classified TM into Types I and II, the latter including neurosensory detachment with subretinal cavitation (9). Often the OCT B-scans show increased light penetration to the choroid with minimal fundus autofluorescence (FAF) signal originating from the lesion (2, 10). Functional testing with visual fields (11) and microperimetry (9) has shown reduced sensitivity in the lesion. Collective responses from electroretinogram (ERG) exams performed on patients with TM have not shown any abnormalities (12). However, multi-focal ERG has shown amplitude reduction with potential latency between pathological and healthy retinal areas of the same eye (12, 13).

In recent years, OCT angiography (OCTA) has been used to evaluate flow profiles in the choriocapillaris and/or choroid in the lesions. Most of these studies have reported decreased flow in the choriocapillaris with vascular alterations at the site of the lesion (11, 14–16). Giannakaki-Zimmermann et al. (17) concluded that attenuation of OCTA signal in choriocapillaris occurs with Type I as well, when there is no subretinal cavitation on structural OCT. Although one publication reported an increase in choroidal vascular density, no explanation was offered as to how this was measured and closer inspection of the key figure in the paper shows reduced choriocapillaris flow density in the lesion, compared with areas outside the lesion (18).

Adaptive optics ophthalmoscopy (AOO) permits cellular level imaging of the retina (19, 20). Recently, Hugo et al. used a commercially available flood-illumination adaptive optics (FIAO) fundus camera to evaluate TM patients and showed decreased cone density in the lesion compared to the healthy retina, suggestive of cone loss (21). Similar findings were reported by Lambart et al. (22) however, they hypothesized that cones were axially displaced rather than lost. Here, we present two new patients with TM who were evaluated using standard clinical imaging tools and AOO, including a commercial FIAO retinal camera and a custom fluorescence adaptive optics scanning laser ophthalmoscope (AOSLO). Compared to FIAO, AOSLO can achieve higher resolution for "reflectance" (i.e., backscattered) light imaging due to its ability to reject out-of-focus light (confocality). Our AOSLO is also equipped with a near-infrared autofluorescence detection channel that we used here to define the morphological alterations to the RPE cell mosaic associated with TM. To our knowledge, this is the first time that RPE morphology has been examined and quantified *in vivo* in TM patients using any modality.

Given the well-circumscribed nature of TM, our hypothesis was that the transition from abnormal to normal cellular mosaics would be relatively abrupt, with abnormalities confined to the immediate vicinity of the lesion. Further, due to the non-progressive clinical course, we hypothesized that the demarcation between abnormal and normal photoreceptor and RPE mosaics would be approximately aligned, without one appearing to lead or lag the other in terms of distance from the lesion border.

TABLE 1 | Optical coherence tomography imaging parameters.

OCT parameters	Patient 1	Patient 2	
	2019	2017	2019
Size X	1,536 pixels (9.8 mm)	768 pixels (9.1 mm)	1,024 pixels (6.1 mm)
Size Z	496 pixels (1.9 mm)	496 pixels (1.9 mm)	496 pixels (1.9 mm)
Scaling X	6.41 μm/pixel	11.79 μm/pixel	6.00 μm/pixel
Scaling Z	3.87 μm/pixel	3.87 μm/pixel	3.87 μm/pixel
ART Mode	ON (16 averaged)	ON (9 averaged)	ON (15 averaged)
Quality	38 dB	42 dB	26 dB
EDI Mode	ON	OFF	ON
Number Of B-Scans	49	61	49
Pattern Size	30° × 10° (9.8 × 3.3 mm)	30° × 25° (9.1 × 7.5 mm)	20° × 20° (6.1 × 6.1 mm)
Distance between B-Scans	68 μm	126 μm	128 μm

METHODS

Clinical imaging included color fundus photography (Topcon/Canon), SLO/OCT (Spectralis, Heidelberg, Germany), and a flood-illumination adaptive optics camera (rtx1-e, Imagine Eyes, France). Detailed OCT imaging parameters are presented in **Table 1**. Microperimetry (MAIA, CenterVue S.p.A, Padova, Italy) was performed using both the macular test and with custom case-specific test patterns that we used to evaluate light sensitivity across the lesions. Before the testing started, optic nerve head was used to calibrate the measurement and for normal control data we used the normative database of the manufacturer. For patient 1, OCTA was also performed (Optovue, Fremont, CA, USA) using an 8 × 8 mm scan area.

Adaptive optics scanning laser ophthalmoscopy imaging was carried out using a system that has been described in detail (23). Briefly, two imaging channels were used for simultaneous confocal reflectance and AO-IRAF imaging. A 795 nm super-luminescent diode was used for simultaneous confocal illumination and AO-IRAF excitation, with AF emission detected between 814 and 850 nm using a double-stacked bandpass filter (FF01-832/37, Semrock, USA). To ensure that no excitation light leaked into the AF detection channel, double-stacked filters were used in the 795 nm illumination path

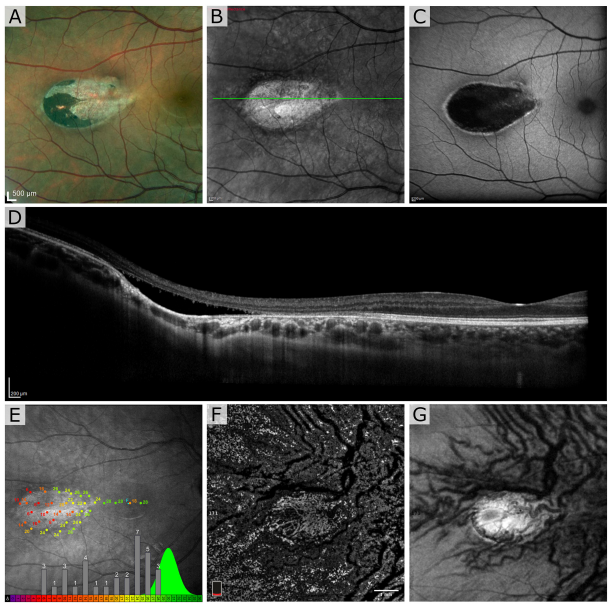

FIGURE 1 | Patient 1 imaged with multimodal clinical imaging. **(A)** Fundus images show a distinct torpedo-shaped lesion at the temporal macular region with the red box indicating the areas for the scanning laser ophthalmoscopy (SLO) and blue autofluorescence (BAF) images. **(B,C)** SLO reflectance and BAF image of the lesion showing the lesion very reflective in the SLO image and exhibiting marked hypo-AF signal at the lesion with a rim of hyper-AF. The green line in **(B)** indicates the B-scan location. **(D)** Optical coherence tomography (OCT) B-scan through the lesion. **(E)** Microperimetry test showing normal sensitivity in the fovea and severely decreased sensitivity at lesion with overall sensitivity well outside the normal distribution. The green distribution represents reference data from normal subjects. OCT *en face* angiogram **(F)** projection and corresponding structural image **(G)** taken with the OptoVue using a slab thickness of 70 μm about 150 μm below the retinal pigment epithelium (RPE).

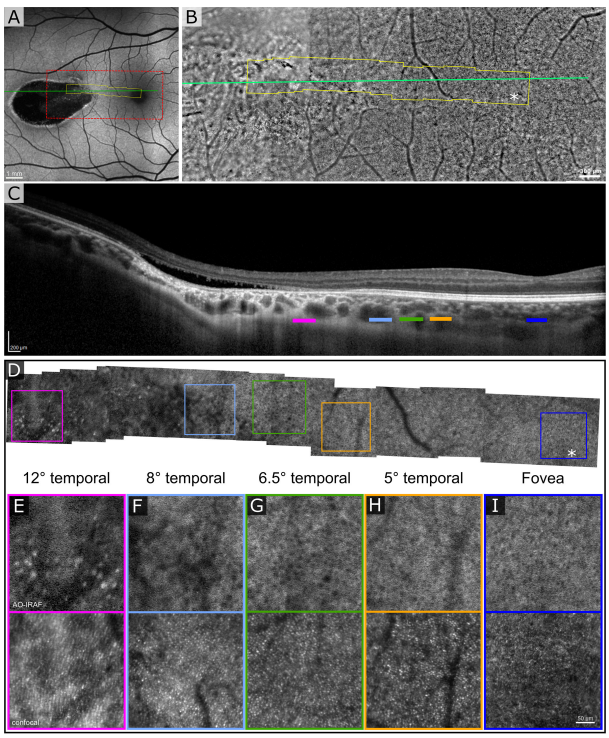

FIGURE 2 | Adaptive optics (AO) assisted imaging of patient 1. **(A)** Blue autofluorescence image showing the location of the lesion with red dashed box indicating the area imaged with the flood-illumination adaptive optics (FIAO) retinal camera and green line showing the location of the OCT scan. **(B)** FIAO montage showing typical photoreceptor mosaic in the region of the fovea. Near the lesion, the cone signature becomes irregular and cannot be distinguished anymore. The yellow area indicates the area that was imaged with the AOSLO. **(C)** OCT B-scan showing the cavity, indicating Type II torpedo maculopathy. Different color bars indicate roughly the location where AO-IRAF images where obtained. **(D)** AO-IRAF montage showing typical RPE cell mosaic. The cell size increases when moving to higher eccentricities and when reaching the lesion border, the mosaic eventually disappears. **(E–I)** Zoomed images of the regions of interest from the montage. Hypo-fluorescent spots are seen in **(E)** suggesting fluorophore accumulation in the lesion itself. Bottom row showing corresponding confocal image from the areas **(E–I)**.

(ET775/50x, Chroma, Bellows Falls VT, USA) to block any spontaneous emission in longer bands. The adaptive optics subsystem used a 909 nm laser diode beacon to detect the ocular aberrations and correct them in closed-loop mode with a deformable mirror. Imaging data were acquired at 30 Hz across a 1.5° × 1.5° field of view for a duration of 60–70 s.

The confocal images were used to co-register the weak signals in the AO-IRAF images using custom strip-based image registration software (24), permitting averaging to increase the signal-to-noise ratio in the AO-IRAF images. For the cell quantification from the AO-IRAF images, a semi-automated algorithm was used (25).

Patients were recruited through the clinics of the UPMC Eye Center. Written informed consent was obtained from both subjects following an explanation of experimental procedures and risks both verbally and in writing. All experiments were approved by the University of Pittsburgh Institutional Review Board and adhered to the tenets of the Declaration of Helsinki. To ensure safe imaging, all light levels were kept below the ANSI laser safety limits (26) and were calculated in accordance with best practices for multi-wavelength ophthalmic imaging (27).

RESULTS

Patient 1, a woman in her early 30s was found to have a pigmented lesion in her right eye during pre-screening for laser refractive surgery that was diagnosed later as TM. Best corrected visual acuity (BCVA) was 20/15 in each eye. The patient had no history of retinal laser nor injections prior to our imaging. Patient 2 was a woman in her early 20s diagnosed with TM. Her BCVA was 20/20 in each eye. The left eye had received a single intravitreal bevacizumab injection 2 years earlier for neovascularization within the lesion. Her angiography images have been published previously (28).

The first patient exhibited a typical torpedo-shaped lesion (**Figures 1A–C**) in the temporal macula with neurosensory detachment. Microperimetry showed decreased sensitivity in the lesion in both patients but in patient 1 with subretinal

cavitation (**Figure 1D**), the expected zero sensitivity did not occur, suggesting some visual function remaining (**Figure 1E**). In the OCTA, image slices taken from approximately 150 μm below the RPE showed some dense vascularization (**Figures 1F,G**) and what appears to be false positive flow signal temporal to the lesion. **Figure 2A** shows the blue autofluorescence image with areas marked where the B-scan and flood AO imaging was done. The cone mosaic in the flood AO (**Figure 2B**) shows typical cone mosaic with structure disappearing with eccentricity when approaching the lesion (yellow box indicating the AO-IRAF imaging area). This is consistent with the structural information on the B-scan (**Figure 2C**), showing the cavity fully starting at the edge of the AO-IRAF montage (**Figure 2D**). AO-IRAF showed the RPE mosaic (**Figures 2E–I**) visible from the fovea up to the margin of the lesion with an expected increase in cell size with increasing eccentricity. At the margin of the lesion, we observed heterogeneity in cell sizes as well as a decrease in the fluorescence signal corresponding to areas larger than individual RPE cells. Within the lesion, few individual RPE cells were seen on AO-IRAF and we observed several hyper-fluorescent spots with a diameter of 15–20 μm (**Figure 2E**).

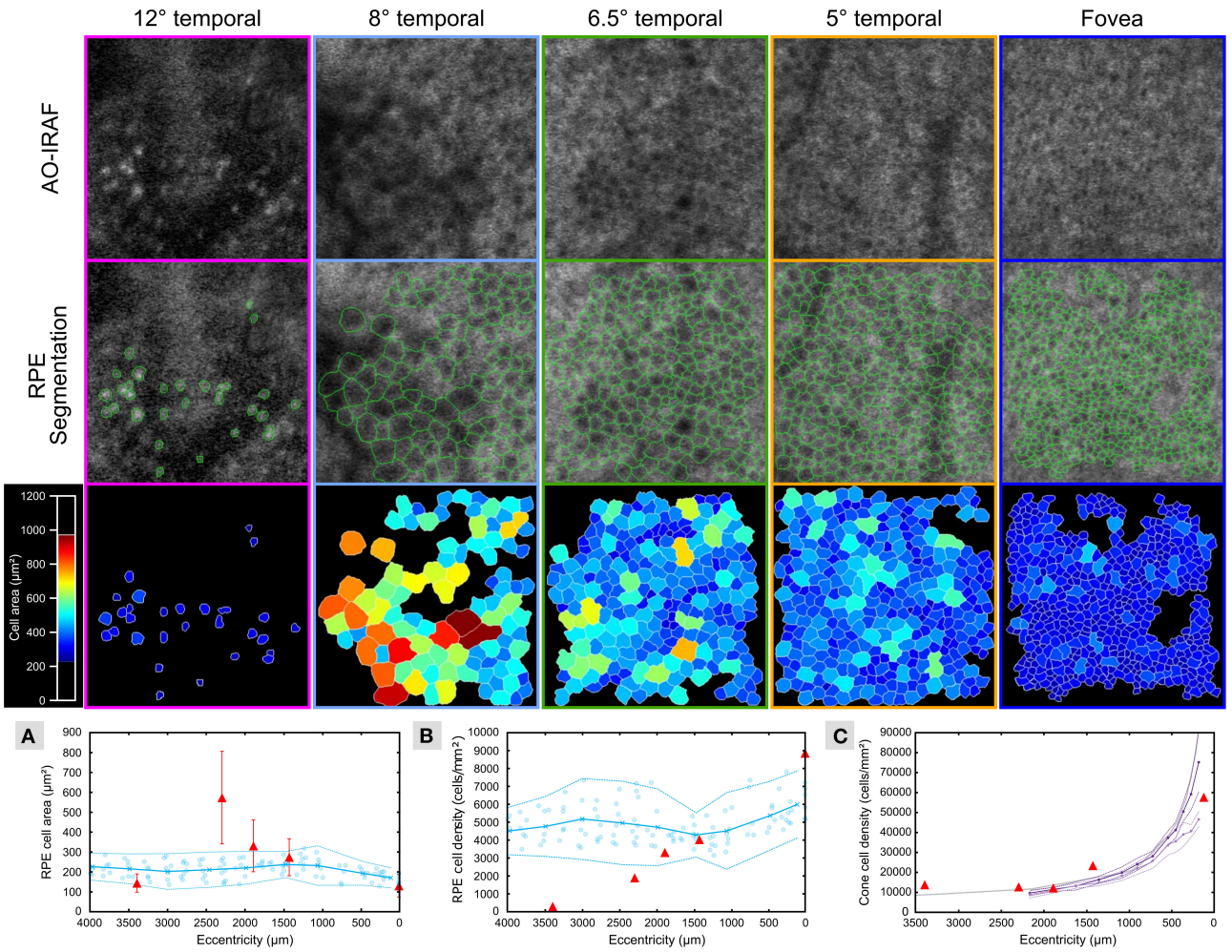

FIGURE 3 | RPE cells are altered in TM outside of the lesion area. AO-IRAF images from patient 1 (top row; see **Figures 2E–I**) were semi-automatically segmented (middle row; green outlines). The bottom row of images shows the segmentation images colored by cell area. Near the fovea (far right images), the cells were relatively uniform in size across the region of interest, while cell size heterogeneity increased with increasing eccentricity approaching the margin of the lesion. Within the lesion (left column), some punctate hyper-AF structures were seen but they did not resemble normal RPE cells. Quantitative plots compare the RPE cell area **(A)** and density **(B)** from this patient (red triangles in A and B, respectively) to the normative data from Granger et al. (29) (blue circles are individual data points; circle markers and solid line show mean; dotted lines are ± 2 SD). Average cell area was greater than the normal range at the margin of the lesion (see data point at approximately 2,300 μm) and greater than 400 μm away from the lesion (see data point at approximately 1,900 μm), while closer to the fovea (approximately 1,400 μm) and at the fovea (0 μm) the average cell area was within the normal range. Similarly, RPE cell density began to diverge from the normal range at the 1,900 μm measurement point and fell below 2 standard deviations from normal at the lesion margin (approximately 2,300 μm) and within the lesion (approximately 3,400 μm). Cone density was measured in 100 × 100 μm FOV within each RPE ROI **(C)** and was close to the range expected for normal eyes (violet and purple lines plot the mean cone density from the *in vivo* AOSLO data of Song et al. (30) for their younger and older cohort, respectively; dashed lines are ± 2SEM; gray line is the mean cone density from the histology data of Curcio et al. (31).

Figure 3 shows the segmentation of RPE cells from the different eccentricities (from 0 to 3,400 μm) from patient 1. Average cell area (**Figure 3A**) was greater than the normal range [data from Granger et al. (29)] at the margin of the lesion (see data point at approximately 2,300 μm) and greater than 400 microns away from the lesion (see data point at approximately 1,900 μm), while closer to the fovea (approximately 1,400 μm); and at the fovea (0 μm), the average cell area was within the normal range. The RPE cell density (**Figure 3B**) deviated from the normative data at the 1,900 microns measurement point and fell below 2 standard deviations from normal at the lesion margin (approximately 2,300 μm) and within the lesion (approximately 3,400 μm). The cone density was measured in 100 × 100 μm FOV within each RPE ROI (**Figure 3C**) and was close to the range expected for normal eyes.

Since the second patient (**Figure 4**) was treated with intravitreal injection, we have shown the SLO fundus image, and an OCT B-scan taken prior to the injection in **Figures 4A,B**. A characteristic torpedo shaped lesion with irregular margins on its temporal aspect is seen in **Figure 4C**. Standard clinical FAF imaging shows reduced AF signal (**Figures 4D-F**) from the lesion area and substantial light penetration to the choroid on the OCT B-scan (**Figure 4H**) suggesting extensive disruption to the RPE. As in patient 1, microperimetry in patient 2 showed reduced sensitivity within the lesion but it was not reduced to same extent seen in patient 1 (**Figure 4D**).

Figure 5A shows the clinical SLO image with red rectangle indicating the area imaged with flood-illumination AO (**Figure 5B**) and green line showing the location of the B-scan (**Figure 5C**). Despite a very low AO-IRAF signal in some areas (**Figure 5E**), the cone mosaic was well defined and clearly visible at many locations within the lesion on FIAO (**Figure 5B**) and confocal AOSLO (**Figure 5D**). AO-IRAF did now show the typical RPE mosaic within the lesion but trace signatures of the mosaic and RPE cells are seen in the bottom left corner of the montage just outside the margins of the TM lesion as well as at the right edge of the AO-IRAF montage.

DISCUSSION

Herein, we show the *in vivo* morphology of both the cone and RPE cell mosaics in TM for the first time. These findings suggest that outside the TM lesion, RPE morphometry is relatively normal. However, near the margin of the lesion, we see marked changes in RPE morphometry characteristic of a disrupted cell mosaic. Within the TM lesion, we observed differences between the two cases that may reflect differences between type I and type II lesions. In patient 1 (**Figures 1–3**), with a type II lesion (neurosensory detachment), we saw reduced AO-IRAF compared to the normal appearing areas outside the lesion but there was still well-defined structure within the lesion such as several areas of hyper-autofluorescence similar in size to individual RPE cells. It is possible that these hyper-autofluorescent areas represent RPE cells that have been altered due to the TM and accumulated additional NIR fluorophores. Another possible explanation of the hyperautofluorescence in the lesion borders could be RPE rounding/stacking but we did not

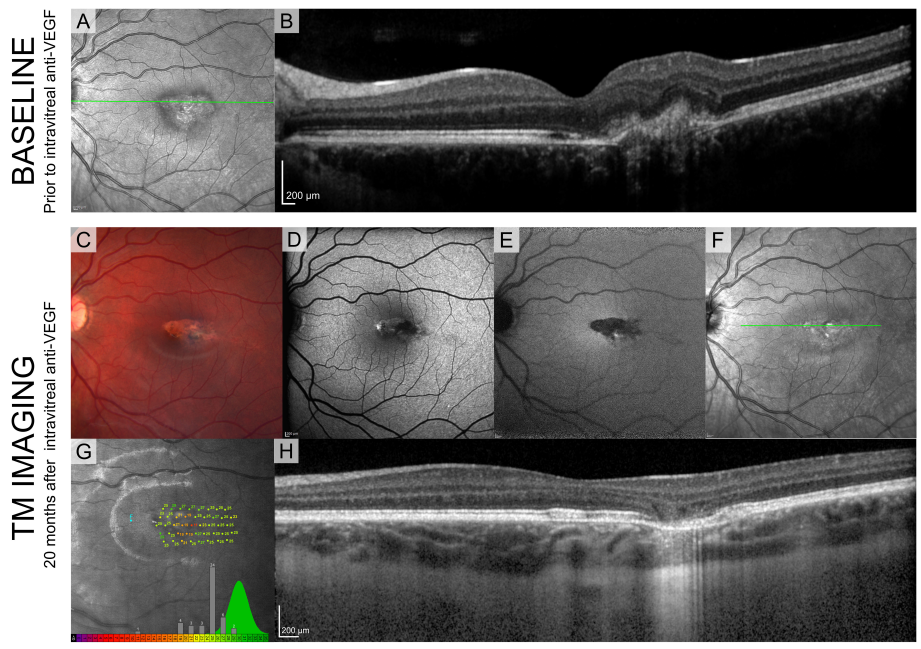

FIGURE 4 | Standard clinical imaging of patient 2. **(A,B)** SLO reflectance image and OCT B-scan taken from the location marked with a green line before the injection. **(C)** Fundus photograph 20 months after the injection. **(D-F)** SLO images from Spectralis (BAF, IRAF, reflectance) showing reduced FAF signal from the lesion. **(G)** Sensitivity estimates from MAIA show decreased values but compared to patient 1 they are substantially higher, suggesting intact visual sensitivity within the lesion. Green distribution represents normative data from the manufacturer's database. **(H)** OCT B-scan taken from the location marked with a green line in **(D)**.

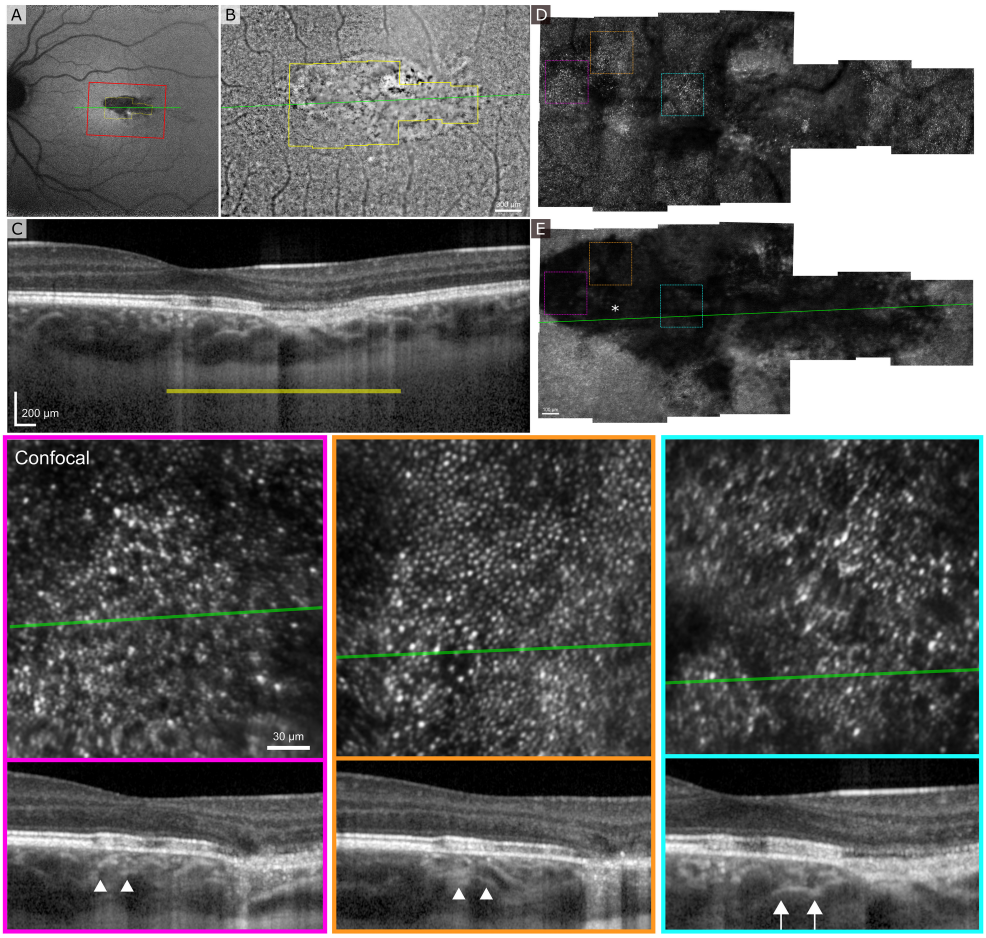

FIGURE 5 | Adaptive optics ophthalmoscopy imaging of the patient 2. **(A)** A clinical SLO reflectance image showing the location of the FIAO montage with red box and OCT B-scan with a green line going through the lesion. **(B)** FIAO montage showing typical photoreceptor mosaic outside the lesion. The yellow outline indicates the area imaged using AOSLO, with yellow bar showing the FIAO image location in the OCT B-scan. **(C)** B-scan showing extensive damage at the RPE layer with slightly increased light penetration to the choroid. **(D)** Confocal AOSLO montage of the lesion area. Compared to FIAO, the cone mosaic is sharper and has more contrast due to confocality and rejection of out-of-focus light. Even within the lesion patches of photoreceptor mosaic are seen. **(E)** AO-IRAF shows highly reduced FAF from the lesion throughout, even within areas where the photoreceptor mosaic seemed healthy, suggesting that the RPE underlying the photoreceptors is damaged. The colored dashed squares mark the location of the zoomed in areas at the bottom with colors indicating the areas. The B-scan locations are marked with a green line and in the B-scans the white arrow heads show the edges of the zoomed in area. The location of the fovea is marked with an asterisk in **(E)**.

see evidence of this when we examined the B-scan stack going through the lesion, particularly the hyperAF areas.

In the second case, there was very little well-defined RPE structure within the TM lesion; though some areas of hyper- and hypo-autofluorescence were seen, no hyper-AF structures were seen that had a similar appearance to what was seen in the first case. Since the photoreceptor mosaic in the confocal channel was well-resolved we do not think that this is an artifact due to poor image quality but rather is reflective of the distribution of fluorophores within the RPE.

Compared to other studies that have implemented commercial flood-illumination adaptive optics retinal cameras in their studies, the confocal reflectance images show similar morphology with no clear photoreceptor mosaic visible (21, 22). Most likely the photoreceptors are there but are misaligned resulting in an altered reflectance signal.

Interestingly, some retinal sensitivity was preserved within the lesion bounds in both patients. This was unsurprising in patient 2, with the type I TM lesion, since it appeared both clinically and on AO-IRAF that sufficient RPE was present to support some photoreceptor survival and function. It was more surprising to see some evidence of photoreceptor function in patient 1, in whom the RPE appeared macroscopically and on AO-IRAF to be mostly obliterated. Given that eyes with complete and chronic RPE atrophy often exhibit severe outer retinal disruption, this observation led us to speculate that neurosensory detachment from a pathological RPE might have been relatively protective to the photoreceptors. It also caused us to question whether TM is congenital, for if so, the observations suggest that it must arise relatively late in development, after outer retinal development and photoreceptor packing are completed. Considering our sensitivity losses in comparison to the literature, it appears that

sensitivity losses in TM vary across a spectrum ranging from little to mild losses, such as the case of patient 3 with Wong et al. (9) to moderate losses such as seen in our case 2 to the more severe losses accompanied by cavitation such as in our case 1 and Wong's patient 4.

As patient 2 underwent a single intravitreal bevacizumab injection prior to being imaged in our study, it is possible that that previous neovascularization might have altered the structure of the RPE. However, based on the literature (3, 14), it appears relatively common to have neovascularization on this rare condition, especially with type I. It is possible that there are some different alterations to the retina in TM with and without neovascularization. Without additional data, it is hard to interpret the level of influence on the AF signal itself.

Although the sample size for this descriptive study was limited by the low prevalence of TM, we were able to image both variants, type I and II, in detail. Clinically, TM can present with varying appearance and new possible lesion subtypes (32) may still be discovered such as those presenting with vitelliform material (33). Near infrared autofluorescence imaging using adaptive optics is an exciting new field and more quantitative results are possible in future studies.

CONCLUSION

Contrary to our expectation that the transition from abnormal to normal cellular mosaics would be relatively abrupt, with abnormalities confined to the immediate vicinity of the lesion, we found that RPE morphometric alterations extended well beyond the bounds of the clinically defined TM lesion. Additionally, the demarcation between abnormal and normal cone and RPE mosaics were not aligned, as cone density appeared to fall within the normal range at each of the locations where RPE cells were quantified in case 1, even though RPE cell morphometry was abnormal in several of these locations. The fluorescence signal that we detect with adaptive optics ophthalmoscopy can show alterations in the RPE when the structural cone images still appear normal. This was shown here in the case of TM patients, but this methodology can be adapted to various diseases and when accompanied by complimentary imaging modalities such as OCT, is a promising tool for clinicians to study the health of the retina.

DATA AVAILABILITY STATEMENT

The raw data supporting the conclusions of this article will be made available by the authors, without undue reservation.

ETHICS STATEMENT

The studies involving human participants were reviewed and approved by University of Pittsburgh Institutional Review Board. The patients/participants provided their written informed consent to participate in this study.

AUTHOR CONTRIBUTIONS

ER and KV conceived and conducted the experiment(s) and also drafted the manuscript. ER, KD, and KV analyzed and interpreted the results. VS conducted the clinical imaging. JM and AE critically revised the manuscript for important intellectual content. All co-authors carefully reviewed the final manuscript.

FUNDING

This research was supported by departmental startup funds from the University of Pittsburgh to ER. This work was also supported by the NIH CORE Grant P30 EY08098 to the University of Pittsburgh, Department of Ophthalmology, the Eye and Ear Foundation of Pittsburgh, NVIDIA GPU Grant Program and from an unrestricted grant from Research to Prevent Blindness, New York, NY, USA.

ACKNOWLEDGMENTS

The authors would like to thank Austin Roorda for sharing their AOSLO software, Pavan Tiruveedhula for electronics fabrication and software guidance and support, Jeff Speakman and Andrew Holmes for manufacturing custom mechanical components, and finally Jie Zhang, for sharing his original AOSLO optical design.

SUPPLEMENTARY MATERIAL

The Supplementary Material for this article can be found online at: https://www.frontiersin.org/articles/10.3389/fmed.2021.769308/full#supplementary-material

REFERENCES

1. Teitelbaum BA, Hachey DL, Messner LV. Torpedo maculopathy. *J. Am. Optom. Assoc.* (1997) 68:373–6
2. Golchet PR, Jampol LM, Mathura JR, Daily MJ. Torpedo maculopathy. *Br J Ophthalmol.* (2010) 94:302–6. doi: 10.1136/bjo.2009.162669
3. Shirley K, O'Neill M, Gamble R, Ramsey A, McLoone E. Torpedo maculopathy: disease spectrum and associated choroidal neovascularisation in a paediatric population. *Eye.* (2018) 32:1315–20. doi: 10.1038/s41433-018-0074-7
4. Williams PJ, Salek S, Prinzi RA, Bergstrom C, Hubbard GB. Distribution patterns of torpedo maculopathy: further evidence of a congenital retinal nerve fiber layer-driven etiology. *Saudi J Ophthalmol.* (2019) 33:260–267. doi: 10.1016/j.sjopt.2019.07.010
5. Gass JDM. Focal congenital anomalies of the retinal pigment epithelium. *Eye.* (1989) 3:1–8. doi: 10.1038/eye.1989.2
6. Roseman RL, Gass JDM. Solitary hypopigmented nevus of the retinal pigment epithelium in the macula. *Arch Ophthalmol.* (1992) 110:1358–9. doi: 10.1001/archopht.1992.01080220020005

7. Su Y, Gurwood AS. Neurosensory retinal detachment secondary to torpedo maculopathy. *Optometry.* (2010) 81:405–7. doi: 10.1016/j.optm.2010.06.001
8. Bedar MS, Holz FG, Lischka T. Hypopigmentierung temporal der Makula. Fallvorstellung: Torpedo-Makulopathie. *Der Ophthalmologe.* (2013) 110:173–4. doi: 10.1007/s00347-012-2705-x
9. Wong EN, Fraser-Bell S, Hunyor AP, Chen FK. Novel optical coherence tomography classification of torpedo maculopathy. *Clin Experim Ophthalmol.* (2015) 43:342–8. doi: 10.1111/ceo.12435
10. Pilotto E, Zannin ME, Convento E, Cortese M, Midena E. Torpedo maculopathy: a morphofunctional evaluation. *Int Ophthalmol.* (2013) 33:71–4. doi: 10.1007/s10792-012-9618-1
11. Hamm C, Shechtman D, Reynolds S. A deeper look at torpedo maculopathy. *Clin Exp Optom.* (2017) 100:563–8. doi: 10.1111/cxo.12540
12. Buzzonetti L, Petroni S, Catena G, Iarossi G. Optical coherence tomography and electrophysiological findings in torpedo maculopathy. *Doc Ophthalmol.* (2015) 130:65–70. doi: 10.1007/s10633-014-9472-8
13. Barbazetto IA, Maris PJG, Greenstein VC. Solitary albinotic spot of the retinal pigment epithelium: a functional and imaging study. *Klin Monbl Augenheilkd.* (2008) 225:295–297. doi: 10.1055/s-2008-1027236
14. Jurjevic D, Böni C, Barthelmes D, Fasler K, Becker M, Michels S, et al. Torpedo maculopathy associated with choroidal neovascularization. *Klin Monbl Augenheilkd.* (2017) 234:508–14. doi: 10.1055/s-0043-100230
15. Grimaldi G, Scupola A, Sammarco MG, Marullo M, Blasi MA. Morpho-functional evaluation of torpedo maculopathy with optical coherence tomography angiography and microperimetry. *Am J Ophthalmol Case Rep.* (2018) 10:16568. doi: 10.1016/j.ajoc.2018.02.019
16. Papastefanou VP, Vázquez-Alfageme C, Keane PA, Sagoo MS. multimodality imaging of torpedo maculopathy with swept-source, en face optical coherence tomography and optical coherence tomography angiography. *Retin Cases Brief Rep.* (2018) 12:153–57. doi: 10.1097/ICB.0000000000000456
17. Giannakaki-Zimmermann H, Munk MR, Dysli C, Ebneter A, Wolf S, Zinkernagel MS. Optical coherence tomography angiography features of torpedo maculopathy. *Retin Cases Brief Rep.* (2019) 13:337–42. doi: 10.1097/ICB.0000000000000589
18. Ding Y, Yao B, Ye H, Yu Y. Multimodal imaging of torpedo maculopathy in a Chinese woman: a case report. *BMC Ophthalmol.* (2019) 19:154. doi: 10.1186/s12886-019-1161-7
19. Liang J, Williams DR, Miller DT. Supernormal vision and high-resolution retinal imaging through adaptive optics. *J Opt Soc Am A.* (1997) 14:2884–92. doi: 10.1364/JOSAA.14.002884
20. Roorda A, Romero-Borja F, Donnelly III WJ, Queener H, Hebert TJ, Campbell MCW. Adaptive optics scanning laser ophthalmoscopy. *Opt Express.* (2002) 10:405–12. doi: 10.1364/OE.10.000405
21. Hugo J, Beylerian M, Denion E, Aziz A, Gascon P, Denis D, et al. Multimodal imaging of torpedo maculopathy including adaptive optics. *Eur J Ophthalmol.* (2019) 30:NP27–31. doi: 10.1177/1120672119827772
22. Lambert NG, Grigorian F, Vasconcelos H, Watzke RC, Pennesi ME. (2020) Adaptive optics ophthalmoscopy, multifocal ERG and OCTA in unique case of suspected torpedo maculopathy presenting with vitelliform lesion. *Am J Ophthalmol Case Rep.* 20:100996. doi: 10.1016/j.ajoc.2020.100996
23. Vienola KV, Zhang M, Snyder VC, Sahel JA, Dansingani KK, et al. Microstructure of the retinal pigment epithelium near-infrared autofluorescence in healthy young eyes and in patients with AMD. *Sci Rep.* (2020) 10:9561. doi: 10.1038/s41598-020-66581-x
24. Zhang M, Gofas-Salas E, Leonard BT, Rui Y, Snyder VC, Reecher HM, et al. Strip-based digital image registration for distortion minimization and robust eye motion measurement from scanned ophthalmic imaging systems. *Biomed Opt Exp.* (2021) 12:2353–2372. doi: 10.1364/BOE.418070
25. Rangel-Fonseca P, Gómez-Vieyra A, Malacara-Hernández D, Wilson MC, Williams DR, Rossi EA. Automated segmentation of retinal pigment epithelium cells in fluorescence adaptive optics images. *J Opt Soc Am A.* (2013) 30:2595–604. doi: 10.1364/JOSAA.30.002595
26. Laser Institute of America (2014). *American National Standard for Safe Use of Lasers Z136.1.*
27. Delori FC, Webb RH, Sliney DH. Maximum permissible exposures for ocular safety (ANSI 2000), with emphasis on ophthalmic devices. *J Opt Soc Am A.* (2007) 24:1250–65. doi: 10.1364/JOSAA.24.001250
28. Banaee T, Doss M, Eller AW. Torpedo maculopathy complicated by choroidal neovascularization. *Am J Ophthalmol Case Rep.* (2020) 19:100772. doi: 10.1016/j.ajoc.2020.100772
29. Granger CE, Yang Q, Song H, Saito K, Nozato K, Latchney LR, et al. Human retinal pigment epithelium: *in vivo* cell morphometry, multispectral autofluorescence, and relationship to cone mosaic. *Invest Ophthalmol Vis Sci.* (2018) 59:5705–16. doi: 10.1167/iovs.18-24677
30. Song H, Rossi EA, Yang Q, Granger CE, Latchney LR, Chung MM. High-resolution adaptive optics *in vivo* autofluorescence imaging in stargardt disease. *JAMA Ophthalmol.* (2019) 137:603–9. doi: 10.1001/jamaophthalmol.2019.0299
31. Curcio CA, Sloan KR, Kalina RE, Hendrickson AE. Human photoreceptor topography. *J Comparat Neurol.* (1990) 292:497–523. doi: 10.1002/cne.902920402
32. Light JG, Alvin Liu TY. A novel phenotype of torpedo maculopathy on spectral-domain optical coherence tomography. *Am J Ophthalmol Case Rep.* (2020) 20:100956. doi: 10.1016/j.ajoc.2020.100956
33. Dolz-Marco R, Saffra NA, Freund KB. Torpedo maculopathy presenting with a vitelliform lesion. *Retina.* (2017) 37:e19–e20. doi: 10.1097/IAE.0000000000001305

Conflict of Interest: Some aspects of this work include technologies that ER is an inventor on for patents that are owned by the University of Rochester (US Patent No.: US 10,123,697 and US 10,092,181).

The remaining authors declare that the research was conducted in the absence of any commercial or financial relationships that could be construed as a potential conflict of interest.

Publisher's Note: All claims expressed in this article are solely those of the authors and do not necessarily represent those of their affiliated organizations, or those of the publisher, the editors and the reviewers. Any product that may be evaluated in this article, or claim that may be made by its manufacturer, is not guaranteed or endorsed by the publisher.

frontiers in Medicine

ORIGINAL RESEARCH
published: 16 December 2021
doi: 10.3389/fmed.2021.795038

MRI-Based Radiomics for Differentiating Orbital Cavernous Hemangioma and Orbital Schwannoma

Liang Chen[1], Ya Shen[1], Xiao Huang[1], Hua Li[2], Jian Li[1], Ruili Wei[1] and Weihua Yang[3]**

[1] Department of Ophthalmology, Shanghai Changzheng Hospital, Shanghai, China, [2] Department of Imaging, Shanghai Changzheng Hospital, Shanghai, China, [3] Affiliated Eye Hospital, Nanjing Medical University, Nanjing, China

Aim: The purpose of this work was to develop and evaluate magnetic resonance imaging (MRI)-based radiomics for differentiation of orbital cavernous hemangioma (OCH) and orbital schwannoma (OSC).

Methods: Fifty-eight patients (40 OCH and 18 OSC, confirmed pathohistologically) screened out from 216 consecutive patients who presented between 2015 and 2020 were divided into a training group (28 OCH and 12 OSC) and a validation group (12 OCH and 6 OSC). Radiomics features were extracted from T1-weighted imaging (T1WI) and T2-weighted imaging (T2WI). *T*-tests, the least absolute shrinkage and selection operator (LASSO), and principal components analysis (PCA) were used to select features for use in the classification models. A logistic regression (LR) model, support vector machine (SVM) model, decision tree (DT) model, and random forest (RF) model were constructed to differentiate OCH from OSC. The models were evaluated according to their accuracy and the area under the receiver operator characteristic (ROC) curve (AUC).

Results: Six features from T1WI, five features from T2WI, and eight features from combined T1WI and T2WI were finally selected for building the classification models. The models using T2WI features showed superior performance on the validation data than those using T1WI features, especially the LR model and SVM model, which showed accuracy of 93% (85–100%) and 92%, respectively, The SVM model showed high accuracy of 93% (91–96%) on the combined feature group with an AUC of 98% (97–99%). The DT and RF models did not perform as well as the SVM model.

Conclusion: Radiomics analysis using an SVM model achieved an accuracy of 93% for distinguishing OCH and OSC, which may be helpful for clinical diagnosis.

Keywords: orbit, radiomics, cavernous hemangioma, schwannoma, machine learning

OPEN ACCESS

Edited by:
Peng Xiao,
Sun Yat-sen University, China

Reviewed by:
Huasheng Yang,
Sun Yat-sen University, China
Jiang Qian,
Fudan University, China

****Correspondence:***
Ruili Wei
ruiliwei@smmu.edu.cn
Weihua Yang
benben0606@139.com

Specialty section:
This article was submitted to Ophthalmology, a section of the journal Frontiers in Medicine

Received: *14 October 2021*
Accepted: *29 November 2021*
Published: *16 December 2021*

Citation:
Chen L, Shen Y, Huang X, Li H, Li J, Wei R and Yang W (2021) MRI-Based Radiomics for Differentiating Orbital Cavernous Hemangioma and Orbital Schwannoma. Front. Med. 8:795038. doi: 10.3389/fmed.2021.795038

INTRODUCTION

Orbital cavernous hemangioma (OCH) is a common primary tumor representing ∼8% of all orbital lesions (1). Patients with OCH typically show slow-moving progression and painless proptosis, although some suffer from disturbance in vision and visual fields (2). Though having a similar clinical manifestation to OCH (3), orbital schwannoma (OSC) accounts for <1% of

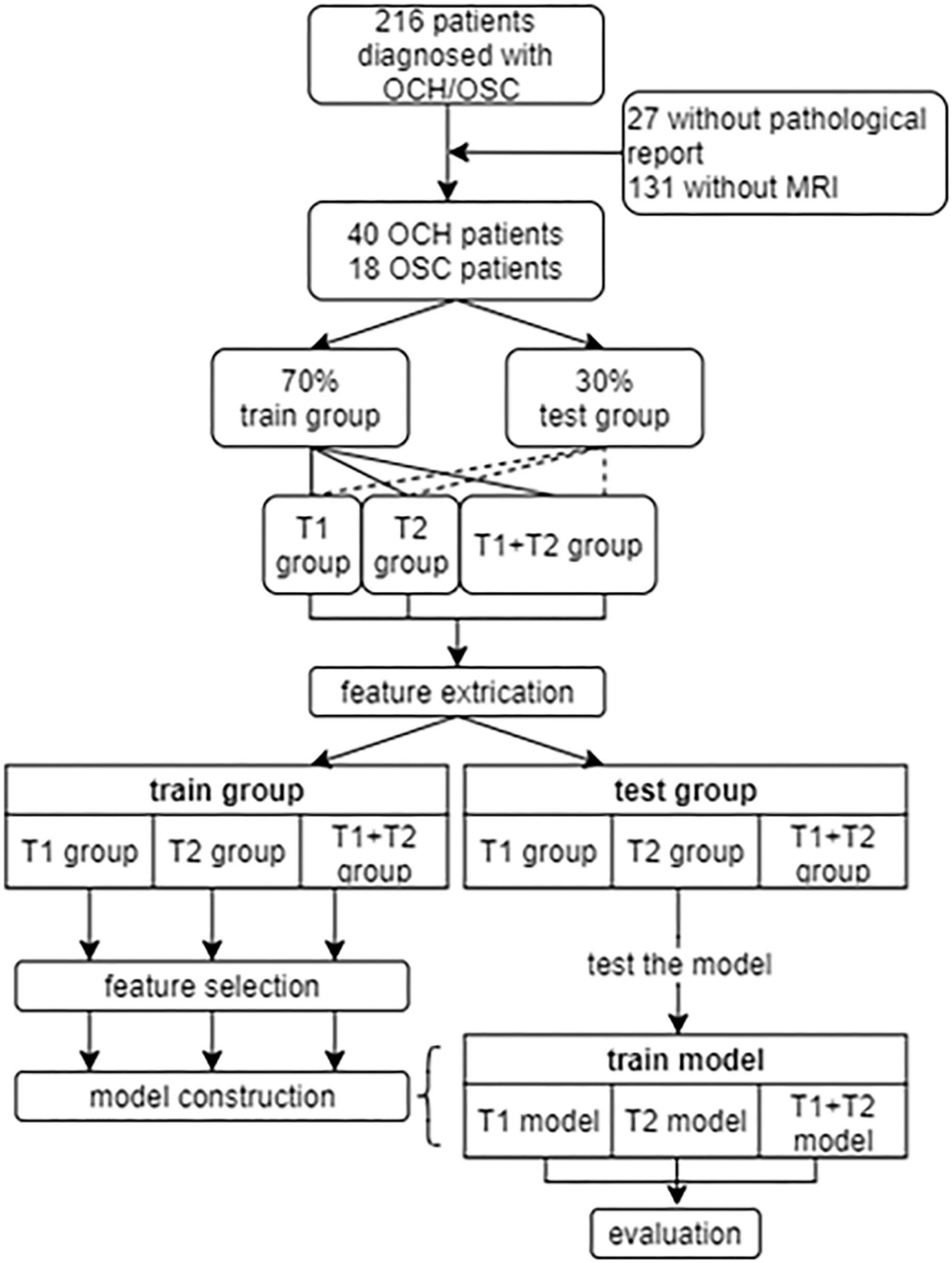

FIGURE 1 | The recruitment of patients and design of this study. OCH, orbital cavernous hemangioma; OSC, orbital schwannoma.

orbital lesions. However, the prognosis and therapeutic strategies for the two tumors are always different. Observation is a possible choice for those patients newly diagnosed with OCH, but surgical intervention is often needed for OSC patients, as OSC typically shows progressive growth (4, 5). Therefore, it is necessary to identify the two tumors (3, 6, 7).

Because of their similar clinical features, the identification of OCH and OSC can be clinically challenging. Several imaging studies attempted to clarify the differences between them (8–10), indicating that OCH has a more regular shape than OSC, and that markedly homogeneous hyperintense signal on T2-weighted magnetic resonance imaging (MRI) favors OCH rather than OSC. Furthermore, the contrast enhancement on dynamic contrast-enhanced MRI may also be helpful for distinguishing the two tumors; OCH shows "progressive" enhancement starting from a small point or portion, with the contrast media later filling up the tumor, whereas OSC shows enhancement starting from a wide area, with heterogeneous or homogeneous enhancement occurring later (8). However, these findings may not always work well in the clinic, with some images being indistinguishable and dividing opinion with an absence of objective evidence. Therefore, an objective identification method would be preferred by the clinician.

Radiomics, a promising and rapidly growing discipline, can be defined as the quantification of the phenotypic features of a lesion from medical images. It involves the extraction of a large number of quantitative features from medical images and their subsequent analysis to support clinical decision-making (11–13). It can overcome some of the limitations of subjective analysis with the human eye, squeezing out more information from each image (14). Radiomics approaches are currently becoming more and more popular in clinical auxiliary diagnosis and prognosis (15–17).

However, to the best of our knowledge, there is no published study using radiomics to distinguish OCH from OSC. In this study, we applied radiomics analysis to the differentiation of the two tumors and evaluated the results.

SUBJECTS AND METHODS

Patients

Two hundred and sixteen consecutive patients diagnosed with OCH or OSC between 2015 and 2020 were identified in the electronic medical record system (EMR) of Shanghai Changzheng Hospital. All patients were retrospectively recruited and signed informed consent before this study.

The inclusion criteria were: (1) patients newly diagnosed with OCH or OSC with biopsy confirmation; (2) tumor involving the eye of only one side; (3) complete and clear MRI data collected on scanners of the same model; (4) no surgical or other therapy prior to MRI scanning. Patients with incomplete MRI or with imaging of insufficient

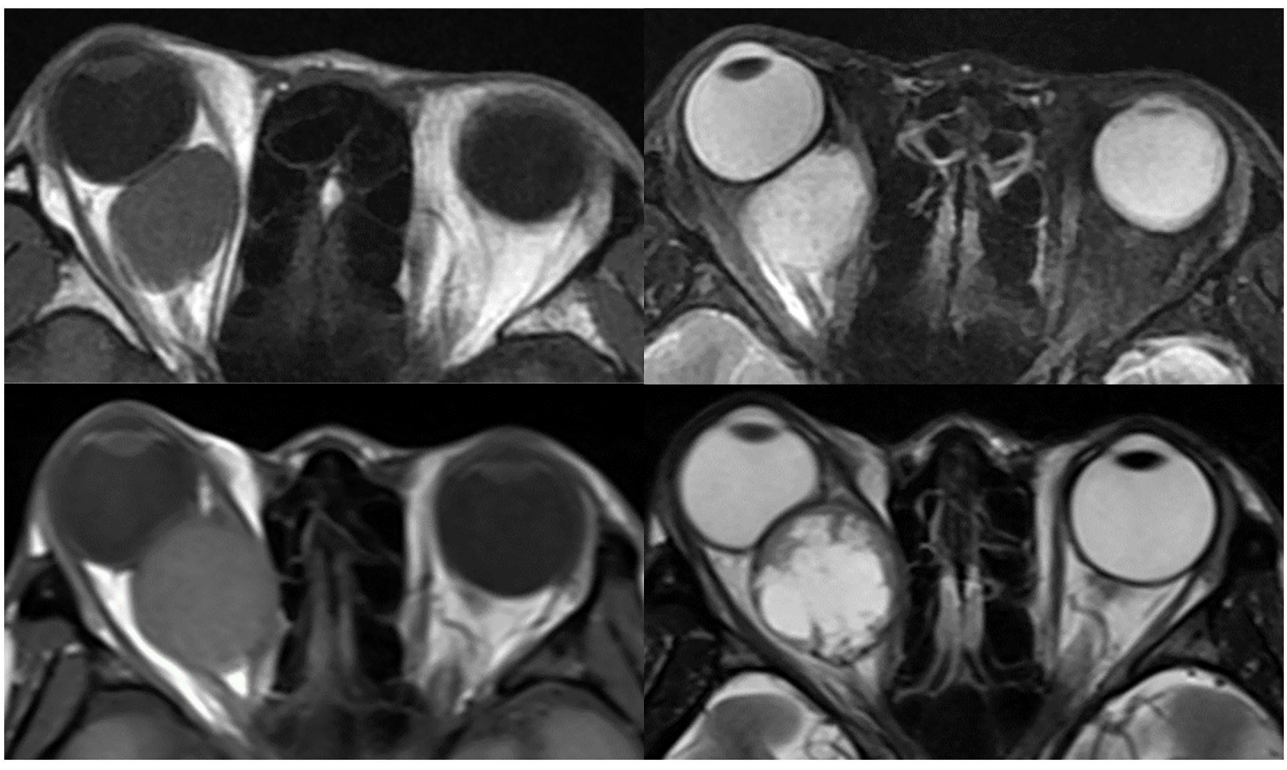

FIGURE 2 | Example images of OCH and OSC. Top left is a T1-weighted image of a patient with OCH, top right is a T2-weighted image of the same patient. Bottom left is a T1-weighted image of a patient with OSC, bottom right is a T2-weighted image of the same patient.

quality were excluded. **Figure 1** summarizes the patient recruitment process.

MRI Pre-processing

The DICOM format MRI of all included patients were acquired from the picture archiving and communication system of Shanghai Changzheng Hospital. The MRI examinations were performed on a 3.0-T scanner [Achieva 3.0T (TX) DS MR system, Philips Healthcare] with heart of FreeWave, an advanced modular 32-channel digital data acquisition system, and high-resolution head coil. Pre-contrast turbo spin-echo (TSE) T1-weighted imaging (T1WI) and T2-weighted imaging (T2WI) with fat suppression were acquired. The parameters were set as follows, for T1WI, the repetition time (TR) was 470 ms, echo time (TE) 12 ms, 16 slicers with thickness of 3 mm and a gap of 0.3 mm, 200–400 mm field of view (FOA), the flip angle (FA) was 90° and the number of signal acquisition (NSA) was 1; for T2WI, the driven equilibrium technology was used and the TR 3,000 ms, TE 80 ms, 16 slicers with thickness of 4 mm and a gap of 0.4 mm, 200–400 mm FOA, FA 90° and NSA was 2. To compare the efficiency of the different sequences, radiomics analyses were performed separately on the T1WI, T2WI, and combined (T1WI + T2WI) sequences. For each sequence, ∼70% (28 OCH and 12 OSC) of the acquisitions were selected as the training data and the remaining 30% formed the validation data.

First, MRI bias was corrected using the N4ITK MRI bias correction (18), then all images were horizontally mirrored. Regions of interest (ROIs) were then outlined on each slice by an ophthalmologist and a radiologist using the free open-source software package 3D Slicer version 4.11(https://download.slicer.org/). The ROIs for each patient were outlined separately in the original images and mirror images, to reduce bias. The intraclass correlation coefficients (ICCs) between the two researchers were calculated for all extracted features to determine the reliability of the ROIs.

Feature Extraction and Selection

The feature extraction was performed for all selected MRIs and their corresponding ROI masks using Python 3.7 (https://www.python.org/downloads/release/python-3711/) with Official default parameters (http://www.radiomics.io/pyradiomicsnotebook.html). The features included first order features, shape features, gray level co-occurrence matrix (GLCM), gray level dependence matrix (GLDM), gray level run length matrix (GLRLM), gray level size zone matrix (GLSZM), and neighboring gray tone difference matrix (NGTDM). These features are defined in the Results section. Zero-mean normalization was applied to these quantitative features following deletion of null values and features stored as string type.

In this analysis, to avoid overfitting and balance the limited samples and redundant features, we adopted four methods to select features. After simple *t*-tests, the LASSO linear regression model was applied, a model that can avoid overfitting and is suitable for analyzing small samples with high-dimensional features (19). However, many features still remained after the application of LASSO, so we then applied recursive feature elimination-cross validation (RFE-CV), a feature selection method that iteratively removes the least important features until the optimal number is reached. Despite these measures, the results were still not significant. Considering the potential for collinearity among the features, we created a correlation heat map, which confirmed out suspicions. Therefore, the dimensionality reduction method of PCA was adopted, which works by recombining a new set of composite variables unrelated to each other from the original features, and a few of these composite variables were extracted to faithfully reflect the original features as much as possible. Finally, fewer features were selected to construct the models (six features on T1WI, five features on

TABLE 1 | Patient demographic information.

	OCH ($n = 40$)	OSC($n = 18$)	*P*-value
Gender			
Female	24 (60%)	8 (44%)	
Male	16 (40%)	10 (56%)	0.41
Age	49 (40–57)	47 (41–50)	0.62
Involvement			
Left	20 (50%)	8 (44%)	
Right	20 (50%)	10 (56%)	0.91
Intraconal	39	18	
Extraconal	1	0	
Tumor			
Size(mm^3)	4776.07	7602.30	0.03
Sphericity	0.70 (0.69–0.74)	0.66 (0.64–0.69)	0.11
T1WI MEAN SIGNAL INTENSITY	573.43 (358.29–765.61)	711.15 (400.96–917.29)	0.30
T2WI mean signal intensity	662.62 (574.92–769.09)	792.05 (608.97–971.64)	0.15

Tumor size was calculated based on the ROI. Tumor sphericity took values between 0 and 1, the higher the value (closer to 1), the closer to sphere the tumor. All values of tumor size, sphericity and signal intensity were from the features extracted.

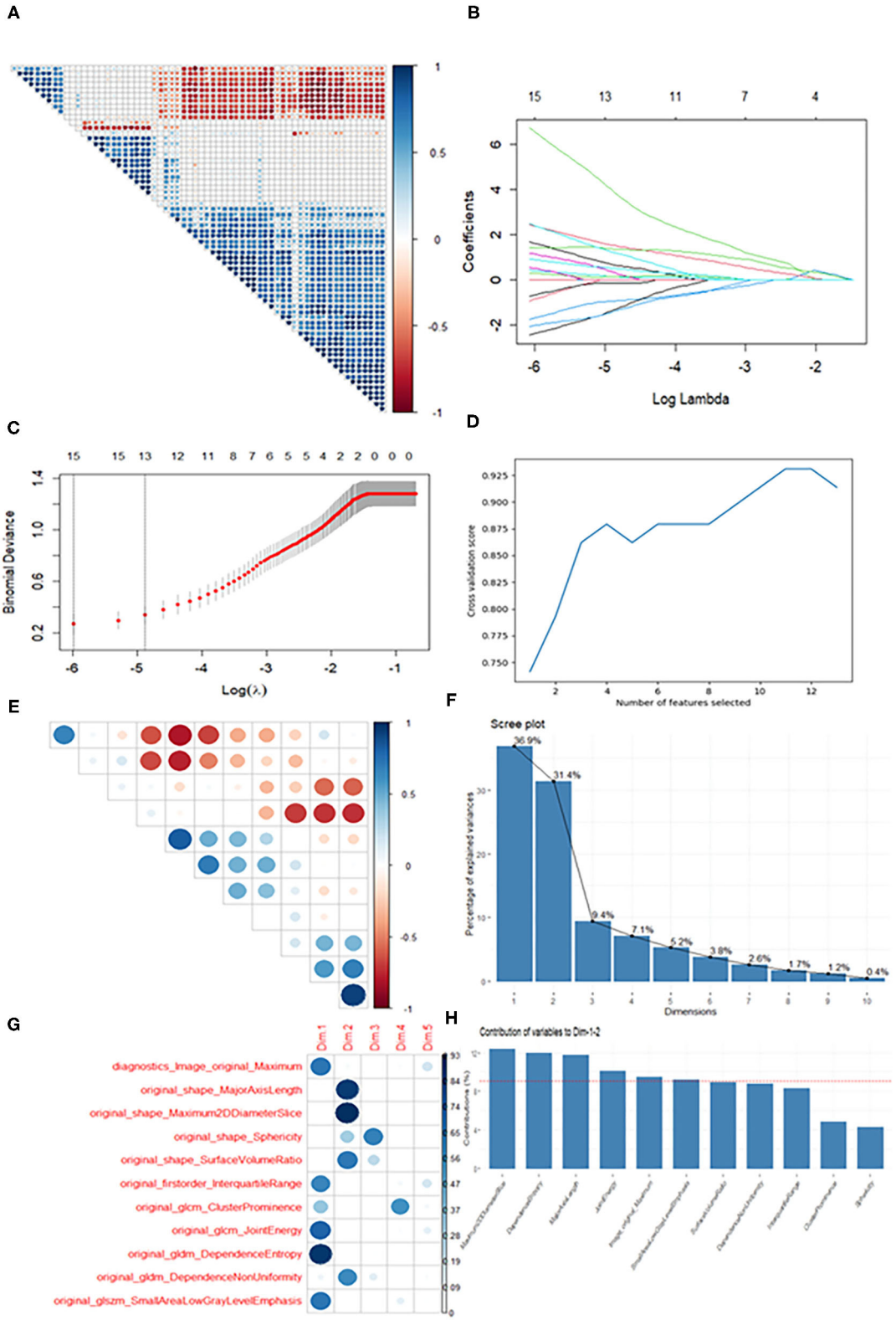

FIGURE 3 | Diagram of the feature selection process. Images **(A,E)** are correlation heat maps demonstrating correlations between features. The deeper the color, the stronger the correlation. Red indicates negative correlation and blue positive correlation. Image **(B)** shows the results of the LASSO regression. With increasing penalty parameter the coefficients of the features approach zero and finally converge on an optimal solution. Image **(C)** shows the results of LASSO-CV. The right dotted line

(Continued)

FIGURE 3 | indicates the standard error of the minimum mean square error (the left dotted line) and corresponds to the feature number on the top coordinate. Image **(D)** shows the RFE-CV, which provided the highest score with the remaining 11 features. Images **(F–H)** show the results of the PCA. Ten recombined dimensions are shown, with the first five explaining 90% of the original data [image **(F)**]. Image g shows the feature distributions of the first five dimensions. We finally selected the features whose contribution was higher than average (the dotted line) on Dimension 1 and Dimension 2 [image **(H)**].

T2WI, eight features on T1 + T2). Statistical analysis and plotting were performed with R (R vision 4.0.3, https://cran.r-project.org/).

Model Construction and Evaluation

The selected features were used to build the classification models. In this analysis, a logistic regression (LR) model, support vector machine (SVM) model (linear kernel), random forest (RF) model, and decision tree (DT) model were constructed. All four models were evaluated on the validation data according to their accuracy score and the area under the receiver operating characteristics (ROC) curve (AUC). A nomogram was also built to visualize a multiparametric MRI prognostication model using radiomics features. Statistical analyses were performed using R statistical software (R version 4.0.3). A P-value <0.05 was considered statistically significant.

RESULTS

Patients and MRI

As shown in **Figure 1**, 58 patients were eventually included in our study. From these patients, 1640 T1 or T2-weighted MR images in DICOM format were finally selected for further analysis. The lesions showed hypointensity on T1WI and hyperintensity on T2WI. **Figure 2** shows example MR images. The demographic information of the included patients is shown in **Table 1**.

Feature Extraction and Selection

A total of 107 features were selected from either T1 or T2 sequences for further analysis. These 107 features included 14 shape features, 18 first order features, 24 GLCMs, 14 GLDMs, 16 GLRLMs, 16 GLSZMs, and 5 NGTDMs. Of the above features, the shape features mainly describe the size and shape of the ROI and are only calculated for the non-derived image and mask, the first order features describe the distribution of voxel intensities within the image region defined by the mask and are computed using common basic metrics, and the remaining features describe texture and gray level intensity distributions with different algorithms and complexity. The ICCs of all extracted features were over 75%.

For the T1WI, t-tests were first employed to screen out 64 features showing a significant difference between OCH and OSC in the training data. A correlation heat map (**Figure 3A**) then revealed multicollinearity among the features, and LASSO regression was therefore used to reduce the dimensionality of the features. **Figure 3B** shows the results of the LASSO regression, and **Figure 3C** the results of a LASSO-Cross validation (LASSO-CV). Then, 13 features were filtered out and RFE-CV based on an SVM was employed for further feature selection. **Figure 3D** indicates that the cross validation score reached a peak with 11 features. In view of the limited number of samples, PCA was then applied to these 11 selected features to avoid overfitting due to the large number of features. **Figure 3E** shows a correlation heat map of the above 11 features and **Figures 3F–H** the results of the PCA, and eventually, 6 features were selected for building the classification models. Using similar feature reduction methods, 5 features from T2 sequences and 8 features from T1 + T2 sequences were finally selected, and these finally selected features were listed in **Table 2**.

TABLE 2 | The features selected for model construction.

Sequences	Features
T1	Image_original_Maximum
	shape_MajorAxisLength
	shape_Maximum2DdiameterSlice
	glcm_JointEnergy
	gldm_DependenceEntropy
	glszm_SmallAreaLowGrayLevelEmphasis
T2	**shape_MajorAxisLength**
	shape_Maximum2DdiameterSlice
	glcm_Imc1
	glcm_MCC
	gldm_DependenceEntropy
T1 + T2	**shape_MajorAxisLength**
	shape_Maximum2DdiameterSlice
	shape_Maximum2DdiameterColumn
	shape_SurfaceVolumeRatio
	glcm_DifferenceVariance
	glcm_MCC
	glcm_Imc2
	glcm_SumSquares

Bold font indicates the universal features used for all three sequences. glcm, gray level co-occurrence matrix; gldm, gray level dependence matrix; glszm, gray level size zone matrix; Imc, informational measure of correlation; MCC, maximal correlation coefficient.

Model Building and Evaluation

Four models were built using the features described in **Table 2**. **Table 3** shows the accuracy and AUC of each model, and indicates that for all models the T2WI seemed to be superior to the T1WI, both in terms of accuracy and AUC. This table also reveals that the SVM model showed better performance than the other models. Using the T1 + T2 features, the SVM model demonstrated high accuracy of 93% (95% CI: 91–96%) and an AUC of 98% (95% CI: 97–99%). The LR model using T2 features also showed good performance, and a nomogram of this model is exhibited in **Figure 4**. The LR model had a C-index of 0.93 on the training set and 0.96 on the validation set.

TABLE 3 | The ACC and AUC of each model.

Sequences	Models	ACC	AUC
T1	LR	77% (67%∼83%)	91% (84%∼97%)
	SVM	86% (82%∼95%)	93% (89%∼98%)
	DT	85% (82%∼92%)	97% (95%∼99%)
	RF	83% (75%∼92%)	96% (94%∼98%)
T2	**LR**	**93% (85%∼100%)**	**91% (89%∼92%)**
	SVM	**92% (91%∼100%)**	**95% (94%∼97%)**
	DT	89% (83%∼92%)	97% (96%∼99%)
	RF	89% (83%∼100%)	97% (94%∼100%)
T1 + T2	LR	88% (84%∼91%)	85% (84%∼86%)
	SVM	**93% (91%∼96%)**	**98% (97%∼99%)**
	DT	83% (79%∼87%)	96% (95%∼97%)
	RF	88% (83%∼92%)	97% (95%∼98%)

Models with an ACC over 90% are marked in bold font. ACC, accuracy; AUC, area under the curve; LR, logistic regression; SVM, support vector machine; DT, decision tree; RF, random forest.

DISCUSSION

The differentiation of OCH and OSC has long been a clinical problem. In this study, we attempted to solve this problem with radiomics, and the results demonstrated the technique's potential for differentiating between the two disorders.

For orbital tumor patients, T1WI and T2WI are more commonly used than contrast-enhanced MRI, especially for those with renal failure or contrast medium allergy (20). Therefore, our results obtained using only these two routine sequences could be widely used and verified in clinical practice. To explore the contributions of each single sequence and a combined sequence (T1 + T2), we compared radiomics features extracted from each image type. Our results showed that the T2WI provided better accuracy than the T1WI, a conclusion also found in some other studies (16, 21, 22). Hopewell et al. considered that the greater contribution of T2WI may be associated with the heterogeneous angiogenesis of the tumor (23). It is known that ischemia, angioedema, and avascular necrosis are more likely to be observed on T2WI. Furthermore, the much longer echo time on T2WI in comparison with T1WI may also be a factor influencing the results (22). The model using both sequences combined achieved a higher score and AUC than either of the sequences alone, just as Han et al. observed in their studies (16, 24).

OSC may tend to grow rapidly. Of all the selected features, we found that the features of shape_ MajorAxisLength and shape_Maximum2DdiameterSlice were present in all sequence groups. The shape feature MajorAxisLength is defined as the largest axis length of the ROI-enclosing ellipsoid, while the shape feature Maximum2DdiameterSlice is defined as the largest pairwise Euclidean distance between tumor surface mesh vertices in the row-column (generally the axial) plane. As can be seen in **Figure 2**, a large tumor size may be more indicative of OSC, which may be related to the progressive growth of OSC. Accordingly, a substantial portion of the OCH tumors were found incidentally, whereas almost all the OSC patients were suffering from symptoms of tumor rapid growth. Furthermore, OCH is often found in middle age at 40–50 years, whereas OSC can present at any age (3, 25–27). OSC may manifest heterogeneous on MRI just as a "geographic map." Except for the above-mentioned two shape features, the other selected features, such as gldm_DependenceEntropy and glcm_MCC, all implied that OSC presented with heterogenous signal intensity. As Tanaka et al. mentioned in their studies (8, 10, 28), OSC is more likely to present heterogeneous than OCH.

The use of radiomics provided a number of advantages compared with previous studies. 1) This was the first attempt to differentiate OCH and OSC with radiomics, and it worked well. 2) Digital features were extracted rather than qualitative assessment through the reader's eye, and detailed data were provided for the analysis rather than a simple statement such as "high signal intensity." 3) Radiomics can make the reading of images and the analysis automated, thereby reducing human error. 4) Objective and repeatable results are more valuable for the clinician than a subjective judgement. However, there are inevitably some limitations to our study. 1) The limited sample size due to the low incidence of the two disorders may have led to a bias in the results, although we restricted the number of features to avoid overfitting. 2) The data used in this study were from a single center, which may affect the robustness of the model. 3) The absence of an external validation cohort because of the limited samples could also limit the final efficiency. 4) The disproportionate numbers of individuals with OSC and OCH is another limitation, and might have affected the statistics and the results. Therefore, a further multi-center analysis is needed to support our results.

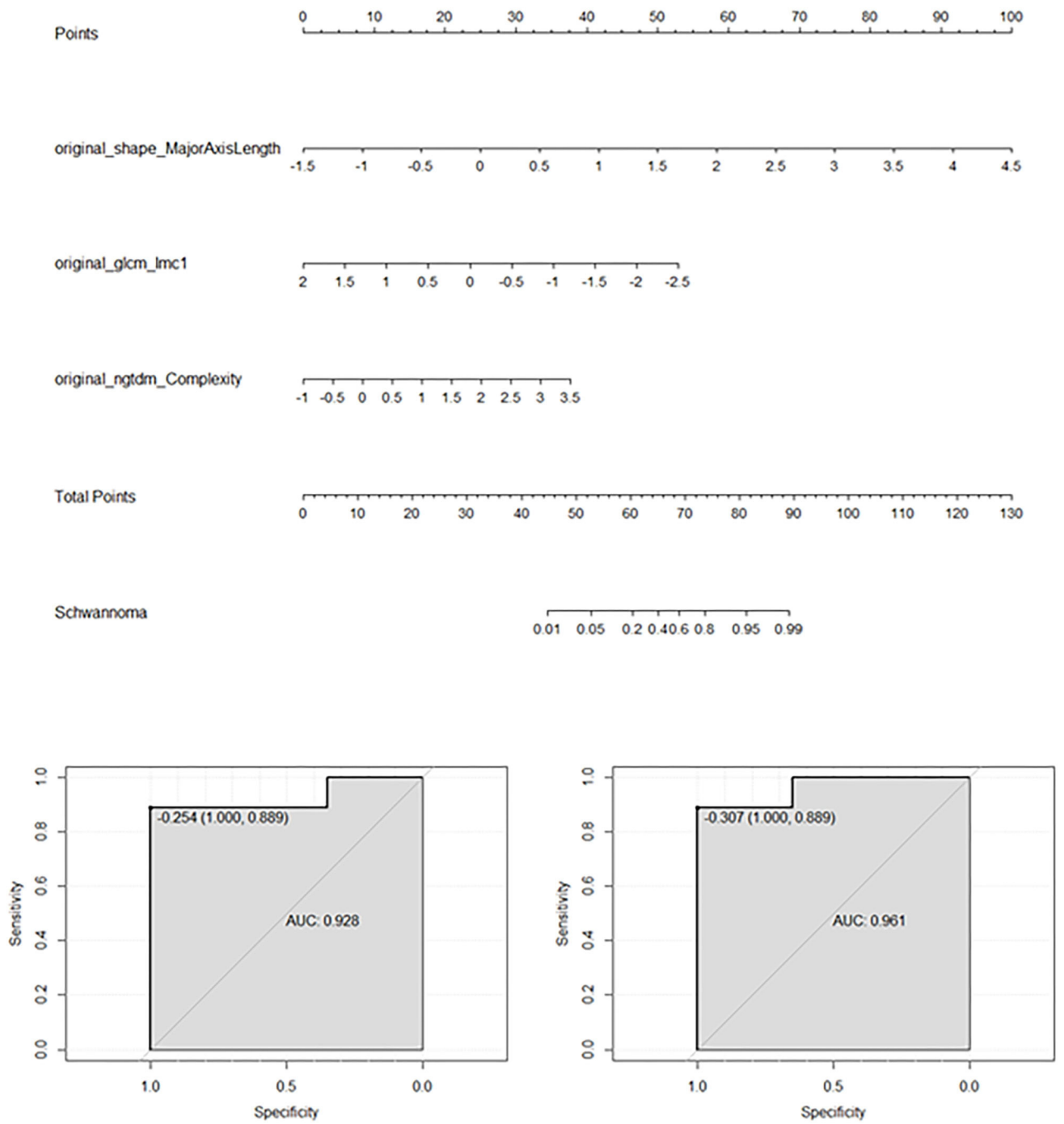

FIGURE 4 | Results of the logistics regression model applied to T2WI. The feature data were standardized with zero-mean normalization. This nomogram is mainly used to predict the odds of OSC rather than OCH according to the three features. The bottom images show the AUCs of the logistic regression model for the training set (left) and validation set (right).

DATA AVAILABILITY STATEMENT

The raw data supporting the conclusions of this article will be made available by the authors, without undue reservation.

ETHICS STATEMENT

The studies involving human participants were reviewed and approved by Ethics Committee of Shanghai Changzheng

Hospital Affiliated with Naval Military Medical University. The patients/participants provided their written informed consent to participate in this study. Written informed consent was obtained from the individual(s) for the publication of any potentially identifiable images or data included in this article.

AUTHOR CONTRIBUTIONS

LC: methodology, software, formal analysis, investigation, data curation, writing—original draft, review and editing, and visualization. WY: methodology, writing—review and editing, supervision, and project administration. RW: conceptualization, methodology, validation, investigation, writing—review and editing, supervision, and project administration. JL: data curation and writing—review and editing. HL: resources and data curation. XH: methodology, validation, writing—review and editing. YS: validation, formal analysis, resources, writing—review and editing. All authors contributed to the article and approved the submitted version.

FUNDING

This work was supported by National Natural Science Foundation of China (Grant No. 81770959); National Natural Science Foundation of China (Grant No. 81570885).

ACKNOWLEDGMENTS

We would like to extend our deep gratitude to all those who have offered cordial and selfless support in this work. We thank Karl Embleton, Ph.D., from Liwen Bianji (Edanz) (www.liwenbianji.cn/), for editing the English text of a draft of this manuscript.

REFERENCES

1. Zhang L, Li X, Tang F, Gan L, Wei X. Diagnostic imaging methods and comparative analysis of orbital cavernous hemangioma. *Front Oncol.* (2020) 10:577452. doi: 10.3389/fonc.2020.577452
2. Claros P, Choffor-Nchinda E, Lopez-Fortuny M, Claros A, Quintana S. Orbital cavernous haemangioma; profile and outcome of 76 patients managed surgically. *Acta Otolaryngol.* (2019) 139:720–5. doi: 10.1080/00016489.2019.1618913
3. Chaskes MB, Rabinowitz MR. Orbital schwannoma. *J Neurol Surg B Skull Base.* (2020) 81:376–80. doi: 10.1055/s-0040-1713935
4. Kapur R, Mafee MF, Lamba R, Edward DP. Orbital schwannoma and neurofibroma: role of imaging. *Neuroimaging Clin N Am.* (2005) 15:159–74. doi: 10.1016/j.nic.2005.02.004
5. Scheuerle AF, Steiner HH, Kolling G, Kunze S, Aschoff A. Treatment and long-term outcome of patients with orbital cavernomas. *Am J Ophthalmol.* (2004) 138:237–44. doi: 10.1016/j.ajo.2004.03.011
6. Yong KL, Beckman TJ, Cranstoun M, Sullivan TJ. Orbital schwannoma-management and clinical outcomes. *Ophthalmic Plast Reconstr Surg.* (2020) 36:590–5. doi: 10.1097/IOP.0000000000001657
7. Colletti G, Biglioli F, Poli T, Dessy M, Dessy M, Petrillo M, et al. Vascular malformations of the orbit (lymphatic, venous, arteriovenous): diagnosis, management and results. *J Craniomaxillofac Surg.* (2019) 47:726–40. doi: 10.1016/j.jcms.2018.09.009
8. Xian J, Zhang Z, Wang Z, Li J, Yang B, Chen Q, et al. Evaluation of MR imaging findings differentiating cavernous haemangiomas from schwannomas in the orbit. *Eur Radiol.* (2010) 20:2221–8. doi: 10.1007/s00330-010-1774-y
9. Hasegawa M, Fujisawa H, Hayashi Y, Yamashita J, Suzuki M, Matsui O. CT arteriography for orbital tumors: diagnostic and surgical value. *J Clin Neurosci.* (2005) 12:548–52. doi: 10.1016/j.jocn.2004.08.012
10. Tanaka A, Mihara F, Yoshiura T, Togao O, Kuwabara Y, Natori Y, et al. Differentiation of cavernous hemangioma from schwannoma of the orbit: a dynamic MRI study. *AJR Am J Roentgenol.* (2004) 183:1799–804. doi: 10.2214/ajr.183.6.01831799
11. Lambin P, Leijenaar RTH, Deist TM, Peerlings J, de Jong EEC, van Timmeren J, et al. Radiomics: the bridge between medical imaging and personalized medicine. *Nat Rev Clin Oncol.* (2017) 14:749–62. doi: 10.1038/nrclinonc.2017.141
12. Christie JR, Lang P, Zelko LM, Palma DA, Abdelrazek M, Mattonen SA. Artificial intelligence in lung cancer: bridging the gap between computational power and clinical decision-making. *Can Assoc Radiol J.* (2021) 72:86–97. doi: 10.1177/0846537120941434
13. Bi WL, Hosny A, Schabath MB, Giger ML, Birkbak NJ, Birkbak NJ, et al. Artificial intelligence in cancer imaging: clinical challenges and applications. *CA Cancer J Clin.* (2019) 69:127–57. doi: 10.3322/caac.21552
14. Sala E, Mema E, Himoto Y, Veeraraghavan H, Brenton JD, Snyder A, et al. Unravelling tumour heterogeneity using next-generation imaging: radiomics, radiogenomics, and habitat imaging. *Clin Radiol.* (2017) 72:3–10. doi: 10.1016/j.crad.2016.09.013
15. Hassani C, Varghese BA, Nieva J, Duddalwar V. Radiomics in pulmonary lesion imaging. *AJR Am J Roentgenol.* (2019) 212:497–504. doi: 10.2214/AJR.18.20623
16. Han Y, Yang Y, Shi ZS, Zhang AD, Yan LF, Hu YC, et al. Distinguishing brain inflammation from grade II glioma in population without contrast enhancement: a radiomics analysis based on conventional MRI. *Eur J Radiol.* (2021) 134:109467. doi: 10.1016/j.ejrad.2020.109467
17. Su Y, Xu X, Zuo P, Xia Y, Qu X, Chen Q, et al. Value of MR-based radiomics in differentiating uveal melanoma from other intraocular masses in adults. *Eur J Radiol.* (2020) 131:109268. doi: 10.1016/j.ejrad.2020.109268
18. Tustison NJ, Avants BB, Cook PA, Zheng Y, Egan A, Yushkevich PA, et al. N4ITK: improved N3 bias correction. *IEEE Trans Med Imaging.* (2010) 29:1310–20. doi: 10.1109/TMI.2010.2046908
19. Mueller-Using S, Feldt T, Sarfo FS, Eberhardt KA. Factors associated with performing tuberculosis screening of HIV-positive patients in Ghana: LASSO-based predictor selection in a large public health data set. *BMC Public Health.* (2016) 16:563. doi: 10.1186/s12889-016-3239-y
20. Marasini R, Thanh Nguyen TD, Aryal S. Integration of gadolinium in nanostructure for contrast enhanced-magnetic resonance imaging. *Wiley Interdiscip Rev Nanomed Nanobiotechnol.* (2020) 12:e1580. doi: 10.1002/wnan.1580
21. Petrujkic K, Milosevic N, Rajkovic N, Stanisavljević D, Gavrilović S, DŽelebdŽić D, et al. Computational quantitative MR image features - a potential useful tool in differentiating glioblastoma from solitary brain metastasis. *Eur J Radiol.* (2019) 119:108634. doi: 10.1016/j.ejrad.2019.08.003
22. Chen X, Wei X, Zhang Z, Yang R, Zhu Y, Jiang X. Differentiation of true-progression from pseudoprogression in glioblastoma treated with radiation therapy and concomitant temozolomide by GLCM texture analysis of conventional MRI. *Clin Imaging.* (2015) 39:775–80. doi: 10.1016/j.clinimag.2015.04.003
23. Hopewell JW, Calvo W, Jaenke R, Reinhold HS, Robbins ME, Whitehouse EM. Microvasculature and radiation damage. *Recent Results Cancer Res.* (1993) 130:1–16. doi: 10.1007/978-3-642-84892-6_1
24. Han Y, Yan Lf, Wang XB, Sun YZ, Zhang X, Liu ZC, et al. Structural and advanced imaging in predicting MGMT promoter methylation of primary glioblastoma: a region of interest based analysis. *BMC Cancer.* (2018) 18:215. doi: 10.1186/s12885-018-4114-2
25. Bachelet JT, Berhouma M, Shipkov H, Kodjikian L, Jouanneau E, Gleizal A. Orbital cavernous hemangioma causing spontaneous compressive hemorrhage. *J Craniofac Surg.* (2018) 29:706–8. doi: 10.1097/SCS.0000000000004285

26. Ansari SA, Mafee MF. Orbital cavernous hemangioma: role of imaging. *Neuroimaging Clin N Am.* (2005) 15:137–58. doi: 10.1016/j.nic.2005.02.009
27. Lopez J, Hamill EB, Burnstine M. Orbital schwannoma management: a case report, literature review, and potential paradigm shift. *Orbit.* (2021) 1–13. doi: 10.1080/01676830.2020.1858431. [Epub ahead of print].
28. Xian J, Zhang Z, Wang Z, Li J, Yang B, Man F, et al. Value of MR imaging in the differentiation of benign and malignant orbital tumors in adults. *Eur Radiol.* (2010) 20:1692–702. doi: 10.1007/s00330-009-1711-0

Conflict of Interest: The authors declare that the research was conducted in the absence of any commercial or financial relationships that could be construed as a potential conflict of interest.

Publisher's Note: All claims expressed in this article are solely those of the authors and do not necessarily represent those of their affiliated organizations, or those of the publisher, the editors and the reviewers. Any product that may be evaluated in this article, or claim that may be made by its manufacturer, is not guaranteed or endorsed by the publisher.

frontiers in Medicine

ORIGINAL RESEARCH
published: 16 December 2021
doi: 10.3389/fmed.2021.796778

High-Resolution Image Analysis Reveals a Decrease in Lens Thickness and Cone Density in a Cohort of Young Myopic Patients

Xiaoyu Xin[1,2], *Qingge Guo*[1,2], *Shuai Ming*[1,2], *Changgeng Liu*[1,2], *Zhongfeng Wang*[3] and *Bo Lei*[1,2,4*]

[1] Department of Ophthalmology, Henan University People's Hospital, Henan Provincial People's Hospital, Zhengzhou, China, [2] Henan Eye Institute, Henan Eye Hospital, Henan Provincial People's Hospital, Zhengzhou, China, [3] State Key Laboratory of Medical Neurobiology and MOE Frontiers Center for Brain Science, Institutes of Brain Science, Fudan University, Shanghai, China, [4] Department of Ophthalmology, Zhengzhou University People's Hospital, Zhengzhou University, Zhengzhou, China

OPEN ACCESS

Edited by:
Peng Xiao,
Sun Yat-sen University, China

Reviewed by:
Haoyu Chen,
Shantou University & The Chinese University of Hong Kong, China
Kari Vienola,
University of California, Davis, United States

***Correspondence:**
Bo Lei
bolei99@126.com
orcid.org/0000-0002-5497-0905

Specialty section:
This article was submitted to Ophthalmology, a section of the journal Frontiers in Medicine

Received: 17 October 2021
Accepted: 16 November 2021
Published: 16 December 2021

Citation:
Xin X, Guo Q, Ming S, Liu C, Wang Z and Lei B (2021) High-Resolution Image Analysis Reveals a Decrease in Lens Thickness and Cone Density in a Cohort of Young Myopic Patients. Front. Med. 8:796778. doi: 10.3389/fmed.2021.796778

Purpose: To study the association between axial length (AL) and the thickness of the lens, retina, choroid, and cone density with swept-source optical coherence tomography (SS-OCT) and an adaptive optics (AO) fundus camera.

Design: A prospective cross-sectional study.

Methods: This study included 136 eyes in 68 subjects. SS-OCT was used to quantify the thickness of the lens, ganglion cell complex (GCC) layer, inner nuclear layer (INL), outer retinal layer (ORL), and choroid layer. Adaptive optics was used to quantify spatial features of the cone photoreceptors, including density, spacing, regularity, and dispersion. The associations among the AL and the thickness of lens, retina, choroid, and cone features were evaluated with linear regression.

Results: With the severity of myopia, the increased AL was associated with thinning of the lens ($P < 0.001$, 95% CI: −100.42 to −49.76). The thickness of the ORL and choroid decreased significantly (all $P < 0.001$), whereas the thickness of the GCC and INL decreased only in the outer ring (both $P < 0.01$). There was a significant correlation between the cone density/spacing and AL (both $P < 0.001$). Although cone density was reduced from 25,160/mm^2 to 19,134/mm^2 in the inner region and from 17,458/mm^2 to 13,896/mm^2 in the outer region, the best-corrected visual acuity (BCVA) was 20/20 or greater.

Conclusions: We found that the lens thickness (LT), ORL, and cone density decreased in myopia. While decreasing cone density and ORL thickness should be related to axial elongation, decreasing of LT might imply intrinsic physical accommodation. These results provide further morphological changes of myopia.

Keywords: myopia, retina, cone, lens, adaptive optics

INTRODUCTION

Myopia is a common refractive condition where parallel rays entering the eye are imprinted in front of the retina rather than focusing on it when ocular accommodation is relaxed (1). The prevalence of myopia is increasing dramatically on a global basis (2), particularly in East Asia, where the prevalence of myopia reaches >80% in young adults (3). It is assumed that 50% and 10% of the world population will develop myopia and high myopia (HM), respectively (4). Myopia is regarded as a major global public health problem (3). Accordingly, understanding the anatomical changes of myopia is of great importance for understanding the mechanisms of this condition, as well as making strategic plans to control it.

Recently, it has been generally believed that myopia may be the result of a disruption of the balance between axial elongation and loss of refraction power of the cornea and lens (5, 6). It was reported that corneal power became stabilized early in life, at approximately 1–2 years after birth (7, 8). Consequently, the importance of lens power and axial length (AL) in myopia is exaggerated (9). To maintain an emmetropization status, AL continues to elongate while the lens tends to be thin and flatten during human growth and development (3). However, when the lens reaches a limit where it can no longer compensate for the growth of the axis, myopia occurs (7, 9).

With the development of myopia, the fundus also changes. Several studies reported that choroidal thickness (10, 11) and choroidal blood perfusion (10, 12) reduced dramatically in HM eyes. Meanwhile, reductions in retinal thickness and vascular density have been demonstrated (13, 14). These changes observed in HM eyes were regarded mainly as the consequence of axial elongation (15, 16). The primary function of the choroid is to supply oxygen and nourishment to the outer retina (17). When the choroid thickness and blood perfusion decrease, the outer retina is affected, which may lead to dysfunction of the photoreceptors (18).

However, reports concerning whether the thickness of the lens and whether the photoreceptors are changed concurrently during the progression of myopia are limited, partially because of lacking applicable technology that could reveal the detailed morphological changes. To explore the changes of cone photoreceptors in myopia, we used an adaptive optics (AO) fundus camera to measure the parameters of the cone photoreceptors in patients. Simultaneously, the thicknesses of the lens, retina, and choroid were obtained from high resolution swept-source optical coherence tomography (SS-OCT), which presented higher penetration up to 6 mm and made as detailed a measurement as possible. We analyzed the relationship between AL and the lens thickness (LT), choroidal thickness, retinal thickness, and spatial features of the cone photoreceptors in a cohort of young myopic patients.

METHODS

Subjects

A total of 68 subjects between the ages of 21 and 32 years were recruited from Henan Provincial People's Hospital from December 2020 to February 2021. Approval for the study was obtained from the Ethics Committee of Henan Eye Hospital. All participants signed written informed consent after being informed about the nature and possible consequences of the project, in compliance with the tenets of the Declaration of Helsinki.

All the participants underwent the collection of disease history and a comprehensive ophthalmic examination, including best-corrected visual acuity (BCVA), refraction error (non-cycloplegic), non-contact tonometer (NT-530, NIDEK, Gamagori, Japan) for intraocular pressure (IOP), slit-lamp, and fundus photography (DRS, Padova, Italy). Axial length was measured (IOL Master 500; Carl Zeiss Meditec AG, Jean, Germany). The spherical equivalent (SE) of all eyes was calculated followed by the spherical power plus half of the

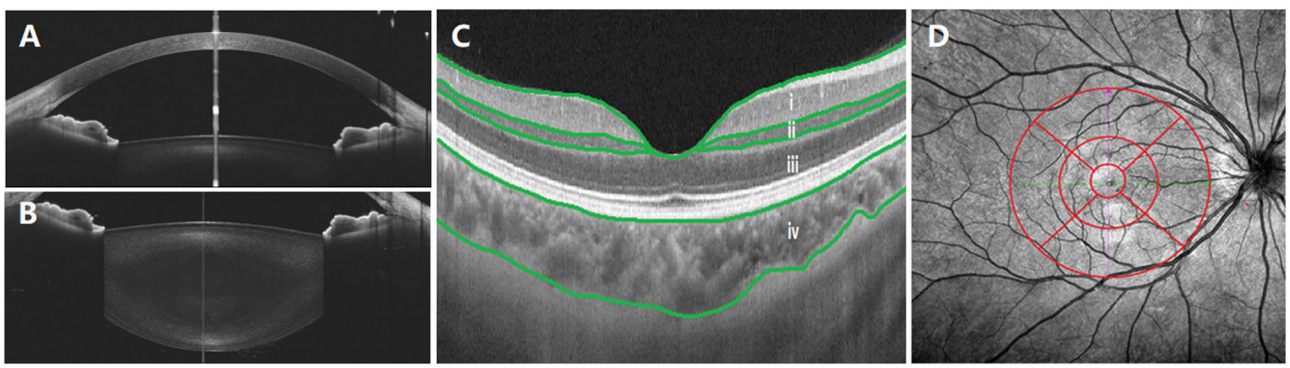

FIGURE 1 | Examination of central corneal thickness (CCT), anterior chamber depth (ACD), lens thickness (LT), choroid, and retina. **(A)** CCT and ACD; **(B)** LT; **(C)** optical coherence tomography (OCT) image. The built-in software in swept-source OCT (SS-OCT) automatically divided fundus structure into four layers: (i) ganglion cell complex (GCC) layer; (ii) inner nuclear layer (INL); (iii) outer retinal layer (ORL); (iv) choroid layer. **(D)** OCT angiography (OCTA) image. The white vertical line is "corneal reflex" in **(A,B)**, the red region is the Early Treatment Diabetic Retinopathy Study (EDTRS) grid in **(C)**. CCT, central corneal thickness; ACD, anterior chamber depth; LT, lens thickness; OCT, optical coherence tomography; SS-OCT, swept-source optical coherence tomography; OCTA, optical coherence tomography angiography; EDTRS, Early Treatment Diabetic Retinopathy Study.

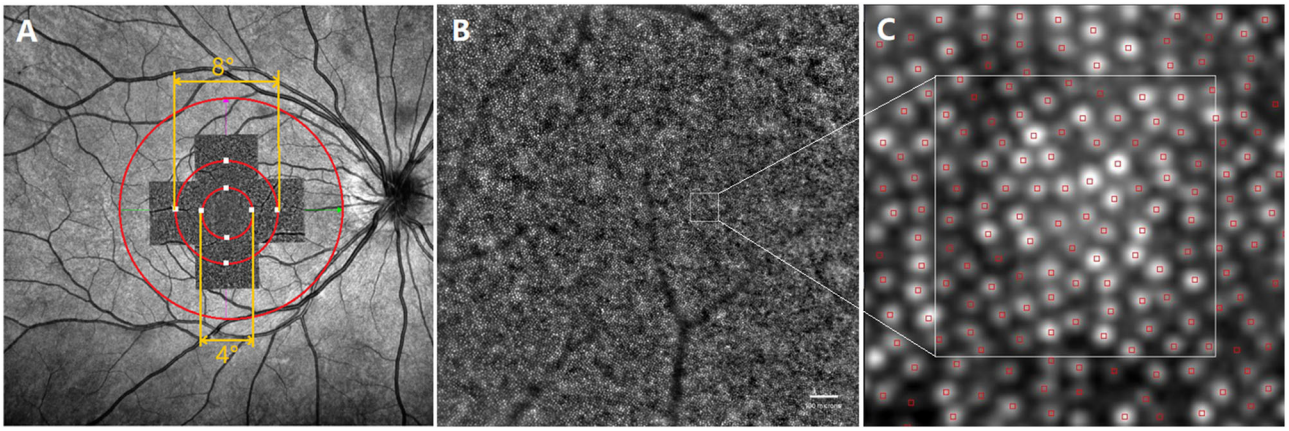

FIGURE 2 | Representative images of swept -optical coherence tomography angiography (SS-OCTA) and adaptive optics (AO). **(A)** The AO image is superimposed on the fundus image by SS-OCTA. The AO montage with a window size of 10° × 10° was created centered on the fovea. The eight white squares shown in the figure represent the measured locations, including four for the inner region (the circle with a diameter of 4°) and four for the outer region (the circle with a diameter of 8°); **(B)** one of the images that made up the AO montage. ROI, white square, represented acquisition window (the size of 100 × 100 μm); **(C)** The white square is a magnified view of an ROI. SS-OCTA, swept-optical coherence tomography angiography; AO, adaptive optics; ROI, region of interest.

negative cylinder power. The inclusion criteria were 20–35 years of age; BCVA 20/20 or better; 10–21 mmHg of IOP; no eye tremor, and good fixation. The exclusion criteria were the use of any eye drops recently, abnormal physical development in eyes, any history of general diseases, ocular diseases and eye surgeries, and pregnant and lactating women.

Swept-Source Optical Coherence Tomography and Swept-Source Optical Coherence Tomography Angiography Measurements

All subjects were imaged using SS-OCT (VG200D SVision Imaging, Henan, China) with a central wavelength of 1,050 nm and a scanning speed of 200,000 A-scans per second. The system provided axial resolutions of 5 μm and transverse resolutions of 20 μm. Only high-quality scans which had signal strength >8 (0 = poor, 10 = good) were selected. The data of both eyes of the subjects were collected. All scans were performed by the same experienced operator.

In anterior segment scanning, two sets of images (the anterior chamber was included in the cornea group) were obtained from 18 consecutive radial B-scans (Star 18 Line R32 mode) of the cornea/lens by the axial shifting of the focal planes on the cornea and the lens, respectively. During imaging, the examiner observed the position of the eyes to achieve optimal alignment, which was defined as a "corneal reflex" (an optically vertical line through the center of the image, **Figures 1A,B**) was seen. The central corneal thickness (CCT), anterior chamber depth (ACD), and LT were measured with built-in software. The images were excluded from the analysis when their quality from one eye was poor.

Posterior segment scanning mode (Angio 6 × 6 mm, 512 × 512 R4 modes) was used to obtain macular SS-OCTA (a 6 × 6 mm radial scan centered on the fovea). In this mode, a total of 512 lines were scanned each time. In total, 512 A-scans were performed for each line, and each line was scanned four times. Retinal/choroidal thickness was automatically divided into four layers (**Figure 1C**) with the built-in software: (i) ganglion cell complex (GCC) layer, perpendicularly from the inner edge of the retinal nerve fiber layer to the outer edge of the inner

TABLE 1 | Patient demographics.

Variable	Total (n = 136)
Age, years	
Range	21–32
Mean ± SD	24.07 ± 2.33
Min, Median, Maximum	21, 24, 32
Gender	
Men	52 (38%)
Women	84 (62%)
SE, D	
EM/LM	37 (27%)
Range	+0.50 to −2.75
Mean ± SD	−1.60 ± 1.12
Min, Median, Maximum	−2.75, −2.00, 0.00
MM	52 (38%)
Range	−3. 00 to −5.75
Mean ± SD	−4.92 ± 0.81
Min, Median, Maximum	−5.75, −5.00, −3.00
HM	47 (35%)
Range	≤-6.00
Mean ± SD	−7.69 ± 1.20
Min, Median, Maximum	−11.50, −7.25, −6.00

Data values are n (%) or mean ± SD. SD, standard deviation; SE, spherical equivalent; EM/LM, emmetropia and low myopia; MM, moderate myopia; HM, high myopia.

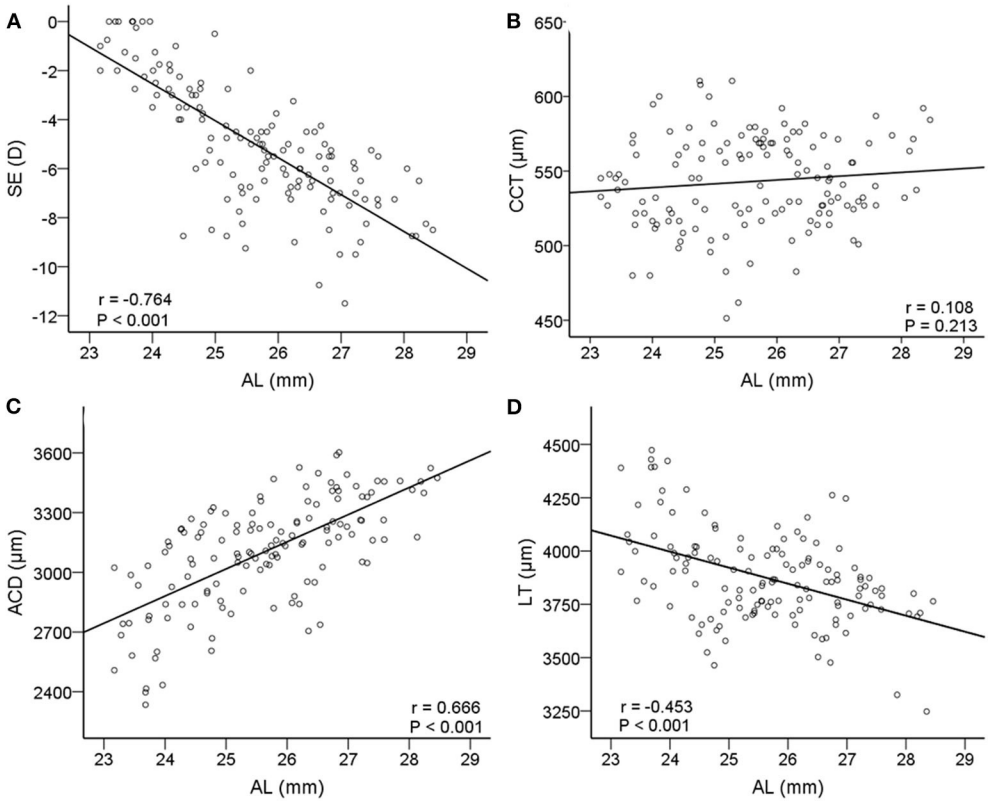

FIGURE 3 | Correlations between axial length (AL) and other relative biometric parameters. Scatterplots showing AL vs. **(A)** spherical equivalent (SE); **(B)** CCT; **(C)** ACD; **(D)** LT. AL, axial length; SE, spherical equivalent; CCT, central corneal thickness; ACD, anterior chamber depth; LT, lens thickness.

plexiform layer; (ii) inner nuclear layer (INL), perpendicularly from the inner edge of the INL to the outer edge of the INL; (iii) outer retinal layer (ORL), perpendicularly from the inner edge of the outer plexiform layer to the inner edge of the RPE; (iv) choroid layer, perpendicularly from the outer edge of the RPE to the choroid–sclera junction. A retinal/choroidal thickness map was established based on the Early Treatment Diabetic Retinopathy Study (ETDRS) grid (**Figure 1D**), which was centered on the fovea, separating the region into nine subfields by three concentric circles: an inner circle (diameter of 1 mm), a middle circle (diameter of 3 mm), and an outer circle (diameter of 6 mm). The inner ring (between the inner and middle circles) and the outer ring (between the middle and outer circle) were divided into four quadrants: superior, temporal, inferior, and nasal. The built-in SS-OCT software automatically calculated the average values of the eight regions, including four quadrants from the inner and outer rings. The images of two eyes were poor and were excluded from the analysis.

AO Measurements

An AO fundus camera (rtx1, Imagine Eyes, Orsay, France) was used to reveal the spatial features of cone photoreceptors. One captured field of imaging was $4^\circ \times 4^\circ$ which was equivalent to $1{,}200 \times 1{,}200\,\mu m$. The initial coordinate was $(0^\circ, 0^\circ)$, which corresponded to the fovea. The subjects were asked to consecutively fixate at 3° of eccentricity along the four meridians of superior, temporal, inferior, and nasal, to image the parafoveal regions. After the image acquisition, five pictures were analyzed with the built-in software (i2k Retina Pro) to generate a montage size of approximately $10^\circ \times 10^\circ$ which was equivalent to 3×3 mm. The inner ring of the ETDRS was the area between the inner circle (diameter 1 mm) and the middle circle (diameter 3 mm), corresponding to the view of the AO montage image (3×3 mm) (**Figure 2**, red cycle).

The spatial features of the cone photoreceptors were analyzed with software provided by the manufacturer (AO Detect 0.2; Imaging Eyes, Orsay, France). The cones were analyzed at 2° (inner region) and 4° (outer region) eccentricity along the four meridians of superior, temporal, inferior, and nasal. Three $100 \times 100\,\mu m$ regions of interest (ROIs) avoiding blood vessels were chosen. The spatial characteristics of cones, including density, spacing, regularity, and dispersion were recorded. Cone density was defined as the number of cells per square millimeter, cone spacing was defined as the center-to-center spacing of adjacent cones, cone regularity was defined as the percentage of cells that had five to seven neighbor cells, and cone dispersion was defined as the spread of cones, which was the coefficient of variation of the cone spacing. The average values of the three parameters were

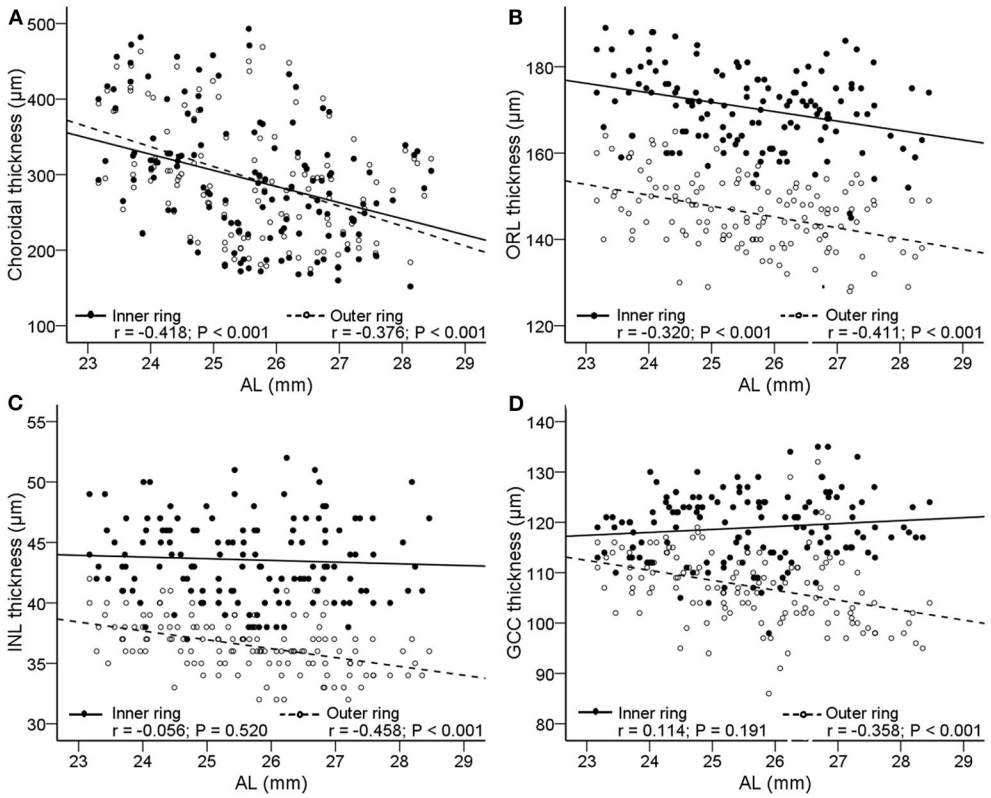

FIGURE 4 | Correlations between AL and the thickness of choroid and retina. Scatterplots showing AL vs. **(A)** choroidal thickness; **(B)** outer retinal layer (ORL); **(C)** inner nuclear layer (INL); **(D)** ganglion cell complex (GCC). The *solid lines* and *filled circles* represent the results in the inner ring. The *dashed lines* and *open circles* represent the results in the outer ring. AL, axial length; ORL, outer retinal layer; INL, inner nuclear layer; GCC, ganglion cell complex.

obtained. The AO images of 40 eyes were poor and were excluded from the analysis.

Statistical Analysis

Statistical analyses were performed using SPSS (version 21.0; IBM SPSS, Chicago, Illinois, USA). Age differences were analyzed by Spearman's correlation. Pearson's correlation and regression were used to analyze the relationship between AL and the biological parameters of anterior and posterior segments. A *P*-value of 0.05 was chosen to denote statistical significance.

RESULTS

General Information

A total of 136 eyes were included. The demographics are presented in **Table 1**, and the ocular biometric parameters are presented in **Supplementary Table 1**. There were 52 eyes from 26 men and 84 eyes from 42 women including 37 emmetropia and low myopia (EM/LM, +0.50 to −2.75 D of the sphere), 52 moderate myopia (MM, −3. 00 to −5.75 D of the sphere), and 47 HM (HM, ≤ −6.00 D of the sphere) eyes. The mean age of the patients was 24.07 ± 2.33 years, with a range between 21 and 32 years.

Associations Between Axial Length and Ocular Parameters

We investigated linear relationships between AL and SE. Axial length was negatively correlated with SE ($r = -0.764$, $P < 0.001$, 95% CI: −1.72 to −1.29, **Figure 3**). In **Figure 3**, with the increase of AL, ACD increased significantly ($r = 0.666$, $P < 0.001$, 95% CI: 100.20 to 162.61) and LT decreased significantly ($r = -0.453$, $P < 0.001$, 95% CI: −100.42 to −49.76), while CCT did not change ($r = 0.108$, $P = 0.213$, 95% CI: −1.48 to 6.58).

Figure 4 shows the scatter plots and linear regression of retinal and choroidal thickness as functions of AL. With axial elongation, the thickness of ORL and choroid decreased significantly both in the inner ring and outer ring ($r = -0.418$ to -0.320, all $P < 0.001$, **Figure 4**), whereas the GCC and INL layers tended to decrease in the outer ring ($r = -0.458$ to -0.358, both $P < -0.01$, **Figure 4**). In addition, we found that as AL increased, the GCC thickness of the superior, temporal, and inferior sectors in the outer ring decreased, but that of the nasal sector had no change (**Supplementary Table 2**).

Associations Between Axial Length and the Spatial Features of Cones

The cone spatial distribution has four characteristics: density, spacing, regularity, and dispersion. Axial length elongation was

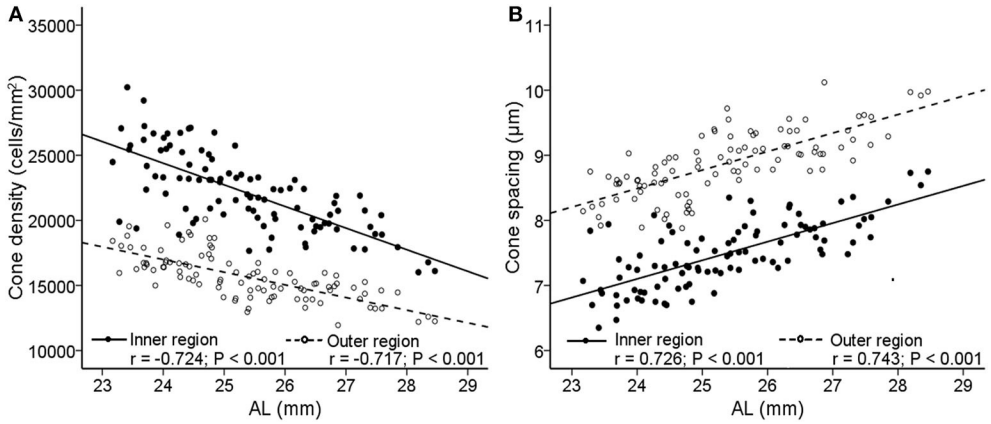

FIGURE 5 | Correlations between AL and cone photoreceptor spatial distribution features. Scatterplots show AL vs. **(A)** cone density; **(B)** cone spacing. The *solid lines* and *filled circles* represent the results in the inner region. The *dashed lines* and *open circles* represent the results in the outer region. AL, axial length.

significantly correlated with density and spacing both in the inner and outer regions ($r = -0.724$ to.743, all $P < 0.001$, **Figure 5**; **Table 2**), while was not related to the regularity and dispersion (both $P > 0.05$, **Table 2**).

TABLE 2 | Correlations between AL and cone spatial distribution features.

	Inner region		Outer region	
	r	*P*	*r*	*P*
Density	−0.724	**<0.001**	−0.717	**<0.001**
Spacing	0.726	**<0.001**	0.743	**<0.001**
Regularity	−0.168	0.101	−0.139	0.176
Dispersion	0.372	0.053	0.194	0.057

Significant difference bolded.

The Relationship Between the Cone Spatial Features and the Thickness of Choroid and Retina

We further analyzed the association between the spatial characteristics of cone photoreceptors with the thickness of the choroid and retina. We found that thickness of the choroid/ORL was significantly correlated with cone density ($r = 0.297$ to.332, both $P < 0.01$, **Table 3**) and cone spacing ($r = -0.311$ to -0.292, both $P < 0.01$, **Table 3**), but not with cone regularity and dispersion (all $P > 0.05$, **Table 3**). However, with the decrease of INL, cones were less regular ($r = 0.224$, $P = 0.028$, 95% CI: 0.01 to 0.18, **Table 3**) and more dispersed ($r = -0.228$, $P = 0.025$, 95% CI: −0.15 to −0.01, **Table 3**), whereas GCC was not associated with cone density and spacing (both $P > 0.05$, **Table 3**).

DISCUSSION

We evaluated the changes of major biometric parameters of the myopic eyes by SS-OCT and cone photoreceptor spatial features by AO. This study was a comprehensive evaluation of the changes of the anterior and posterior segment parameters simultaneously in myopic eyes. We found that among the changes of the refractive system and fundus structure in young myopic adults, the changes with regards to the lens and cones were particularly prominent, in addition to the choroidal thickness.

Our findings are in agreement with previous studies that AL was negatively correlated with LT (19, 20), positively correlated with ACD (20), and not correlated with CCT (21, 22). Central corneal thickness, ACD, and LT are important components of AL. Before axial myopia occurs, the image could still focus on the retina through adaptive thinning of the lens. However, when the thinning of the lens fails to neutralize the growing axis of the eye (9), the image is focused in front of the retina, which may be the so-called irreversible true axial myopia. Because an accommodative lens may play a key role in the development of myopia, it is crucial to understand the changes of the lens during this process. While such data are still limited, partially because of lacking adequate and accurate detecting instruments.

During human growth and development, the thickness and shape of the lens change by producing new protein fibers (7, 20, 23, 24). Studies have shown that most children are far-sighted in the first few years of their life. With the growth of the eye, the AL gradually increases and the lens becomes relatively thinner to achieve a state of emmetropia (23, 24). There were a few reports concerning lens changes in myopia, nevertheless, the conclusions were controversial. Some studies showed that thinning of the lens was correlated with myopia (20, 24, 25), while some suggested that there was no correlation between LT and myopia (26, 27). Our findings are consistent with the former. A possible explanation for the difference in the results may be the methods or the subjects enrolled in these studies, such as the age of the patients and instruments used. In our study, the mean age of the participants was 24.07 ± 2.33 years, which was younger than other studies (26, 27). On the other hand, we used SS-OCT, which provided micron-scale accuracy, and we strongly believe it was better than instruments applied in previous studies. In most studies, myopia was thought to be caused mainly by

TABLE 3 | Correlations between cone features and the thickness of choroid and retina.

	Cone density, cells/mm^2		Cone spacing, μm		Cone regularity, %		Cone dispersion, %	
	r	*p*	*r*	*p*	*r*	*p*	*r*	*p*
Choroidal thickness, μm	0.297	**0.003**	−0.292	**0.004**	0.052	0.617	0.016	0.880
ORL thickness, μm	0.332	**0.001**	−0.311	**0.002**	0.195	0.057	−0.221	**0.031**
INL thickness, μm	0.111	0.282	−0.101	0.327	0.224	**0.028**	−0.228	**0.025**
GCC thickness, μm	0.051	0.621	−0.046	0.655	0.157	0.127	−0.160	0.119

Significant difference bolded.

the lengthening of the vitreous cavity (28), while little attention was paid to the changes of the lens. Our study provided solid evidence that reducing LT may be crucial in counteracting axial elongation functionally. During the progress of myopia, thinning of LT may, to some extent, compensate for the elongation of AL, which helps the eye maintain better vision. However, thinning of the lens should have certain limitations. When the limitation was reached, a focused image would be formed in front of the retina and near sight happens. Therefore, the importance of the changes of LT in myopia, especially in the earlier stages, was exaggerated.

Concerning the posterior segment, several studies have shown the relationship between the thinning of the retina and choroid with increasing myopia (29–32). Our findings further confirmed that of previous studies that thinning of ORL and choroid occurs in the inner and outer rings. In addition, we found that there was a significant negative correlation between AL and GCC or INL in the outer ring, but there was no correlation in the inner ring. The findings supported the opinion proposed by Lim et al. and Liu et al. that the thinning of the retina is more common in the outer ring (16, 33). In addition, as the AL increased, the GCC thickness of the superior, temporal, and inferior quadrants in the outer ring decreased, but the nasal quadrant did not change. A possible explanation was that as the eye stretched axially, the retina moved temporally away from the optic disc, which was also a reason for the formation of the tilted optic disc and the temporal crescent in high myopia.

We found that increased AL was significantly associated with decreased cone density and increased cone spacing in the inner and outer regions. One possible explanation was that the changes in cone photoreceptor distribution in young myopia were due to mechanical tension caused by axial elongation. The area covered by the retina was expanded along with the increase of the AL, which in turn caused the covering of a larger area with the same number of photoreceptors. Although cone density was reduced from 25,160/mm^2 to 19,134/mm^2 in the inner region and from 17,458/mm^2 to 13,896/mm^2 in the outer region in this cohort of patients, their BCVA, however, was 20/20 or greater. These data suggested that the decrease of cone density measured at 2 and 4 degrees of eccentricity did not affect the visual acuity in this cohort, even though the cone density at the fovea was still unknown. The notion was supported by our previous study where the cone system function was not affected in a similar cohort of myopia cases as tested by an electroretinogram (34). On the other hand, we did not see the association between AL and cone regularity, as observed in previous studies in myopia (18). It should be noticed that the current AO cannot ensure a high-quality image in each individual, even in young subjects. Factors that affect image acquisition include vitreous floc opacity, which is not uncommon in myopia patients. On the other hand, the quality of AO imaging is limited by pupil size and refractive compensation. Therefore, useful images were not obtained from all subjects. In addition, an AO retinal camera cannot resolve the cones in the center of the fovea because of the density, hence the software probably limits the closest analysis to two-degree eccentricity. Clearly, further research is necessary when an adequate standard is established.

In summary, we observed changes in the anterior and posterior segments in a cohort of myopic patients with high-resolution image systems. In addition to the decreasing of retinal and choroidal thickness, we found that the LT and cone density were remarkably decreased. Our study indicated that the change of the lens happened concurrently with the mosaic of cone photoreceptors. Thus, clinical assessment in myopia should consider these changes in the development of the common disorder, which may, in turn, result in further revealing their underlying mechanisms and developing novel interventions for this complicated condition.

DATA AVAILABILITY STATEMENT

The original contributions presented in the study are included in the article/**Supplementary Material**, further inquiries can be directed to the corresponding author/s.

ETHICS STATEMENT

The studies involving human participants were reviewed and approved by the Ethics Committee of Henan Eye Hospital. The patients/participants provided their written informed consent to participate in this study. Written informed consent was obtained from the individual(s) for the publication of any potentially identifiable images or data included in this article.

AUTHOR CONTRIBUTIONS

BL conceived and designed this study. XX and QG collected the clinical samples and clinical data. XX and SM analyzed

the sequencing data. XX collected the information and drafted and revised the manuscript. BL and ZW directed the work and finalized the manuscript. All authors contributed to the article and approved the submitted version.

FUNDING

This work was supported by National Natural Science Foundation of China Grants (81770949 and 82071008) and the Henan Key Laboratory of Ophthalmology and Vision Science.

ACKNOWLEDGMENTS

The author would like to thank all participants for participating in this study and their agreement to the use of their clinical data in this study.

SUPPLEMENTARY MATERIAL

The Supplementary Material for this article can be found online at: https://www.frontiersin.org/articles/10.3389/fmed.2021.796778/full#supplementary-material

REFERENCES

1. Flitcroft DI, He M, Jonas J. B., Jong, M., Naidoo, K., Ohno-Matsui, K., et al. IMI - defining and classifying myopia: a proposed set of standards for clinical and epidemiologic studies. *Invest Ophthalmol Vis Sci.* (2019) 60:M20–30. doi: 10.1167/iovs.18-25957
2. Dolgin E. The myopia boom. *Nature*. (2015) 519:276–8. doi: 10.1038/519276a
3. Baird PN, Saw SM, Lanca C, Guggenheim JA, Smith Iii E. L., Zhou, X., et al. Myopia. *Nat Rev Dis Primers*. (2020) 6:99. doi: 10.1038/s41572-020-00231-4
4. Holden, B. A., Fricke, T. R., Wilson, D. A., Jong, M., Naidoo, K. S., Sankaridurg, P., et al. (2016). Global prevalence of myopia and high myopia and temporal trends from 2000 through 2050. *Ophthalmology*. 123:1036–42. doi: 10.1016/j.ophtha.2016.01.006
5. Flitcroft DI. Is myopia a failure of homeostasis? *Exp Eye Res.* (2013) 114:16–24. doi: 10.1016/j.exer.2013.02.008
6. Mutti DO, Sinnott LT, Lynn Mitchell G, Jordan LA, Friedman NE, Frane SL, et al. Ocular component development during infancy and early childhood. *Optom Vis Sci.* (2018) 95:976–85. doi: 10.1097/opx.0000000000001296
7. Iribarren R. Crystalline lens and refractive development. *Prog Retin Eye Res.* (2015) 47:86–106. doi: 10.1016/j.preteyeres.2015.02.002
8. Gordon RA, Donzis PB. Refractive development of the human eye. *Arch Ophthalmol.* (1985) 103:785–9. doi: 10.1001/archopht.1985.01050060045020
9. Rozema J, Dankert S, Iribarren R, Lanca C, Saw SM. Axial growth and lens power loss at myopia onset in Singaporean children. *Invest Ophthalmol Vis Sci.* (2019) 60:3091–9. doi: 10.1167/iovs.18-26247
10. Wu Q, Chen Q, Lin B, Huang S, Wang Y, Zhang L, et al. Relationships among retinal/choroidal thickness, retinal microvascular network and visual field in high myopia. *Acta Ophthalmol.* (2020) 98:e709–14. doi: 10.1111/aos.14372
11. Cheng T, Deng J, Xu X, Zhang B, Wang J, Xiong S, et al. Prevalence of fundus tessellation and its associated factors in Chinese children and adolescents with high myopia. *Acta Ophthalmol.* (2021) 99:e1524–33. doi: 10.1111/aos.14826
12. Yang YS, Koh JW. Choroidal blood flow change in eyes with high myopia. *Korean J Ophthalmol.* (2015) 29:309–14. doi: 10.3341/kjo.2015.29.5.309
13. Qin Y, Zhu M, Qu X, Xu G, Yu Y, Witt RE, et al. Regional macular light sensitivity changes in myopic Chinese adults: an MP1 study. *Invest Ophthalmol Vis Sci.* (2010) 51:4451–7. doi: 10.1167/iovs.09-4642
14. Yang Y, Wang J, Jiang H, Yang X, Feng L, Hu L, et al. Retinal microvasculature alteration in high myopia. *Invest Ophthalmol Vis Sci.* (2016) 57:6020–30. doi: 10.1167/iovs.16-19542
15. Jagadeesh D, Philip K, Fedtke C, Jong M, Ly A, Sankaridurg P. Posterior segment conditions associated with myopia and high myopia. *Clin Exp Optom.* (2020) 103:756–65. doi: 10.1111/cxo.13060
16. Liu X, Shen M, Yuan Y, Huang S, Zhu D, Ma Q, et al. Macular thickness profiles of intraretinal layers in myopia evaluated by ultrahigh-resolution optical coherence tomography. *Am J Ophthalmol.* (2015) 160:53.e2–61.e2. doi: 10.1016/j.ajo.2015.03.012
17. Liu Y, Wang L, Xu Y, Pang Z, Mu G. The influence of the choroid on the onset and development of myopia: from perspectives of choroidal thickness and blood flow. *Acta Ophthalmol.* (2021) 99:730–8. doi: 10.1111/aos.14773
18. Wang Y, Ye J, Shen M, Yao A, Xue A, Fan Y, et al. Photoreceptor degeneration is correlated with the deterioration of macular retinal sensitivity in high myopia. *Invest Ophthalmol Vis Sci.* (2019) 60:2800–10. doi: 10.1167/iovs.18-26085
19. Yuan Y, Zhang Z, Zhu J, He X, Du E, Jiang K, et al. Responses of the ocular anterior segment and refraction to 0.5% tropicamide in chinese school-aged children of myopia, emmetropia, and hyperopia. *J Ophthalmol.* (2015) 2015:612728. doi: 10.1155/2015/612728
20. Muralidharan G, Martínez-Enríquez E, Birkenfeld J, Velasco-Ocana M, Pérez-Merino P, Marcos S. Morphological changes of human crystalline lens in myopia. *Biomed Opt Express.* (2019) 10:6084–95. doi: 10.1364/boe.10.006084
21. Fam HB, How AC, Baskaran M, Lim KL, Chan YH, Aung T. Central corneal thickness and its relationship to myopia in Chinese adults. *Br J Ophthalmol.* (2006) 90:1451–3. doi: 10.1136/bjo.2006.101170
22. Sedaghat MR, Momeni-Moghaddam H, Azimi A, Fakhimi Z, Ziaei M, Danesh Z, et al. Corneal biomechanical properties in varying severities of myopia. *Front Bioeng Biotechnol.* (2020) 8:595330. doi: 10.3389/fbioe.2020.595330
23. Cheng T, Deng J, Xiong S, Yu S, Zhang B, Wang J, et al. Crystalline lens power and associated factors in highly myopic children and adolescents aged 4 to 19 years. *Am J Ophthalmol.* (2021) 223:169–77. doi: 10.1016/j.ajo.2020.07.007
24. Zadnik K, Mutti DO, Fusaro RE, Adams AJ. Longitudinal evidence of crystalline lens thinning in children. *Invest Ophthalmol Vis Sci.* (1995) 36:1581–7.
25. Wong HB, Machin D, Tan SB, Wong TY, Saw SM. Ocular component growth curves among Singaporean children with different refractive error status. *Invest Ophthalmol Vis Sci.* (2010) 51:1341–7. doi: 10.1167/iovs.09-3431
26. McBrien NA, Adams DW. A longitudinal investigation of adult-onset and adult-progression of myopia in an occupational group. Refractive and biometric findings. *Invest Ophthalmol Vis Sci.* (1997) 38:321–33.
27. Pan CW, Chen Q, Sheng X, Li J, Niu Z, Zhou H, et al. Ethnic variations in myopia and ocular biometry among adults in a rural community in China: the Yunnan minority eye studies. *Invest Ophthalmol Vis Sci.* (2015) 56:3235–41. doi: 10.1167/iovs.14-16357
28. Coletta NJ, Watson T. Effect of myopia on visual acuity measured with laser interference fringes. *Vision Res.* (2006) 46:636–51. doi: 10.1016/j.visres.2005.05.025
29. Gupta P, Saw SM, Cheung CY, Girard MJ, Mari JM, Bhargava M, et al. Choroidal thickness and high myopia: a case-control study of young Chinese men in Singapore *Acta Ophthalmol.* (2015) 93:e585–92. doi: 10.1111/aos.12631
30. Barteselli G, Chhablani J, El-Emam S, Wang H, Chuang J, Kozak I, et al. Choroidal volume variations with age, axial length, and sex in healthy subjects: a three-dimensional analysis. *Ophthalmology*. (2012) 119:2572–8. doi: 10.1016/j.ophtha.2012.06.065
31. Flores-Moreno I, Ruiz-Medrano J, Duker JS, Ruiz-Moreno JM. The relationship between retinal and choroidal thickness and visual acuity in highly myopic eyes. *Br J Ophthalmol.* (2013) 97:1010–3. doi: 10.1136/bjophthalmol-2012-302836
32. Ikuno Y, Tano Y. Retinal and choroidal biometry in highly myopic eyes with spectral-domain optical coherence tomography. *Invest Ophthalmol Vis Sci.* (2009) 50:3876–80. doi: 10.1167/iovs.08-3325
33. Lim MC, Hoh ST, Foster PJ, Lim TH, Chew SJ, Seah SK, et al. Use of optical coherence tomography to assess variations in macular retinal thickness in myopia. *Invest Ophthalmol Vis Sci.* (2005) 46:974–8. doi: 10.1167/iovs.04-0828

34. Wan W, Chen Z, Lei B. Increase in electroretinogram rod-driven peak frequency of oscillatory potentials and dark-adapted responses in a cohort of myopia patients. *Doc Ophthalmol.* (2020) 140:189–99. doi: 10.1007/s10633-019-09732-4

Conflict of Interest: The authors declare that the research was conducted in the absence of any commercial or financial relationships that could be construed as a potential conflict of interest.

Publisher's Note: All claims expressed in this article are solely those of the authors and do not necessarily represent those of their affiliated organizations, or those of the publisher, the editors and the reviewers. Any product that may be evaluated in this article, or claim that may be made by its manufacturer, is not guaranteed or endorsed by the publisher.

frontiers in Medicine

ORIGINAL RESEARCH
published: 17 December 2021
doi: 10.3389/fmed.2021.761550

Segmentation Errors in the Measurement of Volumetric Parameters by Swept-Source Anterior Segment Optical Coherence Tomography

Hailiu Chen[1,2†], Jie Meng[1†], Peng Lu[1], Dan Ye[1], Yunxuan Li[1], Lu Cheng[1], Yangyunhui Li[1], Xiaoling Liang[1], Wenyong Huang[1] and Jingjing Huang[1*]*

[1] State Key Laboratory of Ophthalmology, Zhongshan Ophthalmic Center, Sun Yat-sen University, Guangdong Provincial Key Laboratory of Ophthalmology and Visual Science, Guangdong Provincial Clinical Research Center for Ocular Diseases, Guangzhou, China, [2] Department of Ophthalmology, Joint Shantou International Eye Center, Shantou University, Chinese University of Hong Kong, Shantou, China

Purpose: To investigate the error rate of segmentation in the automatic measurement of anterior chamber volume (ACV) and iris volume (IV) by swept-source anterior segment optical coherence tomography (SS-ASOCT) in narrow-angle and wide-angle eyes.

Methods: In this study, fifty eyes from 25 narrow-angle subjects and fifty eyes from 25 wide-angle subjects were enrolled. SS-ASOCT examinations were performed and each SS-ASOCT scan was reviewed, and segmentation errors in the automatic measurement of ACV and IV were classified and manually corrected. Error rates were compared between the narrow-angle and the wide-angle groups, and ACV and IV before and after manual correction were compared.

Results: A total of 12,800 SS-ASOCT scans were reviewed. Segmentation error rates of angle recess, iris root, posterior surface of the iris, pupil margin, and anterior surface of the lens were 84.06, 93.30, 13.15, 59.21, and 25.27%, respectively. Segmentation errors of angle recess, iris root, posterior surface of the iris, and pupil margin occurred more frequently in narrow-angle eyes, while more segmentation errors of the anterior surface of the lens were found in wide-angle eyes (all $P < 0.001$). ACV decreased and IV increased significantly after manual correction of segmentation errors in both groups (all $P < 0.01$).

Conclusion: Segmentation errors were prevalent in the volumetric measurement by SS-ASOCT, particularly in narrow-angle eyes, leading to mismeasurement of ACV and IV.

Keywords: segmentation error, anterior chamber volume, iris volume, swept-source anterior segment optical coherence tomography, narrow angle

OPEN ACCESS

Edited by:
Yali Jia,
Oregon Health and Science University, United States

Reviewed by:
Hideo Akiyama,
Gunma University, Japan
Lijun Qu,
The Second Affiliated Hospital of Harbin Medical University, China

***Correspondence:**
Wenyong Huang
hweny@mail.sysu.edu.cn
Jingjing Huang
hjjing@mail.sysu.edu.cn

†These authors have contributed equally to this work and share first authorship

Specialty section:
This article was submitted to Ophthalmology, a section of the journal Frontiers in Medicine

Received: *20 August 2021*
Accepted: *22 November 2021*
Published: *17 December 2021*

Citation:
Chen H, Meng J, Lu P, Ye D, Li Y, Cheng L, Li Y, Liang X, Huang W and Huang J (2021) Segmentation Errors in the Measurement of Volumetric Parameters by Swept-Source Anterior Segment Optical Coherence Tomography. Front. Med. 8:761550. doi: 10.3389/fmed.2021.761550

INTRODUCTION

Anterior segment optical coherence tomography (AS-OCT) is a non-contact, rapid imaging device that uses low-coherence interferometry to obtain cross-sectional images of the anterior segment (1). The swept-source anterior segment OCT (SS-ASOCT) delivers high-resolution images of the anterior segment along a large image depth, at a fast acquisition speed (2). The high scan speed facilitates 360 degrees imaging of the anterior segment, providing a more precise and representative measurement of the anterior chamber volume (ACV) and iris volume (IV) (3).

Recent studies have found that ACV and IV were important parameters in the screening, diagnosis, and treatment decisions for narrow-angle or angle-closure patients. Wang et al. reported that the ethnic Chinese tended to have smaller ACV than Caucasians, which was the main contributor to the narrower drainage angle in the Chinese (4). Foo et al. reported that angle width was largely dependent on variation in ACV, anterior chamber area, and lens vault (5). Li et al. tested the power of volumetric parameters to differentiate narrow angle from open angle with gonioscopy as reference standard and found that the patients with narrow angle could be more easily detected using the measurement of ACV (6). These studies indicated that the measurement of ACV could be an important factor in the screening and early detection for anatomically narrow angle, which is beneficial in preventing the development of angle closure glaucoma. Esfandiari et al. reported that eyes with a shallower anterior chamber and thinner irises were more likely to experience angle opening from a laser peripheral iridotomy (LPI), which aided clinicians to decide whether an LPI should be attempted or a primary lens extraction might be indicated for primary angle closure suspects (7). These findings indicated that an accurate and stable measurement of ACV and IV plays an important role in the decision-making of treatment among the narrow-angle subjects.

The built-in segmentation algorithm of SS-ASOCT was commonly used for the automatic measurement of ACV and IV, which detected the anterior and posterior boundaries of the iris and cornea in the individual scans. Previous studies reported that using the automated OCT segmentation algorithm could lead to segmentation errors in the retinal thickness measurement, resulting in the misinterpretation of glaucoma or retinopathy (8, 9). Similarly, in clinical practice, we have noticed quite a few segmentation errors in the automatic measurement of ACV and IV using the built-in caliper software of SS-ASOCT. The inaccuracy of ACV and IV would generate errors in the evaluation of the anatomic characteristics of the angle and iris, leading to unreliable results in both clinical research and the diagnosis or management of subjects with narrow or closed angle. Therefore, in the measurement of ACV and IV, manual adjustment of errors was usually made if the software failed to detect the iris and corneal boundaries at the correct location (3). Moreover, a previous study reported that segmentation errors of OCT were more frequently noticed when the structure was distorted and indistinguishable (10). Analogously, in eyes with narrow angle, the congestion of the anterior segment structure might make it more difficult for the automatic algorithm to identify the border of the anterior segment structure, leading to more segmentation errors.

However, there was no investigation of the prevalence, associated factors, and impact of segmentation errors in volume measurements by SS-ASOCT. In addition, the distribution of segmentation errors in narrow-angle and wide-angle eyes remains unknown. The purpose of the current study was to investigate the error rate of segmentation in the automatic measurement of ACV and IV by SS-ASOCT between narrow-angle and wide-angle eyes, as well as the determinants and the impact of segmentation errors on volume measurements. The study would be helpful to prevent misestimation of the volume parameters determined by SS-ASOCT.

METHODS

Participants

Participants from the Guangzhou Diabetic Eye Study were included in this cross-sectional study. Details of the protocol and eligibility of Guangzhou Diabetic Eye Study have been described previously (11, 12). Subjects who underwent SS-ASOCT imaging at the Zhongshan Ophthalmic Center of Sun Yat-sen University (Guangzhou, China) between December 2017 and July 2018 were considered in the current analysis. The study protocol was approved by the Institutional Review Board and all procedures conformed to the tenets of the Declaration of Helsinki. Written informed consent was obtained from all participants in the study. All participants underwent complete ophthalmic evaluation, such as best-corrected visual acuity measurement, slit-lamp examination, gonioscopy examination, stereoscopic optic disc examination and fundus evaluation with a 90-diopter lens, fundus photographs by a retinal camera (CR-2; Canon, Tokyo, Japan), and intraocular pressure (IOP) measurement by Goldmann applanation tonometry.

Inclusion criteria for the subjects in the current study were: (1) age between 40 and 80 years; (2) best-corrected visual acuity better than 20/200; (3) spherical equivalent < -6 D, astigmatism <3 D; (4) IOP <21 mmHg; (5) without iridotrabecular contact as verified by gonioscopy and SS-ASOCT; and (6) normal appearance of optic nerve under stereoscopic examination.

Exclusion criteria were: (1) history of ocular surgeries; (2) history of ocular trauma; (3) disorders of anterior segment, such as corneal opacity, iridocyclitis, and lens dislocation; (4) fundus diseases except for diabetic retinopathy; (5) inability to fixate for eye examination; and (6) other systemic diseases except for diabetes mellitus.

Gonioscopy was performed in each subject by two independent glaucoma specialists (JH and WH) using a Goldmann-style one-mirror lens (Model 902; Haag Streit, Bern, Switzerland) with low ambient illumination. The angle width of each eye was classified according to the Shaffer grading system. A narrow angle was defined as Shaffer grade one or lower, and a wide angle was defined as Shaffer grade two or higher in all quadrants (13). If a discrepancy of the classification existed, then, two glaucoma specialists performed a second examination and

confirmed the state of the anterior chamber angle. Twenty-five wide-angle and 25 narrow-angle subjects who met the inclusion criteria were included in the current study.

Swept-Source Anterior Segment Optical Coherence Tomography (SS-ASOCT)

Swept-source anterior segment OCT (CASIA SS-1000 OCT; Tomey, Nagoya, Japan) examinations and measurements were performed by the same trained physician (JM) who was masked to the clinical data. Miotic or mydriatic medications were not used in any of the subjects for at least 7 days prior to imaging. All SS-ASOCT images were taken under dark conditions (0.16 lux measured with a digital luminometer IM-2D; Topcon, Tokyo, Japan) with sitting posture. To avoid eyelid artifact, the operator gently opened the upper and lower lid without compressing the bulb. The participants were asked to fixate on an internal fixation target during the scan, with refractive correction to perform the measurements in an unaccommodated state. Horizontal standard anterior segment single-scan mode (0–180 degrees) was used for perpendicular scans centered on the pupil and was repeated three times. A volume scan comprising of 128 radial scans was used to image the iris and anterior chamber. Alignment that results in a central corneal reflex ensures good repeatability as recommended by the manufacturer. Images with poor quality due to eye movement or lid overlapping were excluded from analysis.

Swept-source anterior segment OCT linear parameters were measured at the horizontal (0–180 degrees) and vertical B-scan (90–270 degrees) once the scleral spur was manually marked using the built-in caliper software (V.7J.8; Tomey, Nagoya, Japan) by 1 experienced physician (JM). Briefly, anterior chamber depth (ACD) was defined as the axial distance from the corneal endothelium to the anterior lens surface. Anterior chamber width (ACW) was the distance between the two scleral spurs. Lens vault (LV) was defined as the perpendicular distance between the anterior pole of the crystalline lens and the horizontal line connecting the two scleral spurs. Central corneal thickness (CCT) was defined as a distance from the anterior to posterior cornea along a perpendicular line that extends from the median point of the line connecting the two scleral spurs. Each parameter was measured three times and the average value was recorded. All parameters were calculated by the average of the measurements from the horizontal and vertical cross-sections (**Figure 1**).

The measurement of IV and ACV was conducted automatically by the instrument software, with 128 radial scans of each eye included in analysis (images were analyzed for every 1.4 degrees). In the measurement process, the instrument software (V.7J.8; Tomey, Nagoya, Japan) automatically detected the anterior and posterior boundaries of the cornea and iris, and the anterior boundary of lens in the individual scan (**Figure 1**). The iris root was defined as the intersection of the anterior and posterior iris boundaries and the ciliary body. The anterior iris boundary was defined as the anterior chamber-anterior iris surface interface, whereas the posterior iris boundary was defined as the external border of the iris pigment epithelium. The iris and anterior chamber volume were calculated as a summation of pixel volume derived from individual scans by the algorithm of the software (14).

An experienced glaucoma specialist (HC) reviewed each SS-ASOCT scan and manually corrected segmentation errors using the built-in software when the boundaries of cornea, iris, and lens delineated automatically did not conform with the actual borders. Each scan after manual correction was checked by a second experienced glaucoma specialist (JH) to ensure the accuracy of the manual correction. The categories of segmentation errors and the number of scans with each type of segmentation error were recorded in both the narrow-angle and the wide-angle groups. Furthermore, the IV and ACV of each eye were remeasured and recorded after correction of errors.

Statistical Analysis

Statistical analyses were performed using SPSS software version 25.0 (SPSS, Inc., Chicago, IL, USA). Age between the two groups was compared using an independent *t*-test. Gender and

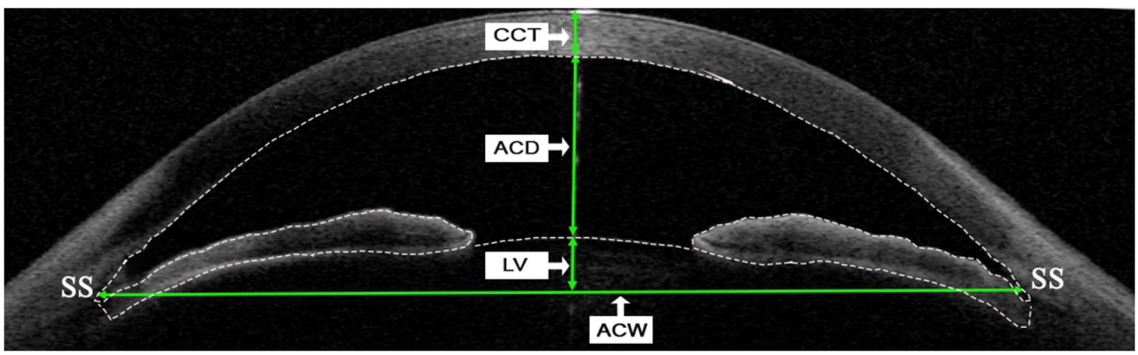

FIGURE 1 | Determinations of linear parameters of the anterior segment by swept-source anterior segment optical coherence tomography (SS-ASOCT). Central corneal thickness (CCT) was defined as a distance from anterior to posterior cornea along a perpendicular line that extends from the median point of the line connecting the two scleral spurs. Anterior chamber depth (ACD) was defined as the axial distance from the corneal endothelium to the anterior lens surface. Lens vault (LV) was defined as the perpendicular distance between the anterior pole of the crystalline lens and the horizontal line connecting the two scleral spurs. Anterior chamber width (ACW) was defined as the distance between the two scleral spurs. The dotted line indicates boundaries of the cornea, iris, and anterior surface of lens, which are detected automatically by the built-in software when measuring the anterior chamber volume (ACV) and iris volume (IV). SS, scleral spur.

TABLE 1 | Demographics and clinical characteristics of narrow angle and wide angle eyes.

Variables	Total (*N* = 50)	Narrow-angle (*N* = 25)	Wide-angle (*N* = 25)	*P* value
Age (y)	68.6 ± 9.1	68.9 ± 8.0	68.3 ± 9.9	0.653
Gender (male/female)	37/13	18/7	19/6	0.891
ACD (mm)	2.49 ± 0.45	2.08 ± 0.17	2.80 ± 0.33	**<0.001**
CCT (μm)	537 ± 29	536 ± 25	538 ± 31	0.691
LV (mm)	0.60 ± 0.36	0.83 ± 0.20	0.42 ± 0.34	**<0.001**
ACW (mm)	11.88 ± 0.49	11.55 ± 0.38	12.14 ± 0.40	**<0.001**

Data are presented as mean ± SD. Bold values indicate statistical significance. ACD, anterior chamber depth; CCT, central corneal thickness; LV, lens vault; ACW, anterior chamber width.

TABLE 2 | Comparison of segmentation error rates of narrow-angle and wide-angle eyes.

Categories	Total (*n* = 12,800)	Narrow angle (*n* = 6,400)	Wide angle (*n* = 6,400)	*P* value
Angle recess	10,760 (84.06%)	5,520 (86.24%)	5,240 (81.88%)	**<0.001**
Iris root	11,942 (93.30%)	6,135 (95.86%)	5,807 (90.73%)	**<0.001**
Posterior surface of iris	1,683 (13.15%)	943 (14.74%)	740 (11.56%)	**<0.001**
Pupil margin	7,579 (59.21%)	4,546 (71.03%)	3,033 (47.40%)	**<0.001**
Anterior surface of lens	3,234 (25.27%)	1,407 (21.98%)	1,827 (28.54%)	**<0.001**

n refers to numbers of SS-ASOCT scans reviewed. Data are presented as no. (%). Bold values indicate statistical significance.

segmentation error rates of all categories between the two groups were compared using the chi-square test. IV and ACV before and after manual correction were compared using the paired *t*-test. Differences before and after manual correction of the actual value of IV and ACV were compared using the chi-square test. In addition, univariate logistic regression analyses were performed. The dependent variables were the segmentation error rates of angle recess, iris root, posterior surface of the iris, pupil margin, and anterior surface of lens, respectively, and the independent variables were SS-ASOCT linear parameters, such as CCT, ACD, ACW, and LV. A $P < 0.05$ was considered statistically significant.

RESULTS

Fifty eyes from 25 narrow-angle subjects and fifty eyes from 25 wide-angle subjects met the inclusion criteria and were included in the current study. Demographic and biometric characteristics are summarized in **Table 1**. There were no significant differences concerning age, gender, and CCT between the groups ($P = 0.653$, 0.891, and 0.691, respectively). ACD and ACW were significantly smaller while LV was larger in the narrow-angle group when compared with the wide-angle group (all $P < 0.001$).

Comparisons of rates of different segmentation errors between the groups are displayed in **Table 2**. Segmentation errors were classified by their location. The definition of angle recess segmentation error was that the posterior boundary of the cornea did not reach the angle recess (**Figures 2A,B**); the definition of a pupil margin segmentation error or iris root segmentation error was that the boundary of iris did not conclude the pupil margin or the iris root (**Figures 2C–F**); the segmentation error of posterior surface of the iris was defined as the dislocation of boundary of the posterior surface of iris (**Figures 2G,H**); the segmentation error of lens surface was defined as the dislocation of the boundary of the anterior surface of the lens (**Figures 2I,J**). A total of 12,800 SS-ASOCT scans were reviewed. Segmentation errors of angle recess, iris root, posterior surface of iris, pupil margin, and anterior surface of lens were noted in 10,760 (84.06%), 11,942 (93.30%), 1,683 (13.15%), 7,579 (59.21%), and 3,234 (25.27%) scans, respectively. Segmentation errors of angle recess, iris root, posterior surface of the iris, and pupil margin occurred more frequently in narrow-angle eyes than wide-angle eyes, while more segmentation errors of the anterior surface of the lens were found in wide-angle eyes (all $P < 0.001$).

Comparisons of volume parameters before and after manual correction of segmentation errors between the two groups are shown in **Table 3**. ACV decreased and IV increased significantly after manual correction of segmentation errors in the narrow-angle group ($P = 0.003$ and 0.001, respectively) and the wide-angle group (both $P \leq 0.001$). As for changes in ACV and IV before and after correction (ΔACV, ΔIV), as well as the percentage of ΔACV or ΔIV in actual ACV or IV (ΔACV/ACV-AC and ΔIV/IV-AC), there were no significant differences between narrow-angle and wide-angle eyes (all $P > 0.05$).

Associations between total segmentation error rates of different types and anterior segment parameters were evaluated by univariable logistic regression analysis (**Table 4**). Smaller ACD was significantly associated with more segmentation errors in angle recess, iris root, posterior surface of the iris, and pupil margin, while larger ACD was associated with more incorrect delineation of the anterior surface of lens (all $P < 0.001$). In addition, a thicker CCT was associated with more segmentation errors of the anterior surface of lens ($P < 0.001$). Besides, smaller ACW was associated with more segmentation errors in angle recess ($P = 0.001$) and iris root ($P < 0.001$), while larger ACW was associated with more failure of delineation of the anterior surface of lens ($P < 0.001$). Furthermore, larger LV was associated with more angle recess segmentation error ($P < 0.001$).

DISCUSSION

Swept-source anterior segment OCT provides objective and repeatable measurements of the anterior segment structures (15). Studies have revealed that accurate measurement of ACV and IV played an important role in screening, diagnosis, and treatment decisions for patients with glaucoma, especially for narrow-angle individuals. However, in the current study, we found that failure of correct segmentation algorithms in the measurement of ACV and IV was very common even in images with good quality. Segmentation errors of angle recess, iris root, posterior surface of iris, and pupil margin were more frequent in narrow-angle

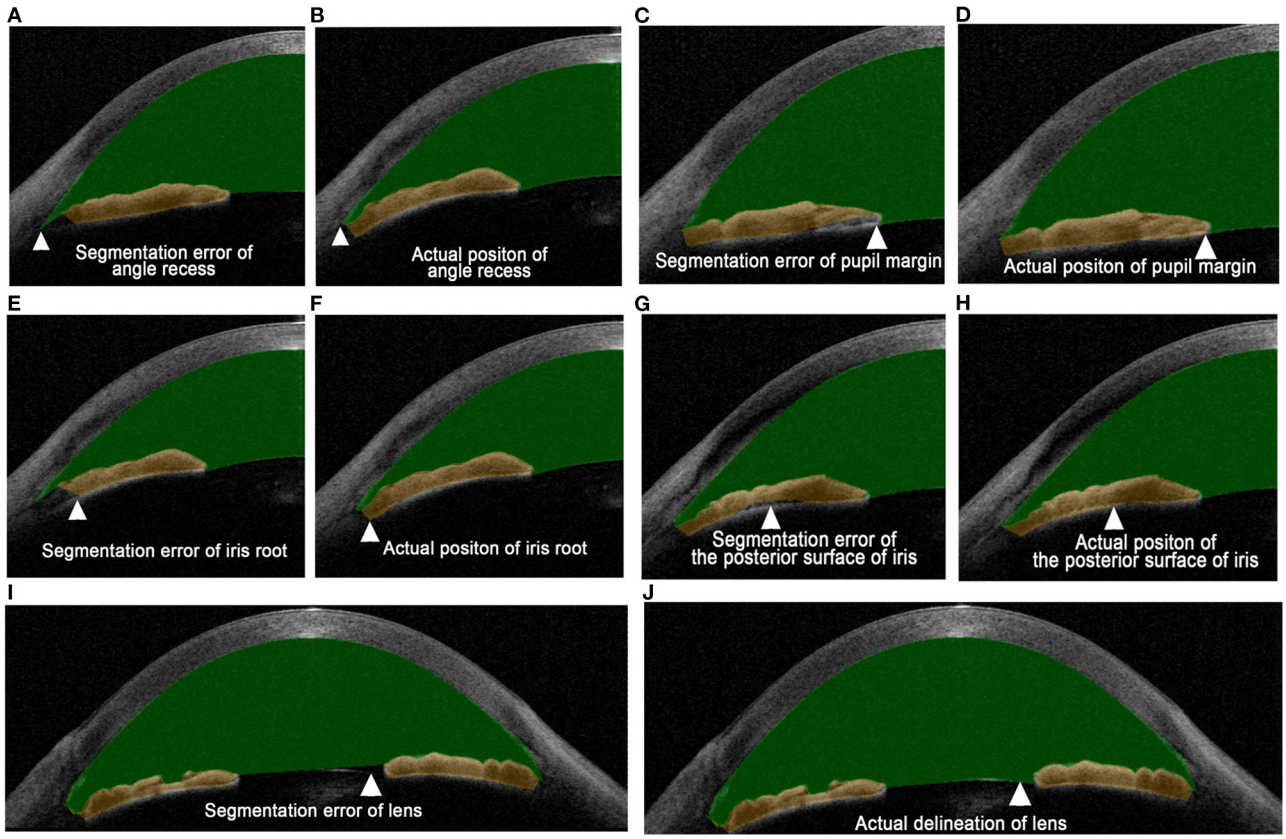

FIGURE 2 | Definitions of different types of segmentation errors. **(A)** Angle recess segmentation error occurs when the posterior boundary of the cornea does not reach the angle recess. **(B)** The angle recess is accurately located after manual correction. **(C)** The pupil margin segmentation error occurs when the boundary of the iris does not conclude the pupil margin. **(D)** The boundary of the iris concludes the pupil margin after manual correction. **(E)** The iris root segmentation error occurs when the boundary of the iris does not conclude the iris root. **(F)** The iris root is concluded in the volume measurement after manual correction. **(G)** The segmentation error of posterior surface of the iris is defined as the dislocation of boundary of the posterior surface of the iris. **(H)** The posterior surface of the iris is accurately delineated after manual correction. **(I)** The segmentation error of lens surface is defined as the dislocation of the boundary of anterior surface of lens. **(J)** The anterior surface of the lens is accurately delineated after manual correction. Arrowheads indicate the location of the segmentation error where the manual correction is carried out.

eyes while the error rate of the anterior surface of lens was higher in wide-angle eyes. SS-ASOCT automated segmentation errors resulted in larger ACV and smaller IV, which were associated with ACD, ACW, LV, and CCT. To the best of our knowledge, this is the first study investigating the error rate of segmentation and its determinants in the automatic measurements of ACV and IV using SS-ASOCT.

The misidentification of iris root was the most common algorithm software–related error, counting 93.3% in this study. The main limitation of SS-ASOCT is that light energy is unable to penetrate tissues behind the iris pigment epithelium. Therefore, the ciliary body cannot be visualized in SS-ASOCT images (2). Thus, the iris root, which inserts into the ciliary body, was probably unidentifiable in most SS-ASOCT images. As shown in our previous study and other studies, ciliary bodies were thinner and more anteriorly rotated in eyes with primary angle closure glaucoma as well as in their fellow eyes (16–18). With the anteriorly rotated ciliary bodies plastering to the posterior surface of the iris, iris root in narrow-angle eyes is harder to be recognized, and therefore the error rate of iris root was higher in narrow-angle eyes. Furthermore, in this study, smaller ACD and ACW were associated with more segmentation errors of iris root, indicating that the recognition of iris root was affected by the degree of stenosis of anterior chamber angle.

In the current study, the segmentation error rate of angle recess was as high as 84.06%. The deviation in the automatic location of scleral spurs by the built-in software of SS-ASOCT leads to segmentation errors of angle recess. In 15–28% of ASOCT images, operators were unable to identify the scleral spur, which made the automatic identification of angle recess difficult (19, 20). To conduct an accurate measurement of volume parameters with SS-ASOCT, manual adjustment of the scleral spur was usually made (3). SS-ASOCT software performs the automated segmentation through the identification of the difference of signal intensity between adjacent layers (21). However, in narrow-angle eyes, the distance from the iris to the scleral spur in the angle is short and the scleral spur is difficult to be detected precisely, leading to more segmentation

errors of angle recess in these eyes (22). In the current study, smaller ACD, ACW, and larger LV were associated with more segmentation errors in angle recess, indicating that the shallow anterior chamber and narrow angle added more difficulty in discriminating the angle structures.

The position of the lens is far away from the zero optical path plane of the B-scan, which may result in segmentation errors of the anterior surface of lens. For the same reason, more segmentation errors of the anterior surface of lens were found in wide-angle eyes which had a deeper anterior chamber, and were associated with thicker CCT. On the contrary, narrow-angle eyes had smaller ACD and larger LV, which meant a shorter distance from the lens to the zero optical path plane, making the imaging of the anterior surface of lens clearer and reducing the segmentation error.

The optic signal of ASOCT significantly attenuates when penetrating iris. The contrast effect of the intraocular structure reduces, resulting in more errors in the segmentation algorithm (23, 24). Thus, the boundary of the posterior surface of the iris and pupil margin was misidentified by the built-in software in some scans. In the previous studies, iris curvature is larger in narrow-angle eyes, which indicates that the iris bent more forwardly to the cornea because of a pupillary block (25, 26). In this condition, the iris surface is obviously tilted, and an oblique transmission of OCT light is expected, leading to an improper alignment of the OCT light and image blurring of the OCT scan (10). The same problem was found in OCT imaging of the retina in high myopia eyes and age-related macular degeneration eyes (27, 28). Therefore, segmentation errors in posterior surface of the iris were more frequent in narrow-angle eyes. Otherwise, because of pupillary block in narrow-angle eyes, the margin of iris was plastered to the surface of lens, which makes the pupil margin harder to be recognized. Since ACD could be an indicator of the extent of pupillary block (22), smaller ACD could result in more segmentation errors of the posterior surface of the iris and pupil margin in the current study.

In this study, ACV decreased and IV increased significantly after manual correction of segmentation errors in the two groups (**Table 3**). According to **Figure 2A**, the angle recess was always located incorrectly on the ciliary body, which occurred in 84.06% of the B-scans. The retrodeviation of the positioning of angle recess led to an overestimation of the ACV. According to **Figures 2I,J**, ACV increased after the correction of segmentation errors in the anterior surface of lens. But segmentation errors of the anterior surface of lens only occurred in 25.27% of the B-scans, which had less effect on ACV than segmentation errors of angle recess. On the other hand, according to **Figures 2C,E,G**, the automated segmentation of the pupil margin, iris root, and posterior surface of the iris did not reach the actual border of the iris, which accounts for 93.30, 13.15, and 59.21%, respectively. These errors made IV significantly smaller than its actual value. The remarkable effect of the correction of these errors indicated that an accurate measurement of the ACV and IV required a manual correction of the segmentation after the automatic measurement or an update of the built-in software of SS-ASOCT to improve the accuracy of image edge recognition.

TABLE 3 | Comparison of volume parameters of two groups before and after manual correction.

	Narrow-angle	Wide-angle	*P* value
ACV (mm^3)			
Before correction (ACV-BC)	85.47 ± 19.40	159.34 ± 26.37	
After correction (ACV-AC)	84.46 ± 19.51	157.51 ± 26.71	
ΔACV	−1.00 ± 0.78	−1.83 ± 1.13	0.09
ΔACV / ACV-AC, %	−1.18 ± 1.06	−1.16 ± 0.76	0.89
P value (ACV-BC vs. ACV-AC)	**0.003**	**0.001**	
IV (mm^3)			
Before correction (IV-BC)	29.94 ± 5.99	38.38 ± 2.73	
After correction (IV-AC)	33.43 ± 5.56	41.49 ± 2.46	
ΔIV	3.49 ± 2.10	3.11 ± 1.13	0.61
ΔIV / IV-AC, %	10.43 ± 11.23	7.50 ± 3.24	0.450
P value (IV-BC vs. IV-AC)	**0.001**	**<0.001**	

Data are presented as mean ± SD. Bold values indicate statistical significance. ACV, anterior chamber volume; IV, iris volume; and Δ, changes in volume before and after manual correction.

TABLE 4 | Univariable logistic regression analysis of the total segmentation error rates in different categories.

Characteristic	Angle recess		Iris root		Posterior surface of iris		Pupil margin		Anterior surface of lens	
	OR, (95% CI)	*P*	OR, (95% CI)	*P*	OR, (95% CI)	*P*	OR, (95% CI)	*P*	OR, (95% CI)	*P*
ACD	0.11 (0.03–0.40)	**<0.001**	0.03 (0.01–0.06)	**<0.001**	0.09 (0.05–0.13)	**<0.001**	0.12 (0.09–0.16)	**<0.001**	4.07 (1.40–6.87)	**<0.001**
CCT	1.03 (0.65–1.75)	0.470	0.66 (0.03–1.19)	0.387	1.30 (0.37–2.69)	0.486	0.76 (0.45–2.23)	0.753	1.02 (1.01–1.03)	**<0.001**
LV	5.30 (2.72–7.37)	**<0.001**	2.40 (0.57–10.03)	0.230	1.69 (0.61–4.71)	0.315	2.42 (0.72–8.16)	0.154	2.85 (0.65–12.55)	0.165
ACW	0.652 (0.51–0.84)	**0.001**	0.016 (0.003–0.09)	**<0.001**	1.50 (0.48–4.69)	0.486	0.96 (0.75–1.23)	0.753	8.32 (3.42–20.25)	**<0.001**

Bold values indicate statistical significance. OR, odds ratio; CI, confidence interval; ACD, anterior chamber depth; CCT, central corneal thickness; LV, lens vault; ACW, anterior chamber width.

There were several limitations in this study. First, because the subjects of this study were recruited from the Guangzhou Diabetic Eye Study, eyes with peripheral anterior synechiae in the angle were not included, and the results of the current study are not applicable to angle-closure eyes. However, considering that segmentation errors by SS-ASOCT were more prevalent in narrow-angle eyes in the current research, it is probable that the automated segmentation is more inaccurate and unreliable in angle-closure eyes, in which the angle structures are more difficult to discriminate. Further research should be conducted to analyze the segmentation errors in eyes with iridotrabecular contact. Second, since we did not investigate the segmentation errors in other ASOCT devices or segmentation algorithms, our results are only applicable to CASIA SS-1000 OCT and the current built-in software (V.7J.8, Tomey, Nagoya, Japan).

In conclusion, segmentation errors were prevalent in the automatic measurement of ACV and IV by SS-ASOCT, particularly in narrow-angle eyes, leading to an overestimation of ACV and underestimation of IV. Manual correction of the segmentation errors after the automatic measurement or an update of the built-in software of SS-ASOCT to improve the accuracy of image edge recognition should be considered.

DATA AVAILABILITY STATEMENT

The raw data supporting the conclusions of this article will be made available by the authors, without undue reservation.

ETHICS STATEMENT

The studies involving human participants were reviewed and approved by Zhongshan Ophthalmic Center, Sun Yat-sen University. The patients/participants provided their written informed consent to participate in this study.

AUTHOR CONTRIBUTIONS

All authors listed have made a substantial, direct, and intellectual contribution to the work and approved it for publication.

FUNDING

This work was supported by the Natural Science Foundation of Guangdong Province in China (Grant No. 2021A1515012142).

REFERENCES

1. Radhakrishnan S, Rollins AM, Roth JE, Yazdanfar S, Westphal V, Bardenstein DS, et al. Real-time optical coherence tomography of the anterior segment at 1310 nm. *Arch Ophthalmol.* (2001) 119:1179–85. doi: 10.1001/archopht.119.8.1179
2. Maslin JS, Barkana Y, Dorairaj SK. Anterior segment imaging in glaucoma: an updated review. *Indian J Ophthalmol.* (2015) 63:630–40. doi: 10.4103/0301-4738.169787
3. Mak H, Xu G, Leung CK. Imaging the iris with swept-source optical coherence tomography: relationship between iris volume and primary angle closure. *Ophthalmology.* (2013) 120:2517–24. doi: 10.1016/j.ophtha.2013.05.009
4. Wang D, Qi M, He M, Wu L, Lin S. Ethnic difference of the anterior chamber area and volume and its association with angle width. *Invest Ophthalmol Vis Sci.* (2012) 53:3139–44. doi: 10.1167/iovs.12-9776
5. Foo LL, Nongpiur ME, Allen JC, Perera SA, Friedman DS, He M, et al. Determinants of angle width in Chinese Singaporeans. *Ophthalmology.* (2012) 119:278–82. doi: 10.1016/j.ophtha.2011.07.049
6. Li F, Zhou R, Gao K, Jin L, Zhang X. Volumetric parameters-based differentiation of narrow angle from open angle and classification of angle configurations: an SS-OCT study. *Br J Ophthalmol.* (2020) 104:92–7. doi: 10.1136/bjophthalmol-2018-313386
7. Esfandiari H, Pakravan M, Amouhashemi N, Yaseri M, Torkian P, Jadidi K, et al. Low iris and anterior chamber volume is associated with deepening after laser peripheral iridotomy in primary angle closure suspects. *Graefes Arch Clin Exp Ophthalmol.* (2018) 256:2173–9. doi: 10.1007/s00417-018-4092-8
8. Ray R, Stinnett SS, Jaffe GJ. Evaluation of image artifact produced by optical coherence tomography of retinal pathology. *Am J Ophthalmol.* (2005) 139:18–29. doi: 10.1016/j.ajo.2004.07.050
9. Ho J, Sull AC, Vuong LN, Chen Y, Liu J, Fujimoto JG, et al. Assessment of artifacts and reproducibility across spectral- and time-domain optical coherence tomography devices. *Ophthalmology.* (2009) 116:1960–70. doi: 10.1016/j.ophtha.2009.03.034
10. Hwang YH, Kim MK, Kim DW. Segmentation errors in macular ganglion cell analysis as determined by optical coherence tomography. *Ophthalmology.* (2016) 123:950–8. doi: 10.1016/j.ophtha.2015.12.032
11. Wang W, He M, Gong X, Wang L, Meng J, Li Y, et al. Association of renal function with retinal vessel density in patients with type 2 diabetes by using swept-source optical coherence tomographic angiography. *Br J Ophthalmol.* (2020) 104:1768–73. doi: 10.1136/bjophthalmol-2019-315450
12. Liu S, Wang W, Tan Y, He M, Wang L, Li Y, et al. Correlation between renal function and peripapillary choroidal thickness in treatment-naive diabetic eyes using swept-source optical coherence tomography. *Curr Eye Res.* (2020) 45:1526–33. doi: 10.1080/02713683.2020.1753213
13. Radhakrishnan S, Goldsmith J, Huang D, Westphal V, Dueker DK, Rollins AM, et al. Comparison of optical coherence tomography and ultrasound biomicroscopy for detection of narrow anterior chamber angles. *Arch Ophthalmol.* (2005) 123:1053–9. doi: 10.1001/archopht.123.8.1053
14. Aptel F, Denis P. Optical coherence tomography quantitative analysis of iris volume changes after pharmacologic mydriasis. *Ophthalmology.* (2010) 117:3–10. doi: 10.1016/j.ophtha.2009.10.030
15. Li H, Leung CK, Cheung CY, Wong L, Pang CP, Weinreb RN, et al. Repeatability and reproducibility of anterior chamber angle measurement with anterior segment optical coherence tomography. *Br J Ophthalmol.* (2007) 91:1490–2. doi: 10.1136/bjo.2007.118901
16. Wang Z, Chung C, Lin J, Xu J, Huang J. Quantitative measurements of the ciliary body in eyes with acute primary-angle closure. *Invest Ophthalmol Vis Sci.* (2016) 57:3299–305. doi: 10.1167/iovs.16-19558
17. Marchini G, Pagliarusco A, Toscano A, Tosi R, Brunelli C, Bonomi L. Ultrasound biomicroscopic and conventional ultrasonographic study of ocular dimensions in primary angle-closure glaucoma. *Ophthalmology.* (1998) 105:2091–8. doi: 10.1016/S0161-6420(98)91132-0
18. Yao BQ, Wu LL, Zhang C, Wang X. Ultrasound biomicroscopic features associated with angle closure in fellow eyes of acute primary angle closure after laser iridotomy. *Ophthalmology.* (2009) 116:444–8 e2. doi: 10.1016/j.ophtha.2008.10.019
19. Sakata LM, Lavanya R, Friedman DS, Aung HT, Seah SK, Foster PJ, et al. Assessment of the scleral spur in anterior segment optical coherence tomography images. *Arch Ophthalmol.* (2008) 126:181–5. doi: 10.1001/archophthalmol.2007.46
20. Wang BS, Narayanaswamy A, Amerasinghe N, Zheng C, He M, Chan YH, et al. Increased iris thickness and association with primary angle closure glaucoma. *Br J Ophthalmol.* (2011) 95:46–50. doi: 10.1136/bjo.2009.178129
21. Kong M, Eo DR, Han G, Park SY, Ham DI. Error rate of automated choroidal segmentation using swept-source optical coherence tomography. *Acta Ophthalmol.* (2016) 94:e427–31. doi: 10.1111/aos.12989

22. Huang J, Wang Z, Wu Z, Li Z, Lai K, Ge J. Comparison of ocular biometry between eyes with chronic primary angle-closure glaucoma and their fellow eyes with primary angle-closure or primary angle-closure suspect. *J Glaucoma.* (2015) 24:323–7. doi: 10.1097/IJG.0b013e31829e55cd
23. Folio LS, Wollstein G, Ishikawa H, Bilonick RA, Ling Y, Kagemann L, et al. Variation in optical coherence tomography signal quality as an indicator of retinal nerve fibre layer segmentation error. *Br J Ophthalmol.* (2012) 96:514–8. doi: 10.1136/bjophthalmol-2011-300044
24. Falavarjani KG, Mehrpuya A, Amirkourjani F. Effect of spectral domain optical coherence tomography image quality on macular thickness measurements and error rate. *Curr Eye Res.* (2017) 42:282–6. doi: 10.1080/02713683.2016.1179332
25. Lin J, Wang Z, Chung C, Xu J, Dai M, Huang J. Dynamic changes of anterior segment in patients with different stages of primary angle-closure in both eyes and normal subjects. *PLoS ONE.* (2017) 12:e0177769. doi: 10.1371/journal.pone.0177769
26. Kalenak JW. A physical analysis of the factors that determine the contour of the iris. *Am J Ophthalmol.* (1991) 112:219–21. doi: 10.1016/S0002-9394(14)76713-3
27. Suwan Y, Rettig S, Park SC, Tantraworasin A, Geyman LS, Effert K, et al. Effects of circumpapillary retinal nerve fiber layer segmentation error correction on glaucoma diagnosis in myopic eyes. *J Glaucoma.* (2018) 27:971–5. doi: 10.1097/IJG.0000000000001054
28. Alten F, Lauermann JL, Clemens CR, Heiduschka P, Eter N. Signal reduction in choriocapillaris and segmentation errors in spectral domain OCT angiography caused by soft drusen. *Graefes Arch Clin Exp Ophthalmol.* (2017) 255:2347–55. doi: 10.1007/s00417-017-3813-8

Conflict of Interest: The authors declare that the research was conducted in the absence of any commercial or financial relationships that could be construed as a potential conflict of interest.

frontiers in Medicine

ORIGINAL RESEARCH
published: 03 March 2022
doi: 10.3389/fmed.2022.821565

A Few-Shot Learning-Based Retinal Vessel Segmentation Method for Assisting in the Central Serous Chorioretinopathy Laser Surgery

Jianguo Xu[1], Jianxin Shen[1], Cheng Wan[2], Qin Jiang[3], Zhipeng Yan[3] and Weihua Yang[3]**

[1] College of Mechanical and Electrical Engineering, Nanjing University of Aeronautics and Astronautics, Nanjing, China, [2] College of Electronic and Information Engineering, Nanjing University of Aeronautics and Astronautics, Nanjing, China, [3] The Affiliated Eye Hospital of Nanjing Medical University, Nanjing, China

Background: The location of retinal vessels is an important prerequisite for Central Serous Chorioretinopathy (CSC) Laser Surgery, which does not only assist the ophthalmologist in marking the location of the leakage point (LP) on the fundus color image but also avoids the damage of the laser spot to the vessel tissue, as well as the low efficiency of the surgery caused by the absorption of laser energy by retinal vessels. In acquiring an excellent intra- and cross-domain adaptability, the existing deep learning (DL)-based vessel segmentation scheme must be driven by big data, which makes the densely annotated work tedious and costly.

Methods: This paper aims to explore a new vessel segmentation method with a few samples and annotations to alleviate the above problems. Firstly, a key solution is presented to transform the vessel segmentation scene into the few-shot learning task, which lays a foundation for the vessel segmentation task with a few samples and annotations. Then, we improve the existing few-shot learning framework as our baseline model to adapt to the vessel segmentation scenario. Next, the baseline model is upgraded from the following three aspects: (1) A multi-scale class prototype extraction technique is designed to obtain more sufficient vessel features for better utilizing the information from the support images; (2) The multi-scale vessel features of the query images, inferred by the support image class prototype information, are gradually fused to provide more effective guidance for the vessel extraction tasks; and (3) A multi-scale attention module is proposed to promote the consideration of the global information in the upgraded model to assist vessel localization. Concurrently, the integrated framework is further conceived to appropriately alleviate the low performance of a single model in the cross-domain vessel segmentation scene, enabling to boost the domain adaptabilities of both the baseline and the upgraded models.

Results: Extensive experiments showed that the upgraded operation could further improve the performance of vessel segmentation significantly. Compared with the listed methods, both the baseline and the upgraded models achieved competitive results on the three public retinal image datasets (i.e., CHASE_DB, DRIVE, and STARE). In the

OPEN ACCESS

Edited by:
Peng Xiao,
Sun Yat-sen University, China

Reviewed by:
Chiara M. Eandi,
Università degli Studi di Torino, Italy
Xiaoying Tang,
Southern University of Science and Technology, China

***Correspondence:**
Weihua Yang
benben0606@139.com
Jianxin Shen
cadatc@nuaa.edu.com

Specialty section:
This article was submitted to Ophthalmology, a section of the journal Frontiers in Medicine

Received: *24 November 2021*
Accepted: *28 January 2022*
Published: *03 March 2022*

Citation:
Xu J, Shen J, Wan C, Jiang Q, Yan Z and Yang W (2022) A Few-Shot Learning-Based Retinal Vessel Segmentation Method for Assisting in the Central Serous Chorioretinopathy Laser Surgery. Front. Med. 9:821565. doi: 10.3389/fmed.2022.821565

practical application of private CSC datasets, the integrated scheme partially enhanced the domain adaptabilities of the two proposed models.

Keywords: retinal vessel segmentation, few-shot learning, multi-scale class prototype, feature fusion, domain adaptability, integrated framework

INTRODUCTION

Retinal vessels are important structures of our eyes, which are responsible for transporting oxygen, nutrients, and waste to ensure the normal function of the eyes. The vessels contain important information including tortuosity, diameter, angle of branches, and density, and their segmentation is crucial to the measurement of the above parameters which assist in the automatic analysis and diagnosis of various fundus diseases, such as Diabetic Retinopathy (1), Age-Related Macular Degeneration (2), and Glaucoma (3). The traditional manual segmentation method is exceedingly time-consuming and laborious, and the segmentation accuracy is easily affected by the subjective factors of doctors. Therefore, some researchers have developed segmentation methods based on traditional image processing techniques, such as the matched filtering method (4), the mathematical morphology method (5), the vessel tracking method (6), and so on. With the help of the image processing technology, the above schemes realize the transformation from manual segmentation to automatic segmentation and improve the efficiency of vessel segmentation, but there is still much room for further promotion in segmentation accuracy.

In addition, with the rapid development of artificial intelligence technology, machine learning has been widely used in various segmentation scenes (7–9) and provides a new impetus for the retinal vessel segmentation task. Various excellent machine learning-based automatic segmentation methods (10) have been designed, which can be divided into two categories (11): the unsupervised methods and the supervised methods. Among them, the unsupervised methods do not rely on pixel-wise labeling information to guide the vessel segmentation process. The typical representative is clustering. Wiharto and Suryani (12) used fuzzy c-means (FCM) algorithm to extract the vessels. They employed a channel separation, contrast limited adaptive histogram equalization (CLAHE), and median filtering to preprocess the fundus images, followed by dimension transformation, clustering, thresholding, and masking operations. The impact of the number of clusters on the segmentation effect of vessel structures was also explored in their work, which provides a direction for further improvement of the scheme. A k-means clustering-based method (13) was presented to segment the vessels, which achieved a comparable performance. The authors binarized the vessel-enhanced images, and a logical OR operation was applied on the binary vessels to produce the final results. However, it is worth noting that although the unsupervised methods do not require any label information, the single segmentation rule may lead to an unstable performance because of the differences in contrast and brightness between the retinal images.

In view of this, some ideas of vessel segmentation based on supervised learning have been proposed (14–29) and the related research work will be briefly introduced in the following. An ensemble classification-based approach was presented by Fraz et al. (14). This typical solution combined the decision tree with the conventional feature extraction steps (i.e., gradient vector field, morphological transformation, line strength measures, and Gabor filter responses), which worked well on the public datasets. With the help of image preprocessing and feature selection operation, Krishna and Gnanasekaran (15) applied the modified adaboost extreme learning machine to extract the retinal vessels, and the method performed well on pathological retinal images. To enhance the local information with better discrimination for vessel and non-vessel pixels, Aslani et al. (16) incorporated a set of robust features into a hybrid feature vector for better characterizing the retinal vessels, closely followed by a random forest classifier. Orlando et al. (17) put forward a discriminatively trained and fully connected conditional random field model to tackle the thin and elongated vessel structures, which obtained better results in terms of sensitivity, f1-score, G-mean, and Matthews correlation coefficient. A novel method (18), which regarded the segmentation task as cross-modality learning, was skillfully designed. By establishing the deep neural network with strong induction ability, they achieved satisfactory results without the feature design and preprocessing. Srinidhi et al. (19) explored the visual attention mechanism to automatically capture the most discriminative features for the random forest classifier, and a significant improvement was achieved. A simple yet effective vessel segmentation method was proposed by Jebaseeli et al. (20), the highlights of which were the operation of feature generation based on the Tandem Pulse Coupled Neural Network, and the classifier called it the Deep Learning-Based Support Vector Machine. Kaur and Mittal (21) developed a generalized scheme for retinal vessel detection and obtained a good performance. This method improved the quality of the constructed vessel features through the initial segmentation and post-processing strategy, and then, the neural network-based classifier further enhanced the accuracy of vessel segmentation.

In recent years, deep learning (DL), as one of the important technologies to realize the machine learning idea, has shown great potential in the field of medical image segmentation. Liskowski and Krawiec (22) designed a DL-based model for detecting the vessel structures. The model, with or without max-pooling layers, was trained on about 4,00,000 examples that are preprocessed with global contrast normalization, zero-phase whitening, and were augmented using geometric transformations and gamma corrections, while the area under the curve (AUC) was up to 0.99. Similarly, a deeply supervised network was established by Mo and Zhang (23), and the novelty is that the multi-level hierarchical feature extraction technique and

the auxiliary classifiers are integrated into the network, which enhanced its discriminative capability on the vessel and the non-vessel pixels. Jiang et al. (24) proposed a supervised method based on the fully convolutional network (FCN) and transfer learning; the accuracy of which was 1–2% higher than other related research. To further improve the segmentation performance, a scheme inspired by a dense conditional random field was presented in (25). By training the convolutional neural network (CNN) to generate discriminative features, the scheme aimed to solve the sub-optimal problem of the hand-crafted unary features in the linear models. In order to alleviate the issue of inaccurate segmentation of thin vessels caused by the highly imbalanced pixel ratio between thick and thin vessels, a novel DL-based vessel segmentation model (26) is constructed delicately. They designed a segment-level loss to emphasize more on the thickness consistency of thin vessels in the training process and combined it with the pixel-wise loss to improve the accuracy of the vessel segmentation. Filipe et al. (27) adopted a multiscale FCN framework for the vessel segmentation. In consideration of the varying width and direction of the vessel structure, the stationary wavelet transform (SWT) was introduced into the framework to sufficiently exploit the multi-scale nature of the retinal vessels, and then, the experimental results showed the effectiveness of the method. To achieve accurate and precise retinal vessel segmentation, Park et al. (28) presented a conditional generative adversarial network called M-GAN that is composed of an M-generator and an M-discriminator. With the help of the deep residual blocks and the deeper network, the framework acquired good results. For exploring the DL-based segmentation method on the other retinal imaging modalities, a framework based on the U-net shape was established to gain the vessel mask from the scanning laser opthalmoscopy retinal images and has performed well (29).

Undoubtedly, the methods based on deep learning have greatly improved the efficiency, accuracy, sensitivity, and specificity of retinal vessel segmentation, and the end-to-end training mode also accelerates the deployment of the DL-based model in practical application scenarios. Nevertheless, this kind of scheme is driven by big data to acquire excellent intra- and cross-domain adaptability, which is challenging for medical image collection. Meanwhile, to optimize the weights of the network by the loss function, the densely annotated task is essential, which is tedious and costly. Therefore, to alleviate the above issues, a few-shot learning-based method, undertaking the task of vessel segmentation with only a few annotated training images, is proposed in this paper. The main contributions of our research are as follows: (1) Firstly, a key solution is presented for transforming the vessel segmentation scene into the few-shot learning task; (2) Then, to adapt to the vessel segmentation task, we improve the existing few-shot learning framework as the baseline model for the vessel segmentation in our work; (3) Next, we upgrade the baseline model for better utilizing the information from the support images by designing a multi-scale class prototype extraction technique; (4) After that, the skip connection technique is integrated into the upgraded model to promote the gradual fusion of the multi-scale vessel features of the query images inferred by the support image class prototype information; (5) Moreover, a multi-scale attention module is built and applied to the high-level features for the upgrade model to capture the global information to assist in vessel localization; and (6) Finally, the integrated framework is further constructed to boost the performance of both the baseline and the upgraded models in the cross-domain vessel segmentation scene.

The rest of the paper is organized as follows: Section Related Work presents the related work of few-shot learning; Section The Proposed Methods describes the details of our proposed method; Section Results and Discussions shows the experiments and discussions; and Section Conclusion and Future Work comes up with conclusions.

RELATED WORK

Few-Shot Learning

Few-shot learning aims to improve the network generalization ability under the condition of a few training examples. Some methods based on this learning paradigm have been explored and applied to the classification of natural and medical images. Huang et al. (30) proposed a few-shot model for fine-grained classification. The advantage of the low-rank pairwise bilinear block was that it enhanced the effective distance metric between the support and query images. Similarly, Sun et al. (31) also studied the fine-grained classification issue based on the few-shot learning. Notably, they utilized the location mechanism to discover the similar characteristics among the objects and captured the rich discriminative information with a high-order integration. Related works are also reflected in the medical disease detection. To make up for the deficiency of the DL model in predicting rare fundus diseases, Quellec et al. (32) extended the CNN model with the few-shot learning paradigm, which improved the discrimination ability on rare pathologies through an unsupervised probabilistic way. A few-shot learning-based method (33) was presented to transfer knowledge from a well-defined source domain to a target domain, the goal of which was so the CNN model could obtain new concepts and representations from a few training samples.

Few-Shot Segmentation

In addition, the few-shot method also performs well in the natural image segmentation field. Seeing that the pixel-wise segmentation is tedious and costly, a segmentation network (34), consisting of a two-branch dense comparison module and an iterative optimization module, which is followed by an attention block, was proposed and has achieved better performance. Li et al. (35) exploited a similar technique that integrated the attention mechanism and the refinement network into the segmentation model, which improved the model performance. Compared with the natural images, the task of the medical image segmentation is more complex and difficult due to the similarity between the normal tissues and the pathological regions, and the extreme professionalism of the pixel-wise annotation process. Some of the few-shot segmentation methods have been successfully applied to the medical image segmentation, which affords new ideas for solving the medical image segmentation problem. Feyjie et al. (36) designed a few-shot learning-based framework for the

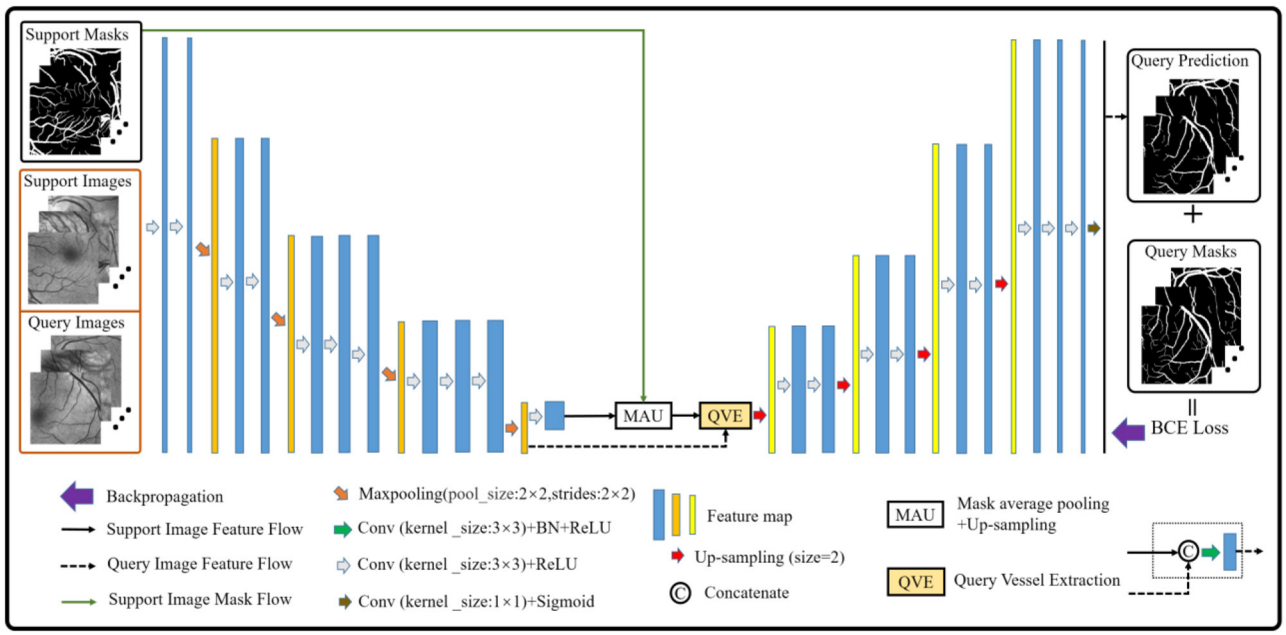

FIGURE 1 | An overview of the baseline model.

skin lesion segmentation, the excellent performance of which also provided inspiration for our research work. To enhance its segmentation ability, they also incorporated the semi-supervised block into the framework. Besides, a unified framework (37), which worked under the condition of the scarcity of both the medical images and the corresponding annotations, was put forward and has contributed to the rare disease segmentation. Additionally, Ouyang et al. (38) further developed creatively a few-shot-based method without any annotations and trained the network with only the pseudo labels, which opened up a new direction for few-shot-based segmentation schemes.

It can be found that the few-shot learning has been widely used in the field of natural image classification and segmentation, which promotes the paradigm to show its head in the similar fields of medical images. Also, its successful application in practice drives us to further apply it in the retinal vessel segmentation to assist in fundus CSC laser surgery. The motivation of introducing the few-shot learning into the fundus blood vessel segmentation task is that the paradigm can guide the vessel segmentation model training under the condition of a small number of annotated images, which is different from most machine learning models that rely on a large amount of image resources for an effective feature learning. This does not only reduce the cost of data collection but also helps ease the pressure of label making. However, we are faced with a thorny problem that has to be solved, that is, how to transform the vessel segmentation scene into a few-shot segmentation task? Specifically, how to construct the support and query sets in our vessel segmentation task? The solution will be introduced in Section The Proposed Methods.

THE PROPOSED METHODS

Methods

The vessel segmentation scheme based on the few-shot learning paradigm consists of two parts. The first part is how to construct the support and the query sets in vessel segmentation task by imitating the natural image scene. As we all know, the vessel structure of each person is not exactly the same. Therefore, in this paper, the vessel images from different people are regarded as different classes, and the patches of each class are regarded as its members. Then, we sampled the members of different classes as the support set, and the remaining members of the corresponding classes as the query set. Especially, given a C-way K-shot learning task, this simple yet effective solution can smoothly build the corresponding episodes for the vessel segmentation task. The second part is to establish the vessel segmentation model. Inspired by (36), we build a model in which the semi-supervised module in (39) is removed to suit our task. Simultaneously, the dilated convolution kernels are also replaced by the ordinary convolution kernels to prevent information loss caused by the gridding effect. Finally, we obtain the baseline model for retinal vessel segmentation as shown in **Figure 1**.

Preprocessing

After solving the problem that transformed the vessel segmentation scene into a few-shot segmentation task, here comes the preprocessing operation. In this paper, the gamma correction and the CLAHE are employed, respectively, aiming at improving the brightness and the contrast of the retinal images. In addition, we separate the green channel, which is a routine

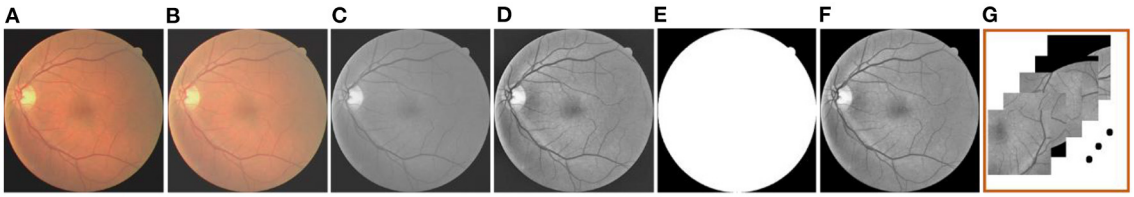

FIGURE 2 | The preprocessing operation: **(A)** Original image; **(B)** Gamma-corrected image; **(C)** Green channel image; **(D)** CLAHE image; **(E)** Mask; **(F)** Mask-processed image; and **(G)** Patches.

operation in the vessel segmentation scenario, to show the vessel structures more clearly. The masks are used to eliminate the disturbance outside the region of interest. Furthermore, in response to the construction of the support and the query sets, the clipping operation is applied to the previous operation result. Meanwhile, the overlapping technique is also adopted here to ensure the similarity and the quantity of patches in the same retinal image. Specifically, we firstly set the size of the image patch template to 224 × 224 pixels, and then the clipping function is realized by moving the template in the horizontal and vertical directions. In the process, we realize the overlapping function by setting the moving step as 64 (i.e., the overlapping size is 160) among each image patches in the above directions. The whole preprocessing is shown in **Figure 2**.

Problem Definition

The task of this paper is to construct the vessel segmentation model based on the few-shot learning paradigm, which possesses a strong generalization ability to the similar unseen targets by learning only a few annotated examples. In this scenario, we are given an annotated retinal image set $\mathcal{D} = \{X_i, Y_i\}_{i=1}^{N}$, where X_i is the i^{th} sample and Y_i corresponds to its label. The N is the number of the annotated retinal images. In order to train the model, D is divided into the training set $\mathcal{D}_{train} = \{X_j, Y_j\}_{j=1}^{N_1}$, validation set $\mathcal{D}_{valid} = \{X_k, Y_k\}_{k=1}^{N_2}$, and testing set $\mathcal{D}_{test} = \{X_l, Y_l\}_{l=1}^{N_3}$, where *N1*, *N2*, and *N3* represent the number of images in each set, respectively. As mentioned above, in order to adapt to the few-shot segmentation task, each retina image X_i is regarded as a unique class and is cropped into patches to build the support set $\mathcal{S}_{i_s} = \{x_{is}, y_{is}\}_{s=1}^{K}$ and the query set $\mathcal{Q}_{iq} = \{x_{iq}, y_{iq}\}$, where K denotes the sampling numbers from the class i, x_{i_s} is the s^{th} support patch extracted from the image X_i with its annotation y_{is}, and x_{iq} is the query patch extracted from the remaining patches in the image X_i with its annotation y_{iq}. So, given a C-way K-shot segmentation task, the training episodes can be described as $\left(\mathcal{S}_{j_s}, \mathcal{Q}_{j_q}\right)$ by randomly extracting C classes from *N1* and K members from each corresponding class during the training stage. To verify the model performance in the training process and to save the optimal weight parameters, the same technique, such as building the training episodes, is also applied to the validation set $\mathcal{D}_{valid}$.

Few-Shot Learning-Based Segmentation Architecture

Although the baseline model performs well in the vessel segmentation task (refer to Section Results and Discussions), it is defective to derive the label information of the query images by only using the support image class prototype information from the high-level layer. The reason is that part of the foreground and the background contents of the support images will be lost in the down-sampling process, which will provide an incomplete guidance for the query image label prediction and render inaccurate results. Therefore, the baseline model is further upgraded to alleviate the above problems (as shown in **Figure 3**). Specifically, a multi-scale class prototype extraction technique, which is embedded into the parallel positions of the down-sampling steps in the encoder composed of the first four modules from the VGG16 (40), is designed for the information derivation of the query images. Besides, the gradual fusion scheme for the multi-scale vessel features is also integrated in the upgraded model. In this paper, the mask average pooling (36, 38) is also employed to extract the class prototype information of the support images, and the formulation can be expressed as:

$$P_s^l = \frac{1}{W \times H} \sum_{w=1}^{W} \sum_{h=1}^{H} f_\omega(x_s^l) \circ y_s^l, l \in (1, 2, 3, 4, 5) \tag{1}$$

where P_s^l represents the class prototype of the support image feature map x_s^l with the width W and height H and l is the parallel position mark. The f_ω is the feature mapping function composed of weight parameters ω and the network framework, and y_s^l denotes the annotation obtained by the linear interpolation sampling on the support image mask. The Hadamard product, denoted by the symbol $\circ$, is used to extract the class prototype of x_s^l. Then, the same operation is adopted as (29), that is, to apply the up-sampling operation on each class prototype P_s^l and convolve the sampling result with the corresponding query image feature map x_q^l to obtain the multi-scale vessel maps. Meanwhile, the skip connection technique is integrated into the upgraded model to fuse the multi-scale information for better segmentation results. Finally, the binary cross-entropy loss function is established based on the probability prediction

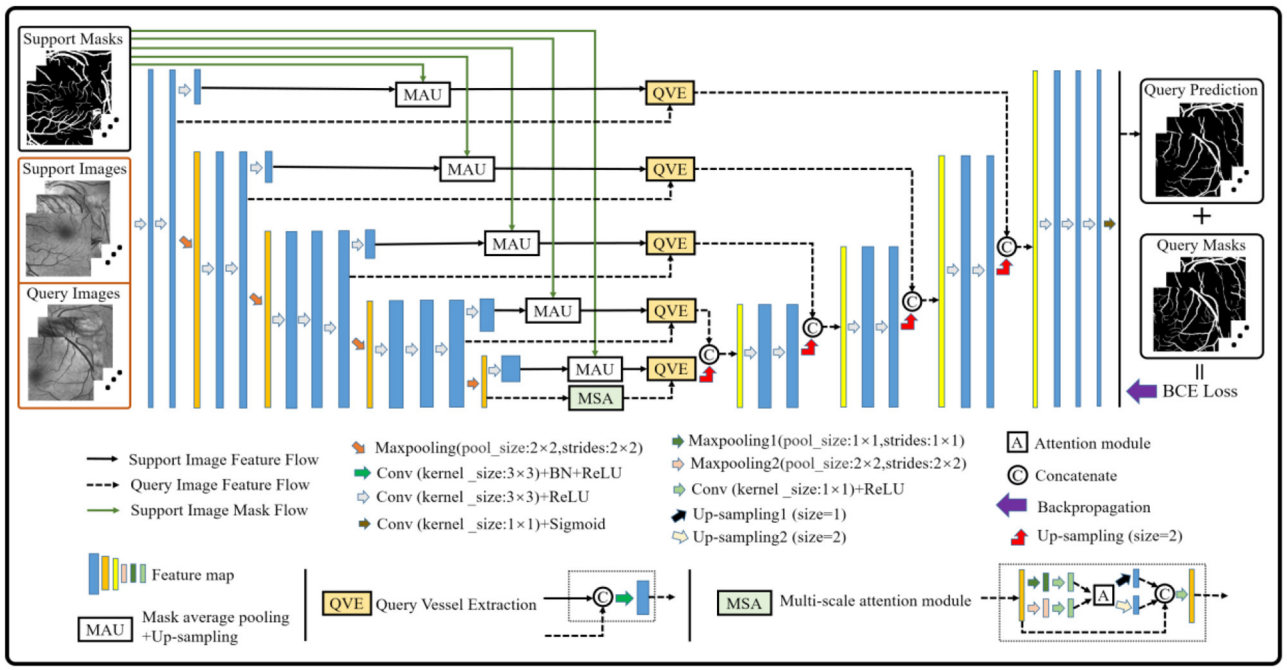

FIGURE 3 | An overview of the upgraded model.

map p_{jk}^{q} and its corresponding true annotation y_{jk}, which can be expressed as:

$$L(\omega, b) = -\frac{1}{C \times K} \sum_{j=1}^{C} \sum_{k=1}^{K} [y_{jk} \cdot log(p_{jk}^{q}) + (1 - y_{jk}) \cdot log(1 - p_{jk}^{q})] \quad (2)$$

$$p_{jk}^{q} = sigmoid(x_Q(k)) = \frac{1}{1 + e^{-x_Q(k)}} \quad (3)$$

where p_{jk}^{q} and $x_Q(k)$ denote the probability prediction map of the query patches with its true annotation, and the k^{th} feature map of the query patches of the model outputs, respectively. In addition, it is well-known that the convolution module is a local operation and ignores the global information, which may lead to the failure of a pixel-level prediction task. Considering this, a block (i.e., the MSA module in **Figure 3**) based on the non-local attention operation (41) and multi-scale operation is established to seek the global information integration of the query feature maps at different scales, aiming at assisting the upgraded model to approach the retinal vessel segmentation task. In view of the rich semantic information of high-level features and the cost of mathematical calculation, the attention operation is just performed on the query feature map with two scales at the last layer of the encoder, and the details are shown in **Figure 3**.

Furthermore, in order to obtain the good performance of both the baseline and upgraded models in the cross-domain retinal vessel segmentation task, an integrated framework (as shown in **Figure 4**) is conceived according to the principle that the minority obeys the majority, the mathematical idea of which can be parameterized as follows:

$$p_{jk}^{l} = F_l(x_Q(k)),\ l = 1, ..., N_1 \quad (4)$$

$$p_{N1} = 1\left\{\left(\sum_{l=1}^{N_1} 1\left\{p_{jk}^{l} > T\right\}\right) > T_1\right\} \quad (5)$$

where N_1 and $F_l$are the total number of models in the integrated framework and the l^{th} model, respectively. The $p_{jk}^{l}$and p_{N1} denote the probability prediction map from the l^{th} model and the statistical prediction result of N_1 models, respectively. The $1\{\bullet\}$ is an indicator function which outputs 1 if the parameters meet the threshold condition T or T_1, and these two values are set to 0.5 and 1 in this paper, respectively. Then, the final probability prediction map p_{jk}^{F} of the query patches can be expressed as:

$$p_{jk}^{F} = \begin{cases} \max\{p_{jk}^{l}(m,n)\},\ if\ p_{N_1}(\mathrm{m,n}) = 1 \\ \min\{p_{jk}^{l}(m,n)\},\ otherwise \end{cases} \quad (6)$$

where (m, n) represents the position coordinate of the element in p_{jk}^{l} or p_{N1}.

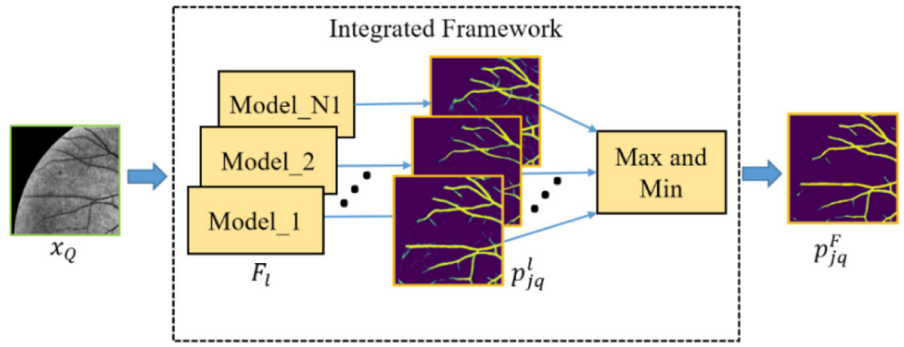

FIGURE 4 | An overview of the integrated framework.

TABLE 1 | The basic configuration of the segmentation architecture.

Encoder	Decoder
Conv3-64	Up-sampling
Conv3-64	Conv3-512
Maxpooling	Conv3-256
Conv3-128	Up-sampling
Conv3-128	Conv3-256
Maxpooling	Conv3-128
Conv3-256	Up-sampling
Conv3-256	Conv3-128
Conv3-256	Conv3-64
Maxpooling	Up-sampling
Conv3-512	Conv3-64
Conv3-512	Conv3-32
Conv3-512	Conv3-3
Maxpooling	Conv3-1

Segmentation Architecture Configuration

In this paper, no matter our baseline model or upgraded model, the basic architecture configuration is the same, which is composed of encoder and decoder. The encoder consists of the first four modules of VGG16 (40), and the decoder consists of conventional neural network layer. **Table 1** shows the specific configuration.

RESULTS AND DISCUSSIONS

Retinal Image Datasets and Experimental Settings

To assess the performance of the proposed baseline and upgraded models based on the few-shot learning paradigm, we have carried out extensive experiments on the public retinal image datasets, namely, CHASE_DB (42) (abbreviated as CHASEDB), DRIVE (43), and STARE (44), to demonstrate the excellent potential of the paradigm. In our experiments, for each dataset, only 10 images, namely, 10 classes, are used as the candidate set for constructing episodes composed of the support and query sets, which is different from the machine-learning-based segmentation models that are generally trained with more than 10 images. In fact, we randomly selected no more than five types of vessel images, that is, C is set to 5, 4, or 3, to drive the vessel segmentation model in the training process. The remaining images are divided into the validation and testing sets. Of note, in order to deduce the label information of the testing set based on the structural similarity between retinal vessels, the testing images share the support images of the validation set. In addition, taking the calculation cost and the reliability verification of both the baseline and the upgraded models into consideration, five groups of C-way K-shot modes (Hereinafter referred to as CK modes), namely, 5-way 3-shot, 4-way 3-shot, 3-way 3-shot, 3-way 4-shot, and 3-way 5-shot, are set up to construct different episodes for training the above vessel segmentation models, respectively. In addition, we conducted application experiments on ophthalmic clinical CSC dataset composed of 20 fundus images to test the effectiveness of the two models and the feasibility of the integrated framework. All experiments are performed on the NVIDIA-3080ti GPU with the Tensorflow framework, and the learning rate, epoch, iteration, and gradient optimizer are set to 0.0001, 30,100, and Adam, respectively.

Evaluation Metrics

In this section, the performance of the baseline and upgraded models in the training, validation, and testing processes is comprehensively evaluated based on the accuracy and the loss of training process, the segmentation metrics, namely, sensitivity (Sen), specificity (Spe), accuracy (Acc), f1-score (F1), and AUC, and the actual segmentation results on the testing images. Meanwhile, the superiority and the potential of the proposed method is also discussed by comparing it with some typical machine learning based vessel segmentation methods. The segmentation metrics mentioned above are written as:

$$sensitivity = tp/(tp + fn), specificity = tn/(tn + fp) \quad (7)$$

$$accuracy = (tp + tn)/(tp + fn + tn + fp),$$
$$f1\text{-}score = 2tp/(2tp + fn + fp) \quad (8)$$

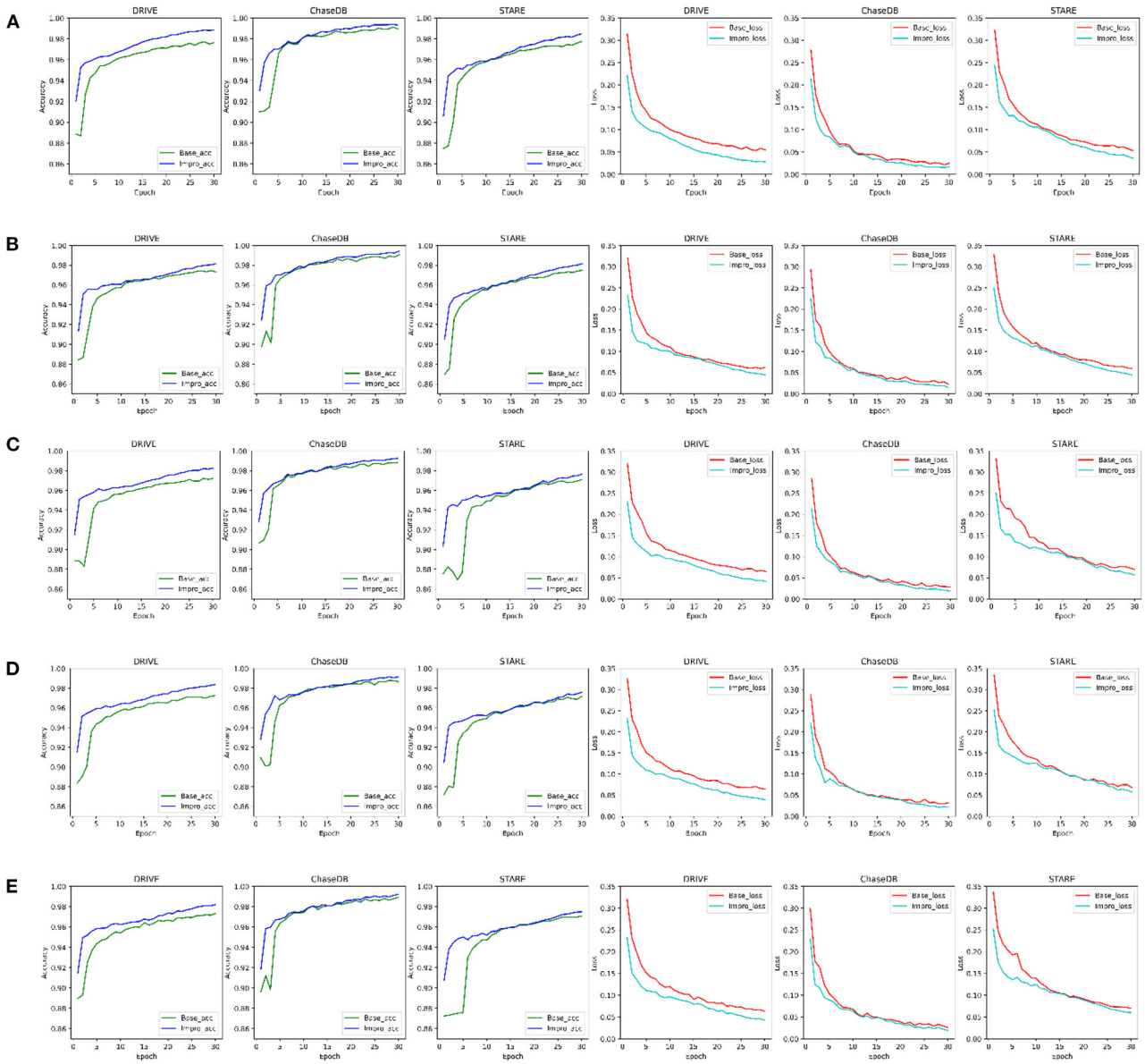

FIGURE 5 | Comparison of the baseline and upgraded models on training set: **(A)** 5-way 3-shot; **(B)** 4-way 3-shot; **(C)** 3-way 3-shot; **(D)** 3-way 4-shot; and **(E)** 3-way 5-shot.

where *tp*, *tn*, *fn*, and *fp* denote true positive, true negative, false negative, and false positive, respectively.

Comparison of the Baseline and Upgraded Models on the Training and Validation Sets

For convenience, in the following sections, the baseline and upgraded models are represented by "Base" and "Impro", respectively. As shown in **Figure 5**, it can be found that both models can achieve more than 95% accuracy in the end. The segmentation accuracy of the Impro model is higher than that of the Base model in most cases under different *CK* modes on three datasets during the training process. Similarly, compared with the Base model, the loss value of the Impro model keeps a low state on the whole. Even in some training epochs, the difference of this loss value between the two models is relatively small, but it is maintained for a short time. In addition, it can also be found that the upgraded model shows the advantages in the initial stage of training, whether it is the accuracy value or the loss value. Specifically, at the beginning, the initial accuracy of the upgraded model is higher than that of the baseline model, and the loss value is also small, which means that the upgraded operation can effectively improve the learning ability of the model and promote the model to quickly capture the vessel and

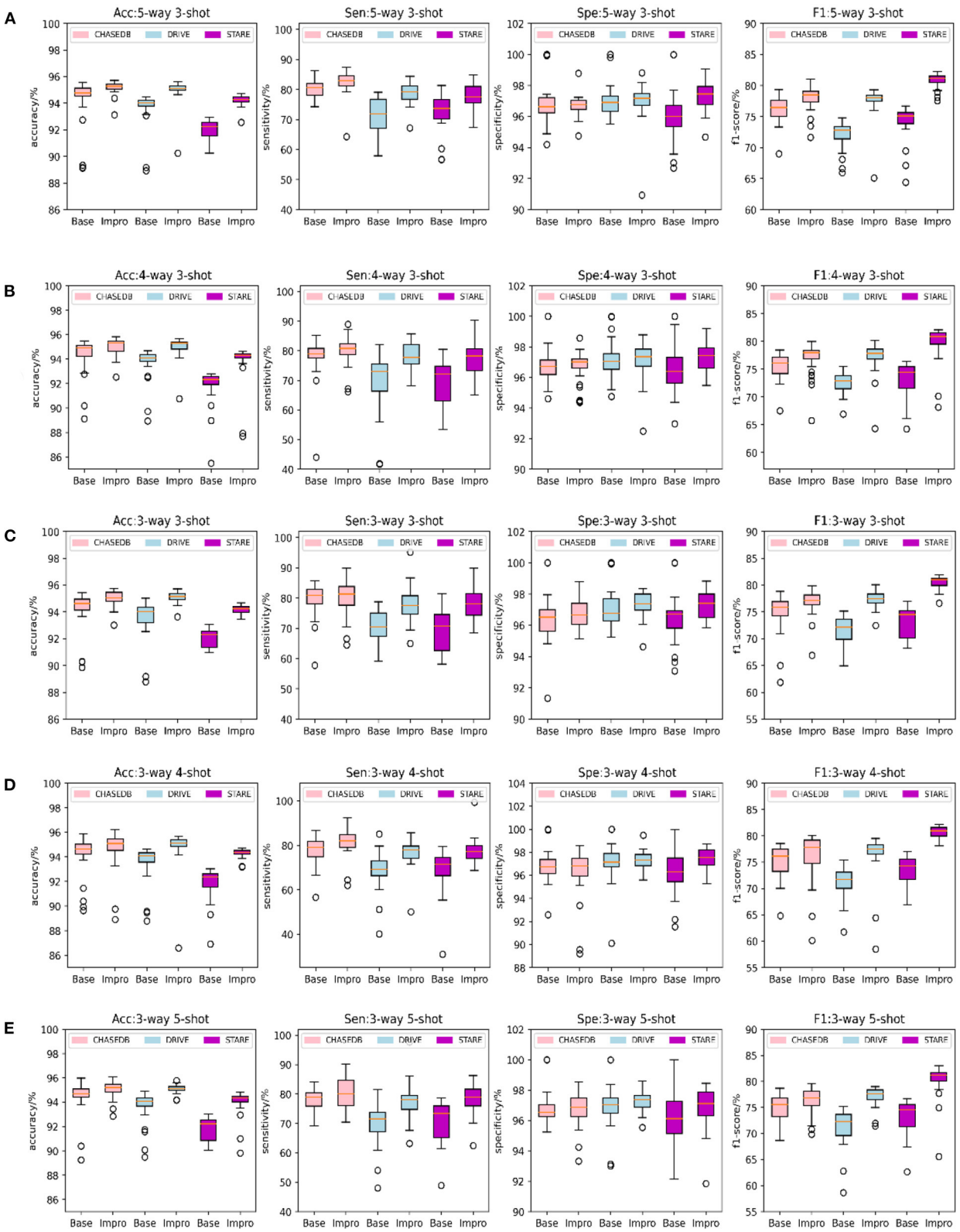

FIGURE 6 | Comparison of the baseline and upgraded models on validation set: **(A)** 5-way 3-shot; **(B)** 4-way 3-shot; **(C)** 3-way 3-shot; **(D)** 3-way 4-shot; and **(E)** 3-way 5-shot.

the non-vessel information in the fundus images. In general, the performance of the upgraded model is slightly superior to that of the baseline model in terms of accuracy and loss on the training set.

Furthermore, to check the generalization ability of the model to the unseen vessel images after each epoch and to save the optimal weights in time, the accuracy, sensitivity, specificity, and f1-scores of the two models on the validation set are specially counted and plotted as shown in **Figure 6**. It shows that the Impro model surpasses the Base model in terms of the average segmentation accuracy and average f1-score in different *CK* modes from **Figure 6**, which implies that the upgraded model has a better segmentation performance. When referring to the other two metrics (i.e., average sensitivity and average specificity), we can also get the conclusion that the segmentation performance of the baseline model is inferior to that of the upgraded model in most cases. Moreover, the experiment can also show that there are some differences in the performance of either the baseline model or the upgraded model on different datasets, which is mainly caused by the inconsistent data distribution of each datasets. Nevertheless, compared with the baseline model, the average values of various metrics of the upgraded model are relatively consistent on different datasets, which reflects its strong learning ability. However, it is worth noting that although the Impro model performs well on the whole, its robustness still needs to be enhanced.

Comparison of the Baseline and Upgraded Models on the Testing Set

It can be obviously revealed from **Figures 7A–E** that both models can achieve higher AUC values. Especially on the DRIVE dataset, the AUC value of the Impro model is as high as 98.03% under the combination of 3-way 5-shot mode and is better than most of the listed methods. Under different *CK* modes, the AUC values of the Impro model on the DRIVE, CHASEDB, and STARE datasets are higher than those of the Base model, which not only explicitly proves the excellent performance of the upgraded model, but also shows the necessity and the effectiveness of the upgraded operation. Moreover, from **Figures 7A–E**, we can directly see that the AUC values of the Base model or of the Impro model are different in each dataset, which indicates that the dataset, itself, is an import factor affecting the model performance, and also proves once again that the inconsistency of data distribution is a significant part leading to a difference of the model performance.

In addition to the AUC value, we also evaluate the generalization ability of the models on the testing set from the other four evaluation metrics shown in **Figure 8**. Under different *CK* modes, both the two models achieve more than 90% in terms of the accuracy and specificity values, and overall, the Impro model surpasses the Base model on the above values. Besides, in consideration of the sensitivity and the f1-score values, the conclusion can be drawn that the Impro model is significantly better than those of the baseline model in most cases on the three testing sets, which is similar to their performance on the validation set. In general, the performance of the two models in the testing sets is consistent with that in the training and validation sets, which implies that both the two models can better transfer the knowledge learned from the training set to the unseen vessel images. However, it can still be found that the test results of the two models in different datasets are slightly different, which is also consistent with the previous experimental observations. The difference in the model performance caused by the inconsistent data distribution of different datasets is the common factor of almost all the current vessel detection methods based on machine learning, and it is also a problem to be alleviated in the future.

Comparison of the Baseline and Upgraded Models on the Segmentation Results

Through the above analysis, on the one hand, it shows the excellent performance of both the Base and the Impro models in the vessel segmentation task, while on the other hand, the Impro model outperforms the Base model overall, which proves the necessity for the upgraded operation. Furthermore, **Figure 9** shows the details of the two models in the vessel segmentation task on three datasets. It can be found that the two models have good segmentation ability for the wide vessels and can extract the main vessel structures. At the same time, by observing the overall segmentation performance of the two models on the three datasets, compared with the Base model, the Impro model, still, has the upper hand, which is embodied in the vessel continuity and adhesion. Specifically, it can be clearly seen from **Figure 9B** that the wide vessels segmented from the Base model may adhere to each other, but the Impro model performs better and can properly deal with the vessel adhesion events. Meanwhile, the Base model is generally inferior to the Impro model in terms of the vessel continuity. For instance, as shown in **Figure 9C**, there is a certain degree of discontinuity between the branch vessel located by the baseline model and the main vessel located by the same model. However, compared with this, the continuity between the main and the branch vessels detected by the upgraded model is relatively satisfactory.

However, although the Impro model has made progress in the above segmentation performance, it cannot be ignored that the baseline and upgraded models still have shortcomings in small vessel segmentation, and this defect is also a common weakness of the existing vessel segmentation methods. The upgraded operation, indeed, improves the recognition ability of the Base model for small vessels, but there is still much room for improvement, which is also the direction of our future efforts.

Comparison of the Baseline and the Upgraded Models With the Previous Studies

In this section, we compare the proposed baseline and upgraded models with the existing typical segmentation schemes based on machine learning, and the results for each dataset are summarized in **Tables 2–4**.

For the DRIVE dataset, it can be found that the accuracy, specificity, sensitivity, and AUC values of the Impro model all exceeded the Base model under different *CK* modes, and the sensitivity difference between the two models is the most obvious,

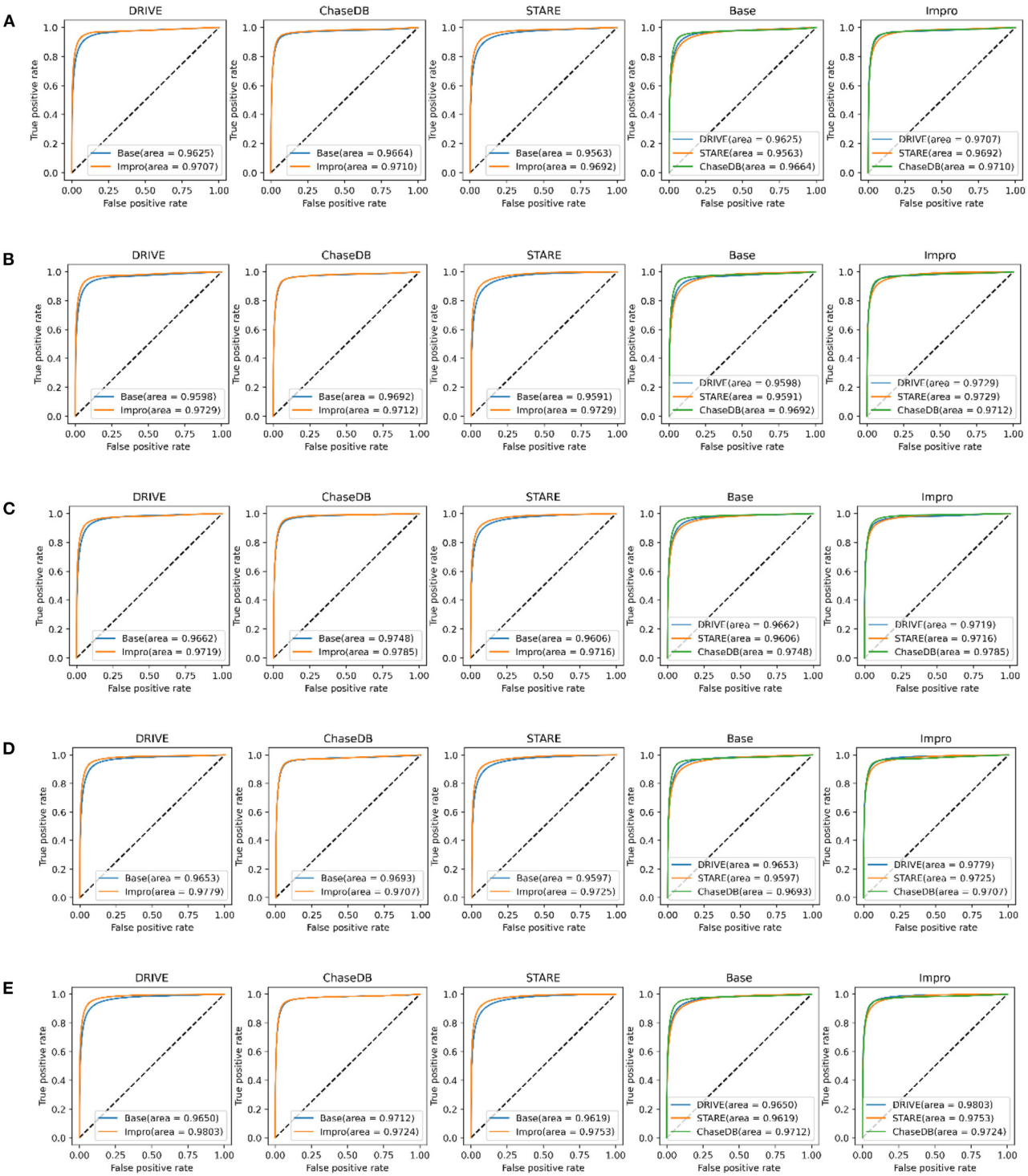

FIGURE 7 | Comparison of the baseline and upgraded models based on the AUC: **(A)** 5-way 3-shot; **(B)** 4-way 3-shot; **(C)** 3-way 3-shot; **(D)** 3-way 4-shot; and **(E)** 3-way 5-shot.

which proves that the upgraded model can better distinguish the vessel pixels from the background pixels. Besides, the highest accuracy, specificity, and sensitivity of the Impro model are 96.64, 98.29, and 84.95%, respectively, which are not only higher than those of the Base model but are also significantly competitive compared with most of the schemes listed. In addition, the AUC

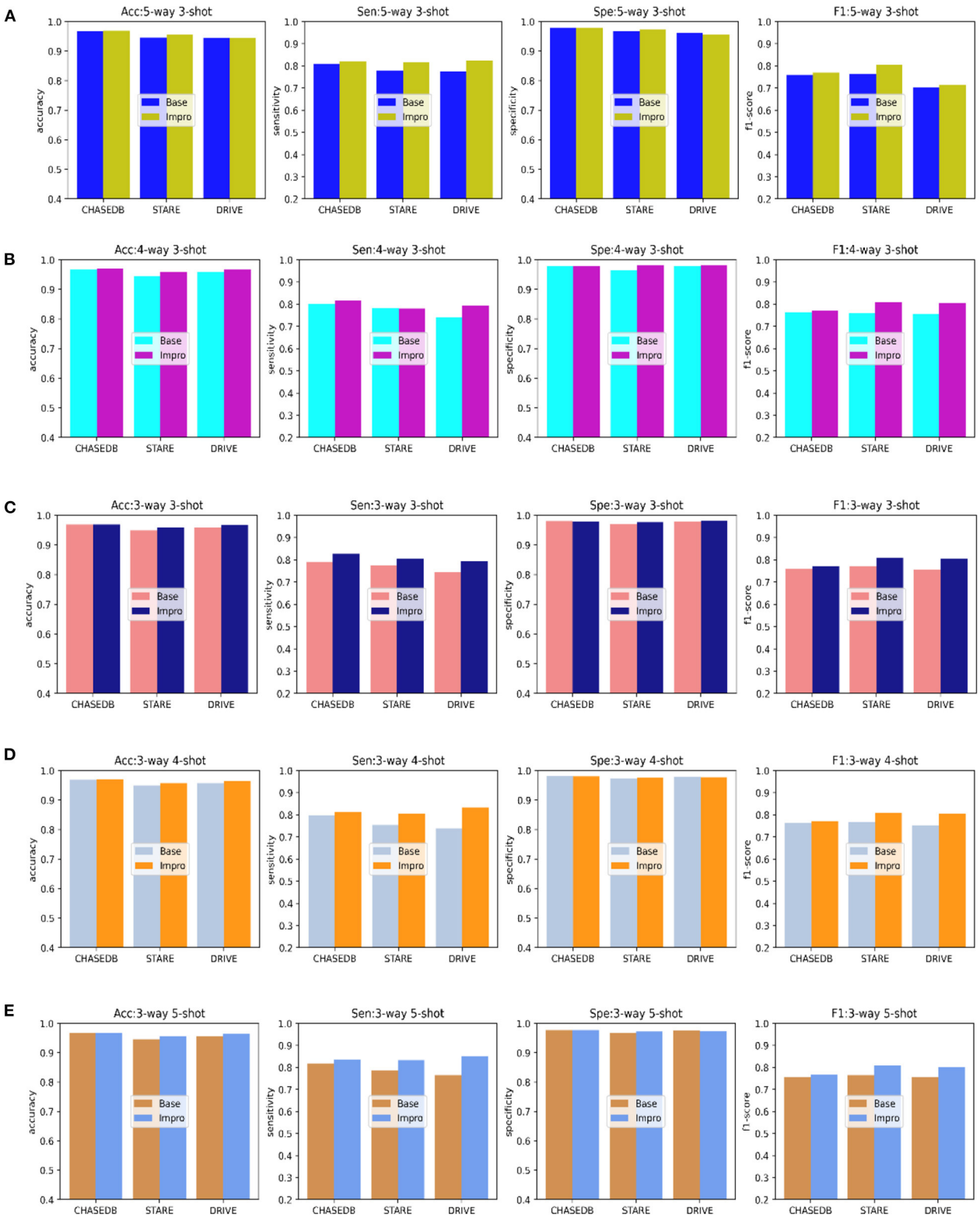

FIGURE 8 | Comparison of the baseline and upgraded models based on the sensitivity, specificity, accuracy, and f1-score: **(A)** 5-way 3-shot; **(B)** 4-way 3-; **(C)** 3-way 3-shot; **(D)** 3-way 4-shot; and **(E)** 3-way 5-shot.

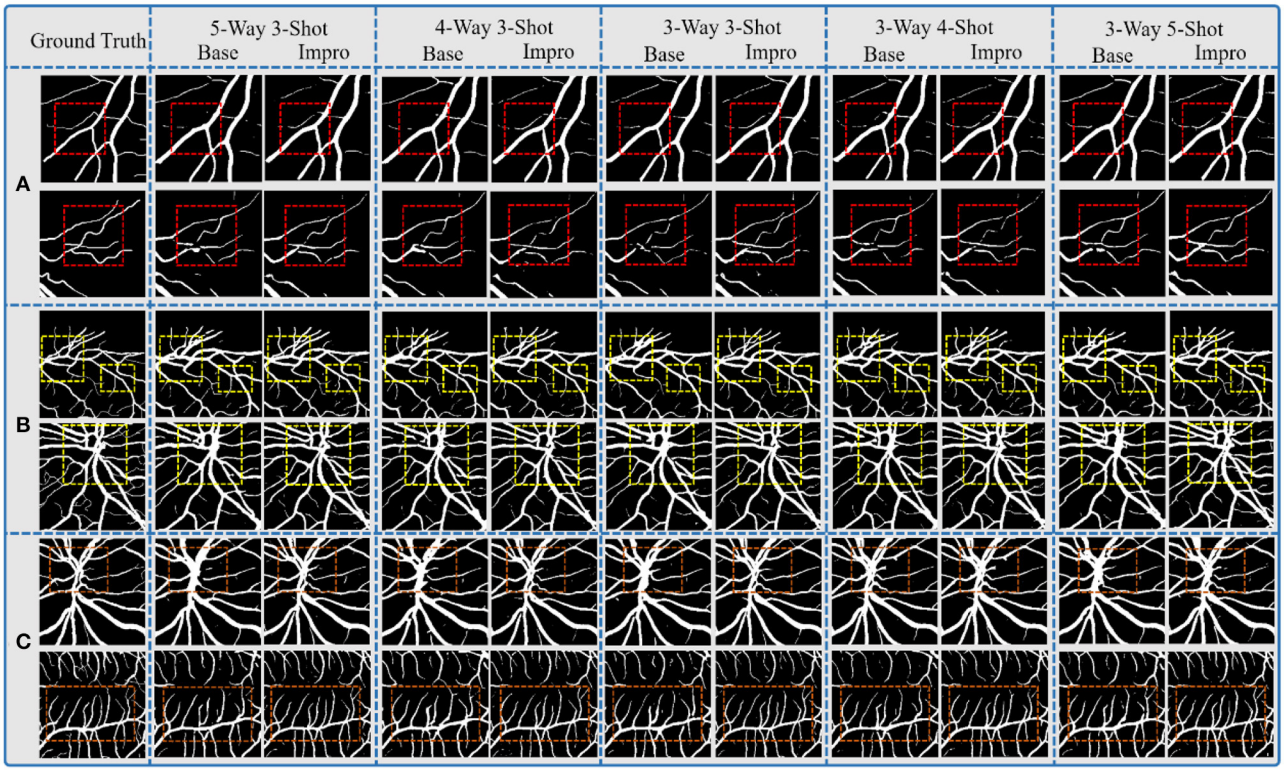

FIGURE 9 | Comparison of the baseline and upgraded models on segmentation results: **(A)** CHASEDB; **(B)** DRIVE; and **(C)** STARE.

value of the upgraded model is also visibly superior to the baseline model, and the biggest difference is 1.53%. Moreover, the Impro model is just 0.65% smaller in this metric than the optimal one that is listed, which not only reveals its potential superiority but also means that there is still room for improvement of the upgraded model based on the few-shot learning paradigm.

Additionally, **Table 3** shows the performance of our models on the STARE dataset. Apparently the Impro model generally obtains better results than the Base model, especially in the accuracy, specificity, and AUC metrics. Compared with other methods, our Impro model performs well in sensitivity and achieves 83.37%, which shows that the model possesses good capability to segment vessel pixels. Nevertheless, this may make the upgraded model recognize the more true negatives as true positives and result in poor performance on other metrics, which encourages us to continue to optimize the few-shot based method for vessel segmentation comprehensively. In addition, we can find that the data-driven models are still dominant in these four metrics overall. This is because more images can make this kind of vessel segmentation model, learn the characteristics of blood vessels more fully, and enhance its sensitivity to the information of blood vessels.

Moreover, the two models also performed well on the CHASEDB dataset, as shown in **Table 4**. The performance of the Impro model is still outstanding, and most of its segmentation evaluation metrics are beyond the Base model under different *CK* modes. The optimal accuracy, sensitivity, specificity, and AUC values achieved by the Impro model are 96.96, 83.44, 98.05, and 97.85%, respectively, which are inferior to those in (24, 27, 28). The reason is that the methods in (24) and (27) both utilized the data augmentation strategy that makes the deep learning framework obtain a more powerful ability to capture the vessel information, and the adversarial learning strategy promotes the scheme (28) to gain strong data distribution learning ability in the vessel segmentation task. Nevertheless, the above accuracy, sensitivity, and specificity values achieved by the Impro model are generally higher than those acquired by the other listed methods, and even the lowest sensitivity value (i.e., 79.08%) obtained from the Base model shows its advantages, which demonstrates the competitiveness of the two models to a certain extent.

Comparison of the Domain Adaptability of Single Model

The performance of the DL model in the intra- and cross-domain tasks is the key reference and an important basis to observe its generalization level. Therefore, the intra- and cross-domain vessel segmentation based on a single model (i.e., the baseline model or upgraded model) is performed in this part, and the results are shown in **Figures 10**, **11**. Here, we give an example to illustrate the experimental setup. When experiments

TABLE 2 | Performance comparison on DRIVE.

Methods		Acc (%)		Spe (%)		Sen (%)		AUC (%)	
		Base	Impro	Base	Impro	Base	Impro	Base	Impro
Proposed	5-way 3-shot	94.52	94.46	96.08	95.56	77.48	82.45	96.25	97.07
	4-way 3-shot	95.82	96.61	97.91	98.28	73.97	79.21	95.98	97.29
	3-way 3-shot	95.82	**96.64**	97.88	**98.29**	74.35	79.47	96.62	97.19
	3-way 4-shot	95.77	96.45	97.87	97.70	73.90	83.35	96.53	97.79
	3-way 5-shot	95.66	96.34	97.50	97.43	76.55	**84.95**	96.50	**98.03**
Machine learning	Fraz et al. (14)	94.80		98.07		74.06		97.47	
	Krishna et al. (15)	96.19		**98.36**		74.35		-	
	Aslani and Sarnel (16)	95.13		98.01		75.45		96.82	
	Orlando et al. (17)	-		96.84		78.97		95.07	
	Li et al. (18)	95.27		98.16		75.69		97.38	
	Srinidhi et al. (19)	95.89		96.67		**86.44**		97.01	
	Liskowski and Krawiec (22)	95.35		98.07		78.11		97.90	
	Mo and Zhang (23)	95.21		97.80		77.79		97.82	
	Jiang et al. (24)	96.24		98.25		75.40		98.10	
	Zhou et al. (25)	94.69		96.74		80.78		-	
	Yan et al. (26)	95.42		98.18		76.53		97.52	
	Filipe et al. (27)	95.76		98.04		80.39		98.21	
	Park et al. (28)	**97.06**		**98.36**		83.46		**98.68**	

The bold values indicate the maximum value of the corresponding metric in the manuscript.

are conducted on the STARE dataset, the Base-STARE or Impro-STARE represents an intra-domain experiment, which means that the training set of STARE is used to train the model, and the STARE testing set is used to test the model. On the premise of STARE dataset, the Base-DRIVE or Impro-DRIVE denotes a cross-domain experiment, which represents training the model with a training set from the DRIVE dataset and testing the model based on the STARE testing set.

As shown in **Figure 10**, the baseline model or the upgraded model generally performs better in the intra-domain task, especially the sensitivity and f1-score metrics. As for the cross-domain scene, the above metric values of the two models are inferior to those in the intra-domain scene. However, as for the other two metrics, it can be found that the performance of the two models in the cross-domain task is close to or even higher than that in the intra-domain task. In addition, it can be seen from the AUC metric in **Figure 11** that the retinal vessel segmentation of the two models in the intra-domain scene is superior to that in the cross-domain task in most cases. However, in some instances, the cross-domain segmentation results of the Impro model are even better. For example, when the upgraded model trained based on the STARE dataset was tested on the DRIVE dataset, the AUC values of 97.27, 97.76, and 97.39% were obtained under the conditions of 5-way 3-shot, 4-way 3-shot, and 3-way 3-shot modes respectively, which were 0.2, 0.47, and 0.2% more than the intra-domain values of the corresponding upgraded model. Yet, with the same *CK* modes, the baseline model performs slightly worse in AUC value. The above observations show that the adaptability of a single model in intra- and cross-domain tasks is different, and overall, the intra-domain segmentation level of the model is superior to its cross-domain performance. Nevertheless, in some cases, the good results of the model in cross-domain task also suggest its potential application value in this scenario.

Comparison of the Domain Adaptability Between the Single Model and the Integrated Framework

The above experiments tested the performance of the baseline and the upgraded models on the public retinal image datasets, which not only showed the effectiveness of the two models in the fundus vessel segmentation task, but also implied their potential competitiveness compared with the existing methods. Of note, whether it is the baseline model or the upgraded model, their performance in the intra-domain task is relatively better than that in the cross-domain task to a certain extent. However, we are

TABLE 3 | Performance comparison on STARE.

Methods		Acc (%)		Spe (%)		Sen (%)		AUC (%)	
		Base	Impro	Base	Impro	Base	Impro	Base	Impro
Proposed	5-way 3-shot	94.59	95.63	96.71	97.39	77.70	81.53	95.63	96.92
	4-way 3-shot	94.46	**95.92**	96.50	98.16	78.18	78.04	95.91	97.29
	3-way 3-shot	94.89	95.81	97.06	97.73	77.56	80.47	96.06	97.16
	3-way 4-shot	94.88	95.77	97.33	97.69	75.39	80.46	95.97	97.25
	3-way 5-shot	94.63	95.65	96.64	97.19	78.51	**83.37**	96.19	**97.53**
Machine learning	Fraz et al. (14)	95.34		97.63		75.48		97.68	
	Aslani and Sarnel (16)	96.05		98.37		75.56		97.89	
	Orlando et al. (17)	-		97.38		76.80		-	
	Li et al. (18)	96.28		98.44		77.26		98.79	
	Srinidhi et al. (19)	95.02		97.46		83.25		96.70	
	Liskowski and Krawiec (22)	97.29		98.62		**85.54**		**99.28**	
	Mo and Zhang (23)	96.74		98.44		81.47		98.85	
	Jiang et al. (24)	97.34		98.46		83.52		99.00	
	Zhou et al. (25)	95.85		97.61		80.65		-	
	Yan et al. (26)	96.12		98.46		75.81		98.01	
	Filipe et al. (27)	96.94		98.58		83.15		99.05	
	Park et al. (28)	**98.76**		**99.38**		83.24		98.73	

The bold values indicate the maximum value of the corresponding metric in the manuscript.

TABLE 4 | Performance comparison on CHASEDB.

Methods		Acc (%)		Spe (%)		Sen (%)		AUC (%)	
		Base	Impro	Base	Impro	Base	Impro	Base	Impro
Proposed	5-way 3-shot	96.76	96.91	97.83	97.92	80.82	81.86	96.64	97.10
	4-way 3-shot	96.85	96.96	97.97	97.99	80.14	81.60	96.92	97.12
	3-way 3-shot	96.85	96.91	98.05	97.87	79.08	82.60	97.48	**97.85**
	3-way 4-shot	96.90	**96.96**	**98.05**	98.02	79.63	81.18	96.93	97.07
	3-way 5-shot	96.70	96.82	97.70	97.72	81.83	**83.44**	97.12	97.24
Machine learning	Fraz et al. (14)	94.69		97.11		72.24		97.12	
	Orlando et al. (17)	-		97.12		72.77		95.24	
	Li et al. (18)	95.81		97.93		75.07		97.16	
	Mo and Zhang (23)	95.99		98.16		76.61		98.12	
	Jiang et al. (24)	96.68		97.45		**86.40**		98.10	
	Zhou et al. (25)	95.20		97.51		75.53		-	
	Yan et al. (26)	96.10		98.09		76.33		97.81	
	Filipe et al. (27)	96.53		**98.64**		77.79		98.55	
	Park et al. (28)	**97.36**		-		-		**98.59**	

The bold values indicate the maximum value of the corresponding metric in the manuscript.

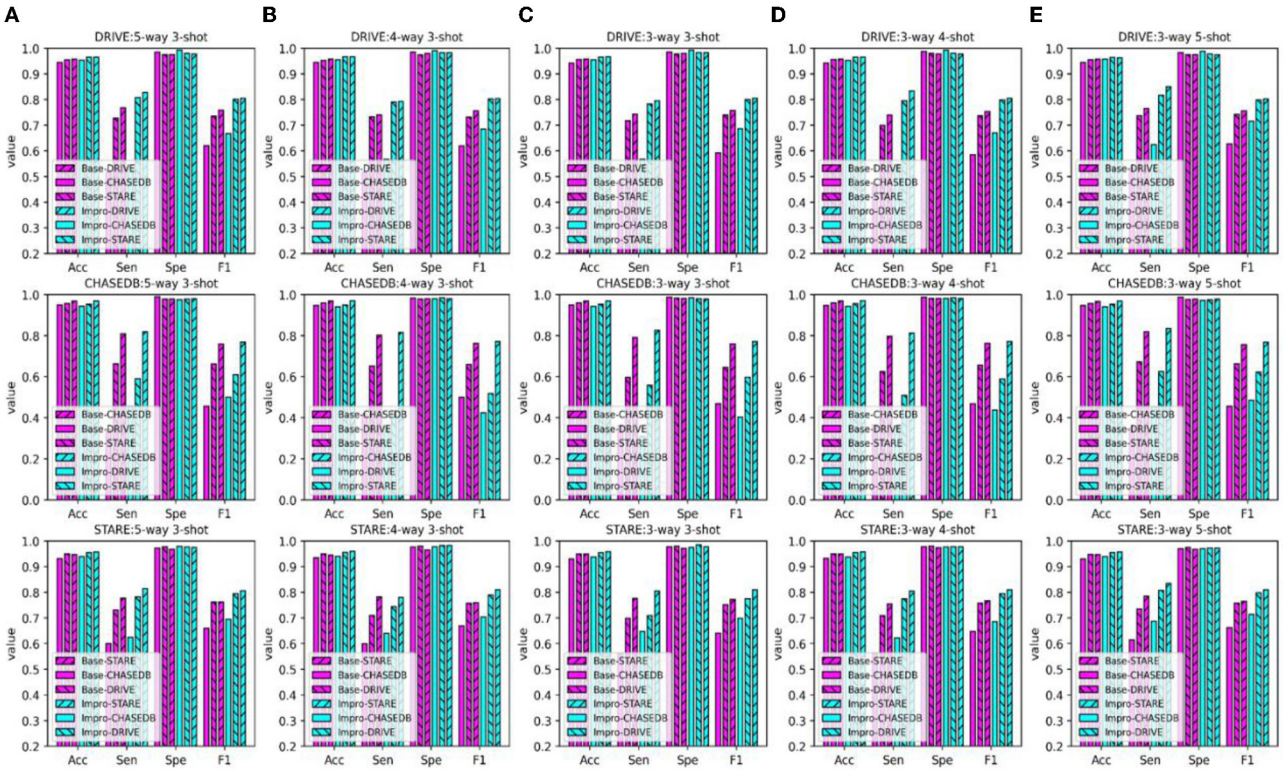

FIGURE 10 | Comparison of the domain adaptability based on the Acc, Sen, Spe, and F1: **(A)** 5-way 3-shot; **(B)** 4-way 3-shot; **(C)** 3-way 3-shot; **(D)** 3-way 4-shot; and **(E)** 3-way 5-shot.

also pleased to observe that the cross-domain adaptability of the upgraded model is, sometimes, even more prominent than that of the intra-domain model.

In order to improve the cross-domain adaptability of the two models, we proposed an integrated framework (as shown in **Figure 4**) and verified it on the ophthalmic clinical CSC dataset. The CSC is a common fundus disease caused by the impairment of retinal pigment epithelium function due to the increased choroidal permeability, characterized by neurosensory retinal detachment (NRD), with or without pigment epithelium detachment (PED) (45–47), or detachment area (DA), and leakage point (LP). As shown in **Figure 12**, the NRD and PED can be clearly displayed on the optical coherence tomography (OCT) B-scan image and DA, and the LP can also be drawn on a fundus color image by an ophthalmologist according to the corresponding angiography image. In recent years, either the traditional laser photocoagulation or the micro-pulse laser photocoagulation has become one of the important means of CSC therapy, which plays an effective role in inhibiting the development of CSC. However, the location of retinal vessels is of great importance in the whole process of the above CSC laser surgery, which does not only help the doctors mark the location of the LP on fundus color image, but also avoids the damage of laser spot to vessel tissue and the low efficiency of surgery caused by the absorption of laser energy by retinal vessels.

Therefore, this section applies the proposed single model (i.e., the baseline model and upgraded model) and the integrated framework to the ophthalmic clinical CSC dataset, which is not only a comparison of their performance, but also a practical application test. First, the symbols in the following figures and tables are briefly explained here. The "Base-DRIVE," "Base-CHASEDB," and "Base-STARE" denote the baseline model trained with DRIVE, CHASEDB, and STARE datasets, respectively. the "Base-UNION" represents the integration of the above three models, which means that N_1 is 3. The naming rules for the upgraded models are consistent with the baseline models.

It can be seen from **Figure 13** that both the baseline and the upgraded models can better adapt to the CSC dataset, and more than 90% of the AUC values are obtained. In most cases, the AUC metric of the Base-UNION is better than the Base-DRIVE and the Base-CHASEDB; the maximum values of which are 96.13 and 97% under the conditions of baseline and upgrade schemes, respectively. This preliminarily shows the effectiveness and the feasibility of the integrated idea in improving the cross-domain adaptability of a single model. However, we have to admit that the AUC values of the Base-STARE and the Impro-STARE are slightly better than the corresponding integrated models, the maximum values of which are 96.5 and 97.18%, respectively. The above observations, on the one hand, show the correctness of the integration scheme, and on the other hand, also convey that the performance of this scheme has room for

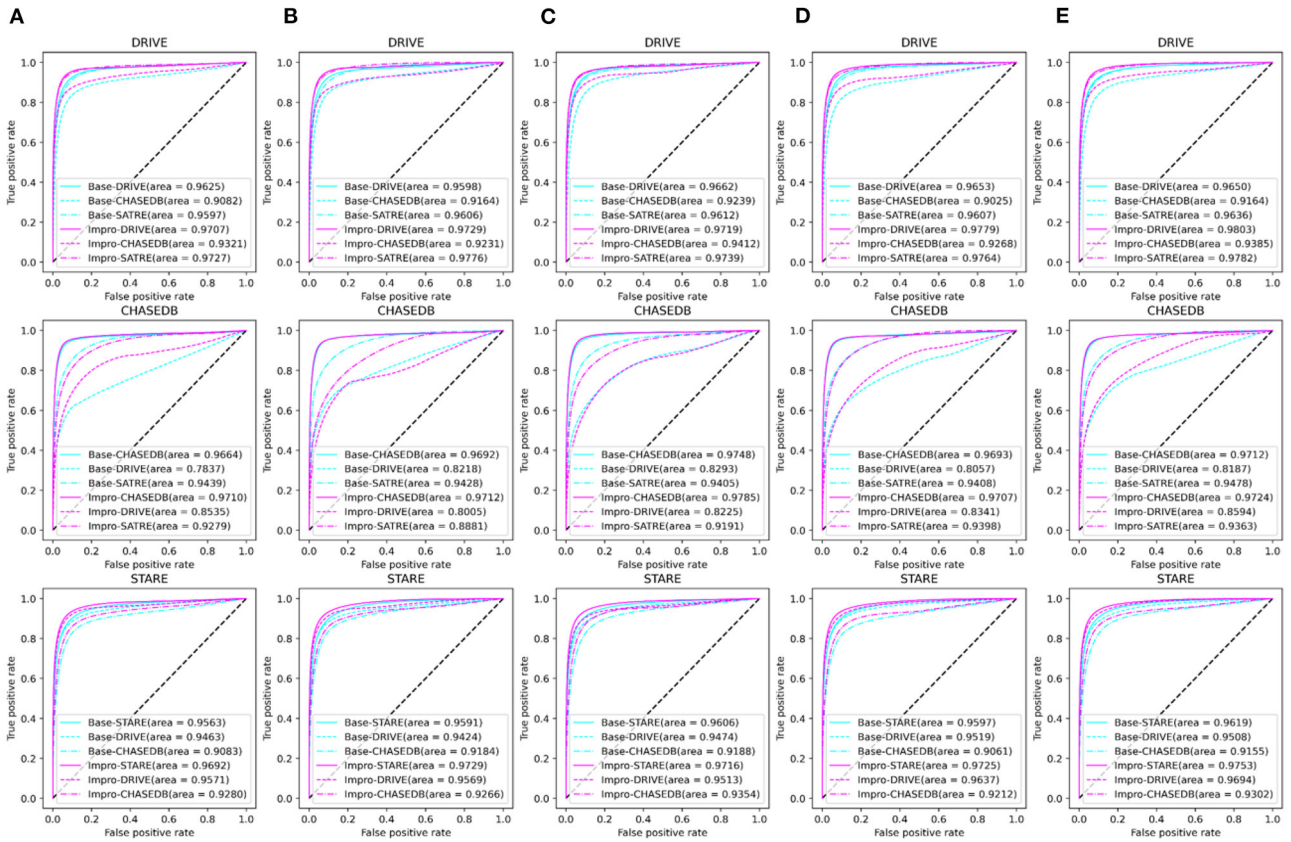

FIGURE 11 | Comparison of the domain adaptability based on the AUC: **(A)** 5-way 3-shot; **(B)** 4-way 3-shot; **(C)** 3-way 3-shot; **(D)** 3-way 4-shot; and **(E)** 3-way 5-shot.

further improvement. At the same time, it can also be found that whether the integration framework is based on the single upgraded model or the single upgraded model itself, their AUC values on the CSC dataset is better than their corresponding baseline model in most cases, which is basically consistent with the performance of the upgraded model and the baseline model on the public datasets. The above analysis not only confirms further the necessity of our upgraded operation, but also hints the potential application ability of the model based on the few-shot learning paradigm in clinical dataset. In addition, **Table 5** clearly shows the values of the other four metrics of the single model and the integrated framework on the CSC dataset. For example, the CSC-U (U represents Union, that is, the integrated framework) represents the application of the integrated framework on the CSC dataset, and CSC-D represents the application of Base-DRIVE or Impro-DRIVE on the CSC dataset. Under different *CK* modes, the ACC and F1 values of the integrated framework are almost better than those of the corresponding single model, especially the F1 value. Although the integrated framework is slightly inferior in the Spe and Sen metrics, it still has the upper hand overall. It can be found that both the Base-CHASEDB and the Impro-CHASEDB achieved the maximum Spe value, but performed poorly in the Sen metric, which implies that they will

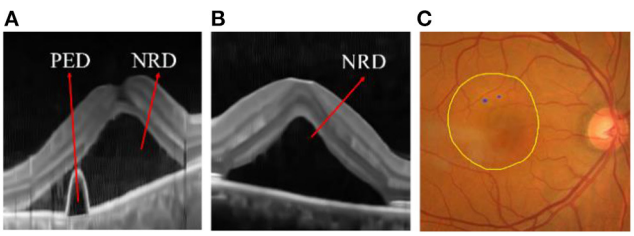

FIGURE 12 | (A) Pigment epithelium detachment (PED) and neurosensory retinal detachment NRD; **(B)** NRD **(C)** detachment area (DA) (the internal area marked by yellow line) and leakage point (LP) (the blue point).

introduce more false positives (refer to **Figure 14** for details) in vessel segmentation task on the CSC dataset. The above implies that a simple model integration can appropriately enhance the poor cross-domain adaptability of a single model, but the integrated principle of the minority obeying the majority needs to be improved.

Figure 14 shows the fusion results of the segmented retinal vessels and the fundus color images, in which the black part represents the position information of vessels,

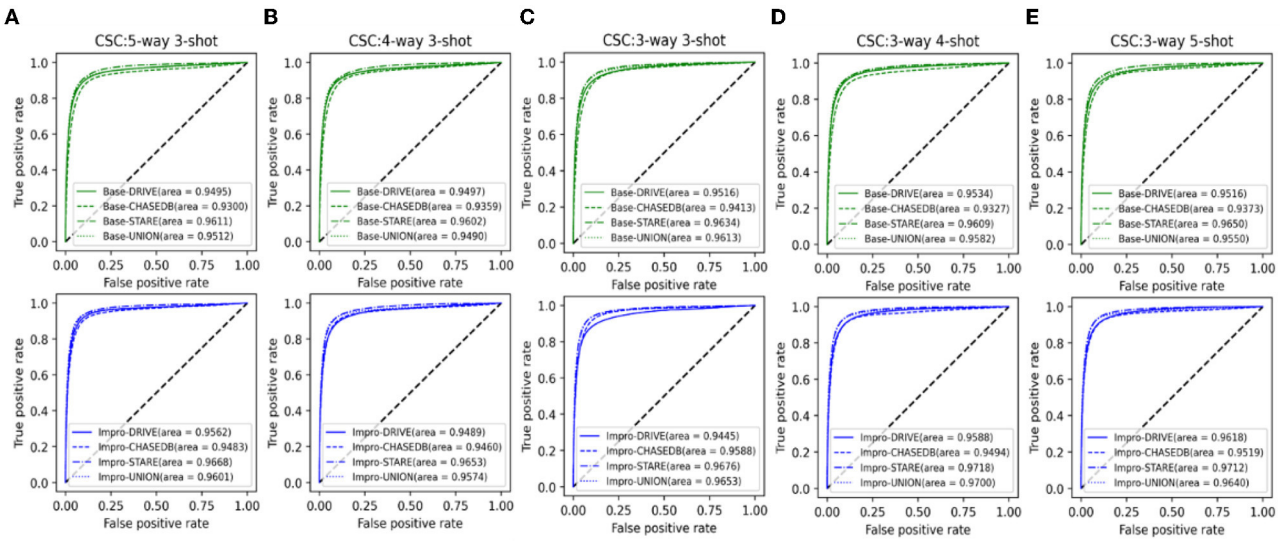

FIGURE 13 | Comparison of the domain adaptability based on the AUC: **(A)** 5-way 3-shot; **(B)** 4-way 3-shot; **(C)** 3-way 3-shot; **(D)** 3-way 4-shot; and **(E)** 3-way 5-shot.

TABLE 5 | Performance comparison of single model and integrated framework on CSC dataset.

Methods		Acc (%)		Spe (%)		Sen (%)		F1 (%)	
		Base	Impro	Base	Impro	Base	Impro	Base	Impro
5-way 3-shot	CSC-U	**94.90**	**95.09**	96.32	96.08	79.40	84.25	**72.30**	**74.20**
	CSC-D	94.52	94.46	96.08	95.56	77.48	82.45	70.33	71.38
	CSC-S	93.93	94.19	94.91	94.83	**83.23**	**87.21**	69.68	71.55
	CSC-C	94.06	94.82	**96.57**	**96.96**	66.63	71.45	65.30	69.83
4-way 3-shot	CSC-U	**95.01**	**95.32**	96.47	96.58	79.07	81.53	**72.65**	**74.48**
	CSC-D	94.74	94.57	96.39	96.09	76.67	77.98	70.96	70.67
	CSC-S	93.83	94.84	94.79	95.90	**83.31**	**83.30**	69.35	73.03
	CSC-C	94.26	94.87	**96.77**	**96.94**	66.90	72.28	66.17	70.28
3-way 3-shot	CSC-U	**95.07**	**95.19**	96.62	96.34	78.09	82.63	**72.64**	**74.24**
	CSC-D	94.60	94.49	96.39	96.07	74.98	77.23	69.94	70.16
	CSC-S	94.29	94.54	95.37	95.31	**82.47**	**86.06**	70.78	72.53
	CSC-C	94.12	94.77	**96.91**	**96.67**	63.61	73.93	64.45	70.31
3-way 4-shot	CSC-U	**95.18**	**95.06**	96.76	96.10	77.82	83.72	**73.01**	**73.97**
	CSC-D	94.72	94.27	96.43	95.49	76.05	80.84	70.73	70.27
	CSC-S	94.43	94.43	95.66	95.17	**81.02**	**86.35**	70.93	72.22
	CSC-C	94.23	94.83	**97.03**	**97.05**	63.53	70.56	64.85	69.60
3-way 5-shot	CSC-U	**94.85**	94.67	96.17	95.45	80.33	86.19	**72.33**	**73.06**
	CSC-D	94.36	93.93	95.93	94.86	77.21	83.68	69.66	69.79
	CSC-S	93.92	93.77	94.79	94.23	**84.40**	**88.78**	69.95	70.50
	CSC-C	94.07	**94.78**	**96.44**	**96.56**	68.16	75.35	65.84	70.77

The bold values indicate the maximum value of the corresponding metric in the manuscript.

the inner area marked by yellow line represents DA, and the blue point is LP. After a careful comparison, it can be found that the integrated framework can segment more retinal vessels than the single model driven by DRIVE or CHASEDB dataset. Although the Base-CHASEDB and the Impro-CHASEDB have advantages in Spe metric, it leads to more false positives (Refer to **Table 5**) in the actual segmentation results. Moreover, the Base-STARE or the Impro-STARE is generally dominant in the task of vessel segmentation. However, it cannot be ignored that they will bring more discrete vessel segments, which may disturb the LP localization process.

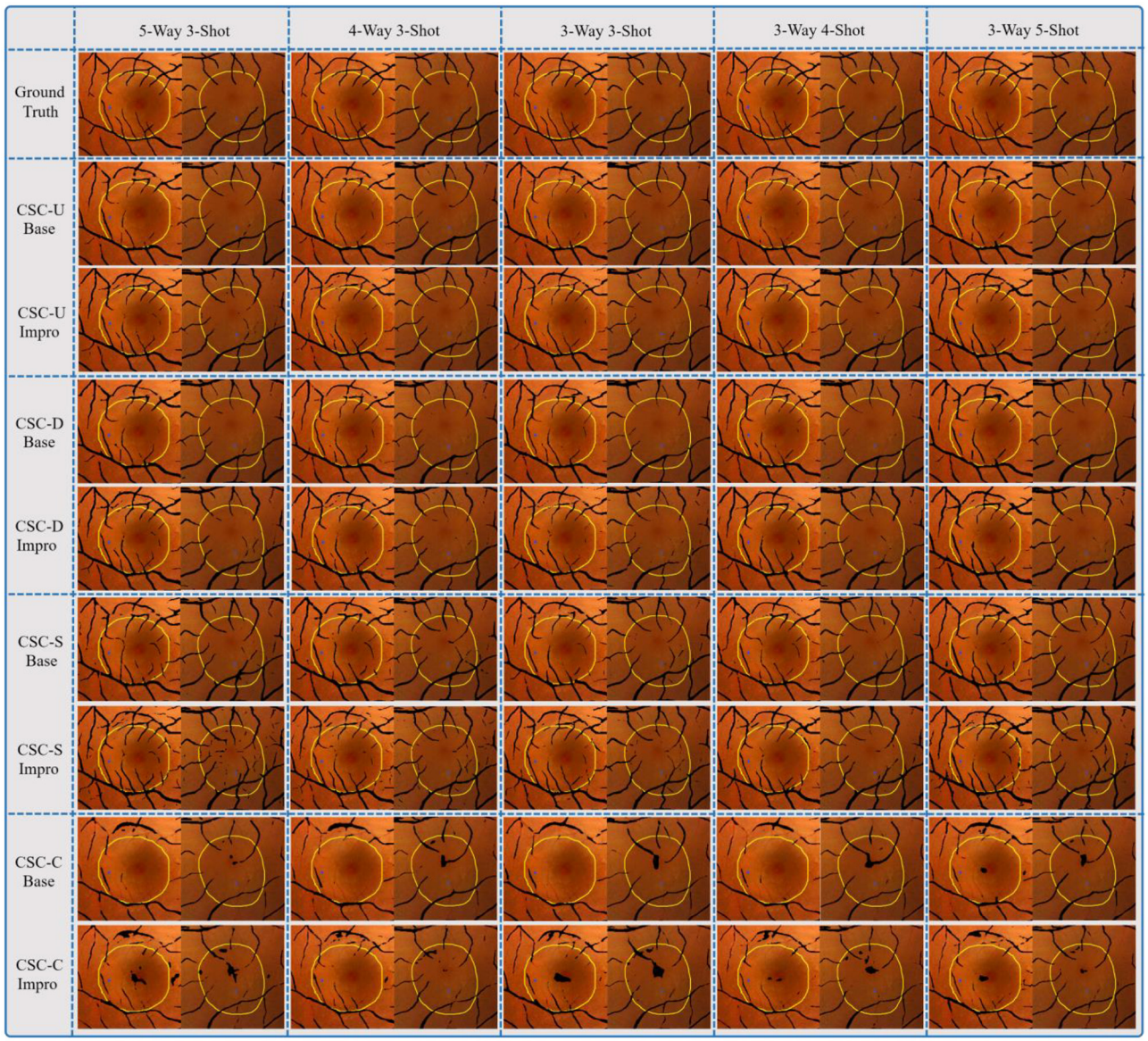

FIGURE 14 | Comparison of the single model and the integrated framework on practical application.

In general, through the above results and discussions, it can be found that the performance of both the Base and Impro models is consistent in the training, validation, and testing processes, which indicates the stability of the two models. In addition, we can see that although the baseline model can adapt to the vessel segmentation task well, it is weaker than the Impro model in terms of adhesion and continuity in wide vessel segmentation as a whole, which also emphasizes the necessity of an upgraded operation. Moreover, compared with some typical machine-learning-based methods listed, the Base and Impro models show superiorities in most cases, but we still need to catch up with the optimal scheme. Furthermore, a single model performs well in the intra- and cross-domain tasks, and overall, either the baseline model or the upgrade model is better in intra-domain tasks. The proposed integrated framework enhanced the vessel segmentation ability of a single model in the cross-domain task to a certain extent, but the integrated idea based on the minority obeying majority needs to be improved in the future to promote the superiority of the integrated framework.

CONCLUSION AND FUTURE WORK

In this paper, a novel few-shot learning-based method for retinal vessel segmentation is proposed. Firstly, from the perspective

of a problem scenario migration, the vessel segmentation scene is skillfully transformed into the few-shot learning task, which lays a foundation for vessel segmentation under the condition of few samples. Then, on the basis of the above, two models based on the few-shot learning paradigm are established. In the first step, we build a baseline segmentation model by improving the existing few-shot learning framework, which adapts to the vessel segmentation task well. In the second step, to improve the segmentation performance of the baseline model, we make further efforts from the following three aspects: (1) A multi-scale class prototype extraction technique is designed to obtain more sufficient vessel features for better utilizing the information from the support images; (2) The multi-scale vessel features of the query images inferred by the support image class prototype information are gradually fused to provide more effective guidance for the retinal vessel segmentation task; and (3) A multi-scale attention module is raised to promote the consideration of the global information in the upgraded model to assist the vessel localization. Moreover, the integrated framework is conceived to appropriately alleviate the low performance of a single model in the cross-domain vessel segmentation scene. Extensive experiments on three public retinal image datasets demonstrate that the few-shot learning-based method can effectively carry out the intra-domain vessel segmentation task with a few annotation samples and possess a potential cross-domain application capability. Practical application experiments on our private CSC dataset not only confirms the effectiveness of the integrated framework to improve the cross-domain adaptability of a single model, but also further indicates the clinical application value of the few-shot learning-based method in assisting the CSC laser surgery for retinal vessel localization. However, although we broaden the research ideas for the vessel segmentation in the case of few samples, the limitations of this method cannot be ignored. In the future, we will focus on enhancing the segmentation ability of the proposed models on the small vessels and alleviate the problem of a discontinuous segmentation issue, and try to explore the vessel segmentation scheme based on the few-shot learning paradigm without any annotations.

DATA AVAILABILITY STATEMENT

The public fundus datasets (i.e., DRIVE, STARE, and CHASEDB datasets) for this study can be found in the corresponding references. The private clinical fundus CSC dataset used and analyzed in our research are available from the corresponding author upon request.

ETHICS STATEMENT

The studies involving human participants were reviewed and approved by Ethics Committee of the Affiliated Eye Hospital of Nanjing Medical University. The patients/participants provided their written informed consent to participate in this study.

AUTHOR CONTRIBUTIONS

JX developed the presented method and drafted the manuscript. JS and WY supervised and reviewed the whole project. CW assisted in improving the manuscript. QJ and ZY provided suggestions for the clinical application of the study and helped to analyze the experimental results. All authors contributed to the article and approved the submitted version.

FUNDING

This work was financially supported by Fundamental Research Funds for the Central Universities (No. NP2020420), China Postdoctoral Science Foundation Funded Project (No. 2019M661832), and the Nanjing Enterprise Expert Team Project.

ACKNOWLEDGMENTS

We would thank the authors of DRIVE, STARE, and CHASEDB datasets for making their databases publicly available and thank the Affiliated Eye Hospital of Nanjing Medical University for providing the clinical fundus CSC dataset for this scientific research. We also appreciate it very much for editors and reviewers with your attention to our paper.

REFERENCES

1. Nguyen PT, Dang V, Vo KD, Phan PT, Yang E, Joshi GP. An optimal deep learning based computer-aided diagnosis system for diabetic retinopathy. *Comput Mater Continua*. (2021) 66:2815–30. doi: 10.32604/cmc.2021.012315
2. Kushol R, Kabir MH, Abdullah-Al-Wadud M, Islam MS. Retinal blood vessel segmentation from fundus image using an efficient multiscale directional representation technique. *Bendlets Math Biosci Eng.* (2020) 17:7751–71. doi: 10.3934/mbe.2020394
3. Rodrigues EO, Conci A, Liatsis P. ELEMENT: multi-modal retinal vessel segmentation based on a coupled region growing and machine learning approach. *IEEE J Biomed Health Inform.* (2020) 24:3507–19. doi: 10.1109/JBHI.2020.2999257
4. Meng X, Yin Y, Yang G, Han Z, Yan X. A framework for retinal vasculature segmentation based on matched filters. *BioMed Eng OnLine.* (2016) 15:120. doi: 10.1186/s12938-015-0089-2
5. Aswini S, Suresh A, Priya S, Krishna BV. Retinal vessel segmentation using morphological top hat approach on diabetic retinopathy images. In: *The Fourth International Conference on Advances in Electrical, Electronics, Information, Communication and Bio-Informatics*, Chennai (2018). p. 1–5.
6. Zhao J, Yang J, Ai D, Song H, Jiang Y, Huang Y, et al. Automatic retinal vessel segmentation using multi-scale superpixel chain tracking. *Digital Signal Proc.* (2018) 81:26–42. doi: 10.1016/j.dsp.2018.06.006
7. Xu M, Qi S, Yue Y, Teng Y, Xu L, Yao Y, Qian W. Segmentation of lung parenchyma in CT images using CNN trained with the clustering algorithm generated dataset. *BioMed Eng OnLine.* (2019) 18:2. doi: 10.1186/s12938-018-0619-9
8. Tian S, Wang M, Yuan F, Dai N, Sun Y, Xie W, Qin J. Efficient computer-aided design of dental inlay restoration: a deep adversarial framework. *IEEE Trans Med Imag.* (2021) 40:2415–27. doi: 10.1109/TMI.2021.3077334

9. Zheng Y, Ai D, Mu J, Cong W, Wang X, Zhao H, et al. Automatic liver segmentation based on appearance and context information. *BioMed Eng OnLine.* (2017) 16:1–12. doi: 10.1186/s12938-016-0296-5
10. Mookiah MR, Hogg S, MacGillivray TJ, Prathiba V, Pradeepa R, Mohan V, et al. A review of machine learning methods for retinal blood vessel segmentation and artery/vein classification. *Med Image Anal.* (2021) 68:101905. doi: 10.1016/j.media.2020.101905
11. Srinidhi CL, Aparna P, Rajan J. Recent advancements in retinal vessel segmentation. *J Med Syst*. (2017) 41:70. doi: 10.1007/s10916-017-0719-2
12. Wiharto W, Suryani E. The analysis effect of cluster numbers on fuzzy C-means algorithm for blood vessel segmentation of retinal fundus image. In: *The International Conference on Information and Communications Technology*. Yogyakarta (2019). p. 106–10.
13. Ali A, Zaki WM, Hussain A. Blood vessel segmentation from color retinal images using K-means clustering and 2D gabor wavelet. In: *International Conference on Applied Physics, System Science and Computers*. Dubrovnik (2018).
14. Fraz MM, Remagnino P, Hoppe A, Uyyanonvara B, Rudnicka AR, Owen CG, et al. An ensemble classification-based approach applied to retinal blood vessel segmentation. *IEEE Trans Biomed Eng.* (2012) 59:2538–48. doi: 10.1109/TBME.2012.2205687
15. Krishna BV, Gnanasekaran T. Retinal vessel extraction framework using modified adaboost extreme learning machine. *Comput Mater Continua.* (2019) 60:855–69. doi: 10.32604/cmc.2019.07585
16. Aslani S, Sarnel H. A new supervised retinal vessel segmentation method based on robust hybrid features. *Biomed Signal Process Control.* (2016) 30:1–12. doi: 10.1016/j.bspc.2016.05.006
17. Orlando JI, Prokofyeva E, Blaschko MB. A discriminatively trained fully connected conditional random field model for blood vessel segmentation in fundus images. *IEEE Trans Biomed Eng.* (2017) 64:16–27. doi: 10.1109/TBME.2016.2535311
18. Li Q, Feng B, Xie L, Liang P, Zhang H, Wang T. A cross-modality learning approach for vessel segmentation in retinal images. *IEEE Trans Med Imag.* (2016) 35:109–18. doi: 10.1109/TMI.2015.2457891
19. Srinidhi CL, Aparna P, Rajan J. A visual attention guided unsupervised feature learning for robust vessel delineation in retinal images. *Biomed Signal Proc Control.* (2018) 44:110–26. doi: 10.1016/j.bspc.2018.04.016
20. Jebaseeli TJ, Durai CA, Peter JD. Retinal blood vessel segmentation from diabetic retinopathy images using tandem PCNN model and deep learning based SVM. *Optik*. (2019) 199:163328. doi: 10.1016/j.ijleo.2019.163328
21. Kaur J, Mittal D. A generalized method for the detection of vascular structure in pathological retinal images. *Biocyber Biomed Eng.* (2017) 37:184–200. doi: 10.1016/j.bbe.2016.09.002
22. Liskowski P, Krawiec K. Segmenting retinal blood vessels with deep neural networks. *IEEE Trans Med Imag.* (2016) 35:2369–80. doi: 10.1109/TMI.2016.2546227
23. Mo J, Zhang L. Multi-level deep supervised networks for retinal vessel segmentation. *Int J Comp Assisted Radiol Surg.* (2017) 12:2181–93. doi: 10.1007/s11548-017-1619-0
24. Jiang Z, Zhang H, Wang Y, Ko SB. Retinal blood vessel segmentation using fully convolutional network with transfer learning. *Comput Med Imaging Graph.* (2018) 68:1–15. doi: 10.1016/j.compmedimag.2018.04.005
25. Zhou L, Yu Q, Xu X, Gu Y, Yang J. Improving dense conditional random field for retinal vessel segmentation by discriminative feature learning and thin-vessel enhancement. *Comp Methods Programs Biomed.* (2017) 148:13–25. doi: 10.1016/j.cmpb.2017.06.016
26. Yan Z, Yang X, Cheng KT. Joint segment-level and pixel-wise losses for deep learning based retinal vessel segmentation. *IEEE Trans Biomed Eng.* (2018) 65:1912–23. doi: 10.1109/TBME.2018.2828137
27. Filipe MO, Rafael MP, Alberto BS. Retinal vessel segmentation based on fully convolutional neural networks. *Expert Syst Appl.* (2018) 112:229–42. doi: 10.1016/j.eswa.2018.06.034
28. Park KB, Choi SH, Lee JY. M-GAN retinal blood vessel segmentation by balancing losses through stacked deep fully convolutional networks. *IEEE Access.* (2020) 8:146308–22. doi: 10.1109/ACCESS.2020.3015108
29. Meyer MI, Costa P, Galdran A, Mendonça AM, Campilho A. A deep neural network for vessel segmentation of scanning laser ophthalmoscopy images. *Int Conf Image Anal Recogn.* (2017) 10317:507–15. doi: 10.1007/978-3-319-59876-5_56
30. Huang H, Zhang J, Zhang J, Xu J, Wu Q. Low-rank pairwise alignment bilinear network for few-shot fine-grained image classification. *IEEE Trans Multimed.* (2021) 23:1666–80. doi: 10.1109/TMM.2020.3001510
31. Sun X, Xv H, Dong J, Zhou H, Chen C, Li Q. Few-shot learning for domain-specific fine-grained image classification. *IEEE Trans Indust Electr*. (2021) 68:3588–98. doi: 10.1109/TIE.2020.2977553
32. Quellec G, Lamard M, Conze PH, Massin P, Cochener B. Automatic detection of rare pathologies in fundus photographs using few-shot learning. *Med Image Anal.* (2020) 61:101660. doi: 10.1016/j.media.2020.101660
33. Medela A, Picon A, Saratxaga CL, Belaret O, Cabezón V, Cicchi R, et al. Few shot learning in histopathological images: reducing the need of labeled data on biological datasets. In *IEEE 16th International Symposium on Biomedical Imaging*. Venice (2019). p. 1860–4.
34. Zhang C, Lin G, Liu F, Yao R, Shen C. CANet: class-agnostic segmentation networks with iterative refinement and attentive few-shot learning. In: *IEEE/CVF Conference on Computer Vision and Pattern Recognition*. Long Beach, CA (2019). p. 5212–21.
35. Li R, Liu H, Zhu Y, Bai Z. Arnet: attention-based refinement network for few-shot semantic segmentation. In: *IEEE International Conference on Acoustics, Speech and Signal Processing*. Barcelona (2020). p. 2238–42.
36. Feyjie AR, Azad R, Pedersoli M, Kauffman C, Ayed IB, Dolz J. Semi-supervised few-shot learning for medical image segmentation. *arXiv* preprint (2020).
37. Cui H, Wei D, Ma K, Gu S, Zheng Y. A unified framework for generalized low-shot medical image segmentation with scarce data. *IEEE Trans Med Imag.* (2020) 40:2656–71. doi: 10.1109/TMI.2020.3045775
38. Ouyang C, Biffi C, Chen C, Kart T, Qiu H, Rueckert D. Self-supervision with superpixels: training few-shot medical image segmentation without annotation. In: *European Conference on Computer Vision*. Glasgow (2020). p. 762–80.
39. Ronneberger O, Fischer P, Brox T. U-Net: convolutional networks for biomedical image segmentation. In: *Proc. International Conference on Medical Image Computing and Computer-Assisted Intervention*. Munich (2015). p. 234–41.
40. Simonyan K, Zisserman A. Very deep convolutional networks for large-scale image recognition. In: *International Conference on Learning Representations*. San Diego, CA (2015). p. 769–84.
41. Wang X, Girshick R, Gupta A, He K. Non-local neural networks. In: *2018 IEEE/CVF Conference on Computer Vision and Pattern Recognition*. Salt Lake (2018).
42. Owen CG, Rudnicka AR, Mullen R, Barman SA, Monekosso D, Whincup PH, et al. Measuring retinal vessel tortuosity in 10-year-old children: validation of the computer-assisted image analysis of the retina (CAIAR) program. *Investig Ophthal Visual Sci.* (2009) 50:2004–10. doi: 10.1167/iovs.08-3018
43. Staal J, Abramoff MD, Niemeijer M, Viergever MA, Ginneken B. Ridge-based vessel segmentation in color images of the retina. *IEEE Trans Med Imaging.* (2004) 23:501–9. doi: 10.1109/TMI.2004.825627
44. Hoover AD, Kouznetsova V, Goldbaum M. Locating blood vessels in retinal images by piecewise threshold probing of a matched filter response. *IEEE Trans Med Imag.* (2000) 19:203–10. doi: 10.1109/42.845178

45. Yang L, Jonas JB, Wei W. Optical coherence tomography assisted enhanced depth imaging of central serous chorioretinopathy. *Invest Ophthalmol Vis.* (2013) 7:4659–65. doi: 10.1167/iovs.12-10991
46. Yu J, Jiang C, Xu G. Study of subretinal exudation and consequent changes in acute central serous chorioretinopathy by optical coherence tomography. *Am J Ophthalmol.* (2014) 158:752–6. doi: 10.1016/j.ajo.2014.06.015
47. Daruich A, Matet A, Dirani A, Bousquet E, Zhao M, Farman N, et al. Central serous chorioretinopathy: recent findings and new physiopathology hypothesis. *Prog Retinal Eye Res.* (2015) 48:82–118. doi: 10.1016/j.preteyeres.2015.05.003

Conflict of Interest: The authors declare that the research was conducted in the absence of any commercial or financial relationships that could be construed as a potential conflict of interest.

frontiers in Medicine

ORIGINAL RESEARCH
published: 11 March 2022
doi: 10.3389/fmed.2022.833487

Validation of the Portable Next-Generation VECTRA H2 3D Imaging System for Periocular Anthropometry

Wanlin Fan[1], Yongwei Guo[2], Xiaoyi Hou[1], Jinhua Liu[1], Senmao Li[1], Sitong Ju[1], Philomena Alice Wawer Matos[1], Michael Simon[1], Alexander C. Rokohl[1†] and Ludwig M. Heindl[1,3*†]*

[1] Department of Ophthalmology, Faculty of Medicine and University Hospital Cologne, University of Cologne, Cologne, Germany, [2] Eye Center, Second Affiliated Hospital, Zhejiang University School of Medicine, Hangzhou, China, [3] Center for Integrated Oncology (CIO), Aachen-Bonn-Cologne-Duesseldorf, Cologne, Germany

OPEN ACCESS

Edited by:
Peng Xiao,
Sun Yat-sen University, China

Reviewed by:
Jules-Raymond Tapamo,
University of KwaZulu-Natal, South Africa
Min Wang,
University of Texas at San Antonio, United States

***Correspondence:**
Alexander C. Rokohl
alexander.rokohl@uk-koeln.de
Ludwig M. Heindl
ludwig.heindl@uk-koeln.de

† These authors have contributed equally to this work and share senior authorship

Specialty section:
This article was submitted to Ophthalmology, a section of the journal Frontiers in Medicine

Received: *11 December 2021*
Accepted: *08 February 2022*
Published: *11 March 2022*

Citation:
Fan W, Guo Y, Hou X, Liu J, Li S, Ju S, Matos PAW, Simon M, Rokohl AC and Heindl LM (2022) Validation of the Portable Next-Generation VECTRA H2 3D Imaging System for Periocular Anthropometry. Front. Med. 9:833487. doi: 10.3389/fmed.2022.833487

Purpose: Portable three-dimensional imaging systems are becoming increasingly common for facial measurement analysis. However, the reliability of portable devices may be affected by the necessity to take three pictures at three time points. The purpose of this study was to evaluate the effectiveness of portable devices for assessing the periocular region.

Methods: In 60 Caucasian volunteers (120 eyes), four facial scans (twice for each instrument) using the portable VECTRA H2 and static VECTRA M3 devices were performed; patients' heads were kept straight, looking ahead, with a neutral facial expression. One assessor set 52 periocular landmarks in the periocular area of each image and subsequently assessed intra- and inter-device reliability by comparing two within-device measurements and one between-device measurement, respectively.

Results: The mean absolute difference (MAD) (0.13 and 0.12 units), relative error of measurement (REM) (0.61 and 0.68%), technical error of measurement (TEM)(1.02 and 0.80 units), relative TEM (rTEM) (5.51 and 4.43%), and intraclass correlation coefficient (ICC) (0.89, 0.89) showed good intra-device reliability for M3 and H2; MAD (0.63, 0.62 units), REM (2.83, 2.69%), TEM (1.31, 1.10 units), rTEM (7.62, 5.57%), and ICC (0.79, 0.83) indicated that inter-device reliability deteriorated compared to intra-device reliability and that the inter-device reliability of the first scan (moderate) was lower than that of the average of the two scans (good).

Conclusions: The portable VECTRA H2 device proved reliable in assessing most periocular linear distances, curve distances, and angles; some improvement in inter-device reliability can be achieved by using the average of two scans.

Keywords: three-dimensional anthropometry, portable stereophotogrammetry devices, validity, reliability, periocular morphology

INTRODUCTION

The anthropometric data of facial soft tissues are widely used in plastic (1) and craniomaxillofacial surgery (2–4). These data are important to develop surgical plans (5) and assess outcome prognosis (6–8). Particularly, the periocular region plays an important role in facial attractiveness, emotional expression, and differentiation by ethnicity (9, 10), gender, and age (11, 12). It is also a major reference indicator for corrective, restorative, or cosmetic surgery (13). In recent years, non-invasive three-dimensional (3D) surface imaging methods, including VECTRA, Artec EVA, and 3D MD systems (14–16) have gradually replaced traditional direct anthropometric techniques (using rulers and calipers) and two-dimensional (2D) photography. Most of the existing 3D photogrammetry systems are static devices, which prominently feature in capturing photos of participants from three different angles at a single time point and composing a 3D photo using a computer. Previous studies have proposed the first standardized periocular anthropometric protocol (17, 18) and showed potential clinical applications, including a novel standardized lower eyelid tension distraction test and a lateral distraction test (19, 20). The reliability (repeatability) and accuracy of the VECTRA M3 static device is very high for linear, curvilinear, angular, area, and volume measurements (21–25). However, the device is expensive, bulky, untransportable, and requires frequent calibration (2, 14, 26–28) to reach this high reliability, which are considerable limitations, especially for patients who cannot walk independently or reside in remote and poor areas.

Currently, portable 3D imaging devices are available in the market. These systems comprise only one digital single-lens reflex camera in addition to a computer system (5). Due to low cost, no need for calibration, and portability, portable 3D photogrammetry systems have high potential to be used extensively in research and routine clinical measurements in the future. Although several publications have conducted facial analyses using older portable devices (5, 16, 29–31), including studies on the reproducibility of these devices (VECTRA H1) in comparison with static devices (3D MD or VECTRA M3) (5, 31), some issues remain to be addressed. First, the primary portable device used in previous studies was the VECTRA H1; the newest generation, VECTRA H2, was not used. Second, there are no studies on the application of portable devices in the periocular area with newly developed standardized landmarks protocols. Finally, many factors, including head and eye movements, camera movements, user dependence, and facial expressions, may affect the reliability of the portable device during the three shots. Therefore, this study aimed to evaluate the reliability of a novel portable stereophotogrammetric device VECTRA H2 compared to the static VECTRA M3 (the current gold-standard 3D imaging system) for three-dimensional periocular analysis and subsequently provide a basis for the feasibility of VECTRA H2 in periocular applications.

METHODS

Study Participants

Sixty Caucasian volunteers (30 men and 30 women, 120 eyes) aged 18–48 years (28.2 ± 6.2 years) were recruited for this study. The study sample size was calculated based on the results of the interdevice comparison between M3 and H2 for 10 volunteers in the pre-test study (LCAm: 67.77 ± 10.65° vs. 62.98 ± 7.09°). With a 2-sided 5% significance level and 80% power, a sample size of 34 patients per group was determined by PASS software (Version 15, UT, USA). Exclusion criteria were deformities, lesions, surgical, or traumatic events involving the face. All participants signed an informed consent form, and this study was performed in accordance with the principles of the Declaration of Helsinki and approved by the ethics committee of Cologne University (approval no: 17-199).

3D Image Acquisition and Data Collection

Before the images were obtained, all volunteers were asked to remove their makeup, take off their jewelry, and pull their

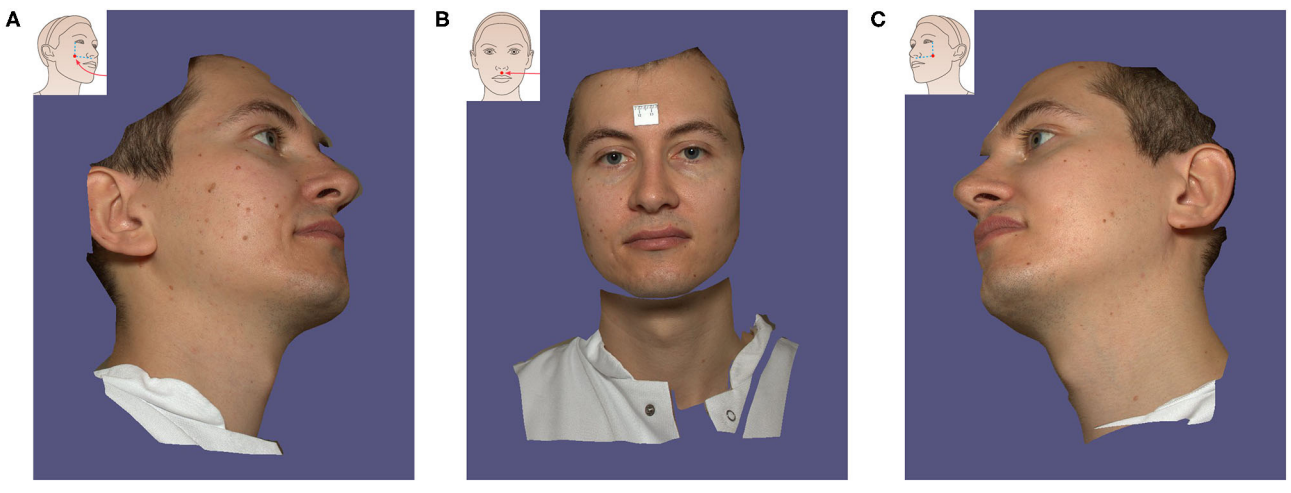

FIGURE 1 | The process of 3D image acquisition with Vectra H2 portable camera. The volunteer follows the instructions to turn the head to the left **(A)**, turn the head to look forward **(B)**, and finally turn the head to the right **(C)**. The application instruction screen for each step is displayed in the upper right corner.

hair back to ensure complete exposure of their forehead and eyebrows. Thereafter, the facial images of each volunteer were captured twice by a static VECTRA M3 and a portable VECTRA H2 system (Canfield Scientific, Inc., Parsippany, NJ, USA). Scanning with both devices was performed consecutively in the same room, and the volunteers sat in a neutral posture. For the static VECTRA M3, calibration was performed according to device guidance before each capture. During acquisition, participants looked at the upper-middle mirror in the machine, keeping their eyes between the vertical and horizontal reference lines on the screen. For the portable VECTRA H2, the operator took three consecutive photographs from three angles as required by the device instructions: the first photograph was taken 30 cm below 45 degrees on the right side of the volunteer's face, and the second photograph was taken with the camera in front of the face. Subsequently, the third picture was taken on the left side of the face at 30 cm below 45 degrees (**Figure 1**). Finally, the computer connected to the camera merged the three photos

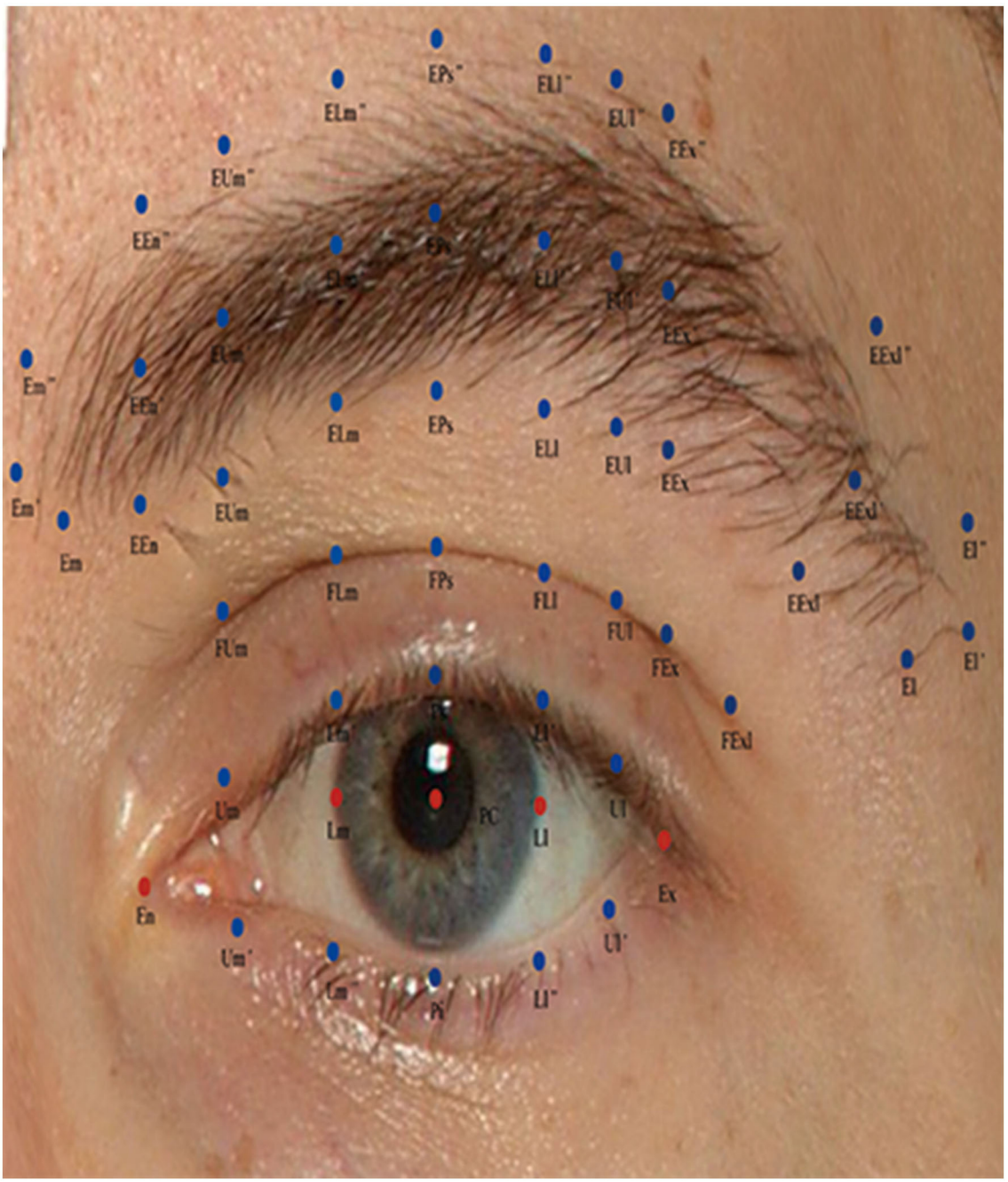

FIGURE 2 | Description of periocular anthropometric landmarks used in this study. Periocular anthropometry was performed according to Guo et al. (17).

TABLE 1 | Definition of abbreviations for periocular landmarks, modified from Guo et al. (17).

Abbreviation of landmarks	Definition
En	Endocanthion, inner commissure of the palpebral fissure
Ex	Exocanthion, outer commissure of the lower and upper eyelash roots of the palpebral fissure
Pc	Pupillary center
Lm	Medial corneoscleral limbus point horizontal to pupillary center
Ll	Lateral corneoscleral limbus point horizontal to pupillary center
Em	Inferior margin point of the medial eyebrow end (sometimes locates at the same place with EEn);
Em"	superior margin point
Em'	middle point
EEn	Inferior margin point of eyebrow vertical to En
EEn"	Superior margin point of eyebrow vertical to En
EEn'	Middle point of eyebrow vertical to En
Um	Middle point between En and Lm' at the upper palpebral margin on the lash roots
Um'	Middle point between En and Lm" at the lower palpebral margin on the lash roots
FUm	Point vertical to Um at the lid fold superioris
EUm	Point vertical to Um at the inferior margin of eyebrows
EUm"	Point vertical to Um at the superior margin point
EUm'	Point vertical to Um at the middle point
Lm'	Point vertical to Lm at the upper palpebral margin on the lash roots
Lm"	Point vertical to Lm at the lower palpebral margin on the lash roots
FLm	Point vertical to Lm at the lid fold superioris
ELm	Point vertical to Lm at the inferior margin of eyebrows
ELm"	Point vertical to Lm at the superior margin of eyebrows
ELm'	Point vertical to Lm at the middle margin of eyebrows
Ps	Palpebrale superioris, Point vertical to Pc at the upper palpebral margin on the lash roots
Pi	Palpebrale inferioris, Point vertical to Pc at the lower palpebral margin on the lash roots
FPs	Point vertical to Pc at the lid fold superioris
EPs	Point vertical to Pc at the inferior margin of eyebrows
EPs"	Point vertical to Pc at the superior margin of eyebrows
EPs'	Point vertical to Pc at the middle margin of eyebrows
Ll'	Point vertical to Ll at the upper palpebral margin on the lash roots
Ll"	Point vertical to Ll at the lower palpebral margin on the lash roots
FLl	Point vertical to Ll at the lid fold superioris
ELl	Point vertical to Ll at the inferior margin of eyebrows
ELl"	Point vertical to Ll at the superior margin of eyebrows
ELl'	Point vertical to Ll at the middle margin of eyebrows
Ul	The middle between Ex and Ll' at the upper palpebral margin on the lash roots
Ul'	The middle between Ex and Ll" at the lower palpebral margin on the lash roots
FUl	FUl Point vertical to Ul at the lid fold superioris
EUl	Point vertical to Ul at the inferior margin of eyebrows
EUl"	Point vertical to Ul at the superior margin of eyebrows
EUl'	Point vertical to Ul at the middle margin of eyebrows
FEx	Point vertical to Ex at the lid fold superioris
EEx	Point vertical to Ex at the inferior margin of eyebrows
EEx"	Point vertical to Ex at the superior margin of eyebrows
EEx'	Point vertical to Ex at the middle margin of eyebrows
FExl	Point vertical to Ex at the lid fold superioris in lateral view
EExl	Point vertical to Ex at the inferior margin of eyebrows in lateral view
EExl"	Point vertical to Ex at the superior margin of eyebrows in lateral view
EExl'	Point vertical to Ex at the middle margin of eyebrows in lateral view
El	inferior margin of the lateral eyebrow end
El"	superior margin of the lateral eyebrow end
El'	middle margin of the lateral eyebrow end

into one 3D photo using VAM software version 2.8.2 (Canfield Scientific, Inc.).

This study employed 52 3D anthropometric landmarks of the periocular region developed and validated by our research group (**Figure 2**). The definitions of these landmarks and measurements are detailed in **Tables 1**, **2**. Subsequently, the study measured three categories of data (linear distances, curves, and angles).

Statistical Analysis

Statistical analysis was performed using SPSS 23.0 software (Armonk, NY: IBM Corp.), and graphs were created by GraphPad Prism 9 (GraphPad Software, San Diego, CA, USA). Differences in the age distribution of men and women among volunteers were assessed using the Wilcoxon's signed rank-sum test. All measured data were tested for normality using the Kolmogorov-Smirnov test. For data conforming to a normal distribution, paired *t*-tests were conducted to assess differences within and between devices. For non-normally distributed data, Wilcoxon's signed-rank test was used. *P*-values <0.05 were considered to indicate statistical significance.

Intra-device reliability was analyzed by comparing the images captured twice by each device (VECTRA M3 and VECTRA H2), and inter-device reliability was analyzed by comparing the metric parameters obtained from the first scan (using VECTRA H2 and VECTRA M3) and the measured average of the images scanned twice with each device. The intraclass correlation coefficient (ICC) has a value between 0 and 1, and a value closer to 1 indicates high reliability. ICC values allowed the classification of the agreement into three classes: <0.4, poor agreement; 0.4–0.75, satisfactory; and ≥ 0.75, excellent (32). Given the small periocular measurements, we set the minimum error threshold for the mean absolute difference (MAD) and technical error of

TABLE 2 | List of linear distance, curve, and angle measurement variables for the periocular region, derived from Guo et al. (17).

Abbreviation	Definition	Landmarks
Liner distances		
PFW	Palpebral fissure width	En-Ex
PFH	Palpebral fissure height	Ps-Pi
EEnD_I	Eyebrow-endocanthion distance of the inferior point	EEn-En
EEnD_M_	Eyebrow-endocanthion distance of the middle point	EEn'-En
EEnD_S_	Eyebrow-endocanthion distance of the inferior, middle, or superior point	EEn"-En
FPDm	Upper lid fold-palpebral margin distance (medial)	FUm-Um
EPDm_I	Eyebrow-palpebral margin distance (medial) of the inferior point	EUm-Um
EPDm_M	Eyebrow-palpebral margin distance (medial) of the middle point	EUm'-Um
EPDm_S	Eyebrow-palpebral margin distance (medial) of the superior point	EUm"-Um
FLmD	Upper lid fold-palpebral margin distance (medial limbus)	FLm-Lm'
ELmD_I	Eyebrow-palpebral margin distance (medial limbus) of the inferior point	ELm-Lm'
ELmD_M	Eyebrow-palpebral margin distance (medial limbus) of the middle point	ELm'-Lm'
ELmD_S	Eyebrow-palpebral margin distance (medial limbus) of the superior point	ELm"-Lm'
FPD	Upper lid fold-palpebral margin distance, similar to upper lid fold height	Ps-FPs
EPD_I	Eyebrow-palpebral margin (Ps) distance of the inferior (similar to upper lid height) point	Ps-EPs
EPD_M	Eyebrow-palpebral margin (Ps) distance of the middle point	Ps-EPs'
EPD_S	Eyebrow-palpebral margin (Ps) distance of the superior point	Ps-EPs"
FLlD	Upper lid fold-palpebral margin distance (lateral limbus)	FLl-Ll'
ELlD_I	Eyebrow-palpebral margin distance (lateral limbus) of the inferior point	ELl-Ll'
ELlD_M	Eyebrow-palpebral margin distance (lateral limbus) of the middle point	ELl'-Ll'
ELlD_S	Eyebrow-palpebral margin distance (lateral limbus) of the superior point	ELl"-Ll'
FPDl	Upper lid fold-palpebral margin distance (lateral)	FUl-Ul
EPDl_I	Eyebrow-palpebral margin distance (lateral) of the inferior point	EUl-Ul
EPDl_M	Eyebrow-palpebral margin distance (lateral) of the middle point	EUl'-Ul
EPDl_S	Eyebrow-palpebral margin distance (lateral) of the superior point	EUl"-Ul
FExD	Upper lid fold-exocanthion distance	FEx-Ex
EExD_I	Eyebrow-exocanthion distance of the inferior point	EEx-Ex
EExD_M	Eyebrow-exocanthion distance of the middle point	EEx'-Ex
EExD_S	Eyebrow-exocanthion distance of the superior point	EEx"-Ex
FExDl	Upper lid fold-exocanthion distance (lateral)	FExl-Ex
EExDl_I	Eyebrow-exocanthion distance (lateral) of the inferior point	EExl-Ex
EExDl_M	Eyebrow-exocanthion distance (lateral) of the middle point	EExl'-Ex
EExDl_S	Eyebrow-exocanthion distance (lateral) of the superior point	EExl"-Ex
ID	Iris diameter	Lm-Ll
EnD	Inner intercanthal distance	En (left)-En (right)
PD	Interpupillary distance	Pc (left)-Pc (right)
ExD	Outer intercanthal distance	Ex (left)-Ex (right)
Curvatures		
UPML	Upper palpebral margin length	En-Um-Lm'-Ps-Ll'-Ul-Ex
UPMLm	Upper palpebral margin length (more points)	Including 4 more midpoints between Lm'-Ps-Ll'-Ul-Ex
LPML	Lower palpebral margin length	En-Um'-Lm"-Pi-Ll"-Ul'-Ex
LPMLm	Lower palpebral margin length (more points)	Including 4 more midpoints between Lm"-Pi-Ll"-Ul'-Ex
EL_I	Inferior eyebrow length	Em-EEn-EUm-ELm-EPs-ELl-EUl-EEx-EExl-El
EL_M	Middle eyebrow length	Em'-EEn'-EUm'-ELm'-EPs'-ELl'-EUl'-EEx'-EExl'-El'
EL_S	Superior eyebrow length	Em"-EEn"-EUm"-ELm"-EPs"-ELl"-EUl"-EEx"-EExl"-El"
Angles		
MCA	Medial canthal angle	Ps-En-Pi
MCAm	Medial canthal angle (medial)	Um-En-Um'
LCA	Lateral canthal angle	Ps-Ex-Pi
LCAm	Lateral canthal angle (medial)	Ul-Ex-Ul'
CT	Canthal tilt	Ex (left)-En (left)-En (right), or Ex (right)-En (right)-En (left)

measurement (TEM) to 1 unit (millimeter or degree). Relative error of measurement (REM) and relative TEM (rTEM) values can be classified into five categories (excellent, <1%; very good, 1–3.9%; good, 4–6.9%; moderate, 7–9.9%; and poor, >10%) based on the scale proposed by Camison et al. and Andrade et al. (5, 33).

RESULTS

The measurement results (means and standard error, SD) of the M3 and H2 system are shown in **Table 3**. Repeatability

parameters (ICC, MAD, TEM, REM, and rTEM) within and between the VECTRA M3 and H2 devices are presented in **Tables 4**, **5**.

Intra-Device Reliability With VECTRA M3

ICC (**Table 4**, **Figure 3**) estimates for most M3 intra-device comparisons were excellent (0.81–1.00), except for two upper lid fold-related variables (FPDI: 0.73, FExDI: 0.70) and one eyelid fissure-related variable (LCAm: 0.68). As shown in **Table 6** and **Figure 4**, MAD was <1 unit for 48 of the 49 parameters, and LCAm was between 1 and 2 units. TEM was <1 unit for 42 parameters (87.5% eyebrow-related variables, 100% upper lid fold-related variables, and 60% palpebral fissure-related variables); the largest measurement error was for the palpebral fissure-related variable MCAm (6.05°). The REM and rTEM results for each comparison are shown in **Figure 5** and **Figure 6**. Of seven upper lid fold-related variables, 57.1% of REM values were <1 and 42.9% of values were between 1 and 3.9%. As for rTEM, 71.4% of variables were >10%, except for FExD, which was <7%, and FDPm, which was <10%. FExDI (rTEM = 13.87%) had the largest value. REM was <1% for 73.3% of palpebral fissure-related variables, and 26.7% were in the 1–3.9% range. Except for MCAm (rTEM = 8.63%) and LCAm (rTEM = 13.61%), 86.7% of palpebral fissure-related values showed an rTEM <7% (20% of variables were <1%, 46.7% were between 1 and 3.9%, and 20% were between 4 and 6.9%). Moreover, the rTEM and REM of all brow-related variables were <7%. Additionally, 95.8% of REM values were <1%, 75% of rTEM and 4.2% of REM values were between 1 and 3.9%, and 25% of rTEM values were between 4 and 6.9%.

Intra-Device Reliability With VECTRA H2

Intra-device ICC (**Table 4**, **Figure 3**) was above 0.75 for most variables measured by device H2, except for one eyebrow-related parameter (EPDl_M) and three upper lid fold-related variables (FPD, FLl, and FPDl), with an ICC between 0.4 and 0.75. **Figure 4** and **Table 6** show that all 49 parameters with a MAD and 41 parameters with TEM had a value of <1 unit (87.5% of eyebrow-related variables, 100% of upper lid fold-related variables, and 60% of palpebral fissure-related variables). The largest measurement error was the palpebral fissure-related variable LCAm (4.03°); 28.6% of upper lid fold-related variables showed an REM <1%, 57.1% had variables between 1 and 3.9%, and the maximum value of FPD was 5.163%. All these variables had an rTEM >7%, 28.6% of these variables had an rTEM between 7 and 10%, and 71.4% had an rTEM >10%; the maximum value was FPD (rTEM = 15.76%). All palpebral fissure-related variables showed an REM and rTEM <7% (80% of REM and 26.7% of rTEM values were <1%, 20% of REM and 40% of rTEM values were between 1 and 3.9%, and 33.3% of rTEM values were between 4 and 6.9%). Except for EPDl_M, ELlD_I, and EPD_I with an rTEM >7%, REM and rTEM were <7% across all brow-related variables (87.5% of variables had an REM <1%, 70.8% of rTEM and 12.5% of REM variables were between 1 and 3.9%, and 16.7% of rTEM values were between 4 and 6.9%).

Inter-Device Reliability Between VECTRA H2 and VECTRA M3

When the first captures of both devices (M3 and H2) were used to compare inter-device reliability; 33 variables showed an ICC (**Table 5**) >0.75 (83.3% of brow-related variables and 73.3% of palpebral fissure-related variables), 15 variables had ICC values between 0.4 and 0.75 (16.7% of brow-related variables, 100% of upper eyelid fold-related variables, and 20% of palpebral fissure-related variables). The smallest ICC value was for a palpebral fissure-related variable, LCAm (ICC = 0.39). Forty-one variables had an MAD <1 unit (100% of eyebrow-related variables, 100% of upper eyelid fold-related variables, and 53.3% of palpebral fissure-related variables), and the highest MAD value was for LCAm (6.825°). Twenty-eight measurements had a TEM <1 unit (62.5% of brow-related variables, 85.7% of upper eyelid fold-related variables, and 40% of palpebral fissure-related variables), and LCAm (8.731°) had the highest TEM value. Only the rTEM of EnD and 14 variables (including EnD) of REM were <1% (41.7% of eyebrow-related variables and 26.7% of palpebral fissure-related variables; **Figure 5**). Thirteen variables of rTEM (37.5% of eyebrow-related variables and 26.7% of palpebral fissure-related variables) and 24 variables of REM (50% of brow-related variables, 42.9% of upper eyelid fold-related variables, and 60% of palpebral fissure-related variables) were between 1 and 3.9%, respectively; 13 rTEM (45.8% of brow-related variables and 13.3% of palpebral fissure-related variables) and five REM (37.5% of brow-related variables, 28.6% of upper eyelid fold-related variables, and 6.7% of palpebral fissure-related variables) variables were between 4 and 6.9%; four rTEM (12.5% of eyebrow-related variables and 28.6% of upper eyelid fold-related variables) and one REM (28.6% of upper eyelid fold-related variables) variables were between 7 and 10%. Nine rTEM (4.2% of brow-related variables, 100% of upper eyelid fold-related variables, and 6.7% [1/15] of palpebral fissure-related variables) and two REM values (28.6% [1/7] of upper eyelid fold-related variables and 6.7% of palpebral fissure-related variables) were >10%. The largest rTEM value was FPD (17.29%), while the largest REM value was LCAm (10.31%).

When the mean of two scans for each device was used for comparison, 39 variables had an ICC >0.75, and the remaining 10 variables were between 0.4 and 0.75. Forty-four measurements had a MAD of <1 unit, and 35 measurements had a TEM of <1 unit. Four rTEM and 16 REM values were <1%, 14 rTEM and 21 REM values were between 1 and 3.9%, and 17 rTEM and 6 REM values were between 4 and 6.9%. Three rTEM and two REM values were between 7 and 10%, and eight rTEM and one REM values were >10%. Overall, applying the average of the two captures mildly improved inter-device reliability compared to using only the first capture.

DISCUSSION

We validated the reliability of portable devices in periocular applications for the first time using a periocular marker developed by Guo et al. (21). The mean results for the intra-device reliability metrics of MAD (0.13 and 0.12 units), REM

TABLE 3 | Means and standard deviations (SDs) of all measurements (mm or degrees).

Parameters	M3				H2			
	Capture 1		Capture 2		Capture 1		Capture 2	
	Mean	SD	Mean	SD	Mean	SD	Mean	SD
Liner distances (mm)								
PFW	29.38	1.76	29.37	1.86	30.05	1.69	30.00	1.68
PFH	12.01	1.28	12.19	1.26	12.28	1.46	12.15	1.49
EEnD_I	16.78	1.95	16.84	2.07	16.46	1.87	16.39	1.72
EEnD_M_	23.81	2.11	23.84	2.11	23.63	2.26	23.58	2.25
EEnD_S_	28.45	2.81	28.55	2.71	28.38	2.91	28.38	2.93
FPDm	4.37	1.16	4.47	1.17	4.83	1.12	4.91	1.13
EPDm_I	13.93	1.95	13.96	2.11	13.94	1.77	13.98	1.71
EPDm_M	21.05	1.97	21.14	2.04	21.32	2.11	21.33	2.09
EPDm_S	25.50	2.49	25.64	2.52	25.83	2.62	25.85	2.59
FLmD	3.96	1.14	3.93	1.16	4.02	0.86	4.04	0.91
ELmD_I	10.88	2.04	10.76	2.17	10.50	1.81	10.60	1.77
ELmD_M	17.75	1.96	17.64	2.15	17.53	2.00	17.65	2.08
ELmD_S	22.23	2.56	22.13	2.69	22.10	2.58	22.21	2.66
FPD	3.39	1.16	3.48	1.18	3.52	0.97	3.71	1.08
EPD_I	10.08	2.01	10.03	1.92	9.43	1.91	9.66	1.83
EPD_M	16.26	1.82	16.28	1.88	15.78	1.98	15.97	2.13
EPD_S	20.83	2.57	20.83	2.70	20.40	2.74	20.59	2.86
FLID	3.77	1.08	3.80	1.08	3.81	1.02	3.87	0.99
ELID_I	11.54	2.43	11.50	2.28	10.76	2.23	10.92	2.04
ELID_M	17.11	1.90	17.06	1.97	16.45	1.80	16.58	1.95
ELID_S	21.68	2.57	21.63	2.82	21.19	2.71	21.30	2.90
FPDl	4.62	0.94	4.63	0.89	4.89	1.20	4.83	1.04
EPDl_I	13.90	2.78	14.01	2.68	13.48	2.51	13.46	2.38
EPDl_M	19.24	2.14	19.32	2.19	18.80	2.53	18.94	2.03
EPDl_S	23.75	2.78	23.83	2.99	23.57	2.75	23.64	2.94
FExD	6.93	1.05	6.89	1.06	7.42	1.47	7.29	1.47
EExD_I	17.88	3.09	18.01	3.11	17.69	2.91	17.58	2.89
EExD_M	23.07	2.35	23.21	2.44	22.96	2.14	22.93	2.14
EExD_S	27.13	2.92	27.30	2.97	27.09	2.71	27.13	2.79
FExDl	4.77	1.17	4.61	1.18	4.31	1.04	4.32	1.02
EExDl_I	14.77	3.21	14.73	3.21	13.65	3.13	13.49	3.03
EExDl_M	19.44	2.58	19.42	2.57	18.60	2.42	18.50	2.38
EExDl_S	23.38	3.19	23.43	3.13	22.71	3.03	22.63	3.04
ID	11.91	0.49	11.97	0.49	11.90	0.46	11.86	0.44
EnD*	32.45	2.60	32.43	2.71	32.40	2.72	32.44	2.75
PD*	62.71	3.24	62.72	3.26	62.39	3.14	62.27	3.19
ExD*	89.93	4.29	90.04	4.22	90.91	4.28	90.87	4.27
Curvatures (mm)								
UPML	38.01	2.75	38.25	2.62	39.03	2.64	38.61	2.55
UPMLm	25.32	2.22	25.46	2.12	26.32	2.18	26.06	1.89
LPML	33.60	2.34	33.75	2.20	34.28	2.41	34.17	2.52
LPMLm	23.20	1.95	23.30	1.71	24.23	1.97	24.19	1.97
EL_I	59.14	5.63	59.22	5.43	59.30	5.64	59.39	5.30
EL_M	70.96	9.28	71.19	9.17	71.37	8.74	71.49	8.55
EL_S	68.91	8.86	69.16	8.84	69.52	8.35	69.59	8.31
Angles (°)								
MCA	41.79	4.45	42.38	4.07	43.04	4.52	42.80	4.78
MCAm	61.65	9.36	62.03	8.71	59.79	9.40	59.07	9.54
LCA	40.93	4.66	41.36	4.63	39.70	4.79	39.55	4.78
LCAm	69.64	10.56	70.65	10.59	62.82	9.44	62.64	9.30
CT	168.33	3.53	168.18	3.44	167.19	3.62	167.13	3.67

**N = 60; for the rest, N = 120; SD, standard deviations.*

TABLE 4 | Intra-device reliability results of VECTRA M3 and H2 for periocular measurements.

Device comparison	M3 vs. M3						H2 vs. H2					
	ICC (CI 95%)	MAD	TEM	rTEM	REM	*p*-value	ICC (CI 95%)	MAD	TEM	rTEM	REM	*p*-value
Liner distances (mm)												
PFW	0.84 (0.77–0.88)	0.02	0.74	2.51	0.06	0.948	0.95 (0.93–0.96)	0.05	0.38	1.27	0.16	0.332
PFH	0.86 (0.79–0.90)	0.19	0.49	4.03	1.56	**<0.001**†	0.87 (0.82–0.91)	0.12	0.54	4.42	1.01	0.078
EEnD_I	0.89 (0.85–0.93)	0.05	0.66	3.91	0.31	0.544	0.92 (0.89–0.94)	0.06	0.51	3.09	0.38	0.349
EEnD_M_	0.90 (0.86–0.93)	0.04	0.68	2.85	0.16	0.665	0.97 (0.96–0.98)	0.05	0.39	1.64	0.22	0.305
EEnD_S_	0.92 (0.89–0.95)	0.10	0.77	2.68	0.34	0.331	0.98 (0.97–0.99)	0.00	0.41	1.45	0.00	0.996
FPDm	0.86 (0.81–0.90)	0.10	0.44	9.88	2.27	0.075	0.89 (0.85–0.92)	0.08	0.37	7.65	1.67	0.062†
EPDm_I	0.88 (0.83–0.91)	0.03	0.71	5.11	0.20	0.765	0.91 (0.87–0.94)	0.05	0.52	3.75	0.32	0.508
EPDm_M	0.91 (0.87–0.93)	0.09	0.62	2.94	0.43	0.259	0.96 (0.94–0.97)	0.01	0.43	2.02	0.06	0.848
EPDm_S	0.93 (0.91–0.95)	0.14	0.65	2.53	0.54	0.100	0.98 (0.97–0.98)	0.03	0.40	1.56	0.10	0.622
FLmD	0.85 (0.79–0.89)	0.02	0.45	11.28	0.60	0.681	0.78 (0.70–0.84)	0.01	0.42	10.34	0.27	0.860
ELmD_I	0.89 (0.85–0.92)	0.12	0.70	6.49	1.12	0.183	0.88 (0.83–0.91)	0.10	0.64	6.02	0.92	0.237
ELmD_M	0.89 (0.84–0.92)	0.11	0.70	3.97	0.62	0.228	0.91 (0.87–0.94)	0.11	0.61	3.49	0.64	0.160
ELmD_S	0.92 (0.88–0.94)	0.09	0.77	3.47	0.42	0.540†	0.94 (0.92–0.96)	0.11	0.65	2.92	0.47	0.211
FPD	0.86 (0.81–0.90)	0.09	0.44	12.76	2.58	0.091†	0.70 (0.59–0.78)	0.19	0.57	15.76	5.16	0.110
EPD_I	0.90 (0.87–0.93)	0.04	0.61	6.07	0.43	0.586	0.79 (0.71–0.85)	0.22	0.86	8.98	2.32	**0.044**
EPD_M	0.88 (0.83–0.92)	0.02	0.64	3.95	0.10	0.854	0.84 (0.77–0.88)	0.19	0.84	5.30	1.19	0.810
EPD_S	0.91 (0.88–0.94)	0.01	0.78	3.75	0.03	0.956	0.92 (0.89–0.95)	0.19	0.78	3.81	0.93	0.057
FLID	0.83 (0.77–0.88)	0.04	0.45	11.76	0.97	0.242†	0.64 (0.53–0.74)	0.07	0.60	15.72	1.68	0.468†
ELID_I	0.92 (0.89–0.94)	0.03	0.67	5.84	0.30	0.695	0.87 (0.81–0.91)	0.16	0.78	7.23	1.51	0.107
ELID_M	0.87 (0.81–0.90)	0.06	0.71	4.17	0.32	0.550	0.84 (0.78–0.89)	0.13	0.75	4.52	0.77	0.185
ELID_S	0.91 (0.87–0.94)	0.05	0.82	3.80	0.21	0.676	0.93 (0.90–0.95)	0.11	0.77	3.62	0.52	0.268
FPDl	0.73 (0.63–0.80)	0.01	0.48	10.31	0.29	0.828	0.73 (0.64–0.81)	0.06	0.59	12.04	1.23	0.430
EPDl_I	0.94 (0.91–0.96)	0.10	0.68	4.86	0.74	0.241	0.94 (0.91–0.96)	0.02	0.61	4.56	0.12	0.840
EPDl_M	0.90 (0.86–0.93)	0.08	0.68	3.53	0.40	0.380	0.67 (0.56–0.76)	0.14	1.33	7.03	0.73	0.421
EPDl_S	0.92 (0.89–0.95)	0.08	0.80	3.35	0.32	0.463	0.95 (0.93–0.97)	0.07	0.63	2.68	0.31	0.373
FExD	0.81 (0.73–0.86)	0.05	0.47	6.73	0.69	0.427	0.83 (0.77–0.88)	0.13	0.60	8.17	1.74	0.169†
EExD_I	0.96 (0.94–0.97)	0.12	0.65	3.63	0.67	0.152	0.97 (0.96–0.98)	0.11	0.51	2.90	0.61	0.105
EExD_M	0.93 (0.91–0.95)	0.14	0.62	2.70	0.62	0.077	0.95 (0.93–0.96)	0.03	0.49	2.13	0.15	0.591
EExD_S	0.94 (0.91–0.96)	0.16	0.74	2.71	0.60	0.086	0.96 (0.95–0.97)	0.04	0.55	2.01	0.14	0.587
FExDl	0.70 (0.59–0.80)	0.16	0.65	13.87	3.51	0.050	0.79 (0.71–0.85)	0.00	0.48	11.03	0.07	0.960
EExDl_I	0.96 (0.95–0.98)	0.03	0.61	4.15	0.22	0.684	0.96 (0.95–0.98)	0.16	0.59	4.32	1.15	**0.039**
EExDl_M	0.95 (0.93–0.96)	0.02	0.60	3.06	0.10	0.801	0.95 (0.93–0.97)	0.10	0.53	2.86	0.54	0.144
EExDl_S	0.94 (0.92–0.96)	0.05	0.76	3.24	0.22	0.609	0.96 (0.94–0.97)	0.08	0.63	2.76	0.34	0.341
ID	0.83 (0.76–0.88)	0.06	0.21	1.74	0.47	**0.037**	0.90 (0.85–0.93)	0.03	0.15	1.22	0.27	0.085
EnD*	0.99 (0.90–1.00)	0.02	0.15	0.66	0.05	0.457†	0.99 (0.99–1.0)	0.04	0.21	0.66	0.12	0.369†
PD*	1.00 (1.00–1.00)	0.00	0.12	0.26	0.01	0.921	0.96 (0.94–0.98)	0.12	0.62	1.00	0.19	0.298
ExD*	0.99 (0.98–0.99)	0.11	0.37	0.42	0.13	0.241	0.99 (0.98–0.99)	0.04	0.52	0.57	0.04	0.692
Curvatures (mm)												
UPML	0.84 (0.78–0.88)	0.24	0.93	2.85	0.56	0.092	0.83 (0.75–0.88)	0.42	1.09	2.81	1.08	**0.002**
UPMLm	0.82 (0.75–0.87)	0.14	0.59	1.74	0.45	0.238	0.78 (0.70–0.84)	0.26	0.97	3.69	0.98	0.141†
LPML	0.93 (0.91–0.95)	0.15	0.67	1.67	0.41	**0.042**	0.90 (0.86–0.93)	0.11	0.78	2.27	0.31	0.286
LPMLm	0.87 (0.81–0.91)	0.10	1.08	1.82	0.13	0.276	0.93 (0.90–0.95)	0.04	0.54	2.24	0.16	0.577
EL_I	0.96 (0.95–0.97)	0.08	1.52	2.15	0.32	0.585	0.94 (0.92–0.96)	0.09	1.32	2.22	0.15	0.617
EL_M	0.97 (0.96–0.98)	0.22	1.32	2.59	0.37	0.354†	0.99 (0.98–0.99)	0.12	1.01	1.42	0.17	0.345
EL_S	0.98 (0.97–0.99)	0.25	1.75	4.15	0.37	0.138	0.99 (0.98–0.99)	0.08	0.92	1.33	0.11	0.513
Angles (°)												
MCA	0.84 (0.77–0.88)	0.58	1.90	4.61	1.05	**0.009**	0.86 (0.81–0.90)	0.23	1.74	4.05	0.55	0.298
MCAm	0.86 (0.80–0.90)	0.38	6.05	8.63	1.43	0.384	0.90 (0.85–0.93)	0.72	3.09	5.20	1.21	0.071
LCA	0.84 (0.77–0.88)	0.43	1.19	6.39	0.09	0.077	0.87 (0.82–0.91)	0.15	1.74	4.39	0.38	0.506
LCAm	0.68 (0.57–0.76)	1.00	0.74	13.16	0.06	0.201	0.82 (0.75–0.87)	0.18	4.03	6.42	0.29	0.730
CT	0.88 (0.84–0.92)	0.15	0.49	1.02	1.56	0.335	0.95 (0.92–0.96)	0.06	0.85	0.51	0.03	0.606
Mean	0.89	0.13	1.02	5.51	0.61		0.89	0.12	0.80	4.43	0.68	

CI, confidence interval.

†*Represents p-values calculated from Wilcoxon's signed-rank test and the rest derived from paired-samples t-test. Results with P < 0.05 are marked in bold.*

TABLE 5 | Inter-device reliability results of VECTRA M3 and H2 for periocular measurements.

Device comparison	M3 vs. H2						M2 vs. H2 (Mean)					
	ICC (CI 95%)	MAD	TEM	rTEM	REM	*p*-value	ICC (CI 95%)	MAD	TEM	rTEM	REM	*p*-value
Liner distances (mm)												
PFW	0.83 (0.46–0.93)	0.67	0.73	2.46	2.25	**<0.001**	0.82 (0.51–0.91)	0.65	0.76	2.55	2.20	**<0.001**
PFH	0.80 (0.70–0.86)	0.27	0.63	5.18	2.23	**0.001**	0.86 (0.81–0.90)	0.12	0.50	4.07	0.94	0.073
EEnD_I	0.79 (0.71–0.85)	0.33	0.88	5.31	1.98	**0.004**	0.85 (0.76–0.90)	0.39	0.73	4.39	2.32	**<0.001**
EEnD_M	0.88 (0.83–0.91)	0.18	0.78	3.27	0.74	0.080	0.92 (0.88–0.95)	0.22	0.61	2.58	0.93	**0.005**
EEnD_S	0.90 (0.87–0.93)	0.07	0.89	3.13	0.24	0.549	0.95 (0.93–0.96)	0.12	0.64	2.27	0.41	0.160
FPDm	0.66 (0.45–0.78)	0.45	0.69	15.10	9.86	**<0.001**	0.72 (0.48–0.84)	0.44	0.61	13.17	9.56	**<0.001**
EPDm_I	0.81 (0.73–0.86)	0.01	0.82	5.91	0.05	0.951	0.85 (0.79–0.90)	0.02	0.71	5.09	0.11	0.869
EPDm_M	0.86 (0.80–0.90)	0.27	0.76	3.60	1.26	**0.006**	0.90 (0.85–0.98)	0.23	0.66	3.11	1.08	**0.007**
EPDm_S	0.89 (0.84–0.92)	0.33	0.85	3.33	1.27	**0.003**	0.92 (0.88–0.95)	0.27	0.73	2.83	1.05	**0.004**
FLmD	0.59 (0.46–0.70)	0.07	0.45	11.15	1.65	0.432	0.68 (0.57–0.77)	0.08	0.56	13.97	2.09	0.249
ELmD_I	0.77 (0.67–0.84)	0.38	0.94	8.77	3.53	†	0.80 (0.72–0.86)	0.27	0.86	8.05	2.51	**0.005†**
ELmD_M	0.80 (0.73–0.86)	0.22	0.89	5.02	1.24	0.056	0.84 (0.78–0.88)	0.11	0.81	4.58	0.61	0.304
ELmD_S	0.85 (0.79–0.89)	0.12	0.99	4.48	0.55	0.346	0.88 (0.83–0.92)	0.02	0.90	4.04	0.10	0.848
FPD	0.69 (0.59–0.78)	0.13	0.60	17.29	3.86	0.108†	0.73 (0.63–0.80)	0.18	0.55	15.61	5.18	**0.011†**
EPD_I	0.71 (0.54–0.81)	0.64	1.09	11.15	6.60	**<0.001†**	0.76 (0.63–0.84)	0.51	0.92	9.39	5.22	**<0.001†**
EPD_M	0.71 (0.58–0.79)	0.48	1.05	6.56	2.99	**<0.001**	0.77 (0.67–0.84)	0.39	0.91	5.68	2.44	**0.001**
EPD_S	0.81 (0.73–0.87)	0.43	1.16	5.65	2.08	**0.004**	0.85 (0.79–0.89)	0.34	1.04	5.04	1.62	**0.012**
FLID	0.63 (0.51–0.73)	0.04	0.64	16.85	1.00	0.962†	0.73 (0.63–0.80)	0.05	0.51	13.42	1.36	0.552†
ELID_I	0.83 (0.60–0.91)	0.78	1.00	8.98	6.97	**<0.001**	0.84 (0.64–0.92)	0.68	0.89	7.99	6.07	**<0.001**
ELID_M	0.74 (0.54–0.84)	0.66	0.98	5.86	3.93	**<0.001**	0.78 (0.61–0.87)	0.57	0.88	5.25	3.38	**<0.001**
ELID_S	0.84 (0.76–0.89)	0.48	1.06	4.94	2.26	**<0.001**	0.86 (0.80–0.90)	0.41	1.02	4.75	1.89	**0.002**
FPDI	0.45 (0.29–0.58)	0.27	0.82	17.27	5.68	0.074†	0.56 (0.42–0.68)	0.23	0.64	13.52	4.92	**0.004**
EPDI_I	0.88 (0.82–0.92)	0.43	0.93	6.76	3.10	**<0.001**	0.88 (0.80–0.93)	0.49	0.89	6.51	3.53	**<0.001†**
EPDI_M	0.60 (0.46–0.70)	0.44	1.51	7.94	2.32	**0.001†**	0.74 (0.64–0.81)	0.41	1.09	5.71	2.15	**0.003**
EPDI_S	0.88 (0.83–0.91)	0.18	0.97	4.09	0.78	0.143	0.89 (0.85–0.92)	0.19	0.93	3.92	0.78	0.124
FExD	0.45 (0.28–0.59)	0.49	0.98	13.63	6.80	**0.004**	0.53 (0.36–0.66)	0.45	0.87	12.15	6.28	**<0.001**
EExD_I	0.92 (0.89–0.94)	0.20	0.86	4.85	1.11	0.077	0.94 (0.90–0.96)	0.31	0.76	4.29	1.75	**0.001**
EExD_M	0.90 (0.86–0.93)	0.11	0.72	3.11	0.46	0.255	0.91 (0.87–0.94)	0.19	0.68	2.93	0.84	**0.025**
EExD_S	0.90 (0.86–0.93)	0.05	0.88	3.26	0.17	0.686	0.91 (0.88–0.94)	0.11	0.84	3.08	0.40	0.315
FExDI	0.64 (0.42–0.77)	0.46	0.69	15.15	10.03	**<0.001†**	0.70 (0.51–0.81)	0.37	0.59	13.04	8.26	**<0.001**
EExDI_	0.89 (0.43–0.96)	1.12	1.11	7.80	7.85	**<0.001**	0.89 (0.29–0.96)	1.18	1.09	7.71	8.31	**<0.001**
EExDI_M	0.87 (0.55–0.95)	0.84	0.61	3.21	4.41	**<0.001**	0.88 (0.43–0.96)	0.88	0.88	4.64	4.63	**<0.001**
EExDI_S	0.89 (0.79–0.94)	0.67	1.05	4.58	2.93	**<0.001**	0.90 (0.76–0.95)	0.74	0.97	4.23	3.20	**<0.001**
ID	0.85 (0.79–0.89)	0.02	0.19	1.57	0.15	0.454	0.87 (0.81–0.91)	0.06	0.17	1.39	0.52	**0.003**
EnD*	0.90 (0.98–0.99)	0.05	0.29	0.88	0.14	0.763†	0.99 (0.99–1.0)	0.02	0.22	0.66	0.06	0.713†
PD*	0.96 (0.93–0.98)	0.33	0.65	1.04	0.52	**0.005**	0.98 (0.92–0.99)	0.39	0.44	0.71	0.62	**<0.001**
ExD*	0.95 (0.65–0.98)	0.98	0.96	1.06	1.08	**<0.001**	0.96 (0.91–0.99)	0.90	0.90	1.00	1.00	**<0.001**
Curvatures (mm)												
UPML	0.76 (0.52–0.82)	1.02	1.37	3.56	2.66	**<0.001**	0.82 (0.68–0.89)	0.70	1.09	2.84	1.81	**<0.001**
UPMLm	0.65 (0.39–0.79)	1.00	1.38	5.34	3.87	**<0.001**	0.73 (0.48–0.85)	0.80	1.09	4.21	3.10	**<0.001**
LPML	0.87 (0.69–0.93)	0.68	1.11	3.28	1.99	**<0.001**	0.87 (0.75–0.92)	0.55	0.85	2.51	1.61	**<0.001**
LPMLm	0.72 (0.27–0.87)	1.03	1.12	4.71	4.34	**<0.001**	0.75 (0.24–0.89)	0.96	1.00	4.21	4.05	**<0.001**
EL_I	0.89 (0.84–0.92)	0.16	1.89	3.18	0.27	0.519	0.92 (0.89–0.95)	0.16	1.51	2.54	0.27	0.406
EL_M	0.96 (0.94–0.97)	0.41	1.80	2.52	0.57	**0.048†**	0.97 (0.95–0.98)	0.36	1.65	2.32	0.50	0.096
EL_S	0.95 (0.92–0.96)	0.61	2.02	2.93	0.88	**0.020**	0.96 (0.94–0.97)	0.52	1.78	2.57	0.75	**0.023**
Angles (°)												
MCA	0.77 (0.64–0.85)	1.24	2.18	5.14	2.93	**<0.001**	0.84 (0.75–0.89)	0.84	1.75	4.12	1.96	**<0.001**
MCAm	0.79 (0.70–0.86)	1.86	4.32	7.11	3.06	**0.001**	0.83 (0.69–0.90)	2.41	3.76	6.20	3.98	**<0.001**

(Continued)

TABLE 5 | Continued

Device comparison	M3 vs. H2						M2 vs. H2 (Mean)					
	ICC (CI 95%)	MAD	TEM	rTEM	REM	*p*-value	ICC (CI 95%)	MAD	TEM	rTEM	REM	*p*-value
LCA	0.71 (0.58–0.80)	1.22	2.61	6.49	3.04	**<0.001**	0.77 (0.58–0.86)	1.52	2.26	5.59	3.75	**<0.001**
LCAm	0.39 (0.11–0.58)	6.83	8.73	13.18	10.31	**<0.001**	0.47 (0.04–0.70)	7.42	7.81	11.76	11.17	**<0.001**
CT	0.79 (0.66–0.88)	1.14	1.68	1.00	0.68	**<0.001**	0.84 (0.63–0.91)	1.09	1.46	0.87	0.65	**<0.001**
Mean	0.79	0.63	1.31	7.62	2.83		0.83	0.62	1.10	5.57	2.69	

CI, confidence interval.

†Represents p-values calculated from Wilcoxon's signed-rank test and the rest derived from paired-samples t-test. Results with P < 0.05 are marked in bold.

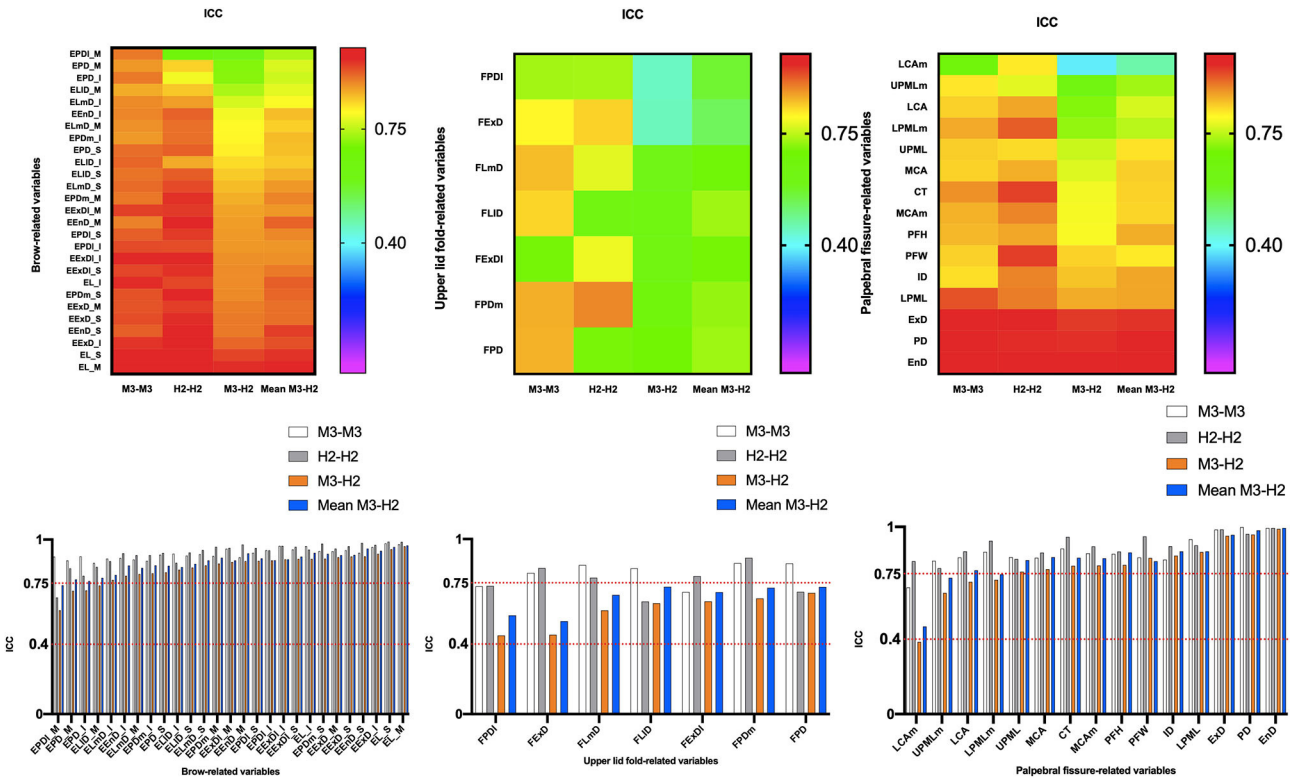

FIGURE 3 | Intra- and inter-device of intraclass correlation coefficient (ICC) for all periocular region measurements of 3D images. ICC values allowed the classification of the agreement into three classes: <0.4, poor agreement; 0.4–0.75, satisfactory; and ≥0.75, excellent.

(0.61 and 0.68%), TEM (1.02 and 0.80 units), rTEM (5.51 and 4.43%), and ICC (0.89 and 0.89) for devices M3 and H2 were highly comparable. For inter-device comparisons, the mean MAD, REM, TEM, rTEM, and ICC were 0.63 units, 2.83%, 1.31 units, 7.62%, and 0.79 units, respectively (0.62 units, 2.69%, 1.10 units, 5.57%, and 0.83 units if the mean values of H2 and M3 were used). Inter-device reliability decreased compared to intra-device reliability and all reliability metrics improved when quoting average values, indicating that we can reduce inter-device variation by using the average of the two captured images when the H2 device is used for photography.

Guo et al. first introduced 52 new periocular landmarks and validated the high reliability of the static VECTRA M3 stereophotogrammetric system for periocular anthropometry (21). The imaging system and landmarks were highly reliable for most measurements. Intra-rater measurements had the highest reliability, followed by inter-rater and intra-device measurements. The results of the M3 intra-device reliability analysis included MAD (0.98 units), REM (4.66%), TEM (0.96 units), rTEM (4.64%), and ICC (0.96). Our results were generally consistent with the aforementioned study, and some indicators were even more reliable.

TABLE 6 | Percentage of different periocular measurement variables in each reliability rating classification for VECTRA M3 and H2.

Variables	Upper lid fold-related variables (7/7)				Palpebral fissure-related variables (15/15)				Eyebrow-related variables (24/24)			
	M3-M3	H2-H2	M3-H2	M3-H2 (Mean)	M3-M3	H2-H2	M3-H2	M3-H2 (Mean)	M3-M3	H2-H2	M3-H2	M3-H2 (Mean)
ICC												
Excellent (≥0.75)	71.4% (5/7)	57.1% (4/7)	0% (0/7)	0% (0/7)	93.3% (14/15)	100% (15/15)	73.3% (11/15)	86.7% (13/15)	100% (24/24)	95.8% (23/24)	83.3% (20/24)	95.8% (23/24)
Satisfactory (0.4–0.75)	28.6% (2/7)	42.9% (3/7)	100% (7/7)	100% (7/7)	6.7% (1/15)	0% (0/15)	20% (3/15)	13.3% (2/15)	0% (0/24)	4.2% (1/24)	16.7% (4/24)	4.2% (1/24)
Poor (<0.4)	0% (0/7)	0% (0/7)	0% (0/7)	0% (0/7)	0% (0/15)	0% (0/15)	6.7% (1/15)	0% (0/15)	0% (0/24)	0% (0/24)	0% (0/24)	0% (0/24)
MAD												
<1 unit	100% (7/7)	100% (7/7)	100% (7/7)	100% (7/7)	93.3% (14/15)	100% (15/15)	53.3% (8/15)	73.3% (11/15)	100% (24/24)	100% (24/24)	100% (24/24)	100% (24/24)
>1 unit	–	–	–	–	6.7% (1/15)	–	46.7% (7/15)	26.7 (4/15)	–	–	–	–
TEM												
<1 unit	100% (7/7)	100% (7/7)	85.7% (6/7)	100% (7/7)	60% (9/15)	60% (9/15)	40% (6/15)	46.7% (7/15)	87.5% (21/24)	87.5% (21/24)	62.5% (15/24)	75% (18/24)
>1 unit	–	–	14.3% (1/7)	–	40% (6/15)	40% (6/15)	60% (9/15)	53.3% (8/15)	12.5% (3/24)	12.5% (3/24)	37.5% (9/24)	25% (6/24)
REM												
Excellent (<1%)	57.1% (4/7)	28.6% (2/7)	–	–	73.3% (11/15)	80% (12/15)	26.7% (4/15)	33.3% (5/15)	95.8% (23/24)	87.5% (21/24)	41.7% (10/24)	45.8% (11/24)
Very good (1–3.9%)	42.9% (3/7)	57.1% (4/7)	42.9% (3/7)	28.6% (2/7)	26.7% (4/15)	20% (3/15)	60% (9/15)	46.7% (7/15)	4.2% (1/24)	12.5% (3/24)	50% (12/24)	45.8% (11/24)
Good (4–6.9%)	0% (0/7)	14.3% (1/7)	28.6% (2/7)	42.9% (3/7)	–	–	6.7% (1/15)	6.7% (1/15)	–	–	4.2% (1/24)	8.3% (2/24)
Moderate (7–9.9%)	–	–	14.3% (1/7)	28.6% (2/7)	–	–	–	–	–	–	4.2% (1/24)	–
Poor (>10%)	–	–	14.3% (1/7)	–	–	–	6.7% (1/15)	6.7% (1/15)	–	–	–	–
rTEM												
Excellent (<1%)	–	–	–	–	20% (3/15)	26.7% (4/15)	46.7% (7/15)	26.7% (4/15)	–	–	–	
Very good (1–3.9%)	–	–	–	–	46.7% (7/15)	40% (6/15)	26.7% (4/15)	26.7% (4/15)	75% (18/24)	70.8% (17/24)	37.5% (9/24)	41.7% (10/24)
Good (4–6.9%)	14.3% (1/7)	–	–	–	20% (3/15)	33.3% (5/15)	–	40% (6/15)	25% (6/24)	16.7% (4/24)	45.8% (11/24)	45.8% (11/24)
Moderate (7–9.9%)	14.3% (1/7)	28.6% (2/7)	–	–	6.7% (1/15)	–	6.7% (1/15)	–	–	12.5% (3/24)	12.5% (3/24)	12.5% (3/24)
Poor (>10%)	71.4% (5/7)	71.4% (5/7)	100% (7/7)	100% (7/7)	6.7% (1/15)	–	6.7% (1/15)	6.7% (1/15)	–	–	4.2% (1/24)	–

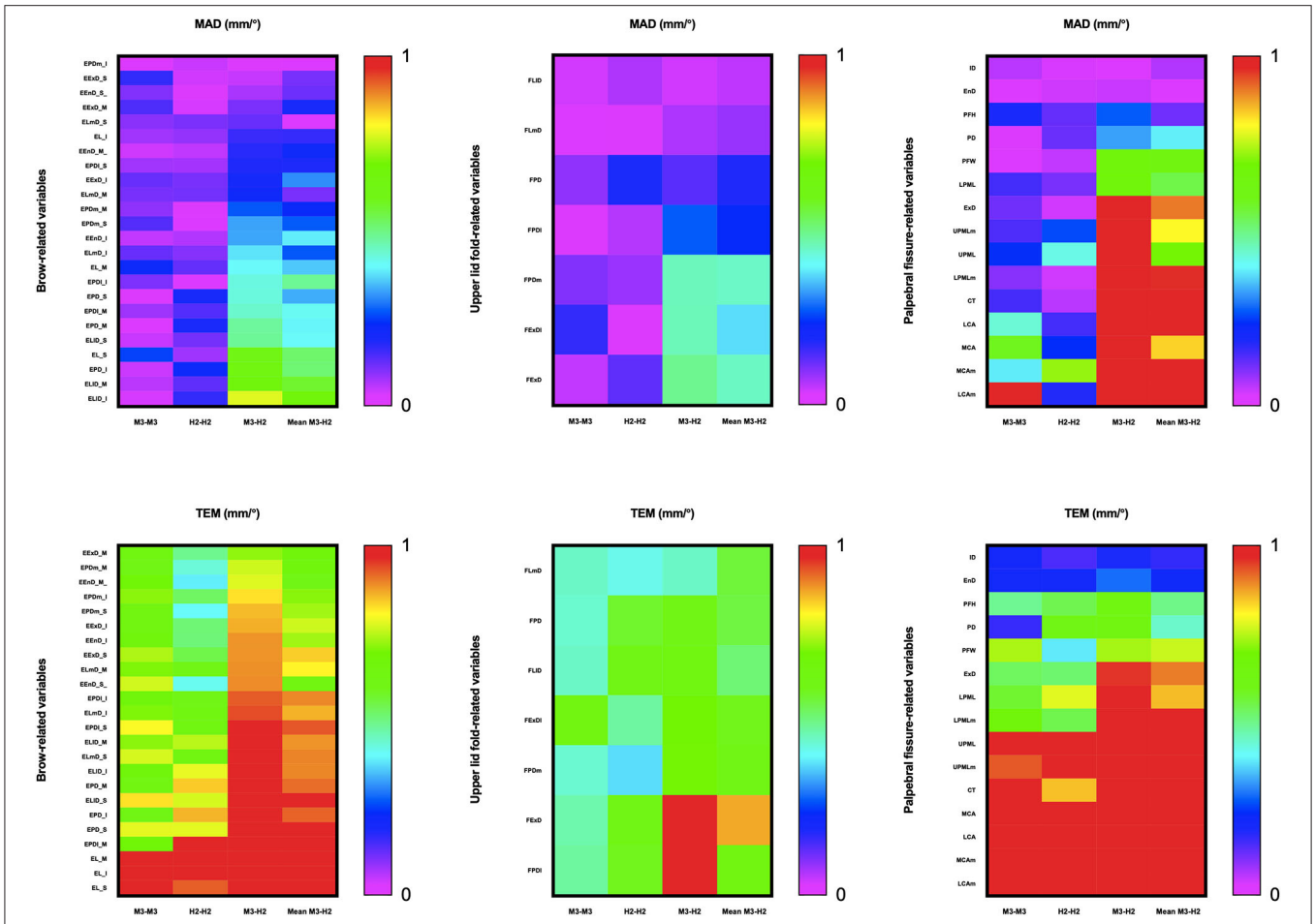

FIGURE 4 | Intra- and inter-device mean absolute difference (MAD) and technical error of measurement (TEM) for periocular measurements on all 3D images. The acceptable error threshold is set to 1 unit.

Several recent studies have validated the reliability of portable stereophotogrammetric devices for facial imaging (5, 31). Camison et al. (5) verified that the portable VECTRA H1 and static 3dMD devices were highly comparable in facial imaging: 136 linear distances had an inter-device mean rTEM value of 1.13% (range, 0.44–2.48%). Fifty-five of these distances (40.4%) were in the "excellent" category (<1%), while the remaining 81 distances (59.6%) were in the "very good" range (<3.9%) (TEM, 0.84 mm). Gibelli et al. (31) and Kim et al. (34) compared the portable VECTRA H1 device with the static VECTRA M3 device in terms of the linear, angular, surface area, and volume measurement for reliability. The results, except for the lip and periocular regions, showed high repeatability for most linear, angular, and surface area measurements in M3 vs. M3, H1 vs. H1, and M3 vs. H1 comparisons (range, 82.2–98.7%; TEM, range, 0.3–2.0 mm, 0.4–1.8 degrees; rTEM, range, 0.2–3.1%). rTEM was primarily classified to provide excellent intra-device and good inter-device comparisons. Notably, they validated the results mainly for the non-periocular regions of the face, thus assessing significant differences in the linear distance and angular type of validation. The current results are generally less reliable than previous studies, possibly due to the eye movements reported in the previous literature (35, 36). Furthermore, the measurements in the periocular region are all small, and previous studies have reported that reliability decreases as measurements decrease (37, 38).

Specifically, the highest reliability was found for most palpebral fissure-related variables in various comparisons, with rTEM primarily categorized as excellent, very good, or good within devices (M3 vs. M3: 0.26–6.39% and H2 vs. H2: 0.51–6.42%). Simultaneously, M3 and H2 comparisons were also excellent, very good, or good (0.02–5.34% and 0.66–6.20%) (first assessment and mean). The next most reliable assessment was for eyebrow-related variables, and within-device rTEM was mainly classified as very good or good (M3 vs. M3: 1.82–6.49% and H2 vs. H2: 1.33–6.02%), while M3 and H2 comparisons were also good (2.52–6.76% and 2.27–6.51%, respectively) (first evaluation and mean). The worst reliability was for the upper eyelid fold-related variables. Within-device rTEM was mainly classified as moderate or poor (M3 vs. M3: 9.88–13.87% and

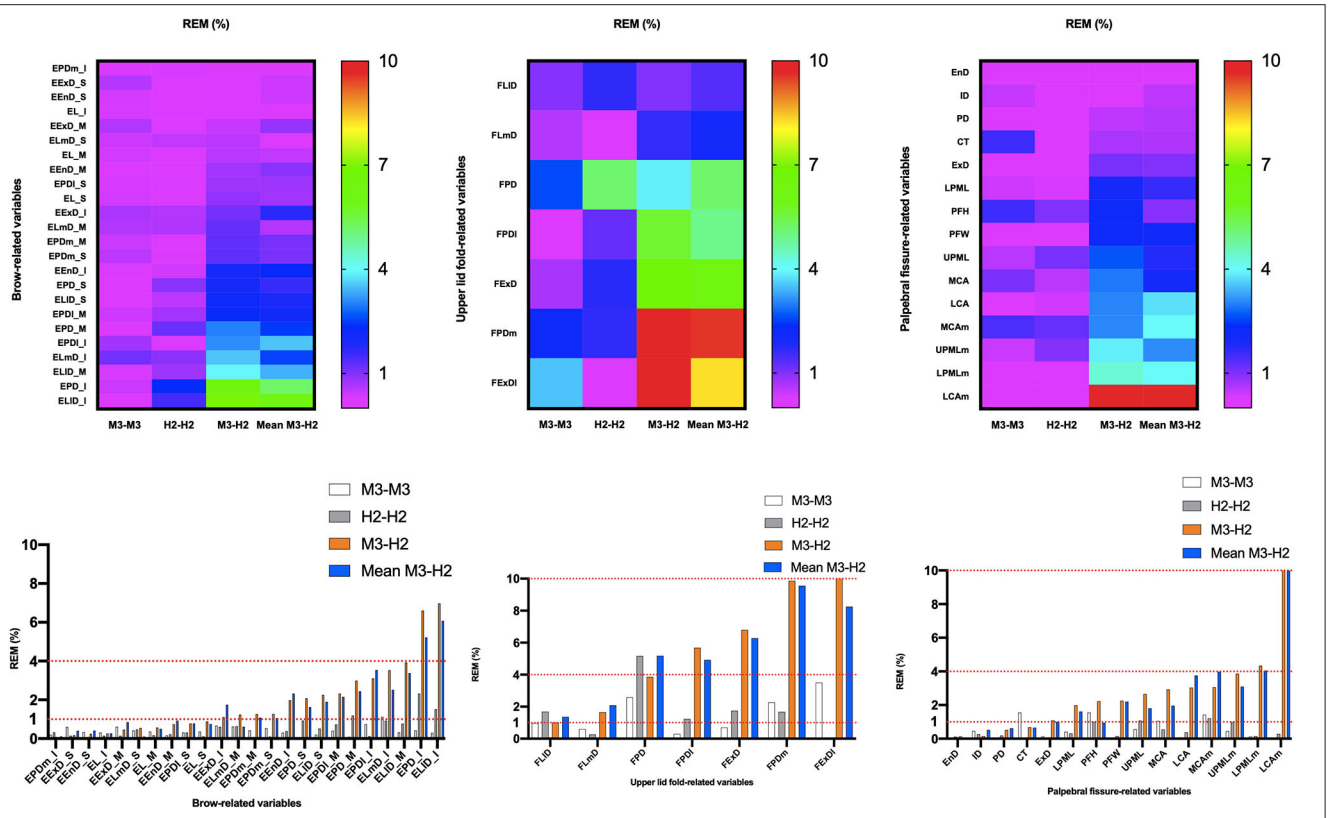

FIGURE 5 | Intra- and inter-device relative error of measurement (REM) for all periocular region measurements of 3D images. Reliability category criteria were as follows: excellent, <1%; very good, 1–3.9%; good, 4–6.9%; moderate, 7–9.9%; and poor, >10%.

H2 vs. H2: 7.65–15.76%), while M3 compared to H1 (first evaluation and mean) had poor rTEM (11.15–17.29% and 12.15–15.61%, respectively).

TEM and rTEM values were generally consistent and reliable in their respective intra-device comparisons when using M3 and H2 scans for periocular data measurements. In contrast, TEM and rTEM values deteriorated in the M3 vs. H2 comparison. This result may be due to the strong effect of involuntary head and eye movements during acquisition using the H2 device as it requires three consecutive images to be acquired, while the static M3 device acquires the same images simultaneously.

One limitation of the current study comes from the volunteers; only cooperative adults could be invited to participate because it is difficult to ensure that head, eye, and eyelid positions do not shift in children and non-cooperative individuals. Additionally, all data were collected at a fixed location, thus not fully reflecting the portability of the H2 device. Furthermore, the current study involved linear distance, curve, and angle measurements of the periocular region, without measuring its area and volume. Therefore, this study focused on comparing the differences in periocular measurements between healthy Caucasian adults on the two devices and did not include age, race, and patients in the study. Further studies should evaluate the device's reliability in different age groups, different ethnicities, bedside or other indoor settings for patients with limited mobility and the periocular area and volume measurement.

CONCLUSIONS

The intra-device reliability of the two categories of devices in this study was generally consistent, with a slightly poorer inter-device agreement. The palpebral fissure-related variables and eyebrow-related variables had good reliability both within and between devices. This validation study explored the measurement of linear distance, angle, and curve values in the periocular region with the new portable device VECTRA H2, making an essential contribution to validating the VECTRA H2 device in the periocular region. Previous studies used the earlier generation of portable devices, VECTRA H1, and mainly verified the reliability in non-ocular locations of the face. Compared to static devices, portable instruments are relatively inexpensive and location-independent, allowing photography for patients with limited mobility or in remote areas. However, it is disadvantageous in that it has slightly lower reliability than static devices. Therefore, we need to select the most suitable

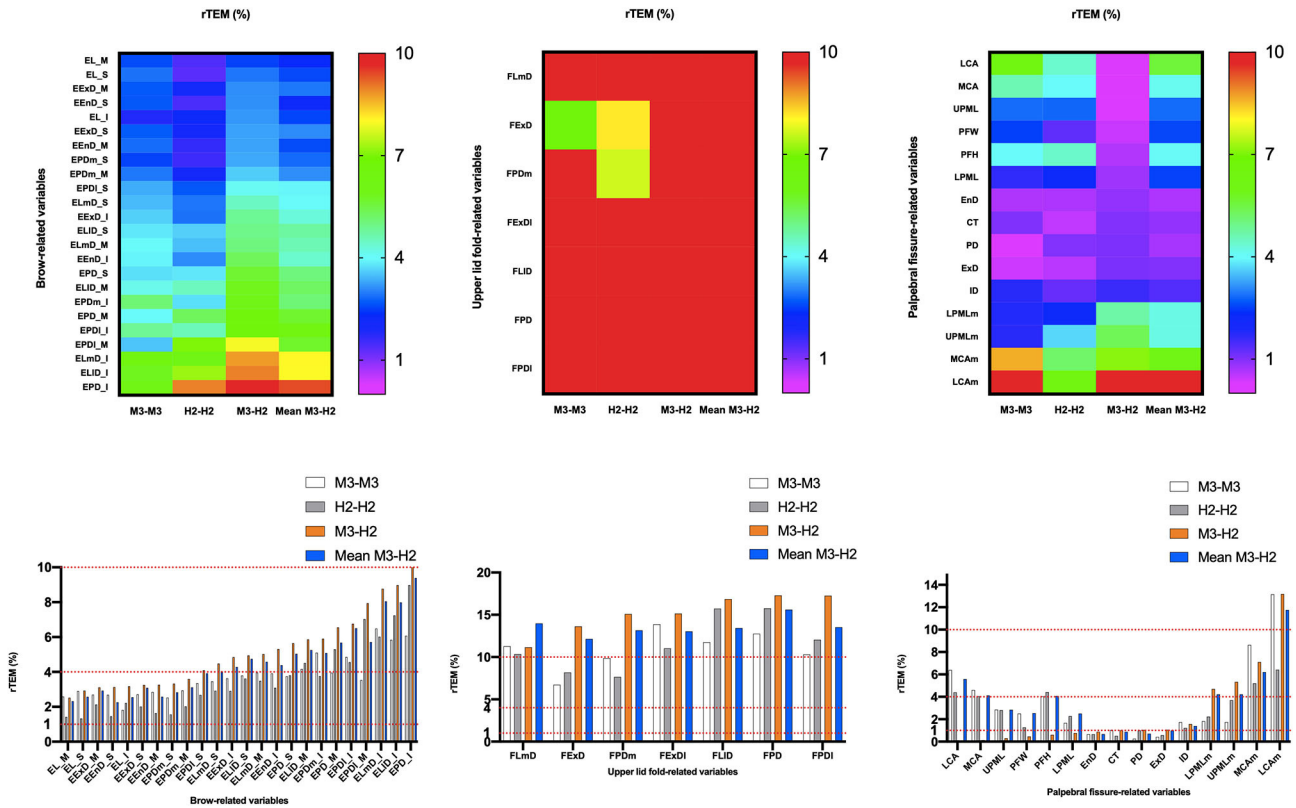

FIGURE 6 | Intra- and inter-device of relative technical error of measurement (rTEM) for all periocular region measurements of 3D images. Reliability category criteria were as follows: excellent, <1%; very good, 1–3.9%; good, 4–6.9%; moderate, 7–9.9%; and poor, >10%.

instrument for future clinical applications according to what the actual situation presents.

DATA AVAILABILITY STATEMENT

The original contributions presented in the study are included in the article/supplementary material, further inquiries can be directed to the corresponding authors.

ETHICS STATEMENT

The studies involving human participants were reviewed and approved by the Ethics Committee of Cologne University. The patients/participants provided their written informed consent to participate in this study. Written informed consent was obtained from the individual(s) for the publication of any potentially identifiable images or data included in this article.

AUTHOR CONTRIBUTIONS

WF, AR, and LH: conception, design, and provision of study materials and participants. LH: administrative support. All authors: collection and assembly of data, data analysis and interpretation, and manuscript writing. All authors contributed to the article and approved the submitted version.

FUNDING

This study was supported by State Scholarship Fund from the China Scholarship Council (No. 202008080258).

ACKNOWLEDGMENTS

The authors thank Editage (www.editage.com) for English language editing. The authors also thank Canfield Scientific GmbH, Bielefeld, Germany for providing the H2 free of charge.

REFERENCES

1. Verhulst A, Hol M, Vreeken R, Becking A, Ulrich D, Maal T. Three-dimensional imaging of the face: a comparison between three different imaging modalities. *Aesthetic Surg J.* (2018) 38:579–85. doi: 10.1093/asj/sjx227

2. Choi JW, Lee JY, Oh T-S, Kwon SM, Yang SJ, Koh KS. Frontal soft tissue analysis using a 3 dimensional camera following two-jaw rotational orthognathic surgery in skeletal class III patients. *J Cranio Maxillofacial Surg.* (2014) 42:220–6. doi: 10.1016/j.jcms.2013.05.004

3. Jung J, Lee CH, Lee JW, Choi BJ. Three dimensional evaluation of soft tissue after orthognathic surgery. *Head Face Med.* (2018) 14:21. doi: 10.1186/s13005-018-0179-z
4. Terzic A, Schouman T, Scolozzi P. Accuracy of morphological simulation for orthognatic surgery. Assessment of a 3D image fusion software. *Rev Stomatol Chir Maxillofac Chir Orale.* (2013) 114:276–82. doi: 10.1016/j.revsto.2013.06.007
5. Camison L, Bykowski M, Lee WW, Carlson JC, Roosenboom J, Goldstein JA, et al. Validation of the Vectra H1 portable three-dimensional photogrammetry system for facial imaging. *Int J Oral Maxillofacial Surg.* (2018) 47:403–10. doi: 10.1016/j.ijom.2017.08.008
6. Meier JD, Glasgold RA, Glasgold MJ. 3D photography in the objective analysis of volume augmentation including fat augmentation and dermal fillers. *Facial Plast Surg Clin North Am.* (2011) 19:725–35, ix. doi: 10.1016/j.fsc.2011.07.012
7. Miller TR. Long-term 3-dimensional volume assessment after fat repositioning lower blepharoplasty. *JAMA Facial Plast Surg.* (2016) 18:108–13. doi: 10.1001/jamafacial.2015.2184
8. Jacono AA, Bryant LM, Ahmedli NN. A novel extended deep plane facelift technique for jawline rejuvenation and volumization. *Aesthet Surg J.* (2019) 39:1265–81. doi: 10.1093/asj/sjy292
9. Kunjur J, Sabesan T, Ilankovan V. Anthropometric analysis of eyebrows and eyelids: an inter-racial study. *Br J Oral Maxillofac Surg.* (2006) 44:89–93. doi: 10.1016/j.bjoms.2005.03.020
10. Liu Y, Kau CH, Pan F, Zhou H, Zhang Q, Zacharopoulos GV. A 3-dimensional anthropometric evaluation of facial morphology among Chinese and Greek population. *J Craniofac Surg.* (2013) 24:e353–8. doi: 10.1097/SCS.0b013e3182902e5d
11. Erbagci I, Erbagci H, Kizilkan N, Gumusburun E, Bekir N. The effect of age and gender on the anatomic structure of Caucasian healthy eyelids. *Saudi Med J.* (2005) 26:1535–8.
12. Sforza C, Grandi G, Catti F, Tommasi DG, Ugolini A, Ferrario VF. Age- and sex-related changes in the soft tissues of the orbital region. *Forensic Sci Int.* (2009) 185:115.e1–8. doi: 10.1016/j.forsciint.2008.12.010
13. Cartwright MJ, Kurumety UR, Nelson CC, Frueh BR, Musch DC. Measurements of upper eyelid and eyebrow dimensions in healthy white individuals. *Am J Ophthalmol.* (1994) 117:231–4. doi: 10.1016/S0002-9394(14)73081-8
14. Metzler P, Sun Y, Zemann W, Bartella A, Lehner M, Obwegeser JA, et al. Validity of the 3D VECTRA photogrammetric surface imaging system for cranio-maxillofacial anthropometric measurements. *Oral Maxillofacial Surg.* (2014) 18:297–304. doi: 10.1007/s10006-013-0404-7
15. Dindaroglu F, Kutlu P, Duran GS, Görgülü S, Aslan E. Accuracy and reliability of 3D stereophotogrammetry: a comparison to direct anthropometry and 2D photogrammetry. *Angle Orthodontist.* (2016) 86:487–94. doi: 10.2319/041415-244.1
16. Modabber A, Peters F, Kniha K, Goloborodko E, Ghassemi A, Lethaus B, et al. Evaluation of the accuracy of a mobile and a stationary system for three-dimensional facial scanning. *J Cranio Maxillofacial Surg.* (2016) 44:1719–24. doi: 10.1016/j.jcms.2016.08.008
17. Guo Y, Schaub F, Mor JM, Jia R, Koch KR, Heindl LM. A simple standardized three-dimensional anthropometry for the periocular region in a European population. *Plast Reconstr Surg.* (2020) 145:514e−23e. doi: 10.1097/PRS.0000000000006555
18. Guo Y, Rokohl AC, Lin M, Heindl LM. Three-dimensional anthropometry in periorbital region. *Ann Eye Sci.* (2020) 6:8. doi: 10.21037/aes-20-99
19. Hou X, Rokohl AC, Meinke MM, Li S, Liu J, Fan W, et al. A novel standardized distraction test to evaluate lower eyelid tension using three-dimensional stereophotogrammetry. *Quantitative Imaging Med Surg.* (2021) 11:3735–48. doi: 10.21037/qims-20-1016
20. Hou X, Rokohl AC, Meinke MM, Liu J, Li S, Fan W, et al. Standardized three-dimensional lateral distraction test: its reliability to assess medial canthal tendon laxity. *Aesthetic Plast Surg.* (2021) 45:2798–807. doi: 10.1007/s00266-021-02440-y
21. Guo Y, Rokohl AC, Schaub F, Hou X, Liu J, Ruan Y, et al. Reliability of periocular anthropometry using three-dimensional digital stereophotogrammetry. *Graefes Arch Clin Exp Ophthalmol.* (2019) 257:2517–31. doi: 10.1007/s00417-019-04428-6
22. Guo Y, Hou X, Rokohl AC, Jia R, Heindl LM. Reliability of periocular anthropometry: a comparison of direct, 2-dimensional, 3-dimensional techniques. *Dermatol Surg.* (2020) 46:e23–31. doi: 10.1097/DSS.0000000000002243
23. Guo Y, Liu J, Ruan Y, Rokohl AC, Hou X, Li S, et al. A novel approach quantifying the periorbital morphology: a comparison of direct, 2-dimensional, 3-dimensional technologies. *J Plast Reconstr Aesthet Surg.* (2021) 74:1888–99. doi: 10.1016/j.bjps.2020.12.003
24. Liu J, Guo Y, Arakelyan M, Rokohl AC, Heindl LM. Accuracy of areal measurement in the periocular region using stereophotogrammetry. *J Oral Maxillofac Surg.* (2021) 79:1106.e1–9. doi: 10.1016/j.joms.2020.12.015
25. Liu J, Rokohl AC, Guo Y, Li S, Hou X, Fan W, et al. Reliability of stereophotogrammetry for area measurement in the periocular region. *Aesthetic Plast Surg.* (2021) 45:1601–10. doi: 10.1007/s00266-020-02091-5
26. Tzou C-HJ, Artner NM, Pona I, Hold A, Placheta E, Kropatsch WG, et al. Comparison of three-dimensional surface-imaging systems. *J Plastic Reconstructive Aesthetic Surg.* (2014) 67:489–97. doi: 10.1016/j.bjps.2014.01.003
27. Birgfeld CB, Saltzman BS, Luquetti DV, Latham K, Starr JR, Heike CL. Comparison of two-dimensional and three-dimensional images for phenotypic assessment of craniofacial microsomia. *Cleft Palate Craniofac J.* (2013) 50:305–14. doi: 10.1597/11-173
28. Naudi KB, Benramadan R, Brocklebank L, Ju X, Khambay B, Ayoub A. The virtual human face: superimposing the simultaneously captured 3D photorealistic skin surface of the face on the untextured skin image of the CBCT scan. *Int J Oral Maxillofac Surg.* (2013) 42:393–400. doi: 10.1016/j.ijom.2012.10.032
29. Yamamoto S, Miyachi H, Fujii H, Ochiai S, Watanabe S, Shimozato K. Intuitive facial imaging method for evaluation of postoperative swelling: a combination of 3-dimensional computed tomography and laser surface scanning in orthognathic surgery. *J Oral Maxillofac Surg.* (2016) 74:2506.e1–10. doi: 10.1016/j.joms.2016.08.039
30. Knoops PG, Beaumont CA, Borghi A, Rodriguez-Florez N, Breakey RW, Rodgers W, et al. Comparison of three-dimensional scanner systems for craniomaxillofacial imaging. *J Plast Reconstr Aesthet Surg.* (2017) 70:441–9. doi: 10.1016/j.bjps.2016.12.015
31. Gibelli D, Pucciarelli V, Cappella A, Dolci C, Sforza C. Are portable stereophotogrammetric devices reliable in facial imaging? A validation study of VECTRA H1 device. *J Oral Maxillofac Surg.* (2018) 76:1772–84. doi: 10.1016/j.joms.2018.01.021
32. Ulijaszek SJ, Kerr DA. Anthropometric measurement error and the assessment of nutritional status. *Br J Nutr.* (1999) 82:165–77. doi: 10.1017/S0007114599001348
33. Andrade LM, Rodrigues da Silva AMB, Magri LV, Rodrigues da Silva MAM. Repeatability study of angular and linear measurements on facial morphology analysis by means of stereophotogrammetry. *J Craniofac Surg.* (2017) 28:1107–11. doi: 10.1097/SCS.0000000000003554
34. Kim AJ, Gu D, Chandiramani R, Linjawi I, Deutsch ICK, Allareddy V, et al. Accuracy and reliability of digital craniofacial measurements using a small-format, handheld 3D camera. *Orthod Craniofac Res.* (2018) 21:132–9. doi: 10.1111/ocr.12228
35. de Menezes M, Rosati R, Allievi C, Sforza C. A photographic system for the three-dimensional study of facial morphology. *Angle Orthod.* (2009) 79:1070–7. doi: 10.2319/111008-570
36. Ferrario VF, Sforza C, Poggio CE, Cova M, Tartaglia G. Preliminary evaluation of an electromagnetic three-dimensional digitizer in facial anthropometry. *Cleft Palate Craniofac J.* (1998) 35:9–15. doi: 10.1597/1545-1569(1998)035<0009:PEOAET>2.3.CO;2
37. Jamison PL, Ward RE. Brief communication: measurement size, precision, and reliability in craniofacial anthropometry: bigger is better. *Am J Phys Anthropol.* (1993) 90:495–500. doi: 10.1002/ajpa.1330900409

38. Ward RE, Jamison PL. Measurement precision and reliability in craniofacial anthropometry: implications and suggestions for clinical applications. *J Craniofac Genet Dev Biol.* (1991) 11:156–64.

Conflict of Interest: The authors declare that the research was conducted in the absence of any commercial or financial relationships that could be construed as a potential conflict of interest.

Publisher's Note: All claims expressed in this article are solely those of the authors and do not necessarily represent those of their affiliated organizations, or those of the publisher, the editors and the reviewers. Any product that may be evaluated in this article, or claim that may be made by its manufacturer, is not guaranteed or endorsed by the publisher.

frontiers | Frontiers in Medicine

REVIEW
published: 04 April 2022
doi: 10.3389/fmed.2022.864824

Functional Optical Coherence Tomography for Intrinsic Signal Optoretinography: Recent Developments and Deployment Challenges

Tae-Hoon Kim[1], *Guangying Ma*[1], *Taeyoon Son*[1] *and Xincheng Yao*[1,2]*

[1] Richard and Loan Hill Department of Biomedical Engineering, University of Illinois at Chicago, Chicago, IL, United States,
[2] Department of Ophthalmology and Visual Sciences, University of Illinois at Chicago, Chicago, IL, United States

Intrinsic optical signal (IOS) imaging of the retina, also termed as optoretinogram or optoretinography (ORG), promises a non-invasive method for the objective assessment of retinal function. By providing the unparalleled capability to differentiate individual retinal layers, functional optical coherence tomography (OCT) has been actively investigated for intrinsic signal ORG measurements. However, clinical deployment of functional OCT for quantitative ORG is still challenging due to the lack of a standardized imaging protocol and the complication of IOS sources and mechanisms. This article aims to summarize recent developments of functional OCT for ORG measurement, OCT intensity- and phase-based IOS processing. Technical challenges and perspectives of quantitative IOS analysis and ORG interpretations are discussed.

Keywords: optoretinography, intrinsic optical signal imaging, retina, phototransduction, optical coherence tomography, retinography, functional retinal imaging, photoreceptor

OPEN ACCESS

Edited by:
Peng Xiao,
Sun Yat-sen University, China

Reviewed by:
Jin Yuan,
Sun Yat-sen University, China
Rene Werkmeister,
Medical University of Vienna, Austria

***Correspondence:**
Xincheng Yao
xcy@uic.edu

Specialty section:
This article was submitted to Ophthalmology, a section of the journal Frontiers in Medicine

Received: *28 January 2022*
Accepted: *16 March 2022*
Published: *04 April 2022*

Citation:
Kim T-H, Ma G, Son T and Yao X (2022) Functional Optical Coherence Tomography for Intrinsic Signal Optoretinography: Recent Developments and Deployment Challenges. Front. Med. 9:864824. doi: 10.3389/fmed.2022.864824

INTRODUCTION

The retina is a neurovascular network complex that can be frequently affected by eye diseases such as age-related macular degeneration (AMD), diabetic retinopathy (DR), glaucoma, and inherited retinal dystrophies (IRDs). Optical imaging methods, such as light fundus photography and fluorescein angiography (1–3), can reveal morphological abnormalities for eye disease diagnosis and treatment assessment. Scanning laser ophthalmoscopy (SLO) (4, 5) can provide improved spatial resolution and image contrast. Optical coherence tomography (OCT) (6, 7) can provide depth-resolved, cross-sectional images of individual retinal neural layers. As one special OCT modality, OCT angiography (OCTA) (8–11) can enhance the visibility of individual retinal capillary plexuses. Adaptive optics (AO) can be incorporated to enhance the resolution of the fundus camera (12, 13), SLO (14, 15), and OCT (16–18). These methods for morphological imaging of the retina provide vital information for clinical management of eye diseases.

However, retinal diseases are often quite advanced before they draw clinical attention, by which time the retina may be functionally abnormal. Structural and functional abnormalities in the retina

are often not correlated in the spatial location and time window. Therefore, an objective method for functional assessment of the retina promises early detection and longitudinal therapeutic assessment of retinal degenerative diseases. Electroretinography (ERG) and multifocal ERG (19, 20) can objectively assess retinal physiological function. However, separate morphological imaging and functional measurement can be costly and time-consuming. Moreover, different spatial resolutions of morphological imaging and functional measurement may challenge clinical evaluation.

Intrinsic optical signal (IOS) imaging of the retina (21–29), also termed as optophysiology (30), optoretinogram (31–35), or optoretinography (25, 36–40) (ORG), promises a non-invasive method for objective assessment of retinal physiological function. The terminology ORG is an analogy to ERG. ERG is based on the electrical measurement of stimulus-evoked electrophysiological activities, while ORG refers to IOS imaging of corresponding light property changes in the retina due to functional activity. Time-lapse light microscopy and fundus camera have been used for two-dimensional IOS imaging study of isolated retinal tissues and intact eyes (21, 22, 28). By providing the unparalleled capability to differentiate individual layers of the retina, OCT has been actively used for IOS imaging of animal and human retinas (25, 29, 31–45). OCT is an interferometric imaging technique that acquires interference fringe patterns generated by the superposition of back-scattered lights from the sample and reference arms. The Fourier transform of the fringe patterns provides intensity information on the scattering object and allows access to information about the axial position of the scattering object within the retina. Thus, intensity and phase information has been utilized in quantifying the stimulus-evoked IOS in the retina. However, clinical deployment of the OCT-based ORG is still challenging due to the lack of a standardized imaging protocol and the complication of signal sources and physiological mechanisms. In the following sections, we will summarize recent developments of functional OCT systems for IOS imaging, OCT intensity and phase-based processing for quantitative IOS analysis. Technical challenges and perspectives of quantitative ORG measurement and interpretation will be discussed.

FUNCTIONAL OCT DEVELOPMENTS FOR INTRINSIC SIGNAL ORG

The retina is thin, transparent, and stratified into distinct cellular layers. Since the stimulus-evoked retinal activity was found to alter intrinsic optical properties at different layers, OCT has been actively investigated for depth-resolved IOS imaging (22, 34). Both time-domain and Fourier-domain OCT systems have been demonstrated for IOS imaging. Time-domain OCT was first demonstrated for depth-resolved observation of IOS in the freshly isolated frog (29) and rabbit (30) retinas. Fourier-domain OCT was later employed to validate *in vivo* IOS imaging of intact rat eyes (46). A hybrid line-scan SLO and OCT system was also employed for confocal-OCT IOS imaging study of isolated retinas (47). Given the improved imaging speed, Fourier-domain OCT has dominated recent IOS imaging studies of both animal (33, 35, 37, 39, 42, 44, 48–52) and human (25, 31, 32, 36, 37, 53–55) retinas.

Figure 1 shows an exemplary Fourier-domain OCT system used for IOS imaging of the human retina. The system is a point-scan spectral-domain OCT, commonly used for clinical and research purposes. A fixation target is used to minimize eye movements during imaging. The system consists of two light sources, one near infrared superluminescent diode (SLD) for OCT imaging, and a visible light source to produce retinal stimulation. The OCT probe beam is raster-scanned over the retinal tissue. A pupil camera helps to align the OCT probe beam for optimal light incidence through the pupil (**Figure 1B1**) and to measure the time course of pupillary light response (**Figure 1B2**). The recording speed is 100 B-scan/s at a 70 kHz A-scan rate. Point-scan OCT benefits from the confocal aperture of the single-mode fiber that rejects multiply scattered light. However, imaging speed is limited for volumetric data acquisition.

Line-scan (40) or full-field (57) OCT can significantly improve the imaging speed by the parallel acquisition of lateral and axial information. Full-field OCT allows imaging without lateral phase noise by employing a collimated illumination over the retinal area with detection by a 2D camera. High-speed 3D imaging can reduce intraframe eye movement artifacts, which permits robust registration of frames and tracking of photoreceptors, returning stable OCT phase information. Access to stable phase information allows detecting cellular deformations much smaller than its axial resolution, and the phase information has been recently used to measure light-evoked photoreceptor outer segment (OS) deformation (32, 36, 55, 58). However, the parallel OCT suffers resolution loss from multiple scattering crosstalk. In addition, a tradeoff for increasing imaging speed is a reduction in the imaging area.

AO can be incorporated to improve further the OCT spatial resolution (36, 40). The AO subsystem generally consists of three elements, including the wavefront sensor, the deformable mirror, and the control computer to dynamically measure and correct low- and high-order wavefront aberrations of the eye. The current state-of-art AO-OCT system has the resolution to reveal the 3D reflectance profile of individual cone photoreceptors and provide sufficient sensitivity to detect light-evoked optical path length (OPL) changes as small as 5 nm in the individual cones (36). Azimipour et al. (31) further demonstrated a combined AO-SLO-OCT for ORG measurement of rod and cone photoreceptors in the human retina. The SLO was utilized to guide the type and location of photoreceptors in the OCT volume. However, clinical deployment of AO-OCT is still challenging due to technical factors such as high cost, optical complexity, system size, data volume, and image postprocessing (59).

OCT DATA PROCESSING FOR INTRINSIC SIGNAL ORG

Both intensity and phase-based processing methods have been developed to quantify the stimulus-evoked IOS in the retina.

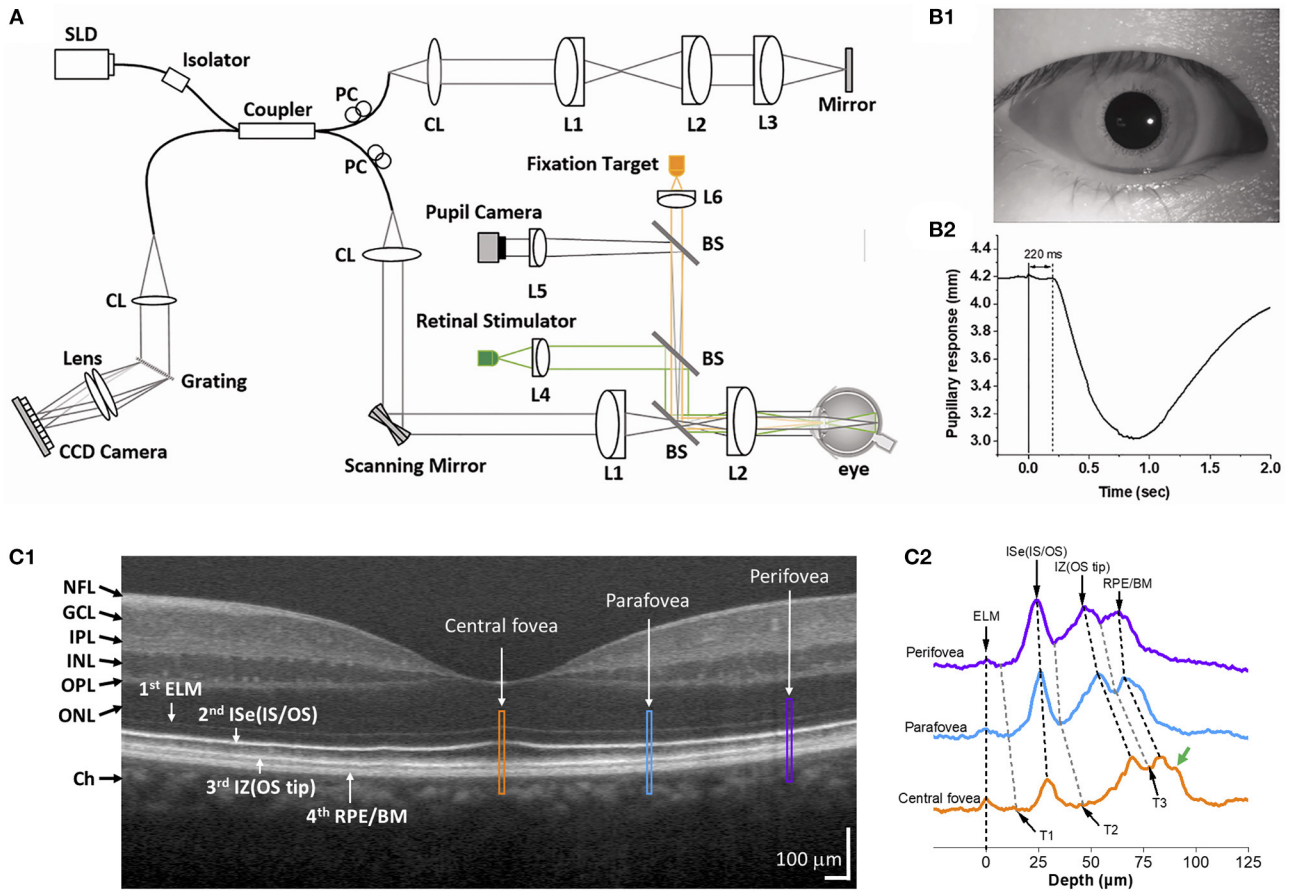

FIGURE 1 | (A) Representative functional OCT system for IOS/ORG imaging. BS, beam splitter; CL, collimation lens; Lenses, L1, L2, L3, L4, L5, and L6; PC, polarization controller; SLD, superluminescent diode. **(B)** Representative pupil image **(B1)** and pupillary response **(B2)**. Reprinted with permission from Son et al. (25). **(C1)** Representative OCT B-scan of the human retina and **(C2)** reflectance profiles of the central fovea (yellow), parafovea (blue), and perifovea (purple). Yellow, blue, and purple windows in **(C1)** indicate retinal regions for comparative reflectance profile analysis. The green arrow in **(C2)** indicates a possible band, i.e., Bruch's membrane. T1–T3 indicate trough positions along the reflectance profiles. NFL, nerve fiber layer; GCL, ganglion cell layer; IPL, inner plexiform layer; INL, inner nuclear layer; OPL, outer plexiform layer; ONL, outer nuclear layer; ELM, external limiting membrane; ISe, inner segment ellipsoid; OS, outer segment; IZ, interdigitation zone; RPE, retinal pigment epithelium; BM, Bruch's membrane. Modified with permission from Yao et al. (56).

OCT Intensity-Based IOS Processing

The OCT intensity-based IOS processing can be divided into two categories: OCT brightness change and OCT band analysis. The intensity-based processing takes advantage of the fact that morphological deformation of the retinal neurons can directly affect IOS, and physiological activities in the retinal neurons and vasculature can cause local variation of optical properties, such as refractive index, scattering, reflection, or birefringence.

OCT Brightness Analysis

The OCT brightness change analysis was devised to detect local variations in pixel intensity value due to light stimulus within the retina. Previous studies using brightness change analysis detected localized IOS change both in the inner and outer retina (42, 51, 60–62). **Figure 2** illustrates representative time-lapse OCT recording and a result from the brightness change analysis (63). The data processing is described as follows (42, 62, 64). First, raw OCT B-scans need to be registered to compensate for eye movements by a sub-pixel registration algorithm. The intensity of each pixel can then be normalized based on the inner retinal intensity to limit the effect of pupillary response (25). Next, from a sequence of the registered B-scans, the "active" IOS pixels are identified. Any pixel that significantly changes its intensity value after the light stimulus is identified as the active-IOS pixel, which can be either positive (intensity increased) or negative sign (intensity decreased). The number of active IOS pixels can be quantified for comparative study (39, 64). In addition, the intensity value of active IOS pixels can be traced over time after subtracting the background pixel intensity value from pre-stimulus B-scans (61, 63). **Figure 2** demonstrates that light-evoked positive (red) and negative (green) IOSs were observed in the human retina. As shown in **Figures 2B–D**, the fast IOS was promptly observed after stimulus onset and primarily confined within the photoreceptor region. Since ∼220 ms time window was available without pupillary response (**Figure 1B2**), it would be feasible to monitor the fast photoreceptor-IOS in

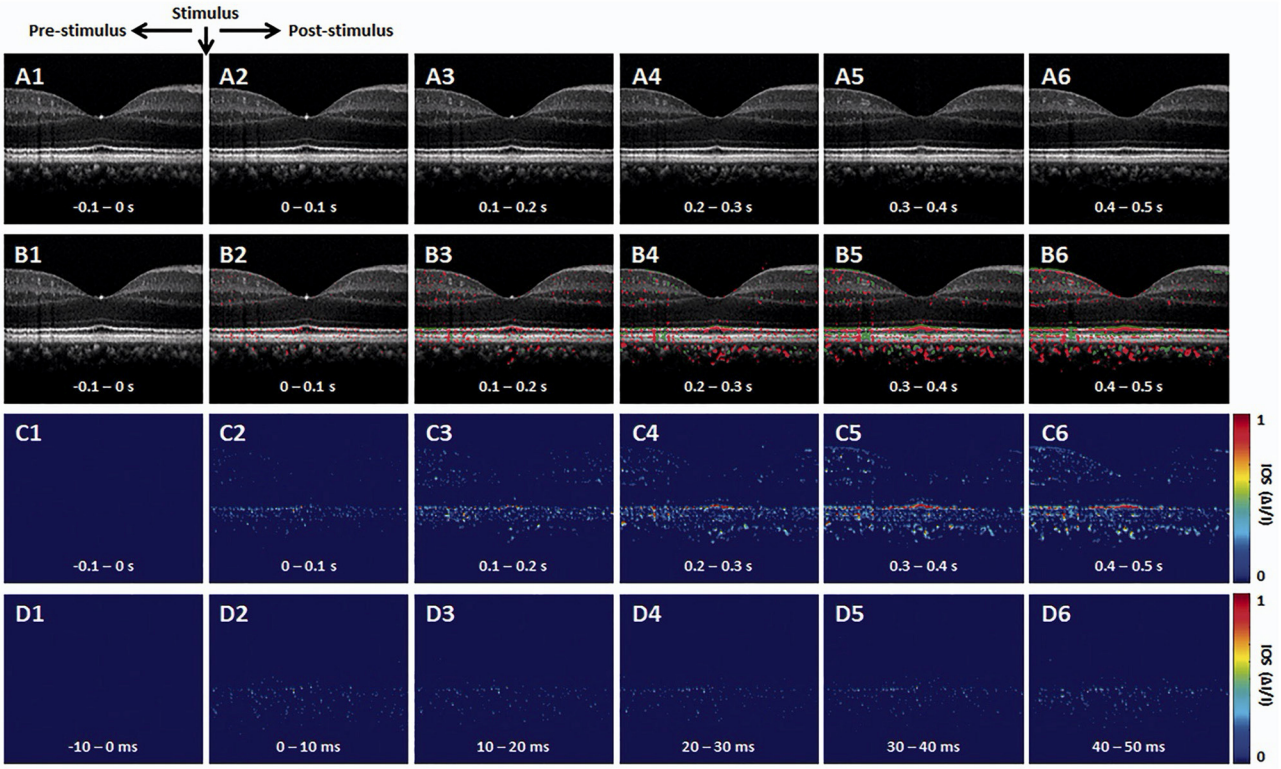

FIGURE 2 | Representative OCT intensity-based IOS imaging. **(A)** Representative OCT image sequence. **(B)** Corresponding IOS distributions of positive (red) and negative (green) changes. **(C)** IOS magnitude sequence with 0.1 s time intervals. **(D)** IOS magnitude sequence with 10 ms time intervals. Reprinted with permission from Son et al. (25).

non-mydriatic conditions (25). The brightness analysis has been demonstrated for robust detection of transient photoreceptor response; however, further investigation is needed to scrutinize IOS origin from the inner retina.

OCT Band Analysis

The retina is stratified into multiple-layered structures. OCT can probe the axial position of each neural and synaptic layer and visualize these layers as hyper- and hypo-reflective bands. Measuring the band alterations under different light conditions is one of the critical parameters in ORG measurement (35, 54, 65–67). There is a growing interest, especially in assessing outer retinal bands, such as photoreceptor inner segment (IS), OS, and subretinal space (SRS), and retinal pigment epithelium (RPE).

Figure 3 illustrates outer retinal bands and analysis methods. Zhang et al. demonstrated a deconvolution method for band analysis in the mouse retina (**Figure 3A**). OCT spectra were initially Fourier transformed after four times zero-padding, and the resultant A-scan profiles were remapped onto a linear scale. Next, they used deconvolution to extract additional information from the hyperreflective bands. Specifically, the averaged A-line profiles were deconvolved with the MATLAB "deconvlucy" function, and the hyperreflective bands from each time point fitted with Gaussian functions, providing three parameters (position, amplitude, and full width at half maximum) that can be used for OCT band analysis. This method was used to measure the length of photoreceptor OS over the diurnal cycle in albino mice (35). Messner et al. demonstrated modeling the OCT A-line profiles by fitting normal distribution curves and observing their position changes over time in the human retina (**Figure 3B**). To better determine the position of outer retinal bands, a signal model for the A-scan averages was developed in the software OriginPro 2019b using the "multiple peak fitting" function. The signal model for the A-scan average provided quantitative parameters by tracking the position of the peaks attributed to the boundaries of the outer retinal layers during baseline and stimulation conditions (54). In addition, Kim et al. recently demonstrated transient band shifting during the initial dark adaptation period in the mouse retina. The high-speed imaging recorded repeated B-scans at the same retinal plane for 5-min dark-adaptation. The volumetric average was conducted for OCT A-line band analysis, and linear interpolation was employed to enhance the sampling density of the average A-line band analysis (65). Yao et al. suggested a more detailed band analysis by accounting for not only hyper-reflective band location but also relative distances between hyper- and hypo-reflective bands to better establish the correlation of each band to the outer retina structure (**Figure 1C2**). This approach may provide additional insight into the outer retinal structure and its dynamics under different light conditions (56). The band analysis

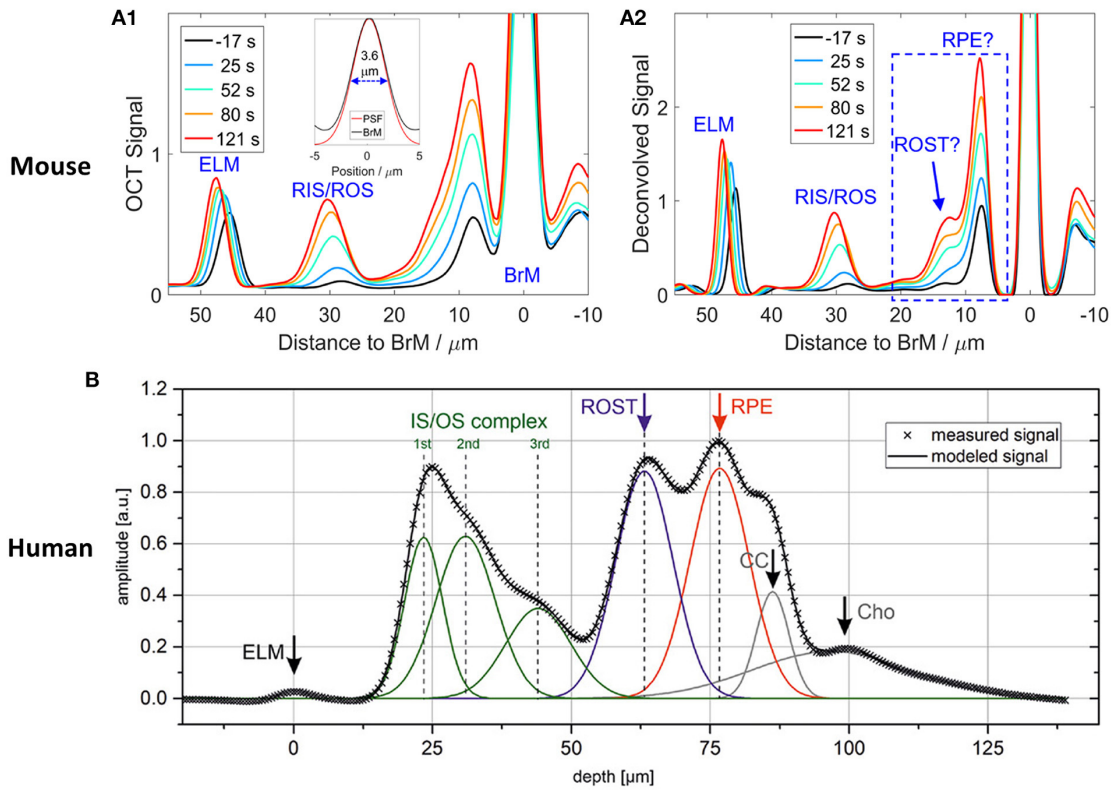

FIGURE 3 | Representative OCT hyper-reflective band analysis. **(A)** Deconvolution method. **(A1)** Depth scattering profiles of the retina of an albino mouse. **(A2)** Deconvolution analysis reveals that the backscatter band nearest to Bruch's membrane (BrM) on the anterior side comprises two distinct components (question marks are used to indicate that the assignment to structures required confirmation). Reprinted with permission from Zhang et al. (35). **(B)** A-line signal modeling by summation of seven Gaussian curves. Gray crosses represent the measured data points, and the black line is the summation of the individual model curves (green, blue, red, and gray lines). ELM, external limiting membrane; IS/OS, inner segment/outer segment complex; ROST, rod outer segment tips; RPE, retinal pigment epithelium; CC, choriocapillaris; Cho, choroid. Reprinted with permission from Messner et al. (54).

requires clear boundary information, and better axial resolution can resolve more detailed morphological alterations. It should also be noted that the band composition is different depending on the eccentricity (56), and different normalization methods can directly impact outputs.

OCT Phase-Based Processing

Evaluation of the phase of interference fringes allows access to information about OPL changes. Given a pair of clear hyper-reflective bands resolved within the retina, the recent development of phase-resolved OCT can offer sensitivities to photoreceptor OS deformation on a nanometer scale, much smaller than the axial resolution of the OCT system.

OCT Band Boundary Measurements for Optical Path Length Estimation

Given the premise that the photoreceptor OSs change in length by light stimulus, OCT phase information has been used to estimate the OPL change of photoreceptor OSs. The photoreceptor OS is long and narrow; thus, it behaves like an optical waveguide (68). In addition, there are relatively strong reflections from each end of the photoreceptor (IS/OS junction and OS tip), well suited for OPL estimation using hyper-reflective band positions. Recent advances in parallel OCT and incorporated AO subsystem enable the measurement of stable phase information. Since the phase in a single layer does not carry information to evaluate the length change of the photoreceptors, it is necessary to compare two phases between two different retinal layers and between two different time points. **Figure 4** demonstrates phase-resolved OCT imaging for OPL estimation. The data processing is described as follows (55). First, the recorded OCT volumes were reconstructed, and each pixel of each reconstructed volume was then referenced to the respective co-registered pixel in one specific volume. Next, the retinal layers carrying the information about the OS length need to be segmented. Two layers used for segmentation are generally photoreceptor OS tips (POST) and inner-outer segment junction (IS/OS). In general, several axial pixels are averaged centered around the peak point of each layer. The temporal evolution of optical phase difference is then computed between the POST and IS/OS (Φ_{POST} - Φ_{ISOS}) to yield a measure of light-induced relative phase changes between POST and IS/OS. The phase difference at

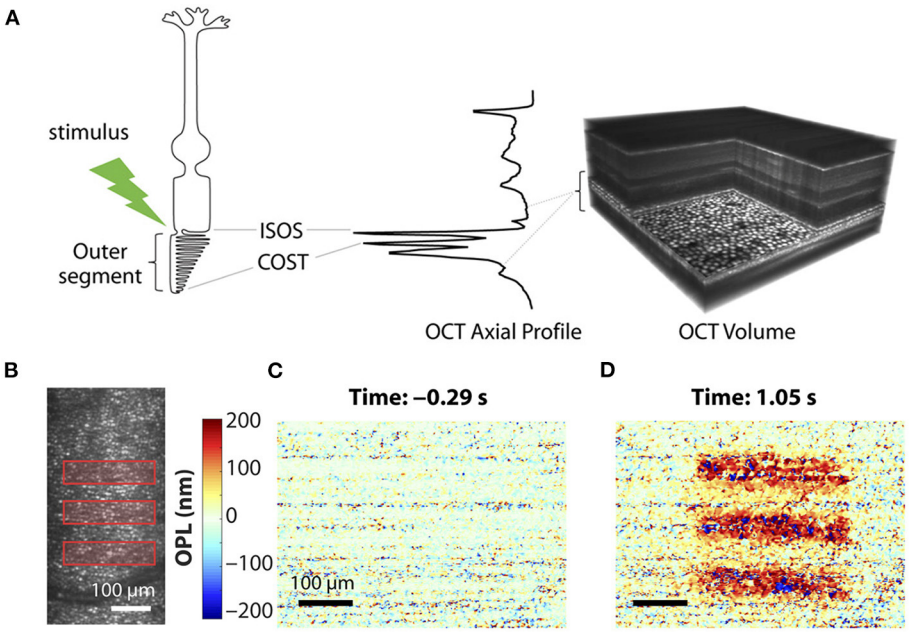

FIGURE 4 | Phase-resolved OCT imaging for optical path length (OPL) estimation. **(A)** Optoretinography experimental paradigm. A three-dimensional (3D) OCT volume with AO allows resolving the cone mosaic in an en face projection and the outer retinal layers in an axial profile corresponding to the ISOS and COST. Stimulus (528 ± 20 nm, green)–driven changes in a cone photoreceptor are accessible by computing the time-varying phase difference between the proximal and distal OCT reflections encasing the outer segment. **(B)** Optoretinography reveals functional activity in cone outer segments. Illumination pattern (three bars) drawn to scale over the line-scan ophthalmoscopic image. **(C,D)** The spatial map of OPL changes between the ISOS and COST before **(C)** and after stimulus **(D)**, measured at 20-Hz volume rate. Reprinted with permission from Pandiyan et al. (32).

the two layers is then converted to OPL using the relation $\Delta OPL = (\lambda_c/4\pi) \times (\Phi_{COST} - \Phi_{ISOS})$, where λ_c = central wavelength of OCT light source. A study showed that the magnitude of these OPL changes was strongly correlated with light-induced activity, and they utilized this correlation to classify three cone classes (69). In principle, relative OPL changes between any two layers, including inner retinal layers, can be estimated (70); however, the two boundaries must present clear peak bands with a high signal-to-noise ratio. The stability of phase data is crucial in the OPL estimation and is often corrupted by ocular movements. Thus, the phase-resolved ORG measurement generally requires ultrahigh-speed recording and voxel-wise registration. It should also be noted that different shapes of cone OSs presented from the central fovea to the parafovea may affect OPL estimation (71).

Differential-Phase Analysis for Spatiotemporal Mapping at Pixel Resolution

Ma et al. (37) recently demonstrated a new approach that simultaneously monitors the phase changes along the whole retinal depths, called differential phase mapping (DPM). DPM was devised to analyze the spatiotemporal phase change at pixel resolution. The processing flow was as follows (**Figure 5A**). Digital dispersion compensation, zero-padding, and fast Fourier transform (FFT) were applied to raw data to get a complex matrix with amplitude and phase information. Then, the OCT phase was unwrapped along the A-scan direction. Finally, the unwrapped phase was differentiated along the A-scan direction. If the scatters of the adjacent pixels are both in the center, the value of the pixel in DPM is $4\pi nL/\lambda_c$, where n denotes the refractive index of the tissue, L denotes the pixel length, λ_c denotes the center wavelength of the light source, and the coefficient 4π is because the OCT measures the back-scattered light. If the distance of two scatterers is less than L, the pixel value of DPM will be smaller than $4\pi nL/\lambda_c$, vice versa. Therefore, the DPM represents the relative scatter distance of the sample. Compared to the OCT amplitude image (**Figure 5B**), DPM also reveals the structural information representing scatter locations (**Figure 5C**). After stimulation, both amplitude and phase IOS appeared at the outer retina layers (**Figures 5D,E**). The phase IOSs of different layers at different time courses indicated the depth association of phototransduction in the outer retina. Compared to conventional phase-resolved OPL measurement, computing the phase change between two selected locations, DPM shows the phase change over all the retina depths simultaneously, which could help understand the phase dynamics between retinal layers.

ORG INTERPRETATIONS AND ITS CHALLENGES

ORG measurement and interpretation are challenging due to the multiple signal sources and variable OCT instruments, and experimental protocols.

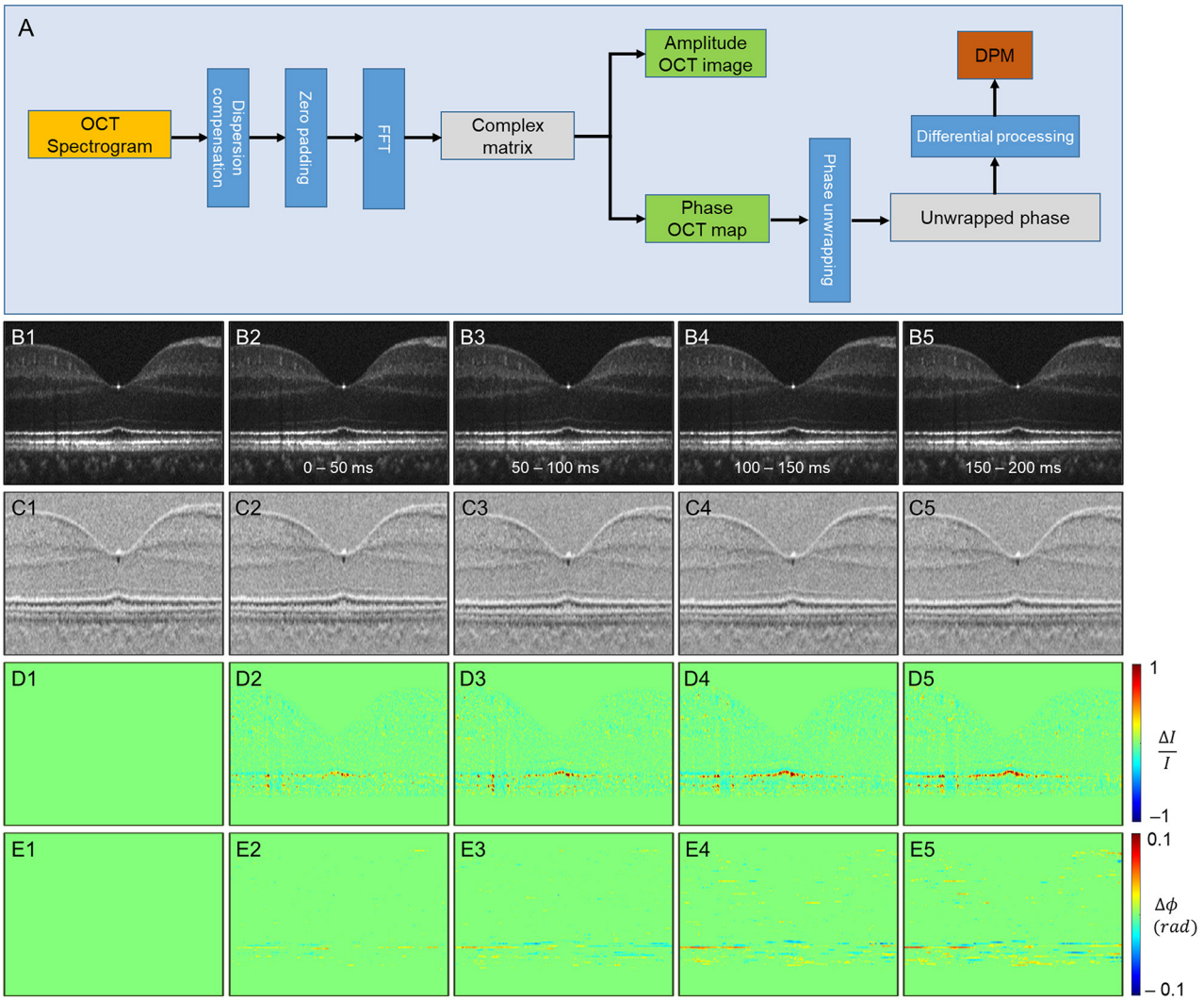

FIGURE 5 | Phase-resolved OCT imaging for differential-phase mapping (DPM) analysis. **(A)** A flow chart of amplitude OCT and DPM processing. **(B–E)** The amplitude-IOS and phase-IOS distribution. **(B)** Amplitude image sequence. **(C)** DPM sequence. **(D)** Amplitude-IOS sequence. **(E)** Phase-IOS sequence. Reprinted with permission from Ma et al. (37).

Retinal Neurovascular Coupling and Inner Retinal Response

Retinal blood flow is actively regulated in response to neuronal activity (72), called neurovascular coupling. The impaired coupling mechanism is commonly associated with microvascular pathologies in the retina (73, 74). Thus, spatiotemporal mapping of transient neural activity and subsequent hemodynamic responses promises early detection of retinal diseases. Based on the intensity-based processing, stimulus-evoked IOS changes have been detected in retinal layers and the vascular network within the retina. Son et al. demonstrated concurrent mapping of neural- and hemodynamic-IOS to monitor retinal neurovascular coupling in the mouse retina (50, 63). They leveraged OCT angiography (OCTA) maps to isolate the retinal vasculature at a single capillary level resolution. The OCTA-guided IOS data processing enables two functional images: a neural-IOS map and a hemodynamic-IOS map. Flicker stimuli were used to induce a robust hemodynamic response. As shown in **Figure 6**, fast photoreceptor-IOS was first observed right after the stimulus onset, while hemodynamic-IOS was revealed with a significant time delay. The temporal progress of hemodynamic-IOS responses was also varied in different vascular plexuses (**Figure 6D**). However, the mechanism of the hemodynamic-IOS responses in large blood vessels and capillaries is not understood yet. Only a few hypotheses have been proposed, such as different neural metabolic demands in individual retinal layers, passive dilation of downstream capillaries, and mural cells' intervention on blood flow regulation (63). In addition, 2D cross-sectional imaging would be challenging for monitoring delayed hemodynamic IOS in the human retina due to motion

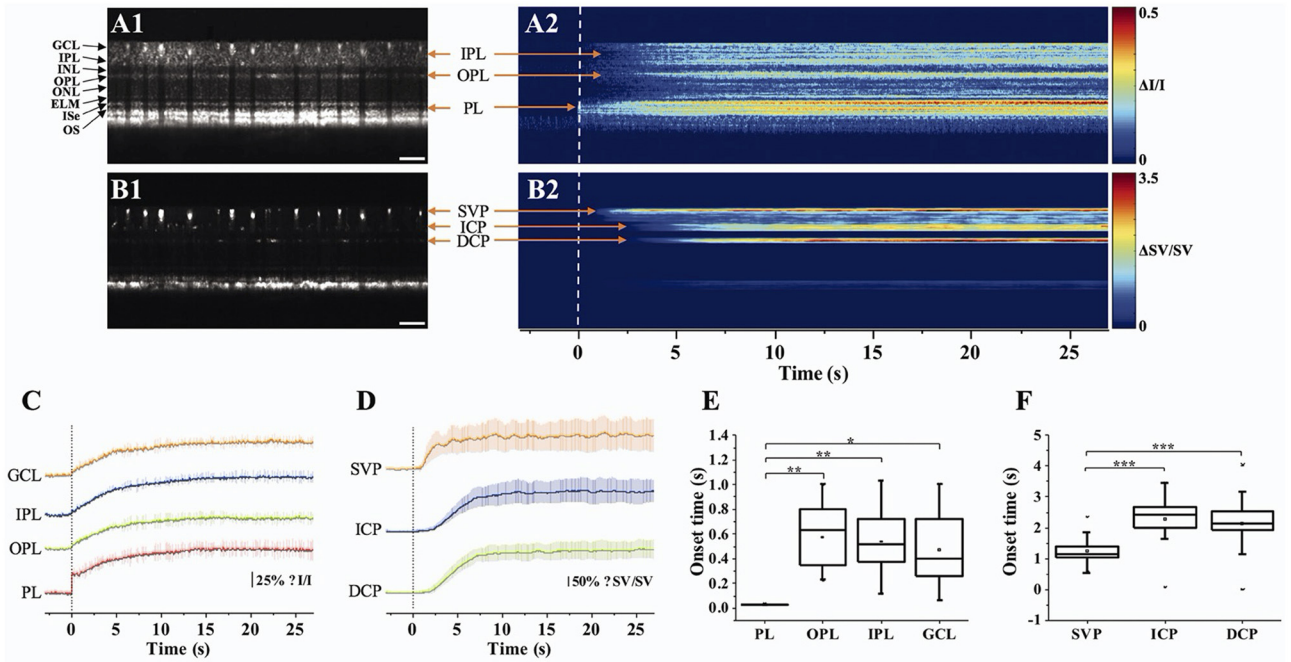

FIGURE 6 | Retinal neurovascular coupling and inner retinal IOS response. **(A)** Representative flattened **(A1)** OCT B-scan and **(A2)** spatiotemporal neural-IOS map. **(B)** Representative flattened **(B1)** OCTA B-scan and **(B2)** spatiotemporal hemodynamic-IOS map. Scale bars in **(A1,B1)** indicate 500 μm. **(C)** Neural-IOS changes of photoreceptor layer (PL), outer plexiform layer (OPL), inner plexiform layer (IPL), and ganglion cell layer (GCL). **(D)** Hemodynamic-IOS changes of superficial vascular plexiform (SVP), intermediate capillary plexiform (ICP), and deep capillary plexiform (DCP). **(E)** Averaged onset times of neural-IOS changes at PL, OPL, IPL, and GCL. **(F)** Averaged onset times of hemodynamic-IOS changes of SVP, ICP, and DCP. Modified with permission from Son et al. (63). P values for statistical significances are indicated by asterisks: $^{*}P < 0.05$; $^{**}P < 0.01$; $^{***}P < 0.001$.

artifacts. Moving correction is impossible if the retina moves perpendicularly to the imaging plane as there is no data to use in correction. High-speed parallel OCT would be desirable for neurovascular coupling study. Another task is to appreciate how local signal variations occur in blood vessel regions associated with flux change, hematocrit, and diameter increase.

Aside from hemodynamic information, the inner retina itself also revealed IOS change (**Figure 6C**). Previous mouse studies reported that a short pulse stimulation mainly induced the fast-photoreceptor IOS, while increased stimulus duration or flicker stimulation can induce IOS changes in the inner retina (41, 42, 50, 75). Although the signal source is underappreciated, it was postulated that the slow inner retinal IOS might be associated with an integral effect of electrophysiological signal transduction between multiple inner retinal neurons, such as bipolar cells, amacrine cells, horizontal cells, and ganglion cells. The plexiform layer in the retina consists of a complex synaptic network containing numerous dendrites from different types of neurons (76, 77). Their synaptic signaling might affect optical signal properties. Pfäffle et al. (70) recently showed simultaneous imaging of the activation in the photoreceptor and ganglion cell layer/inner plexiform layer (GCL/IPL) in the human retina by using phase-sensitive full-field swept-source OCT (FF-SS-OCT). Although the signals from the GCL/IPL were 10-fold smaller than those from the photoreceptor, GCL/IPL signals were still detectable with suppression of motion artifacts and blood flow pulsations in the retinal vessels. The phase difference of the GCL and the IPL was calculated to evaluate the light-evoked OPL changes, and they found that the OPL between GCL and IPL increased about 40 nm in the stimulated area, and the increase in OPL reached its maximum of about 40 nm after approximately 5 s. However, the mechanism of inner retinal IOS changes from both intensity-based and phase-based results is poorly understood. In addition, retinal vasculature is embedded in the inner retina; thus, blood flow pulsation and inhomogeneous intensity distribution may complicate signal interpretations.

Transient Deformations of Photoreceptor Outer Segment

As the center of phototransduction, retinal photoreceptors are responsible for converting photon energy to bioelectric signals for following vision processing in the retina. Retinal photoreceptors are the primary target cell of retinal degenerative diseases such as AMD and retinitis pigmentosa (RP); thus, non-invasive monitoring of functional integrity of photoreceptors is of great interest. The photoreceptors are the most well studied among retinal cell types by intrinsic signal ORG measurement as they exhibit an exceptionally reproducible light-driven response.

At first, time-lapse near-infrared light microscopy was used to image transient IOS changes in freshly isolated retinas, and it was found that the IOS rapidly occurred in the

photoreceptor cells after the visible light stimulus (78, 79). The magnitude and time course of IOS changes were found to be correlated with the stimulus strength (78). In addition, transient shrinkage-induced deformation in photoreceptors was directly observed in both amphibian (80) and mammalian (81) retinas. The shrinkage-induced deformation was mainly observed in the photoreceptor OSs that rapidly shifted toward the direction of the visible light stimulus (47). It turned out that the onset time of the photoreceptor shrinkage was almost identical to that of photoreceptor-IOS change, suggesting that the OS conformational change should correlate with the phototransduction process. A hybrid confocal-OCT study further demonstrated that the photoreceptor OS is the anatomic source of the transient photoreceptor deformation (47). Lu et al. (82) showed vertical shrinkage of isolated frog rod OSs in response to light stimulus, and transmission electron microscopy (TEM) observation confirmed shortened inter-disc spacing in light-adapted rod OSs. To better appreciate the physiological origin of the fast-photoreceptor IOS, comparative measurements of OS deformation and ERG were conducted, and it was consistently observed that the OS deformation occurs earlier than the onset of the ERG a-wave (83). Moreover, substituting a traditional superfusing medium with a low-sodium medium blocked the ERG a-wave response but preserved the stimulus-evoked rod OS deformations (83). In comparative photoreceptor-IOS recording and ERG measurement, previous studies confirmed that the response time of fast photoreceptor-IOS was ahead of the a-wave in the mouse retina (39, 62). This observation provides concrete evidence that the fast-photoreceptor IOS is independent of the OS hyperpolarization, i.e., cyclic guanosine monophosphate (cGMP) gated ion channel closure along the OS plasma membrane, the source of ERG a-wave. Instead, both the fast-photoreceptor IOS and rod OS deformations are associated with the early phase of the phototransduction cascade that involves the sequential activation of rhodopsin, transducin, and cGMP phosphodiesterase (PDE). A recent comparative study of wild-type (WT) and retinal degeneration 10 (rd10) mice demonstrated that fast photoreceptor-IOS occurs even earlier than PDE activation (84). Similarly, recent phase-resolved OCT imaging revealed a stimulus-evoked rapid reduction of OPL in photoreceptor OSs in the human retinas (32, 57, 69). The rapid OPL decrease showed a time course of millisecond level, which is in keeping with the earlier results of stimulus-evoked fast photoreceptor-IOS in animal models (45). Boyle et al. (58) suggested that contraction of the photoreceptor OS may be driven by the charge transfer across the OS disc membrane relevant to early receptor potential (ERP) (32), a fast electrical signal observed in cone photoreceptors under intense flash stimuli (85, 86). The ERP is associated with the conformational change of opsins embedded in the OS disc membrane and is distinct from the changes in the photoreceptor membrane potential.

Intriguingly, phase-resolved OCT imaging revealed not only a rapid (<5 ms) reduction in OPL after the stimulus onset but also a slower (>1 s) increase in OPL of the photoreceptor OSs (31, 32, 57, 69). The elongation response has been consistently observed in phase-resolved ORG studies. Zhang et al. (69) showed that the magnitude of these path length increments was positively correlated with stimulating light dose, and they used the photoreceptor elongation signals to generate maps of the three cone classes. It has been hypothesized that the increase (up to hundreds of nanometers) in the OPL of photoreceptor OSs after light stimulus would be attributable to osmotic swelling, an increase in the cytoplasmic volume due to excess osmolytes produced by phototransduction (66). Based on the intensity-based processing, Lu et al. (87) also observed photoreceptor OS elongation following intense light exposure and subsequent recovery, i.e., photoreceptor OS shortening, in human subjects. Although the increased OPL between IS/OS junction and OS tip is consistent among *in vivo* phase-resolved ORG measurements, there is a lack of direct evidence of the OS elongation. In fact, *ex vivo* studies have often shown conflicting results (**Figures 7A–C**). Comparative TEM observation disclosed shortened inter-disc spacing in rod OSs in light-adapted frog retinas (82). Fast X-ray diffraction studies also revealed a light-induced shrinkage of the disc lattice distance from the frog and mouse rod OSs (90, 91). Moreover, Bocchero et al. (89) recently measured light-evoked 3-axis (X, Y, Z plane) volume changes in the single rod OS from the Xenopus retina. They consistently observed a shortening of the OS on the order of 100–200 nm after a brief flash stimulus. The shortening was transient, and the OS returned to its original size within about 10 s, without further expansion.

Taken together, there is a growing consensus on the photoreceptor OS shrinkage at the early stage of phototransduction. However, more research is necessary to verify the OS swelling or relaxation mechanism. Note that the different dynamics between retinal explant and isolated single photoreceptor responses were demonstrated (90), and fundamentally, photoreceptor morphology and cellular compartment are different among species (92, 93).

Transient Reflectance Changes in Inner Segment Ellipsoid Zone

The photoreceptor ISe is the center of metabolism, consisting of abundant mitochondria (94). Despite contradictory nomenclatures, the ISe is a biomarker of photoreceptor integrity. The integrity of the ISe band has been correlated with different aspects of retinal function (95, 96). In addition, ISe reflectivity has recently emerged as a sensitive biomarker of photoreceptor structure due to the ISe reflectance changes under degenerative retinal conditions (96). In addition, a recent IOS recording showed that the ISe reflectivity dynamically changed in response to different light conditions (61, 65, 66). **Figure 8** shows the ISe IOS in the mouse retina. A study demonstrated that stimulus-evoked IOS change at the ISe appeared with a time delay of ∼12 ms after the stimulation, which is rather slower than fast-OS response, suggesting that the slow ISe IOS might reflect the metabolic reaction of mitochondria, following the phototransduction in the OS (61). Under metabolic stresses, the morphological structure and motion dynamics of mitochondria are all varied (97, 98), which could alter the optical signal properties of the ISe zone, resulting in OCT

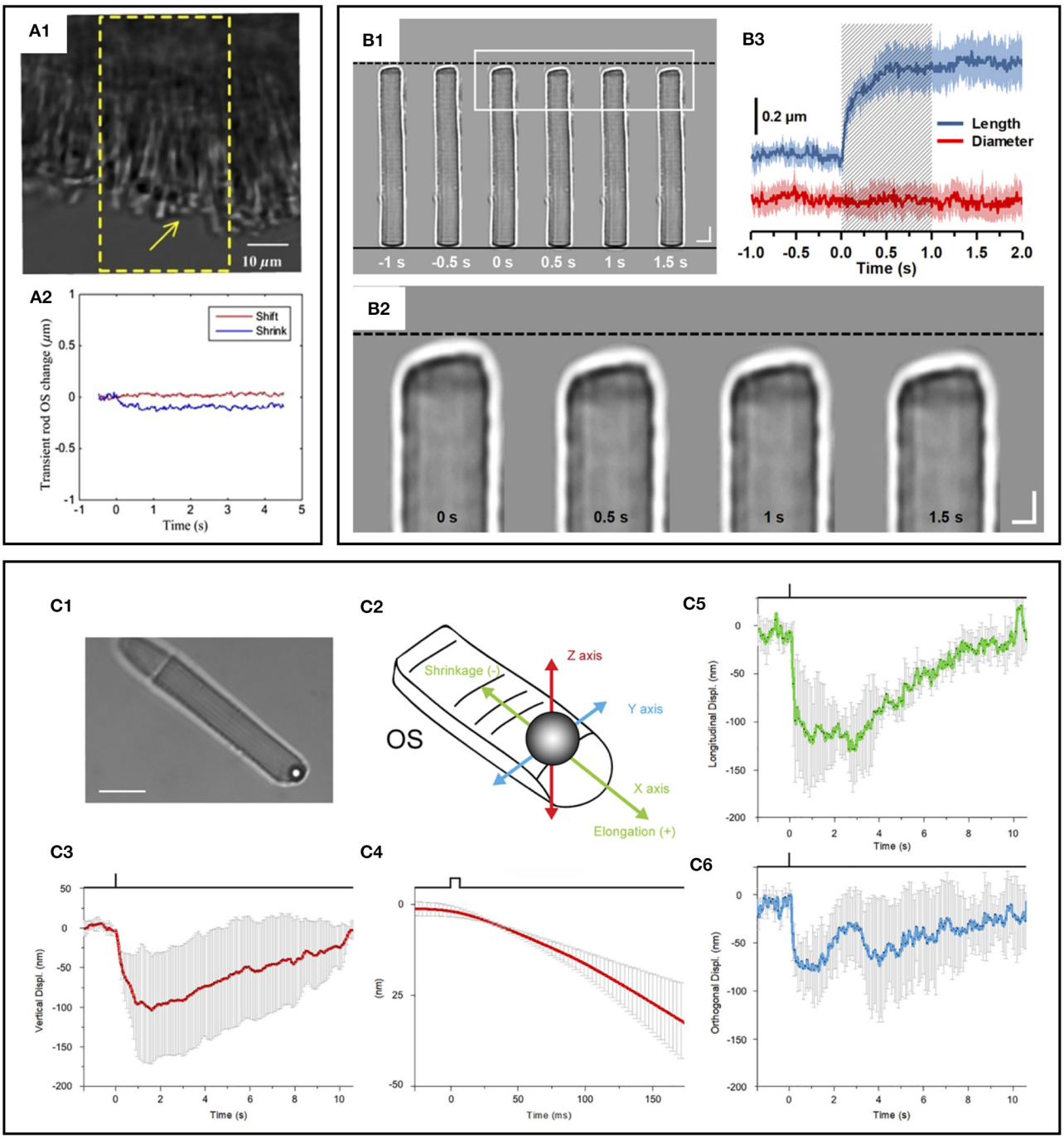

FIGURE 7 | Photoreceptor outer segment (OS) shrinkage due to light stimulus. **(A1)** Stimulus-evoked mouse rod OS movement. The yellow window indicates the stimulation area. **(A2)** OS changes of a mouse rod photoreceptor. In the center of the stimulation region, the length of the OS shrunk, while in the peripheral region, the OS swung toward the center of the stimulation area in the plane perpendicular to the incident stimulus light. Reprinted with permission from Zhao et al. (88). **(B1)** Representative light microscopic images of an isolated frog rod OS acquired with an interval of 0.5 s. To better show the light-evoked OS shrinkage, the base of the rod OS in each image is aligned horizontally as shown by the black solid line at the bottom. The black-dashed line at the top represents the position of the rod OS tip at time −1 s. Scale bars (in white) represent 5 μm. **(B2)** Enlarged picture of the white rectangle in **(B1)**. Scale bars (in white) represent 2 μm. **(B3)** Time course of the averaged rod OS shrinkage in both length and diameter acquired from eight different rod OSs. Colored areas accompanying the curves represent the standard deviations. Shaded area indicates the 1-second stimulation period. Reprinted with permission from Lu et al. (82). **(C)** Mechanical response of an X. laevis rod to light flashes. The position of a bead sealed against the tip of the rod OS is monitored with optical tweezers. Following a bright flash of 491 nm, equivalent to about 10^4 photoisomerization [R*], a transient shrinkage is observed. **(C1)** Bright-field infra-red image, showing a trapped bead in contact with the tip of the rod OS (scale bar,

(Continued)

FIGURE 7 | 10 μm). **(C2)** Detail of the 3D tracking system. **(C3)** Light-induced shifts in the Z axis of the trapped bead (downward is negative). **(C4)** Expansion of the time base in C5 to examine the delay between light stimulus and bead movement. **(C5)** Bead displacement along the direction of the rod OS (shrinkage is negative, and elongation is positive). **(C6)** Bead displacement in the direction perpendicular to the rod OS axis. Data are representative of mean ± SD of 5 different experiments. Reprinted with permission from Bocchero et al. (89).

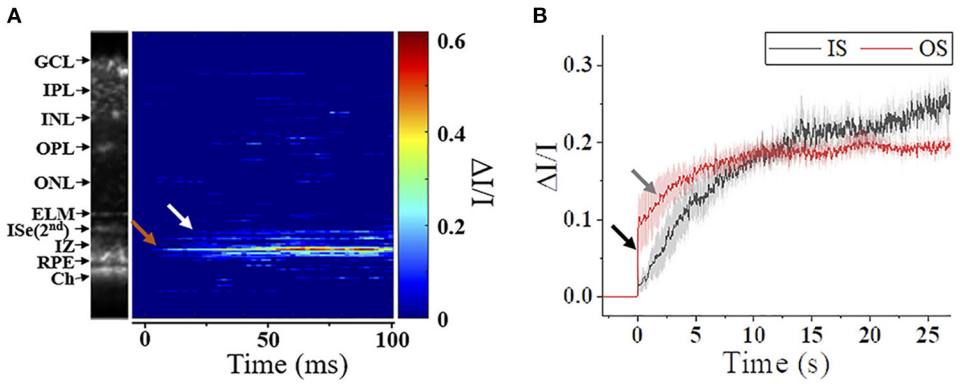

FIGURE 8 | Metabolic response of photoreceptor inner segment. **(A)** IOS M-scan within 100 ms, the white and red arrowheads show the onsets of IS-IOS and OS-IOS, respectively. **(B)** Average IS-IOS and OS-IOS from six mice. The average OS-IOS showed a biphasic curve. The dark and gray arrowheads show the first rapidly increasing phase and the second gradually increasing phase, respectively. GCL, ganglion cell layer; IPL, inner plexiform layer; INL, inner nuclear layer; OPL, outer plexiform layer; ONL, outer nuclear layer; ELM, external limiting membrane; ISe, inner segment ellipsoid; IZ, interdigitation zone; RPE, retinal pigment epithelium; Ch, Choroid; IS, photoreceptor inner segment; OS, photoreceptor outer segment. Reprinted with permission from Ma et al. (61).

reflectance changes. In addition, Kim et al. recently found a significant reduction in ISe reflectance during dark adaptation in the mouse retina. This observation further emphasizes light-modulated ISe reflectivity could serve as a sensitive biomarker for photoreceptor dysfunction (65). However, Zhang et al. (66) hypothesized that phototransduction reactions associated with complete activation of G-protein alpha-subunit transducin might induce osmotic swelling, and the swelling, combined with the mass redistribution of transducing proteins from the disc membranes into the cytosol, might underlie the scattering increases at the IS/OS and OS tips. There is no doubt that the ISe reflectivity can be actively regulated under different light conditions, and it would be a potent biomarker for photoreceptor dysfunction. However, the ISe IOS source is still ill-defined, and both mitochondrial metabolic activity and redistribution of G proteins could simultaneously affect the signal. In addition, there is an unmet need to resolve ambiguity as to how well ISe reflectivity correlates with underlying photoreceptor structure (56).

Subretinal Space Changes Under Different Light Conditions

The SRS is the extracellular fluid space between the ELM and the apical RPE, which is isolated by tight junctions at these two borders, and the ELM and RPE appear as hyper-reflective bands in OCT, which facilitates band change analysis. In fact, the SRS has been a well-recognized region that actively deforms under different light conditions (99). Thus, SRS dynamics could become a potential biomarker for outer retinal dysfunction.

Using Fourier-domain OCT with intensity-based processing, Li et al. (100) found a notable thinning of the outer retina in dark-adapted mouse eyes. They further demonstrated that volume changes in the outer retina varied with the different stages of retinal degeneration in the rd10 mouse model (67). Berkowitz et al. (101) observed that a light-driven expansion of the outer retina was more distinguished in C57BL/6 mice than 129S6/SvEvTac mice. In addition, Gao et al. (102) recently demonstrated a significant reduction of the magnitude and width of a hypo-reflective band between the photoreceptor OS and RPE in the dark-adapted mouse and human retina. Lu et al. (87) also showed a rapid decline in the IS/OS-RPE distance after a light stimulus. **Figure 9** illustrates the dark adaptation effects on the mouse retina. Kim et al. (65) recently demonstrated the dynamic SRS thinning of the mouse retina during light to dark transitional moment and found that dark-induced retinal response was reflected by transient structural (i.e., the SRS thinning) and physiological (i.e., ISe intensity reduction) changes. High-speed OCT recording further identified a strong correlation between the SRS thinning and ISe intensity reduction in the outer retina (65). The SRS thinning mechanism is understood by RPE-mediated water transport from the SRS. The light to dark transition is accompanied by an increase in photoreceptor metabolism, leading to increased oxygen consumption in the retina (103), which can acidify the outer retina due to increased CO_2 and wastewater production, and eventually upregulate water removal co-transporters in the RPE. This removal of the acidified water has been linked to the SRS thinning (99, 104).

However, human study has sometimes shown intriguing but puzzling results. Messner et al. (105) observed a distance

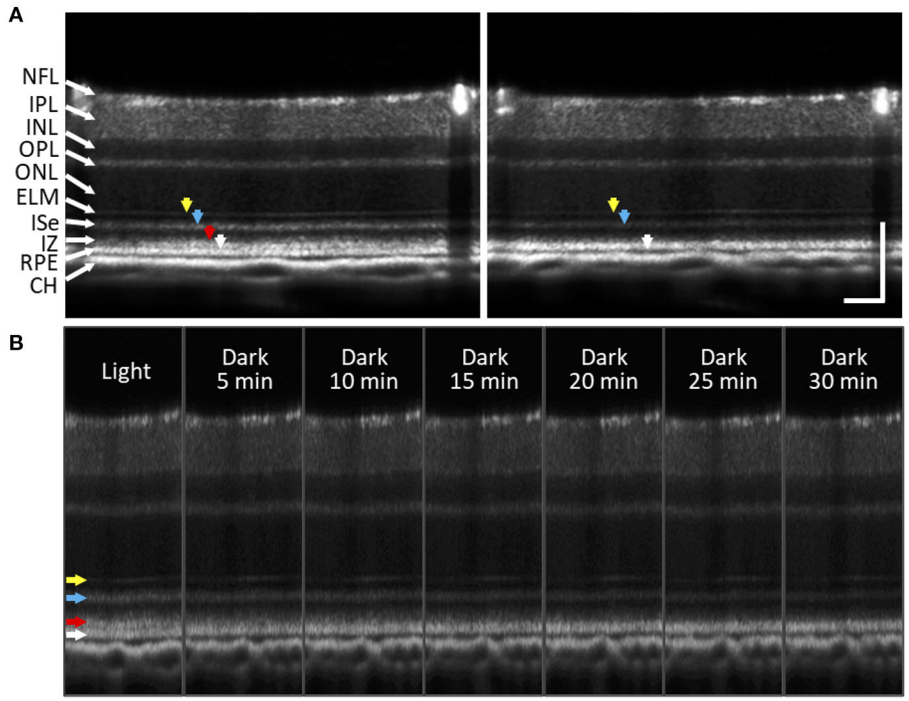

FIGURE 9 | Subretinal space changes during dark adaptation in the mouse retina. **(A)** OCT images of light- and dark-adapted retina of a two-month-old C57BL/6J mouse. Color arrows to indicate outer retinal bands: 1st ELM band (yellow), 2nd ISe band (blue), 3rd IZ and OS tip band (red), 4th RPE band (white). **(B)** A sequence of OCT images obtained every 5 min up to 30 min during dark adaptation. During dark adaptation, ISe intensity reduction rapidly occurred, and the SRS became thinner. In addition, the 3rd outer retinal band (red arrow) faded over time. NFL, nerve fiber layer; IPL, inner plexiform layer; INL, inner nuclear layer; OPL, outer plexiform layer; ONL, outer nuclear layer; ELM, external limiting membrane; ISe, inner segment ellipsoid; IZ, interdigitation zone; RPE, retinal pigment epithelium; CH, choroid. Scale bars: 100 μm. Modified with permission from Kim et al. (65).

decrease between IS/OS junction and RPE after the light stimulus. They observed that the OS tips and RPE were drawn closer together after light exposure, speculating that this might be associated with a decrease in volume of the SRS (105), which is conflicting with previous observations (99). In addition, Azimipour et al. observed that the RPE band appears to split, with its apical portion moving toward the cone OS tip after the light stimulus. They speculated that light-driven translocation of melanin observed in amphibians (49) or a consequence of inward water movement across the RPE/Bruch's complex could be a potential signal source (106). In the human retina, photoreceptor cell population, rod/cone ratio, photoreceptor length, and morphology are largely different depending on eccentricity. The appearance of outer retinal bands also varies among different OCT systems (56). Thus, various factors that can potentially affect ORG measurement should be carefully accounted for and documented.

DISCUSSION

Emerging Issues in ORG Measurements

As demonstrated above, outer retinal structures including the photoreceptor IS and OS, SRS, and RPE have been highlighted in ORG recording because of their structural clarity in OCT and importance as a primary target of retinal degenerative diseases. However, ORG recording has been conducted by different OCT systems and experimental protocols. Thus, there are often challenges for quantitative analysis using OCT reflectance information. Lee et al. (96) recently provided a valuable discussion about challenges associated with ISe intensity measurement using clinical OCT. They emphasized the importance of the pupil entry position of the OCT beam due to the altered reflectivity profile of the retinal image (107, 108). The reproducibility of ISe reflectivity measurements largely depends on the standardization of pupil entry point acquisition. There is also the importance of using appropriate intensity scales. Clinical OCT images are generally presented on a logarithmic scale, but this can misrepresent fundamental differences in reflectivity and a loss of information (109, 110). Adjusting intensity values can result in broadened hyper-reflective retinal bands, and accordingly vertical position of the hyper-reflective bands can be altered within the scan (109). Another issue is inter-device variation in ISe intensity, as each OCT device has different acquisition and optimization methods (111). Thus, it is necessary to establish a standardized normalization method (96). Meleppat et al. further demonstrated that the reflectivity from the inner retinal layers and ELM are also highly directional. The reflectance declines sharply with the angle of incidence of the OCT beam on

the mouse retina (112). Notably, in albino mice, the reflection from Bruch's membrane was highly directional as well (112).

Aside from the issues of image acquisition and analysis, the unmet need for advancing ORG measurement is to establish anatomic correlation with underlying photoreceptor structure. Yao et al. (56) recently provided a valuable discussion about the interpretation of anatomic correlates of outer retinal bands in OCT. Clinical OCT, laboratory prototype OCT without AO, or AO-OCT can resolve four distinct hyperreflective bands in the outer retina (**Figure 1C**). Recent resolution improvement allows further separation of the RPE/Bruch's membrane complex into the individual layers (76). However, our understanding of anatomical correlates to each outer retinal band is not keeping pace with the recent development of OCT imaging technology. Understanding anatomical correlates to OCT bands is crucial to translate ORG information for diagnostic purposes. The interpretations of the 1st ELM and 4th RPE/Bruch's membrane of the outer retina are consistent; however, the interpretations of 2nd band of ISe or IS/OS junction and 3rd band of interdigitation zone (IZ) or OS tips remain a great controversy (109, 113, 114). The inconsistency is mainly found between clinical OCT and AO-OCT images. Comparative alignment of the outer retinal OCT bands with a scale model of outer retinal morphology showed the ISe and IZ as the correlates to the 2nd and 3rd outer retinal bands (115). The 2014 International OCT Nomenclature Meeting also affirmed the ISe and IZ as the anatomic correlates of the 2nd and 3rd bands of the outer retina (116). However, with improved spatial resolution, AO-OCT revealed a much thinner 2nd outer retinal band than the ISe band observed in clinical OCT (117). AO-OCT measurement demonstrated that the 2nd band thickness was about 4.7 μm (117), while the 2nd band thickness in clinical OCT was about 16–20 μm (56). In addition, AO-OCT illustrated that the 2nd band peak is closer to the 3rd band peak, relative to the 1st band peak. Taken together, it was suggested that the 2nd band in AO-OCT corresponds to the IS/OS junction rather than the ISe. A similar phenomenon was also found in the 3rd outer retinal band. The 3rd band thickness was 4.3–6.4 μm and 14–19 μm in AO-OCT and clinical OCT, respectively (118). Yao et al. described that the AO-OCT might enhance the sensitivity for imaging ballistic photons from the IS/OS junction while partially rejecting the diffusive photons within the ISe region due to better sectioning capability (56). Thus, in clinical OCT, both IS/OS junction and ISe can non-exclusively contribute to the 2nd band; and OS tips and RPE apical processes can simultaneously contribute to the 3rd band. Also, weighting factors including system resolution, effective pupil size, imaging orientation, and aberrations can differentially affect the signal detection in clinical OCT and AO-OCT. Moreover, the OCT band profile is also known to be affected by optical dispersion (119). Therefore, it should be acknowledged that the contributing factors for individual band correlates are variable in different instruments, testing protocols, and eye conditions.

Future Perspectives

Growing evidence indicates that morphological examination may be limited to detecting the early stage of retinal degenerative diseases, including but not limited to AMD (120), DR (121), and IRDs (122). Given that timely management of the diseases is the key to the preservation of vision (123–126), functional assessment of retinal photoreceptors and neurovascular coupling has gained increasing importance. Ongoing development in OCT-based ORG measurement is one of the most promising methodologies for screening people at risk. With unparalleled depth-resolved capability, recent advances in OCT further provide multi-modalities, ultrahigh-speed recording, single-cell resolution, and ultrawide field recording. Moreover, advanced ORG processing algorithms allow the mapping of various functional activities over morphological images. While the implementation of OCT-ORG in clinics is still at an early stage, recent studies demonstrated the feasibility of ORG measurement in human subjects (25, 31, 32, 36, 37, 54, 57, 69, 70, 102, 105). To facilitate clinical transition, it would be necessary to refine experimental procedures and shorten the examination time, including the light/dark adaptation to reduce the subject's burden. In addition, there is a broad range of existing testing methods for functional examination, and each has benefits and limitations. In this regard, OCT-ORG should be conducted alongside the existing tests as a multimodal evaluation, which can provide a better understanding of retinal physiology and corresponding IOS sources. Standardized imaging protocol and processing methods also need to be established as there are significant variations in imaging quality, the appearance of the retina, and following results due to different systems and processing algorithms. Above all, our understanding of functional activity and the corresponding IOS is quite limited. Thus, there is an unmet need to seek direct evidence of biological processes to visual stimulus, which helps translate distinct intrinsic signal sources at different retinal locations to target retinal disorders. Both *in vivo* and *ex vivo* studies using mutant animal models would be helpful. We anticipate that further development of the OCT system and ORG processing methods promises an objective measurement of neural and hemodynamic dysfunctions in the retina, allowing early detection and therapeutic assessment of AMD, DR, IRDs, and other retinal diseases.

AUTHOR CONTRIBUTIONS

T-HK conceived the article, performed the literature search, drafted the manuscript, and prepared figures. GM and TS edited the manuscript and prepared figures. XY conceived the article, edited the manuscript, and supervised the study. All authors approved the submitted version.

FUNDING

National Eye Institute: P30 EY001792, R01 EY030101, R01 EY023522, R01 EY029673, R01 EY030842, and R44 EY028786; Richard and Loan Hill endowment; and unrestricted grant from Research to Prevent Blindness.

REFERENCES

1. Li X, Xie J, Zhang L, Cui Y, Zhang G, Wang J, et al. Differential distribution of manifest lesions in diabetic retinopathy by fundus fluorescein angiography and fundus photography. *BMC Ophthalmol.* (2020) 20:471. doi: 10.1186/s12886-020-01740-2
2. Croft DE, van Hemert J, Wykoff CC, Clifton D, Verhoek M, Fleming A, et al. Precise montaging and metric quantification of retinal surface area from ultra-widefield fundus photography and fluorescein angiography. *Ophthalmic Surg Lasers Imaging Retina.* (2014) 45:312–7. doi: 10.3928/23258160-20140709-07
3. Lee JH, Kim SS, Kim GT. Microvascular findings in patients with systemic lupus erythematosus assessed by fundus photography with fluorescein angiography. *Clin Exp Rheumatol.* (2013) 31:871–6. Available online at: https://www.clinexprheumatol.org/abstract.asp?a=6910
4. Fischer J, Otto T, Delori F, Pace L, Staurenghi G. Scanning laser ophthalmoscopy (Slo). In: Bille JF, editor. *High Resolution Imaging in Microscopy and Ophthalmology: New Frontiers in Biomedical Optics*. Cham (CH) (2019). p. 35–57. doi: 10.1007/978-3-030-16638-0_2
5. Calvo-Maroto AM, Esteve-Taboada JJ, Dominguez-Vicent A, Perez-Cambrodi RJ, Cervino A. Confocal scanning laser ophthalmoscopy versus modified conventional fundus camera for fundus autofluorescence. *Expert Rev Med Devices.* (2016) 13:965–78. doi: 10.1080/17434440.2016.1236678
6. Swanson EA, Izatt JA, Hee MR, Huang D, Lin CP, Schuman JS, et al. In vivo retinal imaging by optical coherence tomography. *Opt Lett.* (1993) 18:1864–6. doi: 10.1364/OL.18.001864
7. Leitgeb RA. En face optical coherence tomography: a technology review [invited]. *Biomed Opt Express.* (2019) 10:2177–201. doi: 10.1364/BOE.10.002177
8. Spaide RF, Fujimoto JG, Waheed NK, Sadda SR, Staurenghi G. Optical coherence tomography angiography. *Prog Retin Eye Res.* (2018) 64:1–55. doi: 10.1016/j.preteyeres.2017.11.003
9. Chen CL, Wang RK. Optical coherence tomography based angiography [invited]. *Biomed Opt Express.* (2017) 8:1056–82. doi: 10.1364/BOE.8.001056
10. Gao SS, Jia Y, Zhang M, Su JP, Liu G, Hwang TS, et al. Optical coherence tomography angiography. *Invest Ophthalmol Vis Sci.* (2016) 57:OCT27–36. doi: 10.1167/iovs.15-19043
11. Yao X, Alam MN, Le D, Toslak D. Quantitative optical coherence tomography angiography: a review. *Exp Biol Med.* (2020) 245:301–12. doi: 10.1177/1535370219899893
12. Bessho K, Fujikado T, Mihashi T, Yamaguchi T, Nakazawa N, Tano Y. Photoreceptor images of normal eyes and of eyes with macular dystrophy obtained in vivo with an adaptive optics fundus camera. *Jpn J Ophthalmol.* (2008) 52:380–5. doi: 10.1007/s10384-008-0575-1
13. Soliman MK, Sadiq MA, Agarwal A, Sarwar S, Hassan M, Hanout M, et al. High-resolution imaging of parafoveal cones in different stages of diabetic retinopathy using adaptive optics fundus camera. *PLoS ONE.* (2016) 11:e0152788. doi: 10.1371/journal.pone.0152788
14. Zhang B, Li N, Kang J, He Y, Chen XM. Adaptive optics scanning laser ophthalmoscopy in fundus imaging, a review and update. *Int J Ophthalmol.* (2017) 10:1751–8. doi: 10.18240/ijo.2017.11.18
15. Roorda A. Applications of adaptive optics scanning laser ophthalmoscopy. *Optom Vis Sci.* (2010) 87:260–8. doi: 10.1097/OPX.0b013e3181d39479
16. Godara P, Siebe C, Rha J, Michaelides M, Carroll J. Assessing the photoreceptor mosaic over drusen using adaptive optics and sd-oct. *Ophthalmic Surg Lasers Imaging.* (2010) 41:S104–8. doi: 10.3928/15428877-20101031-07
17. King BJ, Sapoznik KA, Elsner AE, Gast TJ, Papay JA, Clark CA, et al. Sd-Oct and adaptive optics imaging of outer retinal tubulation. *Optom Vis Sci.* (2017) 94:411–22. doi: 10.1097/OPX.0000000000001031
18. Miller DT, Kocaoglu OP, Wang Q, Lee S. Adaptive optics and the eye (super resolution oct). *Eye.* (2011) 25:321–30. doi: 10.1038/eye.2011.1
19. Lai TY, Chan WM, Lai RY, Ngai JW, Li H, Lam DS. The clinical applications of multifocal electroretinography: a systematic review. *Surv Ophthalmol.* (2007) 52:61–96. doi: 10.1016/j.survophthal.2006.10.005
20. McAnany JJ, Persidina OS, Park JC. Clinical electroretinography in diabetic retinopathy: a review. *Surv Ophthalmol.* (2021). doi: 10.1016/j.survophthal.2021.08.011. [Epub ahead of print].
21. Ts'o D, Schallek J, Kwon Y, Kardon R, Abramoff M, Soliz P. Noninvasive functional imaging of the retina reveals outer retinal and hemodynamic intrinsic optical signal origins. *Jpn J Ophthalmol.* (2009) 53:334–44. doi: 10.1007/s10384-009-0687-2
22. Yao X, Wang B. Intrinsic optical signal imaging of retinal physiology: a review. *J Biomed Opt.* (2015) 20:090901. doi: 10.1117/1.JBO.20.9.090901
23. Hanazono G, Tsunoda K, Kazato Y, Tsubota K, Tanifuji M. Evaluating neural activity of retinal ganglion cells by flash-evoked intrinsic signal imaging in macaque retina. *Invest Ophthalmol Vis Sci.* (2008) 49:4655–63. doi: 10.1167/iovs.08-1936
24. Begum M, Joiner DP, Ts'o DY. Stimulus-driven retinal intrinsic signal optical imaging in mouse demonstrates a dominant rod-driven component. *Invest Ophthalmol Vis Sci.* (2020) 61:37. doi: 10.1167/iovs.61.8.37
25. Son T, Kim TH, Ma G, Kim H, Yao X. Functional intrinsic optical signal imaging for objective optoretinography of human photoreceptors. *Exp Biol Med.* (2021) 246:639–43. doi: 10.1177/1535370220978898
26. Wang B, Yao X. In vivo intrinsic optical signal imaging of mouse retinas. *Proc SPIE Int Soc Opt Eng.* (2016) 9693:96930H. doi: 10.1117/12.2212810
27. Zhang QX, Zhang Y, Lu RW, Li YC, Pittler SJ, Kraft TW, et al. Comparative intrinsic optical signal imaging of wild-type and mutant mouse retinas. *Opt Express.* (2012) 20:7646–54. doi: 10.1364/OE.20.007646
28. Yao XC. Intrinsic optical signal imaging of retinal activation. *Jpn J Ophthalmol.* (2009) 53:327–33. doi: 10.1007/s10384-009-0685-4
29. Yao XC, Yamauchi A, Perry B, George JS. Rapid optical coherence tomography and recording functional scattering changes from activated frog retina. *Appl Opt.* (2005) 44:2019–23. doi: 10.1364/AO.44.002019
30. Bizheva K, Pflug R, Hermann B, Povazay B, Sattmann H, Qiu P, et al. Optophysiology: depth-resolved probing of retinal physiology with functional ultrahigh-resolution optical coherence tomography. *Proc Natl Acad Sci U S A.* (2006) 103:5066–71. doi: 10.1073/pnas.0506997103
31. Azimipour M, Valente D, Vienola KV, Werner JS, Zawadzki RJ, Jonnal RS. Optoretinogram: optical measurement of human cone and rod photoreceptor responses to light. *Opt Lett.* (2020) 45:4658–61. doi: 10.1364/OL.398868
32. Pandiyan VP, Maloney-Bertelli A, Kuchenbecker JA, Boyle KC, Ling T, Chen ZC, et al. The optoretinogram reveals the primary steps of phototransduction in the living human eye. *Sci Adv.* (2020) 6:eabc112. doi: 10.1126/sciadv.abc1124
33. Zhang L, Dong R, Zawadzki RJ, Zhang P. Volumetric data analysis enabled spatially resolved optoretinogram to measure the functional signals in the living retina. *J Biophotonics.* (2021) 15:e202100252. doi: 10.1002/jbio.202100252
34. Jonnal RS. Toward a clinical optoretinogram: a review of noninvasive, optical tests of retinal neural function. *Ann Transl Med.* (2021) 9:1270. doi: 10.21037/atm-20-6440
35. Zhang P, Shibata B, Peinado G, Zawadzki RJ, FitzGerald P, Pugh EN. Measurement of diurnal variation in rod outer segment length in vivo in mice with the OCT optoretinogram. *Invest Ophthalmol Vis Sci.* (2020) 61:9. doi: 10.1167/iovs.61.3.9
36. Lassoued A, Zhang F, Kurokawa K, Liu Y, Bernucci MT, Crowell JA, et al. Cone photoreceptor dysfunction in retinitis pigmentosa revealed by optoretinography. *Proc Natl Acad Sci U S A.* (2021) 118:2107444118. doi: 10.1073/pnas.2107444118
37. Ma G, Son T, Kim TH, Yao X. Functional optoretinography: concurrent oct monitoring of intrinsic signal amplitude and phase dynamics in human photoreceptors. *Biomed Opt Express.* (2021) 12:2661–9. doi: 10.1364/BOE.423733
38. Cooper RF, Brainard DH, Morgan JIW. Optoretinography of individual human cone photoreceptors. *Opt Express.* (2020) 28:39326–39. doi: 10.1364/OE.409193
39. Kim TH, Wang B, Lu Y, Son T, Yao X. Functional optical coherence tomography enables in vivo optoretinography of photoreceptor dysfunction due to retinal degeneration. *Biomed Opt Express.* (2020) 11:5306–20. doi: 10.1364/BOE.399334
40. Pandiyan VP, Jiang X, Maloney-Bertelli A, Kuchenbecker JA, Sharma U, Sabesan R. High-speed adaptive optics line-scan oct for cellular-resolution optoretinography. *Biomed Opt Express.* (2020) 11:5274–96. doi: 10.1364/BOE.399034

41. Yao X, Son T, Kim TH, Lu Y. Functional optical coherence tomography of retinal photoreceptors. *Exp Biol Med.* (2018) 243:1256–64. doi: 10.1177/1535370218816517
42. Zhang Q, Lu R, Wang B, Messinger JD, Curcio CA, Yao X. Functional optical coherence tomography enables in vivo physiological assessment of retinal rod and cone photoreceptors. *Sci Rep.* (2015) 5:9595. doi: 10.1038/srep09595
43. Wang B, Lu R, Zhang Q, Jiang Y, Yao X. En face optical coherence tomography of transient light response at photoreceptor outer segments in living frog eyecup. *Opt Lett.* (2013) 38:4526–9. doi: 10.1364/OL.38.004526
44. Moayed AA, Hariri S, Choh V, Bizheva K. In vivo imaging of intrinsic optical signals in chicken retina with functional optical coherence tomography. *Opt Lett.* (2011) 36:4575–7. doi: 10.1364/OL.36.004575
45. Yao X, Kim TH. Fast intrinsic optical signal correlates with activation phase of phototransduction in retinal photoreceptors. *Exp Biol Med.* (2020) 245:1087–95. doi: 10.1177/1535370220935406
46. Srinivasan VJ, Wojtkowski M, Fujimoto JG, Duker JS. In vivo measurement of retinal physiology with high-speed ultrahigh-resolution optical coherence tomography. *Opt Lett.* (2006) 31:2308–10. doi: 10.1364/OL.31.002308
47. Wang B, Zhang Q, Lu R, Zhi Y, Yao X. Functional optical coherence tomography reveals transient phototropic change of photoreceptor outer segments. *Opt Lett.* (2014) 39:6923–6. doi: 10.1364/OL.39.006923
48. Akhlagh Moayed A, Hariri S, Choh V, Bizheva K. Correlation of visually evoked intrinsic optical signals and electroretinograms recorded from chicken retina with a combined functional optical coherence tomography and electroretinography system. *J Biomed Opt.* (2012) 17:016011. doi: 10.1117/1.JBO.17.1.016011
49. Zhang QX, Lu RW, Messinger JD, Curcio CA, Guarcello V, Yao XC. In vivo optical coherence tomography of light-driven melanosome translocation in retinal pigment epithelium. *Sci Rep.* (2013) 3:2644. doi: 10.1038/srep02644
50. Son T, Wang B, Thapa D, Lu Y, Chen Y, Cao D, et al. Optical coherence tomography angiography of stimulus evoked hemodynamic responses in individual retinal layers. *Biomed Opt Express.* (2016) 7:3151–62. doi: 10.1364/BOE.7.003151
51. Son T, Wang B, Lu Y, Chen Y, Cao D, Yao X. Concurrent oct imaging of stimulus evoked retinal neural activation and hemodynamic responses. *Proc SPIE Int Soc Opt Eng.* (2017) 10045:1004522. doi: 10.1117/12.2252480
52. Suzuki W, Tsunoda K, Hanazono G, Tanifuji M. Stimulus-induced changes of reflectivity detected by optical coherence tomography in macaque retina. *Invest Ophthalmol Vis Sci.* (2013) 54:6345–54. doi: 10.1167/iovs.13-12381
53. Srinivasan VJ, Chen Y, Duker JS, Fujimoto JG. In vivo functional imaging of intrinsic scattering changes in the human retina with high-speed ultrahigh resolution oct. *Opt Express.* (2009) 17:3861–77. doi: 10.1364/OE.17.003861
54. Messner A, Aranha dos Santos V, Stegmann H, Puchner S, Schmidl D, Leitgeb R, et al. Quantification of intrinsic optical signals in the outer human retina using optical coherence tomography. *Ann N Y Acad Sci.* (2021). doi: 10.1111/nyas.14721. [Epub ahead of print].
55. Hillmann D, Pfäffle C, Spahr H, Sudkamp H, Franke G, Hüttmann G. In vivo ff-ss-oct optical imaging of physiological responses to photostimulation of human photoreceptor cells. In: Bille JF, editor. *High Resolution Imaging in Microscopy and Ophthalmology: New Frontiers in Biomedical Optics*. Cham: Springer International Publishing (2019). p. 181–94. doi: 10.1007/978-3-030-16638-0_8
56. Yao X, Son T, Kim T-H, Le D. Interpretation of anatomic correlates of outer retinal bands in optical coherence tomography. *Exp Biol Med.* (2021) 246:2140–50. doi: 10.1177/15353702211022674
57. Hillmann D, Spahr H, Pfaffle C, Sudkamp H, Franke G, Huttmann G. In vivo optical imaging of physiological responses to photostimulation in human photoreceptors. *Proc Natl Acad Sci U S A.* (2016) 113:13138–43. doi: 10.1073/pnas.1606428113
58. Boyle KC, Chen ZC, Ling T, Pandiyan VP, Kuchenbecker J, Sabesan R, et al. Mechanisms of light-induced deformations in photoreceptors. *Biophys J.* (2020) 119:1481–8. doi: 10.1016/j.bpj.2020.09.005
59. Jonnal RS, Kocaoglu OP, Zawadzki RJ, Liu Z, Miller DT, Werner JS. A review of adaptive optics optical coherence tomography: technical advances, scientific applications, and the future. *Invest Ophthalmol Vis Sci.* (2016) 57:OCT51–68. doi: 10.1167/iovs.16-19103
60. Kim T-H, Wang B, Lu Y, Son T, Yao X, editors. Intrinsic signal optoretinography of rod photoreceptor dysfunction due to retinal degeneration. *ProcSPIE.* (2021) 11623:2576897. doi: 10.1117/12.2576897
61. Ma G, Son T, Kim TH, Yao X. In vivo optoretinography of phototransduction activation and energy metabolism in retinal photoreceptors. *J Biophotonics.* (2021) 14:e202000462. doi: 10.1002/jbio.202000462
62. Wang B, Lu Y, Yao X. In vivo optical coherence tomography of stimulus-evoked intrinsic optical signals in mouse retinas. *J Biomed Opt.* (2016) 21:96010. doi: 10.1117/1.JBO.21.9.096010
63. Son T, Alam M, Toslak D, Wang B, Lu Y, Yao X. Functional optical coherence tomography of neurovascular coupling interactions in the retina. *J Biophotonics.* (2018) 11:e201800089. doi: 10.1002/jbio.201800089
64. Kim T-H, Wang B, Lu Y, Son T, Yao X. Retinal intrinsic optical signal imaging of wild-type and Rd10 mice. *Invest Ophth Vis Sci.* (2020) 61:198. Available online at: https://iovs.arvojournals.org/article.aspx?articleid=2769057
65. Kim T-H, Ding J, Yao X. Intrinsic signal optoretinography of dark adaptation kinetics. *Sci Rep.* (2022) 12:1–11. doi: 10.1038/s41598-022-06562-4
66. Zhang P, Zawadzki RJ, Goswami M, Nguyen PT, Yarov-Yarovoy V, Burns ME, et al. In vivo optophysiology reveals that G-protein activation triggers osmotic swelling and increased light scattering of rod photoreceptors. *Proc Nat Acad Sci.* (2017) 114:E2937. doi: 10.1073/pnas.1620572114
67. Li Y, Zhang Y, Chen S, Vernon G, Wong WT, Qian H. Light-dependent oct structure changes in photoreceptor degenerative Rd 10 mouse retina. *Invest Ophthalmol Vis Sci.* (2018) 59:1084–94. doi: 10.1167/iovs.17-23011
68. Roorda A, Williams DR. Optical fiber properties of individual human cones. *J Vis.* (2002) 2:4. doi: 10.1167/2.5.4
69. Zhang F, Kurokawa K, Lassoued A, Crowell JA, Miller DT. Cone photoreceptor classification in the living human eye from photostimulation-induced phase dynamics. *Proc Nat Acad Sci.* (2019) 116:7951. doi: 10.1073/pnas.1816360116
70. Pfäffle C, Spahr H, Kutzner L, Burhan S, Hilge F, Miura Y, et al. Simultaneous functional imaging of neuronal and photoreceptor layers in living human retina. *Opt Lett.* (2019) 44:5671–4. doi: 10.1364/OL.44.005671
71. Tschulakow AV, Oltrup T, Bende T, Schmelzle S, Schraermeyer U. The anatomy of the foveola reinvestigated. *PeerJ.* (2018) 6:e4482. doi: 10.7717/peerj.4482
72. Riva CE, Logean E, Falsini B. Visually evoked hemodynamical response and assessment of neurovascular coupling in the optic nerve and retina. *Prog Retin Eye Res.* (2005) 24:183–215. doi: 10.1016/j.preteyeres.2004.07.002
73. Lim LS, Ling LH, Ong PG, Foulds W, Tai ES, Wong TY. Dynamic responses in retinal vessel caliber with flicker light stimulation and risk of diabetic retinopathy and its progression. *Invest Ophthalmol Vis Sci.* (2017) 58:2449–55. doi: 10.1167/iovs.16-21008
74. Mandecka A, Dawczynski J, Blum M, Müller N, Kloos C, Wolf G, et al. Influence of flickering light on the retinal vessels in diabetic patients. *Diabetes Care.* (2007) 30:3048–52. doi: 10.2337/dc07-0927
75. Li YC, Strang C, Amthor FR, Liu L, Li YG, Zhang QX, et al. Parallel optical monitoring of visual signal propagation from the photoreceptors to the inner retina layers. *Opt Lett.* (2010) 35:1810–2. doi: 10.1364/OL.35.001810
76. Zhang T, Kho AM, Srinivasan VJ. In vivo morphometry of inner plexiform layer (Ipl) stratification in the human retina with visible light optical coherence tomography. *Front Cell Neurosci.* (2021) 15:147. doi: 10.3389/fncel.2021.655096
77. Ghassabi Z, Kuranov RV, Schuman JS, Zambrano R, Wu M, Liu M, et al. In vivo sublayer analysis of human retinal inner plexiform layer obtained by visible-light optical coherence tomography. *Invest Ophthalmol Vis Sci.* (2022) 63:18. doi: 10.1167/iovs.63.1.18
78. Zhao Y-B, Yao X-C. Intrinsic optical imaging of stimulus-modulated physiological responses in amphibian retina. *Opt Lett.* (2008) 33:342–4. doi: 10.1364/OL.33.000342
79. Yao X, George JS. Near-infrared imaging of fast intrinsic optical responses in visible light-activated amphibian retina. *J Biomed Opt.* (2006) 11:1–8. doi: 10.1117/1.2393155
80. Lu Y, Liu C, Yao X. In vivo super-resolution imaging of transient retinal phototropism evoked by oblique light stimulation. *J Biomed Opt.* (2018) 23:1–4. doi: 10.1117/1.JBO.23.5.050502

81. Lu R, Levy AM, Zhang Q, Pittler SJ, Yao X. Dynamic near-infrared imaging reveals transient phototropic change in retinal rod photoreceptors. *J Biomed Opt.* (2013) 18:1–7. doi: 10.1117/1.JBO.18.10.106013
82. Lu Y, Benedetti J, Yao X. Light-induced length shrinkage of rod photoreceptor outer segments. *Transl Vis Sci Technol.* (2018) 7:29. doi: 10.1167/tvst.7.6.29
83. Lu Y, Wang B, Pepperberg DR, Yao X. Stimulus-evoked outer segment changes occur before the hyperpolarization of retinal photoreceptors. *Biomed Opt Express.* (2017) 8:38–47. doi: 10.1364/BOE.8.000038
84. Lu Y, Kim T-H, Yao X. Comparative study of wild-type and RD10 mice reveals transient intrinsic optical signal response before phosphodiesterase activation in retinal photoreceptors. *Exp Biol Med.* (2019) 245:360–7. doi: 10.1177/1535370219896284
85. Brown KT, Murakami M. A. New receptor potential of the monkey retina with no detectable latency. *Nature.* (1964) 201:626–8. doi: 10.1038/201626a0
86. Hestrin S, Korenbrot JI. Activation kinetics of retinal cones and rods: response to intense flashes of light. *J Neurosci.* (1990) 10:1967. doi: 10.1523/JNEUROSCI.10-06-01967.1990
87. Lu CD, Lee B, Schottenhamml J, Maier A, Pugh EN, Fujimoto JG. Photoreceptor layer thickness changes during dark adaptation observed with ultrahigh-resolution optical coherence tomography *Invest Ophthalmol Vis Sci.* (2017) 58:4632–43. doi: 10.1167/iovs.17-22171
88. Zhao X, Thapa D, Wang B, Lu Y, Gai S, Yao X. Stimulus-evoked outer segment changes in rod photoreceptors. *J Biomed Opt.* (2016) 21:1–8. doi: 10.1117/1.JBO.21.6.065006
89. Bocchero U, Falleroni F, Mortal S, Li Y, Cojoc D, Lamb T, et al. Mechanosensitivity is an essential component of phototransduction in vertebrate rods. *PLoS Biol.* (2020) 18:e3000750. doi: 10.1371/journal.pbio.3000750
90. Chabre M. X-Ray Diffraction Studies of Retinal Rods. I structure of the disc membrane, effect of illumination. *Biochimica et Biophysica Acta Biomembrane.* (1975) 382:322–35. doi: 10.1016/0005-2736(75)90274-6
91. Yagi N. Structural changes in rod outer segments of frog and mouse after illumination. *Exp Eye Res.* (2013) 116:395–401. doi: 10.1016/j.exer.2013.09.016
92. Pearring JN, Salinas RY, Baker SA, Arshavsky VY. Protein sorting, targeting and trafficking in photoreceptor cells. *Prog Retin Eye Res.* (2013) 36:24–51. doi: 10.1016/j.preteyeres.2013.03.002
93. Morshedian A, Fain GL. The evolution of rod photoreceptors. *Philos Trans R Soc B Biol Sci.* (2017) 372:20160074. doi: 10.1098/rstb.2016.0074
94. Stone J, van Driel D, Valter K, Rees S, Provis J. The locations of mitochondria in mammalian photoreceptors: relation to retinal vasculature. *Brain Res.* (2008) 1189:58–69. doi: 10.1016/j.brainres.2007.10.083
95. Le D, Son T, Lim JI, Yao X. Quantitative optical coherence tomography reveals rod photoreceptor degeneration in early diabetic retinopathy. *[Preprint]. arXiv.* (2021). doi: 10.48550/arXiv.2112.07780
96. Lee KE, Heitkotter H, Carroll J. Challenges associated with ellipsoid zone intensity measurements using optical coherence tomography. *Transl Vis Sci Technol.* (2021) 10:27. doi: 10.1167/tvst.10.12.27
97. Westermann B. Mitochondrial fusion and fission in cell life and death. *Nat Rev Mol Cell Biol.* (2010) 11:872–84. doi: 10.1038/nrm3013
98. Pham N-A, Richardson T, Cameron J, Chue B, Robinson BH. Altered mitochondrial structure and motion dynamics in living cells with energy metabolism defects revealed by real time microscope imaging. *Microsc Microanal.* (2004) 10:247–60. doi: 10.1017/S143192760404005X
99. Berkowitz BA, Qian H. Oct imaging of rod mitochondrial respiration in vivo. *Exp Biol Med.* (2021) 246:2151–8. doi: 10.1177/15353702211013799
100. Li Y, Fariss RN, Qian JW, Cohen ED, Qian H. Light-induced thickening of photoreceptor outer segment layer detected by ultra-high resolution oct imaging. *Invest Ophthalmol Vis Sci.* (2016) 57:OCT105–11. doi: 10.1167/iovs.15-18539
101. Berkowitz BA, Podolsky RH, Qian H, Li Y, Jiang K, Nellissery J, et al. Mitochondrial respiration in outer retina contributes to light-evoked increase in hydration in vivo. *Invest Ophthalmol Vis Sci.* (2018) 59:5957–64. doi: 10.1167/iovs.18-25682
102. Gao S, Li Y, Bissig D, Cohen ED, Podolsky RH, Childers KL, et al. Functional regulation of an outer retina hyporeflective band on optical coherence tomography images. *Sci Rep.* (2021) 11:10260. doi: 10.1038/s41598-021-89599-1
103. Adijanto J, Banzon T, Jalickee S, Wang NS, Miller SS. Co2-induced ion and fluid transport in human retinal pigment epithelium. *J Gen Physiol.* (2009) 133:603–22. doi: 10.1085/jgp.200810169
104. Wangsa-Wirawan ND, Linsenmeier RA. Retinal oxygen: fundamental and clinical aspects. *Arch Ophthalmol.* (2003) 121:547–57. doi: 10.1001/archopht.121.4.547
105. Messner A, Werkmeister RM, Seidel G, Stegmann H, Schmetterer L, Aranha dos Santos V. Light-induced changes of the subretinal space of the temporal retina observed via optical coherence tomography. *Sci Rep.* (2019) 9:13632. doi: 10.1038/s41598-019-50057-8
106. Azimipour M, Migacz JV, Zawadzki RJ, Werner JS, Jonnal RS. Functional retinal imaging using adaptive optics swept-source Oct at 16 Mhz. *Optica.* (2019) 6:300–3. doi: 10.1364/OPTICA.6.000300
107. Lujan BJ, Roorda A, Knighton RW, Carroll J. Revealing henle's fiber layer using spectral domain optical coherence tomography. *Invest Ophthalmol Vis Sci.* (2011) 52:1486–92. doi: 10.1167/iovs.10-5946
108. Gao W, Cense B, Zhang Y, Jonnal RS, Miller DT. Measuring retinal contributions to the optical stiles-crawford effect with optical coherence tomography. *Opt Express.* (2008) 16:6486–501. doi: 10.1364/OE.16.006486
109. Litts KM, Zhang Y, Freund KB, Curcio CA. Optical coherence tomography and histology of age-related macular degeneration support mitochondria as reflectivity sources. *Retina.* (2018) 38:445–61. doi: 10.1097/IAE.0000000000001946
110. Thiele S, Isselmann B, Pfau M, Holz FG, Schmitz-Valckenberg S, Wu Z, et al. Validation of an automated quantification of relative ellipsoid zone reflectivity on spectral domain-optical coherence tomography images. *Transl Vision Sci Technol.* (2020) 9:17. doi: 10.1167/tvst.9.11.17
111. Hu Z, Hariri A, Wu X, Sadda SR. Comparison of retinal layer profiles between spectral-domain optical coherence tomography devices. *Invest Ophthalmol Vis Sci.* (2014) 55:4785. Available online at: https://iovs.arvojournals.org/article.aspx?articleid=2270332
112. Meleppat RK, Zhang P, Ju MJ, Manna SK, Jian Y, Pugh EN, et al. Directional optical coherence tomography reveals melanin concentration-dependent scattering properties of retinal pigment epithelium. *J Biomed Opt.* (2019) 24:1–10. doi: 10.1117/1.JBO.24.6.066011
113. Bloom SM, Singal IP. Revised classification of the optical coherence tomography outer retinal bands based on central serous chorioretinopathy analysis. *Retina.* (2021) 41:181–8. doi: 10.1097/IAE.0000000000002792
114. Cuenca N, Ortuño-Lizarán I, Pinilla I. Cellular characterization of oct and outer retinal bands using specific immunohistochemistry markers and clinical implications. *Ophthalmology.* (2018) 125:407–22. doi: 10.1016/j.ophtha.2017.09.016
115. Spaide RF, Curcio CA. Anatomical correlates to the bands seen in the outer retina by optical coherence tomography: literature review and model. *Retina.* (2011) 31:1609–19. doi: 10.1097/IAE.0b013e3182247535
116. Staurenghi G, Sadda S, Chakravarthy U, Spaide RF. Proposed lexicon for anatomic landmarks in normal posterior segment spectral-domain optical coherence tomography: the in•oct consensus. *Ophthalmology.* (2014) 121:1572–8. doi: 10.1016/j.ophtha.2014.02.023
117. Jonnal RS, Kocaoglu OP, Zawadzki RJ, Lee S-H, Werner JS, Miller DT. The cellular origins of the outer retinal bands in optical coherence tomography images. *Invest Ophthalmol Vis Sci.* (2014) 55:7904–18. doi: 10.1167/iovs.14-14907
118. Jonnal RS, Gorczynska I, Migacz JV, Azimipour M, Zawadzki RJ, Werner JS. The properties of outer retinal band three investigated with adaptive-optics optical coherence tomography. *Invest Ophthalmol Vis Sci.* (2017) 58:4559–68. doi: 10.1167/iovs.16-21138
119. Ahmed SA, Le D, Son T, Adejumo T, Yao X. Adc-Net: an open-source deep learning network for automated dispersion compensation in optical coherence tomography. *arXiv. [Preprint].* (2022). doi: 10.48550/arXiv.2201.12625
120. Haddad WM, Seres A, Coscas G, Soubrane G. Presentation delay in patients affected with exudative age-related macular degeneration. *Graefes Arch Clin Exp Ophthalmol.* (2002) 240:31–4. doi: 10.1007/s00417-001-0404-4

121. Lee SC, Lee ET, Kingsley RM, Wang Y, Russell D, Klein R, et al. Comparison of diagnosis of early retinal lesions of diabetic retinopathy between a computer system and human experts. *Arch Ophthalmol.* (2001) 119:509–15. doi: 10.1001/archopht.119.4.509
122. Suppiej A, Marino S, Reffo ME, Maritan V, Vitaliti G, Mailo J, et al. Early onset retinal dystrophies: clinical clues to diagnosis for pediatricians. *Ital J Pediatr.* (2019) 45:168. doi: 10.1186/s13052-019-0760-5
123. Gonzales CR, Clinical-Trial-Group VISION. Enhanced efficacy associated with early treatment of neovascular age-related macular degeneration with pegaptanib sodium: an exploratory analysis. *Retina.* (2005) 25:815–27. doi: 10.1097/00006982-200510000-00001
124. Loewenstein A. The significance of early detection of age-related macular degeneration: richard & hinda rosenthal foundation lecture, the macula society 29th annual meeting. *Retina.* (2007) 27:873–8. doi: 10.1097/IAE.0b013e318050d2ec
125. Oh K, Kang HM, Leem D, Lee H, Seo KY, Yoon S. Early detection of diabetic retinopathy based on deep learning and ultra-wide-field fundus images. *Sci Rep.* (2021) 11:1897. doi: 10.1038/s41598-021-81539-3
126. Hafler BP. Clinical progress in inherited retinal degenerations: gene therapy clinical trials and advances in genetic sequencing. *Retina.* (2017) 37:417–23. doi: 10.1097/IAE.0000000000001341

Conflict of Interest: The authors declare that the research was conducted in the absence of any commercial or financial relationships that could be construed as a potential conflict of interest.

frontiers | Frontiers in Medicine

ORIGINAL RESEARCH
published: 08 April 2022
doi: 10.3389/fmed.2022.864879

ADC-Net: An Open-Source Deep Learning Network for Automated Dispersion Compensation in Optical Coherence Tomography

Shaiban Ahmed[1], *David Le*[1], *Taeyoon Son*[1], *Tobiloba Adejumo*[1], *Guangying Ma*[1] *and Xincheng Yao*[1,2]*

[1] *Department of Biomedical Engineering, University of Illinois Chicago, Chicago, IL, United States,* [2] *Department of Ophthalmology and Visual Science, University of Illinois Chicago, Chicago, IL, United States*

Chromatic dispersion is a common problem to degrade the system resolution in optical coherence tomography (OCT). This study is to develop a deep learning network for automated dispersion compensation (ADC-Net) in OCT. The ADC-Net is based on a modified UNet architecture which employs an encoder-decoder pipeline. The input section encompasses partially compensated OCT B-scans with individual retinal layers optimized. Corresponding output is a fully compensated OCT B-scan with all retinal layers optimized. Two numeric parameters, i.e., peak signal to noise ratio (PSNR) and structural similarity index metric computed at multiple scales (MS-SSIM), were used for objective assessment of the ADC-Net performance and optimal values of 29.95 ± 2.52 dB and 0.97 ± 0.014 were obtained respectively. Comparative analysis of training models, including single, three, five, seven and nine input channels were implemented. The mode with five-input channels was observed to be optimal for ADC-Net training to achieve robust dispersion compensation in OCT.

Keywords: dispersion compensation, deep learning, fully convolutional network (FCN), automated approach, optical coherence tomography

OPEN ACCESS

Edited by:
Peng Xiao,
Sun Yat-sen University, China

Reviewed by:
Pengfei Zhang,
Dalian University of Technology, China
Weiye Song,
Shandong University, China

****Correspondence:***
Xincheng Yao
xcy@uic.edu

Specialty section:
This article was submitted to Ophthalmology, a section of the journal Frontiers in Medicine

Received: *28 January 2022*
Accepted: *14 March 2022*
Published: *08 April 2022*

Citation:
Ahmed S, Le D, Son T, Adejumo T, Ma G and Yao X (2022) ADC-Net: An Open-Source Deep Learning Network for Automated Dispersion Compensation in Optical Coherence Tomography. Front. Med. 9:864879. doi: 10.3389/fmed.2022.864879

INTRODUCTION

Optical coherence tomography (OCT) is a non-invasive imaging modality that can provide three-dimensional information for clinical assessment (1, 2). By providing micrometer scale resolution to visualize retinal neurovasculature, it has been widely used for fundamental research and clinical management of eye conditions (3–5). Given the reciprocal relationship between the axial resolution and bandwidth of the light source, high resolution OCT requires a broadband light source (6, 7). However, the broadband light source induces chromatic dispersion, i.e., light wavelength dependence of the optical pathlength difference between the sample and the reference arms. The reference arm generally houses a reference mirror that has a uniform reflectance profile, but the sample arm usually contains dispersive media (such as a biological tissue). Optical dispersion induces phase shifts among different wavelength signals in OCT detection, and thus degrades the axial resolution. Dispersion can also produce chirping noise and hence reduce the quality of the OCT image. Both hardware and numeric methods have been developed for dispersion compensation to enhance OCT image quality.

The hardware-based method involves additional dispersive media, such as water, BK7 glass (8), fused silica (9), etc. in the reference arm to balance the dispersion in the sample arm. Physical dispersion compensation can also be achieved by using grating-based group and phase delay detectors (10). Faster speed and a higher range of tunability were achieved by using acousto-optic modulator (11) and tunable optical fiber stretchers (12). However, hardware compensation leads to a bulky optical system due to the need of additional components. Moreover, the hardware compensation is typically effective only when the sample subject is stable with a fixed dispersion.

Numerical dispersion compensation has been established as a useful alternative to hardware-based techniques. Numeric dispersion correction is based on the digital processing of OCT spectrogram, providing the flexibility of adjustable correction values of the dispersion induced phase error. Fercher et al. (13) proposed a numeric compensation technique where a depth-dependent kernel was correlated with the spectrogram to compensate dispersion. However, this method relies on the availability of information related to the dispersive characteristics of the sample which can vary for biological tissues. Fractional Fourier transform for dispersion compensation was introduced by Lippok et al. (14) where the performance is dependent on the accuracy of the value of an order parameter and acquiring this value for biological samples can be challenging. A spectral domain phase correction method, where the spectral density function is multiplied with a phase term, was demonstrated by Cense et al. (15). However, to determine the precise phase term, isolated reflections from a reference interface with a uniform reflectance profile, which might not be available in clinical setup, are required. A numeric algorithm based on the optimization of a sharpness function, which was termed to be divided by the number of intensity points above a specified threshold, was presented by Wojtkowski et al. (16) where a pair of dispersion compensation coefficients were derived to compensate dispersion in the entire B-scan. But due to the depth varying changes in biological tissues, the dispersion effect can vary at different depths and hence a single pair of dispersion compensation coefficients may not be able to compensate dispersion for all depths effectively in one B-scan.

Entropy information of the signal acquired in the spatial domain was utilized as the sharpness metric by Hofer et al. (17) to compensate dispersion. However, the numeric techniques which are based on sharpness metrics are susceptible to the prevalent speckle noise in OCT B-scans and can lead to overestimation or underestimation when the system lacks high sensitivity. A depth-reliant method was proposed by Pan et al. (18) where an analytical formula was developed to estimate the second-order dispersion compensation coefficients in different depths based on a linear fitting approach. But this method relies on the accurate estimation of second order coefficients at specific depths and the analytical formula can differ for different biological subjects. Besides, the lower degree of freedom available in a linear fitting method can lead to inaccurate estimation of the coefficients at different depths. Spectroscopic analysis of A-scan's spectrogram was conducted to estimate and correct dispersion by Ni et al. (19) where information entropy estimated from a centroid image was used as a sharpness metric. However, this technique leads to lower resolution and requires a region of analysis without transversely oriented and regularly arranged nanocylinder. In general, these classical numerical methods can be computationally extensive when it comes to the widescale application as they are usually designed based on specific conditions and may require additional optimization for the generalized application. Hence these methods may lead to computational complexity in real-time application.

Deep learning has garnered popularity in medical image processing (20–24), with demonstrated feasibility for real-time application due to its capability to handle large datasets, computational efficiency, high accuracy, and flexibility for widescale application. Deep learning-based algorithms have been used in image denoising (25, 26), segmentation (27–31), classification (32–34), etc. In this study, we propose a deep learning network for automated dispersion compensation (ADC-Net) that is based on a modified UNet architecture. Input to ADC-Net comprises OCT B-scans which are compensated by different second-order dispersion coefficients and hence are partially compensated for certain retinal layers only. The output is a fully compensated OCT B-scan image optimized for all retinal layers. We quantitatively analyzed the proposed model using two parameters namely MS-SSIM and PSNR. Comparative analysis of training models, including single, three, five, seven and nine input channels were implemented. The source code along with necessary instructions on how to implement it have been provided here: github.com/dleninja/adcnet.

MATERIALS AND METHODS

This study has been conducted in compliance with the ethical regulations reported in the Declaration of Helsinki and has been authorized by the institutional review board of the University of Illinois at Chicago.

Data Acquisition

Five healthy human subjects (mean age: 30 $\pm$ 4.18 years; mean refractive error: -2.28 ± 1.53D) were recruited to acquire the OCT images for training and testing the proposed ADC-Net. These subjects had no history of ocular medical conditions. All human subjects affirmed their willful consent before participating in the experimental study. Moreover, two patients diagnosed with proliferative diabetic retinopathy (DR) were recruited for technical validation of the ADC-Net performance on OCT with eye conditions. Patient 1 was a 58-year-old female diagnosed with proliferative DR without macular edema. Patient 2 was a 68-year-old male also diagnosed with proliferative DR but with macular edema. Data were acquired from the left eye for both the patients. For OCT imaging, the illumination power on the cornea was 600 mW which is within the limit set by the American National Standards Institute. The light source used for this experiment was a near infrared (NIR) superluminescent diode (D-840-HPI, Superlum, Cork, Ireland). A pupil camera and a dim red light were used for localizing the retina and as a fixation target, respectively. The purpose of the fixation target is to minimize voluntary eye movements. Axial and lateral pixel

resolutions were achieved as 1.5 and 5.0 mm respectively. The OCT spectrometer that was used for data recording consisted of a line-scan CCD camera. The total number of pixels in the CCD camera was 2,048 pixels and the line rate was 70,000 Hz. The recording speed for OCT imaging was 100 B-scans per second with a frame resolution of 300 A-lines per B-Scan. A total of 9 OCT volumes were captured. Each OCT volume consists of 1200 B-scans. Seven of these OCT volumes (8400 B-scans) were used for training the model, and another two (2400 B-scans) were used as testing set.

Dispersion Compensation

The signal acquisition in OCT involves recording the spectrogram obtained by interfering back-reflected light from different interfaces of the sample with the back-reflected light from the reference mirror. The fringe pattern generated by this interference signal is detected by the spectrometer and corresponding OCT signal can be represented by the following equation (18):

$$S_{int}\ (k) = 2Re\left\{\sum\sqrt{I_n\left(k\right)I_r\left(k\right)}\exp\left\{i\left[k.\Delta z_n + \phi\left(k.\Delta z_n\right)\right]\right\}\right\} \quad (1)$$

In this equation, $I_n\left(k\right)$ and $I_r\left(k\right)$ represent the back-reflected light intensity obtained from the n-th sample layer and reference arm respectively. The wavenumber is denoted by k while the difference in optical path length is denoted by Δz_n. The phase term $\phi\left(k.\Delta z_n\right)$ denotes the phase difference between the sample interfaces and the reference mirror and this includes the higher order dispersive terms. We can express the phase term as:

$$\begin{aligned}
&\phi\left(k,\Delta z_n\right) = \beta_n\left(k\right)\cdot\Delta z_n\\
&= \left[n_n\left(k_o\right)\cdot k_o + n_{g,n}\left(k_o\right)\cdot\left(k - k_o\right) +\right.\\
&\left.\beta''_n\left(k_o\right)\cdot\frac{\left(k-k_o\right)^2}{2!} + \beta'''_n\left(k_o\right)\cdot\frac{\left(k-k_o\right)^3}{3!} + \ldots\right]\cdot\Delta z_n\\
&= n_n\left(k_o\right)\cdot k_o\cdot\Delta z_n + n_{g,n}\left(k_o\right)\cdot z_n\cdot\left(k - k_o\right) + a_2\cdot\left(k-k_o\right)^2 +\\
&a_3\cdot\left(k-k_o\right)^3 + \ldots
\end{aligned} \quad (2)$$

Where β_n represents dispersion coefficient, while a_2 and a_3 are second and third order dispersion compensation coefficients. While n_n is the sample's n-th layer's refractive index, $n_{n,g}$ is the effective group refractive index. Numeric dispersion compensation can be done by modifying the phase term through the addition of a phase correction term which eliminates the dispersive phase. The following equation shows second and third order dispersion compensation phase correction:

$$\overline{\phi}\left(k\right) = -a_2\left(k - k_o\right)^2 - a_3\left(k - k_o\right)^3 \quad (3)$$

Where a_2 and a_3 can be adjusted to compensate second-order group velocity and third-order phase dispersion. However, since dispersion in biological tissue is different at different depths, dispersion compensation using a single pair of second and third-order coefficients might not be sufficient for all depths. Numerically estimating and applying different compensation coefficients for different depths can be computationally extensive for widescale application. In following Section Model Architecture, we present ADC-Net, a deep learning-based dispersion compensation algorithm for automated implementation of full depth compensation. Input to ADC-Net can be of single or multiple channels of partially compensated B-scans. These partially compensated B-scans can be obtained by using the phase correction method in Equation (3). For simplicity, we have compensated the B-scans using second order compensation only. All depth dispersion compensated ground truth data were also crafted from an array of partially compensated B-scans and the detailed procedure is elaborated in Section Data Pre-Processing.

Model Architecture

The ADC-Net is a fully convolutional network (FCN) based on a modified UNet algorithm, which consists of an encoder-decoder architecture (**Figure 1**). The input to the ADC-Net can be of a single channel or a multichannel system. Each input is an OCT B-scan image which was compensated by different second-order dispersion compensation coefficients and hence the B-scans in each channel are optimally compensated at different layers or depths. The output is dispersion compensated OCT B-scans where all layers in different depths are compensated effectively.

The encoder segment is a combination of convolutional, max pooling, dense, and transitional blocks. The primary function of the decoder segment is to deduce useful features from the image. To ensure precise feature localization and mapping for generating output images, bridging between the encoder and the decoder is established. The convolution blocks, which perform summing operations, constitute the dense blocks. The skip connections, which alleviate the vanishing gradient problem, are used to link each subsequent block to previous blocks. A transition block is connected to each dense block, which is to reduce the dimension of output feature map.

The decoder segment consists of up-sampling operations along with the decoder blocks. Using the decoder block, the outputs obtained from the convolution operation of the fitting transition blocks and the up-sampling operations are concatenated. Image features can then be localized precisely by convolving the generated feature maps.

In the ADC-Net, two types of functions, namely batch normalization function and ReLU activation function trail all the convolution operations. On the other hand, a SoftMax activation function follows the terminal convolutional layer.

Moreover, transfer learning is employed to avoid overfitting errors by utilizing the ImageNet dataset. The ImageNet dataset is a visual database that consists of millions of everyday images. These images differ from the OCT B-scans but facilitate in training the CNN model to learn about simple features such as edges, color codes, geometric shapes, etc. in the primary layers and complex features in the deeper layers by utilizing CNN's bottom-up hierarchical learning structure. Transfer learning can then facilitate the network to relay these simple features to learn complex features which are related to the OCT B-scans. A fully connected layer that consists of 1,000 neurons along with a SoftMax activation function exists in the pre-trained encoder

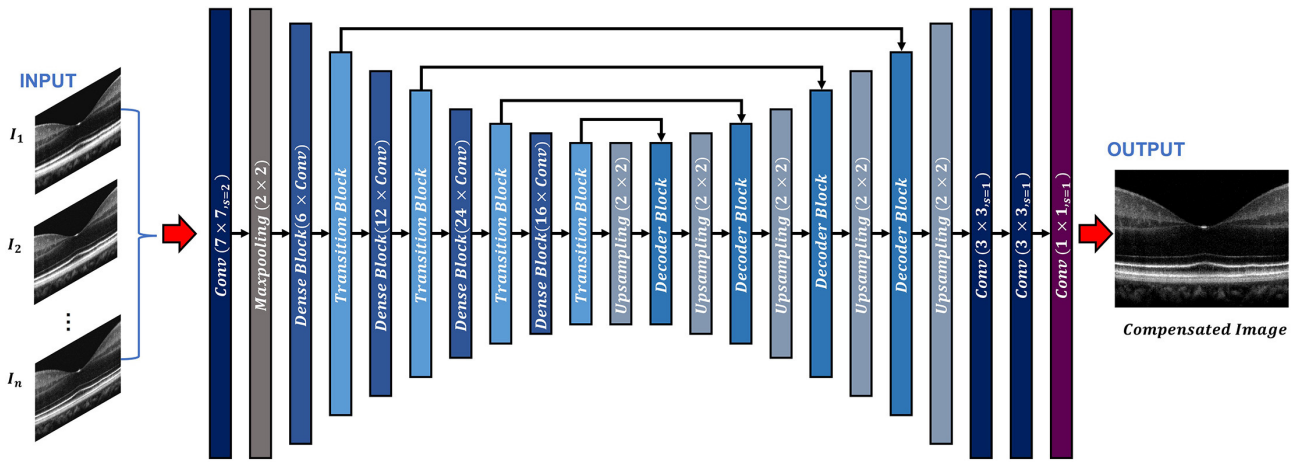

FIGURE 1 | Overview of the ADC-Net architecture. Conv stands for convolution operation. The input section is comprised of OCT B-scans compensated by different second order coefficients ($n = 3$, 5, 7, and 9 for three, five, seven, and nine input channel models. A single image is used as input for the single input channel model). The output image is a corresponding fully compensated OCT B-scan.

network model. When the pre-training was concluded (after achieving about 75% classification accuracy on the ImageNet validation dataset), the fully connected layer was removed. The decoder network was then fed with transitional outputs from the encoder network. Adam optimizer which had a learning rate of 0.0001 was used to train the FCN model along with a dice loss function. The proposed network has a deeper layer and utilizes lesser parameters compared to the classical UNet model which ensures higher learning capability with reduced computational burden and thus makes it more robust. It is similar to a previously reported model (33) where it has been shown that this network can generate higher mean IOU and F1 scores when compared to classical UNet architecture.

The hardware environment used for implementing the proposed ADC-Net had Windows 10 operating system equipped with NVIDIA Quadro RTX Graphics Processing Unit (GPU). The software model was written on Python (v3.7.1) utilizing Keras (v2.2.4) with Tensorflow (v1.31.1) backend.

Data Pre-processing

Figure 2 briefly illustrates the ground truth preparation method for a single B-scan. Raw OCT data were acquired using the SD-OCT system described in Section Data Acquisition. An array of B-scans ranging from I_1 to I_N (In this study, $N = 5$) were reconstructed from the same raw data frame using the usual procedure that involves background subtraction, k-space linearization, dispersion compensation, FFT, etc. However, each of the B-scans were compensated with different second order dispersion compensation coefficients ranging from C_1 to C_N ($N = 5$). Technical rationale of numeric compensation has been explained in Section Dispersion Compensation. Since the tissue structure in a biological subject differ at different depths, the dispersion effect also varies accordingly and thus a single second order coefficient can effectively compensate dispersion errors at a specific layer only. Thus, required values of second order dispersion compensation co-efficient, ranging from C_1 to C_N, were selected empirically so that dispersion at all depths were compensated optimally. In I_1, the region demarcated by the red box along the inner retina had been dispersion compensated and optimized using C_1. However, as we move further away from the inner layers the dispersion effects appear to be more prominent due to ineffective compensation. Image I_N on the contrary has the region demarcated by the yellow box at the outer retina optimized and well compensated. To prepare the ground truth B-scan, the red and yellow demarcated region from I_1 and I_N were extracted and stitched in proper sequence to obtain dispersion compensated layers at the inner and outer retina. Similarly, the remaining layers acquired from I_2 to I_{N-1} which were compensated by C_2 to C_{N-1} respectively. Optimally compensated layers were extracted and stitched sequentially to obtain the all-depth compensated ground truth B-scan. To prepare the training and test data for the single, three, five, seven, and nine input channel models, 1, 3, 5, 7, and 9 arrays of B-scans were re-constructed respectively from each raw volume while each array were compensated with different second order dispersion compensation coefficients. These coefficients were selected in equal intervals between C_1 to C_N. To acquire the OCT data and for digital image processing, LabView (National Instruments) and MATLAB 2021 software environments were used, respectively.

Quantitative Parameters

Two parameters, namely peak signal to noise ratio (PSNR) and structural similarity index metric at multiple scales (MS-SSIM) were used for quantitative analysis and objective assessment of our proposed method. The two parameters are defined as follows:

Peak Signal to Nose Ratio

PSNR can be defined as the ratio of maximum signal strength to the corrupting background noise which was computed using the

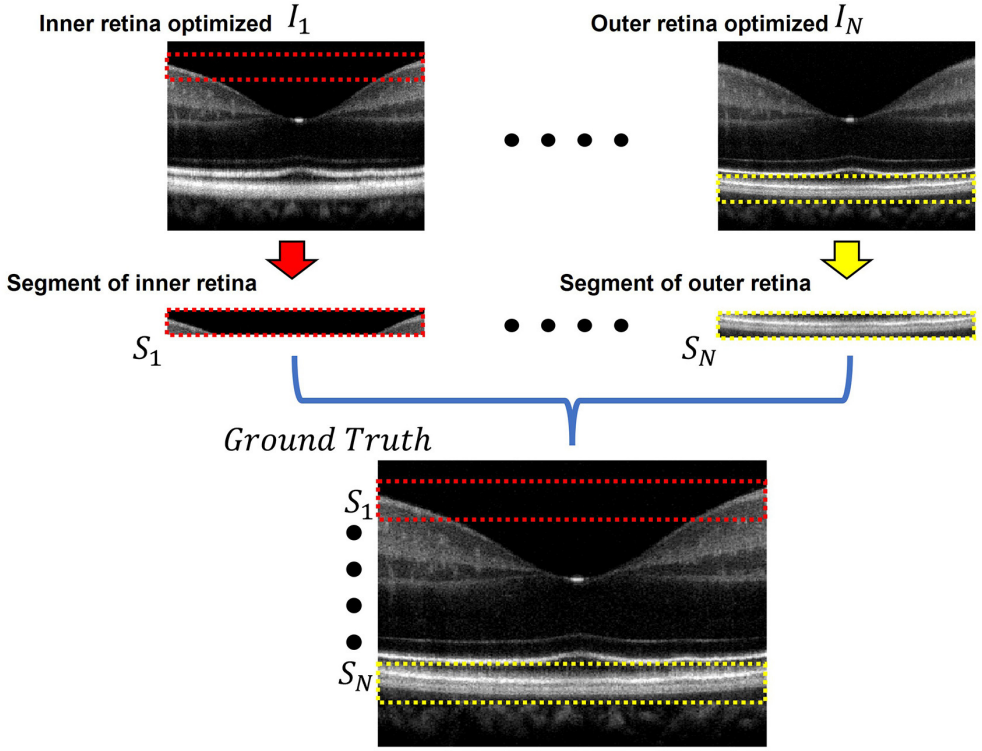

FIGURE 2 | Ground truth preparation. An array of images ranging from I_1 to I_N were utilized to prepare the ground truth image. Each image was compensated by a single second order co-efficient ranging from C_1 to C_N. Well compensated layers from each image were extracted and stitched together to form the ground truth image. In I_1 the inner retinal segment (demarcated by the dashed red box) is better compensated compared to the inner retinal segment in I_N. On the other hand, the outer retinal segment in I_N (demarcated by the dashed yellow box) is better compensated compared to that of I_1. The ground truth was prepared by stitching the inner retinal segment S_1 from I_1 and outer retinal segment S_N from I_N. The adjacent layers were similarly extracted and stitched from the subsequent images between I_1 and I_N.

following equation (35):

$$PSNR = 10\log_{10}\left(\frac{s^2}{MSE(f,g)}\right) \tag{4}$$

Where s is the maximum pixel intensity value in the reconstructed image. Mean squared error (MSE) between the reference image f (ground truth) and reconstructed image g (output) can be defined by the following equation:

$$MSE(f,g) = \frac{1}{MN}\sum_{i=1}^{M}\sum_{j=1}^{N}(f_{ij} - g_{ij})^2 \tag{5}$$

Where M, N denotes the number of rows and columns while $(f_{ij} - g_{ij})$ denote the pixel-wise error difference between f and g.

Structural Similarity Index Metric at Multiple Scale

MS-SSIM was computed to quantify the structural similarities between the ground truth and the corresponding output images obtained from the ADC-Net when implemented with different input channels models. MS-SSIM utilizes three visual perception parameters namely the luminance, contrast and structural parameters when calculated at multiple scales and thus it incorporates detailed image information at different resolutions and visual perceptions which make it a robust and accurate quality metric.

If x and y denote two image patches which are to be compared, the luminance parameter is defined by (36):

$$l(x,y) = \frac{2\mu_x\mu_y + C_1}{\mu^2{}_x + \mu^2{}_y + C_1} \tag{6}$$

The contrast parameter is defined by:

$$c(x,y) = \frac{2\sigma_x\sigma_y + C_2}{\sigma^2{}_x + \sigma^2{}_y + C_2} \tag{7}$$

The structural parameter is defined by:

$$s(x,y) = \frac{\sigma_{xy} + C_3}{\sigma_x\sigma_y + C_3} \tag{8}$$

Where μ_x and μ_y represent the mean, σ_{xy} represents the co-variance, σ_x and σ_y represent the standard deviation of x and y respectively. The constants C_1, C_2, and C_3 can be obtained by:

$$C_1 = (K_1\,L)^2,\ C_2 = (K_2L)^2 \quad and \quad C_3 = C_2/2 \tag{9}$$

Where, L is the pixel dynamic image range and K_1 *(0.01)* and K_2 *(0.03)* are two scalar constants. Thus, SSIM can be defined as:

$$SSIM\left(x,y\right) = [l\left(x,y\right)]^{\alpha} \cdot [c\left(x,y\right)]^{\beta} \cdot [s\left(x,y\right)]^{\gamma}$$
$$or,\ SSIM\left(x,y\right) = \frac{(2\mu_x\mu_y + C_1)(2\sigma_{xy} + C_2)}{(\mu^2{}_x + \mu^2{}_y + C_1)(\sigma^2{}_x + \sigma^2{}_y + C_2)}$$
$$[\alpha = \beta = \gamma = 1] \quad (10)$$

In order to obtain multi scale SSIM, an iterative approach is employed where the reference and the output images are scaled *M-1* times and down sampled by a factor of 2 after each iteration. The contrast and structural parameter are calculated at each scale while the luminance parameter is computed only at the *M*-th scale. The final quantitative parameter is obtained by the combining the values obtained at all the scales using the following relation:

$$MSSSIM\left(x,y\right) = \left[l_M\left(x.y\right)\right]^{\alpha M} \cdot \prod_{j=1}^{M} \left[c_j\left(x,y\right)\right]^{\beta j} \left[s_j\left(x,y\right)\right]^{\gamma j} \quad (11)$$

RESULTS

Qualitative Assessment

Figure 3A shows representative OCT B-scan images obtained from different input channels models along with a raw uncompensated OCT B-scan. For better visualization, 6 neighboring B-scans at the macula region of a human retina were averaged and the images are displayed on a logarithmic scale. **Figure 3A1** represents the uncompensated image and due to the dispersion effect, the B-scan suffers from low axial resolution and the different retinal layers appear to be blurry and overlapping as the detailed structural information is lost. **Figures 3A2–A6** illustrate the representative OCT B-scans obtained from single to nine input channels models respectively. In **Figure 3A2**, which was obtained from the single input channel model, even though the inner retinal layer appears to be well compensated, the central and outer bands suffer from blurring and the dispersion effect is not optimally compensated. When the input was increased to 3, 5, 7, and 9 B-scans, the quality of the output image was enhanced. As shown in **Figures 3A3–A6**, both the inner and outer layers were better compensated compared to single input channel model and showed sharp microstructural information. As described in Section Data Acquisition, input models with 3, 5, 7, and 9 input channels had input B-scans with both inner and outer retinal layers compensated. However, 5, 7, and 9 input channels performed slightly better compensation compared to the model with 3 input channels and this improvement can be better visualized in **Figure 3B** which were generated for a detailed illustration of the differences in performance of the different models. To generate these images, pixel-wise, intensity difference between the corresponding ground truth and **Figures 3A1–A6** were computed, and the resultant intensity differential images were displayed in a jet colourmap. Here, the bright regions indicate higher differences in intensity while the darker blue region indicates lower to no difference. These images serve two purposes. First, the pixel wise extent of dissimilarity between each of the images and the ground truth can be observed. The lesser difference with the ground truth means higher similarity and thus indicates better performance. Second, the detailed differences in performance between the different input models and the uncompensated image can be better visualized using the difference between these images and the ground truth as a qualitative metric. **Figure 3B1** shows that the uncompensated image depicts more difference from the compensated ground truth due to lack of dispersion compensation. While **Figure 3B2** shows slightly better performance but more bright regions at the outer retina depict that the single input model could not compensate dispersion properly at the lower depths. **Figure 3B3** illustrates that the model with three input channels performed better than the single input channel model. However, **Figures 3B4–B6** show almost similar performance and the least amount of difference with the ground truth and thus the higher performance than the other two models.

Quantitative Assessment

The two quantitative parameters described in Section Quantitative Parameterswere calculated from the resultant images obtained from different input channels models along with the corresponding uncompensated images to perform a quantitative assessment of the proposed ADC-Net. Before computing the quantitative parameters, the four repetitive B-scans at the same locations were averaged. MS-SSIM and PSNR were calculated, and the result is graphically represented in **Figure 4**. Mean values with standard deviation were used for representative purpose. In **Figure 4**, UC represents uncompensated images while M1, M3, M5, M7, and M9 represent the output obtained from single, three, five, seven, and nine input channels models respectively. In **Figure 4A**, we can observe that the lowest mean MS-SSIM score was obtained for UC (0.85 ± 0.025) which depicts the least similarity with the ground truth image. Due to the dispersion effect the image quality degrades significantly without compensation. The MS-SSIM score obtained from the single input channel model (M1) is 0.94 ± 0.021 which shows an improved performance in terms of dispersion compensation compared to the raw uncompensated image. The similarity score for three (M3) and five (M5) input channels models show a gradual improvement in performance with MS-SSIM values of 0.95 ± 0.018 and 0.97 ± 0.016 respectively. However, the graph flattens after M5 as seven (M7) and nine (M9) input channels models show a similarity score of 0.97 ± 0.014 and 0.97 ± 0.014 which are within the 1 standard deviation range of the five-input channels model. We can observe a similar trend in **Figure 4B** which depicts the mean PSNR. Highest PSNR of 29.95 ± 2.52 dB was calculated for the five input channels model (M5) while seven and nine input channels model had a mean PSNR of 29.91 ± 2.134 dB and 29.64 ± 2.259 dB respectively. Output from the three input channels model recorded a slightly lower PSNR value of 27.49 ± 1.606 dB and the downward slope continued for the single input channel model (M1) with a mean value of 25.86 ± 1.677 dB and the least PSNR of 20.99 ± 0.021 dB was observed for the uncompensated B-scans.

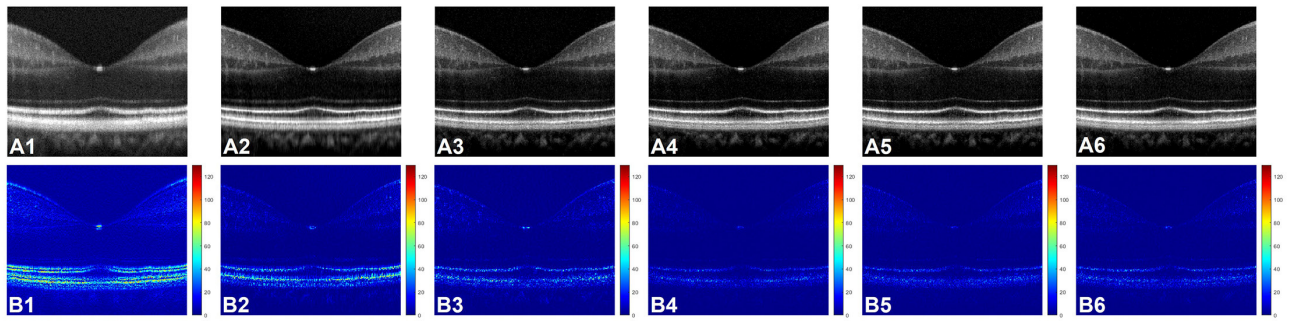

FIGURE 3 | (A) Representative OCT of a human retina with no dispersion compensation **(A1)**, and dispersion compensated by single **(A2)**, three **(A3)**, five **(A4)**, seven **(A5)**, and nine **(A6)** input channel models. **(B)** Corresponding differential intensity images which were generated by computing the pixel-to-pixel intensity differences between the ground truth image and the images in **(A1–A6)**, respectively.

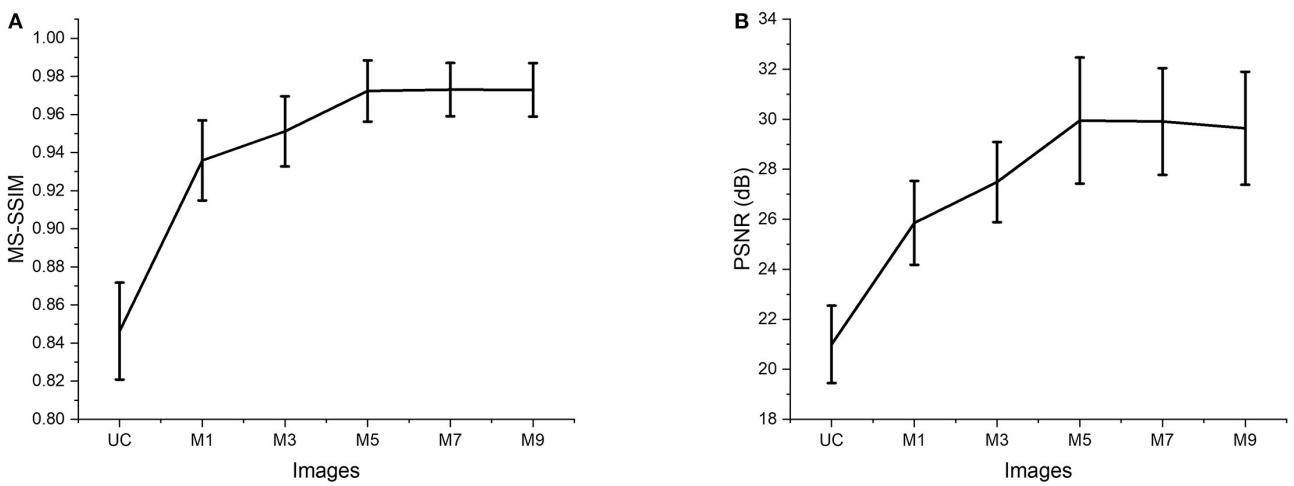

FIGURE 4 | Quantitative evaluation of MS-SSIM **(A)** and PSNR **(B)**. Average values are used for the graphical representation. UC represents the uncompensated images; M1, M3, M5, M7, and M9 represent the images acquired from ADC-Net with the single, three, five, seven, and nine input channel models.

Intensity Profile Analysis

Figure 5 illustrates comparative reflectance intensity profile analysis of the outer retina. The yellow vertical line in **Figure 5A** shows the retinal region for OCT intensity profile analysis (**Figure 5B**). **Figure 5B** illustrates axial intensity profiles at the parafovea and encompasses the outer retinal bands. Six neighboring B-scans were averaged and 5 adjacent A-lines at the region of interest were averaged from the averaged B-scan before generating the intensity profiles. **Figure 5A** is displayed in logarithmic scale for enhanced visualization, but the intensity profile analysis in **Figure 5B** is shown in linear scale. The intensity profiles are depicted in **Figure 5** where GT and UC represent the intensity profiles obtained from the ground truth and the uncompensated images, respectively. Whereas M1, M3, M5, M7, and M9 stand for the intensity profiles obtained from single, three, five, seven, and nine input channels models respectively.

The ELM band profile is known to reflect the point spread function (PSF), i.e., the axial resolution. From GT we can observe a sharper and narrower PSF at the ELM layer when compared to UC and M1, where the PSF is flat and wider. The ELM band profile becomes slightly better for M3, but M5, M7, and M9 depict thinner and analogous band profile to GT. Blurred RPE band profiles can also be observed for UC and M1 at the RPE which overlaps with the Bruch's Membrane (BM) region (37). On the contrary, GT, M3, M5, M7, and M9 show sharper peaks which can be distinguished separately. This means that the RPE and Bruch's membrane can be observed separately from the reconstructed images. The IS/OS and OPR bands in UC have distinguishable peaks but still depict thicker profiles, compared to GT. M1 and M3 show slightly thinner IS/OS and OPR bands, compared to UC. On the other hand, GT, M5, M7, and M9 depict sharper and thinner OCT band profiles.

Dispersion can also shift the location of the interfaces in a multilayered sample which can affect the depth measurement of different layers (38). We comparatively evaluate the peak locations of the ELM, IS/OS, OPR, and RPE in the intensity profiles demonstrated in **Figure 5** to assess the performance of

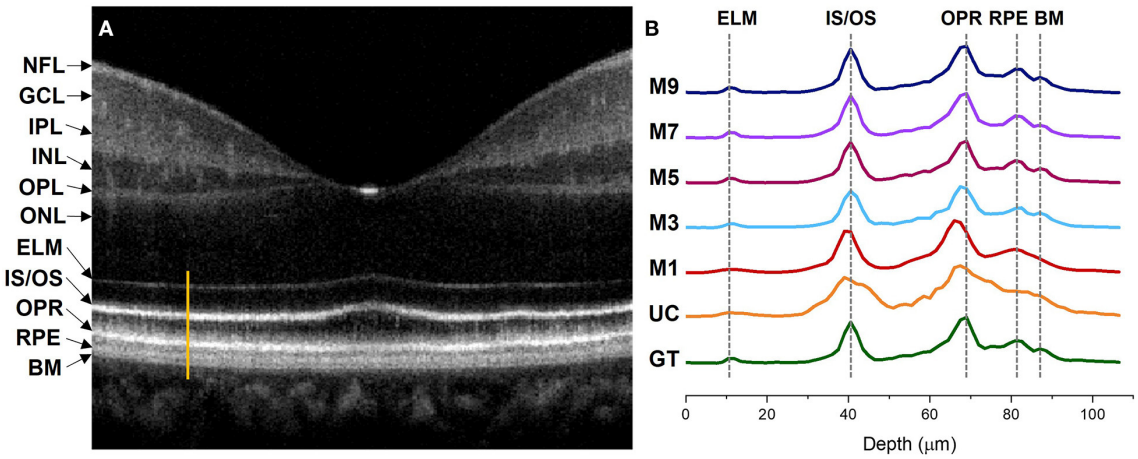

FIGURE 5 | Intensity profile analysis of the outer retinal bands. **(A)** OCT B-scan of a human retina at the macula region with different retinal layers labeled accordingly. The bright orange line represents the A-line segment of the outer retina at the parafovea region where the intensity profiles in **(B)** were computed. **(B)** Intensity profiles generated from different image models. GT, ground truth; UC, uncompensated; M1, single input channel; M3, three input channels; M5, five input channels; M7, seven input channels; M9, nine input channels; NFL, nerve fiber layer; GCL, ganglion cell layer; IPL, inner plexiform layer; INL, inner nuclear layer; OPL, outer plexiform layer; INL, outer nuclear layer; ELM, external limiting membrane; IS/OS, inner segment/outer segment junction; OPR, outer plexiform layer; RPE, retinal pigment epithelium; BM, bruch's membrane.

our proposed method in terms of depth measurement where the GT was taken as the reference of assessment. The GT's peak location at the ELM and IS/OS layer aligns with M3, M5, M7, and M9. However, the peak location for M3 shifts at the OPR and RPE when compared to the peak location of the GT where M5, M7, and M9 demonstrate aligned peaks with the GT. For M1 and UC, the peaks observed at ELM and RPE are flat and overlapping while the peaks are shifted at the IS/OS and OPR layer.

Automated Dispersion Compensation in 3D Volume OCT

Figure 6 illustrated the performance of the ADC-Net model for automated processing of 3D volume OCT. **Figure 6A** shows an OCT enface image. For 3D volumetric OCT, with the model of five input channels, the ADC-Net was used to compensate for individual B-scans sequentially. **Figures 6B,C** show three representative B-scans before (**Figure 6B**) and after (**Figure 6C**) dispersion compensation. **Figures 6C1–C3** have higher contrast, sharpness and retain better structural integrity when compared to the uncompensated images in **Figures 6B1–B3**.

Performance Validation With OCT Images of DR

Performance of the proposed ADC-Net was also assessed using OCT images with eye conditions. Two OCT volumes acquired from two different subjects diagnosed with DR were used for this technical validation. Patient details have been discussed in Section Data Acquisition. and the representative B-scans have been illustrated in **Figure 7**. **Figures 7A1,B1** depicts the raw uncompensated images obtained from patient 1 and 2, respectively. **Figures 7A2,B2** depicts the corresponding compensated B-scans obtained from our proposed ADC-Net when implemented using 5 input channels. Compared to the uncompensated B-scans, **Figures 7A2,B2** depict better contrast and signal quality, and the retinal layers are sharper and can be visualized more effectively. The distortion in retinal layers can also be depicted from the compensated images.

DISCUSSION

Dispersion compensation is necessary to obtain high axial resolution and retain detailed structural information in OCT. Traditional numeric dispersion compensation approaches can be computationally expensive. Numerically devised methods also require optimization based on specific contexts, and thus may lack flexibility for generalized application. The demonstrated ADC-Net can be automated for real-time implementation due to its higher computational flexibility and simplicity. Once trained with the optimum number of input channels and well-crafted ground truth data, ADC-Net can automatically compensate dispersion effectively and generate OCT B-scans with high quality. We made the proposed ADC-Net available through an open-source platform (github.com/dleninja/adcnet-) for easy accessibility to a robust and automated dispersion compensation algorithm.

The performance of ADC-Net peaked when employed using five, seven, and nine input channels models. While a single input channel model performed better than a raw uncompensated image in terms of image resolution, the output images still depicted blurring effects. The output obtained from the three input channels model was better than the single input channel model but slightly worse than the five, seven, and nine input channels.

Since the proposed FCN is built on a modified UNet structure and follows an encoder-decoder pipeline, the model trains itself by acquiring features from the input and the

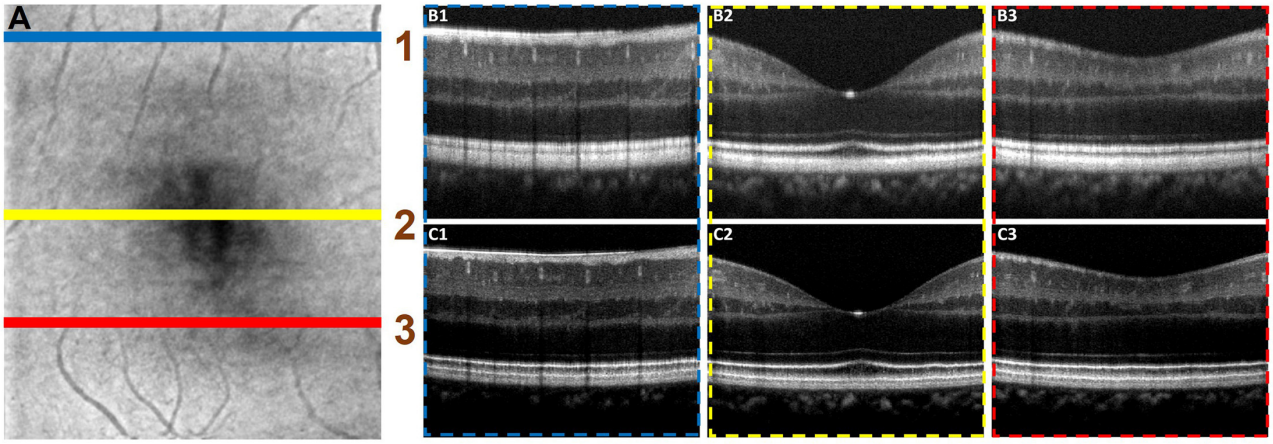

FIGURE 6 | Automated processing of 3D volume OCT dataset. **(A)** Depicts an enface image with the horizontal lines, line 1 (blue), line 2 (yellow), and line 3 (red), demarcating the regions from where representative B-scans were extracted. The corresponding B-scans are shown in **(B,C)**. The compensated B-scans **(C1–C3)** demonstrate higher sharpness, contrast and better visibility of structural layers when compared to the raw uncompensated B-scans **(B1–B3)**.

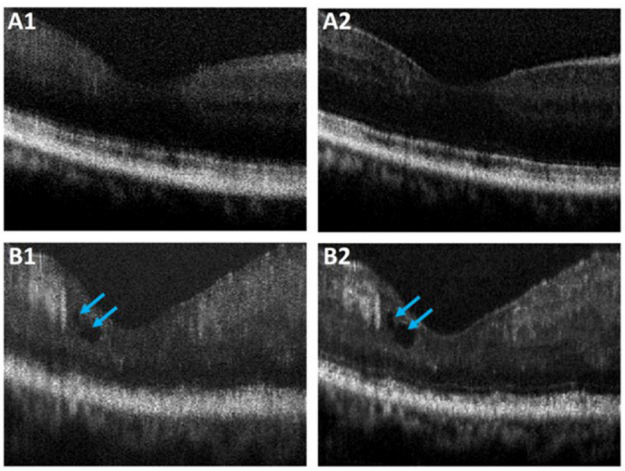

FIGURE 7 | Representative OCT B-scans of proliferative diabetic retinopathy (DR) patients without **(A)** and with **(B)** macular edema (blue arrowheads). The compensated B-scans **(A2,B2)** obtained from the proposed ADC-Net illustrate higher contrast and sharpness compared to the raw uncompensated B-scans **(A1,B1)**.

ground truth data to reconstruct dispersion compensated images. For a single input channel model, the input B-scans were compensated by a single second-order dispersion compensation co-efficient which can optimize dispersion in a specific retinal layer only. For our experiment, the second-order dispersion compensation parameter was selected close to C_1 and thus the input B-scans had optimum compensation along with the inner retinal layer only. Consequently, the output B-scans had the inner retinal layer optimized only. The input model with three input channels had three arrays of B-scans and each array was compensated by different second-order dispersion compensation coefficients which were selected equally spaced between C_1 to C_N. The three input channels thus provided more information related to more layers being compensated and thus the model performed better compared to the single input channel model. Similarly, for five, seven, and nine input channels models, the input channels had more B-scans with more layers being compensated which in terms provided more features to the model to train itself better. Hence the performance was better compared to single and three input channels models. However, quantitative analysis revealed that five, seven, and nine input channels models depict similar performance, and thus optimum all-depth dispersion can be obtained using five input channels.

The dispersion effect broadens OCT band profiles and thus degrade the axial resolution. In a well-compensated OCT image, such as the ground truth image, this blur effect would be minimized, corresponding to thinner and sharper band profiles. On the other hand, as illustrated in the intensity profile obtained from the uncompensated image, the band profiles would be thicker due to dispersion effect which in terms would affect the image resolution. This would impact the thickness measurement of the retinal bands as they would appear to be thicker than the actual value. From our proposed ADC-Net we obtained sharp and thin OCT band profiles from input models with five, seven, and nine channels which were analogous to the intensity profile obtained from the ground truth image. The peaks for the outer retinal layers were also aligned which shows the promise for accurate depth measurement. Hence the proposed ADC-Net demonstrates its capability to generate B-scans with high resolution that can retain intricate structural information. Implementation of this automated process can be beneficial in clinical assessment and ophthalmic research by providing accurate retinal thickness and depth measurement in healthy and diagnosed patients. Artificial intelligence may reduce the technical complexities and streamlining tasks in a clinical setting.

The major challenge of our proposed ADC-Net is the availability of finetuned ground truth data which requires all depth compensation. However, once the required values of the coefficients for different depths and ranges are obtained for one volume, it can be applied to other volumes directly. Thus, for one OCT system, calibrating the system once would be enough. Once our proposed ADC-Net is trained with all depth compensated ground truth, it can automatically generate fully compensated B-scans with retinal layers optimized. Therefore, this ADC-Net process can be effectively implemented for real-time application. The performance of the ADC-Net has been validated with OCT images acquired from both healthy and diseased eyes. We are aware that the OCT image quality of diseased eyes in **Figure 7** was relatively poor, compared to that of healthy subjects. However, the feasibility of automatically generating dispersion compensated images from diseased eyes has been validated with the ADC-Net.

In conclusion, a deep learning network ADC-Net has been validated for automated dispersion compensation in OCT. The ADC-Net is based on a redesigned UNet architecture which employs an encoder-decoder pipeline. With input of partially compensated OCT B-scans with individual retinal layers optimized, the ADC-Net can output a fully compensated OCT B-scans with all retinal layers optimized. The partially compensated OCT B-scans can be produced automatically, after a system calibration to estimate the dispersion range. Comparative analysis of training models, including single, three, five, seven and nine input channels were implemented. The five-input channels implementation was observed to be sufficient for ADC-Net training to achieve robust dispersion compensation in OCT.

DATA AVAILABILITY STATEMENT

The raw data supporting the conclusions of this article will be made available by the authors, without undue reservation. Source code for implementing ADC-Net is available at: https://github.com/dleninja/adcnet.

ETHICS STATEMENT

The studies involving human participants were reviewed and approved by Institutional Review Board of the University of Illinois at Chicago. The patients/participants provided their written informed consent to participate in this study.

AUTHOR CONTRIBUTIONS

SA contributed to data processing, analysis, model implementation, and manuscript preparation. DL contributed to network design, model implementation, and manuscript preparation. TS contributed to experimental design, data acquisition, and manuscript preparation. TA contributed to data processing. GM contributed to the data collection of the diseased patients. XY supervised the project and contributed to manuscript preparation. All authors contributed to the article and approved the submitted version.

FUNDING

This research was supported in part by National Institutes of Health (NIH) (R01 EY023522, R01 EY029673, R01 EY030101, R01 EY030842, and P30 EY001792), Richard and Loan Hill endowment, and Unrestricted grant from Research to prevent blindness.

REFERENCES

1. Huang D, Swanson EA, Lin CP, Schuman JS, Stinson WG, Chang W, et al. Optical coherence tomography. *Science.* (1991) 254:1178–81. doi: 10.1126/science.1957169
2. Fujimoto JG, Brezinski ME, Tearney GJ, Boppart SA, Bouma B, Hee MR, et al. Optical biopsy and imaging using optical coherence tomography. *Nat Med.* (1995) 1:970–2. doi: 10.1038/nm0995-970
3. Wojtkowski M, Bajraszewski T, Gorczyńska I, Targowski P, Kowalczyk A, Wasilewski W, et al. Ophthalmic imaging by spectral optical coherence tomography. *Am J Ophthalmol.* (2004) 138:412–9. doi: 10.1016/j.ajo.2004.04.049
4. Gao SS, Jia Y, Zhang M, Su JP, Liu G, Hwang TS, et al. Optical coherence tomography angiography. *Invest Ophthalmol Vis Sci.* (2016) 57:OCT27–36. doi: 10.1167/iovs.15-19043
5. Yao X, Son T, Kim T-H, Lu Y. Functional optical coherence tomography of retinal photoreceptors. *Exp Biol Med.* (2018) 243:1256–64. doi: 10.1177/1535370218816517
6. Povazay B, Bizheva K, Unterhuber A, Hermann B, Sattmann H, Fercher AF, et al. Submicrometer axial resolution optical coherence tomography. *Opt Lett.* (2002) 27:1800–2. doi: 10.1364/OL.27.001800
7. Unterhuber A, PovaŽay B, Hermann B, Sattmann H, Drexler W, Yakovlev V, et al. Compact, low-cost Ti: Al 2 O 3 laser for in vivo ultrahigh-resolution optical coherence tomography. *Opt Lett.* (2003) 28:905–7. doi: 10.1364/OL.28.000905
8. Yao XC, Yamauchi A, Perry B, George JS. Rapid optical coherence tomography and recording functional scattering changes from activated frog retina. *Appl Opt.* (2005) 44:2019–23. doi: 10.1364/AO.44.002019
9. Drexler W, Morgner U, Ghanta RK, Kärtner FX, Schuman JS, Fujimoto JG. Ultrahigh-resolution ophthalmic optical coherence tomography. *Nat Med.* (2001) 7:502–7. doi: 10.1038/86589
10. Tearney G, Bouma B, Fujimoto J. High-speed phase-and group-delay scanning with a grating-based phase control delay line. *Opt Lett.* (1997) 22:1811–3. doi: 10.1364/OL.22.001811
11. Xie T, Wang Z, Pan Y. Dispersion compensation in high-speed optical coherence tomography by acousto-optic modulation. *Appl Opt.* (2005) 44:4272–80. doi: 10.1364/AO.44.004272
12. Iyer S, Coen S, Vanholsbeeck F. Dual-fiber stretcher as a tunable dispersion compensator for an all-fiber optical coherence tomography system. *Opt Lett.* (2009) 34:2903–5. doi: 10.1364/OL.34.002903
13. Fercher AF, Hitzenberger CK, Sticker M, Zawadzki R, Karamata B, Lasser T. Numerical dispersion compensation for partial coherence interferometry and optical coherence tomography. *Opt Express.* (2001) 9:610–5. doi: 10.1364/OE.9.000610
14. Lippok N, Coen S, Nielsen P, Vanholsbeeck F. Dispersion compensation in fourier domain optical coherence tomography using the fractional Fourier transform. *Opt Express.* (2012) 20:23398–413. doi: 10.1364/OE.20.023398

15. Cense B, Nassif NA, Chen TC, Pierce MC, Yun S-H, Park BH, et al. Ultrahigh-resolution high-speed retinal imaging using spectral-domain optical coherence tomography. *Opt Express.* (2004) 12:2435–47. doi: 10.1364/OPEX.12.002435
16. Wojtkowski M, Srinivasan VJ, Ko TH, Fujimoto JG, Kowalczyk A, Duker JS. Ultrahigh-resolution, high-speed, Fourier domain optical coherence tomography and methods for dispersion compensation. *Opt Express.* (2004) 12:2404–22. doi: 10.1364/OPEX.12.002404
17. Hofer B, PovaŽay B, Hermann B, Unterhuber A, Matz G, Drexler W. Dispersion encoded full range frequency domain optical coherence tomography. *Opt Express.* (2009) 17:7–24. doi: 10.1364/OE.17.000007
18. Pan L, Wang X, Li Z, Zhang X, Bu Y, Nan N, et al. Depth-dependent dispersion compensation for full-depth Oct image. *Opt Express.* (2017) 25:10345–54. doi: 10.1364/OE.25.010345
19. Ni G, Zhang J, Liu L, Wang X, Du X, Liu J, et al. Detection and compensation of dispersion mismatch for frequency-domain optical coherence tomography based on a-scan's spectrogram. *Opt Express.* (2020) 28:19229–41. doi: 10.1364/OE.393870
20. Lakhani P, Sundaram B. Deep learning at chest radiography: automated classification of pulmonary tuberculosis by using convolutional neural networks. *Radiology.* (2017) 284:574–82. doi: 10.1148/radiol.2017162326
21. Mohsen H, El-Dahshan E-SA, El-Horbaty E-SM, Salem A-BM. Classification using deep learning neural networks for brain tumors. *Future Comput Inform J.* (2018) 3:68–71. doi: 10.1016/j.fcij.2017.12.001
22. Baltruschat IM, Nickisch H, Grass M, Knopp T, Saalbach A. Comparison of deep learning approaches for multi-label chest X-Ray classification. *Sci Rep.* (2019) 9:1–10. doi: 10.1007/s41906-018-0376-1
23. Tanaka H, Chiu S-W, Watanabe T, Kaoku S, Yamaguchi T. Computer-aided diagnosis system for breast ultrasound images using deep learning. *Phys Med Biol.* (2019) 64:235013. doi: 10.1088/1361-6560/ab5093
24. Riquelme D, Akhloufi MA. Deep learning for lung cancer nodules detection and classification in Ct scans. *AI.* (2020) 1:28–67. doi: 10.3390/ai1010003
25. Devalla SK, Subramanian G, Pham TH, Wang X, Perera S, Tun TA, et al. A Deep learning approach to denoise optical coherence tomography images of the optic nerve head. *Sci Rep.* (2019) 9:1–13. doi: 10.1038/s41598-019-51062-7
26. Mehdizadeh M, MacNish C, Xiao D, Alonso-Caneiro D, Kugelman J, Bennamoun M. Deep feature loss to denoise oct images using deep neural networks. *J Biomed Opt.* (2021) 26:046003. doi: 10.1117/1.JBO.26.4.046003
27. Wang Z, Camino A, Hagag AM, Wang J, Weleber RG, Yang P, et al. Automated detection of preserved photoreceptor on optical coherence tomography in choroideremia based on machine learning. *J Biophotonics.* (2018) 11:e201700313. doi: 10.1002/jbio.201700313
28. Guo Y, Hormel TT, Xiong H, Wang B, Camino A, Wang J, et al. Development and validation of a deep learning algorithm for distinguishing the nonperfusion area from signal reduction artifacts on oct angiography. *Biomed Opt Express.* (2019) 10:3257–68. doi: 10.1364/BOE.10.003257
29. Guo Y, Hormel TT, Xiong H, Wang J, Hwang TS, Jia Y. Automated segmentation of retinal fluid volumes from structural and angiographic optical coherence tomography using deep learning. *Transl Vis Sci Technol.* (2020) 9:54. doi: 10.1167/tvst.9.2.54
30. Wang J, Hormel TT, You Q, Guo Y, Wang X, Chen L, et al. Robust non-perfusion area detection in three retinal plexuses using convolutional neural network in oct angiography. *Biomed Opt Express.* (2020) 11:330–45. doi: 10.1364/BOE.11.000330
31. Guo Y, Hormel TT, Gao L, You Q, Wang B, Flaxel CJ, et al. Quantification of nonperfusion area in montaged wide-field optical coherence tomography angiography using deep learning in diabetic retinopathy. *Ophthalmol Sci.* (2021) 1:100027. doi: 10.1016/j.xops.2021.100027
32. Alam M, Le D, Lim JI, Chan RV, Yao X. Supervised machine learning based multi-task artificial intelligence classification of retinopathies. *J Clin Med.* (2019) 8:872. doi: 10.3390/jcm8060872
33. Alam M, Le D, Son T, Lim JI, Yao X. Av-Net: deep learning for fully automated artery-vein classification in optical coherence tomography angiography. *Biomed Opt Express.* (2020) 11:5249–57. doi: 10.1364/BOE.399514
34. Qiao L, Zhu Y, Zhou H. Diabetic retinopathy detection using prognosis of microaneurysm and early diagnosis system for non-proliferative diabetic retinopathy based on deep learning algorithms. *IEEE Access.* (2020) 8:104292–302. doi: 10.1109/ACCESS.2020.2993937
35. Hore A, Ziou D. Image quality metrics: Psnr Vs. Ssim. In: *Proceedings of 2010 20th International Conference on Pattern Recognition*. Istanbul: IEEE (2010). p. 2366–9. doi: 10.1109/ICPR.2010.579
36. Wang Z, Simoncelli EP, Bovik AC. Multiscale structural similarity for image quality assessment. In: *Proceedings of The Thirty Seventh Asilomar Conference on Signals, Systems & Computers*. Pacific Grove, CA: IEEE (2003). p. 1398–402. doi: 10.1109/ACSSC.2003.129216
37. Yao X, Son T, Kim T-H, Le D. Interpretation of anatomic correlates of outer retinal bands in optical coherence tomography. *Exp Biol Med.* (2021) 246:15353702211022674. doi: 10.1177/15353702211022674
38. Al-Saeed TA, Shalaby MY, Khalil DA. Dispersion compensation in fourier domain optical coherence tomography. *Appl Opt.* (2014) 53:6643–53. doi: 10.1364/AO.53.006643

Conflict of Interest: The authors declare that the research was conducted in the absence of any commercial or financial relationships that could be construed as a potential conflict of interest.

frontiers | Frontiers in Medicine

ORIGINAL RESEARCH
published: 12 May 2022
doi: 10.3389/fmed.2022.886576

A Baseline Study of Oxygen Saturation in Parafoveal Vessels Using Visible Light Optical Coherence Tomography

Jingyu Wang[1], *Weiye Song*[2,3], *Natalie Sadlak*[3], *Marissa G. Fiorello*[3], *Manishi Desai*[3] *and Ji Yi*[1,4]*

[1] Department of Ophthalmology, School of Medicine, Johns Hopkins University, Baltimore, MD, United States, [2] School of Mechanical Engineering, Shandong University, Jinan, China, [3] Department of Ophthalmology, Boston Medical Center, Boston, MA, United States, [4] Department of Biomedical Engineering, Johns Hopkins University, Baltimore, MD, United States

The retinal macula is at the center of our visual field, and thus pathological damage in the macula significantly impacts an individual's quality of life. The parafoveal vessels form the inner retina provide oxygen perfusion, and the measurement of parafoveal oxygen saturation (sO_2) can evaluate macular metabolism and provide pathophysiological insight. In this paper, for the first time, we present a baseline study of microvascular oxygen saturation (sO_2) in perifoveal macular region using visible light optical coherence tomography (VIS-OCT) on normal eyes. The arterial and venous sO_2 from all eyes was 92.1 ± 7.1 (vol %) and 48.4 ± 5.0 (vol %) (mean ± SD), respectively. Arteriovenous sO_2 difference was 43.8 ± 9.5 (vol %). Marginal correlation was found between venous sO_2 and intraocular pressure (IOP) among eyes. No significant correlation was found between sO_2 and vessel topological features, including length, diameter, and distance to fovea. This baseline study could serve as a benchmark for the future sO_2 investigation of retinal macular pathologies.

Keywords: visible light optical coherence tomography, retinal oximetry, baseline study, parafoveal vessels, segmentation

OPEN ACCESS

Edited by:
Peng Xiao,
Sun Yat-sen University, China

Reviewed by:
Yan Li,
Oregon Health and Science University, United States
Vivek Srinivasan,
NYU Grossman School of Medicine, United States

***Correspondence:**
Ji Yi
jiyi@jhu.edu

Specialty section:
This article was submitted to Ophthalmology, a section of the journal Frontiers in Medicine

Received: *28 February 2022*
Accepted: *20 April 2022*
Published: *12 May 2022*

Citation:
Wang J, Song W, Sadlak N, Fiorello MG, Desai M and Yi J (2022) A Baseline Study of Oxygen Saturation in Parafoveal Vessels Using Visible Light Optical Coherence Tomography. Front. Med. 9:886576. doi: 10.3389/fmed.2022.886576

INTRODUCTION

Oxygen supply supports the metabolism of the human retina, and abnormal oxygen perfusion is associated with various retinal conditions leading to vision damage and blindness, including glaucoma, age-related macular degeneration, diabetic retinopathy, and vascular occlusions (1). Therefore, the measurement of blood oxygen saturation within the retinal circulation is not only essential to understanding the physiopathology of retinal diseases, but also can play important role for detection and monitoring.

Label-free optical retinal oximetry harnesses the oxygen-dependent spectral contrast of endogenous hemoglobin to non-invasively measure oxygen saturation quantitatively in the human retina (2–6). A fundus camera based multi-wavelength oximetry has been previously reported in several clinical studies on retinal conditions (7). However, the technique lacks depth resolution, and the measurement is complicated by the reflections from vessel surface. So far, only readings from large vessels in the peri-papillary region have been reported.

Visible light optical coherence tomography (VIS-OCT) is a recent development that provides the necessary 3D imaging capacity to eliminate confounding signals from other retinal layers and the choroid (8–12). The much stronger absorption in visible light range than conventional near infrared light (8), in conjunction with 3D segmentation of retinal blood vessels, permits reliable spatio-spectral analysis for microvascular retinal oximetry (11). By combining OCT angiography, capillary oximetry in the human retina has been recently reported which is a significant technical contribution. The initial report of *in vivo* oximetry using VIS-OCT was introduced in 2011 (13), then VIS-OCT oximetry was applied in rat's retina in 2013 (8). After several years of development, the technique has been successfully demonstrated in human retina in pathological cases for clinical research, including glaucoma, retinal ischemia, diabetic retinopathy (DR), central retinal vein occlusion (CRVO) and sickle cell retinopathy (SCR) (14–16).

Being responsible for the central vision field and acuity, macular region contains >30% of the total ganglion cells in the whole retina (17) in addition to being enriched with cone photoreceptors. The quantification of macular vascular sO_2 has important implications for macular retinal function and metabolism. However, existing reports so far have evaluated the sO_2 of large retinal vessel around the optic nerve head (ONH) (4, 18–20). Due to lack of resolution in fundus-based 2D oximetry, macular region vascular sO_2 has not been sufficiently studied before. In this study, for the first time, we report a baseline study of sO_2 of parafoveal arterioles and venules. We analyze the association of the arterial and venous sO_2 with ophthalmic exam, and OCT macular and ONH scans. The result will serve as an important reference for the future comparison with pathological data.

MATERIALS AND METHODS

Human Subjects

This study was conducted at Boston Medical Center, whose Institutional Review Board reviewed and approved the study. The study was compliant with the Health Insurance Portability and Accountability Act and adhered to the tenets of the Declaration of Helsinki. Written informed consent was obtained from all subjects before participation. Healthy subjects were recruited through the Boston Medical Center Optometry clinics. Cataracts were evaluated using the Lens Opacification System II based upon color and opalescence (21). The system uses a 4-point grading system with increasing number consistent with increasing maturity. Severe cataracts graded more than 2+ were excluded. All the subjects went through a regular ophthalmic examination including refractive error, tonometry for intraocular pressure (IOP), stereoscopic optic disc assessment, as well as clinical OCT scans of optic nerve head (ONH) and macula by Zeiss Cirrus OCT device. The OCT thickness of circumpapillary retinal nerve fiber layer (cpRNFL) and macular ganglion cell complex (GCC: ganglion cell layer + inner plexiform layer) were recorded, as well as cup to disc ratio (CDR). Dual-channel VIS-OCT was performed subsequently, and parafoveal vessel oxygen saturation (sO_2) were quantified by post-processing. The subjects were imaged by trained technicians.

Study Device and Method

The detailed setup of self-built vis-OCT system can be referenced in our previous publication (22). The pattern of raster scanning was 512 × 256 pixels and signals were received by a line camera with a line rate of 50 kHz and an exposure time of 19.1 μs. The image field of view (FOV) was 5 × 5 mm taking 2.62 s to acquire. The laser power on the cornea was <0.25 mW which is safe under the ANSI standard of ophthalmic instrument. After acquiring the raw interference signals, 3D data vis-OCT was generated by removing DC, converting the signals in k-space, digitally compensating the dispersion, and performing Fourier transform to prepare for later retinal boundary segmentation.

Image Segmentation

We first detected the retinal pigmented epithelium (RPE) layer as the outer retina boundary. We blurred each B-scan by the Gaussian filter with a standard deviation of 7, then identified the RPE depth by detecting the maximum intensities along the A-line. Several factors can influence the accuracy of detection results, including the vessel shadows, high intensities in the retinal nerve fiber layer (RNFL) and system noise. To address these factors, we performed a correction by using a two-step outlier detection and replacement, as detailed below.

We used a third-order polynomial to fit the detected RPE curve within each B-scan, then calculated the difference between the fitted and detected curves. The mean and standard deviation (SD) of the difference were obtained. When the difference is outside the range of mean $\pm 1.8 \times$ SD, this point on the detected RPE curve was considered as an outlier and deleted. Then we used the remaining points to generate the new polynomial fitting curve to replace the outliers and iterated this process until no outlier was found. We also calculated the coefficient of variation (COV) of each final fitted curve within each B-scan. After processing all B-scans, we obtained a COV curve over all B-scans, then we performed the outlier detection in the COV curve using the same standard to find the outliers. The values of COV of each fitting curve in adjacent images is expected to be similar. If the COV of two adjacent curves changed greatly in some frames, that usually mean the segmentation failed, and we discarded the outlier curve and used the previous curve to replace it. After this method, the retina was flattened based on accurate RPE labeling as shown in **Figures 1A,B**. In the next step, the inner limiting membrane (ILM) can be easily determined by the greatest gradient changes of intensities in the region above the RPE (**Figure 1B**).

We averaged the signals 20 pixels above RPE to generate the *en face* image. The vessel mask was obtained by binarizing the *en face* image with an adaptive threshold (23). Based on this vessel mask, we manually selected the vessel in the region of interest (ROI) as illustrated in **Figure 1C**. We considered the vessels branching from grandparents, to parents, and to children. Because of the strong blood absorption in VIS-OCT, the large grandparent vessels can be challenging to locate the vessel bottom and lack regional specification. Therefore, we focused on

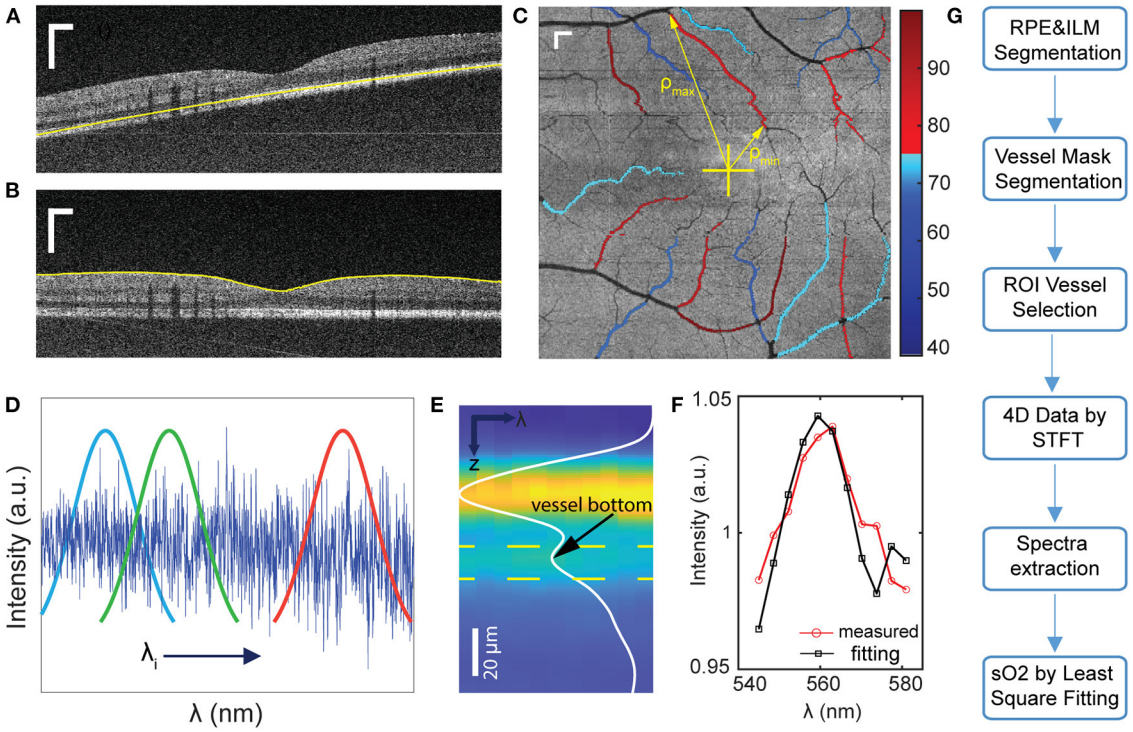

FIGURE 1 | Illustration of the data processing workflow for sO_2 calculation. **(A,B)** Examples of image segmentation for RPE detection, and (b) retina flattening and ILM layer detection. **(C)** Illustration of sO_2 mapping of parafoveal vessels. ρ_{min} and ρ_{max} is the minimum and maximum distance from each vessel segment to fovea. **(D,E)** Short time Fourier transform to extract depth-resolved spectra. Yellow dashlines indicated the depth range for spectra extraction **(F)** sO_2 regression by least square fitting. **(G)** Flow chart of data processing procedures. Scale bar: 250 μm.

smaller parafoveal vessels and stopped at major branching points. When the two vessels were intersecting, we avoided selecting the overlaying portions. Tiny children vessels were also neglected as the adaptive threshold algorithm failed to recognize them.

Oxygen Saturation Calculation

We generated the wavelength-dependent four-dimensional (4D) data I (x, y, z, λ) by the Short-time Fourier transform with 11 Gaussian windows sweeping the spectral interferogram (**Figure 1D**). We flatten all A-lines within each vessel ROI with respect to ILM and averaged all the A-lines of 4D data to generate the spectra in terms of depth I (z, λ) (**Figure 1E**). These spectra were then normalized by the averaged spectrum from non-vascular RNFL (22). To locate the vessel bottom, we averaged over λ and obtained an averaged A-line signal as the curve shown in **Figure 1E**. The location of the second reflective peak from ILM is identified as the vessel bottom. We then averaged the signals in the range of 5 pixels above and 10 pixels below the vessel bottom (area between the two yellow dash line in **Figure 1E**) in I (z, λ) to generate the single spectrum (**Figure 1F**).

Finally, we used a least square fitting on the extracted spectra to calculate the sO_2 of ROI vessels. The model and algorithm were clarified in our previous work (22).

$$I(sO_2|\lambda, z) = I_0(\lambda)\sqrt{R_0 r(\lambda)}e^{-[sO_2 \times \mu_{HbO_2}(\lambda)+(1-sO_2)\times \mu_{Hb}(\lambda)]z} \quad (1)$$

Where $I_0(\lambda)$ is the spectrum of light sources; R_0 is the reflectance of reference arm which is assumed to be constant; $r(\lambda)$ (dimensionless) is the reflectance at the vessel wall, modeled by a power law $r(\lambda) = A\lambda^{-\alpha}$, with A being a dimensionless constant and α modeling the decaying scattering spectrum from the vessel wall. Both A and α were included in the spectral fitting process. The detailed calculation for $r(\lambda)$ can be found in reference (22). For the parameters μ_{HbO_2} and μ_{Hb}, the optical attenuation coefficient μ is determined by the coefficients of absorption μ_a and scattering μ_s, where. $\mu(\lambda) = \mu_a(\lambda) + W\mu_s(\lambda)$. W is the scaling factor for the scattering coefficient which was 0.2 used here (8).

Vessel Topographic Feature Analysis

Several topographic features of manually selected vessels were quantified, including length (L), area (A), diameter (D), the minimum distance (ρ_{min}) and maximum distance (ρ_{max}) from fovea to vessel segments. Based on the *en face* images, the length and area were defined as the converted length of vessel centerline and area of whole vessel ROI segment. The diameter D was obtained by top and bottom of the vessels from averaged A-line signals. The accurate location of fovea was targeted manually by going through the 3D data combined with the *en face* image. With the known fovea location and selected vessel masks, we calculated ρ_{min} *and* ρ_{max} *for* each vessel segment.

TABLE 1 | Demographic information of subjects.

Subject numbers	10
Gender (female/male)	5/5
Eyes (OD/OS)	8/8
Ages (years)	61 ± 13.3
Race (White/AA/NA)	3/4/3
Ethnicity (Not Latino/Latino/NA)	7/2/1

AA, African American; NA, Not available.

TABLE 2 | Characteristics of ocular measurements from all eyes.

Characteristics	Mean (std)
Sphere (Diopter)	−0.50 (1.53)
Cylinder (Diopter)	0.77 (0.97)
IOP (mmHg)	15.4 (2.3)
CDR	0.33 (0.09)
GCC (μm)	78.0 (8.9)
cpRNFL (μm)	90.7 (10.0)
Superior cpRNFL (μm)	115.9 (14.0)
Nasal cpRNFL (μm)	70.3 (14.9)
Inferior cpRNFL (μm)	116.6 (17.4)
Temporal cpRNFL (μm)	61.6 (10.3)
AsO_2 (vol %)	92.1 (7.1)
VsO_2 (vol %)	48.4 (5.0)
A-V sO_2 (vol %)	43.8 (9.5)

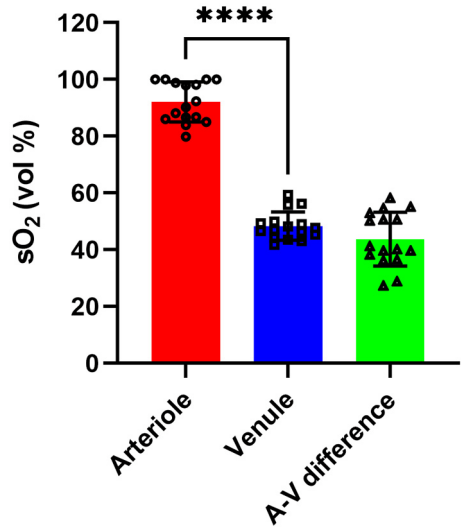

FIGURE 2 | The sO_2 of arterioles, venules, and A-V sO_2 difference from all eyes. ****$p < 0.0001$.

TABLE 3 | Correlation between clinical parameters and vessel sO_2 based on eyes.

Clinical Parameter	AsO_2		VsO_2		A-V sO_2	
	R	*p*	*r*	*p*	*r*	*p*
Sphere	−0.185	0.492	−0.368	0.160	0.055	0.838
Cylinder	0.195	0.524	0.184	0.546	0.045	0.884
IOP	0.253	0.344	−0.530	**0.035**	0.466	0.069
CDR	−0.173	0.521	0.514	**0.042**	−0.398	0.127
GCC	−0.007	0.980	−0.168	0.534	0.083	0.760
cpRNFL	−0.180	0.504	0.283	0.288	−0.282	0.291
Age	0.174	0.520	−0.546	**0.029**	0.414	0.110

Pearson's correlation was performed. Bold: $p < 0.05$.

Statistical Analysis

Statistical analysis was performed by MATLAB (The MathWorks, Inc.). Pearson's linear correlation coefficients were calculated between each pair of parameters, and unpaired parametric t-statistics were executed for the *p*-values. When the $p < 0.05$, the statistics was defined as the significant.

RESULTS

Fourteen healthy subjects in total were recruited in this study. Four subjects were excluded due to the failure of fixation, or low image quality. Fixation failures were due to significant eye movements during imaging where fovea was not present in the images, or the vessel locations were not recognizable. Lower image qualities caused the unsuccessful segmentation, leading to the failure of vessel selection and sO_2 calculation. Additional four eyes were excluded by the same criterion within the left ten subjects. The demographic information and the ophthalmic measurements are summarized in **Tables 1**, **2**. Sixteen eyes in total were used for the analysis. Nine eyes have mild Grade 1 cataract.

The sO_2 value for all arterioles and venules were first averaged within each eye, as shown in **Figure 2**. The mean arterial (AsO_2) and venous sO_2 (VsO_2) were 92.1 ± 7.1 (vol %) and 48.4 ± 5.0 (vol %) respectively. The mean arteriovenous sO_2 difference (A-V sO_2) was 43.8 ± 9.5 (vol %). The mean and standard deviation of vessel sO_2 for both arterioles and venules from all eyes are shown in **Supplementary Figure 3**.

Table 3 summarizes the correlation coefficients and *p* values between parafoveal AsO_2, VsO_2, A-V sO_2 and ophthalmic measurements including refractive errors, IOP, thickness of macular ganglion cell complex (GCC) and circumpapillary RNFL (cpRNFL). No significant correlation was found except between VsO_2 and IOP, cup/disk ratio (CDR) and age. **Figure 3** shows the correlation matrix map between sO_2 per eye and other ophthalmic parameters.

We further analyzed the correlation between sO_2 and vessel topographic parameters, which were in the **Supplementary Figures 1**, **2**. No significant correlation was found between sO_2 and vessel length (*L*), area (*A*), diameter (*D*), and the distance of ρ_{min} and ρ_{max}.

For the venules, *A* and *L* is significantly correlated as expected by geometry. The diameter positively correlated with the length and area of venules but with no significance. The minimum distance (ρ_{min}) has a negative correlation with length, area, and

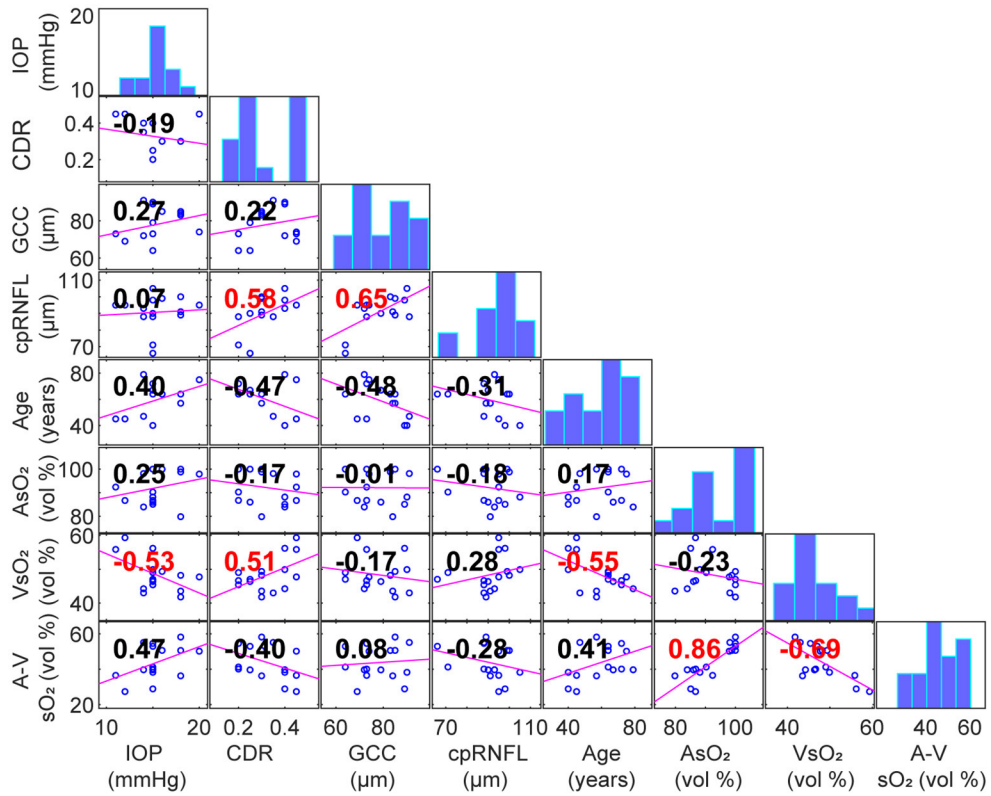

FIGURE 3 | Scatterplot with linear fit for a pair of correlated variables (Panels below the diagonal. Correlation coefficients area labeled in panels. Red: $p < 0.05$). Diagonal panels are histograms of each variable.

TABLE 4 | Vessel segment topographic parameters and sO_2 ($n = 57$ for arterioles, $n = 43$ for venules).

	Arterioles	Venules	*p*
L (mm)	1.19 ± 0.48	1.23 ± 0.42	0.709
A (10^{-3} mm^2)	32.5 ± 17.3	37.1 ± 16.6	0.184
D (μm)	24.8 ± 3.9	28.4 ± 3.2	**<0.001**
ρ_{min} (mm)	1.11 ± 0.39	1.16 ± 0.53	0.604
ρ_{max} (mm)	2.06 ± 0.51	2.26 ± 0.52	0.061
sO_2 (vol %)	91.0 ± 8.0	50.9 ± 8.8	**<0.001**

Two sample t-tests. Bold: $p < 0.05$.

diameter, but only has a significant dependency on the latter two. The maximum distance (ρ_{max}) has significant dependencies on all the other dimensions except diameter. For the arterioles, sO_2 has no significant correlation with topographic parameters. All the topographic parameters have significant correlation with each other, except for the ρ_{min} with length, area, and diameter.

Table 4 summarizes the topographic parameters and sO_2 values from all of arterious and venous segments. The AsO_2 and VsO_2 per segments are 91.0 ± 8.0 vol % ($n = 57$) and 50.9 ± 8.8 vol % ($n = 43$), and the diameter of venules is significantly larger than the arterioles' ($P < 0.001$). For the other parameters, no significant difference was found. It is noted that diameters of both arterioles and venules are smaller than 40 μm.

DISCUSSION

In this paper, we report the first baseline study on parafoveal vessel oxygen saturation (sO_2) in healthy eyes. We quantified the topographic features of those vessels and found no significant correlation with sO_2 values. There is no significant correlation between sO_2 and cpRNFL, GCC thickness or refractive error. IOP moderately correlated with VsO_2; however, A-V sO_2 had no significant correlation with IOP. The significant association between VsO_2 and age and CDR was also found.

We found the negative correlation between VsO_2 and age in healthy subjects was significant, which is consistent with previous reports (24–26). We also found correlation between VsO_2 and IOP. There has been sparse literature investigating the association between VsO_2 and IOP. Liu et al. reported no association between IOP and sO_2 for the healthy children under 18 (27). However, there is a significant age difference in our study and thus it is difficult to compare. It is plausible that IOP was positively correlated to the age of people under 60 (28), leading to the negative correlation to the VsO_2. The positive association between VsO_2 and CDR was marginally significant, which can also be found in Vandewalle et al. (29). Despite above significant

correlation, we found no significant correlation between A-V sO_2 with age, IOP or CDR.

Compared to fundus-based or multi wavelength SLO oximetry (7, 30), VIS-OCT provides better depth resolution enabling precise segmentation from the bottom of the vessels, and avoids noise from other layers. The parafoveal vessels in this study have a modest diameter ranging from 20 to 30 μm where visible light may penetrate fully. Without the depth segmentation, the penetrated light would diffuse through other layers and create confounding factors in the fundus camera. This would also compromise the resolution and contrast and make macular oximetry challenging for 2D image-based methods. We also note that the relative smaller caliber of the parafoveal vessels may be better suited for VIS-OCT than larger peripapillary vessels around ONH, since the bottom of the vessels were easier to image than large vessels to create a strong reflectance signal.

While this is the first study of the parafoveal vessel sO_2 in normal human subjects using VIS-OCT oximetry, there are limitations worth noting. First, we had limited subject number in this pilot study. Therefore, we refrained from advanced multivariable statistical analysis and rather performed simple two-sample *t*-tests and Pearson's linear correlation. Marginal significances were found in some parameters stated above. A larger cohort would be needed in the future study to validate those significance by a multiple-variable analysis to incorporate variable interactions and other confounding factors. Second, there are the technical limitations that we would like to improve in the future. The spectral bandwidth in the current device is limited in exchange for large imaging depth for better alignment. With our new linear-K spectrometer design and extended imaging depth (31), the spectral bandwidth can be increased to improve the robustness and accuracy of sO_2 calculation.

In summary, we investigated parafoveal microvascular sO_2 using VIS-OCT on healthy subjects in this initial baseline study. The statistical analysis reveals that no significant association between sO_2 and vessel topographic features. Also, there are no significant correlations for the eye sO_2 and clinical parameters except the relation of VsO_2 and IOP, CDR and age. This study will provide a normal (an initial) database for later sO_2 investigations in ocular diseases.

DATA AVAILABILITY STATEMENT

The raw data supporting the conclusions of this article will be made available by the authors, without undue reservation.

ETHICS STATEMENT

The studies involving human participants were reviewed and approved by Boston Medical Center. The patients/participants provided their written informed consent to participate in this study.

AUTHOR CONTRIBUTIONS

JY supervised this project. JW and JY analyzed the results. JW, WS, MF, MD, and JY contributed the manuscript. WS, NS, MF, and MD assisted in subject screening and recruitment. All authors contributed to the article and approved the submitted version.

FUNDING

NEI/NINDS R01NS108464, R01 EY032163 and R21EY029412.

SUPPLEMENTARY MATERIAL

The Supplementary Material for this article can be found online at: https://www.frontiersin.org/articles/10.3389/fmed.2022.886576/full#supplementary-material

REFERENCES

1. Stefánsson E, Olafsdottir OB, Eliasdottir TS, Vehmeijer W, Einarsdottir AB, Bek T, et al. Retinal oximetry: metabolic imaging for diseases of the retina and brain. *Prog Retin Eye Res.* (2019) 70:1–22. doi: 10.1016/j.preteyeres.2019.04.001
2. Whalen W, Riley J, Nair P. A microelectrode for measuring intracellular PO2. *J Appl Physiol.* (1967) 23:798–801. doi: 10.1152/jappl.1967.23.5.798
3. Olafsdottir OB, Hardarson SH, Gottfredsdottir MS, Harris A, Stefánsson E. Retinal oximetry in primary open-angle glaucoma. *Invest Ophthalmol Vis Sci.* (2011) 52:6409–13. doi: 10.1167/iovs.10-6985
4. Hardarson SH, Stefánsson E. Retinal oxygen saturation is altered in diabetic retinopathy. *Br J Ophthalmol.* (2012) 96:560–3. doi: 10.1136/bjophthalmol-2011-300640
5. Hardarson SH, Stefánsson E. Oxygen saturation in central retinal vein occlusion. *Am J Ophthalmol.* (2010) 150:871–5. doi: 10.1016/j.ajo.2010.06.020
6. Geirsdottir A, Hardarson SH, Olafsdottir OB, Stefánsson E. Retinal oxygen metabolism in exudative age-related macular degeneration. *Acta ophthalmologica.* (2014) 92:27–33. doi: 10.1111/aos.12294
7. Hardarson SH, Harris A, Karlsson RA, Halldorsson GH, Kagemann L, Rechtman E, et al. Automatic retinal oximetry. *Invest Ophthalmol Vis Sci.* (2006) 47:5011–6. doi: 10.1167/iovs.06-0039
8. Yi J, Wei Q, Liu W, Backman V, Zhang HF. Visible-light optical coherence tomography for retinal oximetry. *Opt Lett.* (2013) 38:1796–8. doi: 10.1364/OL.38.001796
9. Chong SP, Bernucci M, Radhakrishnan H, Srinivasan VJ. Structural and functional human retinal imaging with a fiber-based visible light OCT ophthalmoscope. *Biomed Opt Express.* (2017) 8:323–37. doi: 10.1364/BOE.8.000323
10. Pi S, Camino A, Zhang M, Cepurna W, Liu G, Huang D, et al. Angiographic and structural imaging using high axial resolution fiber-based visible-light OCT. *Biomed Opt Express.* (2017) 8:4595–608. doi: 10.1364/BOE.8.004595
11. Shu X, Beckmann LJ, Zhang HF. Visible-light optical coherence tomography: a review. *J Biomed Opt.* (2017) 22:121707. doi: 10.1117/1.JBO.22.12.121707
12. Yi J, Chen S, Shu X, Fawzi AA, Zhang HF. Human retinal imaging using visible-light optical coherence tomography guided by scanning laser ophthalmoscopy. *Biomed Opt Express.* (2015) 6:3701–13. doi: 10.1364/BOE.6.003701
13. Robles FE, Wilson C, Grant G, Wax A. Molecular imaging true-colour spectroscopic optical coherence tomography. *Nature photonics.* (2011) 5:744–7. doi: 10.1038/nphoton.2011.257
14. Wang J, Baker A, Subramanian ML, Siegel NH, Chen X, Ness S, et al. Simultaneous visible light optical coherence tomography and near infrared

OCT angiography in retinal pathologies: a case study. *Exp Biol Med*. (2021) 247:377–84. doi: 10.1177/15353702211063839
15. Ghassabi Z, Tayebi B, Wu M, Palmer S, Zambrano R, Li J, et al. Retinal oximetry revealed glaucomatous eyes had lower retinal metabolism using Visible Light Optical Coherence Tomography (vis-OCT). *Invest Ophthalmol Vis Sci.* (2021) 62:2526.
16. Kfir J, Ghassabi Z, Wu M, Rubinoff I, Kuranov RV, Wang Y, et al. Visible-Light OCT captures *in-vivo* changes in retinal oximetry in ischemic retinal diseases. *Invest Ophthalmol Vis Sci.* (2020) 61:PB00111.
17. Curcio CA, Allen KA. Topography of ganglion cells in human retina. *J Comp Neurol.* (1990) 300:5–25. doi: 10.1002/cne.903000103
18. Yoneya S, Saito T, Nishiyama Y, Deguchi T, Takasu M, Gil T, et al. Retinal oxygen saturation levels in patients with central retinal vein occlusion. *Ophthalmology*. (2002) 109:1521–6. doi: 10.1016/S0161-6420(02)01109-0
19. Olafsdottir OB, Vandewalle E, Pinto LA, Geirsdottir A, De Clerck E, Stalmans P, et al. Retinal oxygen metabolism in healthy subjects and glaucoma patients. *Br J Ophthalmol.* (2014) 98:329–33. doi: 10.1136/bjophthalmol-2013-303162
20. Hardarson SH, Stefánsson E. Oxygen saturation in branch retinal vein occlusion. *Acta Ophthalmol.* (2012) 90:466–70. doi: 10.1111/j.1755-3768.2011.02109.x
21. Chylack LT, Leske MC, McCarthy D, Khu P, Kashiwagi T, Sperduto R. Lens opacities classification system II (LOCS II). *Arch Ophthalmol.* (1989) 107:991–7. doi: 10.1001/archopht.1989.01070020053028
22. Song W, Shao W, Yi W, Liu R, Desai M, Ness S, et al. Visible light optical coherence tomography angiography (vis-OCTA) facilitates local microvascular oximetry in the human retina. *Biomed Opt Express.* (2020) 11:4037–51. doi: 10.1364/BOE.395843
23. Bradley D, Roth G. Adaptive thresholding using the integral image. *J Graph Tools*. (2007) 12:13–21. doi: 10.1080/2151237X.2007.10129236
24. Geirsdottir A, Palsson O, Hardarson SH, Olafsdottir OB, Kristjansdottir JV, Stefánsson E. Retinal vessel oxygen saturation in healthy individuals. *Invest Ophthalmol Vis Sci.* (2012) 53:5433–42. doi: 10.1167/iovs.12-9912
25. Jani PD, Mwanza J-C, Billow KB, Waters AM, Moyer S, Garg S. Normative values and predictors of retinal oxygen saturation. *Retina.* (2014) 34:394–401. doi: 10.1097/IAE.0b013e3182979e7b
26. Bata AM, Fondi K, Szegedi S, Aschinger GC, Hommer A, Schmidl D, et al. Age-related decline of retinal oxygen extraction in healthy subjects. *Invest Ophthalmol Vis Sci.* (2019) 60:3162–9. doi: 10.1167/iovs.18-26234
27. Liu X, He X, Yin Y, Zhang B, Sun S, Zhu J, et al. Retinal oxygen saturation in 1461 healthy children aged 7–19 and its associated factors. *Acta ophthalmologica.* (2019) 97:287–95. doi: 10.1111/aos.14043
28. Nomura H, Ando F, Niino N, Shimokata H, Miyake Y. The relationship between age and intraocular pressure in a Japanese population: the influence of central corneal thickness. *Curr Eye Res.* (2002) 24:81–5. doi: 10.1076/ceyr.24.2.81.8161
29. Vandewalle E, Abegao Pinto L, Olafsdottir OB, De Clerck E, Stalmans P, Van Calster J, et al. Oximetry in glaucoma: correlation of metabolic change with structural and functional damage. *Acta Ophthalmol.* (2014) 92:105–10. doi: 10.1111/aos.12011
30. Ashman RA, Reinholz F, Eikelboom RH. Oximetry with a multiple wavelength SLO. *Int Ophthalmol.* (2001) 23:343–6. doi: 10.1023/A:1014406831412
31. Song W, Shao W, Yi J, editors. *Wide-Field and Micron-Resolution Visible Light Optical Coherence Tomography in Human Retina by a Linear-K Spectrometer*. Bio-Optics: Design and Application (2021) Optical Society of America. doi: 10.1364/BODA.2021.DM2A.4

Conflict of Interest: The authors declare that the research was conducted in the absence of any commercial or financial relationships that could be construed as a potential conflict of interest.

frontiers | Frontiers in Medicine

ORIGINAL RESEARCH
published: 20 May 2022
doi: 10.3389/fmed.2022.889398

Evaluation of the Relationship Between Aniseikonia and Stereopsis Using a New Method

*Lingxian Xu, Lu Liu and Huang Wu**

Department of Optometry, The Second Hospital of Jilin University, Changchun, China

Purpose: To investigate the influence of induced aniseikonia on stereopsis measured by contour-based and random-dot-based stereograms using a new method.

Methods: Unlike previous studies in which aniseikonia was induced using magnifiers, which potentially influenced the position of the test symbols in the half-view, here the image was magnified while maintaining each test symbol's central position within the half-view. A phoropter and two 4K smartphones were used to measure stereopsis in seventeen young adults aged 20–28 years old. Stereopsis was tested using both contour-based and random-dot-based stereograms under overall or meridional aniseikonia with magnifications ranging from 2.5 to 30%. Repeated measures ANOVA was used to evaluate the effect of aniseikonia on stereopsis.

Results: Stereopsis decreased with an increase in aniseikonia magnification in the overall, horizontal, and vertical directions. Stereopsis values (log arcsec) increased from 1.29 ± 0.14 at baseline to 2.38 ± 0.16 with 30% overall aniseikonia of contour-based stereograms. In random-dot based stereograms, stereopsis values increased from 1.29 ± 0.16 at baseline to 2.24 ± 0.23 with 22.5% overall aniseikonia. Overall aniseikonia caused a significantly greater impairment on stereopsis as compared with the changes in meridional directions. In contour-based stereograms, vertical aniseikonia had significantly less impact on stereopsis than horizontal aniseikonia of identical magnification. The opposite phenomenon was found in random-dot-based stereograms.

Conclusion: Stereopsis decreased with an increase of magnification of induced aniseikonia. Magnifying patterns (overall, horizontal, or vertical) also significantly affected stereopsis. The conflicting impact of meridional aniseikonia on stereopsis measured by contour-based and random-dot-based stereograms may be associated with the uniqueness of the two test systems.

Keywords: stereopsis, induced aniseikonia, contour, random-dot, disparity, smartphone

OPEN ACCESS

Edited by:
Peng Xiao,
Sun Yat-sen University, China

Reviewed by:
Paul Barry Hibbard,
University of Essex, United Kingdom
Gang Luo,
Harvard Medical School,
United States

***Correspondence:**
Huang Wu
wuhuang@jlu.edu.cn

Specialty section:
This article was submitted to Ophthalmology, a section of the journal Frontiers in Medicine

Received: *04 March 2022*
Accepted: *05 May 2022*
Published: *20 May 2022*

Citation:
Xu L, Liu L and Wu H (2022) Evaluation of the Relationship Between Aniseikonia and Stereopsis Using a New Method. Front. Med. 9:889398. doi: 10.3389/fmed.2022.889398

INTRODUCTION

Aniseikonia is a condition where images seen with both eyes are perceived as being different in size and/or shape (1, 2). The possible causes of aniseikonia are optical, retinal, and cortical (3, 4). Optical aniseikonia is used to denote aniseikonia due to a physically measured difference in the sizes of the retinal images that typically arises in anisometropia, aphakia, and pseudophakia,

among others (5, 6). Retinal aniseikonia may be due to the stretching or compression of the retina, leading to the alteration in spacing between the photoreceptors, which changes the perceived image size (1). Common causes include epiretinal membrane, macular edema, and central serous chorioretinopathy (7). Cortical aniseikonia may occur when apparent image sizes are perceived as differently due to abnormalities in the higher levels of visual processing system above beyond the retina (1, 3).

The apparent unequal size may be uniform (i.e., magnified or minified for all meridians). However, the size difference can also be meridional, wherein one image is larger or smaller in one specific meridian relative to the corresponding meridian in the other eye. This phenomenon can be observed when astigmatic anisometropia is present (1, 6). Discrepant image sizes may also be perceived by both eyes in retinal diseases such as epiretinal membrane (8) and macular edema (7).

Studies have suggested that the visual system can tolerate low amounts of aniseikonia without complete disruption of binocular fusion (9, 10). As the degree of aniseikonia increases, stereopsis becomes disrupted (11). Several studies discussed this issue by evaluating the effects of various degrees of induced aniseikonia on stereopsis, but the results varied widely, with stereopsis being reported to be perceived in aniseikonia of 4% or lower (4), 5% or lower (10), and 19% or lower (9). Most of these studies used size lenses to enlarge or reduce images in front of one eye. However, we observed that the enlargement of one eye's image may introduce an additional disparity whether the size of the image is changed uniformly or solely in one meridian. This principle can be demonstrated with a four-circle test pattern like the Fly Stereo Acuity Test (Vision Assessment Corporation, Elk Grove Village, IL, United States).

If a size lens is placed in front of the left eye, then the left eye image is uniformly enlarged, whereas the right eye image is unchanged, resulting in aniseikonia. The locations of the centers of the circles viewed by the left eye are changed, whereas the locations of the centers of the circles viewed by the right eye are unchanged; this causes a shift in the position of the centers of the circles of the left eye. More specifically, in the left eye image, the center of the left circle would be shifted to the left for a certain distance, and the center of the right circle would be shifted to the right by the same distance. An uncrossed disparity would be created simply by moving the circle leftward in the left eye image, without considering the effect of magnification. Similarly, a crossed disparity would be created by moving the circle rightward in the left eye image, regardless of the effect of magnification. Consequently, four circles would appear at different depths; the circle on the left would seem farthest, the circle on the right side would seem nearest, and two circles located in the middle position would appear in the middle distance. In this situation, the participant's ability to distinguish the stereo target is affected not only by the magnification effect over one eye, but also by the set disparities of the test material.

A similar situation exists in the random-dot test pattern such as "Pacman" symbol (TNO stereotest; Lameris Ootech BV, Ede, Netherlands). If a size lens is placed in front of the left eye, then the left eye image is uniformly enlarged, whereas the right eye image is unchanged. Consequently, uncrossed disparity would be created on the left side of the fused image, and crossed disparity would be created on the right side of the fused image. The additional induced disparities might rotate the random-dot pattern clockwise along the vertical axis. The "mouth" of the "Pacman" would be identified easily when facing left or right. However, the participant would experience difficulty in judging the orientation of the mouth when facing up or down because of the difficulty of dislocation fusion in the vertical direction.

In summary, the judgment of stereo symbols is complicated because of the newly introduced disparities by a lens that uniformly magnifies images. In order to minimize the introduction of additional disparities in the process of inducing aniseikonia, we adopted a new method to induce aniseikonia. The test image seen by the left eye was magnified. Four test symbols were utilized as conventional measurement methods (one out of four choose mode). For each test unit, the four symbols were arranged vertically in a line and each center of the four symbols was kept unchanged in the process of magnification. Meanwhile, the test image seen by the right eye was unchanged, so the location of each test symbol's center viewed by the right eye was unchanged and the center of each test symbol's pair still coincided in binocular view. Then we measured stereoacuity under induced aniseikonia. Since the interference of additional disparity was minimized as much as possible, the real effect of stereopsis by aniseikonia was evaluated.

Clinically, there are two commonly used stereopsis measurements: the contour-based stereograms (which are used to test local stereopsis) and random-dot-based stereograms (which are used to test global stereopsis). Some studies suggested that stereopsis values varied when measured by these two kinds of stereograms (12, 13). Lovasik et al. (14) reported a more rapid loss of stereoacuity with induced aniseikonia when measured by the contour stereogram relative to the loss measured by the random-dot stereogram. Therefore, in this study, the effect of aniseikonia on stereopsis was measured by both the contour-based and random-dot-based stereograms.

MATERIALS AND METHODS

Participants

A total of 17 participants (5 men and 12 women) aged 20–28 years were recruited to this study. The best-corrected visual acuity of all participants was 0 logMAR or better. The stereothresholds of all participants were 40″ or better, as measured using the Fly Stereo Acuity Test. All participants provided written informed consent before participating in the study. The research protocol observed the tenets of the Declaration of Helsinki and was approved by the ethics committee of the Second Hospital of Jilin University (No. 2020-110).

Test System

Equipment

A stereopsis measurement system was established with two 4K smartphones and a phoropter, as previously described (15–17). The resolution of the smartphone screen was 3840 × 2160 (Sony Xperia XZ Premium; Sony Mobile Communications Inc., Tokyo,

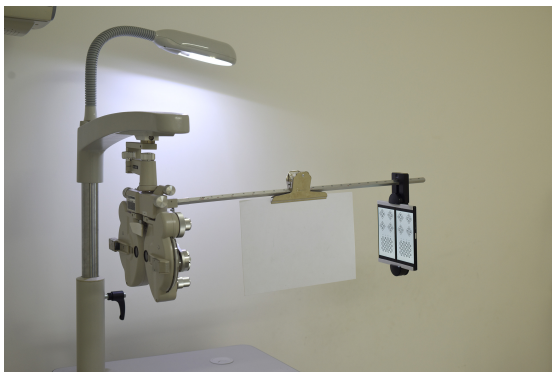

FIGURE 1 | Photograph of the testing system.

Japan). With the aid of two approximately 5.5Δ based out Risley prisms, two smartphones are capable of creating a minimum 10″ (1-pixel) disparity at a viewing distance of 0.65 m at the near-vision test rod of the phoropter (Topcon VT-10, Topcon Corp, Tokyo, Japan) (**Figure 1**).

Test Symbols

Contour-Based Symbols

The contour-based symbols were created to reproduce quantitative measurements using the Fly Stereo Acuity Test. However, the arrangement of the circles was modified in our testing regime. Specifically, four test circles were arranged vertically, and one of them was randomly chosen as the stereo target. The target circle appeared to stand out from the plane due to the crossed disparity. Three comparison circles were set along both sides of the test circles to maintain consistency with the Fly Stereo Acuity Test as much as possible. The participant identified the stereo target when the threshold of their stereopsis was lower than the setting disparity. In the newly designed test system, while magnifying the left eye image to induce aniseikonia, all test circles appeared to be rotated at a certain angle clockwise along the vertical axis of the screen. To minimize the influence of the rotation effect on the disparity evaluation, the test symbols in each test unit were arranged vertically.

Random-Dot-Based Symbols

The random-dot-based pattern comprised four squares composed of random dots arranged vertically. One circle was randomly hidden in one of the four squares. The participant was asked to determine the square comprising a circle protruding from the plane, which occurred when the participants' stereopsis threshold was lower than the disparity of the depth-containing circle. The minimal size of the random dot was 6 × 6 pixels (equivalent to 0 logMAR resolution) to ensure that all of the dots could be distinguished by the participant (18).

Test Pages

Agreement Between Vertical and Conventional Arrangement Pattern

To test the agreement between the vertical arrangement pattern and the conventional arrangement of routine tests, we designed two tests including contour-based and random-dot-based patterns. In the contour-based test, the quantitative measurement section of the Fly Stereo Acuity Test was chosen for comparison (**Figure 2A**). In the random-dot-based test, the

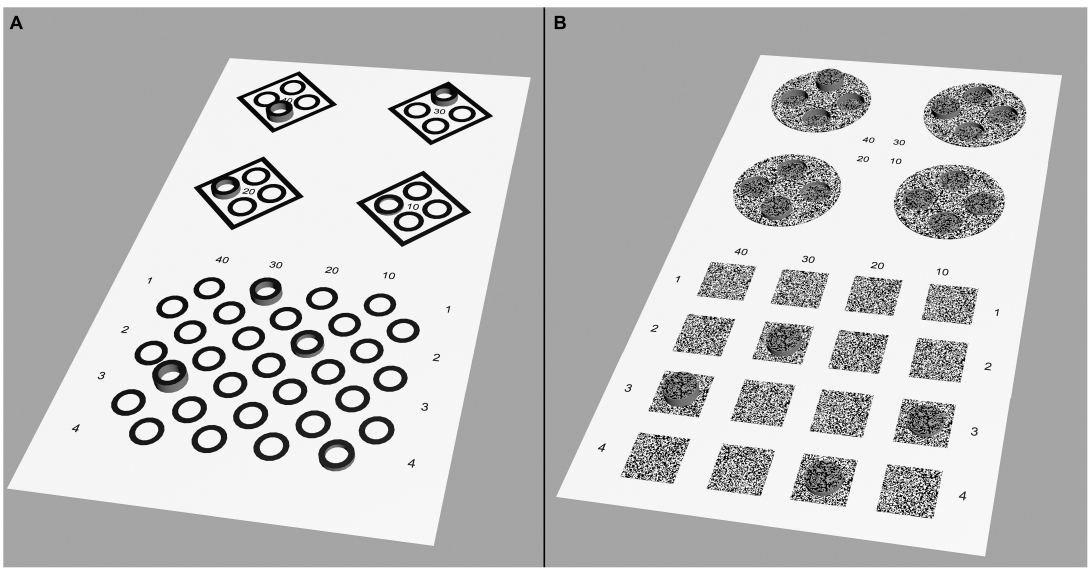

FIGURE 2 | Simulation of the perceptions generated by the test images. If a patient's stereothreshold is lower than the displayed disparity, the target appeared as protruding. **(A)** Contour-based pattern comparison test between four circles arranged in quadrilateral form and vertical line form. The disparity of the four circles arranged in both formations was 40″, 30″, 20″, and 10″, respectively. **(B)** Random-dot pattern comparison test between four circles arranged in quadrilateral and vertical line forms. The disparity of the four circles arranged in both forms was 40″, 30″, 20″, and 10″, respectively. In the quadrilateral arrangement, the other three circles had the same amount of disparity as the target but were designed to be uncrossed and appeared dented into the planes.

quantitative measurement section of the Random Dot 3 Stereo Acuity Test (Vision Assessment Corporation, Elk Grove Village, IL, United States) was chosen for comparison (**Figure 2B**).

Determining the Threshold of Stereopsis

Both the contour-based test and random-dot-based test used the same test pattern. There were two grade menus in the test system. The first grade menu comprised eight test units with a step range of 90″, that is, 640″, 550″, 460″, 370″, 280″, 190″, 100″, and 10″. The second grade menu also comprised eight test units, but the step range was 10″. There were seven test pages in the second grade menu (page 1, 20″–90″; page 2, 110″–180″; page 3, 200″–270″; page 4, 290″–360″; page 5, 380″–450″; page 6, 470″–540″; page 6, 560″–630″). A program written with C# was used to produce all stereograms with crossed disparity.

Aniseikonia Test Unit

To induce aniseikonia, the test image seen by the right eye was unchanged, and the test image seen by the left eye was enlarged to provide either overall, horizontal, or vertical magnification. Overall magnification enlarged the image consistently (**Figure 3**). Horizontal magnification only enlarged the image horizontally without enlarging the image vertically (**Figure 4**), while vertical magnification enlarged the image vertically without horizontal enlargement. The magnification rate ranged from 1.025 to 1.3, with a step range of 2.5%. The specific magnification rates were 1.025, 1.05, 1.075, 1.1, 1.125, 1.15, 1.175, 1.2, 1.225, 1.25, 1.275, and 1.3. While enlarging the test image, each test symbol was enlarged separately, with the location of its center unchanged in order to coincide the center of each test symbol's pair on binocular view.

Test Procedure

Agreement Between Vertical and Conventional Arrangement Pattern

The participant was asked to distinguish the stereo circle from both the original pattern (40″–10″) and vertical arrangement pattern (40″–10″). The minimal stereo symbol that could be distinguished was recorded as the stereopsis threshold of the participant. The test sequence of contour-based and random-dot based stereograms was randomly determined.

Determining the Threshold of Stereopsis Under Induced Aniseikonia Conditions

The test sequence of contour-based pattern or random-dot-based pattern was random. Random test sequences were also used for the overall, horizontal and vertical magnifications. A magnification of 1.3 was adopted at the beginning of the test, and then 1.275, 1.25, and so on, until it reached 1.025. At the beginning of the test, the first grade page was shown, and the participant was asked to find the stereo target from 640″ to 10″. If the participant pointed correctly at 10″, then their stereopsis was recorded as 10″. If the participant could point to the stereo target at 190″ but failed to do so at 100″, then the second page of the second grade menu (including 110″–180″) was chosen for the next examination. At this time, if the participant could ascertain the target circle at 160″ but failed to do so at 150″, then the stereopsis was recorded as 160″. However, if they were unable to point to the stereo circle at 640″, then the stereopsis was recorded as "nil." Under this test procedure, the stereopsis of the participant could be determined from 10″ to 640″ with a measurement accuracy of 10″ (**Figure 5**).

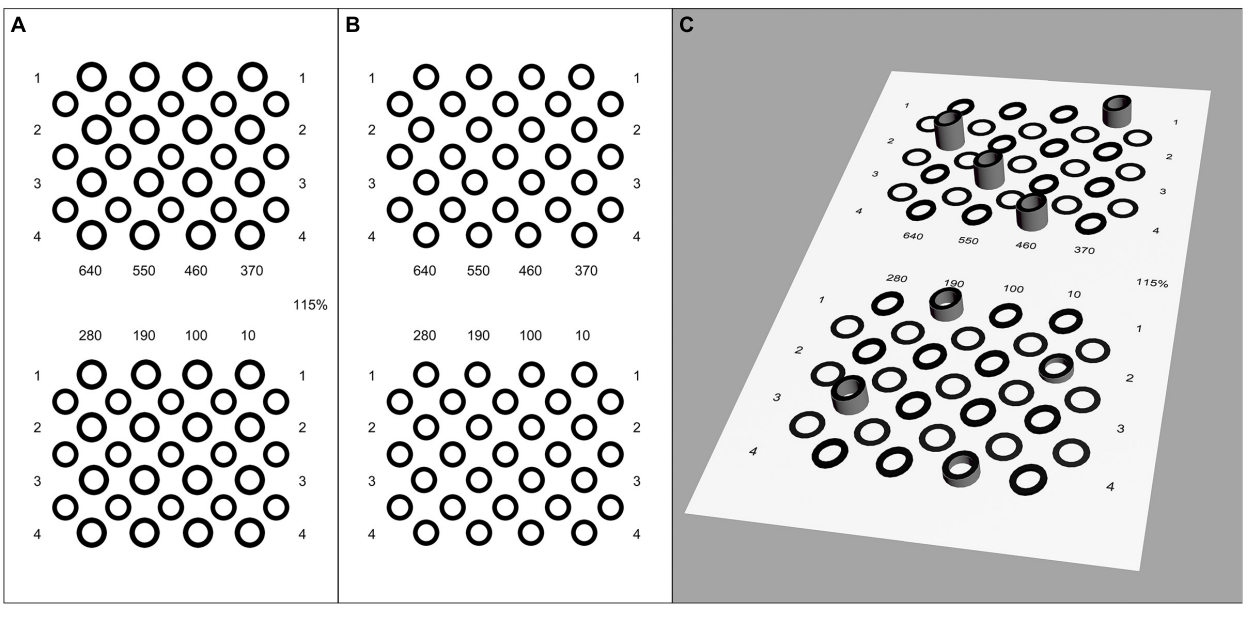

FIGURE 3 | Legend of contour-based pattern of the first grade test page with 15% induced overall aniseikonia. **(A)** Left eye image. **(B)** Right eye image. **(C)** Simulation of the perception of the test images. The disparity of the target circle was 640″, 550″, 460″, 370″, 280″, 190″, 100″, and 10″. The center of the comparison circles was at the same point when fused correctly, but the size of test symbols in left eye image was enlarged by 15% because of the induced aniseikonia. All test circles appeared to be rotated at a certain angle clockwise along the vertical axis of the screen.

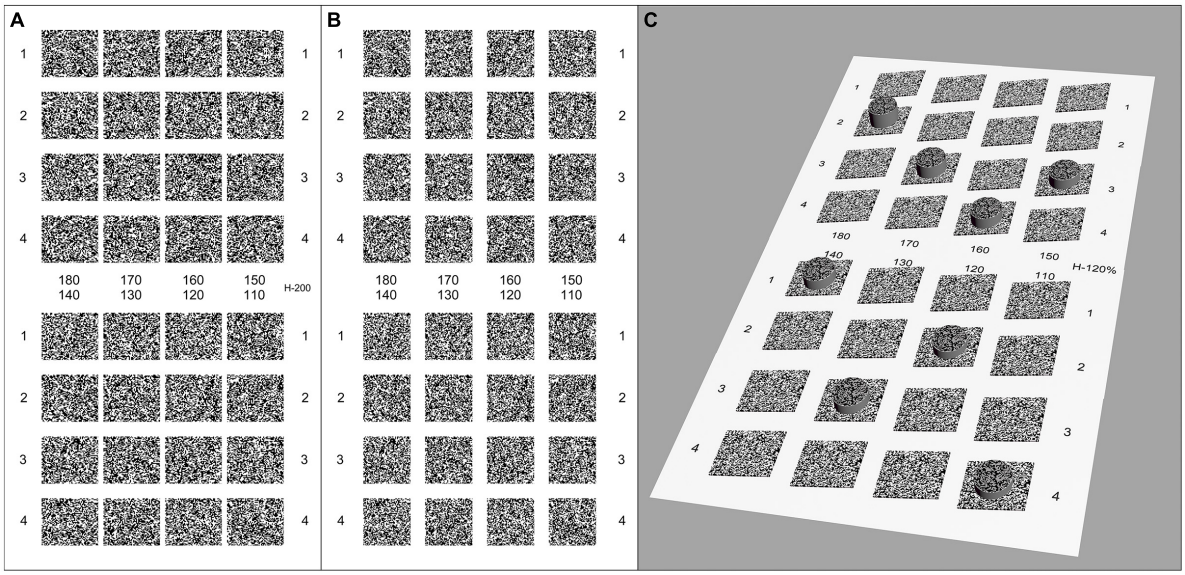

FIGURE 4 | Legend of random-dot pattern of the second grade test page (110″–180″) with 20% induced horizontal aniseikonia. **(A)** Left eye image. **(B)** Right eye image. **(C)** Simulation of the perception of the test images. The disparity of the target circle was 180″, 170″, 160″, 150″, 140″, 130″, 120″, and 110″. The center of the comparison hidden circles was at the same point when fused correctly, but the size of test symbols in left eye image was enlarged by 20% in the horizontal direction to induce aniseikonia. All squares appeared to be rotated at a certain angle clockwise along the vertical axis of the screen.

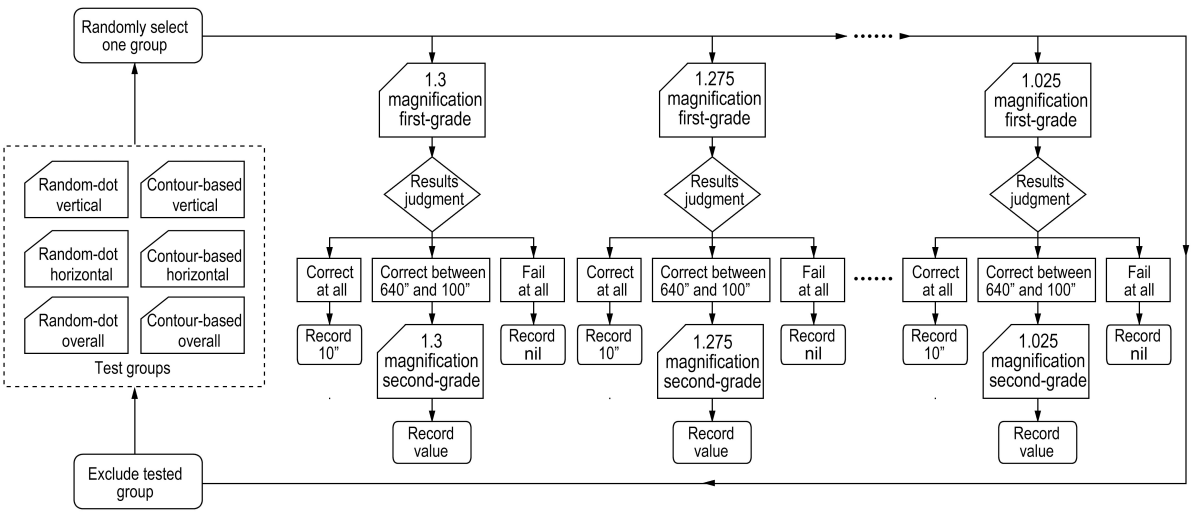

FIGURE 5 | Flowchart of test procedure of determining the threshold for stereopsis under induced aniseikonia conditions. Test groups included three random-dot-based patterns (overall, horizontal, or vertical aniseikonia) and three contour-based patterns (overall, horizontal, or vertical aniseikonia). One group was selected randomly to test a participant. Two-step choices were conducted to measure the stereopsis threshold with a magnification of 1.3, and then 1.275, and so on, until it reached 1.025. Randomly, another group was chosen to do the examination again, and so on, until finishing all the six groups' tests.

Statistical Analysis

Statistical analysis was performed using SPSS (version 20.0; IBM Corp, Armonk, NY, United States) and GraphPad Prism (version 8.0.1; GraphPad Software Inc., San Diego, CA, United States). The Wilcoxon signed-rank test and Kendall's coefficient of concordance (Kendall's W) were conducted to examine the agreement between vertical and conventional arrangement patterns. Stereopsis values under aniseikonia were transformed to log arcsec values for analysis. The normality of the distribution of the stereoacuity (log arcsec) was checked by the D'Agostino and Pearson test, and 64 of 69 sets of data were normally distributed. On this basis, repeated measures ANOVA was applied to determine significant main effects and interactions at $p = 0.05$. Partial eta-squared (η_p^2) was calculated as an effect size measure. Greenhouse-Geisser correction was used if the assumption of sphericity was not met, and the Bonferroni

test was used in *post-hoc* analysis. Minitab Statistical Software (version 19; Minitab Inc., State College, PA, United States) was used to compare the slopes of the change in stereopsis with induced aniseikonia for the contour-based and random-dot based stereograms.

RESULTS

Agreement Between Vertical and Conventional Arrangement Patterns

The Wilcoxon signed-rank test showed that there was no significant difference between the stereopsis threshold measured by vertical and conventional arrangement patterns ($Z = -0.577$, $P = 0.564$ in both contour-based and random-dot-based stereograms). Kendall W tests showed a significant agreement between stereopsis threshold measured by vertical and conventional arrangement patterns (Kendall $W = 0.853$, $P = 0.038$ in contour-based stereograms; Kendall $W = 0.927$, $P = 0.020$ in random-dot-based stereograms).

Stereopsis Changes With Different Aniseikonia

Raw stereopsis values under different conditions of aniseikonia are provided in **Supplementary Tables 1–7**. Stereopsis values were transformed to log arcsec for analysis. The mean ± standard deviation (SD) of stereopsis values (log arcsec) for baseline and each aniseikonia condition for contour-based and random-dot-based stereograms are shown in **Table 1**. The stereopsis values increased with the increase in aniseikonia magnification; this was observed in the overall, horizontal, and vertical directions, in both stereogram types (**Figure 6**). In contour-based stereograms, stereopsis was present until the magnification increased to 30% for overall, horizontal, and vertical patterns. The stereopsis values (log arcsec) at baseline averaged 1.29 and increased to 2.38 with 30% overall aniseikonia. In random-dot-based stereograms, for overall aniseikonia, stereoacuity was measured for magnifications ranging from 2.5 to 22.5%; several of the participants (7/17) failed the stereopsis test under 25%; most participants (12/17) failed the test under 27.5%, and all participants failed the test under 30%. In horizontal and vertical aniseikonia, stereoacuity could be measured under all magnifications ranging from 2.5 to 30%. The stereopsis values (log arcsec) at baseline averaged 1.29 and increased to 2.24 with 22.5% overall aniseikonia.

Differences Between Overall, Horizontal, and Vertical Aniseikonia

Repeated measures ANOVA was conducted with magnification and magnifying pattern (overall, horizontal, or vertical) as within-subject variables. In contour-based stereograms with aniseikonia (2.5–30%), a significant main effect of magnification ($F_{(3,48)} = 190.91$, $P < 0.001$, $\eta_p^2 = 0.923$), of magnifying pattern ($F_{(1,23)} = 163.31$, $P < 0.001$, $\eta_p^2 = 0.911$) and a significant interaction between magnification and magnifying pattern ($F_{(6,96)} = 22.42$, $P < 0.001$, $\eta_p^2 = 0.584$) was found. Bonferroni's *post-hoc* test showed that stereoacuity under each magnifying pattern was significantly different from the other two patterns in identical aniseikonia from 10 to 30% ($P < 0.001$ to $P = 0.015$).

In random-dot-based stereograms with aniseikonia (2.5–22.5%), a significant main effect of magnification ($F_{(2,40)} = 162.30$, $P < 0.001$, $\eta_p^2 = 0.910$), of magnifying pattern ($F_{(2,31)} = 34.38$, $P < 0.001$, $\eta_p^2 = 0.682$) and a significant interaction between magnification and magnifying pattern ($F_{(6,102)} = 17.18$, $P < 0.001$, $\eta_p^2 = 0.518$) was observed. Bonferroni's *post-hoc* test showed that stereopsis values (log arcsec) were significantly higher for overall aniseikonia than for meridional aniseikonia, ranging between 7.5 and 22.5% ($P < 0.001$ to $P = 0.026$). Vertical aniseikonia values of 15, 17.5, and 22.5% yielded significantly ($P = 0.003$ to $P = 0.047$) higher stereothresholds compared with the same values of horizontal aniseikonia.

Differences Between Contour-Based and Random-Dot-Based Stereograms

Repeated measures ANOVA was conducted with magnification and test method (contour-based stereogram, random-dot-based stereogram) as within-subject variables. For overall aniseikonia

TABLE 1 | Mean ± SD of stereopsis values (log arcsec) tested under different conditions of aniseikonia.

Magnification	Contour-based stereograms			Random-dot-based stereograms		
	Overall	Horizontal	Vertical	Overall	Horizontal	Vertical
1		1.29 ± 0.14			1.29 ± 0.16	
1.025	1.34 ± 0.18	1.32 ± 0.18	1.29 ± 0.12	1.41 ± 0.14	1.36 ± 0.13	1.39 ± 0.20
1.05	1.45 ± 0.26	1.40 ± 0.22	1.31 ± 0.15	1.48 ± 0.19	1.42 ± 0.12	1.41 ± 0.21
1.075	1.53 ± 0.23	1.45 ± 0.20	1.32 ± 0.16	1.60 ± 0.15	1.43 ± 0.12	1.50 ± 0.21
1.1	1.65 ± 0.24	1.51 ± 0.17	1.34 ± 0.18	1.68 ± 0.15	1.46 ± 0.14	1.57 ± 0.19
1.125	1.77 ± 0.20	1.59 ± 0.20	1.36 ± 0.20	1.77 ± 0.17	1.52 ± 0.15	1.60 ± 0.21
1.15	1.87 ± 0.16	1.68 ± 0.24	1.37 ± 0.20	1.85 ± 0.18	1.56 ± 0.16	1.67 ± 0.21
1.175	1.96 ± 0.21	1.75 ± 0.22	1.42 ± 0.18	1.98 ± 0.18	1.59 ± 0.16	1.75 ± 0.21
1.2	2.04 ± 0.21	1.82 ± 0.19	1.47 ± 0.13	2.09 ± 0.19	1.67 ± 0.15	1.79 ± 0.20
1.225	2.14 ± 0.20	1.90 ± 0.16	1.54 ± 0.14	2.24 ± 0.23	1.74 ± 0.18	1.88 ± 0.24
1.25	2.22 ± 0.18	1.97 ± 0.18	1.58 ± 0.16	–	1.82 ± 0.17	1.97 ± 0.26
1.275	2.30 ± 0.17	2.05 ± 0.17	1.66 ± 0.17	–	1.92 ± 0.16	2.02 ± 0.29
1.3	2.38 ± 0.16	2.11 ± 0.17	1.76 ± 0.18	–	2.02 ± 0.20	2.08 ± 0.32

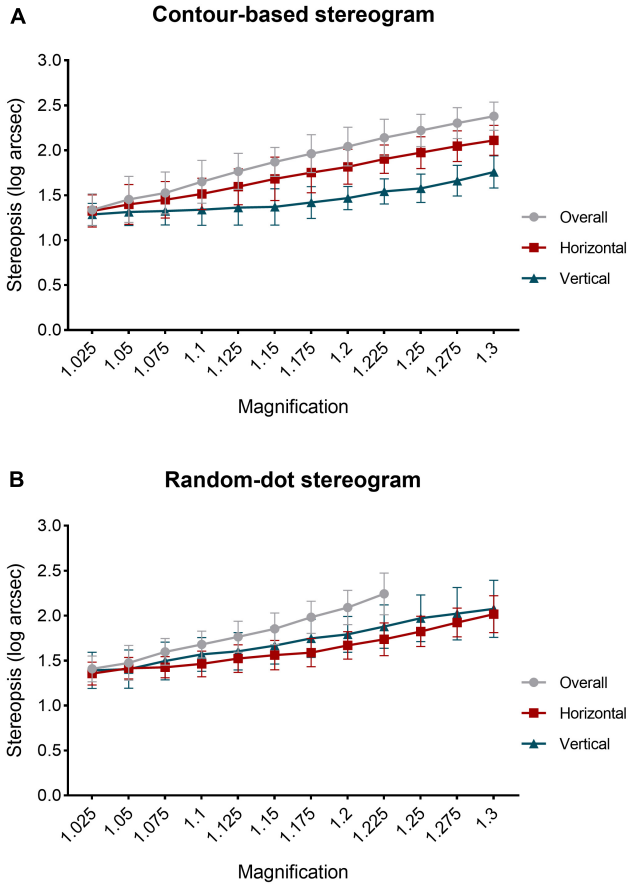

FIGURE 6 | Relationship between induced aniseikonia and stereopsis values (log arcsec). **(A)** Contour-based stereograms. **(B)** Random-dot-based stereograms. Datapoints and error bars represent mean with standard deviation (SD). The final three data points of overall magnification curve in the random-dot stereogram image were not plotted because some participants failed to pass the test when magnification increased to 25, 27.5, and 30%.

(2.5–22.5%), there was a significant main effect of magnification ($F_{(4,58)}$ = 201.92, $P < 0.001$, η_p^2 = 0.927). However, there was no significant main effect of test method and no significant interaction between magnification and test method.

For horizontal aniseikonia, there was a significant main effect of magnification ($F_{(4,60)}$ = 190.31, $P < 0.001$, η_p^2 = 0.922), of test method ($F_{(1,16)}$ = 6.19, P = 0.024, η_p^2 = 0.279), and a significant interaction between magnification and test method ($F_{(5,76)}$ = 4.96, P = 0.001, η_p^2 = 0.237). Bonferroni's *post-hoc* test showed that stereopsis values (log arcsec) under horizontal aniseikonia of 17.5, 20, and 22.5% measured by contour-based stereograms was significantly higher than that of random-dot-based stereograms (P = 0.016 to P = 0.045).

For vertical aniseikonia, a significant main effect of magnification ($F_{(3,42)}$ = 95.79, $P < 0.001$, η_p^2 = 0.857), of test method ($F_{(1,16)}$ = 64.07, $P < 0.001$, η_p^2 = 0.800), and a significant interaction between magnification and test method ($F_{(3,41)}$ = 8.65, $P < 0.001$, η_p^2 = 0.351) was found. Bonferroni's *post-hoc* test showed that stereopsis values (log arcsec) measured under conditions of induced vertical aniseikonia ranging from 7.5 to 30% with contour-based stereograms were lower than those measured using random-dot-based stereograms ($P < 0.001$ to P = 0.008).

For overall aniseikonia, there was no significant difference of the linear regression slopes for stereoacuity over magnification between two test methods (contour-based stereograms slope 3.82; random-dot-based stereograms slope 4.09; P = 0.350). For horizontal aniseikonia, the slope of the regression line of the contour-based stereograms was significantly higher than that of random-dot-based stereograms (2.91 for the contour-based stereograms; 2.30 for the random-dot-based stereograms; P = 0.003). For vertical aniseikonia, the slope of the regression line of the contour-based stereograms was significantly lower than that of the random-dot-based stereograms (1.60 for the contour-based stereograms; 2.60 for the random-dot-based stereograms; $P < 0.001$).

DISCUSSION

The relationship between induced aniseikonia and stereopsis has been investigated for decades (9, 10, 19–21). Highman (9) examined 30 participants with different degrees of myopia. Each participant wore a contact lens in the eye with a smaller diopter and wore the appropriate correcting lens in a trial frame over the more myopic eye to induce aniseikonia of various magnitudes. The Titmus Stereo-circles Chart was used to test stereopsis under different magnifications of aniseikonia. Findings indicated that stereopsis can be measured even with 19% of induced aniseikonia. Oguchi and Mashima (10) investigated the impact of artificial aniseikonia on binocular vision both psychophysically and objectively. They used a random-dot stereogram to measure stereoacuity and visual evoked potential under conditions of aniseikonia induced by size lenses ranging from 2 to 15% in six participants with normal stereoacuity. Their findings showed that stereopsis could be perceived with aniseikonia of 5% or lower. Moreover, they found a declining trend in the amplitude of visual evoked potential as the aniseikonia increased.

The measurement of stereoacuity might be interfered by the additional disparities introduced by size lenses that uniformly magnifies images. To minimize the interference of additional disparities in the process of inducing aniseikonia, the images used in our study were magnified while maintaining the position of each symbol's center. Then the stereoacuity was measured under induced aniseikonia so that the real effect of aniseikonia on stereopsis could be accessed with the minimal interference of additional disparities. The consistency between the vertical and conventional arrangement patterns was first evaluated to ensure the possibility of substitution. There was a high degree of agreement between the vertical and conventional arrangement stereograms in both contour-based and random-dot-based stereograms.

In our study, stereopsis declined with an increase in aniseikonia magnification measured by both contour-based and random-dot-based stereograms. This is consistent

with previous studies (3, 14, 22). Atchison et al. (3) used afocal magnification lenses of 3, 6, 9, and 12% to induce aniseikonia. Stereoacuity was tested using random-dot stereograms with a "Pacman" shape. They transformed the stereoacuity to log values and found that the threshold of stereopsis increased with an increase in aniseikonia, and the loss was approximately proportional to the square of aniseikonia. Lovasik and Szymkiw (14) induced aniseikonia using magnifiers of 26 magnifications ranging from 1.2 to 32.3% and measured stereoacuity using both the Titmus stereo test and the Randot test. Their results indicated that the value of stereopsis (arcsec) increased with increasing aniseikonia in a curvilinear manner.

In our study, the effect of overall aniseikonia was always larger than that of meridional aniseikonia of identical magnification. This was similar to the results of Atchison et al. (3), who found that the mean loss of stereopsis with meridional aniseikonia was approximately 64% of that for overall aniseikonia with identical magnification.

In this study, participants' response to contour-based and random-dot-based stereograms was different in relatively high aniseikonia. For overall aniseikonia, the stereopsis still presented up to 30% when testing with contour-based stereograms, whereas, some participants failed at magnifications of 25, 27.5, and 30% when tested with random-dot-based stereograms.

In the contour-based stereogram, the effect of vertical aniseikonia was significantly smaller than that of horizontal aniseikonia of identical magnification. In random-dot-based stereograms, the opposite trend was found in three out of nine magnifications (15, 17.5, and 22.5%). This difference may be related to variations in the characteristics of the two test targets. Stereopsis is affected primarily in the horizontal meridian. In contour-based stereograms, image matching between the two eyes is determined by the contour. When the vertical direction of the half-view of one eye is enlarged with respect to the fellow half-view, the horizontal direction remains unchanged, which could help participants to distinguish the target symbols more easily. Conversely, when the horizontal direction of the half-view of one eye is enlarged with respect to the fellow half-view, the position of the lines in the horizontal direction changed simultaneously; this is likely to have a greater effect on depth perception and may explain why stereopsis was better under vertical, as opposed to horizontal aniseikonia. Whereas in random-dot-based stereograms, the participant is required to match dense random dots between the left and right eyes and fuse them into a single image. Since vertical disparities are less tolerated by the visual system, the processing capacity of fusing is more powerful in the horizontal than in the vertical direction (23, 24). Thus, it was easier for our participants to fuse images when enlarging one image in the horizontal direction than when enlarging one image in the vertical direction.

This study had some limitations. The participants that were recruited were young and had good stereoacuity; they therefore cannot accurately represent the general population. Induced aniseikonia may differ from that experienced by individuals with actual aniseikonia, and the adaptation of aniseikonia was not considered in this study. Besides, this test could not be achieved in a real circumstance to induce aniseikonia like size lens. It was carried out under an artificial test condition which is partly different from the actual situation of aniseikonia that occurred in the clinic. Moreover, the interference of additional disparities was minimized but was not eliminated completely.

CONCLUSION

In this study, stereopsis decreased with increasing aniseikonia induced by both overall and meridional magnification. Overall aniseikonia decreased stereopsis more than meridional aniseikonia of similar magnitudes. Horizontal aniseikonia impaired the stereopsis of the contour-based stereograms significantly more than random-dot-based stereograms, whereas vertical aniseikonia impaired the stereopsis of random-dot-based stereograms significantly more than the contour-based stereograms.

DATA AVAILABILITY STATEMENT

The original contributions presented in the study are included in the article/**Supplementary Material**, further inquiries can be directed to the corresponding author.

ETHICS STATEMENT

The studies involving human participants were reviewed and approved by the Ethics Committee of The Second Hospital of Jilin University (No. 2020-110). The patients/participants provided their written informed consent to participate in this study.

AUTHOR CONTRIBUTIONS

LX: writing the manuscript, conducting the experiment, and data collection. LL: material preparation and data analysis. HW: design the experiment, material preparation, and revision of the manuscript. All authors contributed to the article and approved the submitted version.

FUNDING

This study was supported by the Jilin Provincial Science and Technology Department, China (no. 20190303150SF) and the Jilin Provincial Special Fund for Talent Team (no. 2019SCZT030).

SUPPLEMENTARY MATERIAL

The Supplementary Material for this article can be found online at: https://www.frontiersin.org/articles/10.3389/fmed.2022.889398/full#supplementary-material

REFERENCES

1. Kulp MAT, Raasch TW, Polasky M. Patients with anisometropia and aniseikonia. 2nd ed. In: Benjamin WJ editor. *Borish's Clinical Refraction*. (Saint Louis, MO: Butterworth-Heinemann) (2006). p. 1479–508. doi: 10.1016/b978-0-7506-7524-6.50037-5
2. Burian HM. Clinical significance of aniseikonia. *Arch Ophthalmol.* (1943) 29:116–33. doi: 10.1001/archopht.1943.00880130136010
3. Atchison DA, Lee J, Lu J, Webber AL, Hess RF, Baldwin AS, et al. Effects of simulated anisometropia and aniseikonia on stereopsis. *Ophthalmic Physiol Opt.* (2020) 40:323–32. doi: 10.1111/opo.12680
4. Furr BA. Aniseikonia: a 21st century look. *J Binocul Vis Ocul Motil.* (2019) 69:43–50. doi: 10.1080/2576117X.2019.1603793
5. Howard IP, Rogers BJ. *Binocular Correspondence and the Horopter: Binocular Vision and Stereopsis*. New York, NY: Oxford University Press (1995). p. 31–68.
6. Rutstein RP. Update on aniseikonia. *Contemp Optom.* (2010) 8:1–7. doi: 10.1097/01.COY.0000384199.73542.02
7. Rutstein RP, Currie DC. Topical review: retinally induced aniseikonia. *Optom Vis Sci.* (2019) 96:780–9. doi: 10.1097/OPX.0000000000001431
8. Ugarte M, Williamson TH. Aniseikonia associated with epiretinal membranes. *Br J Ophthalmol.* (2005) 89:1576–80. doi: 10.1136/bjo.2005.077164
9. Highman VN. Stereopsis and aniseikonia in uniocular aphakia. *Br J Ophthalmol.* (1977) 61:30–3. doi: 10.1136/bjo.61.1.30
10. Oguchi Y, Mashima Y. The influence of aniseikonia on the VEP by random-dot stereogram. *Acta Ophthalmol (Copenh).* (1989) 67:127–30. doi: 10.1111/j.1755-3768.1989.tb00740.x
11. Krarup T, Nisted I, Kjaerbo H, Christensen U, Kiilgaard JF, la Cour M. Measuring aniseikonia tolerance range for stereoacuity – a tool for the refractive surgeon. *Acta Ophthalmol.* (2021) 99:e43–53. doi: 10.1111/aos.14507
12. Hall C. The relationship between clinical stereotests. *Ophthalmic Physiol Opt.* (1982) 2:135–43. doi: 10.1111/j.1475-1313.1982.tb00168.x
13. Fawcett SL. An evaluation of the agreement between contour-based circles and random dot-based near stereoacuity tests. *J AAPOS.* (2005) 9:572–8. doi: 10.1016/j.jaapos.2005.06.006
14. Lovasik JV, Szymkiw M. Effects of aniseikonia, anisometropia, accommodation, retinal illuminance, and pupil size on stereopsis. *Invest Ophthalmol Vis Sci.* (1985) 26:741–50.
15. Wu H, Liu S, Wang R. Stereoacuity measurement using a phoropter combined with two 4K smartphones. *Clin Exp Optom.* (2018) 101:272–5.
16. Sun Y, Wu H, Qiu Y, Yue Z. Stereoacuity of black-white and red-green patterns in individuals with and without color deficiency. *J Ophthalmol.* (2018) 2018:1926736. doi: 10.1155/2018/1926736
17. Zhao L, Wu H. The difference in stereoacuity testing: contour-based and random dot-based graphs at far and near distances. *Ann Transl Med.* (2019) 7:193. doi: 10.21037/atm.2019.03.62
18. Zhao L, Wu H. The effect of dot size in random-dot stereograms on the results of stereoacuity measurements. *BMC Ophthalmol.* (2020) 20:253. doi: 10.1186/s12886-020-01526-6
19. Katsumi O, Miyajima H, Ogawa T, Hirose T. Aniseikonia and stereoacuity in pseudophakic patients. Unilateral and bilateral cases. *Ophthalmology.* (1992) 99:1270–7. doi: 10.1016/s0161-6420(92)31813-5
20. Jiménez JR, Ponce A, del Barco LJ, Díaz JA, Pérez-Ocón F. Impact of induced aniseikonia on stereopsis with random-dot stereogram. *Optom Vis Sci.* (2002) 79:121–5. doi: 10.1097/00006324-200202000-00014
21. Häring G, Gronemeyer A, Hedderich J, de Decker W. Stereoacuity and aniseikonia after unilateral and bilateral implantation of the array refractive multifocal intraocular lens. *J Cataract Refract Surg.* (1999) 25:1151–6. doi: 10.1016/s0886-3350(99)00136-4
22. Hess RF, Ding R, Clavagnier S, Liu C, Guo C, Viner C, et al. A robust and reliable test to measure stereopsis in the clinic. *Invest Ophthalmol Vis Sci.* (2016) 57:798–804. doi: 10.1167/iovs.15-18690
23. Rogers BJ, Bradshaw MF. Vertical disparities, differential perspective and binocular stereopsis. *Nature.* (1993) 361:253–5. doi: 10.1038/361253a0
24. O'Shea RP, Crassini B. The dependence of cyclofusion on orientation. *Percept Psychophys.* (1982) 32:195–6. doi: 10.3758/bf03204280

Conflict of Interest: The authors declare that the research was conducted in the absence of any commercial or financial relationships that could be construed as a potential conflict of interest.

frontiers | Frontiers in Medicine

ORIGINAL RESEARCH
published: 01 June 2022
doi: 10.3389/fmed.2022.885187

Phase-Sensitive Measurements of Depth-Dependent Signal Transduction in the Inner Plexiform Layer

Clara Pfäffle[1], Hendrik Spahr[1], Katharina Gercke[1], Léo Puyo[1,2], Svea Höhl[1], David Melenberg[1], Yoko Miura[1,3], Gereon Hüttmann[1,4,5] and Dierck Hillmann[1,6,7]*

[1] *Institute of Biomedical Optic, University of Lübeck, Lübeck, Germany,* [2] *Medical Laser Center Lübeck GmbH, Lübeck, Germany,* [3] *Department of Ophthalmology, University of Lübeck, Lübeck, Germany,* [4] *Airway Research Center North, Member of the German Center for Lung Research, Grosshansdorf, Germany,* [5] *Center of Brain, Behavior and Metabolism (CBBM), University of Lübeck, Lübeck, Germany,* [6] *Thorlabs GmbH, Lübeck, Germany,* [7] *Department of Physics, Vrije Universiteit Amsterdam, Amsterdam, Netherlands*

Non-invasive spatially resolved functional imaging in the human retina has recently attracted considerable attention. Particularly functional imaging of bipolar and ganglion cells could aid in studying neuronal activity in humans, including an investigation of processes of the central nervous system. Recently, we imaged the activity of the inner neuronal layers by measuring nanometer-size changes of the cells within the inner plexiform layer (IPL) using phase-sensitive optical coherence tomography (OCT). In the IPL, there are connections between the neuronal cells that are dedicated to the processing of different aspects of the visual information, such as edges in the image or temporal changes. Still, so far, it was not possible to assign functional changes to single cells or cell classes in living humans, which is essential for studying the vision process. One characteristic of signal processing in the IPL is that different aspects of the visual impression are only processed in specific sub-layers (strata). Here, we present an investigation of these functional signals for three different sub-layers in the IPL with the aim to separate different properties of the visual signal processing. Whereas the inner depth-layer, closest to the ganglion cells, exhibits an increase in the optical path length, the outer depth-layer, closest to the bipolar cell layer, exhibits a decrease in the optical path length. Additionally, we found that the central depth is sensitive to temporal changes, showing a maximum response at a stimulation frequency of around 12.5 Hz. The results demonstrate that the signals from different cell types can be distinguished by phase-sensitive OCT.

Keywords: optoretinography, optical coherence tomography, phase-sensitive OCT, functional imaging, inner plexiform layer, retina

OPEN ACCESS

Edited by:
Peng Xiao,
Sun Yat-sen University, China

Reviewed by:
Andrea Curatolo,
International Center for Translational Eye Research (ICTER), Poland
Dawid Borycki,
Institute of Physical Chemistry (PAN), Poland

****Correspondence:***
Clara Pfäffle
cl.pfaeffle@uni-luebeck.de

Specialty section:
This article was submitted to Ophthalmology, a section of the journal Frontiers in Medicine

Received: *27 February 2022*
Accepted: *10 May 2022*
Published: *01 June 2022*

Citation:
Pfäffle C, Spahr H, Gercke K, Puyo L, Höhl S, Melenberg D, Miura Y, Hüttmann G and Hillmann D (2022) Phase-Sensitive Measurements of Depth-Dependent Signal Transduction in the Inner Plexiform Layer. Front. Med. 9:885187. doi: 10.3389/fmed.2022.885187

1. INTRODUCTION

Non-invasive, cellular imaging of the neuronal activity in humans is compelling for clinical diagnosis and basic science (1). Currently, only optical methods may achieve the necessary resolution for this purpose. In addition, the retina is the only site, where the central nervous system is directly accessible for optical imaging. Besides being part of the central nervous system

(CNS) and thereby providing diagnostic information on neuronal diseases, the initial information processing of visual impressions, which is mainly performed by the bipolar, amacrine, and ganglion cells, can be studied here (2–4). Each of these cell classes can be further divided into different functional cell types, which are sensitive to specific features of the visual signal. Currently, around 13 different types of bipolar and around 30 types of ganglion cells are known. They are responsible for processing different aspects for the visual information, e.g., brightness, color, as well as spatial and temporal variations, thus splitting the visual information into different feature channels (2, 5).

In recent years, there has been extensive research to identify these different cell types and assign them to different functional tasks (2–5). Although many types have already been classified, there are still gaps in the knowledge about these different cells. To access these cell classes one can use retinal imaging with functional contrast. Suitable functional signals in the inner layers of the retina could be detected with different imaging methods [reviewed in (6)]. Techniques capable of identifying different cell types make, for example, use of calcium imaging (7, 8). However, these methods require insertion of genetically encoded calcium indicators and are thus only available for animal studies.

Several other, non-invasive techniques could be and partially were applied to the living human eye. For example, electroretinogram (ERG) measurements provide information about the overall activity of the retina (9), but cannot spatially resolve contributions from different cell types in the retina. Furthermore, neurovascular coupling using laser Doppler flowmetry (10, 11) or optical coherence tomography angiography (OCTA) (12) can measure increased blood flow when the retina is stimulated. This has already been used to measure the sensitivity of the retina to temporal changes of the visual signal in cats (10, 11) and mice (12). The techniques may also achieve a relatively high resolution by measuring blood flow in the capillaries. Still, these techniques do not allow distinguishing of the functional contributions of individual functional cell types.

Furthermore, it has been shown that light-stimulated activation of the retinal function may lead to a change in reflectivity of the IPL that can be measured with optical coherence tomography (OCT). These changes in reflectivity due to functional activation could be demonstrated in different animals, for example, *ex vivo* in frog retina preparations (13), in paralyzed tree shrews (14), and in a few studies even *in vivo* in human (15). However, such measurements of changing reflectivity exhibit a high noise level, making it particularly challenging to extract the functional information from *in-vivo* measurements.

One technique, that emerged in the past years for non-invasive detection of the functional changes is phase-sensitive OCT. This technique can detect variations in the optical path length between the different retinal layers with a resolution of a few nanometers (16). Additionally, due to the tomographic character of OCT, such variations can be assigned axially and laterally to specific locations with a resolution better than 10 µm, which makes it in principle possible to assign functional changes to single cells. This cellular phase-based functional contrast has so far been demonstrated for the photoreceptor outer segments (OS) with several OCT techniques including Fourier-domain scanning (17–20), line-field (21), and full-field (16, 22) systems. Recently, by using a full-field swept-source OCT (FF-SS-OCT) system, we were able to show functional phase-changes in the inner plexiform layer (IPL) (23), where the synaptic connections of the bipolar, amacrine, and ganglion cells are located. However, low contrast, an order of magnitude smaller optical path length changes, and heart-beat induced pulsatile retinal motion make this endeavor extremely challenging in the inner neuronal layers. In the first demonstration of functional signals in the IPL, the resulting noise was minimized by extensive averaging of the phase over several voxels in the axial dimension. Due to this averaging, the contributions from all different functional bipolar/ganglion cells were integrated and no differentiation of the functional change in the IPL was possible. Unfortunately, the structural sensitivity of FF-SS-OCT has been insufficient to image individual ganglion or bipolar cells, although single ganglion cell imaging was demonstrated for other OCT systems by averaging hundreds of images (24).

Here, we use a recently demonstrated phase evaluation that takes advantage of the statistical properties of random and systematic phase changes to minimize phase noise (25) and use the stratification of the synaptic connections to differentiate signals from different cell types in the living human retina. With this phase evaluation, phase averaging in the axial dimension can be avoided to a large extent, so that the functional changes could be assigned to their origin in the retina with much higher accuracy allowing the evaluation of sub-layers. At the same time, the reduced noise levels enable a better investigation of the lateral dependency of the signal in the IPL. Although, single cell functional imaging of the inner neurons is still not possible due to the limited structural sensitivity, we could use the increased axial resolution and the improved signal-to-noise ratio (SNR) to distinguish the contributions of different functional cell types to the change in optical path length. To this end, we exploit the interconnection behavior of the different cell types in the IPL. Since certain functional bipolar and ganglion cell types form their synaptic connections only in a specific depth of the IPL, the corresponding properties of the visual impression are also processed at a specific depth of the IPL (2–4). Basically, 5 different sub-layers of approximately equal thickness can be distinguished histologically (26) and with visible light OCT (27). Thus, it can be expected that this stratification of the IPL enables a differentiation of functional cell types without resolving individual cells by investigating the phase changes in different depths or sub-layers of the IPL.

2. RESULTS

Here, the functional response of sub-layers to different visual stimuli was investigated in order to see if we can distinguish the response of different bipolar and ganglion cell types. During OCT imaging, the retina of a volunteer with no known diseases or ametropia was stimulated with a white LED combined with a transmission mask that projects a square-shaped pattern at

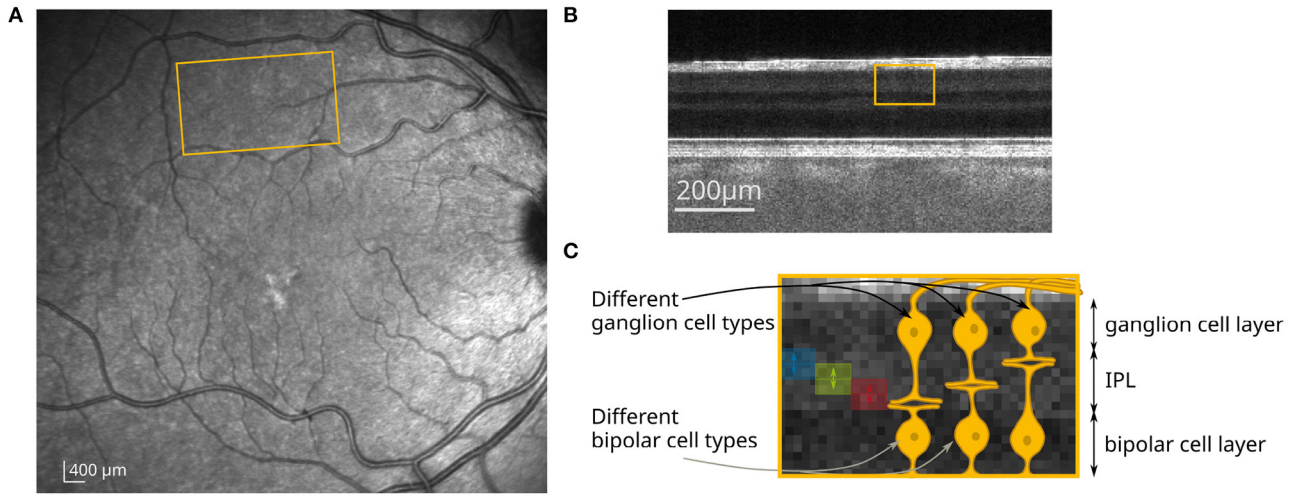

FIGURE 1 | (A) Scanning laser ophthalmoscope (SLO) image at 815 nm (Spectralis, Heidelberg Engineering); yellow marked region corresponds to the field of view at 10° superior to the fovea. **(B)** B-scan of the retina imaged with an FF-SS-OCT system at this position. **(C)** Yellow marked region from **(B)** and close-up with a schematic drawing of the neuronal connections in the IPL. The different sub-layers of the IPL, for which the optical path length changes were obtained, are marked by the blue, green, and red areas.

10° superior of the fovea on the retina (**Figure 1A**). At this position, very little distortion of the actual stimulation pattern and the functional OCT signal was observed (23) due to the wiring of the photoreceptors by the Henle fibers to the inner layers of the retina (28). In addition, at this position in the retina, the size of the dendritic fields of the ganglion cells are in the range between 100 and 200 µm for non-midget cells, or even lower for the midget cells (29). The size of the square shaped stimulation pattern is 1 mm × 1 mm, so that the resolution of the stimulated area in the IPL is expected to be sufficient to analyze the stimulation pattern. The irradiance on the retina was about 57 nW/mm^2, which corresponds to a luminance of 140 cd/m^2 and is therefore in the photopic vision regime (30). In order to investigate the functional phase change in different sub-layers of the IPL, the lower edge of the IPL was segmented (see Section 5 for detailed information). Phase differences were calculated in depths with constant distance to the segmented lower edge of the IPL. Due to the limited axial resolution of the OCT system, it was only possible to evaluate the optical path length change of three different sub-layers in the IPL, in which the 5 histologically differentiable layers partially overlap (see **Figures 1B,C**). The functional phase changes in the three different sub-layers after 8 s of continuous stimulation are shown in **Figures 2A–C**. For comparison, an en-face image showing the functional change in the photoreceptor OS of the same measurement is shown in **Figure 2J**. The response of the photoreceptors OS matches the essentially uniform stimulation pattern. The slightly washed out edges probably result from aberrations of the projection of the stimulation pattern on the retina and ocular motion. In contrast, the functional imaging of the IPL shows a pronounced signal at the edge of the stimulation pattern, while the optical path length changes in the center of the stimulation pattern are weaker for all three layers (**Figures 2G–I**). By this inhomogeneous behavior, the contrast at the edge regions of the stimulation pattern is increased and a prominent contour becomes visible. Furthermore, the functional changes in the sub-layers of the IPL also differ. The greatest change in the optical path length is in the inner sub-layer (closest to the ganglion cell layer). Here, a change in the optical path length of approx. 25 nm is observed in the edges and an increase of approx. 15 nm in the center. In the central layer, only a change in the edges of the stimulation pattern is observed (approx. 10 nm), while no change is observed in the center. Additionally, in the outer layer, the optical path length decreases during stimulation. Here, it is not possible to distinguish between edges and center of the stimulation pattern. The time courses of the three layers are shown in **Figure 2K** (solid lines). The curves were obtained by averaging the phase differences over the central area of the stimulation pattern. Residual motion artifacts, caused for example by vascular pulsation, were corrected by subtracting a background that was obtained by averaging the phase change in an area in a safe distance (at least 200 µm) from the stimulation site.

In **Figures 2D–F** en-face images of the phase change for the three different layers after 8 s of flicker stimulation (square waveform of 12.5 Hz) with the same square pattern are shown. The corresponding time courses are shown in **Figure 2K** (dashed lines). Here, the functional changes in the inner sub-layer (blue, closest to the ganglion cells) and the outer layer (red, closest to the bipolar cells), do not differ significantly from the functional changes caused by continuous stimulation. However, a clear difference can be observed in the central layer. Here, the functional change under flicker stimulation is significantly increased, showing not only a stronger response in the edges of the stimulation pattern, but also a change in the center of the stimulation pattern, which shows an increase in the optical path length of about 15 nm and

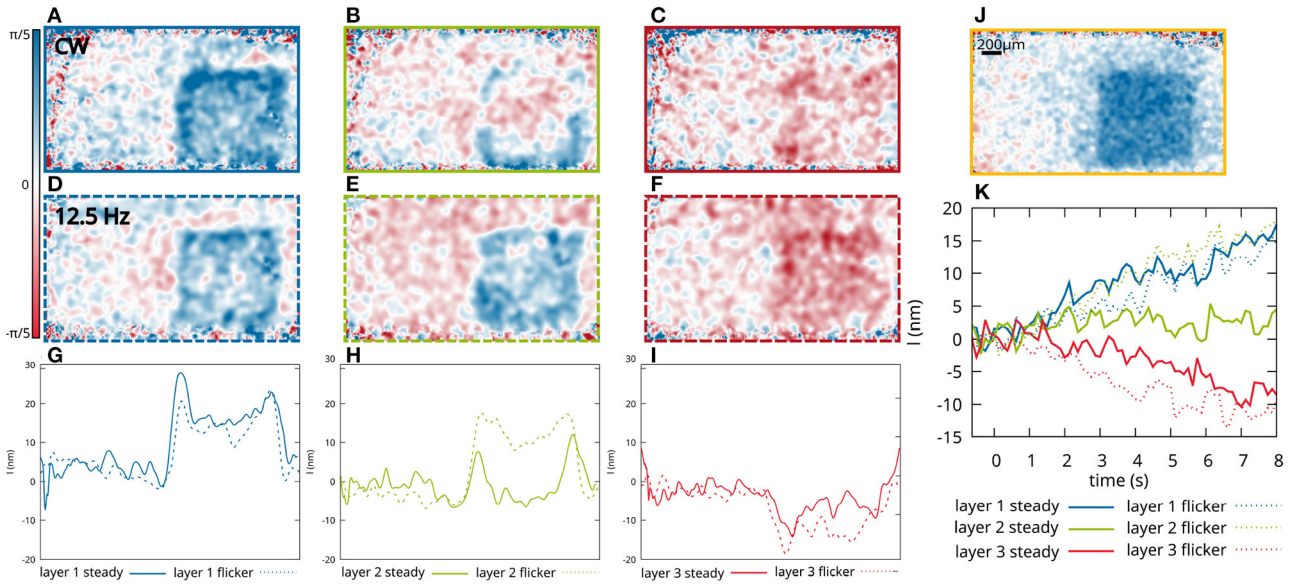

FIGURE 2 | Functional changes of three different layers of the IPL as shown in **Figure 1** after 8 s of stimulation with a square-shaped pattern. En-face images of the phase changes after 8 s of continuous stimulation, of the first layer **(A)**, the second layer **(B)** and the third layer **(C)**. En-face images of the optical path length changes after 8 s stimulation with a 12.5 Hz flickering light, of the first layer **(D)**, the second layer **(E)**, and the third layer **(F)**. **(G–I)** Profile of the optical path length change after 8 s stimulation. The phase changes are vertically averaged over 150 px (600 µm). **(J)** For comparison, phase changes in the photoreceptor OS are shown 0.5 s after the beginning of the stimulation. **(K)** Corresponding time courses of the optical path length changes averaged over the central part of the stimulated area.

is therefore about the same strength as the signal from the inner sub-layer.

Since the central layer is the only one that showed an increased response to flicker stimulation, it was investigated more closely to evaluate the sensitivity to different stimulation frequencies. In order to do so, the stimulation was performed with a continuous illumination and 11 different flicker frequencies of square waveform ranging from 1 to 55 Hz with a duty cycle of 50 %. Consequently, the number of photons reaching the retina was kept constant for all frequencies and halved compared to the constant stimulus. In order to quantify the sensitivity of the phase changes in the central IPL to the temporal frequencies, only the phase changes after 8 s in the central part of the stimulation pattern were evaluated. Signal changes in the edge regions of the stimulation pattern were neglected for this investigation, since they were not effected by different stimulation frequencies in our observations. To reduce the influence of noise or remaining artifacts caused by the arterial pulsation, the optical path length changes over the last 625 ms were averaged. **Figure 3** shows the response of the central layer of the IPL to the different stimulation frequencies. As expected, continuous or low-frequency stimulation with 1 Hz only resulted in a minimal change in the optical path length. The signal increased for higher frequencies (2 – 6.7 Hz) and reached a maximum of around 15 nm for stimulation frequencies of 12.5 – 16.6 Hz. At even higher frequencies, the response decreased again and reached an optical path length change comparable to a continuous stimulation at 50 Hz.

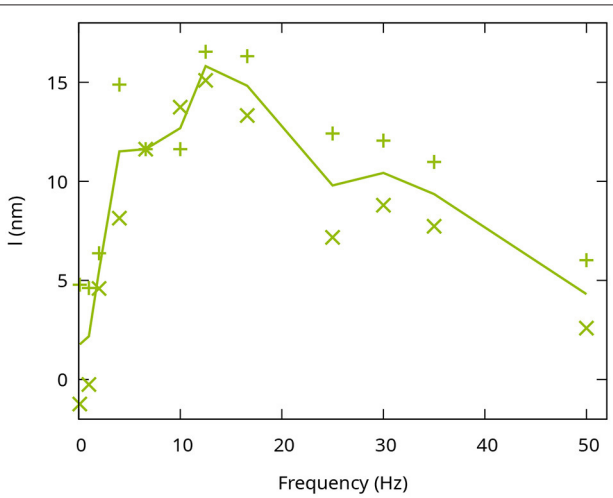

FIGURE 3 | Frequency dependence of the functional phase change in the IPL. The optical path length changes l reached after 8 s were evaluated. Each point corresponds to an individual measurement. The line connects the average of the two measurements at each frequency.

3. DISCUSSION

For a functional evaluation of the phase in the human IPL *in vivo*, it is particularly important to have sufficient stability of the phase. Besides the general requirements for a phase-stable OCT system, as it is needed for the functional evaluation of the photoreceptors,

a robust phase evaluation is crucial for a stable measurement of functional changes in the IPL, since a fast decorrelation of the speckle pattern is observed there, which is likely caused by metabolic processes in the inner retinal layers.

In contrast to other techniques that attempt to more directly assess retinal function and have been mostly used *ex vivo* or in animals, FF-SS-OCT relies on the changes in the phase of the backscattered light. The technique relies heavily on suitable post-processing of the data. As such, even on a state-of-the-art GPU (Radeon VII) accompanied by an Intel i7 8700 and 64 GB of RAM, the processing of the camera's data to suitably segmented OCT volumes takes almost 7 min, when excluding disc I/O. Afterwards almost 2 min are required for the phase evaluation (25), which is done on the CPU (Intel i7) and requires sufficient RAM to achieve this processing time.

The proposed technique is robust enough to be applied to the living human retina as it was demonstrated here. Previous techniques that classified and measured the different ganglion cell types are invasive and can only be applied in animal models or are even limited to cell cultures. An important disadvantages is still that it does not allow functional imaging of individual cells but rather has to rely on the stratification of the dendrite connections in the IPL.

The most important parts to obtain the results presented here is the phase-stable and fast data acquisition, combined with the phase evaluation taking statistical properties into account. In contrast, the exact algorithms used for registration and segmentation could be replaced by other algorithms, however, given the low SNR of the used OCT volumes, many existing solutions fail.

The observed functional changes can be well-explained by the stratification behavior of bipolar and ganglion cell types in the IPL. The OFF-bipolar cells, for instance, only connect in the outer layers (closest to the bipolar cells) with the OFF-ganglion cells, while the synaptic connection of the ON-bipolar and ganglion cells form in the inner layers (closest to the ganglion cells) (2, 3). Since the ON-cells get activated by light onset and the OFF-cells get inactivated, those two cell types react in opposite ways to the same visual stimulus. The increase of the optical path length observed here correlates with the stratification of the ON-bipolar and ganglion cells, while the observed decrease in optical path length coincides with the connection of OFF-bipolar and ganglion cells. Furthermore, we observed a high sensitivity to flickering light in the central layer of the IPL, whereas the response of the innermost and outermost layers was not affected by changes in time of the stimulation. This behavior fits well to the known stratification of sustained and transient cells. Sustained bipolar cells, which process slow visual changes, stratify on the inner and outer edges of the IPL, while transient bipolar cells, which process fast visual changes, tend to stratify in the middle of the IPL (2). Since the functional response in the inner and outermost layer does not change under flicker stimulation, those signals are probably caused by cell types that are sensitive to a different property in the visual signal such as intensity or chromatic information.

The temporal dependence of the IPL response of the middle layer with a maximum between 10 and 20 Hz and a return to the background above 50 Hz fits well to whole retina measurements using flicker ERG, electrical *ex-vivo* measurements on individual cells (31, 32), and measurements of increased blood flow (10). In all these experiments, a decrease in the functional contrast was observed for temporal frequencies at about 30 Hz and above. The frequency dependence measured here also follows the temporal contrast sensitivity curve of the human eye (33). It should be noted, however, that only slow changes in optical path length are measured here and that potential high-frequency changes in optical path length cannot be detected with the used volume rate (8 Hz). Furthermore, based on results obtained for photoreceptors by Tomczweski et al. (22), we expect the amplitude of the fast response to be more than one order of magnitude lower and, at these frequencies, it will be difficult to differentiate from heart-beat induced pulsation (34). Finally, while the observed response is linked to the neuronal activity, the time course of the observed path length changes may differ and show a slower temporal response.

A further interesting effect is the edge sensitivity of the functional changes across the stimulated area, which can be explained by the center-surround processing within the receptive fields of some bipolar and ganglion cell types (35, 36). In this processing scheme, stimulation of the marginal (surround) region of the receptive field acts antagonistically to stimulation in the central region. Areas in which the center of the receptive field and only part of the surrounding are stimulated thus produce a greater functional change than areas in which both the entire center and surround are stimulated. Such a processing scheme makes the cells particularly sensitive to edges in the visual signal (37). However, either the center activation has a higher influence than the surround inhibition, or additional cells contribute that lack the center-surround processing within their receptive field, causing a functional signal in the center of the stimulation pattern.

4. CONCLUSION

Here, we demonstrated that FF-SS-OCT combined with suitable post-processing provides sufficient phase stability and spatial resolution to analyze the neuronal signal processing in the human retina. Although, the functional changes of the optical path length in the IPL detected in this study can so far not be directly correlated with a specific physiological origin or molecular process, they are in good agreement with the existing knowledge of the visual signal processing of bipolar and ganglion cells.

It seems promising that phase-sensitive FF-SS-OCT can be used in the future to study the function of different, so far unclassified cell types *in vivo*. This could help monitoring innovative clinical treatments for ophthalmic diseases such as stem cell or optogenetic therapy in the retina (38, 39). Given the currently time-consuming nature of the measurements presented here, future studies will be required to simplify the procedure, confirm robustness and reproducibility of the signals in multiple individuals, and to evaluate the physiological parameters that can be extracted.

Differentiating functional groups of ganglion and bipolar cells does not need to resolve individual cells, but is possible by studying signals from different depths in the IPL, where their synaptic connections are stratified. This work thus demonstrates the potential of phase-sensitive OCT to study complex neurological function and signal processing *in vivo*, which opens avenues for functional studies in humans.

5. METHODS

5.1. Setup

All measurement were done with a Michelson-interferometer based FF-SS-OCT [see e.g., (40–42)]. It uses a tunable light source (Superlum Broadsweeper, BS-840-1) with 51 nm tuning range centered at $\lambda_0 = 841$ nm, resulting in an axial resolution of 8.4 μm (FWHM) in air. The light source illuminates an area of 2.6 mm × 1.5 mm on the retina. The total radiant flux on the retina from the sample illumination was about 5 mW. The light backscattered by the retina was superimposed with a collimated reference beam and detected by an ultra-high speed camera (Fastcam SA-Z, Photron) at a frame rate of 60 kHz at 640 × 368 pixels. During the wavelength scan the camera acquired 512 images per volume, which results in a volume rate of 117 Hz at full duty cycle. The data had to be stored with 8-bit precision on an internal storage of about 8 GB. With the image size used and the number of frames required for each volume, this ultimately restricts the number of volumes in one imaging sequence to about 70. To achieve 8 s of measurement time, a volume was triggered only every 125 ms, corresponding to a volume rate of 8 Hz. Longer time intervals were hardly useful, because macroscopic and microscopic motion frequently destroyed the phase correlation between successive volumes.

During measurements, the retina was stimulated with a white LED and a transmission mask, which projected a square pattern on the retina. The stimulation light was coupled *via* a cold mirror into the sample arm and an infrared long pass filter in front of the camera ensured that no stimulation light disturbed the OCT imaging. The stimulation irradiance was about 57 nW/mm. The conversion from the irradiance $E_e[\frac{\mathrm{W}}{\mathrm{m}^2}]$, which was obtained from the spectrum of the used LED, to the illuminance $E_v[\frac{\mathrm{lm}}{\mathrm{m}^2}]$ is done by the following equation:

$$E_v = 683\frac{\mathrm{lm}}{\mathrm{W}}\int_0^\infty \mathrm{d}\lambda\, V(\lambda)E_e(\lambda) \tag{1}$$

Here, $V(\lambda)$ is the luminous efficiency function (43) and 683 $\frac{\mathrm{lm}}{\mathrm{W}}$ is a conversion factor. The conversion to luminance $L_v[\frac{\mathrm{cd}}{\mathrm{m}^2}]$ is done according to

$$L_v = E_v\frac{D^2}{A_p}, \tag{2}$$

where A_p is the pupil area for a dilated pupil (50 mm^2) and $D = 17$ mm is the distance from the pupil to the retina.

5.2. Measurements

All measurements shown here were carried out on a single female volunteer with no known diseases or ametropia. Written informed consent was obtained. Compliance with the maximum permissible exposure (MPE) of the retina and all relevant safety rules was confirmed by the ethics board of the University of Lübeck. All methods and measurements were performed in accordance with the relevant guidelines and regulations. The study was approved by the ethics board of the University of Lübeck (ethics approval Ethik-Kommission Lübeck 16-080). To optimize the light detection, the pupil of the volunteer was dilated by mydriatic eye drops to a diameter of approximately 8 mm. Before the beginning of each measurement session, the subject was dark-adapted for at least 20 min and all measurements were performed in a darkened room. Between measurements, a break of at least 5 min enabled a complete regeneration of the stimulated area in the retina. All stimulation (continuous and flicker) started at the 5th recorded volume, and continued for the full duration of the measurement, so that the first 4 volumes served as baseline.

5.3. Data Processing

After the reconstruction of the OCT data, numerical corrections for axial motion, dispersion (44), and aberrations (41, 45) were done for all 70 volumes in a dataset.

5.3.1. Registration

Afterwards, the movement between successive volumes was compensated by a non-rigid registration of the data. The registration utilizes correlation of sub-areas of the different volumes to determine their relative displacement and finally interpolates a three-dimensional displacement map between all volumes.

5.3.2. Segmentation

In order to investigate the functional changes in different layers of the IPL, the lower edge of the IPL was segmented in a volume after aligning the volumes according to their registration. The utilized segmentation was loosely based on the work of Kafieh et al. (46). First, data points with a particularly high axial gradient were selected from a coarse-grained volume. Afterwards, a 3D-graph based algorithm called diffusion maps (47) was used. This algorithm maps the selected data points into a new coordinate system, where they are rearranged according their connectivity, i.e., based on their transition probability after multiple time-steps given only their transition probability in a single time-step. The single time-step transition probability of the graph was thereby determined from the local proximity of the data points to each other and the local curvature of the surface, assuming that transitions along a surface curvature are more likely than those that deviate from the local curvature. The mapped data points are then clustered by a density-based algorithm, called DBSCAN (48), separating them into different layers and finally interpolated to give the respective layers in the high resolution dataset.

Based on the segmentation, the curvature of all 70 complex-valued volumes was removed using the Fourier shift theorem and

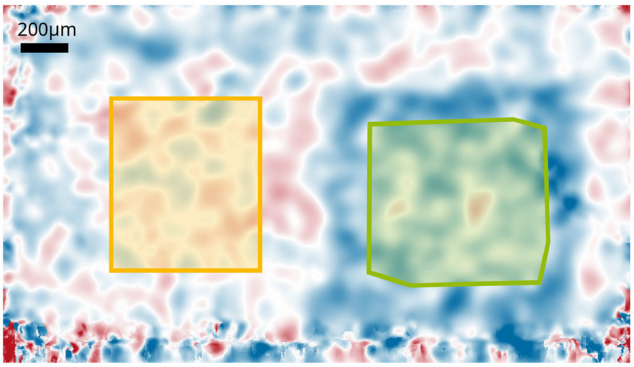

FIGURE 4 | Phase changes of the central layer of the IPL after 8 s stimulation with 12.5 Hz. Areas used for the background corrections are indicated. The green marked area is the mask for the functional changes that is used to extract the time courses; the yellow marked area corresponds to the mask used to obtain the background noise.

the individual A-scans were aligned, resulting in the lower edge of the IPL being flat.

5.3.3. Phase Evaluation

After segmenting, the phase changes of the volumes were evaluated for different sub-layers. This phase evaluation was done by using an adaption of the extended Knox-Thompson algorithm (49–52), which is described in more detail elsewhere (25). For the evaluation, the cross-spectrum $\Delta U\left(x, y, z, t, \Delta t\right)$ is calculated, which contains all possible temporal phase differences between the times t and $t + \Delta t$ for each position (x, y, z),

$$\Delta U(x, y, z; t, \Delta t) = U(x, y, z, t)U^{*}(x, y, z, t + \Delta t), \quad (3)$$

where $U\left(x, y, z, t\right)$ represents the complex-valued OCT volumes.

Following, the spatial phase-differences were calculated between two layers Z_1 and Z_2, each consisting of two voxels in depth, with constant distance to the segmented lower IPL edge. In order to receive a better SNR the phase-information for each layer were averaged over the 2 voxels in depth, according to

$$\Delta U^{Z_1-Z_2}(x, y; t, \Delta t) = \left(\sum_{z\in Z_1} \Delta U(x, y, z; t, \Delta t)\right) \left(\sum_{z\in Z_2} \Delta U(x, y, z; t, \Delta t)\right)^{*}. \quad (4)$$

In the upper layers of the retina, the phase evaluation is especially challenging, since metabolic processes and blood flow cause strong molecular movements here. For this reason, decorrelation of the speckles occurs very fast and makes the phase evaluation difficult.

To minimize this kind of noise, an ensemble average of the phase differences over several adjacent lateral points is formed by convolving the phase with a lateral Gaussian function according to

$$\left\langle \Delta U^{Z_1-Z_2}(x, y; t, \Delta t)\right\rangle \approx G_{\sigma^2}(x, y) * \Delta U^{Z_1-Z_2}(x, y; t, \Delta t). \quad (5)$$

Here, * denotes a circular convolution and $G_{\sigma^2}(x, y)$ is a Gaussian function with standard deviation of $\sigma = 4$ pixels. The resulting, averaged cross-spectrum $\left\langle \Delta U^{Z_1-Z_2}(x, y; t, \Delta t)\right\rangle$ was then used to find a phase function $\phi\left(x, y, t\right)$ that is consistent with all entries of the cross-spectrum (25).

From the resulting en-face phase images, the area in which a functional change occurs were determined. The phases in the area were averaged using an adapted mask to obtain a more stable ensemble average. Additional movement in the IPL, for example by vascular pulsation and other metabolic processes resulted in a continuously changing and non-reproducible background, which is superimposed to the functional signal. For correction and removal of the background noise, the phase changes in a second area that was not stimulated was subtracted from the functional changes (see **Figure 4**). The mask for the functional change was obtained manually for each measurement since the stimulated area could change slightly. The mask for the background noise was the same for all measurements.

DATA AVAILABILITY STATEMENT

The raw data supporting the conclusions of this article will be made available by the authors, without undue reservation.

ETHICS STATEMENT

The studies involving human participants were reviewed and approved by Ethics board of the University of Lübeck. The participant provided written informed consent to participate in this study.

AUTHOR CONTRIBUTIONS

CP worked on the setup, collected, analyzed, and interpreted the data, worked on the post-processing of the data, and wrote the manuscript. HS worked on the setup, collected the data, and worked on the post-processing. KG worked on the post-processing. SH, LP, and DM worked on the setup and collected the data. YM interpreted the data. GH obtained the funding and interpreted the data. DH obtained funding, worked on the post-processing, and interpreted the data. All authors contributed to the article and approved the submitted version.

FUNDING

This work was funded by the German Research Foundation (DFG), Project Number 629/6-1 and the Federal Ministry of Education and Research (BMBF 13N15432).

REFERENCES

1. London A, Benhar I, Schwartz M. The retina as a window to the brain - From eye research to CNS disorders. *Nat Rev Neurol*. (2013) 9:44–53. doi: 10.1038/nrneurol.2012.227
2. Euler T, Haverkamp S, Schubert T, Baden T. Retinal bipolar cells: elementary building blocks of vision. *Nat Rev Neurosci*. (2014) 15:507–19. doi: 10.1038/nrn3783
3. Masland RH. The neuronal organization of the retina. *Neuron*. (2012) 76:266–80. doi: 10.1016/j.neuron.2012.10.002
4. Wässle H. Parallel processing in the mammalian retina. *Nat Rev Neurosci*. (2004). 5:747–57. doi: 10.1038/nrn1497
5. Sanes JR, Masland RH. The types of retinal ganglion cells: current status and implications for neuronal classification. *Annu Rev Neurosci*. (2015) 38:221–46. doi: 10.1146/annurev-neuro-071714-034120
6. Hunter JJ, Merigan WH, Schallek JB. Imaging retinal activity in the living eye. *Annu Rev Vis Sci*. (2019) 5:15–45. doi: 10.1146/annurev-vision-091517-034239
7. Yin L, Geng Y, Osakada F, Sharma R, Cetin AH, Callaway EM, et al. Imaging light responses of retinal ganglion cells in the living mouse eye. *J Neurophysiol*. (2013) 109:2415–21. doi: 10.1152/jn.01043.2012
8. Shiga Y, Alarcon-Martinez L, Belforte N, Villafranca-Baughman D, Dotigny F, Polo AD. Live two-photon calcium imaging in retinal ganglion cells: characterization of early changes in a mouse glaucoma model. *Invest Ophthalmol Vis Sci*. (2020) 61:1437.
9. Balicka A, Trbolova A, Vrbovska T. Electroretinography (A Review). *Folia Vet*. (2016) 60:53–8. doi: 10.1515/fv-2016-0008
10. Toi VV, Riva CE. Variations of blood flow at optic nerve head induced by sinusoidal flicker stimulation in cats. *J Physiol*. (1995) 482:189–202. doi: 10.1113/jphysiol.1995.sp020509
11. Riva CE, Harino S, Shonat RD, Petrig BL. Flicker evoked increase in optic nerve head blood flow in anesthetized cats. *Neurosci Lett*. (1991) 128:291–6. doi: 10.1016/0304-3940(91)90282-X
12. Son T, Alam M, Toslak D, Wang B, Lu Y, Training A, et al. Functional optical coherence tomography of neurovascular coupling interactions in the retina. *J Biophotonics*. (2019) 11:1–20. doi: 10.1002/jbio.201800089
13. Li YC, Strang C, Amthor FR, Liu L, Li YG, Zhang QX, et al. Parallel optical monitoring of visual signal propagation from the photoreceptors to the inner retina layers. *Opt Lett*. (2010) 35:1810. doi: 10.1364/OL.35.001810
14. Erchova I, Tumlinson AR, Fergusson J, White N, Drexler W, Sengpiel F, et al. Optophysiological characterisation of inner retina responses with high-resolution optical coherence tomography. *Sci Rep*. (2018) 8:1–12. doi: 10.1038/s41598-018-19975-x
15. Schmoll T, Kolbitsch C, Leitgeb RA. *In vivo* functional retinal optical coherence tomography. *J Biomed Opt*. (2010) 15:41513–8. doi: 10.1117/1.3463008
16. Hillmann D, Spahr H, Pfäffle C, Sudkamp H, Franke G, Hüttmann G. *In vivo* optical imaging of physiological responses to photostimulation in human photoreceptors. *Proc Natl Acad Sci USA*. (2016) 113:13138–43. doi: 10.1073/pnas.1606428113
17. Azimipour M, Migacz JV, Zawadzki RJ, Werner JS, Jonnal RS. Functional retinal imaging using adaptive optics swept-source OCT at 16 MHz. *Optica*. (2019) 6:300. doi: 10.1364/OPTICA.6.000300
18. Azimipour M, Valente D, Vienola KV, Werner JS, Zawadzki RJ, Jonnal RS. Optoretinogram: optical measurement of human cone and rod photoreceptor responses to light. *Opt Lett*. (2020) 45:4658. doi: 10.1364/OL.398868
19. Zhang P, Zawadzki RJ, Goswami M, Nguyen PT, Yarov-Yarovoy V, Burns ME, et al. *In vivo* optophysiology reveals that G-protein activation triggers osmotic swelling and increased light scattering of rod photoreceptors. *Proc Natl Acad Sci USA*. (2017) 114:E2937–46. doi: 10.1073/pnas.1620572114
20. Ma G, Son T, Kim TH, Yao X. Functional optoretinography: concurrent OCT monitoring of intrinsic signal amplitude and phase dynamics in human photoreceptors. *Biomed Opt Express*. (2021) 12:2661. doi: 10.1364/BOE.423733
21. Pandiyan VP, Maloney-Bertelli A, Kuchenbecker JA, Boyle KC, Ling T, Chen ZC, et al. The optoretinogram reveals the primary steps of phototransduction in the living human eye. *Sci Adv*. (2020) 6:eabc1124. doi: 10.1126/sciadv.abc1124
22. Tomczewski S, Wegrzyn P, Borycki D, Auksorius E, Wojtkowski M, Curatolo A. Light-adapted flicker optoretinograms captured with a spatio-temporal optical coherence-tomography (STOC-T) system. *Biomed Opt Express*. (2022) 13:2186–201. doi: 10.1364/BOE.444567
23. Pfäffle C, Spahr H, Kutzner L, Burhan S, Hilge F, Miura Y, et al. Simultaneous functional imaging of neuronal and photoreceptor layers in living human retina. *Opt Lett*. (2019) 44:5671–4. doi: 10.1364/OL.44.005671
24. Liu Z, Kurokawa K, Zhang F, Lee JJ, Miller DT. Imaging and quantifying ganglion cells and other transparent neurons in the living human retina. *Proc Natl Acad Sci USA*. (2017) 114:12803–8. doi: 10.1073/pnas.1711734114
25. Spahr H, Pfäffle C, Burhan S, Kutzner L, Hilge F, Hüttmann G, et al. Phase-sensitive interferometry of decorrelated speckle patterns. *Sci Rep*. (2019) 9:11748. doi: 10.1038/s41598-019-47979-8
26. Cajal SR. La retine des vertebres. *La Cellule*. (1893) 9:121–255.
27. Zhang T, Kho AM, Srinivasan VJ. *In vivo* morphometry of inner plexiform layer (IPL) stratification in the human retina with visible light optical coherence tomography. *Front Cell Neurosci*. (2021) 15:147. doi: 10.3389/fncel.2021.655096
28. Drasdo N, Millican CL, Katholi CR, Curcio CA. The length of Henle fibers in the human retina and a model of ganglion receptive field density in the visual field. *Vision Res*. (2007) 47:2901–11. doi: 10.1016/j.visres.2007.01.007
29. Dacey DM. The mosaic of midget ganglion cells in the human retina. *J Neurosci*. (1993) 13:5334–5355. doi: 10.1523/JNEUROSCI.13-12-05334.1993
30. Zele AJ, Cao D. Vision under mesopic and scotopic illumination. *Front Psychol*. (2015) 5:1–15. doi: 10.3389/fpsyg.2014.01594
31. Yeh T, Lee BB, Kremers J. Temporal response of ganglion cells of the macaque retina to cone-specific modulation. *J Opt Soc Am A*. (1995) 12:456–64. doi: 10.1364/JOSAA.12.000456
32. Lee BYBB, Martin PR, Valbergt A. Sensitivity of macaque retinal ganglion cells to chromatic and luminance flicker. *J Physiol*. (1989) 414:223–243. doi: 10.1113/jphysiol.1989.sp017685
33. Kolb H, Fernandez E, Nelson R. Webvision: *The Organization of the Retina and Visual System*. Salt Lake City, UT: University of Utah Health Sciences Center (1995).
34. Spahr H, Hillmann D, Hain C, Pfäffle C, Sudkamp H, Franke G, et al. Imaging pulse wave propagation in human retinal vessels using full-field swept-source optical coherence tomography. *Opt Lett*. (2015) 40:4771–4. doi: 10.1364/OL.40.004771
35. Kuffler SW. Discharge patterns and functional organization of mammalian retina. *J Neurophysiol*. (1953) 16:37–68. doi: 10.1152/jn.1953.16.1.37
36. Dacey D, Packer OS, Diller L, Brainard D, Peterson B, Lee B. Center surround receptive field structure of cone bipolar cells in primate retina. *Vis Res*. (2000) 40:1801–11. doi: 10.1016/S0042-6989(00)00039-0
37. Ankri L, Ezra-Tsur E, Maimon SR, Kaushansky N, Rivlin-Etzion M. Antagonistic center-surround mechanisms for direction selectivity in the retina. *Cell Rep*. (2020) 31:107608. doi: 10.1016/j.celrep.2020.107608
38. Sahel JA, Boulanger-Scemama E, Pagot C, Arleo A, Galluppi F, Martel JN, et al. Partial recovery of visual function in a blind patient after optogenetic therapy. *Nat Med*. (2021) 27:1223–29. doi: 10.1038/s41591-021-01351-4
39. McGregor JE, Godat T, Dhakal KR, Parkins K, Strazzeri JM, Bateman BA, et al. Optogenetic restoration of retinal ganglion cell activity in the living primate. *Nat Commun*. (2020) 11:1–9. doi: 10.1038/s41467-020-15317-6
40. Bonin T, Franke G, Hagen-Eggert M, Koch P, Hattmann G. *In vivo* Fourier-domain full-field OCT of the human retina with 1.5 million A-lines/s. *Opt Lett*. (2010) 35:3432–4. doi: 10.1364/OL.35.003432
41. Hillmann D, Spahr H, Hain C, Sudkamp H, Franke G, Pfaffle C, et al. Aberration-free volumetric high-speed imaging of *in vivo* retina. *Sci Rep*. (2016) 6:35209. doi: 10.1038/srep35209
42. Auksorius E, Borycki D, Wegrzyn P, Žičkien e I, Adomavičius K, Sikorski BL, et al. Multimode fiber as a tool to reduce cross talk in Fourier-domain full-field optical coherence tomography. *Opt Lett*. (2022) 47:838–41. doi: 10.1364/OL.449498
43. Sharpe LT, Stockman A, Jagla W, Jaägle H. A luminous efficiency function, V*(λ), for daylight adaptation. *J Vis*. (2005) 5:948–968. doi: 10.1167/5.11.3

44. Hillmann D, Bonin T, Lührs C, Franke G, Hagen-Eggert M, Koch P, et al. Common approach for compensation of axial motion artifacts in swept-source OCT and dispersion in Fourier-domain OCT. *Opt Express*. (2012) 20:6761–76. doi: 10.1364/OE.20.006761
45. Hillmann D, Pfaffle C, Spahr H, Burhan S, Kutzner L, Hilge F, et al. Computational adaptive optics for optical coherence tomography using multiple randomized subaperture correlations. *Opt Lett*. (2019) 44:3905. doi: 10.1364/OL.44.003905
46. Kafieh R, Rabbani H, Abramoff M, Sonka M. Intra-retinal layer segmentation of optical coherence tomography using diffusion map. In: *ICASSP, IEEE International Conference on Acoustics, Speech and Signal Processing - Proceedings*. (2013). p. 1080–4. doi: 10.1109/ICASSP.2013.6637816
47. Coifman RR, Lafon S. Diffusion maps. *Appl Comput Harm Anal*. (2006) 21:5–30. doi: 10.1016/j.acha.2006.04.006
48. Ester M, Kriegel Hp, Sander J, Xu X. A density-based algorithm for discovering clusters in large spatial databases with noise. In: *Proceedings of 2nd International Conference on Knowledge Discovery and Data Mining*. Portland, OR (1996). p. 219–25.
49. Ayers GR, Northcott MJ, Dainty JC. Knox-Thompson and triple-correlation imaging through atmospheric turbulence. *J Opt Soc Am A*. (1988) 5:963–84. doi: 10.1364/JOSAA.5.000963
50. Lannes A. Backprojection mechanisms in phase-closure imaging. Bispectral analysis of the phase-restoration process. *Exp Astron*. (1989) 1:47–76. doi: 10.1007/BF00414795
51. Knox K˜, Thompson B˜. Recovery of images from atmospherically degraded short-exposure photographs. *Astrophysics*. (1974). 193:L45. doi: 10.1086/181627
52. Lohmann AW, Weigelt G, Wirnitzer B. Speckle masking in astronomy: triple correlation theory and applications. *Appl Opt*. (1983) 22:4028–37. doi: 10.1364/AO.22.004028

Conflict of Interest: During the research LP was employed by the Medical Laser Center Lübeck and DH was an employee of Thorlabs GmbH. DH is also listed as inventor on a related patent application. GH is listed as inventor on a related patent application.

The remaining authors declare that the research was conducted in the absence of any commercial or financial relationships that could be construed as a potential conflict of interest.

Publisher's Note: All claims expressed in this article are solely those of the authors and do not necessarily represent those of their affiliated organizations, or those of the publisher, the editors and the reviewers. Any product that may be evaluated in this article, or claim that may be made by its manufacturer, is not guaranteed or endorsed by the publisher.

frontiers | Frontiers in Medicine

SYSTEMATIC REVIEW
published: 15 June 2022
doi: 10.3389/fmed.2022.878946

Diagnostic Value of Spectral-Domain Optical Coherence Tomography for Polypoidal Choroidal Vasculopathy: A Systematic Review and Meta-Analysis

Yang Jiang[1,2] *and Shixin Qi*[1,2]*

[1] *Department of Ophthalmology, Tianjin Baodi Hospital, Tianjin, China,* [2] *Baodi Clinical College, Tianjin Medical University, Tianjin, China*

Purpose: To evaluate the diagnostic value of spectral-domain optical coherence tomography (SD-OCT) for polypoidal choroidal vasculopathy (PCV).

Methods: A search of electronic databases was conducted from 2010 to 2021 to review the relevant literature on SD-OCT to identify PCV and other lesions causing serious or serosanguinous retinal pigment epithelial detachment (PED), specifically neovascular age-related macular degeneration (nvAMD). The QUADAS-2 scale was used to evaluate the quality of the literature. We performed a meta-analysis, including heterogeneity tests, analyze and synthesize the study data, meta-regression analysis, subgroup analysis, Fagan's plot, sensitivity analysis and publication bias tests.

Results: A total of 12 related studies involving 1,348 eyes were included in this study, and the random-effects model was used for meta-analysis. The results showed that the pooled sensitivity of SD-OCT in the diagnosis of PCV was 0.87 (95% CI: 0.84–0.89), the pooled specificity was 0.83 (95% CI: 0.80–0.86), and the pooled positive/negative likelihood ratios were 5.38 (95% CI: 3.28–8.80) and 0.16 (95% CI: 0.10–0.25), respectively. The diagnostic odds ratio (DOR) was 36.07 (95% CI: 15.98–81.40), and the area under the sROC curve (AUC) was 0.9429. When the pre–test probability was set at 20%, the post-test positive and negative probabilities were 58% and 4%, respectively. Meta-regression indicated that race was the primary source of heterogeneity ($P<0.05$). The Deeks' funnel plot showed no significant publication bias in this study ($P>0.05$).

Conclusion: SD-OCT has high sensitivity and specificity for the diagnosis of PCV, as well as significant clinical applicability. Since color fundus photography (CFP) is more clinically available and can improve the diagnostic efficacy, we recommend SD-OCT combined with CFP to diagnose PCV, especially without indocyanine green angiography (ICGA).

Systematic Review Registration:
https://inplasy.com/inplasy-2021-12-0048/, identifier: INPLASY2021120048.

Keywords: spectral-domain optical coherence tomography, polypoidal choroidal vasculopathy, sensitivity, specificity, diagnostic value, meta-analysis

OPEN ACCESS

Edited by:
Yali Jia,
Oregon Health and Science University, United States

Reviewed by:
Carlo Gesualdo,
Università della Campania Luigi Vanvitelli, Italy
Thomas Ach,
University Hospital Bonn, Germany
Nader Fallah,
University of British Columbia, Canada

***Correspondence:**
Shixin Qi
qshxin@126.com

Specialty section:
This article was submitted to Ophthalmology, a section of the journal Frontiers in Medicine

Received: *18 February 2022*
Accepted: *09 May 2022*
Published: *15 June 2022*

Citation:
Jiang Y and Qi S (2022) Diagnostic Value of Spectral-Domain Optical Coherence Tomography for Polypoidal Choroidal Vasculopathy: A Systematic Review and Meta-Analysis. Front. Med. 9:878946. doi: 10.3389/fmed.2022.878946

INTRODUCTION

Polypoidal choroidal vasculopathy (PCV) is characterized by choroidal vascular abnormalities with or without abnormal branching vascular networks (BVNs), as shown by indocyanine green angiography (ICGA). The disease occurs most frequently in Asian populations (1, 2) and presents as a subretinal orange-red lesion in the fundus with recurrent serous or serosanguinous retinal pigment epithelial detachment (PED) (3). In the past, due to the lack of understanding of PCV and limitations of examination methods, many scholars considered it a subtype of neovascular age-related macular degeneration (nvAMD), which is characterized by type 1 aneurysmal choroidal neovascularization (4–6). However, there are significant differences between the two in terms of pathogenesis, clinical characteristics, natural course and prognosis, especially in terms of response to treatment. Photodynamic therapy (PDT) promotes regression or stabilization of choroidal polypoidal lesions and even improves visual acuity in patients with PCV (7), so it has a better therapeutic effect than in AMD (8). Anti-vascular endothelial growth factor (VEGF) drugs are the essential treatment for typical nvAMD. Although they effectively inhibit exudation caused by polypoidal lesions or abnormal BVNs, alleviate retinal edema, and improve visual acuity in PCV patients, they do not fundamentally degenerate polypoidal lesions and abnormal BVNs (2). Recently, the EVEREST II study (9), a 24-month phase IV double-blind, multicenter, randomized clinical test, recommended the combination of PDT and Anti-VEGF drugs to improve patients' vision. Therefore, it is very important to distinguish PCV and nvAMD in the initial diagnosis.

Currently, ICGA is the best visual diagnostic method for PCV, and it has been proven to be the gold standard for diagnosis (7). However, it is an invasive and expensive method, and ICGA is contraindicated in some patients due to impaired liver and kidney function, allergy to contrast agents, and pregnancy. In addition, a shortage of reagents or equipment in developing countries limits its clinical application (10). SD-OCT can clearly display the detailed structure of retinal cross-sections at the histological level. In addition, it is non-invasive, convenient, economical and non-contact, thus gaining increasing use in the diagnosis of PCV. Since De Salvo et al. (11) first diagnosed PCV with SD-OCT in 2014, other studies have used individual SD-OCT diagnostic strategies to diagnose PCV in different populations with varying sensitivity and specificity. At present, no studies have summarized and analyzed these data to draw a consistent conclusion. Therefore, we performed a systematic review and meta-analysis to explore the diagnostic value of SD-OCT for PCV.

MATERIALS AND METHODS

Protocol and Registration

This systematic review and meta-analysis was designed and reported in accordance with the Preferred Reporting Items for Systematic Reviews and Meta-Analyses (PRISMA) (12). The protocol for this systematic review was registered with the International Platform of Registered Systematic Review and Meta-analysis Protocols (INPLASY) (registration number: INPLASY2021120048; https://inplasy.com/inplasy-2021-12-0048/).

Search Strategy

We systematically searched electronic databases such as Pubmed, Embase, Cochrane, Web of Science, China National Knowledge Infrastructure (CNKI), Wanfang database (Wanfang Data), China Science and Technology Journal Database (VIP), and China Biomedical Literature on disc (CBMdisc) from 2010 to 2021. Relevant Chinese and English literature were searched. Database searches were performed using a combination of MeSH and keywords. The search keywords were "polypoidal choroidal vasculopathy," "PCV," "tomography, optical coherence," "coherence tomography, optical," "OCT tomography," "tomography, OCT," "optical coherence tomography," "spectral-domain optical coherence tomography," "spectral domain optical coherence tomography," "SD-OCT," "sensitivity and specificity," "predictive value of tests," and "accuracy." Details of the search strategy are listed in the Supplementary Digital Content (**Supplementary Appendix**). One author (JY) performed the strategy, and the other author (QSX) reviewed the process independently. When the two authors disagreed, the decision was made through open consultation.

Eligibility Criteria

The inclusion criteria for the published articles in this meta-analysis were as follows. (1) Study type: published trials related to PCV diagnosis by SD-OCT; (2) PCV cases confirmed by ICGA (polypoidal hyperfluorescence with or without abnormal BVNs on ICGA). Fundus fluorescein angiography (FFA) may be included as an additional diagnostic criterion; (3) SD-OCT examination or any angiography used to identify serous or serosanguinous PED in the macular area involving nvAMD, central serous chorioretinopathy (CSC), occult or idiopathic choroidal neovascularization (occult or idiopathic CNV), or retinal angiomatous proliferation (RAP).

Exclusion criteria were defined as the following. (1) Basic investigations such as animal experiments; (2) Reviews, systematic reviews, and meta-analyses; (3) Literature without extractable data items of the fourfold table: true positive (TP), false positive (FP), true negative (TN), and false negative (FN); (4) Duplicate studies; (5) Participants with other common eye diseases such as pathological myopia, diabetic retinopathy, and retinal artery or vein occlusion; (6) Participants suffering from low visual acuity, or inferior fixation, or with unobtainable SD-OCT images due to severe refractive interstitial opacification or severe subretinal hemorrhage; (7) Eyes of patients who had received treatment, including photocoagulation, intravitreal injection of anti-VEGF drugs, PDT, or vitrectomy.

Data Extraction and Quality Assessment

The main elements of data extraction included author, year of publication, country or region, sample size of the PCV

group and the control group, control group's disease type, gold standard, SD-OCT diagnostic strategy, detection method, device type and data items of the fourfold table: TP, FP, TN and FN.

Quality assessment was performed according to the QUADAS-2 scale, a revised version of the Quality Assessment of Diagnostic Accuracy Studies published by the QUADAS R&D team (13). This tool is comprised of four domains: patient selection, index test, reference standard, and flow and timing. Each domain is assessed for the risk of bias, and the first three domains are also evaluated for issues of applicability. The degree of risk by bias is determined as "low," "high," or "uncertain" based on "yes," "no," or "uncertain" answers to the relevant landmark questions in each section. A given domain is rated as low risk if all answers are "yes" and high risk if the answer to any informational question is "no." A designation of "uncertain" refers to a lack of clarity in the study that makes it difficult to judge. If one answer is "uncertain," the risk assessment is "uncertain." One author (JY) independently assessed the quality of the literature, while the other author (SQ) independently reviewed the strategy. When the opinions of the two authors differed, the strategy was decided by open consultation.

Statistical Analysis

Quality assessment was performed with Review Manager V5.3 (Cochrane Collaboration, London, UK) software. We performed meta-analyses using Meta-DiSc (Clinical Biostatistics Group, Hospital Ramón y Cajal, Madrid, Spain) software. First, the Spearman correlation coefficient was calculated between the logarithm of sensitivity and the logarithm of (1-specificity), and the summary receiver operating characteristic (sROC) curve was plotted. If the sROC curve shows a typical "shoulder-arm" shape, or if the correlation coefficient is significantly positive, this indicates a threshold effect of heterogeneity. The Cochran-Q test and the I^2 statistic were further used to analyze the heterogeneity of non-threshold effect among the studies. If the included studies were not statistically heterogeneous ($P > 0.05$, $I^2 < 50\%$), a fixed-effects model (Mantel-Haenszel method) was used to pool the effect sizes. Otherwise, we adopted a random-effects model (DerSimonian-Laird method) to pool the effect sizes. Pooled sensitivity (Se), specificity (Sp), positive likelihood ratio (PLR), negative likelihood ratio (NLR), diagnostic odds ratio (DOR), summary receiver operating characteristic (sROC) curve, and area under the curve (AUC) were then calculated. The closer the AUC was to 1, the greater the diagnostic value. If heterogeneity was significant, a meta-regression analysis was performed to analyze the source of heterogeneity, and further subgroup analysis was performed. Fagan's plot was drawn with Stata V15.0 (StataCorp LLC, Texas, America) software to assess the clinical applicability of the diagnostic test. Sensitivity analysis was performed by sequentially omitting individual studies and calculating pooled estimates for the remaining studies to verify the stability and reliability of the results. Publication bias was assessed by Deeks' funnel plot asymmetry test.

RESULTS

Literature Search

A total of 389 studies were identified through the initial database search. After removing duplicates, reviews, systematic reviews, meta-analyses, and animal studies, 190 studies were obtained. Based on the titles and abstracts, we excluded 167 studies with inconsistent content and were left with 23 works. Then, we read the full-text versions in detail according to the eligibility criteria. Finally, 12 studies (11, 14–24) were included in the current meta-analysis, including three Chinese publications (16, 23, 24) and 9 English publications (11, 14, 15, 17–22). The PRISMA flow chart for the literature search is shown in **Figure 1**.

Study Characteristics

After we comprehensively summarized the descriptive characteristics of the 12 studies, 1,348 eyes were included in our study, of which 706 eyes belonged to the PCV group and 642 eyes were in the control group (including nvAMD, dry-type AMD, CSC, serous PED, CNV, occult or idiopathic CNV and RAP). Patients in three studies (11, 20, 22) came from Caucasians, while those in 9 studies (14–19, 21, 23, 24) belonged to Asians. The descriptive characteristics of the eligible studies are presented in **Table 1**. The individual diagnostic strategies of the included studies are summarized in **Supplementary Table 1**.

Quality Assessment

The QUADAS-2 assessment of eligible studies indicated a potential risk of bias in terms of patient selection, index test, flow and timing. In terms of patient selection, seven studies were rated as "unclear" and did not specify whether the included cases were continuous or not. For the index test, since there is currently no standardized consensus OCT diagnosis strategy, seven studies adopted strategies proposed or improved by previous literature, four studies determined their strategy based on AUC $\geq$ 0.8, and one study had an uncertain source of the diagnostic strategy. In terms of flow and timing, not all cases met the eligibility criteria in this part because some patients did not meet the inclusion requirements, or the collection of results was incomplete. With regard to the reference standard, no bias risk was evident. Detailed descriptions of the results are shown in **Figures 2**, **3** and **Supplementary Table 2**.

Heterogeneity Tests

The Spearman correlation coefficient between the logarithm of sensitivity and logarithm of (1-specificity) was −0.865 ($P = 0.000 < 0.05$). Simultaneously, the sROC curve showed a "shoulder-arm" shape, indicating the presence of a threshold effect in this study. The Cochran-Q test for DOR was 64.76, $P = 0.000 < 0.05$, indicating non-threshold effect heterogeneity in this study. In addition, I^2 for Se, Sp, PLR, NLR and DOR were all 50% ($P < 0.05$ for all Cochran-Q tests), so we adopted a random-effects model to pool the five effect sizes mentioned above.

Assessment Criteria for Diagnostic Tests

The pooled sensitivity (Se) was 0.87 (95% CI: 0.84–0.89; **Figure 4A**), pooled specificity (Sp) was 0.83 (95% CI: 0.80–0.86; **Figure 4B**), pooled positive likelihood ratio (PLR) was 5.38 (95%

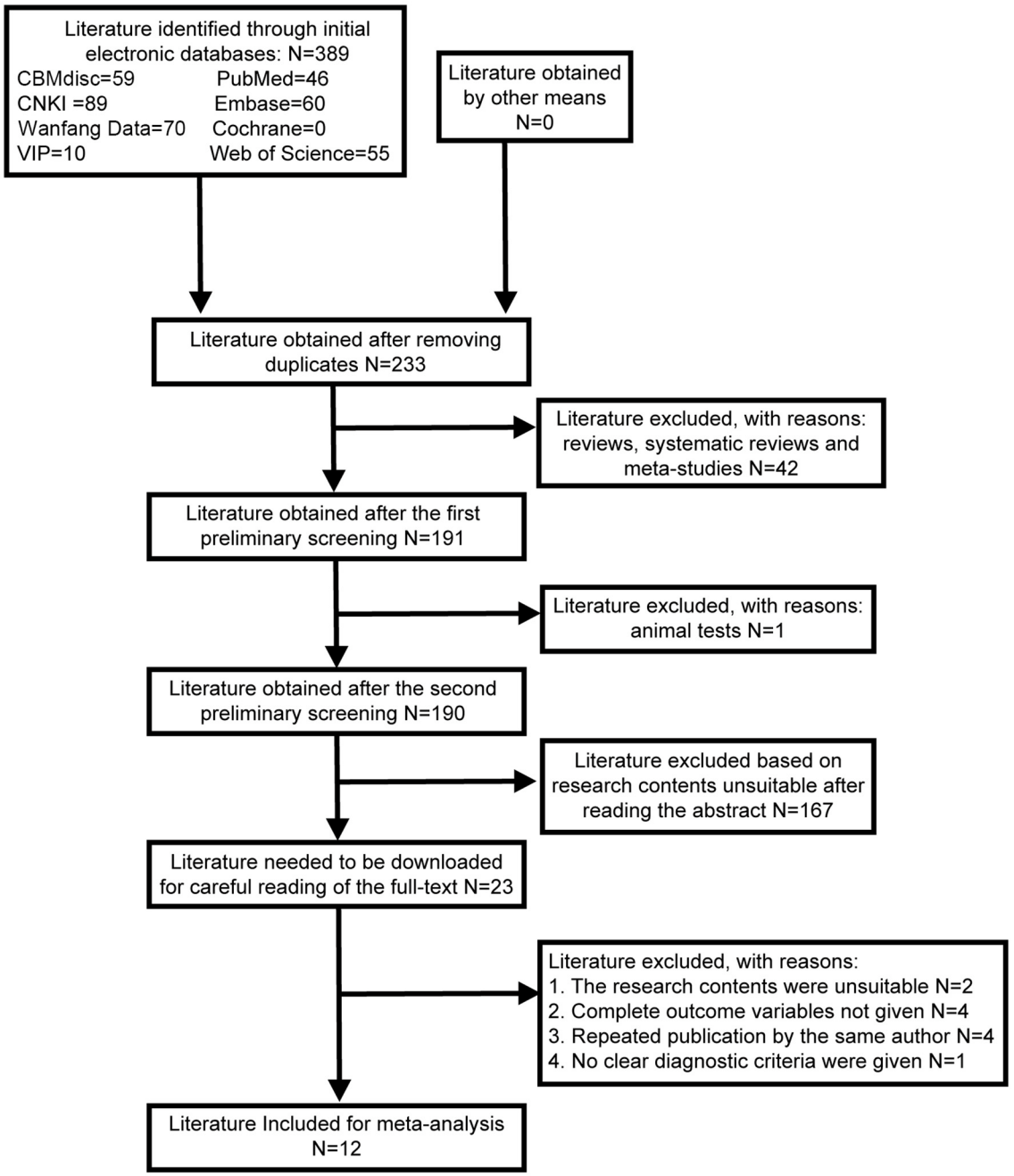

FIGURE 1 | Literature retrieval flow chart.

CI: 3.28–8.80; **Figure 4C**), and pooled negative likelihood ratio (NLR) was 0.16 (95% CI: 0.10–0.25; **Figure 4D**). The pooled diagnostic odds ratio (DOR) was 36.07 (95% CI: 15.98–81.40; **Figure 4E**), area under the sROC curve (AUC) was 0.9429, and Q* index was 0.8812 (**Figure 4F**).

Meta-Regression and Subgroup Analysis

Based on the apparent heterogeneity of non-threshold effect in this study, we extracted race [Asians, n=9 (14–19, 21, 23, 24); Caucasians, $n = 3$ (11, 20, 22)], sample size [eyes <100, $n = 5$ (11, 14, 22–24); eyes≥100, n=7 (15–21)], and device type [Spectralis HRA + OCT or Spectralis OCT, n=7 (11, 14–18, 22); others: including Cirrus HD-OCT, unknown, $n = 5$ (19–21, 23, 24)] to identify the source of heterogeneity by meta-regression. The results indicated that race might be the primary source of heterogeneity in this study (RDOR=5.95, $P = 0.0204 < 0.05$; **Table 2**).

TABLE 1 | Characteristics of the included studies ($n = 12$).

References	Country	Sample size (PCV/ Controls)	Disease type of the controls	Detection method	Gold Standard	Device type	TP	FP	TN	FN
Chaikitmongkol et al. (17)	Thailand	48/71	nvAMD, CSC, RAP, serous PED	CFP+SD-OCT	ICGA	Spectralis OCT	40	12	8	59
Liu et al. (18)	China	113/75	nvAMD	SD-OCT	FFA/ICGA	Spectralis HRA+OCT	101	11	12	64
Cheung et al. (14)	Singapore	23/27	CNV, RAP	SD-OCT	FFA/ICGA	Spectralis OCT	19	13	4	14
Yang et al. (19)	China	52/51	nvAMD	CFP+ SD-OCT	FFA/ICGA	unclear	46	4	6	47
Chang et al. (15)	Korea	147/116	nvAMD	SD-OCT	ICGA	Spectralis HRA+OCT	132	18	15	98
Laíns et al. (20)	Portugal	47/53	occult CNV	SD-OCT	ICGA	Spectralis HRA+OCT and Cirrus HD-OCT	32	23	15	30
Chaikitmongkol et al. (21)	Thailand	65/59	nvAMD, CSC, RAP, idiopathic CNV	CFP+ SD-OCT	FFA/ICGA	unclear	62	3	3	56
De Salvo et al. (11)	United Kingdom	87/14	occult CNV	SD-OCT	FFA/ICGA	Spectralis HRA+OCT	35	1	2	13
Eraydin et al. (22)	Turkey	69/24	dry-type AMD, nvAMD, CSC	SD-OCT	ICGA	Spectralis HRA+OCT	52	6	17	18
Liao et al. (23)	China	24/38	wAMD	SD-OCT	FFA/ICGA	unclear	22	4	2	34
Zhang et al. (24)	China	25/38	wAMD	SD-OCT	FFA/ICGA	Cirrus HD-OCT 4000	23	4	2	34
Xia et al. (16)	China	56/76	wAMD	SD-OCT	FFA/ICGA	Spectralis HRA+OCT	49	10	7	66

PCV, Polypoidal choroidal vasculopathy; nvAMD, neovascular age-related macular degeneration; wAMD, wet age-related macular degeneration; CSC, central serous chorioretinopathy; RAP, retinal angiomatous proliferation; CNV, choroidal neovascularization; PED, pigment epithelial detachment; ICGA, indocyanine green angiography; FFA, fundus fluorescein angiography; SD-OCT, spectral-domain optical coherence tomography; CFP, color fundus photography; Spectralis OCT, Heidelberg Engineering Inc., Heidelberg, Germany; Spectralis HRA+OCT, Heidelberg Engineering Inc., Heidelberg, Germany; Cirrus HD-OCT, Carl Zeiss Meditec Inc., Dublin, United States; Cirrus HD-OCT 4000, Carl Zeiss Meditec Inc., Dublin, United States; TP, true positives; FP, false positives; TN, true negatives; FN, false negatives.

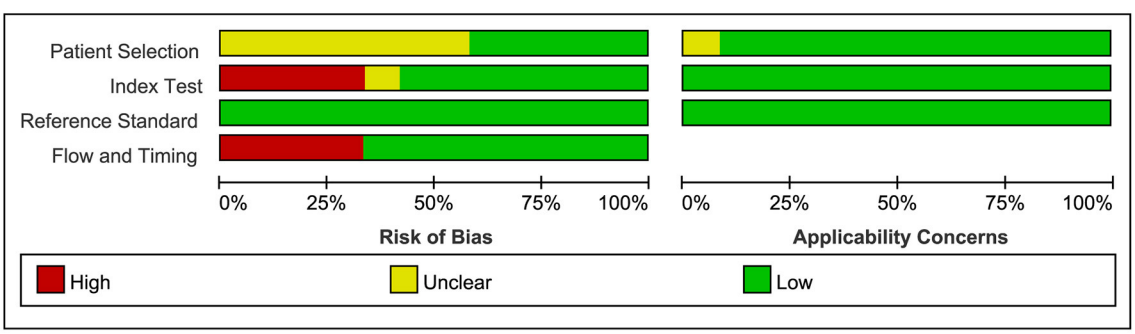

FIGURE 2 | Bar chart of literature quality assessment.

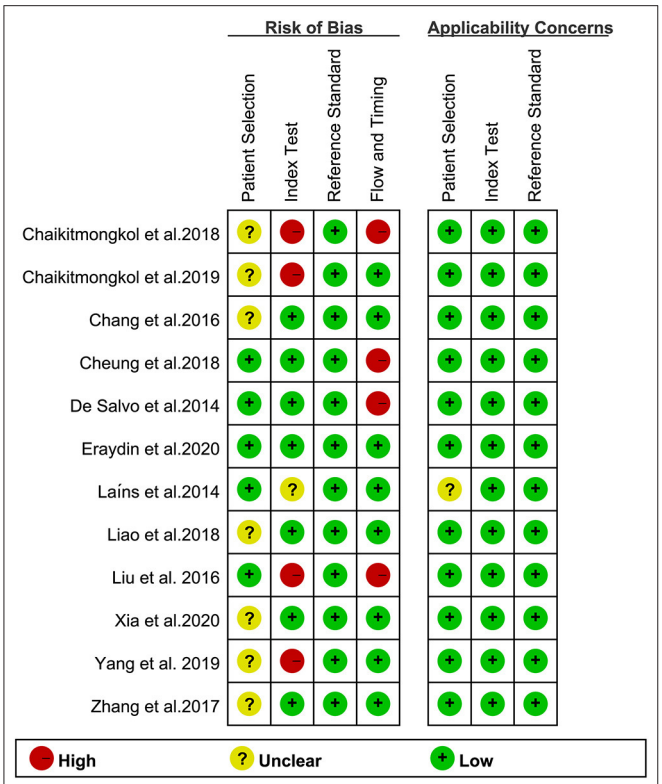

FIGURE 3 | Summary of bias risk and clinical applicability. **Figure 2** combined with **Figure 3** together describe literature quality assessment.

In addition, we performed the subgroup analysis according to race [Asians, $n = 9$ (14–19, 21, 23, 24); Caucasians, $n = 3$ (11, 20, 22)], detection method [SD-OCT alone, $n = 9$ (11, 14–16, 18, 20, 22–24); color fundus photography (CFP) + SD-OCT, $n = 3$ (17, 19, 21)], and disease type in controls [nvAMD only, $n = 6$ (15, 16, 18, 19, 23, 24); others: including dry-type AMD, serous PED, CSC, CNV, idiopathic or occult CNV, RAP with or without nvAMD, $n = 6$ (11, 14, 17, 20–22)]. The results indicate that the diagnostic efficacy of SD-OCT for PCV was more satisfactory in Asians than in Caucasians across all observed indexes (Se, Sp, PLR, NLR, DOR and AUC). Also, the diagnostic efficiency of SD-OCT combined with CFP was superior to that of SD-OCT alone for various observed indexes. Meanwhile, patients were divided according to the type of disease in the control group. The diagnostic accuracy of SD-OCT was better in patients with only nvAMD in the control group than in patients with other types included in the control group (**Table 3**).

Clinical Application Value

We assumed a 20% probability of diagnosing PCV based on symptoms and ophthalmologists' personal experiences. After a positive test by SD-OCT, the accuracy of diagnosing PCV increased to 58% with reference to Fagan's plot (**Figure 5**). Conversely, with a negative test, the diagnostic accuracy was 4%. Therefore, the diagnosis of PCV by SD-OCT provides good accuracy and significant clinical application value.

Sensitivity Analysis

A "leave-one-out" sensitivity analysis was performed by STATA V15.0. The result showed that excluding individual original studies of the current analysis one by one did not cause the calculated results to be sensitive(**Figure 6**).

Publication Bias Tests

Publication bias was assessed by the Deeks' funnel plot asymmetry test with STATA V15.0. The Deeks' funnel plot had DOR as the horizontal axis and the inverse square root of the effective sample size (1/ESS) as the vertical axis. Our study showed that the regression coefficient was −4.83, $P = 0.76 > 0.05$, $t = -0.31$ (95% CI: −39.84–30.18) and the funnel plot was basically symmetrical, indicating that there was no significant publication bias in this meta-study (**Figure 7**).

DISCUSSION

This systematic assessment and meta-analysis first summarized the diagnostic value of SD-OCT for PCV and revealed that SD-OCT has high sensitivity, specificity and significant clinical application value. However, when it was negative, SD-OCT did not identify PCV well. Therefore, we recommend the combined use of color fundus photography (CFP) to improve the diagnostic efficacy.

Characteristic Manifestations of PCV on SD-OCT

The characteristic manifestations of PCV on SD-OCT have been described in previous reports. A polypoidal lesion of PCV on SD-OCT exhibits a thumb-like retinal pigment epithelium (RPE) protrusion or a sharp peak PED (17, 25), as well as a hyporeflective halo surrounded by a hyperreflective ring underneath the PED (15, 18). The abnormal BVNs and exudation can superficially detach the RPE and Bruch's membrane, forming a "double-layer" sign on SD-OCT images (25, 26). A notch-like lesion at the edge of the PED presents a "V"-shaped depression between the two PEDs, which is associated with CNV, especially occult CNV (27). In addition, multiple PEDs and hyperreflective intraretinal hard exudates can also be observed on SD-OCT (11, 16). Although these features are not unique to PCV, many similar studies (11, 15, 16) have demonstrated statistically significant differences in the proportion of these features in patients with PCV and nvAMD, making it possible to diagnose PCV on SD-OCT.

Interpretation of Meta-Analysis Results

This meta-analysis showed that the sensitivity and specificity of SD-OCT to diagnose PCV were high, 87% and 83%, respectively, which is consistent with previous studies. De Salvo et al. (11) first utilized SD-OCT to diagnose PCV in 2014 with the following findings: multiple PEDs, a sharp PED peak, a PED notch, a visible hyporeflective lumen within hyperreflective lesions adherent to the outer surface of the retinal pigment epithelium, and hard exudates. At least three of these features were used to diagnose with a sensitivity of 94.6% and a specificity of 92.9%. Based on

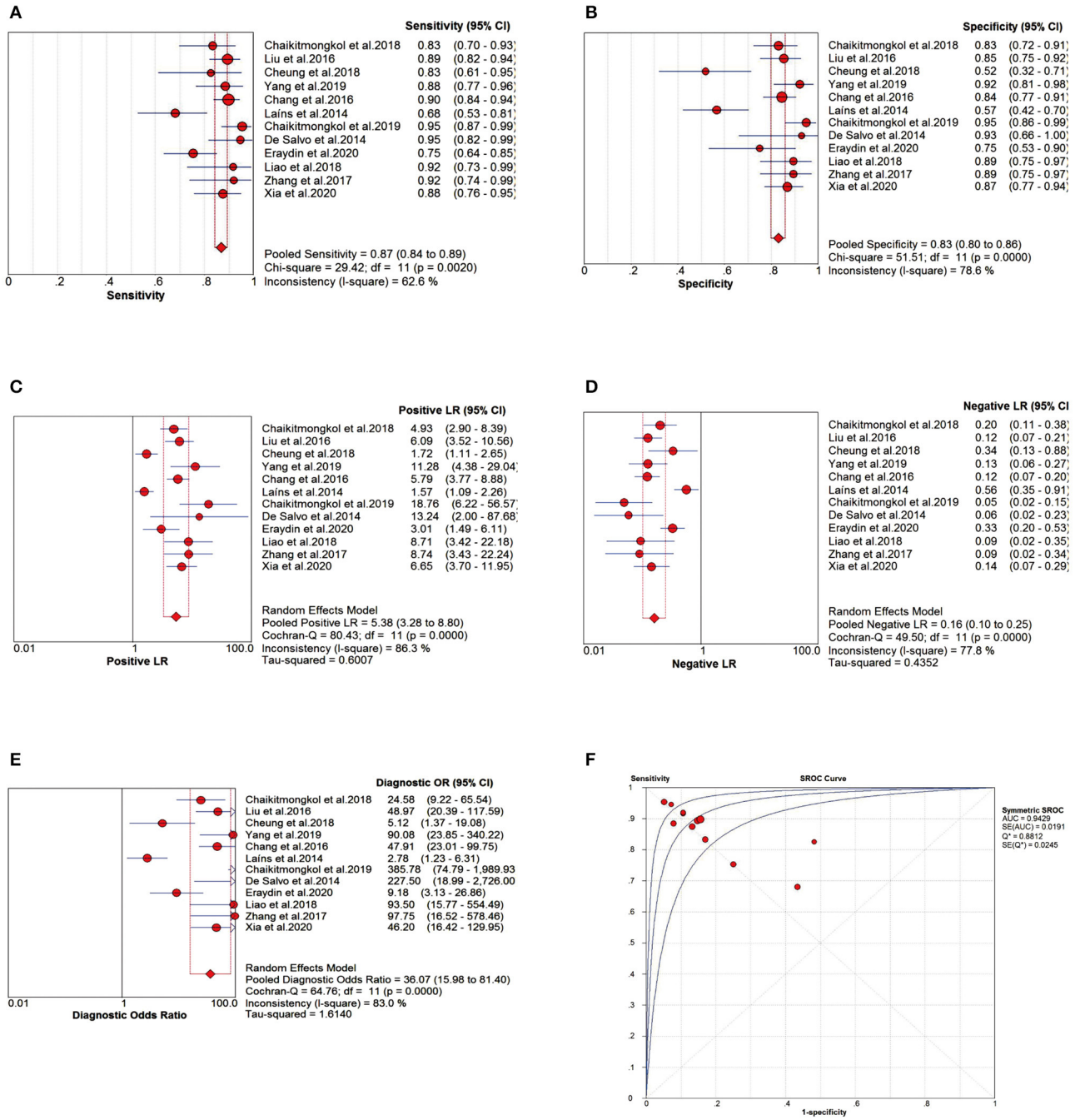

FIGURE 4 | Meta-analysis forest plots of the relevant effect sizes. **(A)** The pooled sensitivity (Se). **(B)** The pooled specificity (Sp). **(C)** The pooled positive likelihood ratio (PLR). **(D)** The pooled negative likelihood ratio (NLR). **(E)** The pooled diagnostic odds ratio (DOR). **(F)** The summary receiver operating characteristic curve (sROC) and area under the curve (AUC).

De Salvo's diagnostic strategy, Xia et al. (16) added a "double-layer" sign representing the abnormal BVNs, and the sensitivity and specificity were 87.5% and 86.8%, respectively. Since PCV is a choroidal thickening disease (28–31), Chang et al. (15) recently adopted the additional criterion of subfoveal choroidal thickness 300 um. They found that the sensitivity increased from 85.7% to 89.8%, while the specificity decreased from 86.2 to 84.5%.

In contrast, the sensitivity and specificity of our results presented slightly reduced because the literature we enrolled in covered a broader selection of samples. In addition to nvAMD, our control group included other diseases such as

CSC, idiopathic or occult CNV and RAP. Our study has greater clinical significance since macular hemorrhage, intraretinal hard exudates, or shallow detachment of the macular neuroepithelial layer accompanying the above diseases can also severely impair patients' vision. According to subgroup analysis, we found that for all test indexes (Se, Sp, PLR, NLR, DOR, and AUC), the diagnostic accuracy of SD-OCT was superior for the group with only nvAMD included in the control group than for other types of disease included in the control group. That resulted in a slight decrease in detection accuracy after the overall combination. Furthermore, PCV is more prevalent in Asians, accounting for 22.3–61.6% of patients with suspected nvAMD diagnosed by ICGA, compared to approximately 8–13% in Caucasians (1, 2), which slightly decreased the PCV detection rate by SD-OCT in this study.

The DOR can objectively reflect the diagnostic value of a diagnostic test. When DOR > 1, the higher the value, the better the discrimination of the test; when the value is <1, a normal person is more likely to be judged positive than a true case; when the value is 1, it means that the test cannot distinguish a normal person from a case. The DOR value in our study was 36.07 (95% CI: 15.98–81.40), which is very satisfactory, indicating that SD-OCT has a high diagnostic value for PCV. To assess the accuracy of the sROC curve, we also calculated the Q* index. The larger the index, the closer the AUC is to 1, indicating the higher accuracy of a diagnostic test. In the present study, the AUC was 0.9429, and the Q* index was 0.8812, indicating that SD-OCT has high diagnostic accuracy.

TABLE 2 | Parameters of meta-regression analysis.

	Coef	Std.Err	*P*	RDOR	95%CI
Race	1.783	0.6346	**0.0204***	5.95	1.42-24.99
Sample size	−0.711	0.6652	0.3165	0.49	0.11–2.28
Device type	0.238	0.6619	0.7298	1.27	0.27–6.07

**Indicates statistical significant P-values.*

The PLR and NLR are not affected by prevalence in the test population and are relatively independent clinically meaningful indicators for assessing the effectiveness of diagnostic tests. The likelihood of identifying or excluding a specific disease is greatly

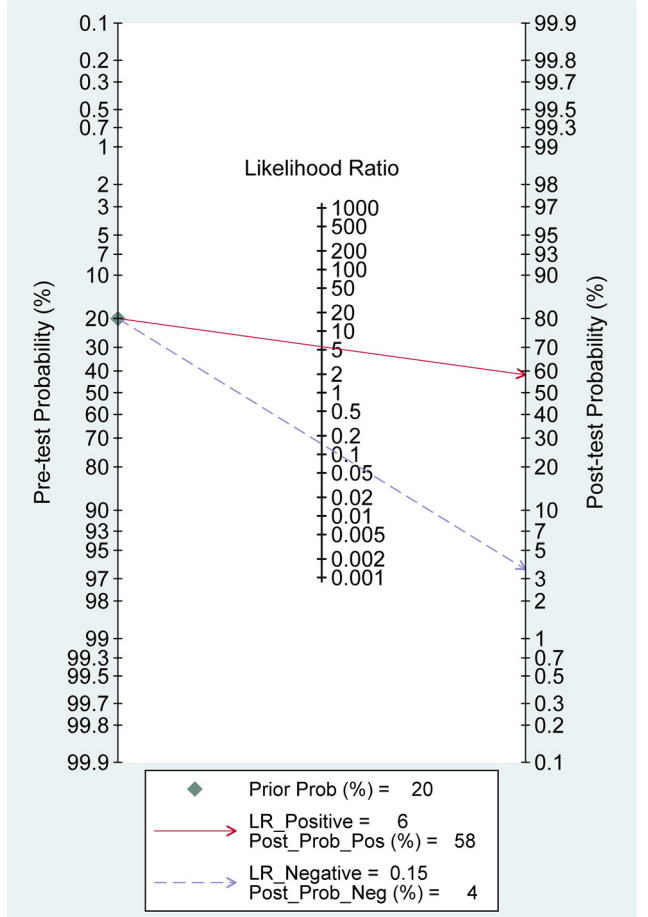

FIGURE 5 | Fagan's plot.

TABLE 3 | Parameters of subgroup analysis.

	Se/95%CI	Sp/95%CI	PLR/95% CI	NLR /95% CI	DOR/95%CI	AUC
Race						
Asians (*n* = 9)	0.89/(0.86–0.92)	0.86/(0.82–0.88)	6.28/(3.87–10.19)	0.13/(0.10–0.16)	49.01/(25.94–92.61)	0.9531
Caucasians (*n* = 3)	0.78/(0.70–0.84)	0.67/(0.56–0.77)	2.92/(1.08–7.87)	0.28/(0.12–0.67)	12.30/(2.00–75.61)	0.9021
Detection method						
SD–OCT (*n* = 9)	0.86/(0.83–0.89)	0.80/(0.77–0.84)	4.49/(2.59–7.79)	0.18/(0.10–0.30)	27.05/(10.47–69.89)	0.9382
SD-OCT + CFP (*n* = 3)	0.90/(0.84–0.94)	0.90/(0.84–0.94)	9.27/(3.75–22.89)	0.12/(0.06–0.25)	85.02/(18.16–398.16)	0.9622
Disease type in controls						
nvAMD (*n* = 6)	0.89/(0.86–0.92)	0.87/(0.83–0.90)	6.78/(5.24–8.78)	0.12/(0.09–0.16)	55.87/(36.61–85.27)	0.9488
Others (*n* = 6)	0.83/(0.78–0.87)	0.77/(0.71–0.82)	3.88/(1.82–8.28)	0.21/(0.10–0.42)	21.21/(5.26–85.54)	0.9302

Se, sensitivity; Sp, specificity; PLR, positive likelihood ratio; NLR, negative likelihood ratio; DOR, diagnostic odds ratio; AUC, area under the sROC curve; 95%CI, 95% confidence interval; SD-OCT, spectral-domain optical coherence tomography; SD-OCT+CFP, spectral-domain optical coherence tomography combined with color fundus photography; nvAMD, neovascular age-related macular degeneration; others, inculding dry-type AMD, central serous chorioretinopathy, serous retinal pigment epithelial detachment, retinal angiomatous proliferation, choroidal neovascularization, idiopathic/occult choroidal neovascularization with and without nvAMD. n, number of included studies.

increased when PLR > 10 or NLR < 0.1. Our study indicated the pooled PLR and NLR were 5.38 and 0.16, respectively, suggesting that SD-OCT does not identify PCV well in the presence of negative results. To improve the diagnostic efficacy, we recommend combining SD-OCT with color fundus photography (CFP). Cackett et al. (32) found that serosanguinous PEDs were more common in eyes with PCV than CNV (PCV vs. CNV = 45.7 vs. 3.9%) in Chinese patients. The drusen are often peripapillary in Caucasians but rare in colored individuals with frequently located in the macular area (33). Furthermore, a Japanese PCV Study Group (34) suggested that definitive diagnostic criteria for PCV should satisfy at least one of these findings: (1) Fundus examination shows protruded elevated orange-red lesions. (2) characteristic polypoidal lesions are seen in ICGA findings. In suspected cases, abnormal BVNs in ICGA or recurrent serous or serosanguinous PED can be observed. Thus characteristic manifestations by fundoscopy can provide ophthalmologists with clues for PCV.

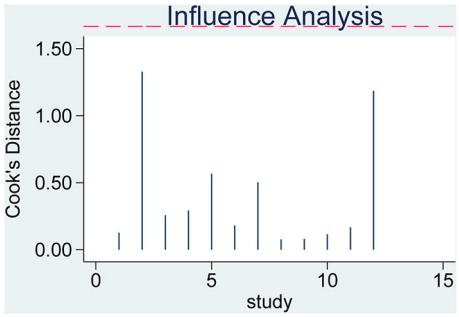

FIGURE 6 | Sensitivity analysis.

Compared with traditional fundoscopy, the use of CFP does not require mydriasis and can avoid the risk of drug-induced glaucoma. It also provides a digital image, which is objective and reliable, easy to store and transmit, and can be used for long-distance diagnosis. In addition, the image capture process is fast, less costly, and has high patient compliance, which is why CFP is widely utilized in small or medium-sized medical institutions in developing countries. We analyzed the diagnostic efficacy of SD-OCT combined with CFP as a detection method. According to the subgroup analysis, the PLR increased from 4.49 to 9.27 and NLR decreased from 0.18 to 0.12 in the

STATISTICAL TESTS FOR SMALL STUDY EFFECTS/PUBLICATION BIAS

yb	Coef.	Std. Err.	t	P>|t|	[95% Conf.	Interval]
Bias	-4.829961	15.71484	-0.31	0.765	-39.84482	30.18489
Intercept	4.225404	1.515546	2.79	0.019	.8485576	7.60225

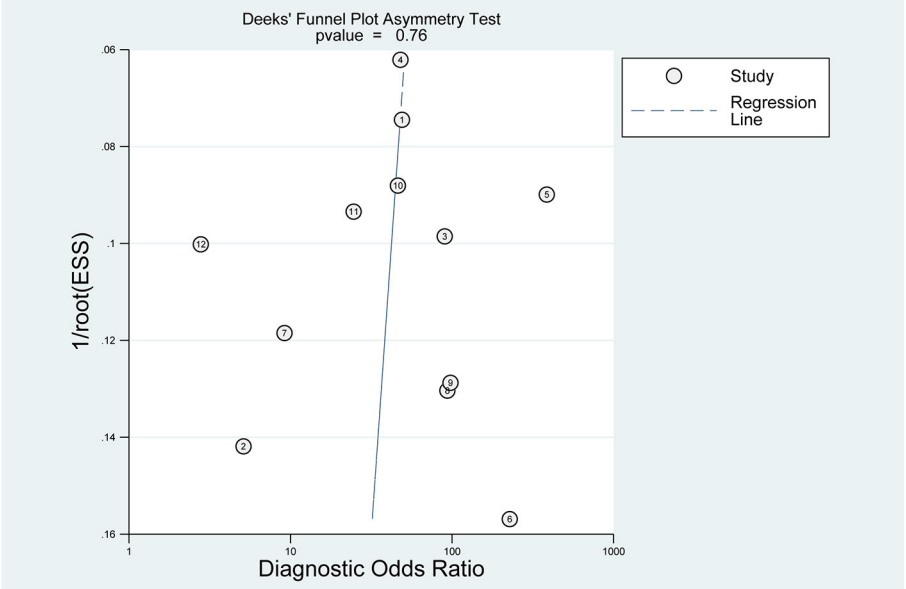

FIGURE 7 | Deeks' funnel plot.

SD-OCT combined with CFP group compared with the SD-OCT alone group. This result indicated that SD-OCT combined with CFP could improve the diagnostic and differential efficiency (**Table 3**). Simultaneously, all diagnostic indicators (Se, Sp, PLR, NLR and AUC) were higher in the SD-OCT combined with CFP group (**Table 3**). Furthermore, Chaikitmongkol et al. (17) found that the accuracy of SD-OCT in diagnosing PCV varied in different prevalent regions due to the different clinical experience and background knowledge of ophthalmologists. However, this difference was not seen in the SD-OCT combined with CFP group, indicating that the diagnosis of SD-OCT combined with CFP is stable. In conclusion, we recommend combing SD-OCT with CFP to diagnose PCV, especially in the absence of ICGA in developing countries.

PCV has a bilateral tendency. The presence of PCV in one eye implies an increased risk of similar clinical changes in the other eye, especially in Caucasians (7, 33). However, ICGA is an invasive test, and it is not realistic to monitor the contralateral eye. In our study, the probability of diagnosing PCV after a positive test by SD-OCT increased to 58%, compared with the pre-test probability set at 20%, which confirms the significant value of SD-OCT in clinical applications. Meanwhile, SD-OCT is non-invasive, convenient, and can be repeated in a follow-up mode. Therefore, SD-OCT examination can be routinely applied to monitor the progression of PCV patients.

Sensitivity analysis is an important indicator to test the stability of a meta-analysis. Our current meta-analysis's robustness was relatively stable by sequentially omitting individual studies. Deeks' publication bias test is based on linear regression to detect whether the funnel plot is symmetrical. The slope of the regression line (regression coefficient) is equal to 0, indicating that the funnel plot is entirely symmetrical. The regression coefficient of our study was −4.83, with $P = 0.76 > 0.05$, $t = -0.31$ (95% CI: −39.84–30.18), and the studies enrolled in this paper were basically symmetrically distributed around the centerline of the funnel plot, so it was concluded that there was no significant publication bias in the current study. In summary, the results of this study are stable and reliable.

Sources of Heterogeneity

The high heterogeneity for our study was caused by both threshold and non-threshold effects. Due to the current lack of a standardized or conventional assessment strategy for SD-OCT, different diagnostic criteria were adopted in individual original studies, thus contributing to the heterogeneity of threshold effect. After summarizing the characteristics of previous literature, we suggest that the SD-OCT diagnostic strategy for PCV should at least include the following findings. (1) Fundus examination shows retinal orange-red elevated lesions. (2) Single or multiple PEDs, a sharp PED peak, PED notches, "double-layer" signs, or a hyporeflective lumen underneath the PED representing the polyp lesion should be observed on SD-OCT. (3) If necessary, the measurement of subfoveal choroidal thickness can be added to the diagnosis.

In addition to the threshold effect, differences in test population, sample size, and test conditions probably contributed to the non-threshold heterogeneity in this study. Therefore, we integrated factors such as race, sample size, and SD-OCT device type into the meta-regression analysis. The results showed that race might be the primary source of non-threshold effect heterogeneity ($P < 0.05$). RDOR=5.95 indicated that the diagnostic accuracy of SD-OCT was 5.08 times higher in Asians than in Caucasians. Several studies have shown that 92% of PCV lesions in Asians occur in the macula (7), while in Caucasians, PCV is more common outside the macula, including around the optic disc and in the peripheral fundus (2, 33, 35). In general, fundus scans on SD-OCT are performed at 30° around the posterior pole, where most maculopathies are located. When PCV lesions are situated away from the macular area or in the peripheral fundus, it is difficult for SD-OCT to detect abnormal lesions.

Limitations

Nevertheless, several other limitations were encountered in this review study. First, the number of cases was limited due to the low prevalence of PCV in the population. Second, our study only covered English and Chinese literature. Although the publication bias of this paper was not significant, the language potentially restricted the quality of our article. Finally, this study only included naïve PCV patients. Whether treatment can reduce the diagnostic efficiency of SD-OCT for PCV remains unknown.

CONCLUSION

In conclusion, our results suggest that SD-OCT has high sensitivity, specificity, and significant clinical applicability for differentiating PCV from diseases such as nvAMD that tend to cause serous or serosanguinous retinal pigment epithelial detachment. Since color fundus photography (CFP) is more accessible in the clinic and can improve the diagnostic efficacy of SD-OCT, we recommend combining SD-OCT with CFP, especially without ICGA.

DATA AVAILABILITY STATEMENT

The original contributions presented in the study are included in the article/**Supplementary Materials**. Further inquiries can be directed to the corresponding author/s.

AUTHOR CONTRIBUTIONS

YJ: concept and design, data analysis, and preliminary draft writing. SQ: participation in manuscript writing and editing. YJ and SQ: literature retrieval, data extraction, and quality assessment. All authors contributed to the article and approved the submitted version.

SUPPLEMENTARY MATERIAL

The Supplementary Material for this article can be found online at: https://www.frontiersin.org/articles/10.3389/fmed.2022.878946/full#supplementary-material

REFERENCES

1. Wong CW, Yanagi Y, Lee WK, Ogura Y, Yeo I, Wong TY, et al. Age-related macular degeneration and polypoidal choroidal vasculopathy in asians. *Prog Retin Eye Res.* (2016) 53:107–39. doi: 10.1016/j.preteyeres.2016.04.002
2. Liu R, Ding X. Xirouyang mailuomo xueguang bingbian yu shenchuxing laonian huangbanbianxing de yitong [Similarities and differences between polypoid choroidal vasculopathy and exudative age-related macular degeneration]. *Chin J Ocul Fundus Dis.* (2012) 9:533–9. doi: 10.3760/cma.j.issn.1005-1015.2012.05.029
3. Zhang S, Zhang J, Xu X, Gao R, Sun X, Huan X. Progress in treatment of submacular hemorrhage due to polypoid choroidal vasculopathy. *Int J Ophthalmol.* (2019) 19:950–5. doi: 10.3980/j.issn.1672-5123.2019.6.13
4. Wong RLM, Lai TYY. Polypoidal choroidal vasculopathy: an update on therapeutic approaches. *J Ophthalmic Vis Res.* (2013) 8:359–71. doi: 10.1136/bjo.2007.116178
5. Khan S, Engelbert M, Imamura Y, Freund KB. Polypoidal cohoroidal vasculopathy simultaneous indocyanine green angiography and eye-tracked spectral optical coherence tomography finding. *Retina.* (2012) 32:1057–68. doi: 10.1097/IAE.0b013e31823beb14
6. Dansingani KK, Gal-Or O, Sadda SR, Yannuzzi LA, Freund KB. Understanding aneurysmal type 1 neovascularization (polypoidal choroidal vasculopathy): A lesson in the taxonomy of 'expanded spectra' - a review. *Clin Exp Ophthalmol.* (2018) 46:189–200. doi: 10.1111/ceo.13114
7. Anantharaman G, Sheth J, Bhende M, Narayanan R, Natarajan S, Rajendran A, et al. Polypoidal: pearls in diagnosis and management. *Indian J Ophthalmol.* (2018) 66:896–908. doi: 10.4103/ijo.IJO_1136_17
8. Gomi F, Ohji M, Sayanagi K, Sawa M, Sakaguchi H, Oshima Y, et al. One-year outcomes of photodynamic therapy in age-related macular degeneration and polypoidal choroidal vasculopathy in japanese patients. *Ophthalmology.* (2008) 115:141–6. doi: 10.1016/j.ophtha.2007.02.031
9. Lim TH, Lai TYY, Takahashi K, Wong TY, Chen LJ, Ruamviboonsuk P, et al. Comparison of ranibizumab with or without verteporfin photodynamic therapy for polypoidal choroidal vasculopathy: The everest ii randomized clinical trial. *JAMA Ophthalmol.* (2020) 138:935–42. doi: 10.1001/jamaophthalmol.2020.2443
10. Lee WK Iida T, Ogura Y, Chen SJ, Wong TY, Mitchell P, et al. Efficacy and safety of intravitreal aflibercept for polypoidal choroidal vasculopathy in the planet study: a randomized clinical trial. *JAMA Ophthalmol.* (2018) 136:786–93. doi: 10.1001/jamaophthalmol.2018.1804
11. De Salvo G, Vaz-Pereira S, Keane PA, Tufail A, Liew G. Sensitivity and specificity of spectral-domain optical coherence tomography in detecting idiopathic polypoidal choroidal vasculopathy. *Am J Ophthalmol.* (2014) 158:1228-38 e1. doi: 10.1016/j.ajo.2014.08.025
12. Mcinnes MDF, Moher D, Thombs BD, Mcgrath TA, Bossuyt PM. and the PRISMA- DTA Group. Preferred reporting items for a systematic review and meta-analysis of diagnostic test accuracy studies: The prisma-dta statement. *JAMA.* (2018) 319:388–96. doi: 10.1001/jama.2017.19163
13. Whiting PF, Rutjes AW, Westwood ME, Mallett S, Deeks JJ, Reitsma JB, et al. Quadas-2: a revised tool for the quality assessment of diagnostic accuracy studies. *Ann Intern Med.* (2011) 155:529–36. doi: 10.7326/0003-4819-155-8-201110180-00009
14. Cheung CMG, Yanagi Y, Akiba M, Tan T, Mathur R, Chan CM. Improved detection and diagnosis of polypoidal choroidal vasculopathy using a combination of optical coherence tomography and optical coherence tomography angiography. *Retina.* (2018) 0:1–9. doi: 10.1097/IAE.0000000000002228
15. Chang YS, Kim JH, Kim JW, Lee TG, Kim CG. Optical coherence tomography-based diagnosis of polypoidal choroidal vasculopathy in korean patients. *Korean J Ophthalmol.* (2016) 30:198–205. doi: 10.3341/kjo.2016.30.3.198
16. Xia S, Yang J, Zhao X, Chen Y. Spectral domain oct for the differentiation of polypoidal choroidal vasculopathy from wet age-related macular degeneration. *Chin J Exp Ophthalmol.* (2020) 38:55–9. doi: 10.3760/cma.j.issn.2095-0160.2020.01.011
17. Chaikitmongkol V, Khunsongkiet P, Patikulsila D, Ratanasukon M, Watanachai N, Jumroendararasame C, et al. Color fundus photography, optical coherence tomography, and fluorescein angiography in diagnosing polypoidal choroidal vasculopathy. *Am J Ophthalmol.* (2018) 192:77–83. doi: 10.1016/j.ajo.2018.05.005
18. Liu R, Li J, Li Z, Yu S, Yang Y, Yan H, et al. Distinguishing polypoidal choroidal vasculopathy from typical neovascular age-related macular degeneration based on spectral domain optical coherence tomography. *Retina.* (2016) 36:778–86. doi: 10.1097/IAE.0000000000000794
19. Yang J, Yuan M, Wang E, Xia S, Chen Y. Noninvasive multimodal imaging in diagnosing polypoidal choroidal vasculopathy. *BMC Ophthalmol.* (2019) 19:229. doi: 10.1186/s12886-019-1244-5
20. Laíns I, Figueira J, Farinha C, Cachulo ML, Costa M, Santos AR. Polypoidal choroidal vasculopathy - is indocyanine green angiography essential for diagnosis? *In: ARVO Annual Meeting Abstract: Association for Research in Vision and Ophthalmology, annual meeting; 2014 May 4–8;* Orlando, Florida, USA: *published in Invest Ophthalmol Vis Sci.* (2014) 55:3915.
21. Chaikitmongkol V, Kong J, Khunsongkiet P, Patikulsila D, Sachdeva M, Chavengsaksongkram P, et al. Sensitivity and specificity of potential diagnostic features detected using fundus photography, optical coherence tomography, and fluorescein angiography for polypoidal choroidal vasculopathy. *JAMA Ophthalmol.* (2019) 137:661–7. doi: 10.1001/jamaophthalmol.2019.0565
22. Eraydin B, Kocak N, Birinci H. The comparison of spectral domain optical coherence tomography and indocyanine green angiography in the diagnosis of polypoidal choroidal vasculopathy. *Int Ophthalmol.* (2020) 41:659–65. doi: 10.1007/s10792-020-01622-y
23. Liao M, Chen Q, Gan R. Analysis of sensitivity and specificity of spectral-domain optical coherence tomography in the diagnosis of polypoidal choroidal vasculopathy. *China Prac Med.* (2018) 13:22–4. doi: 10.14163/j.cnki.11-5547/r.2018.18.010
24. Zhang Y, Yao J, Wang X, Zhao L, Wang L, Wang J, et al. Sensitivity and specificity of optical coherence tomography in diagnosing polypoidal choroidal vasculopathy. *J South Med Univ.* (2017) 37:165–71. doi: 10.3969/j.issn.1673-4254.2017.02.04
25. Alshahrani ST, Al Shamsi HN, Kahtani ES, Ghazi NG. Spectral-domain optical coherence tomography findings in polypoidal choroidal vasculopathy suggest a type 1 neovascular growth pattern. *Clin Ophthalmol.* (2014) 8:1689–95. doi: 10.2147/OPTH.S68471
26. Sato T, Kishi S, Watanabe G, Matsumoto H, Mukai R. Tomographic features of branching vascular networks in polypoidal choroidal vasculopathy. *Retina.* (2007) 27:589–94. doi: 10.1097/01.iae.0000249386.63482.05
27. Sato T, Iida T, Hagimura N, Kishi S. Correlation of optical coherence tomography with angiography in retinal pigment epithelial detachment associat with age-related macular degeneration. *Retina.* (2004) 24:910–4. doi: 10.1097/00006982-200412000-00011
28. Takahashi Y, Koizumi H, Hasegawa T, Izumi T, Maruko I, Sonoda S, et al. Comparison of subfoveal choroidal structures in typical neovascular age-related macular degeneration and polypoidal choroidal vasculopathy. *Jpn J Ophthalmol.* (2018) 62:576–83. doi: 10.1007/s10384-018-0615-4
29. Kilee W, Baek J, Dansingani KK, Lee JH, Freund KB. Choroidal morphology in eyes with polypoidal choroidal vasculopathy and normal or subnormal subfoveal choroidal thickness. *Retina.* (2016) 36:S73–82. doi: 10.1097/IAE.0000000000001346
30. Palkar AH, Khetan V. Polypoidal choroidal vasculopathy: An update on current management and review of literature. *Taiwan J Ophthalmol.* (2019) 9:72–92. doi: 10.4103/tjo.tjo_35_18
31. Koizumi H, Yamagishi T, Yamazaki T, Kawasaki R, Kinoshita S. Subfoveal choroidal thickness in typical age-related macular degeneration and polypoidal choroidal vasculopathy. *Graefes Arch Clin Exp Ophthalmol.* (2011) 249:1123–8. doi: 10.1007/s00417-011-1620-1
32. Japanese Study Group of Polypoidal Choroidal Vasculopathy. Criteria for diagnosis of polypoidal choroidal vasculopathy. *Nippon Ganka Gakkai Zasshi.* (2005) 109:417-27. doi: 10.3969/j.issn.1005-8982.2019.13.011

33. Cackett P, Htoon H, Wong D, Yeo I. Haemorrhagic pigment epithelial detachment as a predictive feature of polypoidal choroidal vasculopathy in a chinese population. *Eye.* (2010) 24:789–92. doi: 10.1038/eye.2009.214
34. Imamura Y, Engelbert M, Iida T, Freund KB, Yannuzzi LA. Polypoidal choroidal vasculopathy: A review. *Surv Ophthalmol.* (2010) 55:501–15. doi: 10.1016/j.survophthal.2010.03.004
35. Zhou N, Wei W. Current advance of polypoidal choroidal vasculopathy in diagnosis and treatment. *Chin J Exp Ophthalmol.* (2019) 37:77–80. doi: 10.3760/cma.j.issn.2095-0160.2019.01.017

Conflict of Interest: The authors declare that the research was conducted in the absence of any commercial or financial relationships that could be construed as a potential conflict of interest.

frontiers | Frontiers in Medicine

ORIGINAL RESEARCH
published: 22 June 2022
doi: 10.3389/fmed.2022.868163

Long Term Time-Lapse Imaging of Geographic Atrophy: A Pilot Study

Michel Paques[1,2]*, *Nathaniel Norberg*[1], *Céline Chaumette*[1], *Florian Sennlaub*[2], *Ethan Rossi*[3], *Ysé Borella*[1,2] *and Kate Grieve*[1,2]

[1] Paris Eye Imaging Group, Clinical Investigation Center 1423, Quinze-Vingts Hospital, INSERM-DHOS, Sorbonne Université, INSERM, Paris, France, [2] Institut de la Vision, Paris, France, [3] Department of Ophthalmology, The University of Pittsburgh School of Medicine, Pittsburgh, PA, United States

Geographic atrophy (GA), the late stage of age-related macular degeneration, is a major cause of visual disability whose pathophysiology remains largely unknown. Modern fundus imaging and histology revealed the complexity of the cellular changes that accompanies atrophy. Documenting the activity of the disease in the margins of atrophy, where the transition from health to disease occurs, would contribute to a better understanding of the progression of GA. Time-lapse imaging facilitates the identification of structural continuities in changing environments. In this retrospective pilot study, we documented the long-term changes in atrophy margins by time-lapse imaging of infrared scanning laser ophthalmoscopy (SLO) and optical coherence tomography (OCT) images in 6 cases of GA covering a mean period of 32.8 months (range, 18–72). The mean interval between imaging sessions was 2.4 months (range, 1.4–3.8). By viewing time-lapse sequences we observed extensive changes in the pattern of marginal hyperreflective spots, which associated fragmentation, increase and/or disappearance. Over the entire span of the follow-up, the most striking changes were those affecting hyperreflective spots closest to margins of atrophy, on the non-atrophic side of the retina; a continuum between the successive positions of some of the hyperreflective spots was detected, both by SLO and OCT. This continuum in their successive positions resulted in a subjective impression of a centrifugal motion of hyperreflective spots ahead of atrophy progression. Such mobilization of hyperreflective spots was detected up to several hundred microns away from atrophic borders. Such process is likely to reflect the inflammatory and degenerative process underlying GA progression and hence deserves further investigations. These results highlight the interest of multimodal time-lapse imaging to document cell-scale dynamics during progression of GA.

Clinical Trial Registration: clinicaltrials.gov, identifier: NCT04128150 and NCT04129021.

Keywords: age-related macular degeneration, geographic atrophy, scanning laser ophthalmoscopy, optical coherence tomography, time-lapse imaging

OPEN ACCESS

Edited by:
Georgios Panos, Nottingham University Hospitals NHS Trust, United Kingdom

Reviewed by:
Alain Gaudric, Université de Paris, France
Weihua Yang, Nanjing Medical University, China
Yuanbo Liang, Affiliated Eye Hospital of Wenzhou Medical University, China

***Correspondence:**
Michel Paques
mpaques@15-20.fr

Specialty section:
This article was submitted to Ophthalmology, a section of the journal Frontiers in Medicine

Received: *02 February 2022*
Accepted: *26 May 2022*
Published: *22 June 2022*

Citation:
Paques M, Norberg N, Chaumette C, Sennlaub F, Rossi E, Borella Y and Grieve K (2022) Long Term Time-Lapse Imaging of Geographic Atrophy: A Pilot Study. Front. Med. 9:868163. doi: 10.3389/fmed.2022.868163

INTRODUCTION

In western countries, dry age-related macular degeneration (AMD) is a major cause of visual disability (1). In its late stage, it progresses to a stage named geographic atrophy (GA), which causes expanding zones of atrophy of the retinal pigment epithelium (RPE). The inexorable expansion of atrophic lesions may have a severe impact on quality of life, in particular when the central zone of the retina, the fovea, is involved. The risk of developing AMD results from an interplay of age, genetic background and chronic inflammation (2–5). The cellular mechanisms underlying the propagation of RPE and photoreceptor atrophy is comparatively less known.

In the margins of GA, where the transition from health to disease occurs, among the most conspicuous changes areas are hypereflective spots, commonly termed pigment mottling. In the early stages of AMD, that is, even before the occurrence of GA, pigment mottling is a biomarker of the risk of progression from early to late AMD (6–10). By histology, several phenotypes and locations of pigment mottling have been described (11–15), which can be intraretinal (therefore called hyperreflective foci, HRF), subretinal or in the subepithelial space. Along margins of atrophy, duplication of the RPE layer has also been described (16), which may account for short wavelength hyperautofluorescence seen clinically (17). Whether this pigment mottling corresponds to detached RPE cells (14, 15) transdifferentiated RPE cells (18, 19) or macrophages that have phagocytozed RPE cells (20, 21) is still a matter of debate.

The mechanisms of atrophy expansion are difficult to ascertain by histology because the latter provides only snapshots; therefore it is likely that the *in vivo* dynamics are of interest to further understand the mechanisms of progression. Time-lapse imaging, which consists of viewing a series of images registered using predefined landmarks, is a practical tool to identify structural continuities in changing environments. We previously reported that time-lapse adaptive optics ophthalmoscopy is helpful to detect motion of pigment spots during GA (22). Using time-lapse OCT, migration of pigment foci (hyperreflective foci, HRF) within the retina has also been reported (23). Here, we investigate if time-lapse sequences of SLO images could improve the characterization of the dynamic changes in fundus features associated with GA progression.

PATIENTS AND METHODS

This institutional retrospective study was carried out according to the principles outlined in the Declaration of Helsinki and was approved by an ethics committee (Comité de Protection des Personnes Sud-Est III), independent from our institution, as required by French law. The present study is an ancillary study on GA imaging registered in clinicaltrials.gov (NCT04128150 and NCT04129021). All participants gave informed consent to take part in this study. Standard procedures were used for multimodal imaging including color fundus photographs (Topcon TRC-501X) and infrared (IR) and short wavelength autofluorescence (swAF) scanning laser ophthalmoscopy (SLO), and optical coherence tomography (OCT) (Spectralis®, Heidelberg Engineering, Heidelberg, Germany). Near infrared autofluorescence (NIRAF) was captured using the Heidelberg Retina Angiograph (Heidelberg Engineering).

Cases were selected based on the quality of images, frequency of follow-up and presence of hyperreflective spots along atrophy margins by IR SLO. Thus, 6 eyes from 6 patients (4 females and 2 males; age range 64 to 80 years; visual acuity, counting fingers to 20/20; refraction range, −2/+0.5) fulfilling these criteria were identified. One (case 4) was reported in a previous paper (22). The mean follow-up was 32.8 months (range, 18–72); mean interval between imaging sessions was 2.4 months (range, 1.4–3.8).

SLO and OCT images were exported in portable network graphic (PNG) format. Careful registration and equalization of successive images of time-lapse videosequences is crucial to neutralize wobbling and hence document a continuum of microscopic features over time. Adjustment of brightness and contrast of each SLO frames was performed manually to smooth differences between frames using Adobe Photoshop 7.0 (Adobe Corporation, Mountain View, CA). To build up time-lapse SLO sequences, successive images were aligned with i2k Align Retina (DualAlign, LLC, Clifton Park, NY) using default settings (rigid registration). The results were evaluated by three of the authors (MP, NN, KG). Accuracy of registration and quality of equalization was based on stability of anatomical landmarks such as retinal and choroidal vessels, and the absence of scintillation. SLO scans that were obviously distorted, overexposed or out of focus were discarded. Low quality frames were easier to identify while viewing the sequence rather than separately. Residual shakes in videosequences were manually corrected using either iterative registration procedures or Photoshop. If not satisfactory, additional registration and equalization procedures were done; this process was iteratively performed as needed. Recently, we used the registration plugin of Fiji (available in the public domain at rsb.inf.nih.gov/ij; National Institutes of Health, Bethesda, MD) which improved the procedure. Then, by manually scrolling the time-lapse sequence back and forth repeatedly at various frame rates (typically 5 - 10fps), microscopic features were visually tracked individually.

Time-lapse OCT B-scan sequences were constructed in a similar way, using the Bruch's membrane and the pattern of choroidal vessels as landmarks. Building time-lapse sequences of OCT was more difficult because of the narrow plane of OCT scans and of the limitations of the performances of eye tracking of the Spectralis system; this often resulted in micrometric displacement of the plane of the scan and hence loss of features to be tracked. Other difficulties were related to the variability of the signal-to-noise ratio and to the scan deformations.

RESULTS

On initial examination, the size of atrophic lesions ranged from 1.03 to 3.2 mm^2 (average, 2.14 mm^2). On OCT scans, atrophic margins presented features typical of complete RPE and outer retinal atrophy (24) bordered by an external limiting membrane descent. On SLO IR images a variable amount of hyperreflective spots were present along the margins

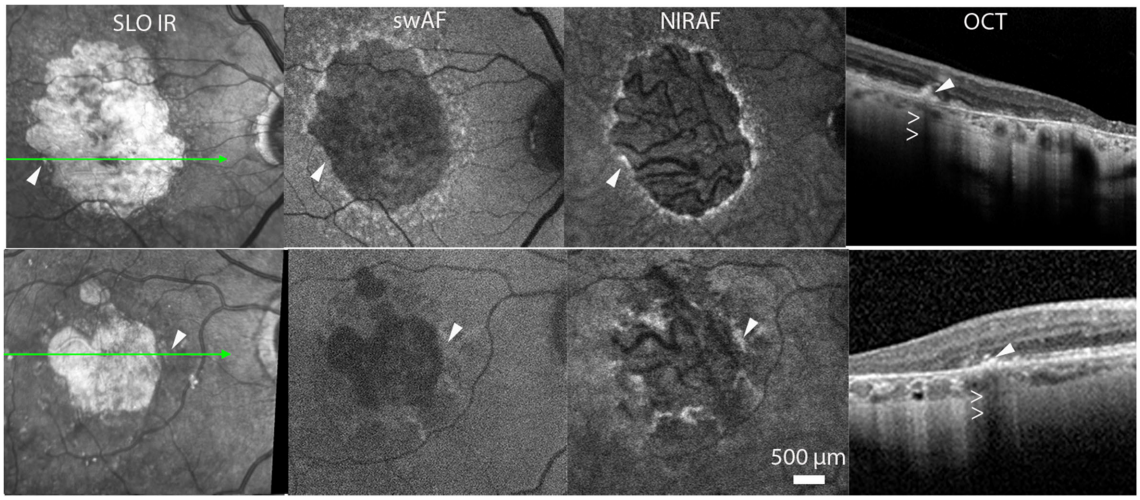

FIGURE 1 | Cases 2 (top row) and 5. Multimodal imaging of GA. Arrowheads show examples of hyperreflective spots. Hollow arrowheads in OCT images point to the shadow effect.

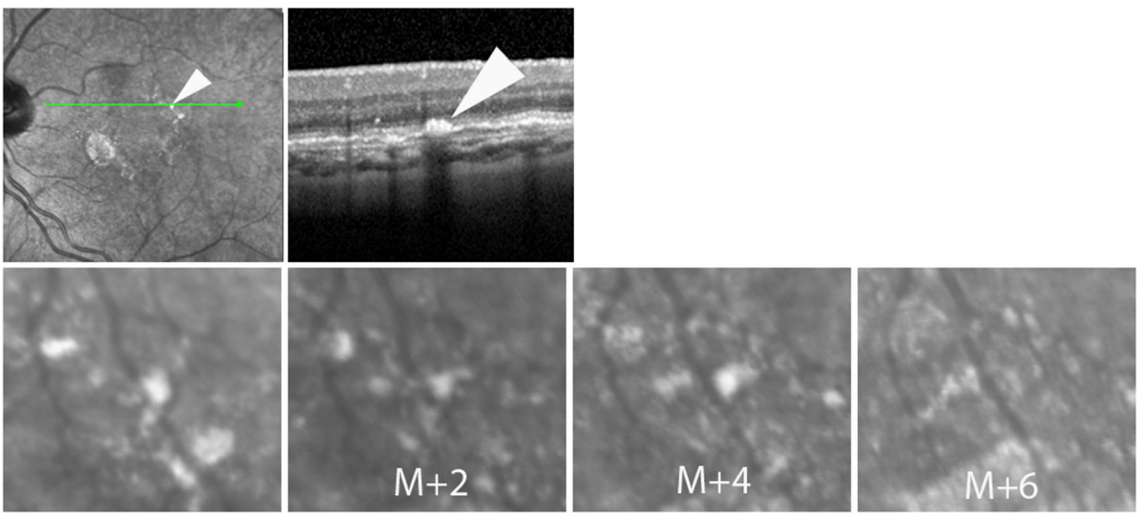

FIGURE 2 | Case 4. Successive SLO images illustrating the change in the shape of a hyperreflective spot during follow-up.

of atrophy (**Figure 1; Supplementary Figure 1**). These spots, which varied in shape, size and amount were mostly NIRAF positive and produced a shadow effect on OCT scans. Short wavelength hyperautofluorescence was less consistent than NIRAF. Accordingly, NIRAF is believed to be both more specific and more sensitive than swAF for the detection of melanin (25–28).

During follow-up, atrophy expanded from an average surface area of 2.14 to 7.47 mm^2 (+349 %; mean progression 1.95 mm^2/year). The median (±SD) radial growth rate of atrophy was 127.2 µm/year (±8.7). On SLO time-lapse videosequences, atrophic areas were seen to expand in all directions (**Supplementary Videos 1**–**3**). In margins, hyperreflective spots showed extensive changes, consisting of a various association of change in shape, fragmentation, expansion or disappearance (**Figure 2**). Despite such variability, careful observation of the entire SLO time-lapse sequence of some of the hyperreflective spots revealed a continuum of the successive positions of hyperreflective spots (**Figure 3**). This continuum gave the impression of a centrifugal motion of some of these spots away from the expanding atrophic area, which is best viewed by the videos.

To provide a more detailed view of these changes, SLO time-lapse sequences were cropped to isolate individual spots and compare their successive positions (**Figure 4; Supplementary Figure 2**, **Supplementary Video 3**). This also showed that the successive positions of these spots were temporally and spatially correlated with atrophy progression.

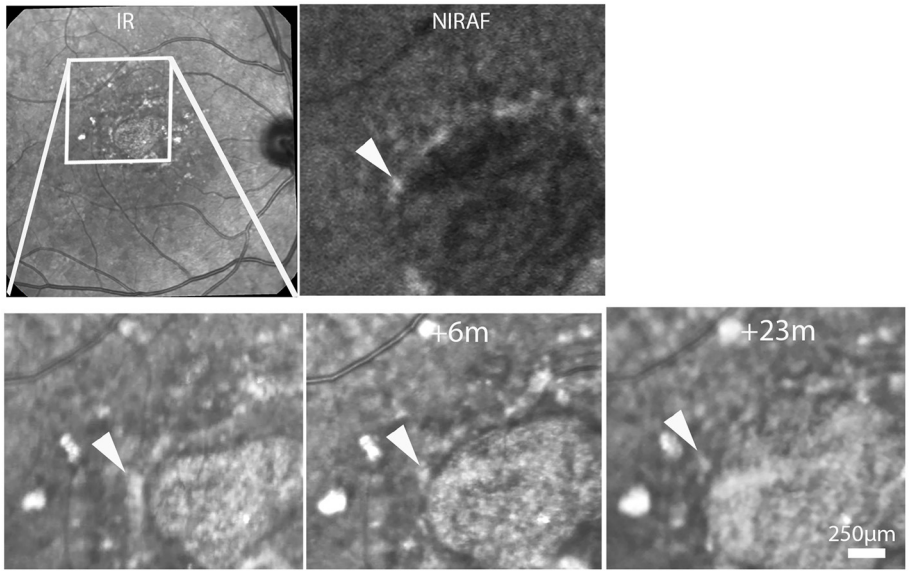

FIGURE 3 | Case 6. Top row, SLO IR and NIRAF images. Bottom row, progression of atrophy. Time-points relative to the first image are indicated in the second and third images. Note the changing aspect of the hyperreflective spot (arrowheads; see also **Supplementary Video 2**).

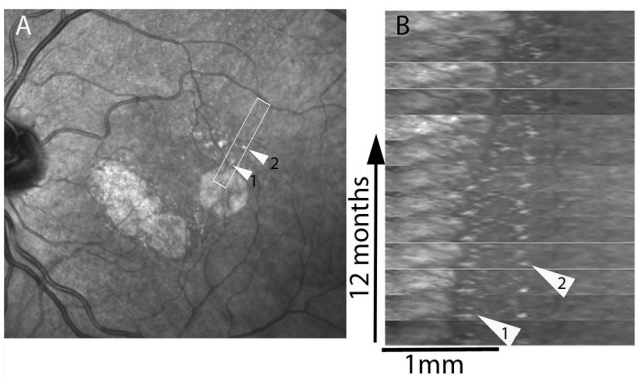

FIGURE 4 | Case 4. Spatiotemporal (xt) plot. Images from regions of interest **(**boxed in **A)** were registered and rotated in **(B)** in order to display the progression from left to right; the x axis represents distance, the y axis time. Arrowheads show two hyperreflective spots that are followed-up. Note the deviation from verticality of the virtual line joining the successive positions of the hyperreflective spot shown by arrowhead 2, which is initially located 620 µm away from the margins. See also **Supplementary Video 3**.

Over the entire follow-up, that is, over several years, some spots could be tracked over distances up to from 41 to 489 µm (examples in **Figure 4**). In addition, some spots located more distally (i.e., several hundred microns from atrophy margins) underwent mobilization and apparent displacement away from atrophy (example in **Figure 4**, shown by arrow 2, **Supplementary Video 3**).

Time-lapse sequences of OCT scans are shown in **Figure 5** and **Supplementary Videos 4–6**. Since OCT scans were seldom placed along the successive position of spots, we experienced more difficulties in tracking individual hyperreflective spots than by SLO. The case showed in **Supplementary Video 4** shows progressive thinning of the outer nuclear layer following atrophy. **Supplementary Video 4** also shows a HRF, that is, a hyperreflective spot located within the outer plexiform layer, which remained at the same location during follow-up. Two time-lapse sequences captured a subretinal hyperreflective spot (**Figure 5**; **Supplementary Videos 5**, **6**). In both cases a subretinal hyperreflective spot could be detected in margins during atrophy progression. No clear evidence of upward migration (i.e., toward inner layers) was noted.

DISCUSSION

Here we used time-lapse sequences of SLO and OCT images to track the changes in microscopic features of margins during GA progression. We paid particular attention to the changes over time in the distribution and aspect of hyperreflective spots, a prominent feature of AMD. We observed that these hyperreflective spots are most often NIRAF positive, suggesting that they contain melanin. They were located within the RPE/Bruch's membrane complex, hence they were not what is called HRFs, which are within the retina, close to the outer plexiform layer. We observed that over the course of months these spots show conspicuous changes, either changing shape, fragmenting, growing or disappearing. Intriguingly, time-lapse imaging also revealed in many case a continuum between the patterns of hyperreflective spots. In fact, over the entire follow-up viewing the time-lapse sequence gave the impression that some of these spots underwent centrifugal displacement in synchrony with atrophy progression. This contrasted with our observation of a HRF which remained static during follow-up.

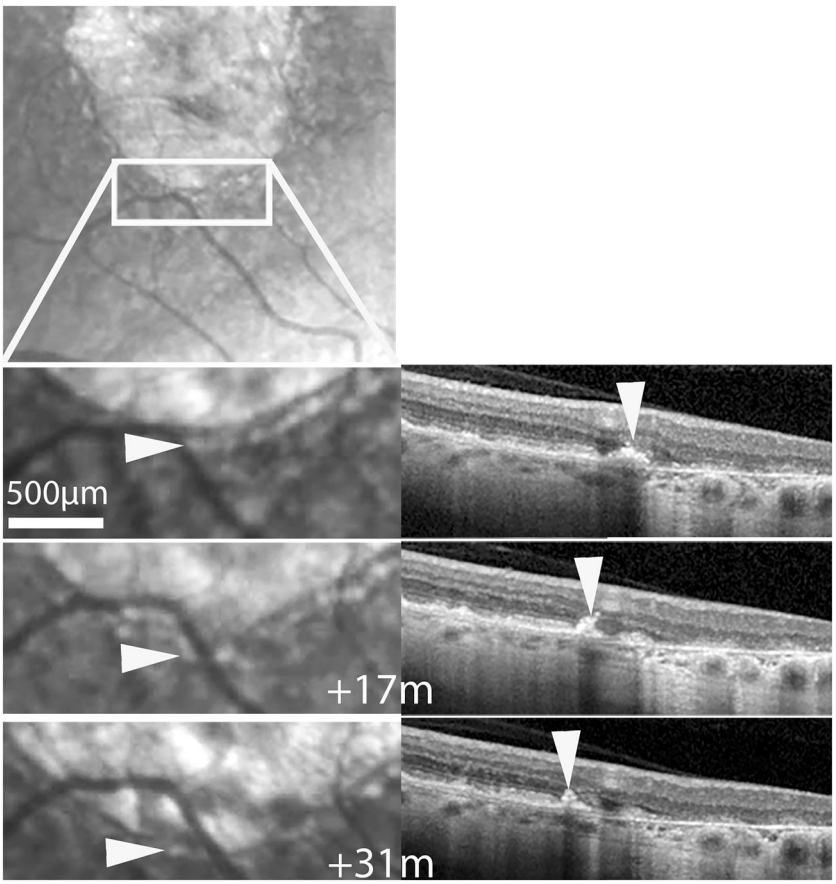

FIGURE 5 | Case 2. Follow-up by SLO and OCT of a subretinalhyperreflective spot. Top, SLO IR image showing the area displayed below. Bottom shows magnifications at three time-points. Arrowheads follow a hyperreflective spot seen by SLO IR (left column) and OCT (See also **Supplementary Video 5**).

In the literature, migration of a HRF toward the inner retina was previously reported (23) as well as stability over several years (19) but not centrifugal migration. Hence, taken collectively, these data suggests that subretinal hyperreflective spots and HRFs may behave differentially.

The fact that hyperreflective spots show mobilization is rather unsurprising since such motion of intraretinal cells has already been shown *in vivo* (29); it may be related to the fact that macrophages, which are migrating in response to inflammatory stimuli, are present in eyes affected by GA and may contain melanin from phagocytized RPE cells (2). The significance of the apparent continuum in the successive positions of these spots is uncertain. This does not necessarily mean that there is physical motion of these spots. Indeed, pigment deposition along margins of atrophy may be agonal changes affecting RPE cells and transmitted *neighbor to neighbor*, hence the apparent displacement could be due to propagation of RPE cell death, more or less like the propagation of a fire; however, the apparent mobilization of more distally located spots challenges this interpretation since it occurs in areas that only transformed into atrophy months later. An alternative hypothesis for centrifugal migration of subretinal hyperreflective spots could be that pigment mottling actually undergoes displacement.

Our study shows that careful construction of time-lapse sequences may be of interest to reveal the microscopic dynamic changes associated with progression of retinal diseases. Time-lapse image sequences can be constructed using commercially available software. Yet, despite the fact that some OCT systems provide built-in registration procedures in our experience there is still a need for manual processing and expert supervision, and often iterative procedures of alignment, sometime with different software to obtain satisfactory time-lapse sequences. Careful pixel-to-pixel registration and expert examination of the successive frames is indeed crucial to neutralize wobbling and hence document a continuum of microscopic features in the long term. The precision of registration is commensurate to the likeliness of distinguishing small changes from background noise. In order to track microscopic features, it is also important, to acquire images at close enough intervals. Indeed, the possibility to detect the continuity of a given feature from one time point to the next is strongly related to the time sampling, that is, the interval between two examinations. This is particularly crucial when addressing a complex and changing environment. A potential limitation of time-lapse imaging in cases with inappropriate time sampling is that it may cause false recognitions of motion patterns, similarly to a stroboscopic

effect. Hence, the shorter the time between two images, the more accurate is the information brought by time-lapse imaging. It is not easy, however, to determine a priori the adequate interval to study a given process, which depends on its particular dynamics. Therefore, the interval between imaging sessions we used here for hyperreflective spots surrounding GA may not be necessarily appropriate for other disease processes. We also observed that display conditions (frame rate and back and forth) affects the possibility to detect features; in particular, back-and-forth viewing greatly improved the recognition of mobilization.

Whatever the interpretation of our data, our observations demonstrate that time-lapse sequences may be useful to investigate the long-term progression of AMD. Our findings may provide new insights into the cellular dynamics accompanying GA. Further work using time-lapse imaging may contribute to better characterize structural changes associated with GA progression. Higher resolution imaging systems such as adaptive optics ophthalmoscopy may provide a better access to the dynamics of microscopic features such as photoreceptors or RPE cells.

DATA AVAILABILITY STATEMENT

The raw data supporting the conclusions of this article will be made available by the authors, without undue reservation.

ETHICS STATEMENT

The studies involving human participants were reviewed and approved by Comité de Protection des Personnes Région Sud-Est III (France). The patients/participants provided their written informed consent to participate in this study.

AUTHOR CONTRIBUTIONS

MP proposed the hypothesis, acquired data, and wrote the first draft of the manuscript. NN managed image analysis. CC acquired images. FS and ER discussed the results. KG discussed the results and wrote the manuscript. All authors contributed to the article and approved the submitted version.

FUNDING

This study was funded by the Region Ile-de-France (EX047007 - SESAME 2019), the LabEx LifeSenses (ANR-10-LABX-65), the Institut Hospitalo-Universitaire ForeSIGHT (ANR-18-IAHU-01) and the Edward N. & Della L. Thome Memorial Foundation. The funding organizations had no role in the design or conduct of this research.

SUPPLEMENTARY MATERIAL

The Supplementary Material for this article can be found online at: https://www.frontiersin.org/articles/10.3389/fmed.2022.868163/full#supplementary-material

Supplementary Figure 1 | Multimodal imaging and evolution of case 1.Top row, SLO, OCT and NIRAF images showing a subretinal hyperpigmented spot (arrows). Bottom row, progression of atrophy. Time-points relative to the first image are indicated in the second and third images (see also **Supplementary Video 1**).

Supplementary Figure 2 | Multimodal imaging and spatiotemporal (xt) plot of cases 3. Registered images from regions of interest (boxed in **A**) were extracted in order to display the progression from left to right **(B)**. Arrow points to a hyperreflective spot.

Supplementary Video 1 | Time-lapse infrared SLO of case 1. Note the hyperreflective spot moving ahead of the progression front (11 frames; real time duration, 24 months). The sequence is displayed back and forth to facilitate the identification of moving features.

Supplementary Video 2 | Time-lapse infrared SLO of case 6. Note the successive positions of a hyperpigmented spot (arrowhead in OCT images) moving ahead of the progression front (15 frames; real time duration, 28 months). The corresponding time-lapse OCT is shown in **Supplementary Video 4**.

Supplementary Video 3 | Time-lapse SLO of case 4, shown in **Figure 4** (16 frames; real time duration, 4 years). The boxed area is displayed in the kymograph.

Supplementary Video 4 | Time-lapse OCT of case 6 (15 frames; real time duration, 28 months). Note the progressive thinning of the retina overlying the RPE loss (center of the OCT image) and the expansion of atrophy (tracked by arrows). Note also on the right a HRF in the outer plexiform layer that remains static over the entire sequence.

Supplementary Video 5 | Time-lapse infrared SLO and OCT of case 2. Note the hyperreflective spot (arrowhead in OCT images) moving ahead of the progression front (9 frames; real time duration, 5 years).

Supplementary Video 6 | Time-lapse infrared SLO and OCT of case 5. Note the hyperreflective spot (arrowhead in SLO and OCT images) moving ahead of the progression front (8 frames; real time duration, 18 months).

REFERENCES

1. Chakravarthy U, Bailey CC, Johnston RL, McKibbin M, Khan RS, Mahmood S, et al. Characterizing disease burden and progression of geographic atrophy secondary to age-related macular degeneration. *Ophthalmology*. (2018) 125:842–9. doi: 10.1016/j.ophtha.2017.11.036
2. Guillonneau X, Eandi CM, Paques M, Sahel JA, Sapieha P, Sennlaub F. On phagocytes and macular degeneration. *Prog Retin Eye Res*. (2017) 61:98–128. doi: 10.1016/j.preteyeres.2017.06.002
3. Fleckenstein M, Keenan TDL, Guymer RH, Chakravarthy U, Schmitz-Valckenberg S, Klaver CC, et al. Age-related macular degeneration. *Nat Rev Dis Primers*. (2021) 7:31. doi: 10.1038/s41572-021-00265-2
4. Beguier F, Housset M, Roubeix C, Augustin S, Zagar Y, Nous C, et al. The 10q26 risk haplotype of age-related macular degeneration aggravates subretinal inflammation by impairing monocyte elimination. *Immunity*. (2020) 53:429–41.e8. doi: 10.1016/j.immuni.2020.07.021
5. Bonilha VL, Bell BA, Hu J, Milliner C, Pauer GJ, Hagstrom SA, et al. Geographic atrophy: confocal scanning laser ophthalmoscopy, histology, and inflammation in the region of expanding lesions. *Invest Ophthalmol Vis Sci*. (2020) 61:15. doi: 10.1167/iovs.61.8.15
6. Ouyang Y, Heussen FM, Hariri A, Keane PA, Sadda SR. Optical coherence tomography-based observation of the natural history of drusenoid lesion in eyes with dry age-related macular degeneration. *Ophthalmology*. (2013) 120:2656–65. doi: 10.1016/j.ophtha.2013.05.029
7. Waldstein SM, Vogl W-D, Bogunovic H, Sadeghipour A, Riedl S, Schmidt-Erfurth U. Characterization of drusen and hyperpigmented spots as biomarkers for disease progression in age-related macular degeneration using artificial intelligence in optical coherence tomography. *JAMA Ophthalmol*. (2020) 138:740–7. doi: 10.1001/jamaophthalmol.2020.1376

8. Nassisi M, Lei J, Abdelfattah NS, Karamat A, Balasubramanian S, Fan W, et al. OCT risk factors for development of late age-related macular degeneration in the fellow eyes of patients enrolled in the HARBOR study. *Ophthalmology*. (2019) 126:1667–74. doi: 10.1016/j.ophtha.2019.05.016
9. Schmidt-Erfurth U, Bogunovic H, Grechenig C, Bui P, Fabianska M, Waldstein S, Reiter GS. Role of deep learning quantified hyperpigmented spots for the prediction of geographic atrophy progression. *Am J Ophthalmol.* (2020) 216:257–70. doi: 10.1016/j.ajo.2020.03.042
10. Chiu CJ, Mitchell P, Klein R, Klein BE, Chang M-L, Gensler G, et al. A risk score for the prediction of advancedage-relatedmaculardegeneration: development and validation in 2 prospective cohorts. *Ophthalmology*. (2014) 121:1421–7. doi: 10.1016/j.ophtha.2014.01.016
11. Curcio CA, Zanzottera EC, Ach T, Balaratnasingam C, Freund KB. Activated Retinal Pigment Epithelium, an Optical Coherence Tomography Biomarker for Progression in Age-Related Macular Degeneration. *Invest Ophthalmol Vis Sci*. (2017) 58:BIO211–26. doi: 10.1167/iovs.17-21872
12. Sarks JP, Sarks SH, Killingsworth MC. Evolution of geographic atrophy of the retinal pigment epithelium. *Eye*. (1988) 2:552–77. doi: 10.1038/eye.1988.106
13. Zanzottera EC, Messinger JD, Ach T, Smith RT, Freund KB, Curcio CA, et al. The project MACULA retinal pigment epithelium grading system for histology and optical coherence tomography in age-related macular degeneration. *Invest Ophthalmol Vis Sci*. (2015) 56:3253–68. doi: 10.1167/iovs.15-16431
14. Li M, Huisingh C, Messinger J, Dolz-Marco R, Ferrara D, Freund BK, et al. Histology of geographic atrophy secondary to age-related macular degeneration: a multilayer approach. *Retina*. (2018) 38:1937–53. doi: 10.1097/IAE.0000000000002182
15. Zanzottera EC, Ach T, Huisingh C, Messinger JD, Spaide RF, Curcio CA, et al. Visualizing retinal pigment epithelium phenotypes in the transition to geographic atrophy in age-related macular degeneration. *Retina.* (2016) 36:S12–25. doi: 10.1097/IAE.0000000000001276
16. Dolz-Marco R, Balaratnasingam C, Messinger JD, Li M, Ferrara D, Freund KB, Curcio CA. The Border of Macular Atrophy in Age-Related Macular Degeneration: a Clinicopathologic Correlation. *Am J Ophthalmol.* (2018) 193:166–77. doi: 10.1016/j.ajo.2018.06.020
17. Rudolf M, Vogt SD, Curcio CA, Huisingh C, McGwin G, Wagner A, et al. Histologic basis of variations in retinal pigment epithelium autofluorescence in eyes with geographic atrophy. *Ophthalmology*. (2013) 120:821–8. doi: 10.1016/j.ophtha.2012.10.007
18. Zanzottera EC, Messinger JD, Ach T, Smith RT, Curcio CA. Subducted and melanotic cells in advanced age-related macular degeneration are derived from retinal pigment epithelium. *Invest Ophthalmol Vis Sci*. (2015) 56:3269–78. doi: 10.1167/iovs.15-16432
19. Cao D, Leong B, Messinger JD, Kar D, Ach T, Yannuzzi LA, Freund KB, Curcio CA. Hyperpigmented spots, OCT progression indicators in age-related macular degeneration, include transdifferentiated retinal pigment epithelium. *Invest Ophthalmol Vis Sci*. (2021) 62:34. doi: 10.1167/iovs.62.10.34
20. Sennlaub F, Auvynet C, Calippe B, Lavalette S, Poupel L, Hu SJ, et al. CCR2(+) monocytes infiltrate atrophic lesions in age-related macular disease and mediate photoreceptor degeneration in experimental subretinal inflammation in Cx3cr1 deficient mice. *EMBO Mol Med.* (2013) 5:1775–93. doi: 10.1002/emmm.201302692
21. Lad EM, Cousins SW, Van Arnam JS, Proia AD. Abundance of infiltrating CD163+ cells in the retina of postmortem eyes with dry and neovascular age-related macular degeneration. *Graefes Arch Clin Exp Ophthalmol*. (2015) 253:1941–5. doi: 10.1007/s00417-015-3094-z
22. Gocho K, Sarda V, Falah S, Sahel J-A, Sennlaub F, Benchaboune M, et al. Adaptive optics imaging of geographic atrophy. *Invest Ophthalmol Vis Sci*. (2013) 54:367–80. doi: 10.1167/iovs.12-10672
23. Ho J, Witkin AJ, Liu J, Chen Y, Fujimoto JG, Schuman JS, et al. Documentation of intraretinal retinal pigment epithelium migration via high-speed ultrahigh-resolution optical coherence tomography. *Ophthalmology*. (2011) 118:687–93. doi: 10.1016/j.ophtha.2010.08.010
24. Sadda SR, Guymer R, Holz FG, Schmitz-Valckenberg S, Curcio CA, Bird AC, et al. Consensus definition for atrophy associated with age-related macular degeneration on OCT: classification of atrophy report 3. *Ophthalmology*. (2018) 125:537–48. doi: 10.1016/j.ophtha.2017.09.028
25. Schmitz-Valckenberg S, Lara D, Nizari S, Normando EM, Guo L, Wegener AR, et al. Localisation and significance of in vivo near-infrared autofluorescent signal in retinal imaging. *Br J Ophthalmol*. (2010) 95:1134–9. doi: 10.1136/bjo.2010.189498
26. Forte R, Querques G, Querques L, Massamba N, Tien VL, Souied EH, et al. Multimodal imaging of dry age-related macular degeneration. *Acta Ophthalmol.* (2012) 90:e281–7. doi: 10.1111/j.1755-3768.2011.02331.x
27. Kellner U, Kellner S, Weinitz S. Fundus autofluorescence (488 nm) and near-infrared autofluorescence (787 NM) visualize different retinal pigment epithelium alterations in patients with age-related macular degeneration. *Retina.* (2010) 30:6–15. doi: 10.1097/IAE.0b013e3181b8348b
28. Heiferman MJ, Fawzi AA. Discordance between blue-light autofluorescence and near-infrared autofluorescence in age-related macular degeneration. *Retina.* (2016) 36:S137–46. doi: 10.1097/IAE.0000000000001254
29. Paques M, Simonutti M, Augustin S, Goupille O, El Mathari B, Sahel JA. In vivo observation of the locomotion of microglial cells in the retina. *Glia*. (2010) 58:1663–8. doi: 10.1002/glia.21037

Conflict of Interest: The authors declare that the research was conducted in the absence of any commercial or financial relationships that could be construed as a potential conflict of interest.

frontiers | Frontiers in Medicine

REVIEW
published: 30 June 2022
doi: 10.3389/fmed.2022.891369

The Development and Clinical Application of Innovative Optical Ophthalmic Imaging Techniques

Palaiologos Alexopoulos[1], *Chisom Madu*[1], *Gadi Wollstein*[1,2,3] *and Joel S. Schuman*[1,2,3,4,5]*

[1] *Department of Ophthalmology, NYU Langone Health, NYU Grossman School of Medicine, New York, NY, United States,* [2] *Department of Biomedical Engineering, NYU Tandon School of Engineering, Brooklyn, NY, United States,* [3] *Center for Neural Science, College of Arts & Science, New York University, New York, NY, United States,* [4] *Department of Electrical and Computer Engineering, NYU Tandon School of Engineering, Brooklyn, NY, United States,* [5] *Department of Neuroscience & Physiology, NYU Langone Health, NYU Grossman School of Medicine, New York, NY, United States*

The field of ophthalmic imaging has grown substantially over the last years. Massive improvements in image processing and computer hardware have allowed the emergence of multiple imaging techniques of the eye that can transform patient care. The purpose of this review is to describe the most recent advances in eye imaging and explain how new technologies and imaging methods can be utilized in a clinical setting. The introduction of optical coherence tomography (OCT) was a revolution in eye imaging and has since become the standard of care for a plethora of conditions. Its most recent iterations, OCT angiography, and visible light OCT, as well as imaging modalities, such as fluorescent lifetime imaging ophthalmoscopy, would allow a more thorough evaluation of patients and provide additional information on disease processes. Toward that goal, the application of adaptive optics (AO) and full-field scanning to a variety of eye imaging techniques has further allowed the histologic study of single cells in the retina and anterior segment. Toward the goal of remote eye care and more accessible eye imaging, methods such as handheld OCT devices and imaging through smartphones, have emerged. Finally, incorporating artificial intelligence (AI) in eye images has the potential to become a new milestone for eye imaging while also contributing in social aspects of eye care.

Keywords: optical coherence tomography, optical coherence tomography (angiography) (OCTA), adaptive optics, visible light OCT, full field OCT, artificial intelligence – AI

OPEN ACCESS

Edited by:
Peng Xiao,
Sun Yat-sen University, China

Reviewed by:
Tanyatuth Padungkiatsagul,
Mahidol University, Thailand
Weiye Song,
Shandong University, China
Eduardo Normando,
Imperial College London,
United Kingdom

***Correspondence:**
Joel S. Schuman
joel.schuman@nyu.edu

Specialty section:
This article was submitted to Ophthalmology, a section of the journal Frontiers in Medicine

Received: *07 March 2022*
Accepted: *23 May 2022*
Published: *30 June 2022*

Citation:
Alexopoulos P, Madu C, Wollstein G and Schuman JS (2022) The Development and Clinical Application of Innovative Optical Ophthalmic Imaging Techniques. Front. Med. 9:891369. doi: 10.3389/fmed.2022.891369

Abbreviations: AI, artificial intelligence; AMD, age-related macular degeneration; AO, adaptive optics; AUC, area under the receiver-operator characteristic curve; CNV, choroidal neovascularization; CSR, central serous retinopathy; DALK, deep anterior lamellar keratoplasty; DED, dry eye disease; DL, deep learning; DR, diabetic retinopathy; FA, fluorescein angiography; FAF, fundus autofluorescence; FD-OCT, fourier-domain optical coherence tomography; FFNN, feed forward neural network; ILM, internal limiting membrane; IPL, inner plexiform layer; GA, geographic atrophy; GCL, ganglion cell layer; INL, inner nuclear layer; IOP, intraocular pressure; IPL, inner plexiform layer; LDH, laser doppler holography; ML, machine learning; NIR-OCT, near-infrared optical coherence tomography; NN, neural network; ONH, optic nerve head; OCT, optical coherence tomography; OCT-A, optical coherence tomography angiography; ORG, optoretinogram; POAG, primary open angle glaucoma; RGC, retinal ganglion cell(s); RNFL, retinal nerve fiber layer; ROP, retinopathy of prematurity; RP, retinitis pigmentosa; RPE, retinal pigment epithelium; SD-OCT, spectral-domain optical coherence tomography; SNR, signal-to-noise ratio; SS-OCT, swept-source optical coherence tomography; TD-OCT, time-domain optical coherence tomography; VF, visual field(s); Vis-OCT, visible light optical coherence tomography.

INTRODUCTION

No more than four decades ago, images of the eyes were limited to just slit-lamp photographs, fundus photographs, fluorescein angiography (FA), and ultrasounds. Since then, a tremendous growth in technology has given birth to a plethora of techniques to image the eye and has drastically transformed patient care. The invention of optical coherence tomography (OCT) in 1991 was a breakthrough in the field of ophthalmology and has shifted the way patients are managed. Several iterations of OCT are currently utilized, and more are being investigated that would allow researchers and clinicians to obtain a much more in-depth insight into ocular diseases. More recently, evolutions in the field of artificial intelligence (AI) and machine learning (ML), termed by many the "fourth industrial revolution," have been proved to outperform human evaluations in several aspects, thus providing potential as powerful supplementary tools to help physicians in all aspects of ophthalmic care. The goal of this review is to summarize major advances in the most important aspects of eye imaging, describe novel emerging imaging techniques, and evaluate their use in clinical settings. Hence, imaging modalities widely used in clinical practice (OCT, fundus imaging) and promising imaging techniques (AO) and analysis tools (AI) were selected to be described in more detail.

OPTICAL COHERENCE TOMOGRAPHY

Optical coherence tomography was introduced in 1991 (1). It is a non-contact and non-invasive technology that uses low-coherence interferometry, in which a beam from a low coherence interferometer is scanned by moving a reference arm that serves as a reference for depth in the axial direction. In the eye, backscattered light from retinal layers is detected sequentially pixel by pixel to form a depth profile (A-scan) (2). Scanning this beam in the transverse plane creates a B-scan, combining all the acquired A-scans. This provides high resolution two-dimensional images of tissue depth structure and can be applied to the entire anatomy of the eye (retina, optic nerve, cornea, and angle). By collecting a sequential series of B-scans, a three-dimensional image can be produced, with volumetric information on the tissue interrogated.

The first iteration of OCT was time-domain OCT (TD-OCT), which interprets the location of the backscattered light as described above. The image acquisition speed of TD-OCT is constrained by the mechanics of the device; in the first TD-OCT systems, a cross sectional image was acquired in roughly 190 s (3). To address this limitation, high-sensitivity interferometric receivers, optical fiber, and galvanometric beam steering devices were implemented that resulted in an increase in scanning speed (up to 100 A-scans/s), producing the first commercial OCT device, launched in 1996 (4). Further developments in TD-OCT allowed for a maximum speed of 400 A-scans/s (third-generation TD-OCT) (3).

Ten years after the introduction of TD-OCT (2001), new methods of signal acquisition were presented. Fourier-domain OCT (FD-OCT) was the next generation of OCT imaging, with the major changes being that the reference mirror remained fixed, and the frequency spectrum of the reflected light was measured simultaneously and transformed from the frequency to the time domain using Fourier transform. These systems are divided into spectral-domain OCT (SD-OCT) and swept-source OCT (SS-OCT): for SD-OCT, the signals are separated by a grating into different wavelengths, whereas, for SS-OCT (introduced in 2012), the light emitted from the laser source sweeps through frequencies in sequence (3). The center wavelength of these two techniques also differs: most commercial SD-OCT devices use a center wavelength of 850-nm versus 1,050 nm of SS-OCT; the longer wavelengths enable for better penetration and thus improved imaging of deeper structures (5). These implementations allowed for a tremendous increase in scan acquisition speed of commercial devices, from 400 A-scans/s to roughly 100,000 A-scans/s for SD-OCT and more than 200,000 A-scans/s for SS-OCT (5–7). Apart from the scanning speed, these techniques also resulted in improved sensitivity and a signal-to-noise ratio, overall better scan quality, and the ability to perform 3-D imaging.

Optical coherence tomography has become standard in ophthalmology, with multiple applications in diagnosis, monitoring, and management of eye conditions across the board (8). Major advances and implementations in OCT are discussed in the following section, which provide novel and exciting applications in the field of ophthalmic imaging.

Optical Coherence Tomography Angiography

Optical coherence tomography angiography (OCT-A) utilizes the motion of red blood cells within blood vessels to image vessels and vascular flow. Commercially available devices developed in 2015 use different algorithms of signal decorrelation from 2 or more repeated B-scans of the same region to display areas of motion: AngioVue (OptoVue, Fremont, CA, United States) uses split-spectrum amplitude-decorrelation angiography (SSADA), whereas Cirrus AngioPlex and PLEX Elite (Zeiss, Dublin, CA, United States) use an OCT-microangiography complex algorithm that is a full-spectrum, complex number-based algorithm (9). The benefits of OCT-A versus other vascular imaging modalities (fluorescent angiography, indocyanine green angiography) are the lack of extrinsic dye injection, leading to adverse effects, and the ability to image vascular networks in different depths (**Figure 1**). While dye-based angiography can reveal vessel leakage, OCT-A cannot.

Scans acquired with OCT-A can be processed to improve the signal-to-noise ratio (SNR) and display very small vessels more accurately. Denoising methods, such as Gaussian filter (10), compressive sensing (11–20), and Bayesian estimation (11, 21), can suppress noise while maintaining vasculature information. Filters that focus on the specific structure of vessels are also applied, such as Frangi filter (22, 23), Gabor wavelets, and Fuzzy-C-Means Classification (24). Quality limiting factors with OCT-A imaging are the presence of artifacts (projection, motion), visibility of vessels dependent on the rate of blood flow and scan speed, and low output image contrast (25, 26).

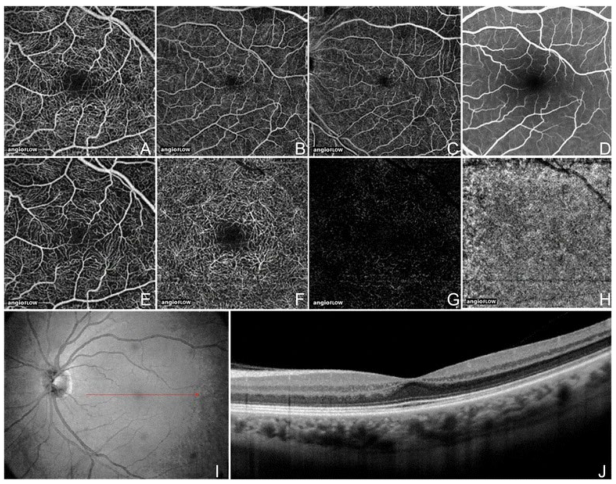

FIGURE 1 | Optical coherence tomography angiography (OCT-A) fields of view and segmentation layers (Angiovue). The normal left eye of a 56-year-old Caucasian man using the Angiovue optical coherence tomography angiography (OCTA) software of the RTVue XR Avanti (Optovue, Inc., Fremont, CA, United States). **(A)** Full-thickness (internal limiting membrane to Bruch's membrane) 3 mm × 3 mm OCT angiogram. **(B)** Full-thickness 6 mm × 6 mm OCT angiogram. **(C)** Full-thickness 8 mm × 8 mm OCT angiogram. **(D)** Fluorescein angiography cropped to approximately 8 mm × 8 mm or 30 degrees demonstrates a less capillary detail than **(A–C)**. **(E)** 3 mm × 3 mm OCT angiogram of the "Superficial" inner retina. **(F)** 3 mm × 3 mm OCT angiogram of the "Deep" inner retina. **(G)** 3 mm × 3 mm OCT angiogram of the outer retina shows absence of vasculature. The white represents noise. **(H)** 3 mm × 3 mm OCT angiogram of the choriocapillaris is generally homogenous. There is black shadowing from retinal vessels. **(I)** Enface intensity OCT image. **(J)** Highly sampled OCT b-scan image. This figure was reprinted from de Carlo et al. (507) with permission.

The OCT-A can be utilized for conditions involving vascular damage or choroidal neovascularization (CNV) (25). Apart from allowing the subjective identification of vascular abnormalities, OCT-A can also provide quantitative data (vessel density, blood flow, and foveal avascular zone size) that could be employed as vascular biomarkers (27–32).

Diabetic retinopathy (DR) is a disease affecting, among other tissues, the retinal microvasculature (33, 34). It is the leading cause of blindness in the middle-aged and elderly population (35). Early in the disease process, deeper retinal capillary plexuses are primarily affected (36–40). OCT-A can detect both microaneurysms (the hallmark of early DR) and neovascularization (in proliferative disease) in various depths (25, 38, 41–44). Being non-invasive and high resolution, OCT-A can be used for early diagnosis and possible screening of DR when compared to fluorescein angiography (FA) (3, 45). Ong et al. and Russell et al. have proposed new models for DR staging and progression based on OCT-A findings (46, 47).

In the setting of age-related macular degeneration (AMD), OCT-A can detect impaired blood flow at sites of drusen or pseudodrusen (48, 49) and geographic atrophy (GA) (50–52) with high reproducibility when compared to SD-OCT (53). It can also identify CNV (sensitivity, 81% and specificity, ≥93%) with more detail and better contrast than FA (54–64).

In glaucoma, various studies have demonstrated reduced blood flow and blood vessel density at the level of the optic nerve head (ONH) and peripapillary area (65–72). OCT-A scans from macular and ONH scans in glaucoma have been shown to display good reproducibility, which supports the use of OCT-A longitudinally as well (73). Vessel density parameters have also been associated with visual field progression (74, 75).

For other conditions, Zhu et al. have recently proposed that OCT-A metrics can be used to assess and detect myopia development in adolescents (76).

A limitation of OCT-A compared to other vessel imaging techniques is the limited area visualized. Kawai et al. have proposed the introduction of a front prism that would generate ultra-wide field panoramic images and allow imaging of the peripheral chorioretinal vessels, while applying image averaging to correct for the drop-off in image quality (77, 78). Miao et al. also introduced the use of megahertz-rate OCT-A as a faster imaging technique that also yields better contrast images (79). Post-processing methods (angiogram subtraction, distortion correction) and eye tracking during scan acquisition have also significantly improved the scan quality and reduced artifacts (80–86). Furthermore, new types of software have been developed to automate the analysis of OCT-A images; Viekash et al. have also established software to automatically quantify the foveal avascular zone, a region affected by various ocular diseases (87), while tools have been constructed to automatically process, segment, and quantitatively analyze the blood vessels (88–90).

Visible Light Optical Coherence Tomography

Vis-OCT, first reported by Povazay and coauthors in 2002 (91), has been developed most intensively in the last decade. It relies on light sources from the visible spectrum (555–800 nm), which provides a better axial resolution than typical OCT devices that use near-infrared (NIR) illumination (1.2–1.4 μm versus 1.7–7.5 μm, respectively) (92–96). Other benefits of Vis-OCT include a smaller bandwidth to achieve the same resolution, leading to easier dispersion compensation, and higher image contrast due to higher scattering coefficients (97). One of the advantages of Vis-OCT is the ability to measure oximetry in blood vessels. Blood, which contains oxyhemoglobin (HbO_2) or deoxyhemoglobin (Hb), exhibits more contrast at the isosbestic point in the wavelengths of Vis-OCT than in the NIR. Combining this property with simultaneous measurement of the blood flow rate using Doppler OCT methods, many metabolic parameters of retinal circulation can be extracted, such as O_2 saturation (sO_2), O_2 extraction fraction, total retinal O_2 delivery, and the metabolic rate; Vis-OCT has been validated and is superior to NIR-OCT for these parameters (97–103).

Vis-OCT has been widely studied in disease models in animals and is now transitioning to clinical practice. Rodents with DR and retinopathy of prematurity (ROP) have been studied using Vis-OCT, and metabolic changes in both conditions were apparent before structural changes (103–105). The first use on humans was performed by Yi et al. on a single healthy subject, with Vis-OCT displaying increased contrast of the inner (the retinal nerve fiber

layer – RNFL) and outer (a photoreceptor inner/outer segment, a retinal pigment epithelial layer, Bruch's membrane) retinal layers compared to NIR-OCT (106). Vis-OCT has since been used for calculating metabolic parameters with upgraded light sources, decreased noise, and great axial resolution (96). Shu et al. also developed a Vis-OCT platform than can be used for humans and demonstrated it successfully in conditions such as retinal occlusive diseases and DR (107). Given its ability to provide metabolic information about oxygenation and circulation, and its advantages of retinal layer imaging over NIR-OCT, Vis-OCT might be a better imaging candidate for conditions affecting these cell layers, for example, the RNFL, inner plexiform layer (IPL), and inner nuclear layer (INL) in glaucoma or the outer retinal layers and retinal pigment epithelium (RPE) in AMD. Its ability to provide metabolic information about oxygenation and circulation, contributors to retinal and optic nerve diseases, reinforces this point.

Vis-OCT has continued to develop. Registration and averaging of multiple volumes have allowed the visualization of single cells, and the concept of Vis-OCT fibergraphy (Vis-OCTF) of imaging-specific retinal ganglion cell (RGC) axon bundles has been introduced in animal models (108–110). Ultrahigh resolution Vis-OCT (UHR Vis-OCT) is capable of imaging sublayers within retinal layers, such as the IPL (**Figure 2**), and improvements in the axial resolution have also been made using rapid spectral shaping, axial tracking, and *in vivo* spatially dependent numerical dispersion compensation (111–113). Zhang et al. have also developed a circumlimbal scanning method to image the anterior segment, capable of visualizing the Schlemm canal and the limbal microvascular network (114). In addition, Wang et al. have recently devised a dual-channel system with both Vis-OCT and NIR-OCT-A capable of simultaneous retinal imaging and metabolic measurement acquisition; the use of a fiber-based dual channel Vis- and NIR-OCT to image the human retina was first reported by Song et al. (115, 116). In a clinical setting, this dual channel system was initially reported to quantify RNFL spectroscopic markers in glaucomatous subjects and glaucoma suspects, which were correlated with disease severity (117). A combination of both Vis-OCT and OCT-A (Vis-OCT-A) has also been reported by Song et al., with narrow bandwidth spectrometers, optimized image protocols, and improved acquisition speed (100,000 A-scans/s) (118).

Handheld Optical Coherence Tomography

In a typical OCT imaging session, the patient sits upright with the head stabilized with a chin rest and headrest. The use of portable or handheld OCT is indicated in cases where this positioning is not possible. Populations included in this category are bedridden or postoperative patients, the pediatric population and cases where access to health care is limited or difficult. Portable HH-OCT would potentially offer an easier-to-use and less-expensive alternative to current commercial OCT devices. Chen et al. displayed that measurements from HH-OCT have good repeatability and reproducibility of both axial and transverse measurements when compared to Heidelberg Spectralis (119).

The HH-OCT is widely used nowadays for pediatric ocular conditions. HH-OCT/OCT-A systems can reliably visualize and measure vitreous opacities and bands, perifoveal vessels, the macular shape, anterior chamber features, retinal tumors,

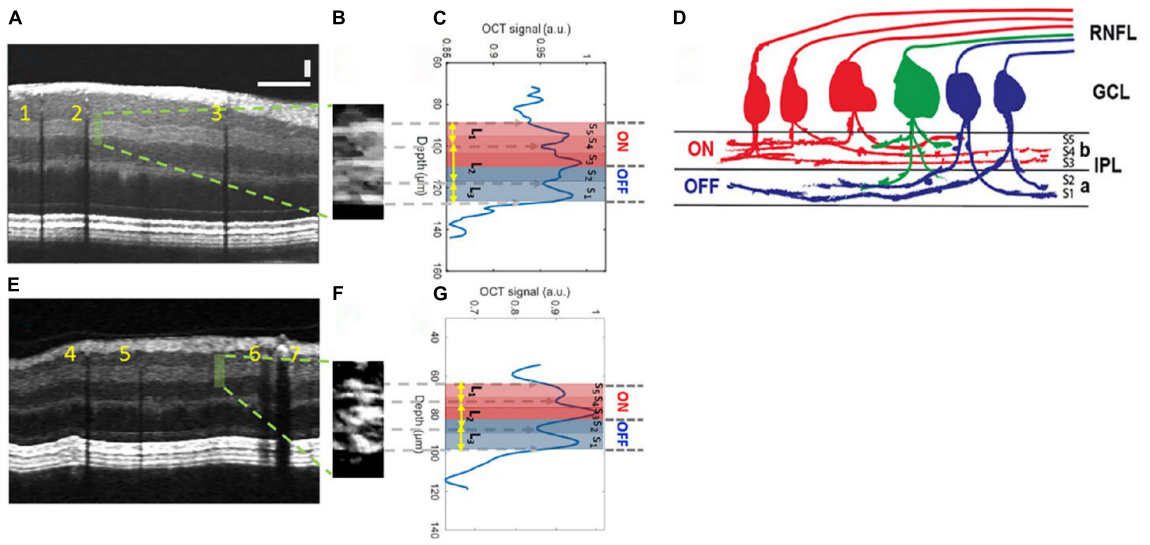

FIGURE 2 | Inner plexiform layer (IPL) sublayer visualization with Vis-OCT. **(A)** A speckle-reduced vis-OCT image from a healthy eye. A horizontal bar: 500 μ m; a vertical bar: 50 μ m. **(B)** A magnified view of the region highlighted by the dashed box in **(A)** (15 srA-lines segments). **(C)** A depth-resolved OCT amplitude profile of the IPL sublayers. We averaged 15 srA-lines, corresponding to approximately 88 μ m along the lateral direction within the highlighted region in **(A)**. **(D)** Illustration of the lamination of ganglion cells from RNFL to the IPL. The "red" ganglion cells (ON center) are laminating dendrites to the "b" sublamella of the IPL whereas "blue" cells (OFF center) laminate to the "a" sublamella. The "green" ganglion cell is bi-laminating. **(E)** A speckle-reduced vis-OCT image from a glaucoma eye. **(F)** A magnified view of the region highlighted by the dashed box in **(E)**. **(G)** A depth-resolved line profile of the glaucoma eye IPL sublayers. This figure was reprinted from Ghassabi et al. (113) with permission under a Creative Commons Attribution 4.0 International License.

and ganglion cell complex (GCC)/IPL/RNFL thickness in both premature and full-term infants (120–130). Hence, they are useful in conditions, such as congenital and pediatric glaucoma, macular edema, macular hole, epiretinal membrane, retinoschisis, retinal dystrophies, and other conditions (128, 129, 131–133). Some measurements obtained, mostly from the fovea, could potentially be used to screen for conditions like ROP (132). HH-OCT-A in specific is extremely useful in cases of CNV in children, such as ROP, retinal dystrophies, inflammatory disorders, trauma or cases of unexplained visual loss (134–136). Ocular measurements, specifically RNFL thickness, have been shown to be associated with systemic health conditions in infants (low birth weight, sepsis, and necrotizing enterocolitis) (137).

The approaches to making OCT devices more mobile are promising. HH-OCT probes have been developed and are currently used in animal experimental models (Leica, Heidelberg); this allows for transportation of the device, although the probes are tied to bulky mobile carts (138, 139). Smaller versions of OCT machines have also been achieved that offer comparable results to bench-top OCT devices, with some offering *en face* reflectance, OCT-A volumes, combination with SLO and supine imaging (140–148). Handheld SS-OCT devices have also been created, containing ultrahigh speed and averaging capabilities (Lu et al.) or capable of imaging both the anterior and posterior segments in quick succession (Nankivil et al.) (149, 150). Ni et al. have recently proposed models for high-speed scanning (the HH-SS-OCT model using a 400 kHz VCSEL light source, scanning speed, 1,720 MHz; volume acquisition time, 1.875 s) and an increased field of view scanning to 105 degrees (**Figure 3**) (151, 152).

Intraoperative Optical Coherence Tomography

Intraoperative OCT (I-OCT) can aid surgeons by providing a live imaging feedback during surgery. The devices currently used for I-OCT are either handheld or integrated in microscopes or probes (153). HH-OCT in this setting is best utilized when mounted onto the surgical microscope to improve stability and precise movement. The images obtained with that method are fast, accurate, and reproducible; drawbacks include pausing the surgery for image acquisition and potential requirement of technician assistance (154). I-OCT integrated within the surgical microscope partially resolves these issues, as it can be used without pausing the operation or additional specialized technical support; additionally, there are opportunities to enhance I-OCT with decision-making algorithms and high-tech instrumentation (e.g., heads-up display) (155). An advanced technique is implementation of OCT scanners in ophthalmic probes, creating an instrument for intraocular use, especially for vitreoretinal surgery (156).

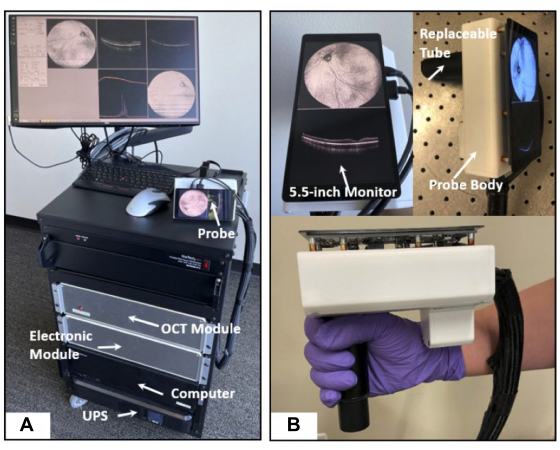

FIGURE 3 | High-speed and widefield handheld SS-OCT-A with a VCSEL light source. **(A)** A photograph of the front of fully assembled handheld OCTA system in a portable cart. **(B)** A photograph of the handheld probe. This figure was reprinted from Ni et al. (151) with permission.

The I-OCT can provide insight into diagnosis and surgical planning, optimal outcome confirmation, complication prevention and control, prognosis, and education. Ehlers et al. in two studies (PIONEER and DISCOVER) reported that I-OCT findings can affect surgical decision-making in 29–68% of select surgery types (154, 157). For epiretinal membrane peeling, I-OCT can precisely locate the margins of the membrane, dictate the best start and end points for peeling, and confirm successful peels without further complications (a point of disagreement between subjective observation and I-OCT) (154, 157–160). In macular hole repairs, I-OCT can confirm the release of traction, effectiveness of the tamponade or flap and hole closure; on the latter, Kumar et al. recognized residual tissue at the hole edge (a "hole-door" sign) as an imaging factor predicting the rate of hole closure (161–166). Recently, Cehajic-Kapetanovic et al. have reported to be the first group using I-OCT to guide a robot-assisted drug delivery during vitreoretinal surgery; in that context, I-OCT can be used to guide all kinds of retinal and subretinal treatments, including highly promising gene therapies for retinal conditions (167–169).

In surgeries of the anterior segment, the ease of imaging of the cornea makes it an attractive I-OCT target (153). For deep lamellar anterior keratoplasty (DALK), where the corneal stroma is dissected, I-OCT allows the surgeon to evaluate the depth of the dissection, make on-the-spot adjustments, and confirm layer separation and integrity of Descemet's membrane (153, 170–173). Implementations of I-OCT in DALK have been shown to lead to successful outcomes (171, 174, 175). Posterior corneal procedures like Descemet stripping (automated) endothelial keratoplasty (DSEK/DSAEK) and Descemet membrane endothelial keratoplasty (DMEK) can also benefit from the use of I-OCT. The handling, unfolding, and positioning of the graft can be performed more quickly and definitively with simultaneous I-OCT, which can also verify its correct orientation (176–181). Apart from this, fluid between the cornea and the graft (interface fluid) and areas of graft non-adherence or folds can be assessed and addressed (176, 182–184). In the setting of cataract extraction surgery, I-OCT could be beneficial for identifying and handling complications, confirming adequate placement of the lens and further improve the accuracy of refractive calculations and aid in the development of future lens designs (153, 185–187).

Whole-Eye Optical Coherence Tomography

Different parts of the eye require imaging configurations specific to the area examined (anterior segment versus retina), mainly due to different natural properties. For anterior segment, imaging light has to pass only through the air to the tissue of interest versus the refractive structures (cornea and lens) for retinal imaging. The scan depth using standard OCT is typically about 2 mm, well below the typical axial length of the eye (188). Whole-eye OCT offers the opportunity to acquire a view of the eye from anterior to posterior segments with a single scan.

Multiple approaches have been implemented for that goal. Commercial systems (Heidelberg Spectralis, OptovueiVue, Leica Bioptigen C-series) are able to scan 2 areas in sequence by changing the scan configurations, for example, the reference arm length. In addition, changing the imaging optics (by adding lenses or using an adjustable lens) or alternating the volume frames helps decrease the differences of the structures imaged (150, 189–191). The main drawback of switching scan configurations is the time gap for changing the settings. Recently, Luo et al. have demonstrated an SS-OCT prototype that utilizes a single source and a single detection channel for sequential imaging (192).

Newer approaches of whole-eye OCT aim to capture images of all structures at the same time and be true whole-eye scanners. Approaches include the use of 2 practically separate subsystems (the first for anterior segment and the second for retina) or a single system with either one or two different imaging depths (193–196). The latter is the most advanced method, with the dual-depth polarization system focusing on both structures at the same time, using either one or two interferometers (197, 198). Its big advantage is the focusing of each area while also achieving standard fields of view greater than 24 degrees to image both the macula and the ONH.

In clinical application, whole-eye OCT can provide biometric data for the entire eye (axial length and lens thickness); this, along with information about possible retinal comorbidities and/or microstructural lenticular changes (for example, posterior capsule integrity), can be useful in planning of refractive or cataract surgeries (199–202). Following cataract extraction surgery, it can also verify correct lens positioning and capsule integrity (202, 203). Moreover, visualization of the entire eye could be relevant to patients with high myopia and potentially provide insight into possible causes of pathologic myopia. In certain conditions involving multiple ocular structures, such as the anterior chamber angle and the RNFL in glaucoma, whole-eye OCT could provide data for multiple regions of interest (204).

Anterior Segment Optical Coherence Tomography

The interest of imaging the anterior segment became apparent soon after OCT's introduction in 1991. A decade and a half later, OCT systems designed specifically for that purpose were developed that utilized TD-OCT [Visante (Carl Zeiss Meditec, Dublin, CA, United States; 2005), Slit-Lamp OCT (Heidelberg Engineering GmbH, Heidelberg, Germany; 2006)] or SS-OCT [Casia SS OCT (Tomey, Nagoya, Japan); 2008] and were able to image the entire anterior segment.

The AS-OCT can be a tool in diagnosing conditions involving the anterior segment. A common condition is dry eye disease (DED), in which diagnosis can be a challenge due to poor association of corneal findings and actual symptoms (205). AS-OCT can measure the precorneal tear film thickness and individual tear film layers (lipid and aqueous) and the tear meniscus (area, height, depth, and radius) (**Figure 4**); these parameters correlate with objective corneal findings, subjective symptoms, and other tests used in DED (such as the Schirmer test) or can be used to evaluate treatment response and monitoring (206–214). For other corneal pathologies, AS-OCT can also be an aid in diagnosing various types of keratitides (fungal, viral, bacterial, and parasitic), ocular surface neoplasias, corneal edema, corneal dystrophies, differentiate pterygium from pseudopterygium and assessing keratoconus morphology (95, 215–223).

A special utilization of AS-OCT is in the setting of glaucoma research. Elevated intraocular pressure (IOP) in primary open angle glaucoma (POAG) is due to increased resistance in the aqueous outflow system, and AS-OCT can be used for evaluation and for better understanding of the pathophysiology. In POAG, the decreased Schlemm canal cross-sectional area has been reported compared to healthy subjects (224, 225). AS-OCT can also visualize the anterior chamber angle qualitatively and quantitatively (angle opening distance, angle recess area, and trabecular-iris space area), with these findings correlating well with ultrasound biomicroscopy (226, 227). Baskaran et al. reported the correlation of angle closure on AS-OCT and gonioscopic angle closure (228). Risk factors for angle closure can be identified using AS-OCT, such as iris thickness/area, anterior chamber width, lens vault, and anterior chamber area/volume (229–231). Further AS-OCT advances would allow better understanding of the inciting events of angle closure glaucoma. The response of the trabecular meshwork to elevated IOP can be visualized and quantified (232). In the laboratory, using automated software, a 3D reconstruction of the entire SC and collector channels is now possible; changes in these structures can help in guiding glaucoma surgeries and predict or monitor IOP-lowering treatment success (both medical and surgical) (233–237). Ruggeri et al. have recently combined AS-OCT with a wavefront-based aberrometer, which was capable of using the OCT beam to acquire refractive error measurements and allow for simultaneous imaging, autorefraction, and biometry (238).

Recent advances in the field of OCT have also been applied to modern AS-OCT, namely, increased scanning speeds (up to 2 million A-scans/s), greater depth, and improved axial resolution (up to 1 μm) (239–246). These have allowed the imaging of most structures of the anterior segment, including all the corneal layers and the precorneal tear film, the outflow system (trabecular meshwork, Schlemm canal, collector channels, and scleral veins), and the anterior chamber angle (247–250).

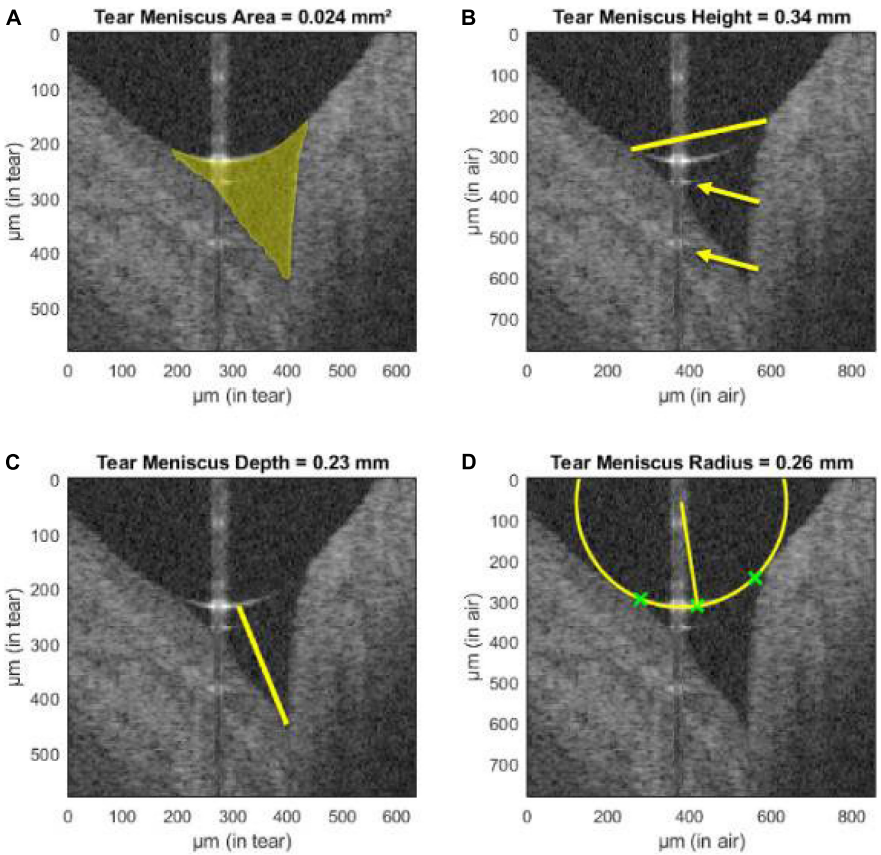

FIGURE 4 | Assessment of tear meniscus using UHR-OCT. Automatic segmentation of the lower tear meniscus in a healthy subject. Calculated parameters (represented in yellow) are **(A)** the tear meniscus area, **(B)** height, **(C)** depth, and **(D)** radius of curvature. Green crosses represent the points used for the estimation of the radius of curvature. The yellow arrows indicate mirror artifacts of the true upper meniscus boundary due to internal reflectors in the optical setup of the system. This figure was reprinted from Stegmann et al. (209) with permission.

Full-Field Optical Coherence Tomography

In FF-OCT, a light emitting diode is used to illuminate the entire scanning field simultaneously, which captures images orthogonal to the optical axis (en face) and avoids transverse scanning (251). Challenges to FF-OCT include eye movements and difficulties matching of the length of the optical path; cameras with high acquisition speeds and combinations with TD-OCT and FD-OCT aim to resolve these issues. Although time-domain FF-OCT (TD-FF-OCT) is possible, its slow volumetric capture capability limits is use (252). Fourier-domain FF-OCT (FD-FF-OCT), on the other hand, can capture 3D volumes of the cornea and retina with scanning speeds reaching 38.6 MHz (253). The single phase of FD-FF-OCT across the entire field does not introduce motion artifacts seen between A-scans in conventional OCT and allows for the use of higher scanning power, leading to fewer aberrations and less signal loss (252, 254).

The FF-OCT can be used to image and study structures of the anterior segment. Mazlin et al. presented the first FD-FF-OCT system capable of corneal imaging the corneal epithelium, stroma, and endothelium (255). The same team later created a system, combining FF-OCT with SD-OCT capable of cellular level imaging of the entire ocular surface (256). Using a common path (NIR light-emitting diode), the SD-OCT arm was used to track axial and lateral eye movements and adjust the optical arm lengths of the FF-OCT accordingly. This allowed for *in vivo* detailed imaging of all the corneal layers, sometimes even to the cellular level (superficial epithelium and stromal keratinocytes), including nerve plexuses. Apart from the cornea, quantitative parameters from structures, such as the tear film (tear flow velocity, amount of particulate matter, and evaporation time after blinking) and the corneal limbus (blood vessel morphology, blood flow velocity, and blood flow direction), were also measured. These can be useful for research studies of relevant anterior segment pathologies (DED, anterior chamber inflammation, and conditions leading to scarring). This approach is comparable to confocal microscopy, as it images the same corneal microscopic features much faster, in a non-contact manner and from a broader (nine times larger) field of view, with high axial resolution and without the requirement of fluorescein administration. These features make FF-OCT an excellent candidate for *in vivo* histological studies without sample preparation.

A similar approach with combination of FF-OCT and SD-OCT has been used for retinal imaging. A device using that principle was presented by Xiao et al., which was able to image the RNFL and photoreceptor layer in great detail (orientation of nerve fibers and cone photoreceptor mosaic, respectively) (257). These images were comparable to AO-OCT commercial devices (discussed below in greater detail), although the SNR was lower in the photoreceptor layer and not adequate to image other retinal layers, such as the ganglion cell layer and RPE; visualization of layers also required averaging of multiple images after acquisition. Other teams have also succeeded in imaging the photoreceptor layer with FF-OCT (258). For remote retinal scanning with FF-OCT, von der Burchard et al. have also proposed a low-cost device, which patients can use to examine themselves and monitor disease progression from their homes (259).

ADAPTIVE OPTICS

By using wavefront technology first utilized in astronomy and defense systems, adaptive optics (AO) systems have been implemented in ophthalmology with the goal of correcting for ocular anatomical and physiological higher order (optical/wavefront) aberrations (cornea, lens, and pupil), which cannot be corrected by glasses, contact lenses or refractive surgery (260). As a result, AO vastly improves the transverse (lateral) resolution as well as the speckle width and increases the SNR *via* imaging through a larger pupil, allowing more light to enter the eye. Further improvements in the lateral resolution have also been made by the addition of mirrors and error budget analyses (261–264). AO has so far been implemented in multiple imaging modalities, such as OCT (AO-OCT), scanning laser ophthalmoscopy (AO-SLO), and two-photon ophthalmoscopy (AO-TPO) (265, 266).

The improved lateral resolution of AO systems has enabled the visualization of single cells within the retina (**Figure 5**). By combining this feature with the high axial resolution of OCT, a resolution voxel smaller than most retinal cells is acquired: the lateral resolution achieved (2–3 μm) is about 5 times higher and overall resolution 36 times greater than commercial OCT (267–272). The big advantage, therefore, of AO is the ability to track cellular changes over time either for studying disease processes or monitoring treatment responses, both of which could be very useful clinical applications.

Cone photoreceptors are the cells most widely studied using both AO-OCT and AO-SLO. Anatomically, they have been shown to possess a wide range of reflectance properties, and their major components (inner segment, outer segment, somas, and axons) can be visualized, with results corresponding to histology. They can also be functionally distinguished by their light sensitivity in different types (short, medium, and long wavelengths). Photoreceptors are normally organized in a lattice hexagonal pattern in the retina, and their architecture can be extracted by semi-automated segmentation methods (273, 274). After identification, mapping the structure formation (Voronoi analysis) allows for descriptive quantitative measurements (cone density, cone spacing, and mosaic regularity), which can be utilized with good inter-device reproducibility (2.5–6.9%) as biomarkers or used to construct normative databases for research or clinical practice (**Figure 6**) (275–278). The calculation of functional biomarkers (cone reflectance) is also possible (279). Rods are more difficult to visualize than cones since they have a smaller diameter (especially peripherally), different refractive indices, and greater interference with the RPE (280). Despite these drawbacks, AO-SLO studies using improved AO systems have demonstrated visualization of rods in both normal and diseased subjects (281).

Imaging of several retinal cell types is possible with AO. These include individual RNFL bundles and sublayers of the ONL, which has been shown to consist of two distinct sublayers (somas and axons) (262, 269). These are mostly visible with AO-OCT, since the limited axial resolution of AO-SLO cannot easily image the transparent, multi-cell thick inner layers (280). Confocal AO-SLO, in which light is focused on a single spot and the backscattered light is refocused on a confocal aperture, is capable of imaging some of these structures (photoreceptor segments and nerve fibers), as well as blood vessels and the lamina cribrosa (282). AO-SLO-FA can also capture blood flow and detect vascular leaks. Other non-confocal detection modes (offset aperture, dark-field, split-detection, and offset pinhole) and the implementation of multi-volume averaging have also been implemented in order to visualize the ganglion cells and RPE (277, 283–285).

These features allow a detailed study of the retina and its cellular microstructure both in normal eyes and in ocular pathologies, making AO a useful adjunct to other OCT imaging technologies. In AMD, retinal layer and RPE changes can be monitored in areas of drusen/pseudodrusen or GA (286). Panorgias et al. have demonstrated both losses in reflectivity between the photoreceptor inner and outer segments in areas of GA (287). This could be extremely helpful in determining the progression of events in AMD and determining which tissues are affected first during the disease onset (277, 288).

Decreased cone density in areas of RNFL thinning was also displayed in glaucoma and other neuropathies (289, 290). Multiple groups have demonstrated that RNFL bundles are lost in areas of scotomas in glaucoma, and that the polarization properties change in the disease course (270, 271, 291). The increased transverse resolution of AO-OCT can also be utilized to better visualize the microstructure of the lamina cribrosa in glaucoma, a site of early damage, and, therefore, aid in earlier diagnosis (291).

The 3D representation of retinal microvasculature with AO-OCT can also make it a valuable tool in the assessment of DR, especially in combination with OCT-A, for study of microaneurysms, vessel tortuosity, and capillary dropout (270, 292–295). Decreased cone density has also been reported to be 10% lower in DR, which could suggest a method for earlier detection (296).

Finally, the cellular identification of either AO-OCT or AO-SLO can be used to study disease mechanisms of inherited color defects and monitor treatment response

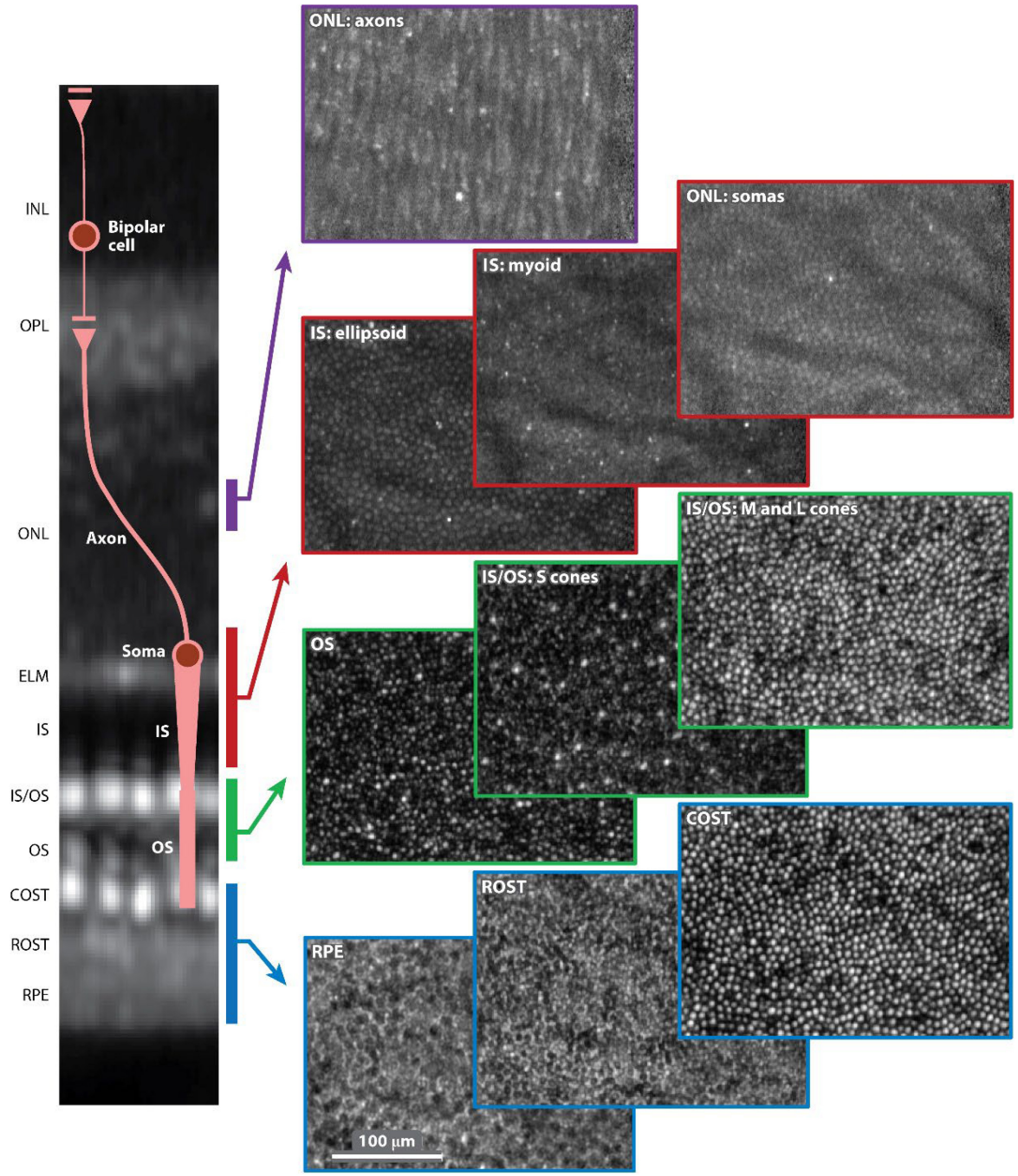

FIGURE 5 | Adaptive optics optical coherence tomography (AO-OCT) volume image of the outer retina of a 52-year-old normal subject. Ten en face (C-scan) images are shown selected from the volume and color-coded by depth in the outer retina, as denoted in the cross-sectional slice (B-scan) on the left. Each C-scan image is normalized to itself and presented on a log intensity scale. The AO-OCT volume image is an average of approximately 2,200 registered volumes that were acquired at 3.7° temporal to the fovea. AO-OCT, adaptive optics optical coherence tomography; COST, cone outer segment tip; ELM, external limiting membrane; INL, inner nuclear layer; IS, inner segment; IS/OS, inner segment/outer segment junction; ONL, outer nuclear layer; OPL, outer plexiform layer; OS, outer segment; ROST, rod outer segment tip; RPE, retinal pigment epithelium. This figure was reprinted from Miller et al. (262) with permission.

in stem cell transplantation therapies for said retinal diseases or central serous chorioretinopathy (280, 297, 298). For treatment of retinitis pigmentosa specifically, multiple AO modalities (AO-OCT and AO-SLO) can be used to stage the disease based on individual cell health, assess visual function from the cellular structure, and select candidates that could benefit from treatment (299, 300).

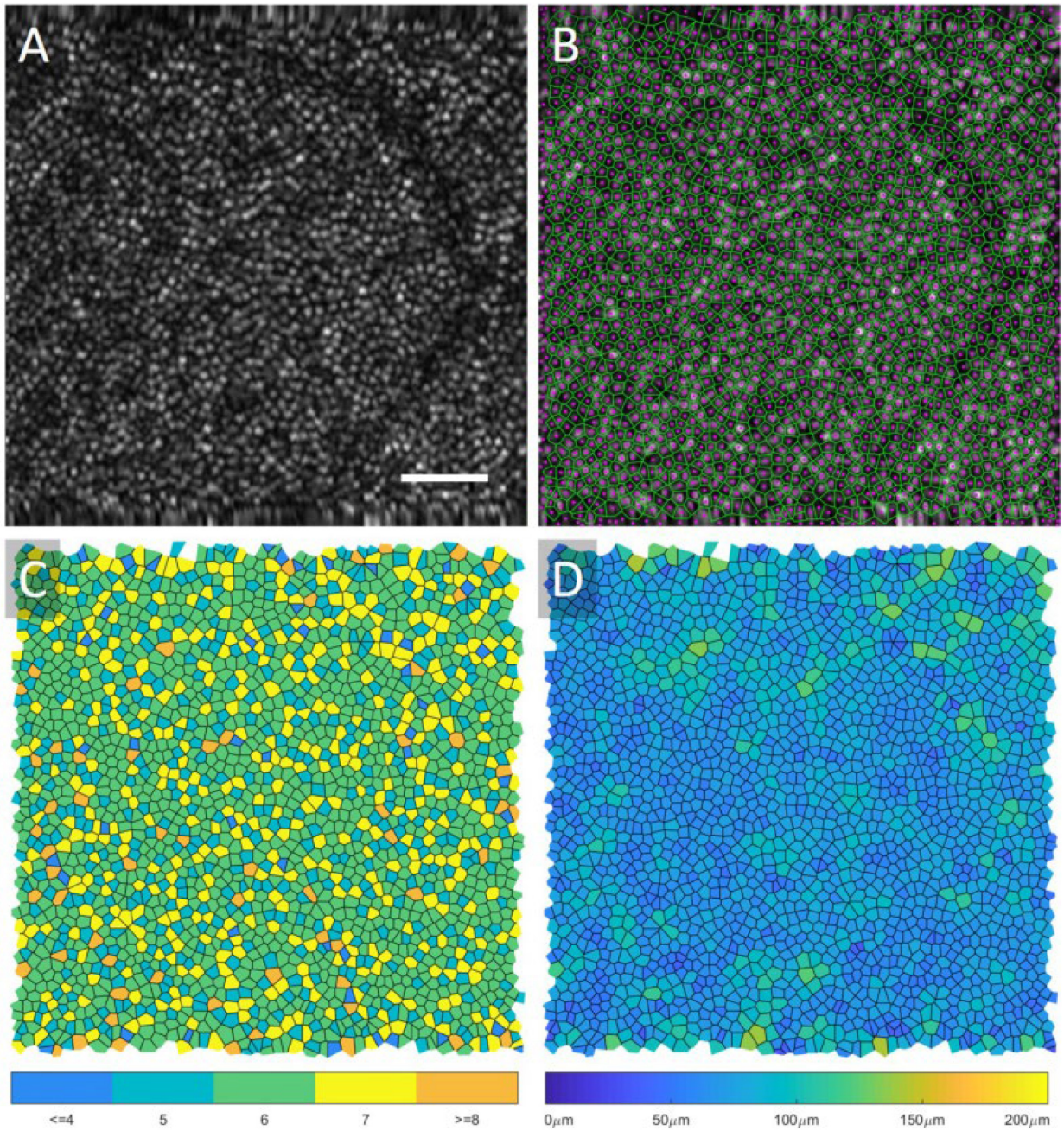

FIGURE 6 | Voronoi analysis of photoreceptors from AO-OCT. An original AO-OCT image taken at ∼6.5° retinal eccentricity is displayed in **(A)**, and the center of the cones (magenta) and the Voronoi map (green) is overlaid onto the image in **(B)**. In **(C)**, the Voronoi cells are shaded based on the number of neighbors, and, in **(D)**, the cells are shaded based on their area. A scale bar, 50 μ m. This figure was reprinted from Heisler et al. (508) with permission.

The application of AO-OCT in routine clinical settings is still challenging, mostly due to high cost, size, and complexity of the devices, time-consuming image acquisition and analysis, a limited scan area (generally no larger than 200 μm × 200 μm transversely), data size, and the lack of established normative databases (280). Some additional limitations are particularly present with specific populations who would benefit from AO applications, for example, unstable fixation in young children with inherited retinal dystrophies. For these reasons, AO-SLO and AO-OCT remain primarily research tools but are applicable to a number of ongoing clinical trials (301).

Despite these challenges, there have been developments over the last few years in the AO systems. Reumueller et al. have recently though developed AO-OCT prototypes that are promising and can be applied in patients with the aforementioned pathologies (302, 303). Improvements over

the standard AO-SD-OCT, such as point-scanning sensorless SD-OCT, computational AO, and line-scanning SD-OCT, are currently being investigated (277, 304, 305). The acquisition speed of images has been improved by various groups up to 1 million A-lines/s, the fastest retinal SD-OCT at the time, while the implementation of AO in SS-OCT systems allows for even higher speeds (262, 269, 291, 306–308). The increased scanning speeds have aided in resolving the issue of motion artifacts, an issue also addressed by means of active retinal tracking (integration of AO-SLO with wide field or tracking SLO) and registration of multiple scans (306, 309–314). The registration and image averaging of scans also allows for temporal tracing of cellular processes in time and improves the SNR and contrast, which make individual cells more apparent; examples include better visualization of the RPE, RGC somas, IPL bands, and hyalocytes on the internal limiting membrane (ILM) (262, 285, 315–319). These cellular parameters are attractive, as they can be used as biomarkers for screening or longitudinal follow-up. As an example, AO-SLO can detect cell destruction in retinal degenerations before the onset of symptoms, which would allow the formation of therapeutic clinical trials, while vision is still salvageable in these patients (280, 320). At the same time, improvements in the axial resolution of OCT devices *via* increasing the bandwidth of imaging sources (greater than 100 nm) have allowed the development of AO ultra-high-resolution OCT (AO-UHR-OCT) (267). Pandiyan et al. implement techniques (increased source bandwidth, improved Nyqyist sampling, increased illumination beam size at the pupil, spherical mirror-based telescopes instead of lens-based telescopes, optimized design software and tools) that improve the resolution of both structure and function, achieving visualization of both individual foveal rods/cones in *en face* projections and RGCs; this has also been achieved by other groups (321, 322).

Phase-Sensitive Optical Coherence Tomography and Optoretinogram

The AO has the potential to capture images of single cells from a snapshot in time. Assessment of the temporal function is also possible through the development of phase-sensitive OCT. It is known that the reflectivity of retinal cells, caused by photoisomerization of pigment chromophores, can vary after application of visual stimuli (optical phase changes) (323). Measurement of these changes is possible with either OCT, hence the term "phase-sensitive OCT" (324). This is the foundational basis of the optoretinogram (ORG), which allows recording of responses to visual stimulation. The ability to detect the function of individual photoreceptors would allow detection of retinal dysfunction in a microscopic scale. As opposed to OCT assessment, where the result is binarized (alive versus lost photoreceptors), ORGs provide a spectrum of function and identify cells that could be salvaged (280).

The implementation of ORG in a clinical setting still has some drawbacks. Studies, so far, have only focused on healthy individuals or patients without severe conditions, whose imaging might pose challenges, such as poor fixation, pathologies hindering image quality, and long periods of dark adaptation not easily tolerable. Furthermore, even after image acquisition, processing of these images is hours long. Despite these difficulties, ORG can potentially be implemented in other devices currently used (SLO and AO-SLO, OCT/OCT-A and AO-OCT) with minimal additions (a stimulus channel and appropriate software) to provide a functional component to structural measurements.

ARTIFICIAL INTELLIGENCE AND INTEGRATED MACHINE LEARNING

The implementation of AI in the field of ophthalmology has been a revelation. Ophthalmology offers a great basis for AI to grow and be utilized, owing to the combination of data availability for highly prevalent conditions (glaucoma, AMD, and DR), which are always rising as the population ages, developments in teleophthalmology, and the reliance of these conditions on low-cost, easily performed images (predominantly fundus images and OCT) (325). AI strives to solve some major obstacles in many aspects of eye care: It can provide valuable feedback for diagnosis, monitoring and follow-up, correct treatment decisions, and prediction of disease course. These benefits are especially relevant to conditions requiring highly specialized care by experts; its use by comprehensive ophthalmologists can provide a highly reliable solution to difficult specialist access, further hindered by the impact of the ongoing pandemic. These obstacles impact specific populations more than others, and broader access to eye care can help unveil true racial variations otherwise attributed to merely genetic differences. Improving medical decisions can also lead to lower eye care cost since the cost of specialist access, referrals, and treatment of advanced eye conditions is very high. As a result, apart from the medical benefits, the implementation of AI also has a strong social aspect, as it could provide solutions to health, clinical, racial, and financial equity.

The utilization of AI in ophthalmic imaging requires the cooperation of a variety of healthcare professionals, including but not limited to physicians, patients, researchers, government officials, and pharmaceutical and imaging device companies. With the collective goal of improving patient care and fostering equity as mentioned above, and with the potential of AI to substantially transform the management of patients, the Collaborative Community on Ophthalmic Imaging (CCOI) was founded in 2019. Experienced experts of the CCOI operate under the values of teamwork, transparency, innovation, and efficiency in a patient-centered approach, strive to resolve any potential issues in eye imaging, and establish the best strategies for the practical use of software in ophthalmology in a way that respects the basic principles of bioethics (325–328).

The Principles of Artificial Intelligence

The foundation of AI is the completion of tasks by computers through mimicking human (natural) intelligence and cognitive functions. Brain neurons receive signals (input), process that information, and generate results (outputs); these neurons are connected and form networks (neural networks – NNs) capable of complex calculations. These calculations are not static, as the brain can learn from previous data and experience. AI replicates

that approach using computer networks, a process referred to as machine learning (ML); inputs are provided to computer models that process them under sets of parameters and give outputs (329). The caveat in that process, which is the basis of supervised learning (SL), is that the real outputs are provided and, accordingly, the model learns to adjust these parameters (training) to calculate the outputs as accurately as possible. Over the past decade, the vast increase in data availability, computer hardware improvement (mostly graphics processing units – GPUs), and the theoretical improvements in NNs have led to an exponential growth of AI.

There are multiple approaches to AI network arrangements, and AI models range from very simple to highly complex. The most simple form of SL is linear regression, where multiple inputs are given to a model that then best adjusts the parameters of each input to provide the most accurate result (330). Logistic regression is an algorithm that adds a sigmoid function to linear regression and displays these results in a probabilistic format (values between 0 and 1) (330). Taking this approach a step further, whereas linear regression tests inputs independently of each other, non-linear regression has the ability to examine interactions between inputs and outputs in several layers (known as multilayer perceptrons), and this is the concept of feed forward neural networks (FFNNs) (330). As the algorithm processes many relationships in several layers, the NN can learn these associations, hence the name deep learning (DL) (331). The metrics of performance for these algorithms are the area under the curve (AUC) in the receiver-operator curve (ROC), sensitivity, specificity, and accuracy.

Specifically in ophthalmology and imaging, NNs have been fine-tuned to process imaging data and are called convolutional NNs (CNNs) (331). Convolution is a mathematical operation that applies filters to images (matrix of parameters) to produce image outputs with different channels (features), whose parameters are continuously tested; this process can be repeated in sequences and actually constructs an FFNN. Inputs can be images in either two- or three-dimensional slices, which is preferred as eye structures between slices are considered as a whole. The final outputs mostly fall into two categories: classification (categorical outputs) or segmentation (image outputs). These can provide both accurate staging of conditions and better-quality images through denoising for clinicians to interpret, since up to 46.3% of SD-OCT scans are prone to artifacts or segmentation errors (330, 332, 333).

Artificial Intelligence and Glaucoma

Glaucoma is a field that has recently attracted a lot of interest in the integration of AI to ophthalmology and imaging due its involvement of multiple eye structures (anterior chamber angle, iris, retina, and ONH), high prevalence, and reliance on multiple methods to establish a diagnosis. Current clinical assessment of glaucoma relies on a combination of various diagnostic tools to assess anatomy, structure, and function, such as gonioscopy, fundus examination of the ONH, tonometry, OCT scans, and perimetry (a visual field) testing, with none being totally sensitive or specific of its own (325, 334). The interpretation of these results also varies among clinicians (335).

The AI can significantly aid in differentiating glaucomatous from healthy eyes. On this matter, emphasis should be given on moderate glaucoma, where symptoms of early vision loss are apparent or very likely (327). DL algorithms can provide segmentation-free image analysis to quantify relevant structures and can even perform better than traditional segmentation approaches of retinal layers (332, 336). For structural assessment, algorithms could detect changes and signs of optic neuropathy from fundus pictures with greater sensitivity and specificity than clinicians (up to 96.2 and 97.7%, respectively); this can be advantageous, given the subjective and inconsistent interpretation by physicians (325, 337–340). AI can be used on fundus pictures to also differentiate glaucoma from other pathologies of the optic disc, such as papilledema, ischemic optic neuropathy, optic nerve atrophy, compressive optic neuropathy, hereditary optic neuropathy, hypoplasia, and toxic optic neuropathy (341–343). The standard modality of assessing structure, though, is OCT imaging; algorithms can provide assessment of the anterior chamber angle as well as segmentation of the RNFL adjusted for other parameters (age, gender, and eye biometry metrics) to improve the accuracy of the measurements (344–346). Studies have focused on many parameters of the retina and ONH (RNFL, prelaminar area, RPE, choroid, peripapillary sclera, Bruch membrane opening, and minimum rim width), and their performance was highly accurate in identifying glaucomatous eyes (>94%); AI analysis of OCT-A vascular abnormalities of the ONH also yields excellent results (347–354). When comparing various ML classifiers, Wu et al. showed that ganglion cell layer measurements were important in early glaucoma detection, whereas RNFL metrics were more useful during disease progression; in fact, Shin et al. showed that wide-field SS-OCT scans can even outperform the conventional parameter-based methods (355–357). In a recent meta-analysis, including data from numerous studies, Wu et al. reported remarkable overall performance in detecting glaucoma from both fundus pictures (AUC, 97%) and OCT (AUC, 96%), with similar outcomes in classifying glaucoma as well (358). Aside from layer segmentation, the analysis of raw unsegmented OCT volumes (feature agnostic approach) of the ONH has been shown to provide better results than classical ML techniques (AUC of 94% versus 89%) (359). The existing issues with AI applications to OCT, though, are the potentially poor image quality, limited generalizability of certain algorithms to multiple devices and patient-specific factors (anatomy and comorbidities) undermining OCT thickness values (325). To detect functional changes in the visual fields, CNN algorithms have been developed by various teams that mark visual field tests as either normal or glaucomatous with high precision (87.4–87.6%) (360, 361).

A very attractive approach is to use AI to combine structural information with functional outcomes. Glaucoma diagnosis is improved when using both ONH parameters and VF outcomes: algorithms capable of predicting 10-2 VF parameters from macular OCT scans, and 24-1 VF parameters from both macular and ONH OCT scans have been developed (362–365). Also, various teams (Lazaridis et al., Christopher et al., Datta et al., and Xiong et al.) have recently developed algorithms (RetiNerveNet and FusionNet) capable of using both OCT metrics (various

layer thickness values) and raw OCT or fundus images to predict VF changes with high accuracy (366–370). Overall, combination of structural and functional information has been shown to outperform structural or functional assessment alone.

These results are especially encouraging when it comes to screening for glaucoma; these imaging techniques are simple and inexpensive and would allow for identification of glaucoma at early stages. As opposed to diagnosis at a more advanced stage, early treatment initiation can both prevent irreversible vision loss and avoid expensive, invasive techniques used for later glaucoma stages, as the cost of management increases with glaucoma progression; its performance, however, still needs to be improved (327). The implementation of DL to AS-OCT is a field-attracting attention; Li et al. have very recently developed a novel 3D deep-learning-based digital gonioscopy system that identified angle closure suspects and that could be used as a screening method for primary angle closure glaucoma (371–376).

AI can also be a valuable tool in establishing the prognosis of glaucomatous progression. Functionally, Wen et al. reported that AI can estimate VF loss up to 5.5 years in the future with minimal error, given only a single test as a starting point (377). Algorithms are also capable of identifying slow disease progression consistently earlier than conventional methods, too (3.5 years versus >3.9 years) (378). Structurally, Christopher et al. reported that RNFL analysis can also predict glaucoma progression more accurately than VF testing (95% versus <86%), and with less error than standard linear regression models (325, 379). Sedai et al. have developed multimodal models using a combination of clinical, structural, and functional information to predict RNFL changes in healthy subjects, patients with glaucoma patients, glaucoma suspects with greater performance than standard linear trend-based estimation (380). These predictive algorithms, however, have not yet been implemented clinically.

Artificial Intelligence and Age-Related Macular Degeneration

With more than 200 million people affected worldwide, AMD constitutes the most common cause of blindness in developed countries (381). Although no AI device has yet been made commercially available for AMD yet, several algorithms to potentially aid physicians' decisions do exist.

Up to 25% of patients with AMD can remain undiagnosed by primary care providers, and the use of AI would not require an advanced skillset to operate or retinal expertise (328, 382). An ideal method of AMD screening should be able to efficiently detect AMD and distinguish it from other similar diseases, be cost-effective, and autonomous. Hence, the low cost and simplicity of fundus photographs make it a great candidate for wide AMD screening; models that can classify AMD based on the need for treatment have been developed, which function with great accuracy compared to professional graders (up to 92%) (383). This distinction is important when evaluating algorithms, as early treatment can significantly prevent vision loss in select cases of AMD (large drusen and intermediate AMD, CNV), and the cost of error is high for missing wet AMD; high sensitivity is, therefore, preferable (384). Macular OCT scans have the advantage of depicting the pathological findings of AMD in 3 dimensions and with high resolution; hence, they can be utilized as a next step, following the initial screening with fundus photographs to rule out false positive cases and further classify the true positives (385). De Fauw et al. have developed a screening algorithm capable of identifying multiple retinal conditions, which was able to outperform retinal specialists on both screening success and avoidance of severe and costly errors (386).

Models can also substantially assist physicians in establishing diagnosis of AMD. This can sometimes be challenging, as AMD findings can potentially go unnoticed or appear similar to other retinal conditions (polypoidal choroidal vasculopathy, macular dystrophies, CSR, and others) (328, 384). For this purpose, a variety of algorithms has been offered, focusing on different imaging modalities (fundus pictures, OCT and OCT-A, FA) to detect multiple pathological findings (drusen and pseudodrusen, intra- and subretinal fluid, GA); similar to DR, structural and vascular biomarkers are also utilized for AMD (387–392). As a representative example, Yan et al. were able to utilize a model for identification of drusen, inactive and active CNV with high precision (84.3–97.7%) and AUC (94.–99.%) (393). Keenan et al. also used SD-OCT data across 10 years from the AREDS2 study to construct a model capable of identifying retinal fluid with high accuracy, sensitivity, and specificity compared to retinal specialists (85.1%, 82.2%, 86.5% versus 80.5%, 46.8%, 97.%, respectively) (394).

Even though the use of AI tools in the context of AMD has not been fully optimized, tools capable of prognosis and monitoring the condition are starting to emerge. Algorithms can perform better than specialists in some cases, but their accuracy can be improved; classification accuracy has been reported to be up to 76% and 5-year prognosis accuracy up to 86% in recent studies (395, 396). For classification, Peng et al. developed a model (DeepSeeNet) that more accurately classified AMD, when compared to retina specialists (397). This is especially important in the setting of edema in wet AMD, where anti-VEGF injections are indicated; Potapenko et al. have recently trained a CNN identifying retinal edema with accuracy of 90.9% (398). Even more so when combined with HH-OCT, algorithms can be proved to be a powerful tool in self-monitoring of the condition and more easily identify patients in need of antiangiogenic treatment. As to predicting the disease course, algorithms will help tackle issues, such as predicting conversion to wet (neovascular) AMD, personalize anti-VEGF treatment and predict their response, and increase the use of supplements to decrease the rate of progression. Sarici et al. have recently reported a set of outer retinal biomarkers (ellipsoid zone and RPE attenuation and thickness) useful to predict evolution of dry AMD to subfoveal GA, while Abdelfattah et al. used drusen volume to predict development of wet AMD within 2 years (399, 400). Finally, tools that could be utilized in predicting response to anti-VEGF treatment have also been developed with accuracy comparable to retinal experts (65.4% vs. 53.8–76.9%) (401). A detailed review of tools for AMD progression prediction by fundus photographs or OCT has been constructed by Romond et al. (402).

The implementation of AI on AMD care still faces some challenges. The limitations of OCT (high cost, artifacts, low signal strength, and poor focus) still apply in this field. There is also a great need for dataset diversity in terms of age, race, and socioeconomic status in data analysis to provide broader and more accurate AI outputs, as baseline factors and phenotypes can vary among populations (389, 403).

In general, the impact of AI tools in the setting of AMD can be proved useful in screening, diagnosis, and differentiation of similar appearing conditions, prognosis, and disease monitoring. Whether or not they can benefit physicians and potentially influence clinical decisions remains to be seen.

Artificial Intelligence and Diabetic Retinopathy

Using AI in the setting of DR is one of the most promising applications in medicine. As opposed to general monitoring of diabetes, which can be performed easily (blood glucose testing, HbA1c levels and others), DR requires qualitative evaluation.

The modalities more commonly used for diagnosis and monitoring of DR are fundus pictures, OCT, and OCT-A scans (as mentioned above). AI has the potential to detect disease in early (even asymptomatic) stages, classify it, predict the disease course, and thus guide treatment in select eyes (404–406). Tools can match or even outperform physicians and can make access to screening broader and less expensive; algorithms and devices are already clinically available (IDx-DR by Digital Diagnostics, Coralville, IA, United States; SELENA+ by EyRIS, Singapore) and have been authorized for use in multiple fundus cameras (407–412). Training models for AI has been steadily increasing for diagnosing DR from fundus pictures, with accuracy, sensitivity, and specificity improving over time (reaching 95.7, 97.5, and 98%, respectively) (412–416).

Similar results are also seen when using CNNs for DR severity grading; Ryu et al. have recently developed a fully automated algorithm to classify DR stages with accuracy of 91–98%, sensitivity of 86–97%, and specificity of 94–99% (417, 418). Application of these models can also establish biomarkers useful for diagnosis and treatment response; these could be structural (retinal layer measurement, hyperreflective foci) or vascular (areas of non-perfusion, vascular leakage, microaneurysm count, and neovascularization) (387).

TELEOPHTHALMOLOGY AND SMARTPHONE FUNDUS IMAGING

Telemedicine is defined as "the use of electronic information and communications technologies to provide and support health care when distance separates the participants" (419). In response to its growing demand in recent years, further enhanced by the COVID-19 pandemic, ophthalmologists have begun to implement techniques and technologies more widely to better facilitate patient care in a remote setting. This would make access to eye care more accessible, easier and more convenient for patients, faster, and more cost-effective. In terms of ophthalmic care, teleophthalmology is mostly applicable to ophthalmic emergencies, screening, and monitoring of chronic conditions.

One such technique is imaging of the eye with a smartphone (smartphone imaging – SI). The use of smartphones for clinical imaging in ophthalmology was first introduced by Lord et al. in 2010 (420). It was demonstrated that an iPhone could be used to capture external photos of the orbit and surrounding structures, indirectly image the anterior segment and the fundus of the eye when used with a slit lamp fitted with a 78D lens or a handheld 20D lens (420).

Since its introduction, external attachments and phone applications that offer features, such as image storage and improved user-interface, have been developed with the aim of improving the image quality and utility of SI. Although many variations and distributors exist, a commonly used attachment is a macro lens that can be clipped over the camera of a smartphone to provide supplemental co-axial illumination, making imaged features of the eye more distinguishable (421). The ability for smartphones to be paired with additional attachments and other devices has given rise to techniques that make it applicable in a wider range of clinical scenarios than most other forms of imaging (421).

The current capability of SI in the observation of anterior segment features is promising. Refined techniques using either gonio or macro lens combinations make it possible to capture high-quality videos and standstill images of the iridocorneal angle (422, 423). A trial conducted by Pujari et al. found that inferior angle measurements acquired using the iPhone-macro lens combination demonstrate excellent correlation with measurements acquired using AS-OCT (424). SI can also be used for the analysis of globe torsion. Using a 360° protractor application, the axis of the eye can be compared between smartphone-macro lens images before and after surgical intervention to quantify torsion of the iris and retina (425, 426). It is possible to perform pupillometry using SI, giving smartphones additional utility in the management of neuro-ophthalmological disease (427, 428). McAnany et al. observed excellent agreement when comparing smartphone pupillometry with infrared camera pupillometry, and found significant correlations in pupillary light reflex and re-dilation size between both methods (429). Additionally, methods have been developed for smartphone photography to be used in measuring implantable contact lens vault and assessing the intraocular lens alignment of patients (430–432).

With respect to posterior segment features and pathology, SI can be used to assess and monitor the fundus of patients. While studies have outlined successful techniques for imaging of the optic disk with smartphones (**Figure 8**) (433–435), Pujari et al. document a strategy to evaluate the ONH using a macro lens phone attachment and 90D handheld lens (436). With a combination of a battery, an LED light source, a barrier, and an excitation filter fitted to an iPhone, Suto et al. also demonstrated for the first time that fundus FA can be captured with a smartphone, producing images comparable to those obtained by indirect ophthalmoscopy (437). More recently, Sivaraman et al. have come forward with a smartphone-coupled device capable of capturing widefield images of the retina beyond

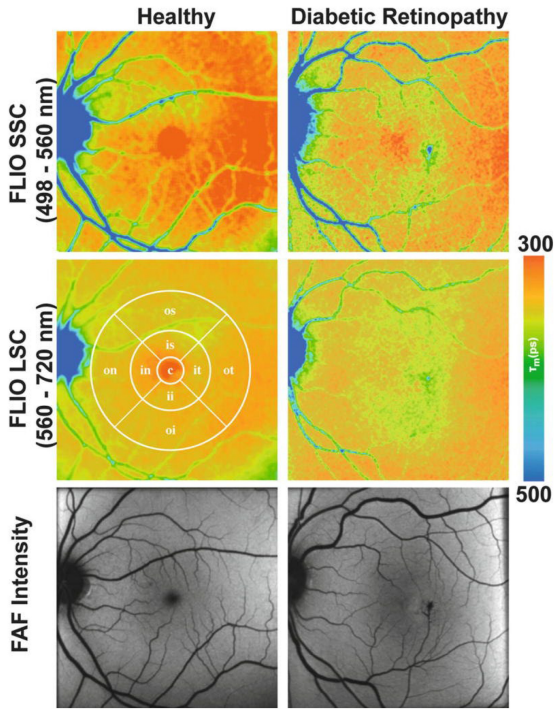

FIGURE 7 | Funds autofluorescence (FAF) lifetime images (FLIO) and FAF intensity images in diabetic retinopathy (DR). Mean funds autofluorescence (FAF) lifetime images (FLIO) from two spectral channels, as well as FAF intensity images from the retina of a healthy control **(Left)** and a diabetic retinopathy patient **(Right)**. The middle left panel comprises a standardized ETDRS grid. This figure was reprinted from Bernstein et al. (455) with permission.

the posterior pole, with a field of view of 65° with a single take (438).

The SI is suited for the screening of common diseases, such as glaucoma, AMD, and DR (439–441). SI-based screening for glaucoma, using frequency doubling technology and a head-mounted display, was found to be comparable to Humphrey VF testing with good agreement and correlation between both techniques (440). Photographs of the ONH can also be acquired with SI, with moderate agreement with in-person evaluation and respectable positive and negative predictive values (77.5 and 82.2%, respectively) (441–443). Home monitoring of IOP with rebound tonometers or contact lenses is also possible (441, 444, 445). Teleophthalmology in the setting of AMD screening mostly aims to detect conversion from dry to neovascular form; Li et al. were the first group to demonstrate similar wait times between remote screening in tertiary clinics and referral to retinal specialists, although with increased wait times for treatment initiation (446). Monitoring for AMD progression with Amsler grids or macular VF testing (for example, a ForeseeHome device by Notal Vision Ltd., Tel Aviv, Israel) is more promising and can be beneficial for high-risk patients (441, 447). For DR, screening can be accomplished with imaging modalities, such as non-mydriatic ultrawide-field and multifield fundus photographs, and has been proved to be reliable and cost-effective; Tan et al. compared smartphone ophthalmoscopy to standardized techniques and found that SI had an overall sensitivity of 87% and specificity of 94% (441, 448–450).

Like with many other current ophthalmic imaging modalities, the future of SI may lie in AI. Algorithms, such as AlexNet, EyeArt, and Medios, are accessible and can be coupled with SI for the screening for disease (451). Studies have demonstrated that SI analysis performed using AI is able to improve the sensitivity and specificity of SI in diagnosing retinal disease (452, 453).

FLUORESCENCE LIFETIME IMAGING OPHTHALMOSCOPY

The retina exhibits intrinsic autofluorescence: reactive to light stimulation, chemical compounds absorb photons, and promote electrons to a higher power state that subsequently return to their stable state, emitting red-shifted protons in the process. The intensity and patterns of fluorescence can be detected with high-sensitivity detectors in fundus cameras and ophthalmoscopes, mapped and used to diagnose and monitor many macular conditions (454). Since the majority of the signals originate from lipofuscin in the RPE, its high intensity predominates and shadows other retinal molecules that also emit fluorescence. The new technique of FLIO measures the decay lifetime of retinal fluorophores (FLIO lifetimes – FLTs), which are unique to molecules (Dysli et al. have described the lifetimes of each fluorophore in detail) and, therefore, more sensitive of weak fluorophores that are masked using fundus autofluorescence (FAF) (455–457). Hence, FLIO can reveal not only structural but also metabolic and biochemical changes in the retina.

In a clinical setting, the first FLIO device used was developed by Heidelberg Engineering in 2012 and has been shown to be highly reproducible (458–460). FLIO patterns have been identified for a variety of retinal diseases and can be valuable in early detection and detailed monitoring. In AMD, FLIO displays a characteristic pattern of ring-shaped prolongation of the FLTs around the fovea, which is present in the early stages of the disease even before the appearance of drusen and increases as the disease progresses (greater in advanced AMD) (461). Apart from this sign, areas of GA and drusen also display FLT prolongation, and this information could be proved useful in the understanding of their pathogenesis and metabolism as well as monitoring their development (461–463). Since AMD can appear similar to Stargardt disease, FLIO can be used to differentiate the two, since FLTs in Stargardt disease are not prolonged, and the typical ring pattern of AMD is not present. Most importantly, retinal flecks in Stargardt disease appear in FLIO about a year earlier than in other imaging methods like FAF (464). In the case of hydroxychloroquine toxicity, where early toxicity detection is challenging, FLIO could provide a better alternative to electroretinogram (ERG) or OCT, since it can detect prolonged FLTs before structural changes appear (465, 466). FLIO has also been used to identify changes in other retinal conditions as well, including DR (**Figure 7**), vascular occlusive diseases, CSR, choroideremia, RP, and macular holes, and is believed to be a promising diagnostic method (463, 467–473).

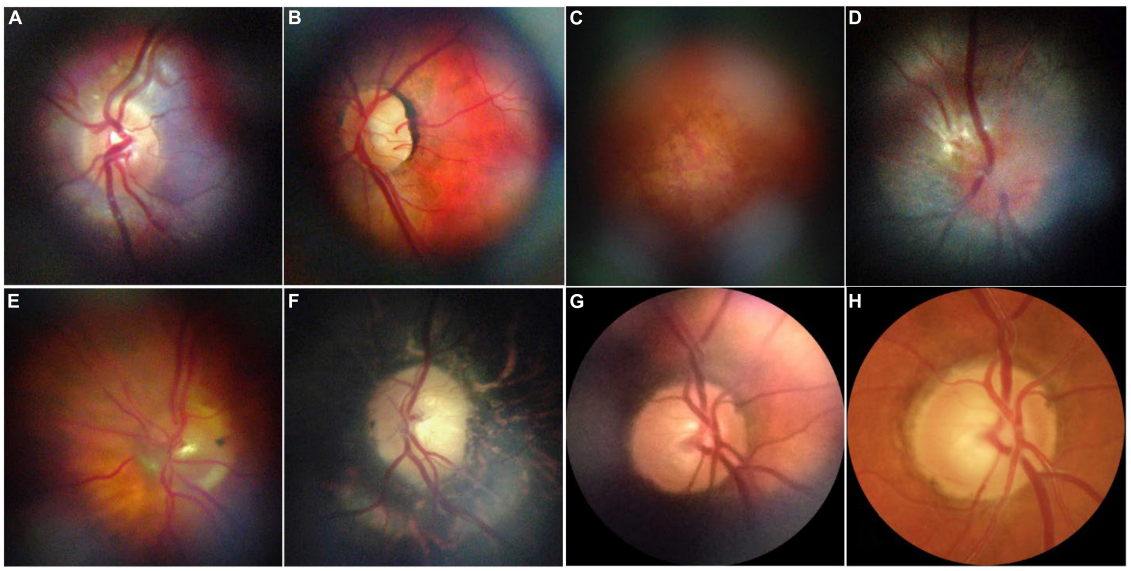

FIGURE 8 | Representative retinal images taken with D-eye. **(A)** A normal optic disk in an undilated child. **(B)** A normal posterior pole in a dilated 29-year-old woman. **(C)** Dry age-related maculopathy in an undilated 75-year-old man. **(D)** Optic nerve glioma in a 23-year-old undilated woman. **(E)** Posterior vitreous detachment in a dilated 72-year-old pseudophakic woman. **(F)** Waxy disk pallor and pigmentary changes in a 50-year-old man with retinitis pigmentosa **(G,H)**. Depiction of the same optic nerve head by D-Eye and Canon CR-2 Retinal Camera. This figure was reprinted from Russo et al. (434) with permission.

MULTIMODAL IMAGING

Multimodal imaging involves the incorporation of two or more imaging technologies for a single purpose. Combinations of imaging modalities make it possible to perform a more comprehensive examination of tissue by compensating for the individual limitations of a single device. Multimodal imaging is often used to improve the utility of commonly used OCT technologies.

The OCT-A is an example of a modality that greatly benefits from multimodal imaging. Although it provides significant clinical utility through its ability to capture the vasculature of the retina, limitations in the acquisition speed of OCT-A create prolonged susceptibility to motion artifacts, and other reductions

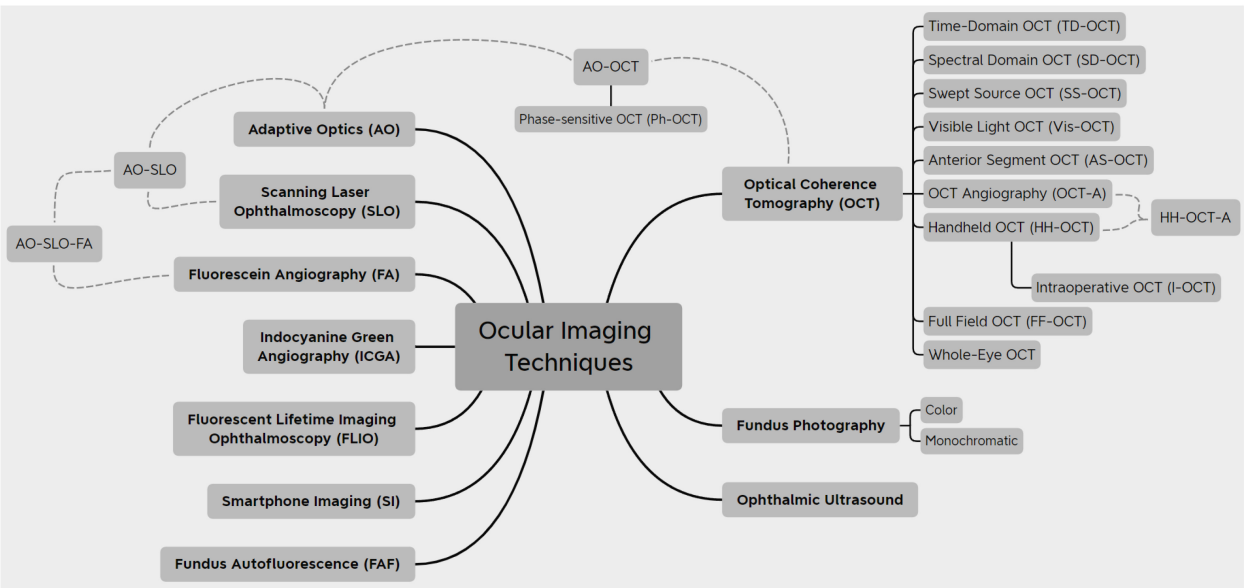

FIGURE 9 | A summary of the modern ocular imaging modalities.

TABLE 1 | Review and evolution of optical coherence tomography (OCT) imaging technologies in chronological order (3, 195, 196, 252, 255, 265, 308, 312, 499–506).

OCT technology	Year introduced	Commercial availability	Axial resolution in tissue (μm)	Lateral resolution in tissue (μm)	Maximum scanning rates (A-scans per second)	Major clinical application(s)	Advantages	Disadvantages
Time-domain OCT (TD-OCT)	1991	Yes	1.7–15	15–20	400	Most retinal pathologies.	Non-contact, non-invasive.	Low image acquisition speed. Poor spatial resolution.
Anterior segment OCT (AS-OCT)	1994	Yes	1.0	15	2,000,000	Anterior segment conditions (dry eye disease, corneal pathologies).	Detailed imaging of most structures of the anterior segment (corneal layers and precorneal tear film, outflow system, anterior chamber).	
Spectral domain OCT (SD-OCT)	2001	Yes	5–8	6–20	100,000 (clinical)	Most retinal pathologies.	Higher imaging speed and sensitivity than TD-OCT. Capture of 3D volumetric data *in vivo*. Retinal layer segmentation.	Imaging artifacts (projection, motion). Segmentation errors.
Full-field OCT	2002	No	5.6	1.7–2.4	40,000,000 (research)	Ocular surface conditions (dry eye disease, corneal inflammation).	Stable phase, no motion artifacts. Higher scanning power supported. Less sensitive to optical aberrations and signal loss.	Eye motion makes scanning difficult. Difficulties with optical path matching. Post-processing and image averaging necessary. Only select retinal layers visible.
Visible light OCT (Vis-OCT)	2002	No	1–1.4	4.6–10	30,000 (research)		Vastly improved axial resolution. Smaller bandwidth for same resolution. Higher image contrast. Oximetry and calculation of circulation metabolic parameters.	Slow imaging.
Adaptive optics OCT (AO-OCT)	2004	Yes	5–8	2–3	1,000,000 (research)		Vastly improved lateral resolution. Improvement of speckle width. Increased SNR. Visualization of single retinal cells and their function (phase-sensitive OCT). Improved lamina cribrosa visualization.	Slow imaging. Multiple scans required for registration. High cost. High complexity of devices. Limited scanning area. Large data size.
Handheld OCT (HH-OCT)	2007	Yes Yes	3–6	8–15	32,000 (clinical). 350,000 (research).	Pediatric conditions (congenital and pediatric glaucoma, macular edema, macular hole, epiretinal membrane, retinoschisis, retinal dystrophies). Intraoperative OCT (see below).	Imaging of challenging patient populations (bedridden and postoperative patients, children, remote access). Less expensive than benchtop OCT. Imaging of anterior and posterior segments in quick succession.	Probes still connected to bulky mobile carts.

(Continued)

TABLE 1 | (Continued)

OCT technology	Year introduced	Commercial availability	Axial resolution in tissue (μm)	Lateral resolution in tissue (μm)	Maximum scanning rates (A-scans per second)	Major clinical application(s)	Advantages	Disadvantages
Intraoperative OCT (I-OCT)						Glaucoma surgeries (trabeculectomies, drainage surgeries, canaloplasty, sclerectomy, and angle surgeries). Cornea surgeries (DALK, DSEK/DSAEK, DMEK). Cataract extraction surgeries. Retinal surgeries (ERM peeling, macular hole repair, gene therapies).	Live imaging feedback during surgery. Valuable information on diagnosis and surgery planning. Confirmation of optimal outcome. Assessment of intraoperative complications.	Technician often required. Pausing of surgery sometimes necessary.
Swept source OCT (SS-OCT)	2012	Yes	8–9	20	200,000 (clinical). 6,700,000 (research).	Most retinal pathologies.	Increased SNR. Improved scan quality. Improved imaging of deeper structures.	
Whole-eye OCT	2012	Yes	12.4–19	73	50,000–580,000 (clinical).	Biometry. Surgery planning (cataract extraction and refractive surgeries). Identification of high myopia causality.	Assessment of the entire ocular anatomy with a single scan in standard fields of view.	Time gap for switching scan configurations between anterior-posterior segment
OCT angiography (OCT-A)	2015	Yes	5	15–24 8–16 (ultra high-definition)	200,000 (clinical).	Conditions involving vasculature damage or neovascularization (glaucoma, AMD, DR, BRVO).	Lack of extrinsic dye. Vascular network imaging at different depths. Vascular biomarker identification.	No detection of vessel leakage. Imaging artifacts (projection and motion). Visibility of vessels dependent on flow. Low image contrast. Limited area of visualization.

in image quality. Combining OCT-A, as well as other OCT variations, with SLO (OCT-SLO) allows for the implementation of motion tracking to compensate for involuntary eye movements during imaging (474–477). Commercially available systems that already currently use integrated OCT-SLO technology include the Zeiss PLEX Elite, Heidelberg Spectralis, and Optos Silverstone. Handheld OCT-SLO devices have also been implemented and have expanded the accessibility of multimodal imaging for pediatric, bedridden, and immobilized patients (143, 144). Additionally, OCT-A devices can be combined with vis-OCT to establish a complementary endogenous contrast, which allows for blood oxygen saturation to be quantified and used as a biomarker for DR and AMD (96, 102, 105, 106, 478–482).

While no clinical system is commercially available, photoacoustic microscopy (PAM) is an imaging modality that can be used in ophthalmology to detect the distribution of emitted acoustic waves in vascular tissue, with the ability to map blood absorption without the use of exogenous contrast. Combining PAM with OCT imaging establishes complementary structural and vascular contrast, which has been used to capture neovascularization associated with DR and wet AMD in animal models (483–487). Nguyen et al. further demonstrated that the multimodal combination of PAM with OCT has utility in monitoring vascular and structural changes associated with vascular occlusion (488, 489). PAM has additionally been combined with Doppler OCT to measure retinal oxygen metabolism with the potential to aid in an earlier diagnosis of DR, AMD, and glaucoma (478, 490).

Other experimental imaging techniques that have begun to make headway in multimodal research include polarization-sensitive OCT, photothermal OCT, and optical coherence elastography, which, when combined with more standard techniques, have been shown to allow for the differentiation between depolarizing and birefringent tissue (491, 492), establishment of molecular contrast (493–496), and biomechanical assessment of tissue, respectively (497, 498).

CONCLUSION

The field of ocular imaging is rapidly advancing. The sheer number of imaging modalities that exist nowadays

provides physicians and researchers with a substantially high number to study eye conditions and gather information. This variety of available technologies (**Figure 9**) provides a multimodal approach to eye imaging, which will inevitably lead to optimization of imaging techniques for each condition individually.

Most innovations are centered around OCT, since it has become the gold standard of managing most retinal diseases; a summary of the OCT imaging modalities is displayed in **Table 1**. As hardware components and image processing improve, OCT is bound to be improved in multiple ways: faster and higher quality scanning, lower costs, and greater population coverage. These are applications that can be applied worldwide and elevate the standard, commercially available OCT scanner. Some of the new technologies described previously, such as AS-OCT, I-OCT, and HH-OCT, are beginning to be used more widely and are already making a significant impact on medical decisions. Others, like Vis-OCT, FF-OCT, and AO-OCT, that are still rapidly evolving, will undoubtedly be improved and optimized for routine clinical use.

The most exciting prospect of eye imaging is the incorporation of AI. AI is becoming more accessible and broadly studied, and ophthalmology provides the perfect foundation for its rapid evolution. As such, it is fairly safe to assume that ophthalmology will be among the first medical specialties to transition from a traditional, physician-only care approach to a collaboration between human and software decision-making. The ability to provide valuable data from simple images can help millions of people get eye care in the first place but also improve and optimize the way patients are managed and treated. There are still, though, issues to be considered before safely applying AI in the routine care; these range from mostly technical, namely, the issue of performing AI tasks in most imaging devices, to medical in order to ensure its efficacy and reliability, as well as ethical. Despite these hurdles, AI will be a huge step toward ultimately decreasing blindness and providing equal health care across the entire population.

In conclusion, the evolution of ocular imaging is truly fascinating. The next years will be critical in its evolution and will definitely contribute to the ultimate goals of minimizing blindness and ensuring optimal care for patients.

AUTHOR CONTRIBUTIONS

JS and PA contributed to conception and design of the study. JS, PA, and CM acquired the data and performed the analysis. PA and CM wrote the first draft of the manuscript. JS, PA, CM, and GW contributed to manuscript revision and approved the submitted version and took responsibility for the integrity of the data and the accuracy of the data analysis. All authors contributed to the article and approved the submitted version.

FUNDING

This study was supported by National Institutes of Health (Bethesda, MD, United States) R01-EY013178 (JS) and U01-EY033001 (JS). An unrestricted grant from Research to Prevent Blindness (New York, NY, United States) to the Department of Ophthalmology, NYU Langone Health, NYU Grossman School of Medicine, New York, NY, United States.

REFERENCES

1. Huang D, Swanson EA, Lin CP, Schuman JS, Stinson WG, Chang W, et al. Optical coherence tomography. *Science.* (1991) 254:1178–81. doi: 10.1126/science.1957169
2. Danielson BL, Boisrobert CY. Absolute optical ranging using low coherence interferometry. *Appl Opt.* (1991) 30:2975–9. doi: 10.1364/AO.30.002975
3. Qin J, An L. Optical coherence tomography for ophthalmology imaging. *Adv Exp Med Biol.* (2021) 3233:197–216. doi: 10.1007/978-981-15-7627-0_10
4. Fujimoto J, Swanson E. The development, commercialization, and impact of optical coherence tomography. *Invest Ophthalmol Vis Sci.* (2016) 57:Oct1–13. doi: 10.1167/iovs.16-19963
5. Geevarghese A, Wollstein G, Ishikawa H, Schuman JS. Optical coherence tomography and glaucoma. *Annu Rev Vis Sci.* (2021) 7:693–726. doi: 10.1146/annurev-vision-100419-111350
6. Leitgeb R, Hitzenberger C, Fercher A. Performance of fourier domain vs. time domain optical coherence tomography. *Opt Express.* (2003) 11:889–94. doi: 10.1364/OE.11.000889
7. Wojtkowski M, Leitgeb R, Kowalczyk A, Bajraszewski T, Fercher AF. In vivo human retinal imaging by Fourier domain optical coherence tomography. *J Biomed Opt.* (2002) 7:457–63. doi: 10.1117/1.1482379
8. Gabriele ML, Wollstein G, Ishikawa H, Xu J, Kim J, Kagemann L, et al. Three dimensional optical coherence tomography imaging: advantages and advances. *Prog Retin Eye Res.* (2010) 29:556–79. doi: 10.1016/j.preteyeres.2010.05.005
9. Jia Y, Tan O, Tokayer J, Potsaid B, Wang Y, Liu JJ, et al. Split-spectrum amplitude-decorrelation angiography with optical coherence tomography. *Opt Express.* (2012) 20:4710–25. doi: 10.1364/OE.20.004710
10. Freund KB, Gattoussi S, Leong BCS. Dense B-Scan optical coherence tomography angiography. *Am J Ophthalmol.* (2018) 190:78–88. doi: 10.1016/j.ajo.2018.03.029
11. Fang L, Li S, Nie Q, Izatt JA, Toth CA, Farsiu S, et al. Sparsity based denoising of spectral domain optical coherence tomography images. *Biomed Opt Express.* (2012) 3:927–42. doi: 10.1364/BOE.3.000927
12. Xu D, Huang Y, Kang JU. Volumetric (3D) compressive sensing spectral domain optical coherence tomography. *Biomed Opt Express.* (2014) 5:3921–34. doi: 10.1364/BOE.5.003921
13. Xu D, Vaswani N, Huang Y, Kang JU. Modified compressive sensing optical coherence tomography with noise reduction. *Opt Lett.* (2012) 37:4209–11. doi: 10.1364/OL.37.004209
14. Schwartz S, Liu C, Wong A, Clausi DA, Fieguth P, Bizheva K, et al. Energy-guided learning approach to compressive FD-OCT. *Opt Express.* (2013) 21:329–44. doi: 10.1364/OE.21.000329
15. Xu D, Huang Y, Kang JU. Compressive sensing with dispersion compensation on non-linear wavenumber sampled spectral domain optical coherence tomography. *Biomed Opt Express.* (2013) 4:1519–32. doi: 10.1364/BOE.4.001519
16. Xu D, Huang Y, Kang JU. Real-time compressive sensing spectral domain optical coherence tomography. *Opt Lett.* (2014) 39:76–9. doi: 10.1364/OL.39.000076
17. Xu D, Huang Y, Kang JU. Real-time dispersion-compensated image reconstruction for compressive sensing spectral domain optical coherence tomography. *J Opt Soc Am A Opt Image Sci Vis.* (2014) 31:2064–9. doi: 10.1364/JOSAA.31.002064
18. Yi L, Sun L. Full-depth compressive sensing spectral-domain optical coherence tomography based on a compressive dispersion encoding method. *Appl Opt.* (2018) 57:9316–21. doi: 10.1364/AO.57.009316

19. Yi L, Sun L, Zou M, Hou B. Dual-channel spectral domain optical coherence tomography based on a single spectrometer using compressive sensing. *Sensors (Basel).* (2019) 19:4006. doi: 10.3390/s19184006
20. Yi L, Guo X, Sun L, Hou B. Structural and functional sensing of biotissues based on compressive sensing spectral domain optical coherence tomography. *Sensors (Basel).* (2019) 19:4208. doi: 10.3390/s19194208
21. Tan B, Wong A, Bizheva K. Enhancement of morphological and vascular features in OCT images using a modified Bayesian residual transform. *Biomed Opt Express.* (2018) 9:2394–406. doi: 10.1364/BOE.9.002394
22. Anegondi N, Kshirsagar A, Mochi TB, Sinha Roy A. Quantitative comparison of retinal vascular features in optical coherence tomography angiography images from three different devices. *Ophthalmic Surg Lasers Imaging Retina.* (2018) 49:488–96. doi: 10.3928/23258160-20180628-04
23. Mochi T, Anegondi N, Girish M, Jayadev C, Sinha Roy A. Quantitative comparison between optical coherence tomography angiography and fundus fluorescein angiography images: effect of vessel enhancement. *Ophthalmic Surg Lasers Imaging Retina.* (2018) 49:e175–81. doi: 10.3928/23258160-20181101-15
24. Taibouni K, Chenoune Y, Miere A, Colantuono D, Souied E, Petit E, et al. Automated quantification of choroidal neovascularization on Optical Coherence Tomography Angiography images. *Comput Biol Med.* (2019) 114:103450. doi: 10.1016/j.compbiomed.2019.103450
25. Chua J, Tan B, Ang M, Nongpiur ME, Tan AC, Najjar RP, et al. Future clinical applicability of optical coherence tomography angiography. *Clin Exp Optom.* (2019) 102:260–9. doi: 10.1111/cxo.12854
26. Anvari P, Ashrafkhorasani M, Habibi A, Falavarjani KG. Artifacts in optical coherence tomography angiography. *J Ophthalmic Vis Res.* (2021) 16:271–86. doi: 10.18502/jovr.v16i2.9091
27. Tan B, Sim R, Chua J, Wong DWK, Yao X, Garhofer G, et al. Approaches to quantify optical coherence tomography angiography metrics. *Ann Transl Med.* (2020) 8:1205. doi: 10.21037/atm-20-3246
28. Ghassemi F, Berijani S, Babeli A, Faghihi H, Gholizadeh A, Sabour S, et al. The quantitative measurements of choroidal thickness and volume in diabetic retinopathy using optical coherence tomography and optical coherence tomography angiography; correlation with vision and foveal avascular zone. *BMC Ophthalmol.* (2022) 22:3. doi: 10.1186/s12886-021-02178-w
29. Xu B, Chen J, Zhang S, Shen S, Lan X, Chen Z, et al. Association between the severity of diabetic retinopathy and optical coherence tomography angiography metrics. *Front Endocrinol (Lausanne).* (2021) 12:777552. doi: 10.3389/fendo.2021.777552
30. Kalra G, Zarranz-Ventura J, Chahal R, Bernal-Morales C, Lupidi M, Chhablani J, et al. Optical coherence tomography (OCT) angiolytics: a review of OCT angiography quantitative biomarkers. *Surv Ophthalmol.* (2021) 67:1118–34. doi: 10.1016/j.survophthal.2021.11.002
31. Hsu CR, Lai TT, Hsieh YT, Ho TC, Yang CM, Yang CH, et al. Combined quantitative and qualitative optical coherence tomography angiography biomarkers for predicting active neovascular age-related macular degeneration. *Sci Rep.* (2021) 11:18068. doi: 10.1038/s41598-021-97652-2
32. Arrigo A, Perra C, Aragona E, Giusto D, Bandello F, Battaglia Parodi M, et al. Total flow intensity, active flow intensity and volume related flow intensity as new quantitative metrics in optical coherence tomography angiography. *Sci Rep.* (2021) 11:9094. doi: 10.1038/s41598-021-88681-y
33. Wang W, Lo ACY. Diabetic retinopathy: pathophysiology and treatments. *Int J Mol Sci.* (2018) 19:1816. doi: 10.3390/ijms19061816
34. Heng LZ, Comyn O, Peto T, Tadros C, Ng E, Sivaprasad S, et al. Diabetic retinopathy: pathogenesis, clinical grading, management and future developments. *Diabet Med.* (2013) 30:640–50. doi: 10.1111/dme.12089
35. Mohamed Q, Gillies MC, Wong TY. Management of diabetic retinopathy: a systematic review. *JAMA.* (2007) 298:902–16. doi: 10.1001/jama.298.8.902
36. Scarinci F, Nesper PL, Fawzi AA. Deep retinal capillary nonperfusion is associated with photoreceptor disruption in diabetic macular ischemia. *Am J Ophthalmol.* (2016) 168:129–38. doi: 10.1016/j.ajo.2016.05.002
37. Moore J, Bagley S, Ireland G, McLeod D, Boulton ME. Three dimensional analysis of microaneurysms in the human diabetic retina. *J Anat.* (1999) 194(Pt 1):89–100. doi: 10.1046/j.1469-7580.1999.19410089.x
38. Hasegawa N, Nozaki M, Takase N, Yoshida M, Ogura Y. New insights into microaneurysms in the deep capillary plexus detected by optical coherence tomography angiography in diabetic macular edema. *Invest Ophthalmol Vis Sci.* (2016) 57:OCT348–55. doi: 10.1167/iovs.15-18782
39. Carnevali A, Sacconi R, Corbelli E, Tomasso L, Querques L, Zerbini G, et al. Optical coherence tomography angiography analysis of retinal vascular plexuses and choriocapillaris in patients with type 1 diabetes without diabetic retinopathy. *Acta Diabetol.* (2017) 54:695–702. doi: 10.1007/s00592-017-0996-8
40. Onishi AC, Nesper PL, Roberts PK, Moharram GA, Chai H, Liu L, et al. Importance of considering the middle capillary plexus on OCT angiography in diabetic retinopathy. *Invest Ophthalmol Vis Sci.* (2018) 59:2167–76. doi: 10.1167/iovs.17-23304
41. Parravano M, De Geronimo D, Scarinci F, Querques L, Virgili G, Simonett JM, et al. Diabetic microaneurysms internal reflectivity on spectral-domain optical coherence tomography and optical coherence tomography angiography detection. *Am J Ophthalmol.* (2017) 179:90–6. doi: 10.1016/j.ajo.2017.04.021
42. Schreur V, Domanian A, Liefers B, Venhuizen FG, Klevering BJ, Hoyng CB, et al. Morphological and topographical appearance of microaneurysms on optical coherence tomography angiography. *Br J Ophthalmol.* (2018):bjohthalmol–2018–312258. [Online ahead of print], doi: 10.1136/bjophthalmol-2018-312258
43. Ishibazawa A, Nagaoka T, Yokota H, Takahashi A, Omae T, Song YS, et al. Characteristics of retinal neovascularization in proliferative diabetic retinopathy imaged by optical coherence tomography angiography. *Invest Ophthalmol Vis Sci.* (2016) 57:6247–55. doi: 10.1167/iovs.16-20210
44. Savastano MC, Federici M, Falsini B, Caporossi A, Minnella AM. Detecting papillary neovascularization in proliferative diabetic retinopathy using optical coherence tomography angiography. *Acta Ophthalmol.* (2018) 96:321–3. doi: 10.1111/aos.13166
45. Palma F, Camacho P. The role of optical coherence tomography angiography to detect early microvascular changes in diabetic retinopathy: a systematic review. *J Diabetes Metab Disord.* (2021) 20:1957–74. doi: 10.1007/s40200-021-00886-0
46. Ong JX, Fawzi AA. Perspectives on diabetic retinopathy from advanced retinal vascular imaging. *Eye (Lond).* (2022) 36:319–27. doi: 10.1038/s41433-021-01825-2
47. Russell JF, Han IC. Toward a new staging system for diabetic retinopathy using wide field swept-source optical coherence tomography angiography. *Curr Diab Rep.* (2021) 21:28. doi: 10.1007/s11892-021-01401-8
48. Cicinelli MV, Rabiolo A, Marchese A, de Vitis L, Carnevali A, Querques L, et al. Choroid morphometric analysis in non-neovascular age-related macular degeneration by means of optical coherence tomography angiography. *Br J Ophthalmol.* (2017) 101:1193–200. doi: 10.1136/bjophthalmol-2016-309481
49. Nesper PL, Soetikno BT, Fawzi AA. Choriocapillaris nonperfusion is associated with poor visual acuity in eyes with reticular pseudodrusen. *Am J Ophthalmol.* (2017) 174:42–55. doi: 10.1016/j.ajo.2016.10.005
50. Choi W, Moult EM, Waheed NK, Adhi M, Lee B, Lu CD, et al. Ultrahigh-speed, swept-source optical coherence tomography angiography in nonexudative age-related macular degeneration with geographic atrophy. *Ophthalmology.* (2015) 122:2532–44. doi: 10.1016/j.ophtha.2015.08.029
51. Sacconi R, Corbelli E, Carnevali A, Querques L, Bandello F, Querques G, et al. Optical coherence tomography angiography in geographic atrophy. *Retina.* (2018) 38:2350–5. doi: 10.1097/IAE.0000000000001873
52. Corbelli E, Sacconi R, Rabiolo A, Mercuri S, Carnevali A, Querques L, et al. Optical coherence tomography angiography in the evaluation of geographic atrophy area extension. *Invest Ophthalmol Vis Sci.* (2017) 58:5201–8. doi: 10.1167/iovs.17-22508
53. Jiang X, Shen M, Wang L, de Sisternes L, Durbin MK, Feuer W, et al. Validation of a novel automated algorithm to measure drusen volume and area using swept source optical coherence tomography angiography. *Transl Vis Sci Technol.* (2021) 10:11. doi: 10.1167/tvst.10.4.11
54. Kuehlewein L, Bansal M, Lenis TL, Iafe NA, Sadda SR, Bonini Filho MA, et al. Optical coherence tomography angiography of Type 1 neovascularization in age-related macular degeneration. *Am J Ophthalmol.* (2015) 160:739–48.e2. doi: 10.1016/j.ajo.2015.06.030
55. Kuehlewein L, Dansingani KK, de Carlo TE, Bonini Filho MA, Iafe NA, Lenis TL, et al. Optical coherence tomography angiography of Type 3

neovascularization secondary to age-related macular degeneration. *Retina.* (2015) 35:2229–35. doi: 10.1097/IAE.0000000000000835
56. Costanzo E, Miere A, Querques G, Capuano V, Jung C, Souied EH, et al. Type 1 choroidal neovascularization lesion size: indocyanine green angiography versus optical coherence tomography angiography. *Invest Ophthalmol Vis Sci.* (2016) 57:OCT307–13. doi: 10.1167/iovs.15-18830
57. Farecki ML, Gutfleisch M, Faatz H, Rothaus K, Heimes B, Spital G, et al. Characteristics of type 1 and 2 CNV in exudative AMD in OCT-Angiography. *Graefes Arch Clin Exp Ophthalmol.* (2017) 255:913–21. doi: 10.1007/s00417-017-3588-y
58. Phasukkijwatana N, Tan ACS, Chen X, Freund KB, Sarraf D. Optical coherence tomography angiography of type 3 neovascularisation in age-related macular degeneration after antiangiogenic therapy. *Br J Ophthalmol.* (2017) 101:597–602. doi: 10.1136/bjophthalmol-2016-308815
59. Schneider EW, Fowler SC. Optical coherence tomography angiography in the management of age-related macular degeneration. *Curr Opin Ophthalmol.* (2018) 29:217–25. doi: 10.1097/ICU.0000000000000469
60. Faridi A, Jia Y, Gao SS, Huang D, Bhavsar KV, Wilson DJ, et al. Sensitivity and specificity of OCT angiography to detect choroidal neovascularization. *Ophthalmol Retina.* (2017) 1:294–303. doi: 10.1016/j.oret.2017.02.007
61. Jia Y, Bailey ST, Wilson DJ, Tan O, Klein ML, Flaxel CJ, et al. Quantitative optical coherence tomography angiography of choroidal neovascularization in age-related macular degeneration. *Ophthalmology.* (2014) 121:1435–44. doi: 10.1016/j.ophtha.2014.01.034
62. Miere A, Querques G, Semoun O, Amoroso F, Zambrowski O, Chapron T, et al. Optical coherence tomography angiography changes in early Type 3 neovascularization after anti-vascular endothelial growth factor treatment. *Retina.* (2017) 37:1873–9. doi: 10.1097/IAE.0000000000001447
63. Miere A, Querques G, Semoun O, El Ameen A, Capuano V, Souied EH, et al. Optical coherence tomography angiography in early Type 3 neovascularization. *Retina.* (2015) 35:2236–41. doi: 10.1097/IAE.0000000000000834
64. Roisman L, Zhang Q, Wang RK, Gregori G, Zhang A, Chen CL, et al. Optical coherence tomography angiography of asymptomatic neovascularization in intermediate age-related macular degeneration. *Ophthalmology.* (2016) 123:1309–19. doi: 10.1016/j.ophtha.2016.01.044
65. Cherecheanu AP, Garhofer G, Schmidl D, Werkmeister R, Schmetterer L. Ocular perfusion pressure and ocular blood flow in glaucoma. *Curr Opin Pharmacol.* (2013) 13:36–42. doi: 10.1016/j.coph.2012.09.003
66. Nakazawa T. Ocular blood flow and influencing factors for glaucoma. *Asia Pac J Ophthalmol (Phila).* (2016) 5:38–44. doi: 10.1097/APO.0000000000000183
67. Geyman LS, Garg RA, Suwan Y, Trivedi V, Krawitz BD, Mo S, et al. Peripapillary perfused capillary density in primary open-angle glaucoma across disease stage: an optical coherence tomography angiography study. *Br J Ophthalmol.* (2017) 101:1261–8. doi: 10.1136/bjophthalmol-2016-309642
68. Chihara E, Dimitrova G, Amano H, Chihara T. Discriminatory power of superficial vessel density and prelaminar vascular flow index in eyes with glaucoma and ocular hypertension and normal eyes. *Invest Ophthalmol Vis Sci.* (2017) 58:690–7. doi: 10.1167/iovs.16-20709
69. Triolo G, Rabiolo A, Shemonski ND, Fard A, Di Matteo F, Sacconi R, et al. Optical coherence tomography angiography macular and peripapillary vessel perfusion density in healthy subjects, glaucoma suspects, and glaucoma patients. *Invest Ophthalmol Vis Sci.* (2017) 58:5713–22. doi: 10.1167/iovs.17-22865
70. Shoji T, Zangwill LM, Akagi T, Saunders LJ, Yarmohammadi A, Manalastas PIC, et al. Progressive macula vessel density loss in primary open-angle glaucoma: a longitudinal study. *Am J Ophthalmol.* (2017) 182:107–17. doi: 10.1016/j.ajo.2017.07.011
71. Wang X, Jiang C, Ko T, Kong X, Yu X, Min W, et al. Correlation between optic disc perfusion and glaucomatous severity in patients with open-angle glaucoma: an optical coherence tomography angiography study. *Graefes Arch Clin Exp Ophthalmol.* (2015) 253:1557–64. doi: 10.1007/s00417-015-3095-y
72. Rao HL, Pradhan ZS, Weinreb RN, Reddy HB, Riyazuddin M, Dasari S, et al. Regional comparisons of optical coherence tomography angiography vessel density in primary open-angle glaucoma. *Am J Ophthalmol.* (2016) 171:75–83. doi: 10.1016/j.ajo.2016.08.030
73. Nishida T, Moghimi S, Hou H, Proudfoot JA, Chang AC, David RCC, et al. Long-term reproducibility of optical coherence tomography angiography in healthy and stable glaucomatous eyes. *Br J Ophthalmol.* (2021):bjohthalmol–2021–320034. [Online ahead of print], doi: 10.1136/bjophthalmol-2021-320034
74. Lee JY, Shin JW, Song MK, Hong JW, Kook MS. Baseline vessel density parameters for predicting visual field progression in open-angle glaucoma eyes with central visual field damage. *Am J Ophthalmol.* (2021) 237:241–58. doi: 10.1016/j.ajo.2021.11.028
75. Shin JD, Wolf AT, Harris A, Verticchio Vercellin A, Siesky B, Rowe LW, et al. Vascular biomarkers from optical coherence tomography angiography and glaucoma: where do we stand in 2021? *Acta Ophthalmol.* (2022) 100:e377–85. doi: 10.1111/aos.14982
76. Zhu Q, Chen C, Yao J. Vessel density and retinal thickness from optical coherence tomography angiography as new indexes in adolescent myopia. *J Ophthalmol.* (2021) 2021:6069833. doi: 10.1155/2021/6069833
77. Kawai K, Murakami T, Sakaguchi S, Yamada T, Kadomoto S, Uji A, et al. Peripheral chorioretinal imaging through a front prism on optical coherence tomography angiography. *Transl Vis Sci Technol.* (2021) 10:36. doi: 10.1167/tvst.10.14.36
78. Kawai K, Uji A, Miyazawa T, Yamada T, Amano Y, Miyagi S, et al. Prevention of image quality degradation in wider field optical coherence tomography angiography images via image averaging. *Transl Vis Sci Technol.* (2021) 10:16. doi: 10.1167/tvst.10.13.16
79. Miao Y, Siadati M, Song J, Ma D, Jian Y, Beg MF, et al. Phase-corrected buffer averaging for enhanced OCT angiography using FDML laser. *Opt Lett.* (2021) 46:3833–6. doi: 10.1364/OL.430915
80. Nesper PL, Fawzi AA. New method for reducing artifactual flow deficits caused by compensation techniques in the choriocapillaris with optical coherence tomography angiography. *Retina.* (2022) 42:328–35. doi: 10.1097/IAE.0000000000003313
81. Wei W, Cogliati A, Canavesi C. Model-based optical coherence tomography angiography enables motion-insensitive vascular imaging. *Biomed Opt Express.* (2021) 12:2149–70. doi: 10.1364/BOE.420091
82. Zhang Q, Zhang A, Lee CS, Lee AY, Rezaei KA, Roisman L, et al. Projection artifact removal improves visualization and quantitation of macular neovascularization imaged by optical coherence tomography angiography. *Ophthalmol Retina.* (2017) 1:124–36. doi: 10.1016/j.oret.2016.08.005
83. Mehta N, Cheng Y, Alibhai AY, Duker JS, Wang RK, Waheed NK, et al. Optical coherence tomography angiography distortion correction in widefield montage images. *Quant Imaging Med Surg.* (2021) 11:928–38. doi: 10.21037/qims-20-791
84. Cheng Y, Chu Z, Wang RK. Robust three-dimensional registration on optical coherence tomography angiography for speckle reduction and visualization. *Quant Imaging Med Surg.* (2021) 11:879–94. doi: 10.21037/qims-20-751
85. Ploner SB, Kraus MF, Moult EM, Husvogt L, Schottenhamml J, Yasin Alibhai A, et al. Efficient and high accuracy 3-D OCT angiography motion correction in pathology. *Biomed Opt Express.* (2021) 12:125–46. doi: 10.1364/BOE.411117
86. Husvogt L, Ploner SB, Chen S, Stromer D, Schottenhamml J, Alibhai AY, et al. Maximum a posteriori signal recovery for optical coherence tomography angiography image generation and denoising. *Biomed Opt Express.* (2021) 12:55–68. doi: 10.1364/BOE.408903
87. Viekash VK, Jothi Balaji J, Lakshminarayanan V. FAZSeg: a new software for quantification of the foveal avascular zone. *Clin Ophthalmol.* (2021) 15:4817–27. doi: 10.2147/OPTH.S346145
88. Untracht GR, Matos RS, Dikaios N, Bapir M, Durrani AK, Butsabong T, et al. OCTAVA: an open-source toolbox for quantitative analysis of optical coherence tomography angiography images. *PLoS One.* (2021) 16:e0261052. doi: 10.1371/journal.pone.0261052
89. Zhang Y, Li H, Cao T, Chen R, Qiu H, Gu Y, et al. Automatic 3D adaptive vessel segmentation based on linear relationship between intensity and complex-decorrelation in optical coherence tomography angiography. *Quant Imaging Med Surg.* (2021) 11:895–906. doi: 10.21037/qims-20-868
90. Miguel A, Legeai J, Silva B. A software for quantification of vessel density in glaucoma: an OCT-angiography study. *J Fr Ophtalmol.* (2021) 44:376–81. doi: 10.1016/j.jfo.2020.06.038

91. Považay B, Apolonskiy A, Unterhuber A, Hermann B, Bizheva K, Sattmann H, et al. Visible light optical coherence tomography. *Proc SPIE.* (2002) 4619:90–4. doi: 10.1117/12.470466
92. Xu J, Song S, Wei W, Wang RK. Wide field and highly sensitive angiography based on optical coherence tomography with akinetic swept source. *Biomed Opt Express.* (2017) 8:420–35. doi: 10.1364/BOE.8.000420
93. Kolb JP, Klein T, Eibl M. *Megahertz FDML Laser with Up to 143nm Sweep Range for Ultrahigh Resolution OCT at 1050nm*. Bellingham, DC: SPIE (2016). doi: 10.1117/12.2214758
94. You Y-J, Wang C, Lin Y-L. Ultrahigh-resolution optical coherence tomography at 1.3μm central wavelength by using a supercontinuum source pumped by noise-like pulses. *Laser Phys Lett.* (2015) 13:025101. doi: 10.1088/1612-2011/13/2/025101
95. Werkmeister RM, Sapeta S, Schmidl D, Garhofer G, Schmidinger G, Aranha Dos Santos V, et al. Ultrahigh-resolution OCT imaging of the human cornea. *Biomed Opt Express.* (2017) 8:1221–39. doi: 10.1364/BOE.8.001221
96. Chong SP, Bernucci M, Radhakrishnan H, Srinivasan VJ. Structural and functional human retinal imaging with a fiber-based visible light OCT ophthalmoscope. *Biomed Opt Express.* (2017) 8:323–37. doi: 10.1364/BOE.8.000323
97. Shu X, Beckmann L, Zhang H. Visible-light optical coherence tomography: a review. *J Biomed Opt.* (2017) 22:1–14. doi: 10.1117/1.JBO.22.12.121707
98. Chong SP, Merkle CW, Leahy C, Srinivasan VJ. Cerebral metabolic rate of oxygen (CMRO2) assessed by combined Doppler and spectroscopic OCT. *Biomed Opt Express.* (2015) 6:3941–51. doi: 10.1364/BOE.6.003941
99. Yi J, Wei Q, Liu W, Backman V, Zhang HF. Visible-light optical coherence tomography for retinal oximetry. *Opt Lett.* (2013) 38:1796–8. doi: 10.1364/OL.38.001796
100. Yi J, Liu W, Chen S, Backman V, Sheibani N, Sorenson CM, et al. Visible light optical coherence tomography measures retinal oxygen metabolic response to systemic oxygenation. *Light Sci Appl.* (2015) 4:e334. doi: 10.1038/lsa.2015.107
101. Werkmeister RM, Schmidl D, Aschinger G, Doblhoff-Dier V, Palkovits S, Wirth M, et al. Retinal oxygen extraction in humans. *Sci Rep.* (2015) 5:15763. doi: 10.1038/srep15763
102. Chen S, Yi J, Zhang HF. Measuring oxygen saturation in retinal and choroidal circulations in rats using visible light optical coherence tomography angiography. *Biomed Opt Express.* (2015) 6:2840–53. doi: 10.1364/BOE.6.002840
103. Soetikno BT, Yi J, Shah R, Liu W, Purta P, Zhang HF, et al. Inner retinal oxygen metabolism in the 50/10 oxygen-induced retinopathy model. *Sci Rep.* (2015) 5:16752. doi: 10.1038/srep16752
104. Liu W, Wang S, Soetikno B, Yi J, Zhang K, Chen S, et al. Increased retinal oxygen metabolism precedes microvascular alterations in Type 1 diabetic mice. *Invest Ophthalmol Vis Sci.* (2017) 58:981–9. doi: 10.1167/iovs.16-20600
105. Nesper PL, Soetikno BT, Zhang HF, Fawzi AA. OCT angiography and visible-light OCT in diabetic retinopathy. *Vision Res.* (2017) 139:191–203. doi: 10.1016/j.visres.2017.05.006
106. Yi J, Chen S, Shu X, Fawzi AA, Zhang HF. Human retinal imaging using visible-light optical coherence tomography guided by scanning laser ophthalmoscopy. *Biomed Opt Express.* (2015) 6:3701–13. doi: 10.1364/BOE.6.003701
107. Shu X, Beckmann L, Wang Y, Rubinoff I, Lucy K, Ishikawa H, et al. Designing visible-light optical coherence tomography towards clinics. *Quant Imaging Med Surg.* (2019) 9:769–81. doi: 10.21037/qims.2019.05.01
108. Grannonico M, Miller DA, Liu M, Norat P, Deppmann CD, Netland PA, et al. Global and regional damages in retinal ganglion cell axon bundles monitored non-invasively by visible-light optical coherence tomography fibergraphy. *J Neurosci.* (2021) 41:10179–93. doi: 10.1523/JNEUROSCI.0844-21.2021
109. Miller DA, Grannonico M, Liu M, Kuranov RV, Netland PA, Liu X, et al. Visible-light optical coherence tomography fibergraphy for quantitative imaging of retinal ganglion cell axon bundles. *Transl Vis Sci Technol.* (2020) 9:11. doi: 10.1167/tvst.9.11.11
110. Pi S, Hormel TT, Wei X, Cepurna W, Morrison JC, Jia Y, et al. Imaging retinal structures at cellular-level resolution by visible-light optical coherence tomography. *Opt Lett.* (2020) 45:2107–10. doi: 10.1364/OL.386454
111. Zhang T, Kho AM, Srinivasan VJ. In vivo Morphometry of Inner Plexiform Layer (IPL) stratification in the human retina with visible light optical coherence tomography. *Front Cell Neurosci.* (2021) 15:655096. doi: 10.3389/fncel.2021.655096
112. Zhang T, Kho AM, Srinivasan VJ. Improving visible light OCT of the human retina with rapid spectral shaping and axial tracking. *Biomed Opt Express.* (2019) 10:2918–31. doi: 10.1364/BOE.10.002918
113. Ghassabi Z, Kuranov RV, Schuman JS, Zambrano R, Wu M, Liu M, et al. In vivo sublayer analysis of human retinal inner plexiform layer obtained by visible-light optical coherence tomography. *Invest Ophthalmol Vis Sci.* (2022) 63:18. doi: 10.1167/iovs.63.1.18
114. Zhang X, Beckmann L, Miller DA, Shao G, Cai Z, Sun C, et al. In Vivo imaging of Schlemm's canal and limbal vascular network in mouse using visible-light OCT. *Invest Ophthalmol Vis Sci.* (2020) 61:23. doi: 10.1167/iovs.61.2.23
115. Wang J, Baker A, Subramanian ML, Siegel NH, Chen X, Ness S, et al. Simultaneous visible light optical coherence tomography and near infrared OCT angiography in retinal pathologies: a case study. *Exp Biol Med (Maywood).* (2022) 247:377–84. doi: 10.1177/15353702211063839
116. Song W, Zhou L, Zhang S. Fiber-based visible and near infrared optical coherence tomography (vnOCT) enables quantitative elastic light scattering spectroscopy in human retina. *Biomed Opt Express.* (2018) 9:3464–80. doi: 10.1364/BOE.9.003464
117. Song W, Zhang S, Sadlak N. Visible and near-infrared optical coherence tomography (vnOCT) in glaucoma suspect, pre-perimetric, and perimetric glaucoma. *Invest Ophthalmol Vis Sci.* (2020) 61:2559–2559. doi: 10.1117/12.2578925
118. Song W, Shao W, Yi W, Liu R, Desai M, Ness S, et al. Visible light optical coherence tomography angiography (vis-OCTA) facilitates local microvascular oximetry in the human retina. *Biomed Opt Express.* (2020) 11:4037–51. doi: 10.1364/BOE.395843
119. Chen X, Tai V, McGeehan B, Ying GS, Viehland C, Imperio R, et al. Repeatability and reproducibility of axial and lateral measurements on handheld optical coherence tomography systems compared with tabletop system. *Transl Vis Sci Technol.* (2020) 9:25. doi: 10.1167/tvst.9.11.25
120. Scoville NM, Legocki AT, Touch P, Ding L, Moshiri Y, Bays-Muchmore C, et al. Vitreous opacities in infants born full-term and preterm by handheld swept-source optical coherence tomography. *J Am Assoc Pediatr Ophthalmol Strabismus.* (2022) 26:20.e1–7. doi: 10.1016/j.jaapos.2021.09.007
121. Patel PR, Imperio R, Viehland C, Tran-Viet D, Chiu SJ, Tai V, et al. Depth-resolved visualization of perifoveal retinal vasculature in preterm infants using handheld optical coherence tomography angiography. *Transl Vis Sci Technol.* (2021) 10:10. doi: 10.1167/tvst.10.9.10
122. Abdeen W, Esmael AF, Gawdat G, El-Fayoumi D. Anterior chamber angle features in primary congenital glaucoma infants using hand-held anterior segment-oct. *Eye (Lond).* (2021) 36:1238–45. doi: 10.1038/s41433-021-01583-1
123. Legocki AT, Moshiri Y, Zepeda EM, Gillette TB, Shariff A, Grant LE, et al. Dome-shaped macula in premature infants visualized by handheld spectral-domain optical coherence tomography. *J AAPOS.* (2021) 25:153.e1–6. doi: 10.1016/j.jaapos.2020.12.007
124. Edawaji BSA, Gottlob I, Proudlock FA. Anterior chamber measurements in healthy children: a cross-sectional study using optical coherence tomography. *Transl Vis Sci Technol.* (2021) 10:13. doi: 10.1167/tvst.10.6.13
125. Shah SD, Haq A, Toufeeq S, Tu Z, Edawaji B, Abbott J, et al. Reliability and recommended settings for pediatric circumpapillary retinal nerve fiber layer imaging using hand-held optical coherence tomography. *Transl Vis Sci Technol.* (2020) 9:43. doi: 10.1167/tvst.9.7.43
126. Nadiarnykh O, McNeill-Badalova NA, Gaillard MC, Bosscha MI, Fabius AWM, Verbraak FD, et al. Optical coherence tomography (OCT) to image active and inactive retinoblastomas as well as retinomas. *Acta Ophthalmol.* (2020) 98:158–65. doi: 10.1111/aos.14214
127. Lim ME, Jiramongkolchai K, Xu L, Freedman SF, Tai V, Toth CA, et al. Handheld optical coherence tomography normative inner retinal layer measurements for children <5 years of age. *Am J Ophthalmol.* (2019) 207:232–9. doi: 10.1016/j.ajo.2019.06.015
128. Pilat AV, Proudlock FA, Shah S, Sheth V, Purohit R, Abbot J, et al. Assessment of the anterior segment of patients with primary congenital glaucoma using handheld optical coherence tomography. *Eye (Lond).* (2019) 33:1232–9. doi: 10.1038/s41433-019-0369-3

129. Pilat AV, Shah S, Sheth V, Purohit R, Proudlock FA, Abbott J, et al. Detection and characterisation of optic nerve and retinal changes in primary congenital glaucoma using hand-held optical coherence tomography. *BMJ Open Ophthalmol.* (2019) 4:e000194. doi: 10.1136/bmjophth-2018-000194
130. Zepeda EM, Shariff A, Gillette TB, Grant L, Ding L, Tarczy-Hornoch K, et al. Vitreous bands identified by handheld spectral-domain optical coherence tomography among premature infants. *JAMA Ophthalmol.* (2018) 136:753–8. doi: 10.1001/jamaophthalmol.2018.1509
131. Ling KP, Mangalesh S, Tran-Viet D, Gunther R, Toth CA, Vajzovic L, et al. Handheld spectral domain optical coherence tomography findings of x-linked retinoschisis in early childhood. *Retina.* (2020) 40:1996–2003. doi: 10.1097/IAE.0000000000002688
132. Anwar S, Nath M, Patel A, Lee H, Brown S, Gottlob I, et al. Potential utility of foveal morphology in preterm infants measured using hand-held optical coherence tomography in retinopathy of prematurity screening. *Retina.* (2020) 40:1592–602. doi: 10.1097/IAE.0000000000002622
133. Chen X, Prakalapakorn SG, Freedman SF, Vajzovic L, Toth CA. Differentiating retinal detachment and retinoschisis using handheld optical coherence tomography in stage 4 retinopathy of prematurity. *JAMA Ophthalmol.* (2020) 138:81–5. doi: 10.1001/jamaophthalmol.2019.4796
134. Padhi TR, Anderson BJ, Abbey AM, Yonekawa Y, Stem M, Alam D, et al. Choroidal neovascular membrane in paediatric patients: clinical characteristics and outcomes. *Br J Ophthalmol.* (2018) 102:1232–7. doi: 10.1136/bjophthalmol-2017-310497
135. Agarwal K, Vinekar A, Chandra P, Padhi TR, Nayak S, Jayanna S, et al. Imaging the pediatric retina: an overview. *Indian J Ophthalmol.* (2021) 69:812–23. doi: 10.4103/ijo.IJO_1917_20
136. Moshiri Y, Legocki AT, Zhou K, Cabrera MT, Rezaei KA, Tarczy-Hornoch K, et al. Handheld swept-source optical coherence tomography with angiography in awake premature neonates. *Quant Imaging Med Surg.* (2019) 9:1495–502. doi: 10.21037/qims.2019.09.01
137. Shen LL, Mangalesh S, Michalak SM, McGeehan B, Sarin N, Finkle J, et al. Associations between systemic health and retinal nerve fibre layer thickness in preterm infants at 36 weeks postmenstrual age. *Br J Ophthalmol.* (2021):bjohthalmol–2021–319254. [Online ahead of print], doi: 10.1136/bjophthalmol-2021-319254
138. Heidelberg. (2021). Available online at: https://business-lounge.heidelbergengineering.com/gb/en/products/spectralis/flex-module/ (accessed June 16, 2022).
139. Leica. (2021). Available online at: https://www.leica-microsystems.com/products/surgical-microscopes/p/envisu-c2300/ (accessed June 16, 2022).
140. Shelton RL, Jung W, Sayegh SI, McCormick DT, Kim J, Boppart SA, et al. Optical coherence tomography for advanced screening in the primary care office. *J Biophotonics.* (2014) 7:525–33. doi: 10.1002/jbio.201200243
141. Song G, Chu KK, Kim S, Crose M, Cox B, Jelly ET, et al. First clinical application of low-cost OCT. *Transl Vis Sci Technol.* (2019) 8:61. doi: 10.1167/tvst.8.3.61
142. Malone JD, El-Haddad MT, Yerramreddy SS, Oguz I, Tao YK. Handheld spectrally encoded coherence tomography and reflectometry for motion-corrected ophthalmic optical coherence tomography and optical coherence tomography angiography. *Neurophotonics.* (2019) 6:041102. doi: 10.1117/1.NPh.6.4.041102
143. Larocca F, Nankivil D, Farsiu S, Izatt JA. Handheld simultaneous scanning laser ophthalmoscopy and optical coherence tomography system. *Biomed Opt Express.* (2013) 4:2307–21. doi: 10.1364/BOE.4.002307
144. LaRocca F, Nankivil D, DuBose T, Toth CA, Farsiu S, Izatt JA, et al. In vivo cellular-resolution retinal imaging in infants and children using an ultracompact handheld probe. *Nat Photonics.* (2016) 10:580–4. doi: 10.1038/nphoton.2016.141
145. Jung W, Kim J, Jeon M, Chaney EJ, Stewart CN, Boppart SA, et al. Handheld optical coherence tomography scanner for primary care diagnostics. *IEEE Trans Biomed Eng.* (2011) 58:741–4. doi: 10.1109/TBME.2010.2096816
146. Viehland C, Chen X, Tran-Viet D, Jackson-Atogi M, Ortiz P, Waterman G, et al. Ergonomic handheld OCT angiography probe optimized for pediatric and supine imaging. *Biomed Opt Express.* (2019) 10:2623–38. doi: 10.1364/BOE.10.002623
147. Cho NH, Park K, Wijesinghe RE, Shin YS, Jung W, Kim J, et al. Development of real-time dual-display handheld and bench-top hybrid-mode SD-OCTs. *Sensors (Basel).* (2014) 14:2171–81. doi: 10.3390/s140202171
148. Song S, Zhou K, Xu JJ, Zhang Q, Lyu S, Wang R, et al. Development of a clinical prototype of a miniature hand-held optical coherence tomography probe for prematurity and pediatric ophthalmic imaging. *Biomed Opt Express.* (2019) 10:2383–98. doi: 10.1364/BOE.10.002383
149. Lu CD, Kraus MF, Potsaid B, Liu JJ, Choi W, Jayaraman V, et al. Handheld ultrahigh speed swept source optical coherence tomography instrument using a MEMS scanning mirror. *Biomed Opt Express.* (2013) 5:293–311. doi: 10.1364/BOE.5.000293
150. Nankivil D, Waterman G, LaRocca F, Keller B, Kuo AN, Izatt JA, et al. Handheld, rapidly switchable, anterior/posterior segment swept source optical coherence tomography probe. *Biomed Opt Express.* (2015) 6:4516–28. doi: 10.1364/BOE.6.004516
151. Ni S, Wei X, Ng R, Ostmo S, Chiang MF, Huang D, et al. High-speed and widefield handheld swept-source OCT angiography with a VCSEL light source. *Biomed Opt Express.* (2021) 12:3553–70. doi: 10.1364/BOE.425411
152. Ni S, Nguyen TP, Ng R, Khan S, Ostmo S, Jia Y, et al. 105 degrees field of view non-contact handheld swept-source optical coherence tomography. *Opt Lett.* (2021) 46:5878–81. doi: 10.1364/OL.443672
153. Muijzer MB, Schellekens P, Beckers HJM, de Boer JH, Imhof SM, Wisse RPL, et al. Clinical applications for intraoperative optical coherence tomography: a systematic review. *Eye (Lond).* (2021) 36:379–91. doi: 10.1038/s41433-021-01686-9
154. Ehlers JP, Dupps WJ, Kaiser PK, Goshe J, Singh RP, Petkovsek D, et al. The Prospective Intraoperative and Perioperative Ophthalmic ImagiNg with Optical CoherEncE TomogRaphy (PIONEER) Study: 2-year results. *Am J Ophthalmol.* (2014) 158:999–1007. doi: 10.1016/j.ajo.2014.07.034
155. Ehlers JP, Srivastava SK, Feiler D, Noonan AI, Rollins AM, Tao YK, et al. Integrative advances for OCT-guided ophthalmic surgery and intraoperative OCT: microscope integration, surgical instrumentation, and heads-up display surgeon feedback. *PLoS One.* (2014) 9:e105224. doi: 10.1371/journal.pone.0105224
156. Mura M, Iannetta D, Nasini F, Barca F, Peiretti E, Engelbrecht L, et al. Use of a new intra-ocular spectral domain optical coherence tomography in vitreoretinal surgery. *Acta Ophthalmol.* (2016) 94:246–52. doi: 10.1111/aos.12961
157. Ehlers JP, Modi YS, Pecen PE, Goshe J, Dupps WJ, Rachitskaya A, et al. The DISCOVER study 3-year results: feasibility and usefulness of microscope-integrated intraoperative OCT during ophthalmic surgery. *Ophthalmology.* (2018) 125:1014–27. doi: 10.1016/j.ophtha.2017.12.037
158. Falkner-Radler CI, Glittenberg C, Gabriel M, Binder S. Intrasurgical microscope-integrated spectral domain optical coherence tomography-assisted membrane peeling. *Retina.* (2015) 35:2100–6. doi: 10.1097/IAE.0000000000000596
159. Leisser C, Hirnschall N, Palkovits S, Doeller B, Kefer K, Findl O, et al. Intraoperative optical coherence tomography-guided membrane peeling for surgery of macular pucker: advantages and limitations. *Ophthalmologica.* (2019) 241:234–40. doi: 10.1159/000493279
160. Leisser C, Hackl C, Hirnschall N, Luft N, Doller B, Draschl P, et al. Visualizing macular structures during membrane peeling surgery with an intraoperative spectral-domain optical coherence tomography device. *Ophthalmic Surg Lasers Imaging Retina.* (2016) 47:328–32. doi: 10.3928/23258160-20160324-04
161. Yee P, Sevgi DD, Abraham J, Srivastava SK, Le T, Uchida A, et al. iOCT-assisted macular hole surgery: outcomes and utility from the DISCOVER study. *Br J Ophthalmol.* (2021) 105:403–9. doi: 10.1136/bjophthalmol-2020-316045
162. Dayani PN, Maldonado R, Farsiu S, Toth CA. Intraoperative use of handheld spectral domain optical coherence tomography imaging in macular surgery. *Retina.* (2009) 29:1457–68. doi: 10.1097/IAE.0b013e3181b266bc
163. Hayashi A, Yagou T, Nakamura T, Fujita K, Oka M, Fuchizawa C, et al. Intraoperative changes in idiopathic macular holes by spectral-domain optical coherence tomography. *Case Rep Ophthalmol.* (2011) 2:149–54. doi: 10.1159/000328752
164. Bruyere E, Philippakis E, Dupas B, Nguyen-Kim P, Tadayoni R, Couturier A, et al. Benefit of intraoperative optical coherence tomography for

vitreomacular surgery in highly myopic eyes. *Retina.* (2018) 38:2035–44. doi: 10.1097/IAE.0000000000001827
165. Lytvynchuk LM, Falkner-Radler CI, Krepler K, Glittenberg CG, Ahmed D, Petrovski G, et al. Dynamic intraoperative optical coherence tomography for inverted internal limiting membrane flap technique in large macular hole surgery. *Graefes Arch Clin Exp Ophthalmol.* (2019) 257:1649–59. doi: 10.1007/s00417-019-04364-5
166. Kumar V, Yadav B. HOLE-DOOR SIGN: a novel intraoperative optical coherence tomography feature predicting macular hole closure. *Retina.* (2018) 38:2045–50. doi: 10.1097/IAE.0000000000001791
167. Cehajic-Kapetanovic J, Xue K, Edwards TL, Meenink TC, Beelen MJ, Naus GJ, et al. First-in-human robot-assisted subretinal drug delivery under local anaesthesia a randomised clinical trial. *Am J Ophthalmol.* (2021) 237:104–13. doi: 10.1016/j.ajo.2021.11.011
168. Vasconcelos HM Jr., Lujan BJ, Pennesi ME, Yang P, Lauer AK. Intraoperative optical coherence tomographic findings in patients undergoing subretinal gene therapy surgery. *Int J Retina Vitreous.* (2020) 6:13. doi: 10.1186/s40942-020-00216-1
169. Hussain RM, Tran KD, Maguire AM, Berrocal AM. Subretinal injection of voretigene Neparvovec-rzyl in a patient with RPE65-associated leber's congenital amaurosis. *Ophthalmic Surg Lasers Imaging Retina.* (2019) 50:661–3. doi: 10.3928/23258160-20191009-01
170. Au J, Goshe J, Dupps WJ Jr., Srivastava SK, Ehlers JP. Intraoperative optical coherence tomography for enhanced depth visualization in deep anterior lamellar keratoplasty from the PIONEER study. *Cornea.* (2015) 34:1039–43. doi: 10.1097/ICO.0000000000000508
171. Steven P, Le Blanc C, Lankenau E, Krug M, Oelckers S, Heindl LM, et al. Optimising deep anterior lamellar keratoplasty (DALK) using intraoperative online optical coherence tomography (iOCT). *Br J Ophthalmol.* (2014) 98:900–4. doi: 10.1136/bjophthalmol-2013-304585
172. De Benito-Llopis L, Mehta JS, Angunawela RI, Ang M, Tan DT. Intraoperative anterior segment optical coherence tomography: a novel assessment tool during deep anterior lamellar keratoplasty. *Am J Ophthalmol.* (2014) 157:334–341.e3. doi: 10.1016/j.ajo.2013.10.001
173. Santorum P, Yu AC, Bertelli E, Busin M. Microscope-integrated intraoperative optical coherence tomography-guided big-bubble deep anterior lamellar keratoplasty. *Cornea.* (2022) 41:125–9. doi: 10.1097/ICO.0000000000002826
174. Scorcia V, Busin M, Lucisano A, Beltz J, Carta A, Scorcia G, et al. Anterior segment optical coherence tomography-guided big-bubble technique. *Ophthalmology.* (2013) 120:471–6. doi: 10.1016/j.ophtha.2012.08.041
175. Guindolet D, Nguyen DT, Bergin C, Doan S, Cochereau I, Gabison EE, et al. Double-docking technique for femtosecond laser-assisted deep anterior lamellar keratoplasty. *Cornea.* (2018) 37:123–6. doi: 10.1097/ICO.0000000000001442
176. Cost B, Goshe JM, Srivastava S, Ehlers JP. Intraoperative optical coherence tomography-assisted descemet membrane endothelial keratoplasty in the DISCOVER study. *Am J Ophthalmol.* (2015) 160:430–7. doi: 10.1016/j.ajo.2015.05.020
177. Patel AS, Goshe JM, Srivastava SK, Ehlers JP. Intraoperative optical coherence tomography-assisted descemet membrane endothelial keratoplasty in the DISCOVER Study: first 100 cases. *Am J Ophthalmol.* (2020) 210:167–73. doi: 10.1016/j.ajo.2019.09.018
178. Sharma N, Sahay P, Maharana PK, Kumar P, Ahsan S, Titiyal JS, et al. Microscope integrated intraoperative optical coherence tomography-guided DMEK in corneas with poor visualization. *Clin Ophthalmol.* (2020) 14:643–51. doi: 10.2147/OPTH.S230195
179. Muijzer MB, Soeters N, Godefrooij DA, van Luijk CM, Wisse RPL. Intraoperative optical coherence tomography-assisted descemet membrane endothelial keratoplasty: toward more efficient. *Saf Surg Cornea.* (2020) 39:674–9. doi: 10.1097/ICO.0000000000002301
180. Steven P, Le Blanc C, Velten K, Lankenau E, Krug M, Oelckers S, et al. Optimizing descemet membrane endothelial keratoplasty using intraoperative optical coherence tomography. *JAMA Ophthalmol.* (2013) 131:1135–42. doi: 10.1001/jamaophthalmol.2013.4672
181. Saad A, Guilbert E, Grise-Dulac A, Sabatier P, Gatinel D. Intraoperative OCT-assisted DMEK: 14 consecutive cases. *Cornea.* (2015) 34:802–7. doi: 10.1097/ICO.0000000000000462
182. Miyakoshi A, Ozaki H, Otsuka M, Hayashi A. Efficacy of intraoperative anterior segment optical coherence tomography during descemet's stripping automated endothelial keratoplasty. *ISRN Ophthalmol.* (2014) 2014:562062. doi: 10.1155/2014/562062
183. Sng CC, Luengo Gimeno F, Mehta JS, Htoon HM, Tan DT. Intraoperative use of spectral-domain optical coherence tomography during Descemet's stripping automated endothelial keratoplasty. *Clin Ophthalmol.* (2012) 6:479–86. doi: 10.2147/OPTH.S28971
184. Steverink JG, Wisse RPL. Intraoperative optical coherence tomography in descemet stripping automated endothelial keratoplasty: pilot experiences. *Int Ophthalmol.* (2017) 37:939–44. doi: 10.1007/s10792-016-0338-9
185. Das S, Kummelil MK, Kharbanda V, Arora V, Nagappa S, Shetty R, et al. Microscope integrated intraoperative spectral domain optical coherence tomography for cataract surgery: uses and applications. *Curr Eye Res.* (2016) 41:643–52. doi: 10.3109/02713683.2015.1050742
186. Lytvynchuk LM, Glittenberg CG, Falkner-Radler CI, Neumaier-Ammerer B, Smretschnig E, Hagen S, et al. Evaluation of intraocular lens position during phacoemulsification using intraoperative spectral-domain optical coherence tomography. *J Cataract Refract Surg.* (2016) 42:694–702. doi: 10.1016/j.jcrs.2016.01.044
187. Hirnschall N, Farrokhi S, Amir-Asgari S, Hienert J, Findl O. Intraoperative optical coherence tomography measurements of aphakic eyes to predict postoperative position of 2 intraocular lens designs. *J Cataract Refract Surg.* (2018) 44:1310–6. doi: 10.1016/j.jcrs.2018.07.044
188. Rodriguez-Aramendia A, Diaz-Douton F, Fernandez-Trullas J, Falgueras P, Gonzalez L, Pujol J, et al. Whole anterior segment and retinal swept source OCT for comprehensive ocular screening. *Biomed Opt Express.* (2021) 12:1263–78. doi: 10.1364/BOE.414592
189. Grulkowski I, Manzanera S, Cwiklinski L, Sobczuk F, Karnowski K, Artal P, et al. Swept source optical coherence tomography and tunable lens technology for comprehensive imaging and biometry of the whole eye. *Optica.* (2018) 5:52–9. doi: 10.1364/OPTICA.5.000052
190. Jeong HW, Lee SW, Kim BM. Spectral-domain OCT with dual illumination and interlaced detection for simultaneous anterior segment and retina imaging. *Opt Express.* (2012) 20:19148–59. doi: 10.1364/OE.20.019148
191. Kim HJ, Kim PU, Hyeon MG, Choi Y, Kim J, Kim BM, et al. High-resolution, dual-depth spectral-domain optical coherence tomography with interlaced detection for whole-eye imaging. *Appl Opt.* (2016) 55:7212–7. doi: 10.1364/AO.55.007212
192. Luo M, Li Y, Zhuo Y. Advances and current clinical applications of anterior segment optical coherence tomography angiography. *Front Med (Lausanne).* (2021) 8:721442. doi: 10.3389/fmed.2021.721442
193. Fan S, Li L, Li Q, Dai C, Ren Q, Jiao S, et al. Dual band dual focus optical coherence tomography for imaging the whole eye segment. *Biomed Opt Express.* (2015) 6:2481–93. doi: 10.1364/BOE.6.002481
194. Jayaraman V, Cole GD, Robertson M, Uddin A, Cable A. High-sweep-rate 1310 nm MEMS-VCSEL with 150 nm continuous tuning range. *Electron Lett.* (2012) 48:867–9. doi: 10.1049/el.2012.1552
195. Grulkowski I, Liu JJ, Potsaid B, Jayaraman V, Lu CD, Jiang J, et al. Retinal, anterior segment and full eye imaging using ultrahigh speed swept source OCT with vertical-cavity surface emitting lasers. *Biomed Opt Express.* (2012) 3:2733–51. doi: 10.1364/BOE.3.002733
196. Grulkowski I, Liu JJ, Zhang JY, Potsaid B, Jayaraman V, Cable AE, et al. Reproducibility of a long-range swept-source optical coherence tomography ocular biometry system and comparison with clinical biometers. *Ophthalmology.* (2013) 120:2184–90. doi: 10.1016/j.ophtha.2013.04.007
197. Kim HJ, Kim M, Hyeon MG, Choi Y, Kim BM. Full ocular biometry through dual-depth whole-eye optical coherence tomography. *Biomed Opt Express.* (2018) 9:360–72. doi: 10.1364/BOE.9.000360
198. McNabb RP, Polans J, Keller B, Jackson-Atogi M, James CL, Vann RR, et al. Wide-field whole eye OCT system with demonstration of quantitative retinal curvature estimation. *Biomed Opt Express.* (2019) 10:338–55. doi: 10.1364/BOE.10.000338
199. Grulkowski I, Manzanera S, Cwiklinski L, Mompean J, de Castro A, Marin JM, et al. Volumetric macro- and micro-scale assessment of crystalline lens

opacities in cataract patients using long-depth-range swept source optical coherence tomography. *Biomed Opt Express.* (2018) 9:3821–33. doi: 10.1364/BOE.9.003821
200. de Castro A, Benito A, Manzanera S, Mompean J, Canizares B, Martinez D, et al. Three-dimensional cataract crystalline lens imaging with swept-source optical coherence tomography. *Invest Ophthalmol Vis Sci.* (2018) 59:897–903. doi: 10.1167/iovs.17-23596
201. Eugui P, Harper DJ, Kummer S, Lichtenegger A, Gesperger J, Himmel T, et al. Three-dimensional visualization of opacifications in the murine crystalline lens by in vivo optical coherence tomography. *Biomed Opt Express.* (2020) 11:2085–97. doi: 10.1364/BOE.387335
202. Pujari A, Yadav S, Sharma N, Khokhar S, Sinha R, Agarwal T, et al. Study 1: evaluation of the signs of deficient posterior capsule in posterior polar cataracts using anterior segment optical coherence tomography. *J Cataract Refract Surg.* (2020) 46:1260–5. doi: 10.1097/j.jcrs.0000000000000246
203. Martinez-Enriquez E, Perez-Merino P, Duran-Poveda S, Jimenez-Alfaro I, Marcos S. Estimation of intraocular lens position from full crystalline lens geometry: towards a new generation of intraocular lens power calculation formulas. *Sci Rep.* (2018) 8:9829. doi: 10.1038/s41598-018-28272-6
204. Kuo AN, McNabb RP, Izatt JA. Advances in whole-eye optical coherence tomography imaging. *Asia Pac J Ophthalmol (Phila).* (2019):10.22608/AO.201901. [Online ahead of print], doi: 10.22608/APO.201901
205. Begley CG, Chalmers RL, Abetz L, Venkataraman K, Mertzanis P, Caffery BA, et al. The relationship between habitual patient-reported symptoms and clinical signs among patients with dry eye of varying severity. *Invest Ophthalmol Vis Sci.* (2003) 44:4753–61. doi: 10.1167/iovs.03-0270
206. Schmidl D, Witkowska KJ, Kaya S, Baar C, Faatz H, Nepp J, et al. The association between subjective and objective parameters for the assessment of dry-eye syndrome. *Invest Ophthalmol Vis Sci.* (2015) 56:1467–72. doi: 10.1167/iovs.14-15814
207. Huang J, Hindman HB, Rolland JP. In vivo thickness dynamics measurement of tear film lipid and aqueous layers with optical coherence tomography and maximum-likelihood estimation. *Opt Lett.* (2016) 41:1981–4. doi: 10.1364/OL.41.001981
208. Dos Santos VA, Schmetterer L, Triggs GJ, Leitgeb RA, Groschl M, Messner A, et al. Super-resolved thickness maps of thin film phantoms and in vivo visualization of tear film lipid layer using OCT. *Biomed Opt Express.* (2016) 7:2650–70. doi: 10.1364/BOE.7.002650
209. Stegmann H, Aranha Dos Santos V, Messner A, Unterhuber A, Schmidl D, Garhofer G, et al. Automatic assessment of tear film and tear meniscus parameters in healthy subjects using ultrahigh-resolution optical coherence tomography. *Biomed Opt Express.* (2019) 10:2744–56. doi: 10.1364/BOE.10.002744
210. Ang M, Baskaran M, Werkmeister RM, Chua J, Schmidl D, Aranha Dos Santos V, et al. Anterior segment optical coherence tomography. *Prog Retin Eye Res.* (2018) 66:132–56. doi: 10.1016/j.preteyeres.2018.04.002
211. Carracedo G, Pastrana C, Serramito M, Rodriguez-Pomar C. Evaluation of tear meniscus by optical coherence tomography after different sodium hyaluronate eyedrops instillation. *Acta Ophthalmol.* (2019) 97:e162–9. doi: 10.1111/aos.13887
212. Wang Y, Zhuang H, Xu J, Wang X, Jiang C, Sun X, et al. Dynamic changes in the lower tear meniscus after instillation of artificial tears. *Cornea.* (2010) 29:404–8. doi: 10.1097/ICO.0b013e3181bd476c
213. Bujak MC, Yiu S, Zhang X, Li Y, Huang D. Serial measurement of tear meniscus by FD-OCT after instillation of artificial tears in patients with dry eyes. *Ophthalmic Surg Lasers Imaging.* (2011) 42:308–13. doi: 10.3928/15428877-20110603-02
214. Wang J, Cui L, Shen M, Perez VL, Wang MR. Ultra-high resolution optical coherence tomography for monitoring tear meniscus volume in dry eye after topical cyclosporine treatment. *Clin Ophthalmol.* (2012) 6:933–8. doi: 10.2147/OPTH.S32384
215. Sharma N, Singhal D, Maharana PK, Agarwal T, Sinha R, Satpathy G, et al. Spectral domain anterior segment optical coherence tomography in fungal keratitis. *Cornea.* (2018) 37:1388–94. doi: 10.1097/ICO.0000000000001715
216. Soliman W, Nassr MA, Abdelazeem K, Al-Hussaini AK. Appearance of herpes simplex keratitis on anterior segment optical coherence tomography. *Int Ophthalmol.* (2019) 39:2923–8. doi: 10.1007/s10792-019-01142-4
217. Oliveira MA, Rosa A, Soares M, Gil J, Costa E, Quadrado MJ, et al. Anterior segment optical coherence tomography in the early management of microbial keratitis: a cross-sectional study. *Acta Med Port.* (2020) 33:318–25. doi: 10.20344/amp.12663
218. Nanji AA, Sayyad FE, Galor A, Dubovy S, Karp CL. High-resolution optical coherence tomography as an adjunctive tool in the diagnosis of corneal and conjunctival pathology. *Ocul Surf.* (2015) 13:226–35. doi: 10.1016/j.jtos.2015.02.001
219. Konstantopoulos A, Kuo J, Anderson D, Hossain P. Assessment of the use of anterior segment optical coherence tomography in microbial keratitis. *Am J Ophthalmol.* (2008) 146:534–42. doi: 10.1016/j.ajo.2008.05.030
220. Fuentes E, Sandali O, El Sanharawi M, Basli E, Hamiche T, Goemaere I, et al. Anatomic predictive factors of acute corneal hydrops in keratoconus: an optical coherence tomography study. *Ophthalmology.* (2015) 122:1653–9. doi: 10.1016/j.ophtha.2015.04.031
221. Siebelmann S, Scholz P, Sonnenschein S, Bachmann B, Matthaei M, Cursiefen C, et al. Anterior segment optical coherence tomography for the diagnosis of corneal dystrophies according to the IC3D classification. *Surv Ophthalmol.* (2018) 63:365–80. doi: 10.1016/j.survophthal.2017.08.001
222. Mohammed ISK, Tran S, Toledo-Espiett LA, Munir WM. The detection of keratoconus using novel metrics derived by anterior segment optical coherence tomography. *Int Ophthalmol.* (2022): [Online ahead of print], doi: 10.1007/s10792-021-02210-4
223. Jin X, Jin H, Shi Y, Zhang N, Zhang H. Clinical observation of corneal endothelial plaques with fungal and bacterial keratitis by anterior segment optical coherence tomography and in vivo confocal microscopy. *Cornea.* (2021): [Online ahead of print], doi: 10.1097/ICO.0000000000002912
224. Wang F, Shi G, Li X, Lu J, Ding Z, Sun X, et al. Comparison of Schlemm's canal's biological parameters in primary open-angle glaucoma and normal human eyes with swept source optical. *J Biomed Opt.* (2012) 17:116008. doi: 10.1117/1.JBO.17.11.116008
225. Hong J, Xu J, Wei A, Wen W, Chen J, Yu X, et al. Spectral-domain optical coherence tomographic assessment of Schlemm's canal in Chinese subjects with primary open-angle glaucoma. *Ophthalmology.* (2013) 120:709–15. doi: 10.1016/j.ophtha.2012.10.008
226. Dada T, Sihota R, Gadia R, Aggarwal A, Mandal S, Gupta V, et al. Comparison of anterior segment optical coherence tomography and ultrasound biomicroscopy for assessment of the anterior segment. *J Cataract Refract Surg.* (2007) 33:837–40. doi: 10.1016/j.jcrs.2007.01.021
227. Console JW, Sakata LM, Aung T, Friedman DS, He M. Quantitative analysis of anterior segment optical coherence tomography images: the Zhongshan Angle Assessment Program. *Br J Ophthalmol.* (2008) 92:1612–6. doi: 10.1136/bjo.2007.129932
228. Baskaran M, Iyer JV, Narayanaswamy AK, He Y, Sakata LM, Wu R, et al. Anterior segment imaging predicts incident gonioscopic angle closure. *Ophthalmology.* (2015) 122:2380–4. doi: 10.1016/j.ophtha.2015.07.030
229. Nongpiur ME, He M, Amerasinghe N, Friedman DS, Tay WT, Baskaran M, et al. Lens vault, thickness, and position in Chinese subjects with angle closure. *Ophthalmology.* (2011) 118:474–9. doi: 10.1016/j.ophtha.2010.07.025
230. Nongpiur ME, Sakata LM, Friedman DS, He M, Chan YH, Lavanya R, et al. Novel association of smaller anterior chamber width with angle closure in Singaporeans. *Ophthalmology.* (2010) 117:1967–73. doi: 10.1016/j.ophtha.2010.02.007
231. Wang B, Sakata LM, Friedman DS, Chan YH, He M, Lavanya R, et al. Quantitative iris parameters and association with narrow angles. *Ophthalmology.* (2010) 117:11–7. doi: 10.1016/j.ophtha.2009.06.017
232. Li P, Reif R, Zhi Z, Martin E, Shen TT, Johnstone M, et al. Phase-sensitive optical coherence tomography characterization of pulse-induced trabecular meshwork displacement in ex vivo nonhuman primate eyes. *J Biomed Opt.* (2012) 17:076026. doi: 10.1117/1.JBO.17.7.076026
233. Huang AS, Belghith A, Dastiridou A, Chopra V, Zangwill LM, Weinreb RN, et al. Automated circumferential construction of first-order aqueous humor outflow pathways using spectral-domain optical coherence tomography. *J Biomed Opt.* (2017) 22:66010. doi: 10.1117/1.JBO.22.6.066010
234. Hong J, Yang Y, Wei A, Deng SX, Kong X, Chen J, et al. Schlemm's canal expands after trabeculectomy in patients with primary angle-closure

glaucoma. *Invest Ophthalmol Vis Sci.* (2014) 55:5637–42. doi: 10.1167/iovs.14-14712
235. Fuest M, Kuerten D, Koch E, Becker J, Hirsch T, Walter P, et al. Evaluation of early anatomical changes following canaloplasty with anterior segment spectral-domain optical coherence tomography and ultrasound biomicroscopy. *Acta Ophthalmol.* (2016) 94:e287–92. doi: 10.1111/aos.12917
236. Chen J, Huang H, Zhang S, Chen X, Sun X. Expansion of Schlemm's canal by travoprost in healthy subjects determined by Fourier-domain optical coherence tomography. *Invest Ophthalmol Vis Sci.* (2013) 54:1127–34. doi: 10.1167/iovs.12-10396
237. Skaat A, Rosman MS, Chien JL, Mogil RS, Ren R, Liebmann JM, et al. Effect of pilocarpine hydrochloride on the schlemm canal in healthy eyes and eyes with open-angle glaucoma. *JAMA Ophthalmol.* (2016) 134:976–81. doi: 10.1001/jamaophthalmol.2016.1881
238. Ruggeri M, Belloni G, Chang YC, Durkee H, Masetti E, Cabot F, et al. Combined anterior segment OCT and wavefront-based autorefractor using a shared beam. *Biomed Opt Express.* (2021) 12:6746–61. doi: 10.1364/BOE.435127
239. Huo T, Wang C, Zhang X, Chen T, Liao W, Zhang W, et al. Ultrahigh-speed optical coherence tomography utilizing all-optical 40 MHz swept-source. *J Biomed Opt.* (2015) 20:030503. doi: 10.1117/1.JBO.20.3.030503
240. Kolb JP, Klein T, Kufner CL, Wieser W, Neubauer AS, Huber R, et al. Ultra-widefield retinal MHz-OCT imaging with up to 100 degrees viewing angle. *Biomed Opt Express.* (2015) 6:1534–52. doi: 10.1364/BOE.6.001534
241. Zhi Z, Qin W, Wang J, Wei W, Wang RK. 4D optical coherence tomography-based micro-angiography achieved by 1.6-MHz FDML swept source. *Opt Lett.* (2015) 40:1779–82. doi: 10.1364/OL.40.001779
242. Gora M, Karnowski K, Szkulmowski M, Kaluzny BJ, Huber R, Kowalczyk A, et al. Ultra high-speed swept source OCT imaging of the anterior segment of human eye at 200 kHz with adjustable imaging range. *Opt Express.* (2009) 17:14880–94. doi: 10.1364/OE.17.014880
243. Ishida S, Nishizawa N. Quantitative comparison of contrast and imaging depth of ultrahigh-resolution optical coherence tomography images in 800-1700 nm wavelength region. *Biomed Opt Express.* (2012) 3:282–94. doi: 10.1364/BOE.3.000282
244. Lim H, Jiang Y, Wang Y, Huang YC, Chen Z, Wise FW, et al. Ultrahigh-resolution optical coherence tomography with a fiber laser source at 1 microm. *Opt Lett.* (2005) 30:1171–3. doi: 10.1364/OL.30.001171
245. Moon S, Kim DY. Ultra-high-speed optical coherence tomography with a stretched pulse supercontinuum source. *Opt Express.* (2006) 14:11575–84. doi: 10.1364/OE.14.011575
246. Nishizawa N, Chen Y, Hsiung P, Ippen EP, Fujimoto JG. Real-time, ultrahigh-resolution, optical coherence tomography with an all-fiber, femtosecond fiber laser continuum at 1.5 microm. *Opt Lett.* (2004) 29:2846–8. doi: 10.1364/OL.29.002846
247. Moutsouris K, Dapena I, Ham L, Balachandran C, Oellerich S, Melles GR, et al. Optical coherence tomography, Scheimpflug imaging, and slit-lamp biomicroscopy in the early detection of graft detachment after Descemet membrane endothelial keratoplasty. *Cornea.* (2011) 30:1369–75. doi: 10.1097/ICO.0b013e31820d86bd
248. Kagemann L, Wollstein G, Ishikawa H, Bilonick RA, Brennen PM, Folio LS, et al. Identification and assessment of Schlemm's canal by spectral-domain optical coherence tomography. *Invest Ophthalmol Vis Sci.* (2010) 51:4054–9. doi: 10.1167/iovs.09-4559
249. Leung CK, Li H, Weinreb RN, Liu J, Cheung CY, Lai RY, et al. Anterior chamber angle measurement with anterior segment optical coherence tomography: a comparison between slit lamp OCT and Visante OCT. *Invest Ophthalmol Vis Sci.* (2008) 49:3469–74. doi: 10.1167/iovs.07-1477
250. Werkmeister RM, Alex A, Kaya S, Unterhuber A, Hofer B, Riedl J, et al. Measurement of tear film thickness using ultrahigh-resolution optical coherence tomography. *Invest Ophthalmol Vis Sci.* (2013) 54:5578–83. doi: 10.1167/iovs.13-11920
251. Dubois A, Vabre L, Boccara AC, Beaurepaire E. High-resolution full-field optical coherence tomography with a Linnik microscope. *Appl Opt.* (2002) 41:805–12. doi: 10.1364/AO.41.000805
252. Auksorius E, Borycki D, Stremplewski P, Lizewski K, Tomczewski S, Niedzwiedziuk P, et al. In vivo imaging of the human cornea with high-speed and high-resolution Fourier-domain full-field optical coherence tomography. *Biomed Opt Express.* (2020) 11:2849–65. doi: 10.1364/BOE.393801
253. Hillmann D, Spahr H, Hain C, Sudkamp H, Franke G, Pfäffle C, et al. Aberration-free volumetric high-speed imaging of in vivo retina. *Sci Rep.* (2016) 6:35209.
254. Xiao P, Fink M, Boccara AC. Full-field spatially incoherent illumination interferometry: a spatial resolution almost insensitive to aberrations. *Opt Lett.* (2016) 41:3920–3. doi: 10.1364/OL.41.003920
255. Mazlin V, Xiao P, Dalimier E, Grieve K, Irsch K, Sahel JA, et al. In vivo high resolution human corneal imaging using full-field optical coherence tomography. *Biomed Opt Express.* (2018) 9:557–68. doi: 10.1364/BOE.9.000557
256. Mazlin V, Xiao P, Scholler J, Irsch K, Grieve K, Fink M, et al. Real-time non-contact cellular imaging and angiography of human cornea and limbus with common-path full-field/SD OCT. *Nat Commun.* (2020) 11:1868. doi: 10.1038/s41467-020-15792-x
257. Xiao P, Mazlin V, Grieve K. In vivo high-resolution human retinal imaging with wavefront-correctionless full-field OCT. *Optica.* (2018) 5:409–12. doi: 10.1364/OPTICA.5.000409
258. Mecê P, Groux K, Scholler J, Thouvenin O, Fink M, Grieve K, et al. Coherence gate shaping for wide field high-resolution in vivo retinal imaging with full-field OCT. *Biomed Opt Express.* (2020) 11:4928–41. doi: 10.1364/BOE.400522
259. von der Burchard C, Moltmann M, Tode J, Ehlken C, Sudkamp H, Theisen-Kunde D, et al. Self-examination low-cost full-field OCT (SELFF-OCT) for patients with various macular diseases. *Graefes Arch Clin Exp Ophthalmol.* (2021) 259:1503–11. doi: 10.1007/s00417-020-05035-6
260. Jayabalan GS, Bille JF. The development of adaptive optics and its application in ophthalmology. In: Bille JF editor. *High Resolution Imaging in Microscopy and Ophthalmology: New Frontiers in Biomedical Optics*. Cham: Springer (2019). doi: 10.1007/978-3-030-16638-0_16
261. Cense B, Gao W, Brown JM, Jones SM, Jonnal RS, Mujat M, et al. Retinal imaging with polarization-sensitive optical coherence tomography and adaptive optics. *Opt Express.* (2009) 17:21634–51. doi: 10.1364/OE.17.021634
262. Miller DT, Kurokawa K. Cellular-scale imaging of transparent retinal structures and processes using adaptive optics optical coherence tomography. *Annu Rev Vis Sci.* (2020) 6:115–48. doi: 10.1146/annurev-vision-030320-041255
263. Zhang Y, Cense B, Rha J, Jonnal RS, Gao W, Zawadzki RJ, et al. High-speed volumetric imaging of cone photoreceptors with adaptive optics spectral-domain optical coherence tomography. *Opt Express.* (2006) 14:4380–94. doi: 10.1364/OE.14.004380
264. Evans JW, Zawadzki RJ, Jones SM, Olivier SS, Werner JS. Error budget analysis for an adaptive optics optical coherence tomography system. *Opt Express.* (2009) 17:13768–84. doi: 10.1364/OE.17.013768
265. Hermann B, Fernandez EJ, Unterhuber A, Sattmann H, Fercher AF, Drexler W, et al. Adaptive-optics ultrahigh-resolution optical coherence tomography. *Opt Lett.* (2004) 29:2142–4. doi: 10.1364/OL.29.002142
266. Roorda A, Romero-Borja F, Donnelly Iii W, Queener H, Hebert T, Campbell M, et al. Adaptive optics scanning laser ophthalmoscopy. *Opt Express.* (2002) 10:405–12. doi: 10.1364/OE.10.000405
267. Jonnal RS, Kocaoglu OP, Zawadzki RJ, Liu Z, Miller DT, Werner JS, et al. A review of adaptive optics optical coherence tomography: technical advances, scientific applications, and the future. *Invest Ophthalmol Vis Sci.* (2016) 57:OCT51–68. doi: 10.1167/iovs.16-19103
268. Zhang Y, Rha J, Jonnal R, Miller D. Adaptive optics parallel spectral domain optical coherence tomography for imaging the living retina. *Opt Express.* (2005) 13:4792–811. doi: 10.1364/OPEX.13.004792
269. Kocaoglu OP, Cense B, Jonnal RS, Wang Q, Lee S, Gao W, et al. Imaging retinal nerve fiber bundles using optical coherence tomography with adaptive optics. *Vision Res.* (2011) 51:1835–44. doi: 10.1016/j.visres.2011.06.013
270. Zawadzki RJ, Choi SS, Jones SM, Oliver SS, Werner JS. Adaptive optics-optical coherence tomography: optimizing visualization of microscopic retinal structures in three dimensions. *J Opt Soc Am A Opt Image Sci Vis.* (2007) 24:1373–83. doi: 10.1364/JOSAA.24.001373
271. Cense B, Koperda E, Brown JM, Kocaoglu OP, Gao W, Jonnal RS, et al. Volumetric retinal imaging with ultrahigh-resolution spectral-domain

optical coherence tomography and adaptive optics using two broadband light sources. *Opt Express.* (2009) 17:4095–111. doi: 10.1364/OE.17.004095
272. Reumueller A, Wassermann L, Salas M, Schranz M, Hacker V, Mylonas G, et al. Three-dimensional composition of the photoreceptor cone layers in healthy eyes using adaptive-optics optical coherence tomography (AO-OCT). *PLoS One.* (2021) 16:e0245293. doi: 10.1371/journal.pone.0245293
273. Curcio CA, Sloan KR, Kalina RE, Hendrickson AE. Human photoreceptor topography. *J Comp Neurol.* (1990) 292:497–523. doi: 10.1002/cne.902920402
274. Li KY, Roorda A. Automated identification of cone photoreceptors in adaptive optics retinal images. *J Opt Soc Am A Opt Image Sci Vis.* (2007) 24:1358–63. doi: 10.1364/JOSAA.24.001358
275. Cooper RF, Wilk MA, Tarima S, Carroll J. Evaluating descriptive metrics of the human cone mosaic. *Invest Ophthalmol Vis Sci.* (2016) 57:2992–3001. doi: 10.1167/iovs.16-19072
276. Cooper RF, Lombardo M, Carroll J, Sloan KR, Lombardo G. Methods for investigating the local spatial anisotropy and the preferred orientation of cones in adaptive optics retinal images. *Vis Neurosci.* (2016) 33:E005. doi: 10.1017/S0952523816000018
277. Akyol E, Hagag AM, Sivaprasad S, Lotery AJ. Adaptive optics: principles and applications in ophthalmology. *Eye (Lond).* (2021) 35:244–64. doi: 10.1038/s41433-020-01286-z
278. Morgan JIW, Vergilio GK, Hsu J, Dubra A, Cooper RF. The reliability of cone density measurements in the presence of rods. *Transl Vis Sci Technol.* (2018) 7:21. doi: 10.1167/tvst.7.3.21
279. Pallikaris A, Williams DR, Hofer H. The reflectance of single cones in the living human eye. *Invest Ophthalmol Vis Sci.* (2003) 44:4580–92. doi: 10.1167/iovs.03-0094
280. Wynne N, Carroll J, Duncan JL. Promises and pitfalls of evaluating photoreceptor-based retinal disease with adaptive optics scanning light ophthalmoscopy (AOSLO). *Prog Retin Eye Res.* (2021) 83:100920. doi: 10.1016/j.preteyeres.2020.100920
281. Wells-Gray EM, Choi SS, Bries A, Doble N. Variation in rod and cone density from the fovea to the mid-periphery in healthy human retinas using adaptive optics scanning laser ophthalmoscopy. *Eye (Lond).* (2016) 30:1135–43. doi: 10.1038/eye.2016.107
282. Burns SA, Elsner AE, Sapoznik KA, Warner RL, Gast TJ. Adaptive optics imaging of the human retina. *Prog Retin Eye Res.* (2019) 68:1–30. doi: 10.1016/j.preteyeres.2018.08.002
283. Scoles D, Sulai YN, Dubra A. In vivo dark-field imaging of the retinal pigment epithelium cell mosaic. *Biomed Opt Express.* (2013) 4:1710–23. doi: 10.1364/BOE.4.001710
284. Rossi EA, Granger CE, Sharma R, Yang Q, Saito K, Schwarz C, et al. Imaging individual neurons in the retinal ganglion cell layer of the living eye. *Proc Natl Acad Sci U S A.* (2017) 114:586–91. doi: 10.1073/pnas.1613445114
285. Liu Z, Kurokawa K, Zhang F, Lee JJ, Miller DT. Imaging and quantifying ganglion cells and other transparent neurons in the living human retina. *Proc Natl Acad Sci U S A.* (2017) 114:12803–8. doi: 10.1073/pnas.1711734114
286. Querques G, Massamba N, Guigui B, Lea Q, Lamory B, Soubrane G, et al. In vivo evaluation of photoreceptor mosaic in early onset large colloid drusen using adaptive optics. *Acta Ophthalmol.* (2012) 90:e327–8. doi: 10.1111/j.1755-3768.2011.02228.x
287. Panorgias A, Zawadzki RJ, Capps AG, Hunter AA, Morse LS, Werner JS, et al. Multimodal assessment of microscopic morphology and retinal function in patients with geographic atrophy. *Invest Ophthalmol Vis Sci.* (2013) 54:4372–84. doi: 10.1167/iovs.12-11525
288. Godara P, Siebe C, Rha J, Michaelides M, Carroll J. Assessing the photoreceptor mosaic over drusen using adaptive optics and SD-OCT. *Ophthalmic Surg Lasers Imaging.* (2010) 41:S104–8. doi: 10.3928/15428877-20101031-07
289. Choi SS, Zawadzki RJ, Lim MC, Brandt JD, Keltner JL, Doble N, et al. Evidence of outer retinal changes in glaucoma patients as revealed by ultrahigh-resolution in vivo retinal imaging. *Br J Ophthalmol.* (2011) 95:131–41. doi: 10.1136/bjo.2010.183756
290. Werner JS, Keltner JL, Zawadzki RJ, Choi SS. Outer retinal abnormalities associated with inner retinal pathology in nonglaucomatous and glaucomatous optic neuropathies. *Eye (Lond).* (2011) 25:279–89. doi: 10.1038/eye.2010.218
291. Torti C, Povazay B, Hofer B, Unterhuber A, Carroll J, Ahnelt PK, et al. Adaptive optics optical coherence tomography at 120,000 depth scans/s for non-invasive cellular phenotyping of the living human retina. *Opt Express.* (2009) 17:19382–400. doi: 10.1364/OE.17.019382
292. Wang Q, Kocaoglu OP, Cense B, Bruestle J, Jonnal RS, Gao W, et al. Imaging retinal capillaries using ultrahigh-resolution optical coherence tomography and adaptive optics. *Invest Ophthalmol Vis Sci.* (2011) 52:6292–9. doi: 10.1167/iovs.10-6424
293. Kurokawa K, Sasaki K, Makita S, Hong YJ, Yasuno Y. Three-dimensional retinal and choroidal capillary imaging by power Doppler optical coherence angiography with adaptive optics. *Opt Express.* (2012) 20:22796–812. doi: 10.1364/OE.20.022796
294. Felberer F, Rechenmacher M, Haindl R, Baumann B, Hitzenberger CK, Pircher M, et al. Imaging of retinal vasculature using adaptive optics SLO/OCT. *Biomed Opt Express.* (2015) 6:1407–18. doi: 10.1364/BOE.6.001407
295. Tam J, Dhamdhere KP, Tiruveedhula P, Manzanera S, Barez S, Bearse MA Jr., et al. Disruption of the retinal parafoveal capillary network in type 2 diabetes before the onset of diabetic retinopathy. *Invest Ophthalmol Vis Sci.* (2011) 52:9257–66. doi: 10.1167/iovs.11-8481
296. Lombardo M, Parravano M, Lombardo G, Varano M, Boccassini B, Stirpe M, et al. Adaptive optics imaging of parafoveal cones in type 1 diabetes. *Retina.* (2014) 34:546–57. doi: 10.1097/IAE.0b013e3182a10850
297. Park SS, Bauer G, Abedi M, Pontow S, Panorgias A, Jonnal R, et al. Intravitreal autologous bone marrow CD34+ cell therapy for ischemic and degenerative retinal disorders: preliminary phase 1 clinical trial findings. *Invest Ophthalmol Vis Sci.* (2014) 56:81–9. doi: 10.1167/iovs.14-15415
298. Nakamura T, Ueda-Consolvo T, Oiwake T, Hayashi A. Correlation between outer retinal layer thickness and cone density in patients with resolved central serous chorioretinopathy. *Graefes Arch Clin Exp Ophthalmol.* (2016) 254:2347–54. doi: 10.1007/s00417-016-3403-1
299. Foote KG, Wong JJ, Boehm AE, Bensinger E, Porco TC, Roorda A, et al. Comparing cone structure and function in RHO- and RPGR-associated retinitis pigmentosa. *Invest Ophthalmol Vis Sci.* (2020) 61:42. doi: 10.1167/iovs.61.4.42
300. Foote KG, Loumou P, Griffin S, Qin J, Ratnam K, Porco TC, et al. Relationship between foveal cone structure and visual acuity measured with adaptive optics scanning laser ophthalmoscopy in retinal degeneration. *Invest Ophthalmol Vis Sci.* (2018) 59:3385–93. doi: 10.1167/iovs.17-23708
301. Thompson DA, Iannaccone A, Ali RR, Arshavsky VY, Audo I, Bainbridge JWB, et al. Advancing clinical trials for inherited retinal diseases: recommendations from the second monaciano symposium. *Transl Vis Sci Technol.* (2020) 9:2. doi: 10.1167/tvst.9.7.2
302. Reumueller A, Schmidt-Erfurth U, Salas M, Sacu S, Drexler W, Pircher M, et al. Three-dimensional adaptive optics-assisted visualization of photoreceptors in healthy and pathologically aged eyes. *Invest Ophthalmol Vis Sci.* (2019) 60:1144–55. doi: 10.1167/iovs.18-25702
303. Reumueller A, Wassermann L, Salas M, Karantonis MG, Sacu S, Georgopoulos M, et al. Morphologic and functional assessment of photoreceptors after macula-off retinal detachment with adaptive-optics OCT and microperimetry. *Am J Ophthalmol.* (2020) 214:72–85. doi: 10.1016/j.ajo.2019.12.015
304. Wong KS, Jian Y, Cua M, Bonora S, Zawadzki RJ, Sarunic MV, et al. In vivo imaging of human photoreceptor mosaic with wavefront sensorless adaptive optics optical coherence tomography. *Biomed Opt Express.* (2015) 6:580–90. doi: 10.1364/BOE.6.000580
305. South FA, Kurokawa K, Liu Z, Liu YZ, Miller DT, Boppart SA, et al. Combined hardware and computational optical wavefront correction. *Biomed Opt Express.* (2018) 9:2562–74. doi: 10.1364/BOE.9.002562
306. Kocaoglu OP, Lee S, Jonnal RS, Wang Q, Herde AE, Derby JC, et al. Imaging cone photoreceptors in three dimensions and in time using ultrahigh resolution optical coherence tomography with adaptive optics. *Biomed Opt Express.* (2011) 2:748–63. doi: 10.1364/BOE.2.000748
307. Lee SH, Werner JS, Zawadzki RJ. Improved visualization of outer retinal morphology with aberration cancelling reflective optical design for adaptive optics - optical coherence tomography. *Biomed Opt Express.* (2013) 4:2508–17. doi: 10.1364/BOE.4.002508

308. Kocaoglu OP, Turner TL, Liu Z, Miller DT. Adaptive optics optical coherence tomography at 1 MHz. *Biomed Opt Express.* (2014) 5:4186–200. doi: 10.1364/BOE.5.004186
309. Kocaoglu OP, Ferguson RD, Jonnal RS, Liu Z, Wang Q, Hammer DX, et al. Adaptive optics optical coherence tomography with dynamic retinal tracking. *Biomed Opt Express.* (2014) 5:2262–84. doi: 10.1364/BOE.5.002262
310. Pircher M, Zawadzki RJ, Evans JW, Werner JS, Hitzenberger CK. Simultaneous imaging of human cone mosaic with adaptive optics enhanced scanning laser ophthalmoscopy and high-speed transversal scanning optical coherence tomography. *Opt Lett.* (2008) 33:22–4. doi: 10.1364/OL.33.000022
311. Felberer F, Kroisamer JS, Baumann B, Zotter S, Schmidt-Erfurth U, Hitzenberger CK, et al. Adaptive optics SLO/OCT for 3D imaging of human photoreceptors in vivo. *Biomed Opt Express.* (2014) 5:439–56. doi: 10.1364/BOE.5.000439
312. Hillmann D, Spahr H, Hain C, Sudkamp H, Franke G, Pfaffle C, et al. Aberration-free volumetric high-speed imaging of in vivo retina. *Sci Rep.* (2016) 6:35209. doi: 10.1038/srep35209
313. Azimipour M, Jonnal RS, Werner JS, Zawadzki RJ. Coextensive synchronized SLO-OCT with adaptive optics for human retinal imaging. *Opt Lett.* (2019) 44:4219–22. doi: 10.1364/OL.44.004219
314. Azimipour M, Zawadzki RJ, Gorczynska I, Migacz J, Werner JS, Jonnal RS, et al. Intraframe motion correction for raster-scanned adaptive optics images using strip-based cross-correlation lag biases. *PLoS One.* (2018) 13:e0206052. doi: 10.1371/journal.pone.0206052
315. Liu Z, Kocaoglu OP, Miller DT. 3D Imaging of Retinal Pigment Epithelial Cells in the Living Human Retina. *Invest Ophthalmol Vis Sci.* (2016) 57:OCT533–43. doi: 10.1167/iovs.16-19106
316. Liu Z, Tam J, Saeedi O, Hammer DX. Trans-retinal cellular imaging with multimodal adaptive optics. *Biomed Opt Express.* (2018) 9:4246–62. doi: 10.1364/BOE.9.004246
317. Wells-Gray EM, Choi SS, Slabaugh M, Weber P, Doble N. Inner retinal changes in primary open-angle glaucoma revealed through adaptive optics-optical coherence tomography. *J Glaucoma.* (2018) 27:1025–8. doi: 10.1097/IJG.0000000000001039
318. Tanna H, Dubis AM, Ayub N, Tait DM, Rha J, Stepien KE, et al. Retinal imaging using commercial broadband optical coherence tomography. *Br J Ophthalmol.* (2010) 94:372–6. doi: 10.1136/bjo.2009.163501
319. Kurokawa K, Crowell JA, Zhang F, Miller DT. Suite of methods for assessing inner retinal temporal dynamics across spatial and temporal scales in the living human eye. *Neurophotonics.* (2020) 7:015013. doi: 10.1117/1.NPh.7.1.015013
320. Csaky K, Ferris F 3rd., Chew EY, Nair P, Cheetham JK, Duncan JL, et al. Report from the NEI/FDA endpoints workshop on age-related macular degeneration and inherited retinal diseases. *Invest Ophthalmol Vis Sci.* (2017) 58:3456–63. doi: 10.1167/iovs.17-22339
321. Pandiyan VP, Jiang X, Kuchenbecker JA, Sabesan R. Reflective mirror-based line-scan adaptive optics OCT for imaging retinal structure and function. *Biomed Opt Express.* (2021) 12:5865–80. doi: 10.1364/BOE.436337
322. Valente D, Vienola KV, Zawadzki RJ, Jonnal RS. Kilohertz retinal FF-SS-OCT and flood imaging with hardware-based adaptive optics. *Biomed Opt Express.* (2020) 11:5995–6011. doi: 10.1364/BOE.403509
323. Cooper RF, Tuten WS, Dubra A, Brainard DH, Morgan JIW. Non-invasive assessment of human cone photoreceptor function. *Biomed Opt Express.* (2017) 8:5098–112. doi: 10.1364/BOE.8.005098
324. Hüllmann D, Spahr H, Pfäffle C, Sudkamp H, Franke G, Hüttmann G, et al. In vivo optical imaging of physiological responses to photostimulation in human photoreceptors. *Proc Natl Acad Sci U S A.* (2016) 113:13138–43. doi: 10.1073/pnas.1606428113
325. Al-Aswad LA, Ramachandran R, Schuman JS. Artificial intelligence for glaucoma: creating and implementing AI for disease detection and progression. *Ophthalmol Glaucoma.* (2022):S2589–4196. [Online ahead of print], doi: 10.1016/j.ogla.2022.02.010
326. Blumenkranz MS, Tarver ME, Myung D, Eydelman MB. The collaborative community on ophthalmic imaging: accelerating global innovation and clinical utility. *Ophthalmology.* (2022) 129:e9–13. doi: 10.1016/j.ophtha.2021.10.001
327. Schuman JS, Ramos Cadena DLAM, McGee R, Al-Aswad LA, Medeiros FA. A case for the use of artificial intelligence in glaucoma assessment. *Ophthalmol Glaucoma.* (2021) 5:e3–13. doi: 10.1016/j.ogla.2021.12.003
328. Abramoff MD, Cunningham B, Patel B, Eydelman MB, Leng T, Sakamoto T, et al. Foundational considerations for artificial intelligence using ophthalmic images. *Ophthalmology.* (2022) 129:e14–32. doi: 10.1016/j.ophtha.2021.08.023
329. Fazal MI, Patel ME, Tye J, Gupta Y. The past, present and future role of artificial intelligence in imaging. *Eur J Radiol.* (2018) 105:246–50. doi: 10.1016/j.ejrad.2018.06.020
330. Benet D, Pellicer-Valero OJ. Artificial intelligence: the unstoppable revolution in ophthalmology. *Surv Ophthalmol.* (2022) 67:252–70. doi: 10.1016/j.survophthal.2021.03.003
331. Salazar H, Misra V, Swaminathan SS. Artificial intelligence and complex statistical modeling in glaucoma diagnosis and management. *Curr Opin Ophthalmol.* (2021) 32:105–17. doi: 10.1097/ICU.0000000000000741
332. Mirzania D, Thompson AC, Muir KW. Applications of deep learning in detection of glaucoma: a systematic review. *Eur J Ophthalmol.* (2021) 31:1618–42. doi: 10.1177/1120672120977346
333. Halupka KJ, Antony BJ, Lee MH, Lucy KA, Rai RS, Ishikawa H, et al. Retinal optical coherence tomography image enhancement via deep learning. *Biomed Opt Express.* (2018) 9:6205–21. doi: 10.1364/BOE.9.006205
334. Prabhakar B, Singh RK, Yadav KS. Artificial intelligence (AI) impacting diagnosis of glaucoma and understanding the regulatory aspects of AI-based software as medical device. *Comput Med Imaging Graph.* (2021) 87:101818. doi: 10.1016/j.compmedimag.2020.101818
335. Zheng C, Johnson TV, Garg A, Boland MV. Artificial intelligence in glaucoma. *Curr Opin Ophthalmol.* (2019) 30:97–103. doi: 10.1097/ICU.0000000000000552
336. Thompson AC, Jammal AA, Berchuck SI, Mariottoni EB, Medeiros FA. Assessment of a segmentation-free deep learning algorithm for diagnosing glaucoma from optical coherence tomography scans. *JAMA Ophthalmol.* (2020) 138:333–9. doi: 10.1001/jamaophthalmol.2019.5983
337. Raghavendra U, Gudigar A, Bhandary SV, Rao TN, Ciaccio EJ, Acharya UR, et al. A two layer sparse autoencoder for glaucoma identification with fundus images. *J Med Syst.* (2019) 43:299. doi: 10.1007/s10916-019-1427-x
338. Li Z, He Y, Keel S, Meng W, Chang RT, He M, et al. Efficacy of a deep learning system for detecting glaucomatous optic neuropathy based on color fundus photographs. *Ophthalmology.* (2018) 125:1199–206. doi: 10.1016/j.ophtha.2018.01.023
339. Liu H, Li L, Wormstone IM, Qiao C, Zhang C, Liu P, et al. Development and validation of a deep learning system to detect glaucomatous optic neuropathy using fundus photographs. *JAMA Ophthalmol.* (2019) 137:1353–60. doi: 10.1001/jamaophthalmol.2019.3501
340. Lee T, Jammal AA, Mariottoni EB, Medeiros FA. Predicting glaucoma development with longitudinal deep learning predictions from fundus photographs. *Am J Ophthalmol.* (2021) 225:86–94. doi: 10.1016/j.ajo.2020.12.031
341. Milea D, Najjar RP, Zhubo J, Ting D, Vasseneix C, Xu X, et al. Artificial intelligence to detect papilledema from ocular fundus photographs. *N Engl J Med.* (2020) 382:1687–95. doi: 10.1056/NEJMoa1917130
342. Liu TYA, Wei J, Zhu H, Subramanian PS, Myung D, Yi PH, et al. Detection of optic disc abnormalities in color fundus photographs using deep learning. *J Neuroophthalmol.* (2021) 41:368–74. doi: 10.1097/WNO.0000000000001358
343. Milea D, Singhal S, Najjar RP. Artificial intelligence for detection of optic disc abnormalities. *Curr Opin Neurol.* (2020) 33:106–10. doi: 10.1097/WCO.0000000000000773
344. Ran AR, Cheung CY, Wang X, Chen H, Luo LY, Chan PP, et al. Detection of glaucomatous optic neuropathy with spectral-domain optical coherence tomography: a retrospective training and validation deep-learning analysis. *Lancet Digit Health.* (2019) 1:e172–82. doi: 10.1016/S2589-7500(19)30085-8
345. Li L, Zhu H, Zhang Z, Zhao L, Xu L, Jonas RA, et al. Neural network-based retinal nerve fiber layer profile compensation for glaucoma diagnosis in myopia: model development and validation. *JMIR Med Inform.* (2021) 9:e22664. doi: 10.2196/22664

346. Porporato N, Tun TA, Baskaran M, Wong DWK, Husain R, Fu H, et al. Towards 'automated gonioscopy': a deep learning algorithm for 360° angle assessment by swept-source optical coherence tomography. *Br J Ophthalmol.* (2021):bjohthalmol–2020–318275. [Online ahead of print], doi: 10.1136/bjophthalmol-2020-318275
347. Devalla SK, Chin KS, Mari JM, Tun TA, Strouthidis NG, Aung T, et al. A deep learning approach to digitally stain optical coherence tomography images of the optic nerve head. *Invest Ophthalmol Vis Sci.* (2018) 59:63–74. doi: 10.1167/iovs.17-22617
348. Thompson AC, Jammal AA, Medeiros FA. A deep learning algorithm to quantify neuroretinal rim loss from optic disc photographs. *Am J Ophthalmol.* (2019) 201:9–18. doi: 10.1016/j.ajo.2019.01.011
349. Schottenhamml J, Würfl T, Mardin S, Ploner SB, Husvogt L, Hohberger B, et al. Glaucoma classification in 3 x 3 mm en face macular scans using deep learning in a different plexus. *Biomed Opt Express.* (2021) 12:7434–44. doi: 10.1364/BOE.439991
350. Bowd C, Belghith A, Zangwill LM, Christopher M, Goldbaum MH, Fan R, et al. Deep learning image analysis of optical coherence tomography angiography measured vessel density improves classification of healthy and glaucoma eyes. *Am J Ophthalmol.* (2021) 236:298–308. doi: 10.1016/j.ajo.2021.11.008
351. Mehta P, Petersen CA, Wen JC, Banitt MR, Chen PP, Bojikian KD, et al. Automated detection of glaucoma with interpretable machine learning using clinical data and multimodal retinal images. *Am J Ophthalmol.* (2021) 231:154–69. doi: 10.1016/j.ajo.2021.04.021
352. Sun S, Ha A, Kim YK, Yoo BW, Kim HC, Park KH, et al. Dual-input convolutional neural network for glaucoma diagnosis using spectral-domain optical coherence tomography. *Br J Ophthalmol.* (2021) 105:1555–60. doi: 10.1136/bjophthalmol-2020-316274
353. Panda SK, Cheong H, Tun TA, Devella SK, Senthil V, Krishnadas R, et al. Describing the structural phenotype of the glaucomatous optic nerve head using artificial intelligence. *Am J Ophthalmol.* (2021) 236:172–82. doi: 10.1016/j.ajo.2021.06.010
354. Andrade De Jesus D, Sánchez Brea L, Barbosa Breda J, Fokkinga E, Ederveen V, Borren N, et al. OCTA multilayer and multisector peripapillary microvascular modeling for diagnosing and staging of glaucoma. *Transl Vis Sci Technol.* (2020) 9:58. doi: 10.1167/tvst.9.2.58
355. Wu CW, Shen HL, Lu CJ, Chen SH, Chen HY. Comparison of different machine learning classifiers for glaucoma diagnosis based on spectralis OCT. *Diagnostics (Basel).* (2021) 11:1718. doi: 10.3390/diagnostics11091718
356. Shin Y, Cho H, Jeong HC, Seong M, Choi JW, Lee WJ, et al. Deep learning-based diagnosis of glaucoma using wide-field optical coherence tomography images. *J Glaucoma.* (2021) 30:803–12. doi: 10.1097/IJG.0000000000001885
357. Raja H, Hassan T, Akram MU, Werghi N. Clinically verified hybrid deep learning system for retinal ganglion cells aware grading of glaucomatous progression. *IEEE Trans Biomed Eng.* (2021) 68:2140–51. doi: 10.1109/TBME.2020.3030085
358. Wu JH, Nishida T, Weinreb RN, Lin JW. Performances of machine learning in detecting glaucoma using fundus and retinal optical coherence tomography images: a meta-analysis. *Am J Ophthalmol.* (2021) 237:1–12. doi: 10.1016/j.ajo.2021.12.008
359. Maetschke S, Antony B, Ishikawa H, Wollstein G, Schuman J, Garnavi R, et al. A feature agnostic approach for glaucoma detection in OCT volumes. *PLoS One.* (2019) 14:e0219126. doi: 10.1371/journal.pone.0219126
360. Kucur SS, Hollo G, Sznitman R. A deep learning approach to automatic detection of early glaucoma from visual fields. *PLoS One.* (2018) 13:e0206081. doi: 10.1371/journal.pone.0206081
361. Li F, Wang Z, Qu G, Song D, Yuan Y, Xu Y, et al. Automatic differentiation of Glaucoma visual field from non-glaucoma visual filed using deep convolutional neural network. *BMC Med Imaging.* (2018) 18:35. doi: 10.1186/s12880-018-0273-5
362. Devalla SK, Liang Z, Pham TH, Boote C, Strouthidis NG, Thiery AH, et al. Glaucoma management in the era of artificial intelligence. *Br J Ophthalmol.* (2020) 104:301–11. doi: 10.1136/bjophthalmol-2019-315016
363. Hashimoto Y, Asaoka R, Kiwaki T, Sugiura H, Asano S, Murata H, et al. Deep learning model to predict visual field in central 10° from optical coherence tomography measurement in glaucoma. *Br J Ophthalmol.* (2021) 105:507–13. doi: 10.1136/bjophthalmol-2019-315600
364. Hashimoto Y, Kiwaki T, Sugiura H, Asano S, Murata H, Fujino Y, et al. Predicting 10-2 visual field from optical coherence tomography in glaucoma using deep learning corrected with 24-2/30-2 visual field. *Transl Vis Sci Technol.* (2021) 10:28. doi: 10.1167/tvst.10.13.28
365. Yu HH, Maetschke SR, Antony BJ, Ishikawa H, Wollstein G, Schuman JS, et al. Estimating global visual field indices in glaucoma by combining macula and optic disc OCT scans using 3-dimensional convolutional neural networks. *Ophthalmol Glaucoma.* (2021) 4:102–12. doi: 10.1016/j.ogla.2020.07.002
366. Lazaridis G, Montesano G, Afgeh SS, Mohamed-Noriega J, Ourselin S, Lorenzi M, et al. Predicting visual fields from optical coherence tomography via an ensemble of deep representation learners. *Am J Ophthalmol.* (2022) 238:52–65. doi: 10.1016/j.ajo.2021.12.020
367. Christopher M, Bowd C, Proudfoot JA, Belghith A, Goldbaum MH, Rezapour J, et al. Deep learning estimation of 10-2 and 24-2 visual field metrics based on thickness maps from macula OCT. *Ophthalmology.* (2021) 128:1534–48. doi: 10.1016/j.ophtha.2021.04.022
368. Datta S, Mariottoni EB, Dov D, Jammal AA, Carin L, Medeiros FA, et al. RetiNerveNet: using recursive deep learning to estimate pointwise 24-2 visual field data based on retinal structure. *Sci Rep.* (2021) 11:12562. doi: 10.1038/s41598-021-91493-9
369. Christopher M, Bowd C, Belghith A, Goldbaum MH, Weinreb RN, Fazio MA, et al. Deep learning approaches predict glaucomatous visual field damage from OCT optic nerve head en face images and retinal nerve fiber layer thickness maps. *Ophthalmology.* (2020) 127:346–56. doi: 10.1016/j.ophtha.2019.09.036
370. Xiong J, Li F, Song D, Tang G, He J, Gao K, et al. Multimodal machine learning using visual fields and peripapillary circular OCT scans in detection of glaucomatous optic neuropathy. *Ophthalmology.* (2022) 129:171–80. doi: 10.1016/j.ophtha.2021.07.032
371. Li F, Yang Y, Sun X, Qiu Z, Zhang S, Tun TA, et al. Digital gonioscopy based on three-dimensional anterior-segment OCT: an international multicenter study. *Ophthalmology.* (2022) 129:45–53. doi: 10.1016/j.ophtha.2021.09.018
372. Fu H, Baskaran M, Xu Y, Lin S, Wong DWK, Liu J, et al. A deep learning system for automated angle-closure detection in anterior segment optical coherence tomography images. *Am J Ophthalmol.* (2019) 203:37–45. doi: 10.1016/j.ajo.2019.02.028
373. Randhawa J, Chiang M, Porporato N, Pardeshi AA, Dredge J, Apolo Aroca G, et al. Generalisability and performance of an OCT-based deep learning classifier for community-based and hospital-based detection of gonioscopic angle closure. *Br J Ophthalmol.* (2021) doi: 10.1136/bjophthalmol-2021-319470 [Epub ahead of print].
374. Li W, Chen Q, Jiang C, Shi G, Deng G, Sun X, et al. Automatic anterior chamber angle classification using deep learning system and anterior segment optical coherence tomography images. *Transl Vis Sci Technol.* (2021) 10:19. doi: 10.1167/tvst.10.6.19
375. Hao H, Zhao Y, Yan Q, Higashita R, Zhang J, Zhao Y, et al. Angle-closure assessment in anterior segment OCT images via deep learning. *Med Image Anal.* (2021) 69:101956. doi: 10.1016/j.media.2021.101956
376. Fu H, Xu Y, Lin S, Wong DWK, Baskaran M, Mahesh M, et al. Angle-closure detection in anterior segment OCT based on multilevel deep network. *IEEE Trans Cybern.* (2020) 50:3358–66. doi: 10.1109/TCYB.2019.2897162
377. Wen JC, Lee CS, Keane PA, Xiao S, Rokem AS, Chen PP, et al. Forecasting future Humphrey Visual Fields using deep learning. *PLoS One.* (2019) 14:e0214875. doi: 10.1371/journal.pone.0214875
378. Yousefi S, Kiwaki T, Zheng Y, Sugiura H, Asaoka R, Murata H, et al. Detection of longitudinal visual field progression in glaucoma using machine learning. *Am J Ophthalmol.* (2018) 193:71–9. doi: 10.1016/j.ajo.2018.06.007
379. Christopher M, Belghith A, Weinreb RN, Bowd C, Goldbaum MH, Saunders LJ, et al. Retinal nerve fiber layer features identified by unsupervised machine learning on optical coherence tomography scans predict glaucoma progression. *Invest Ophthalmol Vis Sci.* (2018) 59:2748–56. doi: 10.1167/iovs.17-23387
380. Sedai S, Antony B, Ishikawa H, Wollstein G, Schuman JS, Garnavi R, et al. Forecasting retinal nerve fiber layer thickness from multimodal temporal data incorporating OCT volumes. *Ophthalmol Glaucoma.* (2020) 3:14–24. doi: 10.1016/j.ogla.2019.11.001

381. Wong WL, Su X, Li X, Cheung CM, Klein R, Cheng CY, et al. Global prevalence of age-related macular degeneration and disease burden projection for 2020 and 2040: a systematic review and meta-analysis. *Lancet Glob Health.* (2014) 2:e106–16. doi: 10.1016/S2214-109X(13)70145-1
382. Neely DC, Bray KJ, Huisingh CE, Clark ME, McGwin G Jr., Owsley C, et al. Prevalence of undiagnosed age-related macular degeneration in primary eye care. *JAMA Ophthalmol.* (2017) 135:570–5. doi: 10.1001/jamaophthalmol.2017.0830
383. Burlina PM, Joshi N, Pekala M, Pacheco KD, Freund DE, Bressler NM, et al. Automated grading of age-related macular degeneration from color fundus images using deep convolutional neural networks. *JAMA Ophthalmol.* (2017) 135:1170–6. doi: 10.1001/jamaophthalmol.2017.3782
384. Dow ER, Keenan TDL, Lad EM, Lee AY, Lee CS, Lowenstein A, et al. From data to deployment: the Collaborative Communities on Ophthalmic Imaging roadmap for artificial intelligence in age-related macular degeneration. *Ophthalmology.* (2022) 129:e43–59. doi: 10.1016/j.ophtha.2022.01.002
385. Pandit RR, Wibbelsman TD, Considine SP, Jenkins TL, Xu D, Levin HJ, et al. Distribution and practice patterns of retina providers in the United States. *Ophthalmology.* (2020) 127:1580–1. doi: 10.1016/j.ophtha.2020.04.016
386. De Fauw J, Ledsam JR, Romera-Paredes B, Nikolov S, Tomasev N, Blackwell S, et al. Clinically applicable deep learning for diagnosis and referral in retinal disease. *Nat Med.* (2018) 24:1342–50. doi: 10.1038/s41591-018-0107-6
387. Kalra G, Kar SS, Sevgi DD, Madabhushi A, Srivastava SK, Ehlers JP, et al. Quantitative imaging biomarkers in age-related macular degeneration and diabetic eye disease: a step closer to precision medicine. *J Pers Med.* (2021) 11:1161. doi: 10.3390/jpm11111161
388. Saha S, Nassisi M, Wang M, Lindenberg S, Kanagasingam Y, Sadda S, et al. Automated detection and classification of early AMD biomarkers using deep learning. *Sci Rep.* (2019) 9:10990. doi: 10.1038/s41598-019-47390-3
389. Waldstein SM, Vogl WD, Bogunovic H, Sadeghipour A, Riedl S, Schmidt-Erfurth U, et al. Characterization of drusen and hyperreflective foci as biomarkers for disease progression in age-related macular degeneration using artificial intelligence in optical coherence tomography. *JAMA Ophthalmol.* (2020) 138:740–7. doi: 10.1001/jamaophthalmol.2020.1376
390. Schmitz-Valckenberg S, Gobel AP, Saur SC, Steinberg JS, Thiele S, Wojek C, et al. Automated retinal image analysis for evaluation of focal hyperpigmentary changes in intermediate age-related macular degeneration. *Transl Vis Sci Technol.* (2016) 5:3. doi: 10.1167/tvst.5.2.3
391. Wang J, Hormel TT, Gao L, Zang P, Guo Y, Wang X, et al. Automated diagnosis and segmentation of choroidal neovascularization in OCT angiography using deep learning. *Biomed Opt Express.* (2020) 11:927–44. doi: 10.1364/BOE.379977
392. Zhang G, Fu DJ, Liefers B, Faes L, Glinton S, Wagner S, et al. Clinically relevant deep learning for detection and quantification of geographic atrophy from optical coherence tomography: a model development and external validation study. *Lancet Digit Health.* (2021) 3:e665–75. doi: 10.1016/S2589-7500(21)00134-5
393. Yan Y, Jin K, Gao Z, Huang X, Wang F, Wang Y, et al. Attention-based deep learning system for automated diagnoses of age-related macular degeneration in optical coherence tomography images. *Med Phys.* (2021) 48:4926–34. doi: 10.1002/mp.15002
394. Keenan TDL, Clemons TE, Domalpally A, Elman MJ, Havilio M, Agrón E, et al. Retinal specialist versus artificial intelligence detection of retinal fluid from OCT: age-related eye disease study 2: 10-year follow-on study. *Ophthalmology.* (2021) 128:100–9. doi: 10.1016/j.ophtha.2020.06.038
395. Burlina PM, Joshi N, Pacheco KD, Freund DE, Kong J, Bressler NM, et al. Use of deep learning for detailed severity characterization and estimation of 5-year risk among patients with age-related macular degeneration. *JAMA Ophthalmol.* (2018) 136:1359–66. doi: 10.1001/jamaophthalmol.2018.4118
396. Peng Y, Keenan TD, Chen Q, Agron E, Allot A, Wong WT, et al. Predicting risk of late age-related macular degeneration using deep learning. *NPJ Digit Med.* (2020) 3:111. doi: 10.1038/s41746-020-00317-z
397. Peng Y, Dharssi S, Chen Q, Keenan TD, Agron E, Wong WT, et al. DeepSeeNet: a deep learning model for automated classification of patient-based age-related macular degeneration severity from color fundus photographs. *Ophthalmology.* (2019) 126:565–75. doi: 10.1016/j.ophtha.2018.11.015
398. Potapenko I, Kristensen M, Thiesson B, Ilginis T, Lykke Sørensen T, Nouri Hajari J, et al. Detection of oedema on optical coherence tomography images using deep learning model trained on noisy clinical data. *Acta Ophthalmol.* (2022) 100:103–10. doi: 10.1111/aos.14895
399. Sarici K, Abraham JR, Sevgi DD, Lunasco L, Srivastava SK, Whitney J, et al. Risk classification for progression to subfoveal geographic atrophy in dry age-related macular degeneration using machine learning-enabled outer retinal feature extraction. *Ophthalmic Surg Lasers Imaging Retina.* (2022) 53:31–9. doi: 10.3928/23258160-20211210-01
400. Abdelfattah NS, Zhang H, Boyer DS, Rosenfeld PJ, Feuer WJ, Gregori G, et al. Drusen volume as a predictor of disease progression in patients with late age-related macular degeneration in the fellow eye. *Invest Ophthalmol Vis Sci.* (2016) 57:1839–46. doi: 10.1167/iovs.15-18572
401. Zhao X, Zhang X, Lv B, Meng L, Zhang C, Liu Y, et al. Optical coherence tomography-based short-term effect prediction of anti-vascular endothelial growth factor treatment in neovascular age-related macular degeneration using sensitive structure guided network. *Graefes Arch Clin Exp Ophthalmol.* (2021) 259:3261–9. doi: 10.1007/s00417-021-05247-4
402. Romond K, Alam M, Kravets S, Sisternes L, Leng T, Lim JI, et al. Imaging and artificial intelligence for progression of age-related macular degeneration. *Exp Biol Med (Maywood).* (2021) 246:2159–69. doi: 10.1177/15353702211031547
403. Kashani AH, Zimmer-Galler IE, Shah SM, Dustin L, Do DV, Eliott D, et al. Retinal thickness analysis by race, gender, and age using Stratus OCT. *Am J Ophthalmol.* (2010) 149:496–502.e1. doi: 10.1016/j.ajo.2009.09.025
404. Alam M, Zhang Y, Lim JI, Chan RVP, Yang M, Yao X, et al. Quantitative optical coherence tomography angiography features for objective classification and staging of diabetic retinopathy. *Retina.* (2020) 40:322–32. doi: 10.1097/IAE.0000000000002373
405. Ting DSW, Cheung CY, Lim G, Tan GSW, Quang ND, Gan A, et al. Development and validation of a deep learning system for diabetic retinopathy and related eye diseases using retinal images from multiethnic populations with diabetes. *JAMA.* (2017) 318:2211–23. doi: 10.1001/jama.2017.18152
406. Walton OB, Garoon RB, Weng CY, Gross J, Young AK, Camero KA, et al. Evaluation of automated teleretinal screening program for diabetic retinopathy. *JAMA Ophthalmol.* (2016) 134:204–9. doi: 10.1001/jamaophthalmol.2015.5083
407. Arsalan M, Owais M, Mahmood T, Cho SW, Park KR. Aiding the diagnosis of diabetic and hypertensive retinopathy using artificial intelligence-based semantic segmentation. *J Clin Med.* (2019) 8:1446. doi: 10.3390/jcm8091446
408. Islam MM, Poly TN, Walther BA, Yang HC, Li YJ. Artificial intelligence in ophthalmology: a meta-analysis of deep learning models for retinal vessels segmentation. *J Clin Med.* (2020) 9:1018. doi: 10.3390/jcm9041018
409. Hassan B, Hassan T, Li B, Ahmed R, Hassan O. Deep ensemble learning based objective grading of macular edema by extracting clinically significant findings from fused retinal imaging modalities. *Sensors (Basel).* (2019) 19:2970. doi: 10.3390/s19132970
410. Verbraak FD, Abramoff MD, Bausch GCF, Klaver C, Nijpels G, Schlingemann RO, et al. Diagnostic accuracy of a device for the automated detection of diabetic retinopathy in a primary care setting. *Diabetes Care.* (2019) 42:651–6. doi: 10.2337/dc18-0148
411. Liu X, Ali TK, Singh P, Shah A, McKinney SM, Ruamviboonsuk P, et al. Deep learning to detect optical coherence tomography-derived diabetic macular edema from retinal photographs: a multicenter validation study. *Ophthalmol Retina.* (2022) 6:398–410. doi: 10.1016/j.oret.2021.12.021
412. Ipp E, Liljenquist D, Bode B, Shah VN, Silverstein S, Regillo CD, et al. Pivotal evaluation of an artificial intelligence system for autonomous detection of referrable and vision-threatening diabetic retinopathy. *JAMA Netw Open.* (2021) 4:e2134254. doi: 10.1001/jamanetworkopen.2021.34254
413. Nuzzi R, Boscia G, Marolo P, Ricardi F. The impact of artificial intelligence and deep learning in eye diseases: a review. *Front Med (Lausanne).* (2021) 8:710329. doi: 10.3389/fmed.2021.710329
414. Gulshan V, Peng L, Coram M, Stumpe MC, Wu D, Narayanaswamy A, et al. Development and validation of a deep learning algorithm for detection of diabetic retinopathy in retinal fundus photographs. *JAMA.* (2016) 316:2402–10. doi: 10.1001/jama.2016.17216

415. Gargeya R, Leng T. Automated identification of diabetic retinopathy using deep learning. *Ophthalmology.* (2017) 124:962–9. doi: 10.1016/j.ophtha.2017.02.008
416. Ardiyanto I, Nugroho HA, Buana RLB. Deep learning-based Diabetic Retinopathy assessment on embedded system. *Annu Int Conf IEEE Eng Med Biol Soc.* (2017) 2017:1760–3. doi: 10.1109/EMBC.2017.8037184
417. Ryu G, Lee K, Park D, Park SH, Sagong M. A deep learning model for identifying diabetic retinopathy using optical coherence tomography angiography. *Sci Rep.* (2021) 11:23024. doi: 10.1038/s41598-021-02479-6
418. Chen YM, Huang WT, Ho WH, Tsai JT. Classification of age-related macular degeneration using convolutional-neural-network-based transfer learning. *BMC Bioinformatics.* (2021) 22:99. doi: 10.1186/s12859-021-04001-1
419. Institute of Medicine (Us) Committee on Evaluating Clinical Applications of Telemedicine [IMCECAT]. *Telemedicine: A Guide to Assessing Telecommunications in Health Care*. Field MJ editor. Washington, DC: National Academies Press (1996).
420. Lord RK, Shah VA, San Filippo AN. Novel uses of smartphones in ophthalmology. *Ophthalmology.* (2010) 117:1274–1274.e3. doi: 10.1016/j.ophtha.2010.01.001
421. Pujari A, Saluja G, Agarwal D, Selvan H, Sharma N. Clinically useful smartphone ophthalmic imaging techniques. *Graefes Arch Clin Exp Ophthalmol.* (2021) 259:279–87. doi: 10.1007/s00417-020-04917-z
422. Kumar N, Bandello F, Sharma A. Smartphone-based gonio-imaging: a novel addition to glaucoma screening tools. *J Glaucoma.* (2019) 28:e149–50. doi: 10.1097/IJG.0000000000001306
423. Pujari A, Behera AK, Agarwal D, Sihota R, Dada T. A new technique of iPhone 11 Pro Max Smartphone-aided angle video and standstill image documentation. *J Glaucoma.* (2020) 29:e28–30. doi: 10.1097/IJG.0000000000001479
424. Pujari A, Selvan H, Asif MI, Gupta B, Dada T. Smartphone-aided quantification of iridocorneal angle. *J Glaucoma.* (2019) 28:e153–5. doi: 10.1097/IJG.0000000000001316
425. Pujari A, Mukhija R, Phuljhele S. Quantification of change in Iris Torsion using a smartphone. *Ophthalmology.* (2019) 126:126. doi: 10.1016/j.ophtha.2018.10.017
426. Pujari A, Phuljhele S, Sharma P. Quantification of Retinal Torsion in strabismus using a smartphone. *Ophthalmol Retina.* (2019) 3:379. doi: 10.1016/j.oret.2018.12.007
427. Sousa AI, Neves CM, Vieira P. Smartphone-based pupillometer with chromatic stimuli to screen neuro-ophthalmological diseases. In: Tiginyanu I, Sontea V, Railean S editors. *Proceeding of the 5th International Conference on Nanotechnologies and Biomedical Engineering*. Berlin: Springer International Publishing (2022). doi: 10.1007/978-3-030-92328-0_19
428. Chang LY, Turuwhenua J, Qu TY, Black JM, Acosta ML. Infrared video pupillography coupled with smart phone LED for measurement of pupillary light reflex. *Front Integr Neurosci.* (2017) 11:6. doi: 10.3389/fnint.2017.00006
429. McAnany JJ, Smith BM, Garland A, Kagen SL. iPhone-based Pupillometry: a novel approach for assessing the pupillary light reflex. *Optom Vis Sci.* (2018) 95:953–8. doi: 10.1097/OPX.0000000000001289
430. Pujari A, Kishore A, Makwana T, Sharma N. A simple tool to assess an implantable collamer lens vault. *J Cataract Refract Surg.* (2019) 45:883–4. doi: 10.1016/j.jcrs.2019.04.022
431. Pujari A, Yadav S, Mukhija R, Urkude J, Sharma N. Smartphone-aided technique to quantify toric intraocular lens alignment. *J Cataract Refract Surg.* (2019) 45:1833–4. doi: 10.1016/j.jcrs.2019.09.013
432. Pallas A, Yeo TK, Trevenen M, Barrett G. Evaluation of the accuracy of two marking methods and the novel toriCAM application for toric intraocular lens alignment. *J Refract Surg.* (2018) 34:150–5. doi: 10.3928/1081597X-20180115-03
433. Bastawrous A, Giardini ME, Bolster NM, Peto T, Shah N, Livingstone IA, et al. Clinical validation of a smartphone-based adapter for optic disc imaging in Kenya. *JAMA Ophthalmol.* (2016) 134:151–8. doi: 10.1001/jamaophthalmol.2015.4625
434. Russo A, Morescalchi F, Costagliola C, Delcassi L, Semeraro F. A novel device to exploit the smartphone camera for fundus photography. *J Ophthalmol.* (2015) 2015:823139. doi: 10.1155/2015/823139
435. Nazari Khanamiri H, Nakatsuka A, El-Annan J. Smartphone fundus photography. *J Vis Exp.* (2017) 125:55958. doi: 10.3791/55958 [Epub ahead of print].
436. Pujari A, Mukhija R, Chawla R, Phuljhele S, Saxena R, Sharma P, et al. Smartphone-based evaluation of the optic nerve head. *Indian J Ophthalmol.* (2018) 66:1617–8. doi: 10.4103/ijo.IJO_394_18
437. Suto S, Hiraoka T, Oshika T. Fluorescein fundus angiography with smartphone. *Retina.* (2014) 34:203–5. doi: 10.1097/IAE.0000000000000041
438. Sivaraman A, Nagarajan S, Vadivel S, Dutt S, Tiwari P, Narayana S, et al. A novel, smartphone-based, teleophthalmology-enabled, widefield fundus imaging device with an autocapture algorithm. *Transl Vis Sci Technol.* (2021) 10:21. doi: 10.1167/tvst.10.12.21
439. Bilong Y, Domngang CN, Nwanlih Gimma G, Katte JC, Afetane TE, Kagmeni G, et al. Smartphone-assisted glaucoma screening in patients with Type 2 diabetes: a pilot study. *Med Hypothesis Discov Innov Ophthalmol.* (2020) 9:61–5.
440. Alawa KA, Nolan RP, Han E, Arboleda A, Durkee H, Sayed MS, et al. Low-cost, smartphone-based frequency doubling technology visual field testing using a head-mounted display. *Br J Ophthalmol.* (2021) 105:440–4. doi: 10.1136/bjophthalmol-2019-314031
441. Rathi S, Tsui E, Mehta N, Zahid S, Schuman JS. The current state of teleophthalmology in the United States. *Ophthalmology.* (2017) 124:1729–34. doi: 10.1016/j.ophtha.2017.05.026
442. Bergua A, Mardin CY, Horn FK. Tele-transmission of stereoscopic images of the optic nerve head in glaucoma via Internet. *Telemed J E Health.* (2009) 15:439–44. doi: 10.1089/tmj.2008.0162
443. Kiage D, Kherani IN, Gichuhi S, Damji KF, Nyenze M. The muranga teleophthalmology study: comparison of virtual (Teleglaucoma) with in-person clinical assessment to diagnose glaucoma. *Middle East Afr J Ophthalmol.* (2013) 20:150–7. doi: 10.4103/0974-9233.110604
444. Sakamoto M, Kanamori A, Fujihara M, Yamada Y, Nakamura M, Negi A, et al. Assessment of IcareONE rebound tonometer for self-measuring intraocular pressure. *Acta Ophthalmol.* (2014) 92:243–8. doi: 10.1111/aos.12108
445. Mansouri K, Medeiros FA, Tafreshi A, Weinreb RN. Continuous 24-hour monitoring of intraocular pressure patterns with a contact lens sensor: safety, tolerability, and reproducibility in patients with glaucoma. *Arch Ophthalmol.* (2012) 130:1534–9. doi: 10.1001/archophthalmol.2012.2280
446. Li B, Powell AM, Hooper PL, Sheidow TG. Prospective evaluation of teleophthalmology in screening and recurrence monitoring of neovascular age-related macular degeneration: a randomized clinical trial. *JAMA Ophthalmol.* (2015) 133:276–82. doi: 10.1001/jamaophthalmol.2014.5014
447. Chew EY, Clemons TE, Bressler SB, Elman MJ, Danis RP, Domalpally A, et al. Randomized trial of a home monitoring system for early detection of choroidal neovascularization home monitoring of the Eye (HOME) study. *Ophthalmology.* (2014) 121:535–44. doi: 10.1016/j.ophtha.2013.10.027
448. Tan CH, Kyaw BM, Smith H, Tan CS, Tudor Car L. Use of smartphones to detect diabetic retinopathy: scoping review and meta-analysis of diagnostic test accuracy studies. *J Med Internet Res.* (2020) 22:e16658. doi: 10.2196/16658
449. Kirkizlar E, Serban N, Sisson JA, Swann JL, Barnes CS, Williams MD, et al. Evaluation of telemedicine for screening of diabetic retinopathy in the Veterans Health Administration. *Ophthalmology.* (2013) 120:2604–10. doi: 10.1016/j.ophtha.2013.06.029
450. Silva PS, Horton MB, Clary D, Lewis DG, Sun JK, Cavallerano JD, et al. Identification of diabetic retinopathy and ungradable image rate with ultrawide field imaging in a national teleophthalmology program. *Ophthalmology.* (2016) 123:1360–7. doi: 10.1016/j.ophtha.2016.01.043
451. Pujari A, Saluja G, Agarwal D, Sinha A, Ananya PR, Kumar A, et al. Clinical role of smartphone fundus imaging in diabetic retinopathy and other neuro-retinal diseases. *Curr Eye Res.* (2021) 46:1605–13. doi: 10.1080/02713683.2021.1958347
452. Rajalakshmi R, Subashini R, Anjana RM, Mohan V. Automated diabetic retinopathy detection in smartphone-based fundus photography using artificial intelligence. *Eye (Lond).* (2018) 32:1138–44. doi: 10.1038/s41433-018-0064-9

453. Sheikh A, Bhatti A, Adeyemi O, Raja M, Sheikh I. The utility of smartphone-based artificial intelligence approaches for diabetic retinopathy: a literature review and meta-analysis. *J Curr Ophthalmol.* (2021) 33:219–26. doi: 10.4103/2452-2325.329064
454. Bernstein PS, Sauer L. Fluorescence lifetime imaging ophthalmoscopy: a new era of autofluorescence imaging of the human retina. *Retina.* (2019) 39:817–9. doi: 10.1097/IAE.0000000000002517
455. Bernstein P, Dysli C, Fischer J, Hammer M, Katayama Y, Sauer L, et al. Fluorescence Lifetime Imaging Ophthalmoscopy (FLIO). In: Bille JF editor. *High Resolution Imaging in Microscopy and Ophthalmology: New Frontiers in Biomedical Optics*. Cham: Springer (2019). doi: 10.1007/978-3-030-16638-0_10
456. Li DQ, Choudhry N. The future of retinal imaging. *Curr Opin Ophthalmol.* (2020) 31:199–206. doi: 10.1097/ICU.0000000000000653
457. Dysli C, Wolf S, Berezin MY. Fluorescence lifetime imaging ophthalmoscopy. *Prog Retin Eye Res.* (2017) 60:120–43. doi: 10.1016/j.preteyeres.2017.06.005
458. Klemm M, Dietzel A, Haueisen J, Nagel E, Hammer M, Schweitzer D, et al. Repeatability of autofluorescence lifetime imaging at the human fundus in healthy volunteers. *Curr Eye Res.* (2013) 38:793–801. doi: 10.3109/02713683.2013.779723
459. Dysli C, Quellec G, Abegg M, Menke MN, Wolf-Schnurrbusch U, Kowal J, et al. Quantitative analysis of fluorescence lifetime measurements of the macula using the fluorescence lifetime imaging ophthalmoscope in healthy subjects. *Invest Ophthalmol Vis Sci.* (2014) 55:2106–13. doi: 10.1167/iovs.13-13627
460. Kwon S, Borrelli E, Fan W, Ebraheem A, Marion KM, Sadda SR, et al. Repeatability of fluorescence lifetime imaging ophthalmoscopy in normal subjects with mydriasis. *Transl Vis Sci Technol.* (2019) 8:15. doi: 10.1167/tvst.8.3.15
461. Sauer L, Gensure RH, Andersen KM, Kreilkamp L, Hageman GS, Hammer M, et al. Patterns of fundus autofluorescence lifetimes in eyes of individuals with nonexudative age-related macular degeneration. *Invest Ophthalmol Vis Sci.* (2018) 59:AMD65–77. doi: 10.1167/iovs.17-23764
462. Dysli C, Fink R, Wolf S, Zinkernagel MS. Fluorescence lifetimes of drusen in age-related macular degeneration. *Invest Ophthalmol Vis Sci.* (2017) 58:4856–62. doi: 10.1167/iovs.17-22184
463. Sauer L, Vitale AS, Modersitzki NK, Bernstein PS. Fluorescence lifetime imaging ophthalmoscopy: autofluorescence imaging and beyond. *Eye (Lond).* (2021) 35:93–109. doi: 10.1038/s41433-020-01287-y
464. Dysli C, Wolf S, Hatz K, Zinkernagel MS. Fluorescence lifetime imaging in stargardt disease: potential marker for disease progression. *Invest Ophthalmol Vis Sci.* (2016) 57:832–41. doi: 10.1167/iovs.15-18033
465. Sauer L, Calvo CM, Vitale AS, Henrie N, Milliken CM, Bernstein PS, et al. Imaging of hydroxychloroquine toxicity with fluorescence lifetime imaging ophthalmoscopy. *Ophthalmol Retina.* (2019) 3:814–25. doi: 10.1016/j.oret.2019.04.025
466. Solberg Y, Dysli C, Moller B, Wolf S, Zinkernagel MS. Fluorescence lifetimes in patients with hydroxychloroquine retinopathy. *Invest Ophthalmol Vis Sci.* (2019) 60:2165–72. doi: 10.1167/iovs.18-26079
467. Schweitzer D, Deutsch L, Klemm M, Jentsch S, Hammer M, Peters S, et al. Fluorescence lifetime imaging ophthalmoscopy in type 2 diabetic patients who have no signs of diabetic retinopathy. *J Biomed Opt.* (2015) 20:61106. doi: 10.1117/1.JBO.20.6.061106
468. Schweitzer D, Quick S, Klemm M, Hammer M, Jentsch S, Dawczynski J, et al. [Time-resolved autofluorescence in retinal vascular occlusions]. *Ophthalmologe.* (2010) 107:1145–52. doi: 10.1007/s00347-010-2195-7
469. Dysli C, Berger L, Wolf S, Zinkernagel MS. Fundus autofluorescence lifetimes and central serous chorioretinopathy. *Retina.* (2017) 37:2151–61. doi: 10.1097/IAE.0000000000001452
470. Sauer L, Gensure RH, Hammer M, Bernstein PS. Fluorescence lifetime imaging ophthalmoscopy: a novel way to assess macular telangiectasia Type 2. *Ophthalmol Retina.* (2018) 2:587–98. doi: 10.1016/j.oret.2017.10.008
471. Vitale AS, Sauer L, Modersitzki NK, Bernstein PS. Fluorescence Lifetime Imaging Ophthalmoscopy (FLIO) in patients with choroideremia. *Transl Vis Sci Technol.* (2020) 9:33. doi: 10.1167/tvst.9.10.33
472. Dysli C, Schuerch K, Escher P, Wolf S, Zinkernagel MS. Fundus autofluorescence lifetime patterns in retinitis pigmentosa. *Invest Ophthalmol Vis Sci.* (2018) 59:1769–78. doi: 10.1167/iovs.17-23336
473. Sauer L, Peters S, Schmidt J, Schweitzer D, Klemm M, Ramm L, et al. Monitoring macular pigment changes in macular holes using fluorescence lifetime imaging ophthalmoscopy. *Acta Ophthalmol.* (2017) 95:481–92. doi: 10.1111/aos.13269
474. Vienola KV, Braaf B, Sheehy CK. Real-time eye motion compensation for OCT imaging with tracking SLO. *Biomed Opt Express.* (2012) 3:2950–63. doi: 10.1364/BOE.3.002950
475. Schwarzhans F, Desissaire S, Steiner S. Generating large field of view en-face projection images from intra-acquisition motion compensated volumetric optical coherence tomography data. *Biomed Opt Express.* (2020) 11:6881–904. doi: 10.1364/BOE.404738
476. Pircher M, Götzinger E, Sattmann H, Leitgeb RA, Hitzenberger CK. In vivo investigation of human cone photoreceptors with SLO/OCT in combination with 3D motion correction on a cellular level. *Opt Express.* (2010) 18:13935–44. doi: 10.1364/OE.18.013935
477. Pircher M, Baumann B, Götzinger E. Simultaneous SLO/OCT imaging of the human retina with axial eye motion correction. *Opt Express.* (2007) 15:16922–32. doi: 10.1364/OE.15.016922
478. Yu DY, Cringle SJ. Retinal degeneration and local oxygen metabolism. *Exp Eye Res.* (2005) 80:745–51. doi: 10.1016/j.exer.2005.01.018
479. Pi S, Camino A, Zhang M, Cepurna W, Liu G, Huang D, et al. Angiographic and structural imaging using high axial resolution fiber-based visible-light OCT. *Biomed Opt Express.* (2017) 8:4595–608. doi: 10.1364/BOE.8.004595
480. Pi S, Camino A, Wei X, Simonett J, Cepurna W, Huang D, et al. Rodent retinal circulation organization and oxygen metabolism revealed by visible-light optical coherence tomography. *Biomed Opt Express.* (2018) 9:5851–62. doi: 10.1364/BOE.9.005851
481. Pi S, Hormel TT, Wei X, Cepurna W, Wang B, Morrison JC, et al. Retinal capillary oximetry with visible light optical coherence tomography. *Proc Natl Acad Sci U S A.* (2020) 117:11658–66. doi: 10.1073/pnas.1918546117
482. Chen S, Shu X, Nesper PL. Retinal oximetry in humans using visible-light optical coherence tomography [Invited]. *Biomed Opt Express.* (2017) 8:1415–29. doi: 10.1364/BOE.8.001415
483. Jiao S, Jiang M, Hu J, Fawzi A, Zhou Q, Shung KK, et al. Photoacoustic ophthalmoscopy for in vivo retinal imaging. *Opt Express.* (2010) 18:3967–72. doi: 10.1364/OE.18.003967
484. Penn JS, Madan A, Caldwell RB, Bartoli M, Caldwell RW, Hartnett ME, et al. Vascular endothelial growth factor in eye disease. *Prog Retin Eye Res.* (2008) 27:331–71. doi: 10.1016/j.preteyeres.2008.05.001
485. Zhang W, Li Y, Nguyen VP. High-resolution, in vivo multimodal photoacoustic microscopy, optical coherence tomography, and fluorescence microscopy imaging of rabbit retinal neovascularization. *Light: Sci Appl.* (2018) 7:103. doi: 10.1038/s41377-018-0093-y
486. Nguyen VP, Li Y, Aaberg M. In Vivo 3D Imaging of Retinal Neovascularization Using Multimodal Photoacoustic Microscopy and Optical Coherence Tomography Imaging. *J Imaging.* (2018) 4:150. doi: 10.3390/jimaging4120150
487. Li Y, Zhang W, Nguyen VP, Rosen R, Wang X, Xia X, et al. Real-time OCT guidance and multimodal imaging monitoring of subretinal injection induced choroidal neovascularization in rabbit eyes. *Exp Eye Res.* (2019) 186:107714–107714. doi: 10.1016/j.exer.2019.107714
488. Nguyen VP, Li Y, Zhang W, Wang X, Paulus YM. High-resolution multimodal photoacoustic microscopy and optical coherence tomography image-guided laser induced branch retinal vein occlusion in living rabbits. *Sci Rep.* (2019) 9:10560. doi: 10.1038/s41598-019-47062-2
489. Nguyen VP, Li Y, Henry J, Zhang W, Wang X, Paulus YM, et al. High resolution multimodal photoacoustic microscopy and optical coherence tomography visualization of choroidal vascular occlusion. *Int J Mol Sci.* (2020) 21:6508. doi: 10.3390/ijms21186508
490. Song W, Wei Q, Liu W. A combined method to quantify the retinal metabolic rate of oxygen using photoacoustic ophthalmoscopy and optical coherence tomography. *Sci Rep.* (2014) 4:6525. doi: 10.1038/srep06525
491. Braaf B, Donner S, Nam AS, Bouma BE, Vakoc BJ. Complex differential variance angiography with noise-bias correction for optical coherence tomography of the retina. *Biomed Opt Express.* (2018) 9:486–506. doi: 10.1364/BOE.9.000486

492. Gong P, Li Q, Wang Q, Karnowski K, Sampson DD. Jones matrix-based speckle-decorrelation angiography using polarization-sensitive optical coherence tomography. *J Biophotonics.* (2020) 13:e202000007. doi: 10.1002/jbio.202000007
493. Gordon AY, Lapierre-Landry M, Skala MC. Photothermal optical coherence tomography of anti-angiogenic treatment in the mouse retina using gold nanorods as contrast agents. *Transl Vis Sci Technol.* (2019) 8:18–18. doi: 10.1167/tvst.8.3.18
494. Adler DC, Huang S-W, Huber R, Fujimoto JG. Photothermal detection of gold nanoparticles using phase-sensitive optical coherence tomography. *Opt Express.* (2008) 16:4376–93. doi: 10.1364/OE.16.004376
495. Lapierre-Landry M, Gordon AY, Penn JS. In vivo photothermal optical coherence tomography of endogenous and exogenous contrast agents in the eye. *Sci Rep.* (2017) 7:9228. doi: 10.1038/s41598-017-10050-5
496. Lapierre-Landry M, Huckenpahler AL, Link BA, Collery RF, Carroll J, Skala MC, et al. Imaging melanin distribution in the zebrafish retina using photothermal optical coherence tomography. *Transl Vis Sci Technol.* (2018) 7:4–4. doi: 10.1167/tvst.7.5.4
497. Kennedy BF, Kennedy KM, Sampson DDA. Review of optical coherence elastography: fundamentals, techniques and prospects. *IEEE J Selected Topics Quantum Electron.* (2014) 20:272–88. doi: 10.1109/JSTQE.2013.2291445
498. Ramier A, Eltony AM, Chen Y, Clouser F, Birkenfeld JS, Watts A, et al. In vivo measurement of shear modulus of the human cornea using optical coherence elastography. *Sci Rep.* (2020) 10:17366. doi: 10.1038/s41598-020-74383-4
499. Li XX, Wu W, Zhou H, Deng JJ, Zhao MY, Qian TW, et al. A quantitative comparison of five optical coherence tomography angiography systems in clinical performance. *Int J Ophthalmol.* (2018) 11:1784–95.
500. Jung W, Kim J, Jeon M, Chaney EJ, Stewart CN, Boppart SA, et al. Handheld optical coherence tomography scanner for primary care diagnostics. *IEEE Trans Biomed Eng.* (2010) 58:741–4. doi: 10.1109/TBME.2010.2096816
501. Hahn P, Migacz J, O'Connell R, Maldonado RS, Izatt JA, Toth CA, et al. The use of optical coherence tomography in intraoperative ophthalmic imaging. *Ophthalmic Surg Lasers Imaging.* (2011) 42:S85–94. doi: 10.3928/15428877-20110627-08
502. Izatt JA, Hee MR, Swanson EA, Lin CP, Huang D, Schuman JS, et al. Micrometer-scale resolution imaging of the anterior eye in vivo with optical coherence tomography. *Arch Ophthalmol.* (1994) 112:1584–9. doi: 10.1001/archopht.1994.01090240090031
503. Považay B, Apolonskiy A, Unterhuber A. Visible light optical coherence tomography. *Proc SPIE.* (2002) 4619:90–4.
504. Zhang T, Kho AM, Yiu G. Visible Light Optical Coherence Tomography (OCT) quantifies subcellular contributions to outer retinal band 4. *Transl Vis Sci Technol.* (2021) 10:30–30. doi: 10.1167/tvst.10.3.30
505. Chong SP, Zhang T, Kho A, Bernucci MT, Dubra A, Srinivasan VJ, et al. Ultrahigh resolution retinal imaging by visible light OCT with longitudinal achromatization. *Biomed Opt Express.* (2018) 9:1477–91. doi: 10.1364/BOE.9.001477
506. Klein T, Wieser W, Reznicek L, Neubauer A, Kampik A, Huber R, et al. Multi-MHz retinal OCT. *Biomed Opt Express.* (2013) 4:1890–908. doi: 10.1364/BOE.4.001890
507. de Carlo TE, Romano A, Waheed NK, Duker JS. A review of optical coherence tomography angiography (OCTA). *Int J Retina Vitreous.* (2015) 1:5. doi: 10.1186/s40942-015-0005-8
508. Heisler M, Ju MJ, Bhalla M, Schuck N, Athwal A, Navajas EV, et al. Automated identification of cone photoreceptors in adaptive optics optical coherence tomography images using transfer learning. *Biomed Opt Express.* (2018) 9:5353–67. doi: 10.1364/BOE.9.005353

Conflict of Interest: JS: Aerie Pharmaceuticals, Inc. and Opticient: consultant/advisor and equity owner. BrightFocus Foundation and National Eye Institute: grant support. Boehringer Ingelheim, Perfuse, Inc., Regeneron, Inc., and SLACK Incorporated: consultant/advisor. Carl Zeiss Meditec: patents/royalty/consultant/advisor. Massachusetts Eye and Ear Infirmary and Massachusetts Institute of Technology, New York University, Tufts University, and University of Pittsburgh: intellectual property. Ocugenix: equity owner, and patents/royalty. Ocular Therapeutix, Inc.: consultant/advisor and equity owner.

The remaining authors declare that the research was conducted in the absence of any commercial or financial relationships that could be construed as a potential conflict of interest.

Publisher's Note: All claims expressed in this article are solely those of the authors and do not necessarily represent those of their affiliated organizations, or those of the publisher, the editors and the reviewers. Any product that may be evaluated in this article, or claim that may be made by its manufacturer, is not guaranteed or endorsed by the publisher.

frontiers | Frontiers in Medicine

ORIGINAL RESEARCH
published: 12 July 2022
doi: 10.3389/fmed.2022.868217

Characterization and Analysis of Retinal Axial Motion at High Spatiotemporal Resolution and Its Implication for Real-Time Correction in Human Retinal Imaging

Yao Cai[1,2], *Kate Grieve*[2,3] *and Pedro Mecê*[1,4]*

[1] *Institut Langevin, ESPCI Paris, CNRS, PSL University, Paris, France,* [2] *Sorbonne Université, INSERM, CNRS, Institut de la Vision, Paris, France,* [3] *CHNO des Quinze-Vingts, INSERM-DGOS CIC 1423, Paris, France,* [4] *DOTA, ONERA, Université Paris Saclay, Palaiseau, France*

High-resolution ophthalmic imaging devices including spectral-domain and full-field optical coherence tomography (SDOCT and FFOCT) are adversely affected by the presence of continuous involuntary retinal axial motion. Here, we thoroughly quantify and characterize retinal axial motion with both high temporal resolution (200,000 A-scans/s) and high axial resolution (4.5 μm), recorded over a typical data acquisition duration of 3 s with an SDOCT device over 14 subjects. We demonstrate that although breath-holding can help decrease large-and-slow drifts, it increases small-and-fast fluctuations, which is not ideal when motion compensation is desired. Finally, by simulating the action of an axial motion stabilization control loop, we show that a loop rate of 1.2 kHz is ideal to achieve 100% robust clinical *in-vivo* retinal imaging.

Keywords: optical coherence tomography, eye motion, high-resolution retinal imaging, eye tracking, OCT angiography

OPEN ACCESS

Edited by:
Hossein Rabbani, Isfahan University of Medical Sciences, Iran

Reviewed by:
Qinqin Zhang, University of Washington, United States
Yousef Ahmed Fouad, Ain Shams University, Egypt

***Correspondence:**
Pedro Mecê
pedro.mece@onera.fr

Specialty section:
This article was submitted to Ophthalmology, a section of the journal Frontiers in Medicine

Received: *02 February 2022*
Accepted: *20 June 2022*
Published: *12 July 2022*

Citation:
Cai Y, Grieve K and Mecê P (2022) Characterization and Analysis of Retinal Axial Motion at High Spatiotemporal Resolution and Its Implication for Real-Time Correction in Human Retinal Imaging. Front. Med. 9:868217. doi: 10.3389/fmed.2022.868217

1. INTRODUCTION

A major challenge for *in vivo* retinal high resolution ophthalmic imaging with optical coherence tomography (OCT) is posed by artifacts caused by constant involuntary axial eye motion, from sources including head and body motion, physiological phenomena such as cardiac cycle, blood flow, pulsation, muscular, and/or respiratory activity (1, 2). For simple B-scan acquisition with SD-OCT devices, motion related artifacts can be automatically corrected during post-processing, but with the growing popularity of imaging methods based on volumetric SDOCT acquisitions with *en face* image reconstruction such as motion contrast-based OCT-Angiography (OCTA) (3), axial eye motion may provoke enough decorrelation to cause the false positive appearance of flow, significantly degrade the image quality, and add distracting artifacts in reconstructed *en face* slices (4).

Axial eye motion is also an important consideration for camera-based OCT techniques which acquire directly in the *en face* direction, such as time-domain full-field optical coherence tomography (FFOCT). FFOCT is an imaging modality capable of recording high-speed en-face sections of a sample at a given depth (5). One very attractive characteristic of FFOCT is the use of spatially incoherent illumination to make the FFOCT lateral resolution robust to symmetric optical aberrations (6), which are the dominant aberrations in the eye (around 90%) (7). By exploiting this

phenomenon, we were able to apply FFOCT for high 3D resolution imaging of the living human retina. This achievement was possible owing to recent advances in FFOCT, including shaping the temporal coherence gate to match the retina curvature, achieving a wide field-of-view ($5 \times 5°$) (8), stabilizing the axial retinal motion in real-time (9), and increasing signal-to-noise ratio (SNR) using the adaptive-glasses approach for ocular aberration correction (10). Given its relative simplicity and small footprint, FFOCT holds promise for adoption by clinicians (11).

When acquiring a single en-face image in FFOCT, a micrometer stabilization precision can be obtained. However, longer acquisition durations on the order of a few seconds may be necessary in the clinical setting in order to allow image averaging to improve SNR. Therefore, it is necessary to accurately compensate for axial motion during image acquisition by moving the reference or the sample arm of FFOCT accordingly (9). A few methods exist, but they are either used in conventional OCT, thus not suitable for FFOCT en-face imaging (12, 13), or are not sufficiently stable to remain within the coherence gate for acquisition durations over several seconds (9). Indeed, our previous work (9) achieved an RMS error of around 10 μm, i.e., greater than the coherence gate width of 8 μm, which was nevertheless sufficient for a satisfactory 60% imaging success rate in subjects with good fixation. However, for imaging in patients who may have poorer fixation, and eventual extension to *in vivo* functional imaging with dynamic FFOCT (14), a greater precision of axial tracking is desirable. Although the causes of axial retinal motion are well understood, the literature on axial retinal motion is still incomplete, as collected data had low temporal and axial resolution (1), and tested relatively few subjects (1, 9, 13), so that general conclusions on the most suitable design of a retinal axial motion stabilization control-loop could not be drawn.

In this article, we present the first characterization of the axial retinal motion with both high temporal resolution (200,000 A-scans/s) and high axial resolution (4.5 μm in water), over a typical data acquisition duration of 3 s. Characterization is performed on a 14-subject population, making it possible to come up with a statistical description reflecting the inter-subject variability. We also evaluate for the first time the direct influence of breathing on axial motion in our population, as this is a parameter that is clinically feasible to control during short image acquisition durations and which may affect stability. Finally, we draw conclusions on design considerations of axial retinal motion stabilization for robust clinical *in vivo* retinal OCTA and FFOCT imaging.

2. METHODS

To measure the retinal axial position, we used a commercial spectral domain OCT system (SD-OCT; GAN611, Thorlabs). The SD-OCT system comprises a broadband superluminescent diode with 930 nm central wavelength and 100 nm bandwidth, providing a theoretical axial resolution of 4 μm in water. It presents an A-scan rate up to 248 kHz with a sensitivity of 84 dB and 1,024 axial pixels, comprising an axial range of 2.2 mm in water. The galvanometer scanners of the SD-OCT were conjugated to the eye's pupil with a 4-f system. The SD-OCT light beam arrives in the eye's pupil with a 4 mm diameter. The experimental setup is shown in **Figure 1**.

To obtain statistics on axial retinal motion, 14 healthy subjects (age 22–80 years) free of ocular disease were invited to participate in the study. Research procedures followed the tenets of the Declaration of Helsinki. Prior to data collection, the nature and possible consequences of the study were explained, and informed consent was obtained from all subjects. This study was authorized by the appropriate ethics review boards [CPP and ANSM (IDRCB number: 2019-A00942-55)]. Subjects were seated in front of the system and stabilized with a chin and forehead rest, without any pupil dilation nor cycloplegia. Image acquisition was realized in a dark room, maximizing the pupil dilation. They were asked to gaze at a yellow fixation cross displayed on a black screen using an LCD projector, maintaining fixation for about 4 s until acquisition was complete. To provide a good trade-off between acquisition speed and SNR, we chose to scan $1°$ field of view (FOV) of the retina with 256 A-scans at 200 kHz A-scan rate, corresponding to 1.28-ms exposure time for a single B-scan. With a 2-ms fly-back time, we were able to achieve a B-scan rate of 300 Hz. During image acquisition, the output power measured at the eye pupil plane was 850 μW, which is below the ocular safety limits established by the ISO standards for group 1 devices. To study the influence of breathing on axial retinal motion, two groups of data were obtained from our 14-subject population: while subjects held their breath for around 5 s or while they were breathing normally. The participants would indicate if they succeeded in holding their breath during acquisition. In the case of ambiguous data, a new dataset would be acquired.

After image acquisition, SD-OCT B-scan images were used to measure the retinal axial position using a previously introduced algorithm based on normalized cross-correlation and parabolic fitting to obtain a subpixel precision (9). Blinks were automatically detected by an intensity-based algorithm (9). We extracted blink-free B-scan sequences, resulting in 3-s time series of retinal axial position data for all 14 subjects. Temporal power spectral densities (PSD) were calculated by a FFT routine.

3. RESULTS AND DISCUSSION

3.1. Temporal Fluctuation of Retinal Axial Position

Figures 2A–D presents four typical examples of retinal axial position as a function of time. A good superposition of measured axial position (red line) and averaged A-scan time series has validated the proposed data processing method. As exemplified here, slow drifts and relative fast oscillations could be observed in all 14 subjects. Still, the slow and fast motion amplitude and frequency varied among subjects. **Figures 2E–H** present the corresponding axial motion power spectra density (PSD) for the same subjects in **Figures 2A–D**. All PSDs present similar behavior, with an energy decay in a f^{-p} power-law, where f is the frequency, before reaching the noise-level plateau around 150 Hz.

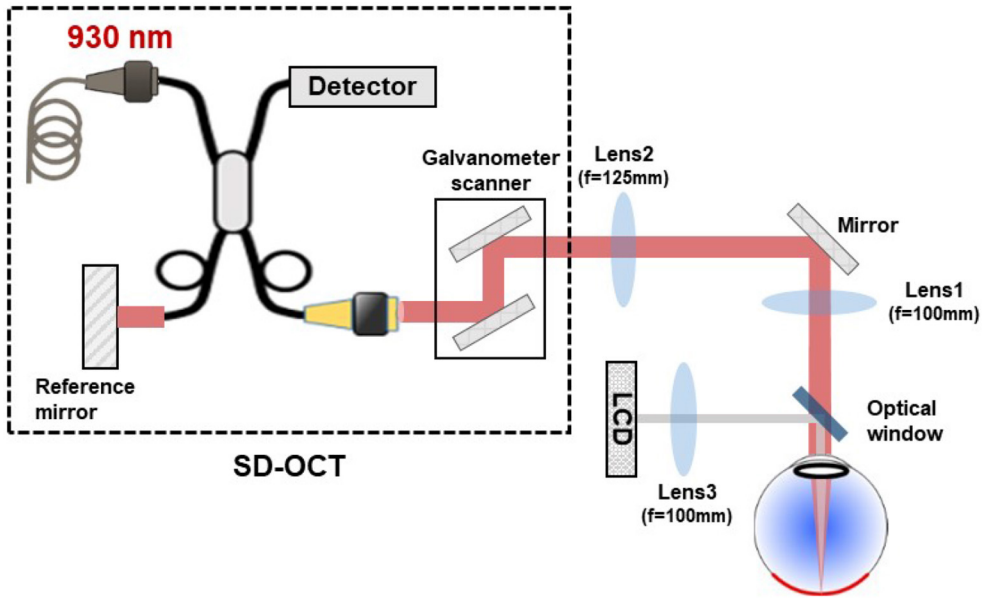

FIGURE 1 | Schematic drawing of the experimental setup used for retinal axial motion measurement, consisting of a commercial SD-OCT, a 4-f system conjugating the scanner in SD-OCT to the eye's pupil, and a LCD projector to display the target for eye fixation. The SD-OCT light beam arrives in the eye's pupil with a 4 mm diameter.

Note that the presence of pronounced peaks between 1 and 4 Hz varied in the population.

To draw statistics of retinal axial motion, and to investigate the effect of breathing on motion, we computed the standard deviation of each axial position time series for each of 14 subjects. **Figure 3** shows temporal fluctuation of axial position under breath holding (blue bars) and normal breathing (red bars) conditions. Note that 9 subjects out of 14 presented a lower temporal fluctuation while holding their breath. Greater variations observed in subjects 12 and 13 are caused by larger drifts, most probably due to head motion. Two participants (subjects 1 and 6) were trained for eye fixation tasks. In contrast to retinal lateral motion, where experience in fixation can play an important role in the temporal fluctuation (15, 16), here no significant difference was noted, apart from a decrease of slow-and-large drifts linked to breathing and head motion. Additionally, although fixational microsaccades, i.e., fast and large amplitude lateral motion (15), took place during acquisition, axial retinal motion is not impacted by microsaccades.

We computed the median ± standard deviation over the population of peak-to-valley (PV) amplitude, mean deviation from zero, root mean square (RMS) value and speed of 3-s time series of retina axial positions for both breath-holding and normal breathing conditions. Results of this statistical analysis is summarized in **Table 1**. During normal breathing, retinal axial motion presents higher PV amplitude, meaning that slow drifts are more important compared with the breath-holding condition. Indeed, it has been shown that breathing may cause slow and large drifts due to the movement of the subject's head (1). Not surprisingly, after filtering out slow drifts corresponding to <2 Hz temporal frequency, we found similar PV amplitude value for both conditions, 158 ± 52 μm for normal breathing compared to 160 ± 46 μm for breath-holding. Similar values of mean deviation from zero (26 ± 15 against 25 ± 11 μm) and RMS (32 ± 18 against 31 ± 12 μm) were also obtained for normal breathing and breath-holding conditions respectively. These results suggest that respiration induces axial motion at temporal frequencies up to 2 Hz, whereas respiration rate is around 0.2 Hz (1). On the other hand, the breath-holding condition exhibited a faster axial movement of 988 ± 209 μm/s, compared to 941 ± 194 μm/s in the case of normal breathing, for which the causes are still unclear. In both cases, computed speeds are in line with 958 μm/s median speed previously reported (2), and are assumed to be related to the systolic phase of the heart pulse.

Figure 4 presents the averaged PSD over all 14 subjects in both breath-holding and normal breathing conditions. The averaged PSD has a $f^{-2.2}$ mean power-law before reaching the experimental noise-level at 150 Hz. Temporal frequencies below 1Hz present a factor of two lower PSD in the breath-holding condition than the normal breathing condition, highlighting the influence of respiration on axial motion. Remarkably, this difference is more pronounced at temporal frequencies associated to heartbeat (1–2 Hz), showing a link between breathing and heartbeat on retinal axial motion. Indeed, apnea can induce a reduction in cardiac output and peripheral vasoconstriction (17, 18). Both normal breathing and breath-holding conditions presented a similar behavior in the range of 3–6 Hz, with some marked peak rises around 3–4 Hz, which may be a high order harmonic of heartbeat rate (1) or related to pulsatile blood flow in the retina or in the choroid (19). Meanwhile, similar to the

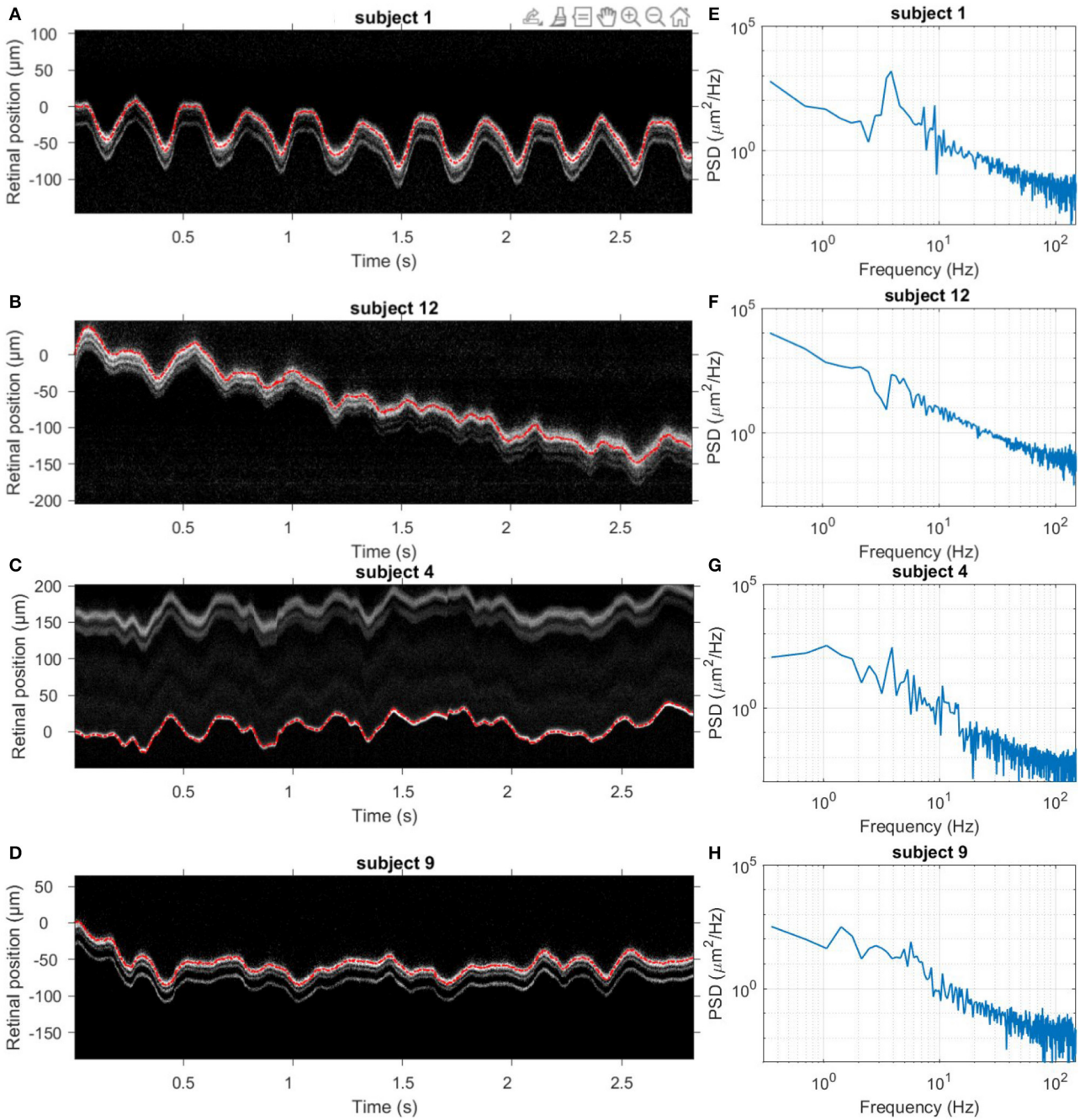

FIGURE 2 | Dynamics of retinal axial position. **(A–D)** Four examples of acquired averaged A-scan time series over 3 s without blinks. The red line indicates the measured axial position temporal evolution. **(E–H)** Corresponding temporal PSD computed for the retinal axial position. Note that subjects 1 and 12 held their breath, while subjects 4 and 9 breathed normally.

computed speed behavior, the PSD in the range of 7–150 Hz is more important in the breath-holding condition than under normal breathing.

3.2. Axial Tracking Loop Simulation

Having characterized retinal axial motion, and knowing that breathing, heartbeat and pulsatile blood flow each play an important role, we next addressed the question of how fast the stabilization control-loop should run to precisely compensate for retinal axial motion in real-time for *in vivo* retinal imaging. To answer this question, we simulated the action of a retinal axial motion stabilization loop and integrator-based control scheme with a 0.5 gain (ensuring 45° stability margin) (20), assuming a two-frame delay (21). **Figure 5** displays the overall distribution

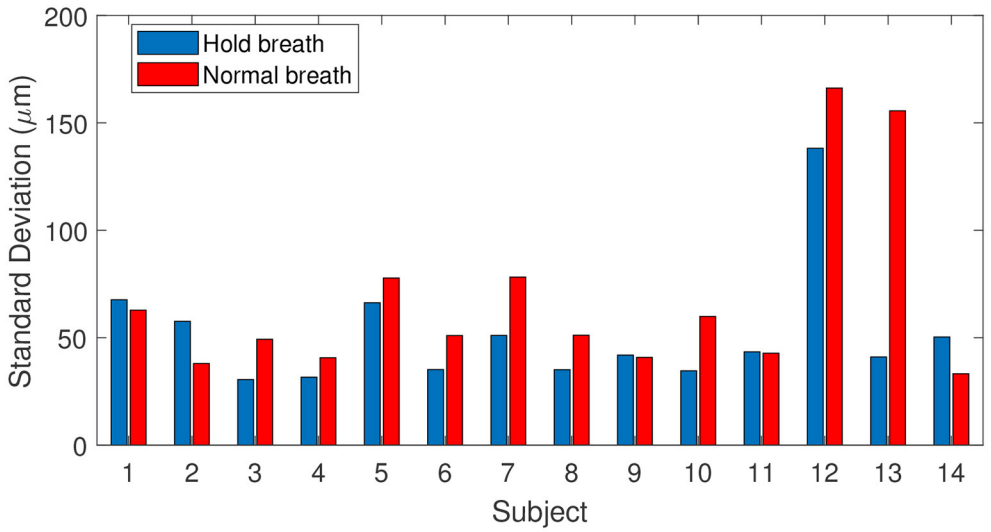

FIGURE 3 | Fluctuations of axial position for 14 subjects tested during breath-holding (blue) and normal breathing (red), calculated as the standard deviation of axial position.

of axial RMS tracking errors among all participants and for different stabilization control loop rates. This result provides a valuable tool for selecting the acquisition frequency for retinal axial motion measurement, and consequently the control-loop rate for stabilization. For instance, it indicates that at 150 Hz loop-rate, the residual axial motion should be ∼10 μm rms in a normal breathing condition.

In the context of applying dynamic (D-) FFOCT *in vivo*, the use of singular value decomposition (SVD) processing was recently proposed to filter out the axial displacement of the sample from the local fluctuations linked to intracellular motility (22). This study showed that axial motion suppression works as long as residual axial motion after correction is smaller than the temporal coherence gate width (22, 23). In FFOCT high-resolution *in vivo* retinal imaging, a temporal coherence gate of 8 μm is used (10). Therefore, if we approximate the temporal fluctuation of retinal axial motion as a Gaussian distribution, one can establish that an RMS error below 4 μm will ensure a residual axial motion of amplitude lower than the 8 μm coherence gate width more than 95% of the time. An RMS error of 4 μm can be achieved on average with a stabilization control-loop rate of 400 Hz under normal breathing conditions. The same precision can be obtained under the breath-holding condition, but with a higher loop rate, here around 600 Hz, showing that holding breath does not necessarily help axial motion stabilization but may in fact hinder it. Indeed, although breath holding decreases low temporal frequencies, these are the frequencies that are better managed by an integrator-based control scheme (9, 20). On the other hand, breath holding amplifies high temporal frequencies, which are also amplified by an integrator-based control scheme (9, 20).

In clinical application of FFOCT, one needs to consider the temporal fluctuation variability among subjects and ensure that the stabilization precision is enough to achieve robust imaging

TABLE 1 | Axial motion statistics (median ± standard deviation) over the 14-subject population.

	PV (μm)	Mean deviation (μm)	RMS (μm)	Speed (μm/s)
Normal breathing	276 ± 154	57 ± 36	68 ± 42	941 ± 194
Holding breath	230 ± 98	42 ± 24	52 ± 28	988 ± 209

Statistics were drawn in both normal breathing and breath-holding conditions in time series of 3-s duration. PV, peak-to-valley amplitude.

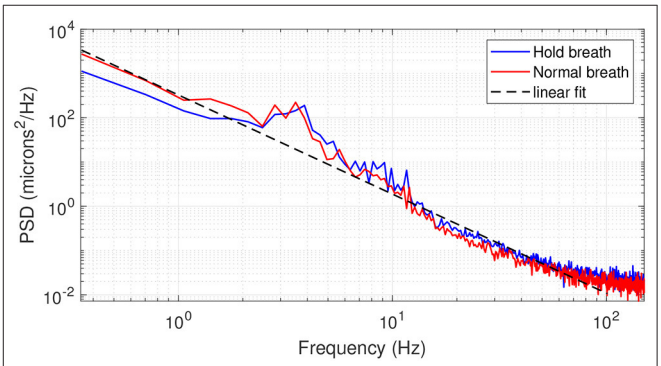

FIGURE 4 | Averaged PSD over 14 subjects in breath-holding (blue trace) and normal breathing (red trace) conditions. The black dashed line gives a linear regression of the PSD following a $f^{-2.2}$ behavior.

for 100% of the patients. **Figure 6** highlights the proportion of subjects (of the 14 in total) where stabilization precision below 4 μm was obtained throughout the entire time series (i.e., 3 s) for different stabilization control-loop rates. To ensure robust FFOCT acquisition in all subjects, a control-loop rate of at least 1.2 kHz is necessary. Enticingly, this level of stability

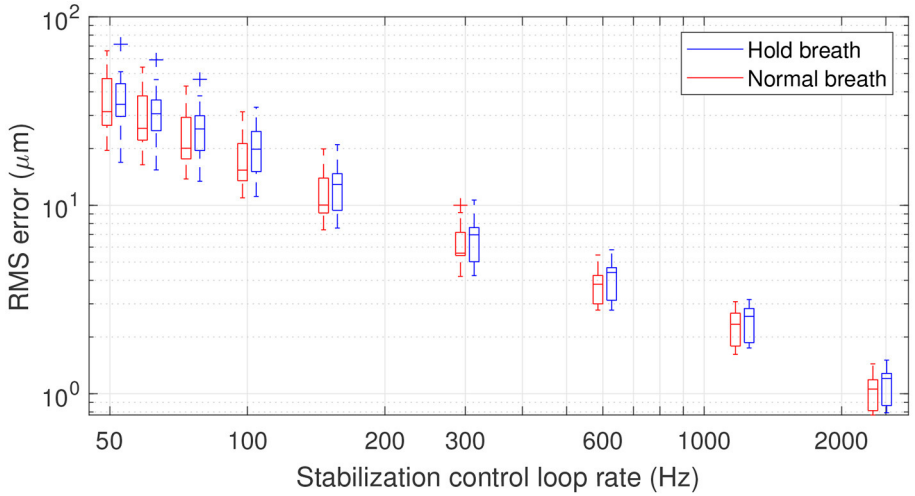

FIGURE 5 | Box plot representation of residual RMS motion for different acquisition frequencies. The line within the box identifies the median. The blue and red traces indicate median RMS tracking errors during breath-holding and normal breathing, respectively. The length of the box represents the interquartile range (IQR), with the edges being the 25th (lower quartile) and 75th (upper quartile) percentiles. The ends of the whiskers represent minimum and maximum values. Values more than 1.5 IQRs are labeled as outliers (+). Note that the figure is plotted in a logarithmic scale.

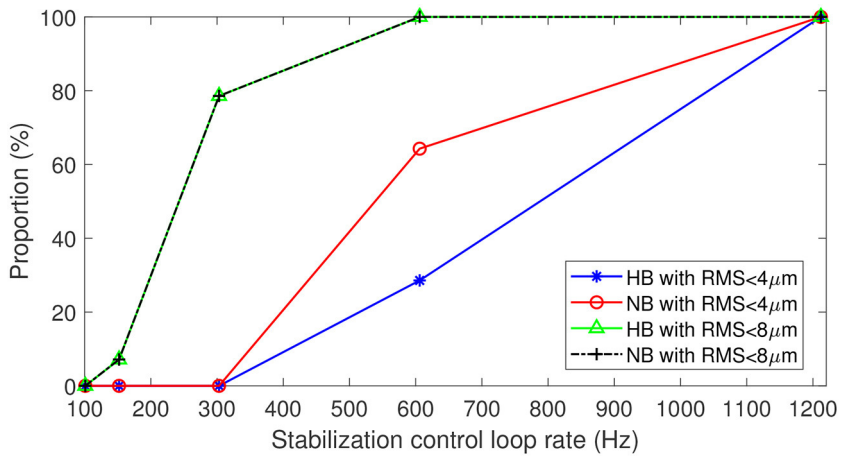

FIGURE 6 | Proportion of data with residual RMS motion below 4 μm with respect to 8 μm axial resolution for *in vivo* FFOCT imaging, and below 8 μm with respect to 16 μm axial resolution for different acquisition frequencies. Blue and green traces for breath-holding, red and black traces for normal breathing.

would also theoretically allow the first *in vivo* acquisition of dynamic FFOCT datasets, as axial motion would remain within the coherence gate width over the 3 s acquisition time required for a dynamic FFOCT image stack to probe temporal frequencies carrying intracellular dynamic signal (typically between 1 and 10 Hz) (14). This finding further supports the work of Pircher et al. (13) who found that increased high loop rate of 1 kHz enabled the reduction of the residual axial motion below 5 μm in transverse-scanning OCT. As commonly done in OCTA, the reduction of the axial resolution can help to decrease the sensitivity to axial motion, thus relaxing the control loop rate (4). For instance, a 600 Hz loop rate would be sufficient to ensure a residual RMS motion less than 8 μm in 100% of the patients for a 16 μm axial resolution (**Figure 6**). Another strategy to alleviate the control loop rate is the use of Linear-quadratic-Gaussian (LQG) control law (24). Indeed, such an LQG approach could incorporate in the control strategy the specific spatio-temporal statistical structure of the axial retinal motion. The implementation of the LQG control strategy will be explored during future system optimization. An interesting way to reduce axial motion dynamics would be to perform measurements when the subject is lying down. Indeed, Kinkelder et al. (1) showed that the movements of the subject's head were reduced in a supine position. However, this posture is impractical for patients in clinical applications and so was not considered in our study. Correcting the axial motion in real-time in volumetric SDOCT

and OCTA en-face projections can also present advantages such as artifact suppression, optimization of SNR—given that the sensitivity decay with depth position would be avoided—access to the highest axial resolution, and decrease in the computational complexity of 3D registration algorithms.

4. CONCLUSION

In conclusion, this study has been one of the first attempts to thoroughly quantify and characterize retinal axial motion with high temporal resolution. The results of this experiment show that head motion during breathing, heartbeat and pulsatile blood flow significantly account for involuntary retinal axial displacement in the low-frequency domain below 5 Hz. We also demonstrated that breath holding can help decrease large-and-slow drifts. However, contrary to expectations, when holding breath, axial motion presented a higher speed and higher PSD for temporal frequencies from 7 to 150 Hz, which is not ideal when motion compensation is desired. Further investigation is necessary to understand the mechanism behind this phenomenon. Finally, by simulating the action of an axial motion stabilization control loop, we showed that a loop rate of 1.2 kHz is ideal to achieve 100% robust FFOCT in *in vivo* human retina, and could even pave the way to acquiring dynamic FFOCT *in vivo*. To relax the loop-rate constraint, a practical solution can be the combination of lower axial resolution and LQG control law.

DATA AVAILABILITY STATEMENT

Data underlying the results presented in this paper are not publicly available at this time but may be obtained from the authors upon reasonable request.

ETHICS STATEMENT

The studies involving human participants were reviewed and approved by CPP and ANSM (IDRCB number: 2019-A00942-55). The patients/participants provided their written informed consent to participate in this study. Written informed consent was obtained from the individual(s) for the publication of any potentially identifiable images or data included in this article.

AUTHOR CONTRIBUTIONS

YC constructed the optical system, collected the data, and drafted the manuscript. YC and PM analyzed the results. PM designed the experiment and developed the algorithm to measure the retinal axial motion. KG and PM provided overall guidance to the project. KG obtained funding to support this research. All authors discussed the results and contributed to the manuscript.

FUNDING

This work was supported by OPTORETINA [European Research Council (ERC)] (#101001841), HELMHOLTZ [European Research Council (ERC)] (#610110), IHU FOReSIGHT [ANR-18-IAHU-0001], Region Ile-De-France fund SESAME 4D-EYE [EX047007], Fondation Visio, French state fund CARNOT VOIR ET ENTENDRE [x16-CARN 0029-01].

ACKNOWLEDGMENTS

The authors thank all participants for their support, and Olivier Thouvenin and Yan Liu for fruitful discussions.

REFERENCES

1. de Kinkelder R, Kalkman J, Faber DJ, Schraa O, Kok PHB, Verbraak FD, et al. Heartbeat-induced axial motion artifacts in optical coherence tomography measurements of the retina. *Invest Ophthalmol Vis Sci*. (2011) 52:3908–13. doi: 10.1167/iovs.10-6738
2. Ginner L, Kumar A, Fechtig D, Wurster LM, Salas M, Pircher M, et al. Noniterative digital aberration correction for cellular resolution retinal optical coherence tomography *in vivo*. *Optica*. (2017) 4:924–31. doi: 10.1364/OPTICA.4.000924
3. Lavia C, Mecê P, Nassisi M, Bonnin S, Marie-Louise J, Couturier A, et al. Retinal capillary plexus pattern and density from fovea to periphery measured in healthy eyes with swept-source optical coherence tomography angiography. *Sci Rep*. (2020) 10:1–11. doi: 10.1038/s41598-020-58359-y
4. Spaide RF, Fujimoto JG, Waheed NK. Image artifacts in optical coherence angiography. *Retina*. (2015) 35:2163. doi: 10.1097/IAE.0000000000000765
5. Beaurepaire E, Boccara AC, Lebec M, Blanchot L, Saint-Jalmes H. Full-field optical coherence microscopy. *Opt Lett*. (1998) 23:244–6. doi: 10.1364/OL.23.000244
6. Barolle V, Scholler J, Mecê P, Chassot JM, Groux K, Fink M, et al. Manifestation of aberrations in full-field optical coherence tomography. *Opt Exp*. (2021) 29:22044–65. doi: 10.1364/OE.419963
7. Jarosz J, Mecê P, Conan JM, Petit C, Paques M, Meimon S. High temporal resolution aberrometry in a 50-eye population and implications for adaptive optics error budget. *Biomed Opt Exp*. (2017) 8:2088–105. doi: 10.1364/BOE.8.002088
8. Mecê P, Groux K, Scholler J, Thouvenin O, Fink M, Grieve K, et al. Coherence gate shaping for wide field high-resolution *in vivo* retinal imaging with full-field OCT. *Biomed Opt Exp*. (2020) 11:4928–41. doi: 10.1364/BOE.400522
9. Mecê P, Scholler J, Groux K, Boccara C. High-resolution *in-vivo* human retinal imaging using full-field OCT with optical stabilization of axial motion. *Biomed Opt Exp*. (2020) 11:492–504. doi: 10.1364/BOE.381398
10. Scholler J, Groux K, Grieve K, Boccara C, Mecê P. Adaptive-glasses time-domain FFOCT for wide-field high-resolution retinal imaging with increased SNR. *Opt Lett*. (2020) 45:5901–4. doi: 10.1364/OL.403135
11. Mecê P, Scholler J, Groux K, Grieve K, Boccara C. Adaptive glasses wavefront sensorless Full-Field OCT for high-resolution retinal imaging over a wide field-of-view. In: *Ophthalmic Technologies XXXI*. Vol. 11623. International Society for Optics and Photonics (2021). p. 1162306. doi: 10.1117/12.2576689
12. Baghaie A, Yu Z, D'Souza RM. Involuntary eye motion correction in retinal optical coherence tomography: hardware or software solution? *Med Image Anal*. (2017) 37:129–45. doi: 10.1016/j.media.2017.02.002
13. Pircher M, Götzinger E, Sattmann H, Leitgeb RA, Hitzenberger CK. *In vivo* investigation of human cone photoreceptors with SLO/OCT in combination with 3D motion correction on a cellular level. *Opt Exp*. (2010) 18:13935–44. doi: 10.1364/OE.18.013935
14. Scholler J, Groux K, Goureau O, Sahel JA, Fink M, Reichman S, et al. Dynamic full-field optical coherence tomography: 3D live-imaging of retinal organoids. *Light Sci Appl*. (2020) 9:1–9. doi: 10.1038/s41377-020-00375-8

15. Mecê P, Jarosz J, Conan JM, Petit C, Grieve K, Paques M, et al. Fixational eye movement: a negligible source of dynamic aberration. *Biomed Opt Exp*. (2018) 9:717–27. doi: 10.1364/BOE.9.000717
16. Zhang M, Gofas-Salas E, Leonard BT, Rui Y, Snyder VC, Reecher HM, et al. Strip-based digital image registration for distortion minimization and robust eye motion measurement from scanned ophthalmic imaging systems. *Biomed Opt Exp*. (2021) 12:2353–72. doi: 10.1364/BOE.418070
17. Schuitema K, Holm B. The role of different facial areas in eliciting human diving bradycardia. *Acta Physiol Scand*. (1988) 132:119–20. doi: 10.1111/j.1748-1716.1988.tb08306.x
18. Delahoche J, Delapille P, Lemaître F, Verin E, Tourny-Chollet C. The role of different facial areas in eliciting human diving bradycardia. *Int J Sports Med*. (2005) 26:177–81. doi: 10.1055/s-2004-820976
19. Puyo L, Paques M, Fink M, Sahel JA, Atlan M. Waveform analysis of human retinal and choroidal blood flow with laser Doppler holography. *Biomed Opt Exp*. (2019) 10:4942–63. doi: 10.1364/BOE.10.004942
20. Roddier F. *Adaptive Optics in Astronomy*. Cambridge University Press (1999). doi: 10.1017/CBO9780511525179
21. Gofas-Salas E, Mecê P, Petit C, Jarosz J, Mugnier LM, Bonnefois AM, et al. High loop rate adaptive optics flood illumination ophthalmoscope with structured illumination capability. *Appl Opt*. (2018) 57:5635–42. doi: 10.1364/AO.57.005635
22. Scholler J. Motion artifact removal and signal enhancement to achieve *in vivo* dynamic full field OCT. *Opt Exp*. (2019) 27:19562–72. doi: 10.1364/OE.27.019562
23. Scholler J, Mecê P, Groux K, Mazlin V, Boccara C, Grieve K. Motion artifact removal and signal enhancement to achieve *in vivo* dynamic full field OCT (Conference Presentation). In: *Optical Coherence Tomography and Coherence Domain Optical Methods in Biomedicine XXIV*. Vol. 11228. San Francisco, CA: International Society for Optics and Photonics (2020). p. 112281N. doi: 10.1117/12.2542635
24. Sivo G, Kulcsár C, Conan JM, Raynaud HF, Gendron É, Basden A, et al. First on-sky SCAO validation of full LQG control with vibration mitigation on the CANARY pathfinder. *Opt Exp*. (2014) 22:23565–91. doi: 10.1364/OE.22.023565

Conflict of Interest: The authors declare that the research was conducted in the absence of any commercial or financial relationships that could be construed as a potential conflict of interest.

Advantages of publishing in Frontiers

OPEN ACCESS
Articles are free to read for greatest visibility and readership

FAST PUBLICATION
Around 90 days from submission to decision

HIGH QUALITY PEER-REVIEW
Rigorous, collaborative, and constructive peer-review

TRANSPARENT PEER-REVIEW
Editors and reviewers acknowledged by name on published articles

Frontiers
Avenue du Tribunal-Fédéral 34
1005 Lausanne | Switzerland

Visit us: www.frontiersin.org
Contact us: frontiersin.org/about/contact

REPRODUCIBILITY OF RESEARCH
Support open data and methods to enhance research reproducibility

DIGITAL PUBLISHING
Articles designed for optimal readership across devices

FOLLOW US
@frontiersin

IMPACT METRICS
Advanced article metrics track visibility across digital media

EXTENSIVE PROMOTION
Marketing and promotion of impactful research

LOOP RESEARCH NETWORK
Our network increases your article's readership